

## University of Tasmania Open Access Repository

### Cover sheet

**Title**

Geology and genesis of the Ridgeway porphyry Au-Cu deposit, NSW

**Author**

Garcia-Cuison, AL

**Bibliographic citation**

Garcia-Cuison, AL (2010). Geology and genesis of the Ridgeway porphyry Au-Cu deposit, NSW. University Of Tasmania. Thesis. <https://doi.org/10.25959/23211200.v1>

Is published in:

**Copyright information**

This version of work is made accessible in the repository with the permission of the copyright holder/s under the following,

**Licence.**

Rights statement: Copyright Copyright The Author

If you believe that this work infringes copyright, please email details to: [oa.repository@utas.edu.au](mailto:oa.repository@utas.edu.au)

Downloaded from [University of Tasmania Open Access Repository](#)

Please do not remove this coversheet as it contains citation and copyright information.

University of Tasmania Open Access Repository

Library and Cultural Collections

University of Tasmania

Private Bag 3

Hobart, TAS 7005 Australia

E [oa.repository@utas.edu.au](mailto:oa.repository@utas.edu.au)

CRICOS Provider Code 00586B | ABN 30 764 374 782

[utas.edu.au](http://utas.edu.au)

# **Geology and genesis of the Ridgeway porphyry Au-Cu deposit, NSW**

by

**Ana Liza Garcia-Cuison (Bsc)**

Submitted in fulfilment of the requirements for the degree of

Doctor of Philosophy

University of Tasmania

November, 2010



University of Tasmania



ARC Centre of Excellence in Ore Deposits

## Declaration

This thesis contains no material that has been accepted for a degree or diploma by the University or by any other institution, except by way of background information and duly acknowledged in the thesis, and to the best of the candidate's knowledge and belief, no material previously published or written by another person except where due acknowledgement is made in the text of the thesis.

Ana Liza Garcia-Cuison

Date:

## Confidentiality

This thesis is not to be made available for loan or copying for 12 months following the date this statement was signed. Following the time, the thesis may be made available for loan and limited copying in accordance with the *Copyright Act 1968*.

Ana Liza Garcia-Cuison

Date:

---

# Abstract

---

The Ridgeway alkalic porphyry Au–Cu deposit is located in the Molong Volcanic Belt of the Macquarie Arc, part of the Lachlan Fold Belt in eastern Australia. Ridgeway is hosted by a Middle Ordovician sequence of volcano-sedimentary rocks that were deposited in an active submarine sedimentary basin. The volcanic sequence evolved from fine grained distal volcanoclastics (Weemalla Formation) to coarse proximal breccias and sandstones (Forest Reef Volcanics). The host sequence was intruded first by pyroxene- and feldspar-phyric dikes and sills, and then by the Ridgeway intrusive complex, a cluster of subvertical porphyry pipes, dikes and stocks of monzodiorite (U–Pb<sub>zircon</sub> age:  $448.2 \pm 2.1$  Ma), mafic monzonite and quartz monzonite (U–Pb<sub>zircon</sub> age:  $444.2 \pm 1.3$  Ma). Cross-sectional shapes of the monzonite intrusions are broadly pipe-like. They swell at the contact between the Weemalla Formation and Forest Reef Volcanics.

The highest Au–Cu grades at Ridgeway are associated with quartz–magnetite–bornite vein stockworks and intense K-silicate alteration that formed during the emplacement of the mafic monzonite. These early stage veins have been truncated by the quartz monzonite porphyry and its lower grade quartz–chalcopyrite  $\pm$  molybdenite veins (Re–Os<sub>molybdenite</sub>:  $445.7 \pm 2.8$  Ma,  $442.8 \pm 2.3$  Ma) associated with less intense K-silicate alteration. A late-stage quartz monzonite cut the earlier phases, and defines the low-grade core of the deposit.

The mafic monzonite and quartz monzonite contain magnetite- and quartz-rich unidirectional solidification textures (USTs), miarolitic cavities and aplite vein-dikes. These textural features imply that magmatic-hydrothermal fluids streamed through and accumulated within the narrow pipes, which acted as a conduit to supply fluids from a deeper magma to the site of ore deposition. Mineralizing fluids were released when the carapace of the crystallizing fluids failed, and were emplaced preferentially into two subvertical vein systems that formed via hydraulic fracturing.



The older veins (set 2) strike N, WNW and NE, whereas the younger mineralized structures (set 3) strike E, NE and NW.

Cathodoluminescence imaging of quartz shows that most of the quartz (Qz-1) crystallized early in the history of vein formation. Dissolution of Qz-1 was then followed by the deposition of a second quartz generation (Qz-2). Cu–Fe sulfides were then deposited together with a later generation of darkly-luminescent quartz (Qz-3). Bright luminescence in Qz-1 correlates with elevated Al, Ti and K concentrations, whereas dull-luminescent Qz-3 is comparatively rich in Fe. High-temperature Qz-1 precipitated during vein stockwork formation at temperatures between 601° and 850°C in equilibrium with hydrothermal K-feldspar. Changes in pressure and temperature occurred during mechanical fracturing that created secondary permeability exploited by Qz-2. Further decrease in pressure and/or temperature facilitated the precipitation of Qz-3 at temperatures below 589°C, synchronous with Fe–Cu sulfides.

Sulfur isotopic compositions of sulfides from Ridgeway show increasing  $\delta^{34}\text{S}$  depletion in the sequence of pyrite (ave. -1.8 ‰), chalcopyrite (ave. -3.6 ‰) and bornite (ave. -4.9 ‰). Low  $\delta^{34}\text{S}_{\text{bornite}}$  and  $\delta^{34}\text{S}_{\text{chalcopyrite}}$  values occur in the core of the deposit. Isotopically light  $\delta^{34}\text{S}_{\text{pyrite}}$  values are also found in the core of the deposit, but these become more negative towards the top of the deposit, in the epidote–chlorite–hematite alteration zone. This is consistent with isotopic fractionation caused by cooling of the magmatic-hydrothermal fluids under oxidizing conditions during late-stage pyrite deposition.

The Ridgeway deposit was localized at the intersection of NW-trending faults and a NNW-trending monocline. The pre-existing NW-trending parallel wedge-shape faults provided the pathways for the deep-seated magma to migrate into the shallow crust. Roof-lifting within the fault wedge provided space for monzonite emplacement. At Ridgeway, there was an intimate link between magmatism and a dynamic structural environment that ultimately controlled the genesis of the high-grade orebody and provided an excellent focus for fluid flow in a well-developed vein stockwork.

---

# Acknowledgements

---

First and foremost, I would like to thank my husband, Al, for all the support, encouragement, love and understanding over the years of this study. You have given up so much for me to pursue my dreams, for this I am truly grateful. To our children, Lean and Aaron, thank you for your understanding.....now the fun part begins.

To my supervisor, Dave Cooke, I would like to extend my sincerest thanks and appreciation, not only for initiating this project in collaboration with Newcrest, but for your support and patience over the years. Thank you Dave for showing little restraint when it came to editing my drafts - for your dedication to enforce the rudiments of the English language, and for your perseverance to instil in your student the importance of technical syntax. Thank you for imparting your expertise - I have learned a lot through the years, for which I am extremely grateful.

I would like to thank my two co-supervisors, Anthony Harris and Ron Berry for providing sound technical input. Thanks Anthony for introducing me to the enigmatic mushy-features of magma. And Ron, thank you for sharing your expertise and providing numerous edits of my structural model. Sincere thanks to Richard Tosdal for his help and patience in explaining the complexities of structures in the field.

Many thanks are extended to Newcrest Mining Limited and the ARC Centre of Excellence in Ore Deposit Research for the financial, technical and logistical support of this research project. Additional research fund also came from the SEG Foundation-McKinstry grant.

Special thanks go to Newcrest geoscientists John Holliday, Ian Tedder, Dean Collett, Collin McMillan, Geoff Smart, among others for the support on the different aspects of the study. Matt Hatzl, Katrina Thiel, Robyn Ransley, Caroline Hassall, and the Rockdoctors are thanked for logistic support extended in the field. Special thanks go to Dave Coates, Raquel Kolkert, Megan Evitt and John Chow, and Lea for being especially hospitable during my stay in Orange. Many thanks to Mark Gabbitus for allowing to me use the MineSight software.

---

I would like to extend my gratitude and appreciation to the academic staffs at CODES which provided expert advice during the course of this study: Tony Crawford for the insightful discussion on my whole rock geochemistry; Garry Davidson for the sulfur isotope 101 lectures and discussions on my isotope data; Sebastien Mefree for his help in concordia plots; and Zhaoshan Chang for always being there, not only as a friend, but also for sharing his expertise on skarn. Karsten Goemann at the CSL is thanked for his assistance in the microprobe.

Big thanks to Jocelyn McPhie, Karin Orth, Isabelle Chamberfort, David Hutchinson and Huayong Chen for the encouragement. Joce – thanks a lot for everything. To Julie Hunt, I cannot thank you enough for all your help to me and my family – it is greatly appreciated.

I wish to thank the School of Earth Sciences support staffs: Simon Stephens for processing my samples, Peter Cornish for the help when we were re-arranging our office (I still use a stool when trying to reach things), Dianne Madden for the help in the admin, Christine Higgins, Helen Scott, Karen Molross and Dianne Steffens, for taking care of the financial aspects (and saved me the worry of financial crisis), Isabella von Lichtan, for the expert advice in taking rock pictures, Sarah Gilbert, for her assistance on trace element mapping, and Keith Dobson, for all the technical support. Special thanks to June Pongratz in the editorial side of this thesis.

To my current and former postgraduate colleagues, thank you for the friendship, support and conversation: Bronto, Taka, Sang, Nathan, Anita, Joe, Ben, Tim, Patrick, Claire (thanks for the wool blanket), Hugo, Andrea, Adam, Sarah, Martin, Heidi, Sofia, Natalee, Olga, Adel, Kyrill and Roisin. Special thanks to Wojciech, Masoe, Jacq, Gisela and Fiona for all the advice and encouragement, especially on the final months in writing my thesis.

Finally, I would like to thank my mother, sisters, brother and in-laws for all the encouragement and support over the years.

To my late father and sister.....I made it.

---

# Table of Contents

---

<b>Abstract .....</b>	<b>i</b>
<b>Acknowledgements .....</b>	<b>iii</b>
<b>Table of Contents.....</b>	<b>v</b>
<b>List of Figures.....</b>	<b>xi</b>
<b>List of Tables.....</b>	<b>xii</b>
<b>List of Appendices.....</b>	<b>xvii</b>
<b>List of Abbreviations.....</b>	<b>xix</b>

## **Chapter 1: Introduction**

1.1. Preamble.....	1
1.2. Projects aims and objectives.....	5
1.3. Methodology.....	6
1.4. Thesis Organization.....	7
1.5. Cadia District - Exploration and mining history.....	8
1.5.1. Ridgeway Au–Cu porphyry deposit.....	10
1.6. Previous research.....	12

## **Chapter 2: Regional Geology**

2.1 Introduction.....	15
2.2 Tasman Fold Belt.....	15
2.3 Lachlan Fold Belt (Lachlan Orogen).....	17
2.4 Deformation in the Lachlan Fold Belt.....	20
2.5 Macquarie Arc.....	22
2.6 Crustal-scale structures and metallogeny of the Macquarie Arc.....	28
2.6.1 Lachlan Transverse Zone.....	29
2.7 Metallogeny in the Macquarie Arc.....	31

## **Chapter 3: Geology, Geochronology and Geochemistry**

3.1 Introduction.....	35
3.2 District Geology.....	35
3.3 Ridgeway Geology.....	37
3.3.1 Weemalla Formation.....	38
3.3.1.1 Feldspathic sandstone and siltstone.....	52
3.3.1.2 Calcareous sandstone and siltstone.....	52

3.3.1.3	Laminated and siliceous siltstone.....	52
3.3.2	Transitional unit.....	53
3.3.3	Forest Reefs Volcanics .....	53
3.3.3.1	Polymictic volcaniclastic lithic conglomerate and breccia.....	54
3.3.3.2	Monomictic volcanic breccia.....	58
3.3.3.3	Massive feldspathic sandstone and siltstone.....	58
3.3.3.4	Pyroxene-phyric and feldspar-phyric intrusions.....	59
3.4	Ridgeway intrusive complex.....	63
3.4.1	Pre-mineralization intrusion.....	65
3.4.1.1	Monzodiorite.....	65
3.4.2	Syn-mineralization intrusions.....	68
3.4.2.1	Mafic monzonite porphyry.....	68
3.4.2.2	Quartz monzonite porphyry.....	71
3.4.3	Late stage intrusion.....	75
3.4.3.1	Late-stage quartz monzonite.....	75
3.5	Mafic xenoliths.....	78
3.6	Tertiary Basalt.....	79
3.7	U–Pb Geochronology.....	79
3.7.1	Ridgeway $^{206}\text{Pb}/^{238}\text{U}$ geochronology.....	80
3.8	Igneous Geochemistry.....	82
3.8.1	Hydrothermal alteration effects and element mobility.....	83
3.8.2	Major element geochemistry.....	84
3.8.3	Trace and rare earth elements geochemistry.....	89
3.8.4	Comparison to Northparkes district.....	96
3.9	Discussion.....	96
3.9.1	Deposition of the Ridgeway host rocks.....	96
3.9.2	Ridgeway intrusive complex.....	97
3.9.3	Timing and nature of magmatism.....	100
3.10	Summary.....	101

#### **Chapter 4: Alteration and Mineralization**

4.1	Introduction.....	103
4.2	Previous work.....	105
4.3	Ridgeway vein paragenesis.....	106
4.3.1	Pre-main mineralization veins - Stage 1.....	114
4.3.1.1	Stage 1A Magnetite veinlets.....	114
4.3.1.2	Stage 1B Actinolite–magnetite veins.....	115

4.3.2	Main mineralization stage veins - Stage 2.....	116
4.3.2.1	Stage 2A Quartz–magnetite veins.....	117
4.3.2.2	Stage 2B Quartz–banded magnetite–bornite veins.....	117
4.3.2.3	Stage 2C Vein-dikes.....	120
4.3.2.4	Stage 2D Quartz–bornite veins.....	121
4.3.3	Main mineralization stage veins - Stage 3.....	121
4.3.3.1	Stage 3A Quartz–chalcopyrite veins.....	121
4.3.3.2	Stage 3B Vein-dikes.....	122
4.3.3.3	Stage 3C Chalcopyrite–epidote veins.....	122
4.3.3.4	Stage 3D Quartz ± chlorite veins.....	122
4.3.4	Late stage veins - Stage 4.....	127
4.3.4.1	Stage 4A Pyrite ± quartz veins.....	127
4.3.4.2	Stage 4B Epidote ± chlorite veins.....	127
4.3.4.3	Stage 4C Chlorite-rich matrix breccias.....	128
4.3.4.4	Stage 4D Calcite–prehnite ± quartz veins.....	129
4.4	Hydrothermal Alteration.....	129
4.4.1	Early alteration stage.....	132
4.4.1.1	Quartz ± albite alteration.....	132
4.4.1.2	Garnet–epidote alteration.....	137
4.4.1.3	Magnetite–actinolite–albite–biotite alteration.....	142
4.4.2	Main stage alteration.....	143
4.4.2.1	Orthoclase–biotite–albite–magnetite–actinolite alteration.....	143
4.4.3	Late stage alteration.....	149
4.4.3.1	Late orthoclase–albite alteration.....	149
4.4.3.2	Epidote–chlorite–hematite alteration.....	149
4.4.3.3	Hematite alteration.....	152
4.4.3.4	Outer propylitic alteration.....	152
4.4.3.5	Albite–quartz–pyrite–sericite alteration.....	153
4.4.4	Fault-related alteration.....	153
4.4.4.1	Clay–chlorite alteration.....	153
4.4.4.2	Epidote–hematite alteration.....	154
4.4.4.3	Carbonate alteration.....	154
4.5	Gold and copper grade distribution.....	154
4.6	Re–Os Geochronology.....	162
4.6.1	Re–Os Analytical Methods.....	162
4.6.2	Previous Re–Os geochronological studies.....	163

4.6.3	Results.....	163
4.7	Discussion.....	164
4.7.1	Pre-mineralization stage.....	164
4.7.2	Fluid evolution in space and time.....	165
4.7.3	K-silicate (Potassic) alteration and Au–Cu ore.....	166
4.7.4	Relationships between unidirectional solidification textures to Au–Cu mineralization.....	166
4.7.5	Ore distribution.....	169
4.7.6	Timing of the Magmatic - Hydrothermal System.....	170
4.8	Summary.....	173

## **Chapter 5: Structural Geology**

5.1	Introduction.....	175
5.2	Field Methods and Data Presentation.....	176
5.3	Previous Work.....	178
5.4	Structure of the Cadia district.....	179
5.4.1	Regional-scale structures.....	179
5.4.2	District-scale structures.....	180
5.5	Structures at Ridgeway.....	182
5.5.1	Folds.....	182
5.5.2	Faults.....	184
5.5.2.1	Northwest-striking, steeply-dipping faults.....	185
5.5.2.2	North-northwest striking, southwest-dipping reverse faults.....	189
5.5.2.3	Low-angle thrust faults.....	191
5.6	Geometry of veins and structures at Ridgeway.....	192
5.6.1	Domain Analysis.....	197
5.6.1.1	Vein set 1.....	197
5.6.1.2	Vein set 2.....	199
5.6.1.3	Vein set 3.....	201
5.6.1.4	Vein set 4.....	203
5.6.2	Comparison with pre-existing mine data.....	204
5.6.3	Dikes and sills.....	205
5.7	Structural level plans.....	206
5.7.1	5100mRL.....	206
5.7.2	5255mRL.....	207
5.7.3	5330mRL.....	209
5.8	Discussion and Summary.....	210

---

5.8.1	Deposit-scale structural interpretations.....	210
5.8.1.1	Pre-mineralization deformation.....	210
5.8.1.2	Mafic dikes as paleostress-direction indicator.....	210
5.8.2	Magma intrusion: a structural model.....	211
5.8.3	Vein formation, fluid pressure and differential stress.....	217
5.8.4	Structural History.....	218
<b>Chapter 6: Hydrothermal Geochemistry</b>		
6.1	Introduction.....	223
6.2	Cathodoluminescence.....	223
6.2.1	Methodology.....	224
6.2.2	Hydrothermal quartz vein textures.....	225
6.2.2.1	Qz-1A: euhedral growth zones.....	226
6.2.2.2	Qz-1B: diffuse zones.....	227
6.2.2.3	Qz-2: quartz overgrowths on dissolution surfaces.....	227
6.2.2.4	Qz-3: CL-dark luminescence.....	227
6.2.3	Electron microprobe results.....	228
6.2.3.1	Stage 2B quartz–banded magnetite–bornite veins.....	228
6.2.3.2	Stage 2D quartz–bornite vein.....	229
6.2.3.3	Stage 3A quartz–chalcopyrite vein.....	234
6.2.3.4	Stage 3D quartz vein.....	236
6.2.4	Titanium-in-quartz geothermometer.....	236
6.2.5	Discussion.....	239
6.2.5.1	Correlation between quartz types, CL intensity and trace elements...	239
6.2.5.2	Temperature of quartz formation and sulfide precipitation.....	241
6.3	Fluid Inclusions.....	241
6.3.1	Previous work.....	242
6.3.2	Methodology.....	243
6.3.3	Classification.....	243
6.3.4	Microthermometry results.....	244
6.3.5	Discussion.....	246
6.3.5.1	Pressure and depth estimates.....	246
6.4	Sulfur Isotopes.....	248
6.4.1	Previous Work.....	248
6.4.2	Methodology.....	248
6.4.3	Results.....	250
6.4.3.1	Stage 2B and 2D veins.....	250

---



6.4.3.2	Stage 3A and 3C veins.....	252
6.4.3.3	Stage 4A pyrite veins and disseminations.....	252
6.4.4	Discussion.....	257
6.4.4.1	Fluid and sulfur sources.....	257
6.5	Oxygen Isotopes.....	259
6.5.1	Previous work.....	260
6.5.2	Methodology.....	261
6.5.3	Results.....	261
6.5.4	Discussion.....	261
6.6	Summary.....	264

## **Chapter 7: Summary and Genetic Model**

7.1	Introduction.....	265
7.2	Volcano-sedimentary succession, magmatism and volcanic setting.....	265
7.3	Ridgeway genetic model.....	267
7.3.1	Structural controls and history of emplacement.....	267
7.3.2	Intrusions, alteration and mineralization.....	270
7.3.2.1	Pre-mineralization: monzodiorite, stage 1 veins and related hydrothermal alteration events.....	271
7.3.2.2	Main-stage mineralization: mafic monzonite porphyry, stage 2 veins and related hydrothermal alteration events.....	270
7.3.2.3	Main-stage mineralization: quartz monzonite porphyry, stage 3 veins and related hydrothermal alteration events.....	272
7.3.2.4	Late-stage: equigranular quartz monzonite, stage 4 veins and related hydrothermal events.....	273
7.3.2.5	Post-mineralization: fault-related hydrothermal alteration events.....	277
7.3.3	Timing of igneous activity and sulfide mineralization.....	278
7.3.4	Sulfide precipitation.....	279
7.3.5	Gold enrichment in the alkaline melts at Ridgeway.....	279
7.4	Exploration Implication.....	280
7.5	Further Work.....	281

<b>References.....</b>	<b>283</b>
------------------------	------------

---

# List of Figures

---

## Chapter 1 Introduction

Figure 1.1	Location of the Cadia district, New South Wales, Australia.....	2
Figure 1.2	Location of porphyry and skarn deposits of the Cadia district.....	3
Figure 1.3	Total resource tonnages versus average grades of selected gold-rich alkalic deposits.....	3
Figure 1.4	Aerial photograph of the subsidence zone on top of the Ridgeway mine....	11

## Chapter 2 Regional Geology

Figure 2.1	Major orogenic belts in the Tasman Fold Belt, eastern Australia.....	16
Figure 2.2	Subprovinces of the Lachlan Fold Belt.....	19
Figure 2.3	Ordovician volcanic belts comprising the Macquarie Arc.....	23
Figure 2.4	Major lithostratigraphic units and magmatic phases in the Macquarie Arc..	24
Figure 2.5	Tectonic evolution of the Macquarie Arc.....	25
Figure 2.6	Major crustal structures in the Tasman Fold Belt.....	29
Figure 2.7	Interpreted crustal-architecture and geological features below the Lachlan Transverse Zone.....	30
Figure 2.8	Aeromagnetic image of the Cadia district.....	32

## Chapter 3 Geology, Geochronology and Geochemistry

Figure 3.1	Geology of the Cadia district.....	36
Figure 3.2	Location plan of logged drillholes at Ridgeway.....	37
Figure 3.3	Regional geology of the Cadia district.....	39
Figure 3.4	Idealized summary of the Ridgeway stratigraphy.....	40
Figure 3.5A	Geological cross-section along 10950mE.....	41
Figure 3.5B	Geological cross-section along 11050mE.....	43
Figure 3.5C	Geological cross-section along 11150mE.....	45
Figure 3.5D	Geological cross-section along 11250mE.....	46
Figure 3.6	Geological long-section along 22650mN.....	47
Figure 3.7	Geological plan maps at different levels from Ridgeway.....	48
Figure 3.8	Photographs and photomicrographs of the Weemalla Formation.....	51
Figure 3.9	Photographs and photomicrographs of the Forest Reefs Volcanics.....	57
Figure 3.10	Photographs and photomicrographs of the coherent lithofacies of the Forest Reefs Volcanics.....	61

Figure 3.11 Photographs and photomicrographs the monzodiorite.....	67
Figure 3.12 Photographs and photomicrographs of the mafic monzonite.....	69
Figure 3.13 Unidirectional solidification textures in the mafic monzonite.....	70
Figure 3.14 Photographs and photomicrographs of the quartz monzonite.....	72
Figure 3.15 Unidirectional solidification textures and miarolitic cavities in the quartz monzonite.....	73
Figure 3.16 Intrusive contacts at Ridgeway.....	74
Figure 3.17 Photographs and photomicrographs of the late-stage quartz monzonite.....	77
Figure 3.18 Mafic xenoliths at Ridgeway.....	78
Figure 3.19 Tera–Wasserburg concordia plots.....	82
Figure 3.20 Assessment of the effect of hydrothermal alteration on the whole rock geochemistry for intrusive rocks from Ridgeway.....	85
Figure 3.21 Major- and trace-element discrimination diagrams for intrusive rocks from Ridgeway.....	86
Figure 3.22 Major-element variation diagrams for intrusive rocks from Ridgeway.....	88
Figure 3.23 Trace-element variation diagrams for intrusive rocks from Ridgeway.....	90
Figure 3.24 Chondrite-normalized rare earth element profiles for intrusive rocks from Ridgeway.....	92
Figure 3.25 Variation on rare earth element concentration versus SiO <sub>2</sub> concentration and absolute age for intrusive rocks from Ridgeway.....	93
Figure 3.26 Geochemical comparisons of the different intrusive rocks from Cadia and Northparkes districts.....	95
Figure 3.27 Simplified schematic diagrams showing the volcanic and magmatic evolution of Ridgeway .....	98

## Chapter 4 Alteration and Mineralization

Figure 4.1 Schematic time-space diagram of alteration assemblages and vein stages for from Ridgeway.....	109
Figure 4.2 Geology, alteration and distribution of vein stages - section 11050mE...	111
Figure 4.3 Geology, alteration and distribution of vein stages - section 22650mN...	113
Figure 4.4 Textures and mineralogy of stage 1 veins.....	115
Figure 4.5 Textures and mineralogy of stage 2 veins.....	119
Figure 4.6 Textures and mineralogy of stage 2B veins.....	120
Figure 4.7 Textures and mineralogy of stage 3 veins.....	125
Figure 4.8 Textures and mineralogy of stage 3 veins.....	126
Figure 4.9 Textures and mineralogy of stage 4A veins.....	128
Figure 4.10 Textures and mineralogy of stage 4 veins.....	131

Figure 4.11 Early alteration stage at Ridgeway.....	139
Figure 4.12 Quartz $\pm$ albite alteration assemblage.....	140
Figure 4.13 Garnet–epidote alteration assemblage.....	141
Figure 4.14 Orthoclase–biotite–albite–magnetite alteration assemblage (inner).....	145
Figure 4.15 Orthoclase - biotite - albite - magnetite alteration assemblage (outer).....	147
Figure 4.16 Late-stage alteration assemblages.....	151
Figure 4.17 Fault-related alteration assemblages.....	154
Figure 4.18 Gold contours (plans).....	157
Figure 4.19 Copper contours (Plans).....	158
Figure 4.20 Gold contours (cross-sections).....	159
Figure 4.21 Copper contours (cross-sections).....	160
Figure 4.22 Gold and copper contours - along section 22650mN.....	161
Figure 4.23 Diagram showing the geology, alteration and grade relationships.....	167
Figure 4.24 Unidirectional solidification textures in the mafic monzonite and quartz monzonite.....	168
Figure 4.25 Summary of geochronology at Ridgeway.....	170
Figure 4.26 Location and results of all geochronology samples in the Cadia district..	172

## Chapter 5 Structural Geology

Figure 5.1 Photograph of core-orientation cradle.....	176
Figure 5.2 Surface geology and location of bedding orientation.....	181
Figure 5.3 Photograph of folding in the Weemalla Formation.....	183
Figure 5.4 Equal-area projection plots of bedding in the Weemalla Formation.....	183
Figure 5.5 Location of major faults at Ridgeway in plan and section.....	186
Figure 5.6 Cross-sections showing the major faults at Ridgeway.....	187
Figure 5.7 Photographs of northwest-striking, steeply-dipping faults.....	188
Figure 5.8 Photographs of northwest-striking, low-angle faults.....	190
Figure 5.9 Diagram showing the stress-field relationship.....	192
Figure 5.10 Rose diagram and contour plots for the different vein stages.....	195
Figure 5.11 Contour plots of the different veins sets by rock types.....	196
Figure 5.12 Plan showing major veins orientations by domains .....	198
Figure 5.13 Photographs of set 1 veins.....	199
Figure 5.14 Photographs of set 2 veins.....	200
Figure 5.15 Photographs of set 3 veins.....	202
Figure 5.16 Photographs of set 4 veins.....	204
Figure 5.17 Contour plots of the different veins sets from digital database.....	205
Figure 5.18 Rose diagram and contour plots of dikes and sill.....	205

Figure 5.19 Vein orientations from different level plans.....	208
Figure 5.20 Schematic diagram showing orientation of dikes of .....	211
Figure 5.21 Geometry of intrusions and pull-apart model analogue.....	212
Figure 5.22 Mechanism for the intrusion of dikes.....	213
Figure 5.23 Emplacement model for the Ridgeway intrusive complex.....	215
Figure 5.24 Structural history of the Ridgeway intrusive complex.....	220

## Chapter 6 Hydrothermal Geochemistry

Figure 6.1 Cathodoluminescence image of quartz textures.....	226
Figure 6.2 Quartz textures in stage 2B vein.....	229
Figure 6.3 Quartz textures in stage 3D barren quartz vein.....	230
Figure 6.4 Trace elements mapping in stage 2B vein.....	231
Figure 6.5 Trace element concentrations in stage 2D vein.....	233
Figure 6.6 Trace elements mapping in stage 2D vein.....	234
Figure 6.7 Trace element concentrations in stage 3A veins.....	235
Figure 6.8 Quartz textures in stage 3D vein.....	236
Figure 6.9 Trace element concentration and temperature.....	238
Figure 6.10 Aluminum and Titanium concentration of quartz compared with other deposits.....	240
Figure 6.11 Types and occurrences of fluid inclusions.....	243
Figure 6.12 Results of microthermometric analyses of fluid inclusion.....	246
Figure 6.13 Photographs of sulfides analyzed for sulfur isotope.....	249
Figure 6.14 Distribution and location of sulfur isotopes at Ridgeway.....	253
Figure 6.15 Sulfur isotope contour in stage 3A and 3C veins.....	255
Figure 6.16 Sulfur isotope contour in stage 4A veins.....	256
Figure 6.17 Ranges of sulfur isotopes associated with other porphyry Au-Cu deposits.....	258
Figure 6.18 Photomicrographs of quartz and magnetite textures .....	260
Figure 6.19 Spatial distribution of oxygen isotope results of garnet at Ridgeway.....	262
Figure 6.20 Plot of calculated composition of fluids in equilibrium with garnet.....	263

## Chapter 7 Summary and Genetic Model

Figure 7.1 Diagram showing the structural position of Ridgeway intrusions.....	269
Figure 7.2 Conceptual genetic model - pre-mineralization.....	275
Figure 7.3 Conceptual genetic model - main-mineralization and late stage.....	276
Figure 7.4 Conceptual genetic model - post-mineralization.....	277

---

# List of Tables

---

## Chapter 1 Introduction

Table 1.1	Resources of the porphyry and skarn deposits of the Cadia district.....	3
Table 1.2	Reserves and resources of selected alkalic- and calc-alkalic porphyry deposits.....	4

## Chapter 2 Regional Geology

Table 2.1	Porphyry groups emplaced into the Macquarie Arc.....	26
Table 2.2	Reserves/resources for the Ordovician Au-Cu deposits of the Macquarie Arc.....	32

## Chapter 3 Geology, Geochronology and Geochemistry

Table 3.1	Rock units of the Weemalla Formation.....	49
Table 3.2	Rock units of the Forest Reefs Volcanics.....	55
Table 3.3	Textural and Mineralogical characteristics of the intrusive rocks.....	64
Table 3.4	Summary of SHRIMP $^{206}\text{Pb}/^{238}\text{U}$ age determinations in the Cadia district..	80
Table 3.5	Summary of $^{206}\text{Pb}/^{238}\text{U}$ LA-ICPMS age determinations from Ridgeway....	82
Table 3.6	PGE and Au abundances of mafic xenoliths at Ridgeway .....	94

## Chapter 4 Alteration and Mineralization

Table 4.1	Definition of alteration and mineralization terminology.....	104
Table 4.2	Veins stages of the Ridgeway deposit.....	107
Table 4.3	Styles, and spatial and temporal distribution of alteration assemblages of the Ridgeway deposit .....	133
Table 4.4	Comparison of alteration assemblages and veins associations observed at Ridgeway during this study with previous studies.....	135
Table 4.5	Re-Os data for molybdenite from the Cadia district.....	164
Table 4.6	Re-Os data for molybdenite from Ridgeway deposit.....	164
Table 4.7	Summary of geochronological data from the Cadia district.....	171

## Chapter 5 Structural Geology

Table 5.1	Summary of veins stages at Ridgeway .....	177
Table 5.2	Bedding orientations in the Weemalla Formation.....	184
Table 5.3	Major faults at Ridgeway.....	185
Table 5.4	Summary of structural.....	193

**Chapter 6 Hydrothermal Geochemistry**

Table 6.1	Vein stages analyzed for SEM-CL and LA-ICPMS at Ridgeway.....	225
Table 6.2	Quartz generations defined by textures using SEM-CL at Ridgeway.....	229
Table 6.3	Calculated temperature of quartz formation using the TitaniQ geothermometry.....	237
Table 6.4	Summary of microthermometric analysis.....	245
Table 6.5	Sulfur isotope compositions of sulfides .....	251
Table 6.6	Summary of sulfur isotope compositions .....	251
Table 6.7	Combined summary of all sulfur compositions from this study and with previous study.....	251
Table 6.8	Measured and calculated oxygen isotope.....	263

---

# List of Appendices

---

## **Appendix A: Graphic core logs**

- A.1 Logged drillholes – collar data and logged depth
- A.2 Scanned/digital graphic logs

## **Appendix B: Chemical staining**

- B.1 Chemical staining procedure
- B.2 List of stained samples

## **Appendix C: Electron microprobe mineral chemistry**

- C.1 Silicates

## **Appendix D: Results of the whole rock geochemistry**

- D.1 Data from the current study
- D.2 Data from the previous study

## **Appendix E: Structural data**

- E.1 Measurements – vein orientations in drillholes
- E.2 Measurements – bedding orientations in drillholes
- E.3 Measurements – dikes and sills orientations in drillholes
- E.4 Measurements – vein orientations underground
- E.5 Bedding orientation data extracted from Newcrest database
- E.6 Vein orientation extracted from Newcrest database
- E.7 Vein orientations extracted from digitized underground map of Newcrest

## **Appendix F: Cathodoluminescence images of hydrothermal quartz**

- F.1 Stage 2B veins
- F.2 Stage 2D veins
- F.3 Stage 3A veins
- F.4 Stage 3D vein

## **Appendix G: Electron microprobe analyses of quartz**

- G.1 Quartz
- G.2 Titanium-in-quartz geothermometry

## **Appendix H: Sulfur isotope results**

- H.1 Data from the current study
- H.2 Data from the previous study

## **Appendix I: Rock sample catalogue**

Appendices are provided electronically on accompanying CD



---

# List of Abbreviations

---

## Minerals

ab	albite	au	gold
act	actinolite	grs	grossular
adr	andradite	hem	hematite
ap	apatite	hbl	hornblende
aug	augite	ill	illite
bt	biotite	Kfs	K-feldspar
bn	bornite	mag	magnetite
cal	calcite	mo	molybdenite
cb	carbonate mineral	or	orthoclase
cc	chalcocite	opx	orthopyroxene
ccp	chalcopyrite	plg	plagioclase
chl	chlorite	prh	prehnite
cpx	clinopyroxene	py	pyrite
cv	covelite	px	pyroxene
dg	digenite	qtz	quartz
ep	epidote	rt	rutile
fsp	feldspar	sa	sanidine
fl	flourite	ser	sericite
grt	garnet	ttn	titanite

## Rocks/structures

LFB	Lachlan Fold Belt	N	north
LTZ	Lachlan Transverse Zone	NE	northeast
P3	late-stage quartz monzonite	NNW	north-northwest
P2	quartz monzonite porphyry	NW	northwest
P1	mafic monzonite porphyry	S	south
MzD	monzodiorite	SE	southeast
Fpo	feldspar-phyric	W	west
Ppo	pyroxene-phyric	E	east
FRV	Forest Reefs Volcanics		

### **Units of measurement**

C	celcius
cm	centrimeter(s)
km	kilometre(s)
m	meter(s)
µm	micrometer(s)
mm	milimeter(s)

### **Laboratories and Analyses**

BSE	back scatter image
CL	cathodoluminescence
CODES	Centre of Excellence in Ore Deposits
CSL	Central Science Laboratory
EMPA	electron microprobe analysis
LA-ICPMS	laser ablation inductively-coupled plasma mass spectrometry
LOI	loss on ignition
REE	rare-earth element(s)
SEM	scanning electron microscope
SHRIMP	sensitive high-resolution ion microprobe
XRD	X-ray diffraction

---

# Chapter 1: Introduction

---

## 1.1 Preamble

The Late Ordovician Lachlan Fold Belt of New South Wales, Australia is a well-endowed metallogenic province that contains some of the world's gold-rich porphyry copper deposits. Alkalic Au–Cu porphyry deposits characterize the Cadia district in the eastern Lachlan Fold Belt (Fig. 1.1), including two high-grade porphyry gold resources at Ridgeway and Cadia East (Table 1.1; Fig. 1.2). Alkalic gold-(copper) deposits are attractive exploration targets of increasing economic significance. They include some of the world's highest grade and largest porphyry-related gold resources, such as Ridgeway (157 Mt at 0.8 g/t Au, 0.39 % Cu) and Galore Creek in British Columbia (1143 Mt at 0.26 g/t Au, 0.47 % Cu; Table 1.2; Fig. 1.3). The Cadia district contains an *in situ* resource of 1280 t Au and 6.9 Mt Cu, making the district the sixth largest gold-rich porphyry district in the world (Cooke *et al.*, 2007).

Alkalic porphyry deposits can be difficult exploration targets due to their spatially restricted hydrothermal alteration zones which may be confined within a few hundred meters from the margins of small, pipe-like monzonite intrusions (Cooke *et al.*, 2007). Weakly developed peripheral alteration domains may also present difficulties when trying to identify the mineralized intrusive center. Hence, in order to better define and understand the characteristics of these atypical but potentially very metal-rich alkalic porphyry systems, it is important to characterize well-exposed deposits over their full vertical and lateral extent.

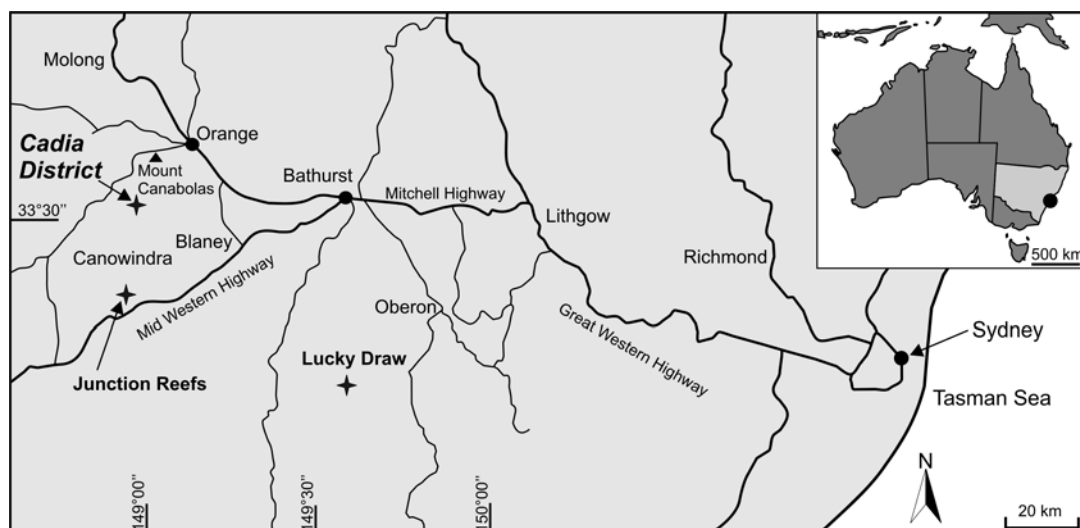


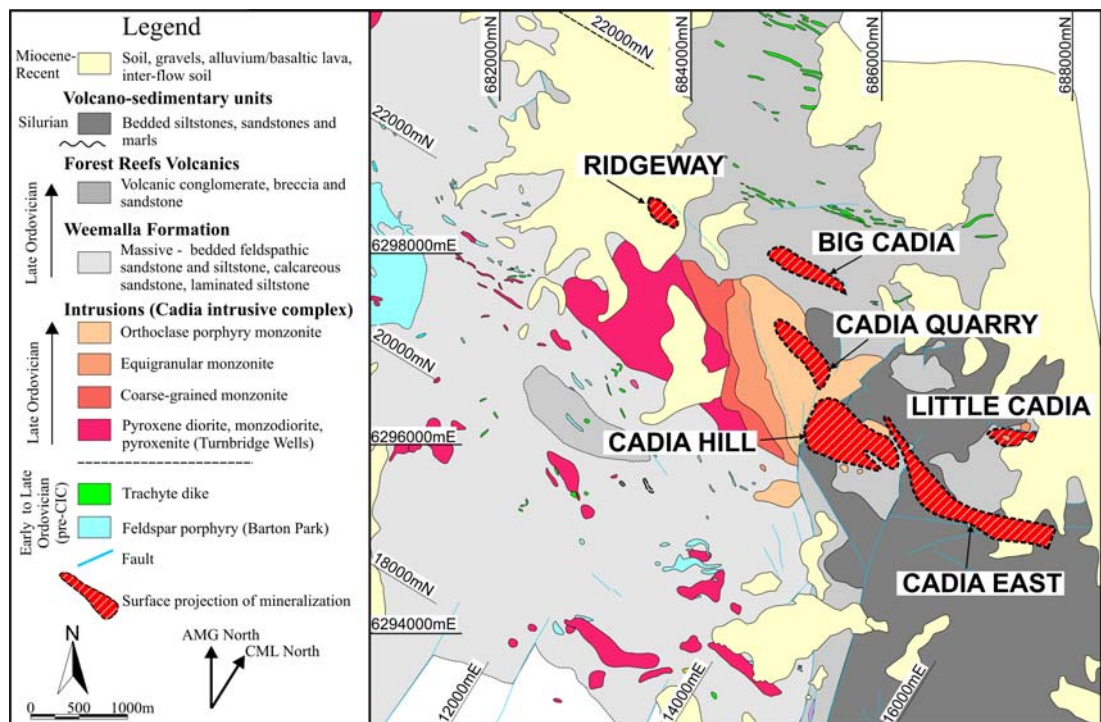
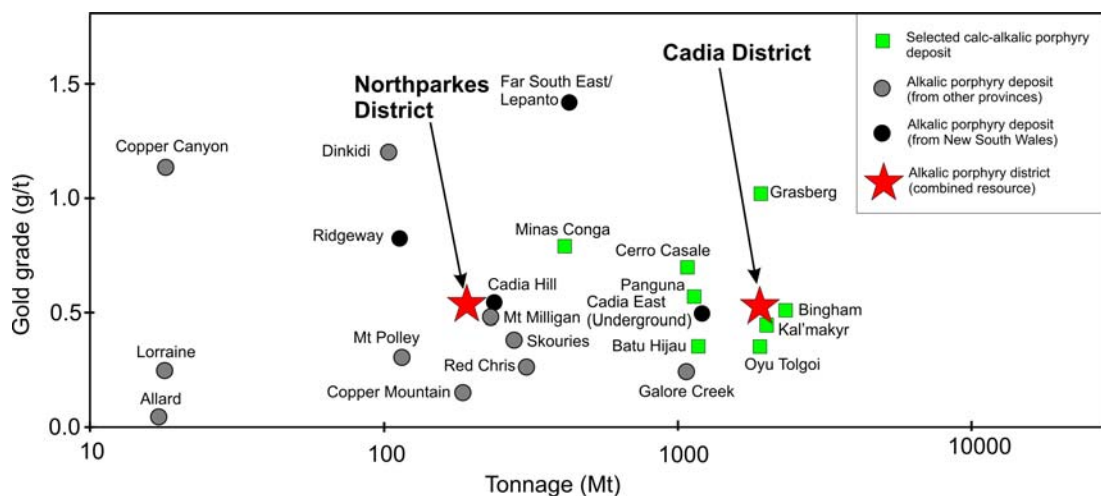
**Figure 1.1** Location of the Cadia district and other selected deposits, New South Wales, Australia (modified from Pogson and Watkins, 1998).

The Ridgeway Au–Cu deposit, with a resource of 126 t Au and 0.61 Mt Cu (Table 1.1), is an ideal place to study the anatomy of one of the highest grade alkalic porphyry deposits. This PhD dissertation seeks to determine the nature of the hydrothermal system at Ridgeway and to investigate likely processes of ore deposition through analysis of the mineralogy, vein and alteration paragenesis, intrusion geometries, and structural architecture so that a genetic model can be formulated. The extensive underground developments, combined with numerous 1.5 km long vertical diamond drillholes, provide an opportunity to constrain the geometry of this porphyry system. Combining new and existing knowledge of magmatic and hydrothermal processes will hopefully lead to an improved understanding of mechanisms that influence porphyry emplacement and Au–Cu mineralization.

This deposit-scale study of Ridgeway is a part of a bigger project that aims to better understand the architecture of Australia’s premier Au–Cu district. The district-wide collaborative research project, “Cadia Valley Alkalic Porphyry Ore Deposits: Deconstructing the System Architecture”, involved staff and students from CODES, the Australian Research Council’s Centre of Excellence in Ore Deposits at the University of Tasmania in collaboration with industry partner Newcrest Mining Limited.

**Table 1.1** Resources of the Cadia district at the end of December 2008 (Newcrest Mining Limited, 2008)

Deposit	Tonnage (Mt)	Au (g/t)	Cu (%)	Contained Au (t)	Contained Cu (Mt)
Cadia Hill (open pit)	417.0	0.50	0.13	208.5	0.54
Cadia Quarry (Cadia extended)	37.0	0.40	0.23	14.8	0.09
Ridgeway (underground)	157.0	0.80	0.39	125.6	0.61
Cadia East (underground)	1834.0	0.50	0.30	917.0	5.50
Big Cadia	34.0	0.40	0.50	13.6	0.17
Little Cadia*	8.0	0.30	0.40	-	0.03
Total metal content				1279.5	6.9

\* Holliday *et al.*, 2002**Figure 1.2** Geology of the Cadia district and location of the different styles of gold-copper mineralization (modified from Holliday *et al.*, 2002; Newcrest Mining Limited, 2006).**Figure 1.3** Alkalic gold-rich porphyry deposits from New South Wales and other selected deposits from other alkalic provinces, plotted as a function of resource tonnage versus gold grades. Also shown are the other 10 largest known calc-alkalic and high-K calc-alkalic gold-rich porphyry copper deposits. Data are listed in Table 1.2 and reference therein (modified from Cooke *et al.*, 2005; 2006; 2007).

**Table 1.2** Reserves and resources of selected alkalic-porphyry deposits from New South Wales and other alkalic provinces compared with the largest (in terms of contained gold) calc-alkalic and high-K calc-alkalic gold-rich porphyry copper deposits.

Deposit/District	Mt	Au (g/t)	Cu (%)	Reference
<b>Alkalic Porphyry Deposits - NSW</b>				
Cadia district	2445.0	0.52	0.28	Table 1.1
Northparkes district (E26, E22, E48, E37)	131.7	0.51	1.12	Cooke <i>et al.</i> (2007)
<b>Other Alkalic Porphyry Deposits</b>				
<i>British Columbia, Canada</i>				
Copper Mountain	345.0	0.13	0.43	Cooke <i>et al.</i> (2007)
Mt Milligan	408.0	0.47	0.18	Cooke <i>et al.</i> (2007)
Galore Creek	1143.4	0.26	0.47	<a href="http://www.novagold.com/">http://www.novagold.com/</a>
Red Chris	522.7	0.27	0.35	Lang (2001)
Mt Polley	141.7	0.30	0.32	<a href="http://www.imperialmetals.com/">http://www.imperialmetals.com/</a>
Copper Canyon	32.4	1.17	0.75	Cooke <i>et al.</i> (2007)
Lorraine	32.0	0.26	0.66	Cooke <i>et al.</i> (2007)
<i>Other Provinces</i>				
Skouries (Greece)	500.0	0.47	0.37	Tobey <i>et al.</i> (1998)
Dinkidi (Philippines)	110.0	1.20	0.50	Wolfe (2001)
Allard (Colorado)	32.0	0.07	0.40	Jensen and Barton (2000)
<b>Ten largest known gold-rich porphyry copper deposits (ranked based on contained gold)</b>				
Grasberg, Irian Jaya	2480.0	1.05	1.13	Cooke <i>et al.</i> (2005)
Bingham, Utah	3228.0	0.50	0.88	Cooke <i>et al.</i> (2005)
Kal'makyr, Uzbekistan	2700.0	0.51	0.40	Cooke <i>et al.</i> (2005)
Lepanto-Far Southeast, Philippines	685.0	1.42	0.80	Cooke <i>et al.</i> (2005)
Cerro Casale, Chile	1285.0	0.70	0.35	Cooke <i>et al.</i> (2005)
Cadia, NSW, Australia	2445.0	0.52	0.28	Newcrest Mining Limited 2008
Panguna, Bougainville	1415.0	0.57	0.46	Cooke <i>et al.</i> (2005)
Oyu Tolgoi, Mongolia	2467.0	0.32	0.83	Cooke <i>et al.</i> (2005)
Batu Hijau, Indonesia	1644.0	0.35	0.44	Cooke <i>et al.</i> (2005)
Minas Conga, Northern Peru	641.0	0.79	0.30	Cooke <i>et al.</i> (2005)

## 1.2 Project aims and objectives

Ridgeway has extensive domains of mineralization and alteration that have been drilled to depths of more than 1.5 km below the present-day surface. Wilson (2003) characterized the upper parts of the orebody in a PhD study that encompassed the four major deposits at the Cadia district (Ridgeway, Cadia East, Cadia Quarry and Cadia Hill; Fig. 1.2). Harper (2000) documented the upper parts of Ridgeway in a BSc (Honours) thesis. Since production at the Ridgeway mine commenced in 2001, new underground developments and deep drilling have provided opportunities to investigate the deeper portions of this gold-rich porphyry deposit. Specifically, Newcrest Mining Limited instigated the Ridgeway Deeps project in 2004, which has involved mining of the mineralized resource to depths to 1.3 km below the surface (Newcrest Mining Limited, 2007). Previous research (e.g. Wilson, 2003) did not have the opportunity to investigate Ridgeway Deeps. The current study therefore seeks to update previous research by Harper (2000) and Wilson (2003) by:

- Determining the vein and alteration paragenesis and intrusive history for Ridgeway Deeps, and integrating it with previously determined results for the upper parts of Ridgeway.
- Establishing the geometry of individual intrusions associated with mineralization.
- Evaluating how space was created for the Ridgeway intrusive complex (RIC) and the associated veins, and assessing the stress field evolution at Ridgeway during Au–Cu mineralization.
- Analyzing the composition of veins and alteration minerals in order to determine the nature of the mineralizing fluids and likely processes of ore deposition.
- Proposing revised genetic and exploration models for Ridgeway.

### 1.3 Methodology

This PhD study included three seasons of fieldwork at Ridgeway for a combined total of 23 weeks. Field observations focused on documenting the deposit geology, including the hydrothermal alteration and vein paragenesis. The mine assay database was interrogated to determine metal distributions and zonation patterns over a ~ 2.0 km vertical extent. Detailed documentation of igneous and hydrothermal textures of individual intrusions focused on recognition of features indicative of the magmatic-hydrothermal transition, including unidirectional solidification textures (USTs), miarolitic cavities and aplite vein-dikes. The distribution of quartz veins and fracture patterns in and around the different intrusions and host rocks were documented through core logging and underground mapping coupled with the use of the mine's digital database of structural measurements.

A principal objective of the core logging was the construction of four cross sections spaced at 100m apart (10950mE, 11050mE, 11150mE and 11250mE; Cadia mine lease [CML] grid system) and one subsidiary long section (22650mN) through Ridgeway and Ridgeway Deeps to investigate the three-dimensional geometry of the deposit. In total, approximately 14 km of core was logged from 37 drillholes. More emphasis was placed on logging core from the deeper extension of the orebody, Ridgeway Deeps, because it has not previously been documented. Several drillholes were also logged from the periphery of the deposit to gain a deposit-wide perspective. Due to mining access and safety reasons, only limited underground mapping was undertaken. A total of ~ 0.3 km of detailed underground mapping was conducted in order to measure vein orientations from three crosscuts.

Petrographic and laboratory analyses were mostly conducted at the University of Tasmania. Geochemical research included X-ray fluorescence (XRF) analyses of major and selected trace element compositions of whole rock samples. Additional trace and rare earth elements (REE) were analyzed by solution-based inductively-coupled plasma mass spectrometry (ICP-MS). Electron microprobe analyses of mineral compositions were performed on a Cameca SX100 at the Central Science Laboratory (CSL). Re–Os age determinations of molybdenite were conducted at the University of Alberta, Canada. Stable isotope analyses were



conducted at the Central Science Laboratory, University of Tasmania (sulfur) and GNS Stable Isotope Laboratory, New Zealand (oxygen). Scanning Electron Microprobe Cathodoluminescence (SEM-CL) of quartz was performed at the CSL.

## **1.4 Thesis Organization**

This thesis has been divided into seven chapters. Following the introductory chapter, the thesis comprises:

- Chapter 2 – a review of the regional tectonic setting of the Cadia district, including a summary of the different ore deposit styles in the Macquarie Arc.
- Chapter 3 – a description of the geology of Ridgeway including the different host rocks and geometry of intrusions. New U–Pb geochronological results for the igneous rocks at Ridgeway are also presented in this chapter, as are whole rock geochemical analyses.
- Chapter 4 – a description of veins and altered rocks and an updated vein paragenesis based on observations from Ridgeway Deeps. The spatial distribution of alteration, vein assemblages and sulfide zonation patterns are also presented. The chapter also presents the results of the new Re–Os molybdenite age that placed the absolute timing of mineralization at Ridgeway.
- Chapter 5 – a documentation and discussion of the geometric and timing relationships of structural elements at Ridgeway. Emplacement mechanism of the Ridgeway intrusive complex is presented in this chapter.
- Chapter 6 – which presents the results of cathodoluminescence and trace element studies of hydrothermal quartz, and stable isotope results. These are discussed in the context of constraining the physico-chemical environment of ore deposition at Ridgeway.
- Chapter 7 – which concludes the thesis by presenting a revised genetic model and discusses the exploration implications of this study.

The local grid at Cadia is called the Cadia Mine Local Grid (CML). The CML is aligned 32° east of grid north (AMG/GDA94). For the purpose of this thesis, all orientations are discussed with reference to the national Australian Map Grid (AMG) system. The local Real Level (mRL) used at the mine is sea level +5000 meters.

## **1.5 Cadia District - Exploration and mining history**

Since the 1870s, Cadia has been mined for copper and gold from small open-cuts and scattered shafts (Wood and Holliday, 1995). A magnetite skarn orebody, Big Cadia, yielded more than 100,000 tonnes of secondary copper at grades of 5 - 7 % Cu by 1971. It had also yielded about 1.5 million tonnes of low-grade iron ore (50 % Fe) from intermittent quarrying between 1918 and 1941 (Newcrest Mining Limited, 1993).

Various companies explored the Cadia district during the 1950s, but it was only in the mid-60s when modern exploration methods began to be employed. The area was acquired by Pacific Copper Limited in 1968, who carried out drilling at the Big Cadia and Little Cadia skarns. The first significant indications of a large, low-grade Cu–Au deposit came in the mid-1970s. The mineralization at Big Cadia was hosted in banded magnetite–hematite skarn.

In the early 1980s, the increased interest in gold exploration led Homestake Australia and Endeavour Resources to enter into a joint venture with Pacific Copper and conducted regional surface sampling and shallow drilling around the old open-cut at Cadia Hill. The soil and rock chip samples taken on the eastern side of the Cadia Hill ridge detected a gold anomaly and subsequent RC drilling showed the presence of low grade gold mineralization (Wood and Holliday, 1995). However, the disappointment of not finding a large, stand-alone gold resource at Big Cadia led Homestake to pull out of the joint venture in 1986. No further exploration was carried out until Newcrest Mining Limited obtained the Cadia tenements in 1991.

With the acquisition of the Cadia property, Newcrest focused its initial investigations at Big Cadia where the potential for a shallow oxide gold resource was noted. Newcrest's review of historical exploration data and their ground verification

of previous results by regional- and district-scale mapping led to the identification of at least three prospect areas where soil and rock-chip sampling and ground magnetics were then conducted (Wood and Holliday, 1995). One rock-chip sample taken from old mine workings yielded 1.4 g/t Au. This sample of altered and copper-mineralized monzonite porphyry encouraged Newcrest geologists to consider the possibility of a large tonnage, low-grade Au–Cu resource at Cadia Hill (Wood and Holliday, 1995). Newcrest geologists then concluded that the Cadia magnetite deposits were most probably magnetite skarns associated with the monzonite porphyry and thus, a part of a porphyry-style hydrothermal alteration system. Subsequently, this led to the discovery of the Cadia Hill porphyry Au–Cu deposit in 1992.

Recognition of a preferred NW-trending orientation of mineralized veins at Cadia Hill and the delineation of an extensive halo of low-grade mineralization northwest of the deposit led to step-out drilling in both the NW and SE directions (Holliday *et al.*, 1999). The exploration drilling strategy led to more discoveries, Cadia Quarry in 1992 and Cadia East in 1994. Continued exploration on the mineralized corridor was followed-up with a regional IP survey northwest of Cadia Quarry by Newcrest Mining Limited in 1994. The survey obtained one anomaly which could not be explained by lithological contrasts and proved to be attractive because it was located on the known NW-SE corridor of mineralization (Holliday *et al.*, 1999).

. In February and March 1995, a total of nine RC percussion holes were collared and drilled down to 200 m to test the IP anomaly. The first hole, RCGRC1 intersected a significant result at 182 m: 8 m at 0.42 g/t Au and 0.53 % Cu, which proved to be a “leakage” vein some 400 m above the Ridgeway deposit (Holliday *et al.*, 1999; Holliday and Cooke, 2007). Other RC holes intersected magnetic diorite and volcanic rocks with disseminated pyrite. The recognition of hematite dusting of feldspar in the drillholes led to a coherent alteration-metal zonation pattern that implied the presence of mineralized body at depth (Holliday *et al.*, 1999). In June 1995, NC371 was drilled beneath RCGRC1 to depth of 513.6 m (Holliday *et al.*, 1999). The assay results from this hole showed increasing anomalous Cu contents at depth and significant narrow high-grade Au intercepts, which prompted Newcrest to deepen the hole down to 858.4 m. Chalcopyrite-bearing sheeted veins were then

intersected from 610 - 711 m of near-economic grades (Holliday *et al.*, 1999; Holliday and Cooke, 2007). This stretch was cut by a fault, below which narrow high-grade zones were intersected. These results were considered encouraging and Newcrest decided to drill deeper core holes around NC371 (Holliday *et al.*, 1999; Holliday and Cooke, 2007).

The siting of the discovery hole, NC498 (collared 175 m west of NC371), was made using a structural interpretation from existing holes. It was interpreted that the fault that cut the vein zone in NC371 extended westwards along the strike direction as determined from core measurements (Holliday *et al.*, 1999). Hence, NC498 was collared in November 1996, with the prediction that the vein zone would be intersected at 550 m downhole. This proved to be accurate. The hole intersected two zones of very high-grade porphyry stockwork-style mineralization: a 145 m thick zone from 598 m with average grade of 4.3 g/t Au and 1.2 % Cu; and an 84 m wide zone from 821 m with grades of 7.4 g/t Au and 1.27 % Cu. This was the discovery of the Ridgeway porphyry Au–Cu deposit (Holliday *et al.*, 1999; Holliday and Cooke, 2007).

### **1.5.1 Ridgeway Au–Cu porphyry deposit**

Newcrest embarked on an extensive campaign of deep-drilling, technical evaluation and underground development of the orebody to fully evaluate the horizontal and vertical extent of Ridgeway. As of February 2007, 643 drill holes have been drilled as part of the Ridgeway Project totalling ~254 km (Newcrest Mining Limited, 2007). The initial resource of 77 Mt averaging 1.87 g/t Au and 0.63 % Cu has been increased to 157.0 Mt at 0.80 g/t Au and 0.39 % Cu (Table 1.1). The Ridgeway deposit has been the most productive mine in the Cadia district, producing 366,520 ounces of gold and 39,938 tonnes of copper-in-concentrate in 2006 (Newcrest Mining Limited, 2006).

Ridgeway has no geological surface expression, with the top of the high-grade zone occurring some 500 m below the surface. Gold and copper sulfides at Ridgeway occur in quartz–sulfide vein stockworks and as disseminations in altered rocks. The orebody is centered on thin, subvertical, pipe-shaped mafic monzonite to

quartz monzonite intrusions and has a maximum length of ~ 200 m, a width of ~50 m, and extends for 1.7 km vertical. The highest grades occur within and around the pencil-shaped monzonite porphyries, extending laterally and vertically into the gently-dipping Ordovician volcano-sedimentary rocks.

Ridgeway is currently an underground sub-level cave mining operation. Construction and commissioning was completed in March 2002. Mining started at the top of the orebody, 500 m below the present-day surface with ore extraction progressing downwards. This type of mining method has created a surface subsidence zone (Fig. 1.4) that continues to increase in size as mining progress.



**Figure 1.4** Aerial photo showing the subsidence zone on top of the Ridgeway mine, *ca.* 2003. Photo courtesy of Newcrest Mining Limited.

In 2004, a drilling program tested the depth extension to mineralization at Ridgeway. Initial results confirmed that mineralization persists at depth in a zone named Ridgeway Deeps. The Newcrest resource definition group then focussed on exploring and defining the down-plunge extent of mineralization (Newcrest Mining Limited, 2007).

Drilling below the lowest mine development level has revealed new alteration and mineralization features. Sulfide assemblages have been found to persist with depth, but the total sulfide content diminishes coincident with a change in the host rocks from andesitic volcanoclastic breccias and conglomerates to laminated siltstone and sandstone with depth.

The Ridgeway Deeps project will extend the depth of the original Ridgeway mine by up to 0.3 km to 1.3 km below the pre-mining surface (Newcrest Mining Limited, 2006). Ridgeway Deeps will be mined by block caving methods underneath the existing Ridgeway sub-level cave. Access development work is currently ongoing and Ridgeway Deeps is expected to be in full production in 2010. With a resource of 4.1 million ounces of gold and 0.61 million tonnes of copper (Newcrest Mining Limited, 2008), this is expected to extend the life of the combined Ridgeway/Ridgeway Deeps mine until 2019.

## 1.6 Previous research

Numerous conference publications have documented Newcrest's discoveries in the Cadia district (Newcrest Mining Limited, 1993; Holliday, 1995; Wood and Holliday, 1995; Holliday *et al.*, 1999, Tedder *et al.*, 2001). These reports provide overviews of the exploration history, geological setting and also brief descriptions of the mineralization from the district. Holliday *et al.* (2002) described the different deposits found at the Cadia district and the association of alkalic (shoshonitic) magmas and Au–Cu porphyry style mineralization. The porphyry deposits of the Cadia district have been described by Wilson (2003), Wilson *et al.* (2003), Wilson *et al.* (2004), and Wilson *et al.* (2007a and b). Forster and Seccombe (2004) described the Big and Little Cadia skarns.

Various postgraduates and honours academic studies have focussed on specific deposits in the Cadia district. Bajwah (1985) suggested a submarine exhalative origin for Big Cadia. Green (1999) concluded that Big Cadia is actually a calcic-iron-copper-gold skarn. Squire (2001) documented the Forest Reef Volcanics (FRV) from the region around Cadia and provided an interpretation of the volcanic facies architecture. Harper (2000) described the alteration and mineralization in and around the Ridgeway porphyry Au–Cu deposit and Close (2000) documented its geophysical properties. Reynolds (2007) characterized the nature of hydrothermal alteration in the distal parts of Ridgeway. The most comprehensive district-scale overview of ore deposits at Cadia, describing the geology, intrusive and hydrothermal paragenesis, was provided by the PhD study of Wilson (2003). Other studies from the district include an evaluation of lithostratigraphy, alteration and geochemistry of the Cadia East Au–Cu deposit (Kitto, 2005), and an appraisal of the late-stage phyllic alteration and late faults in Cadia East (Finn, 2006). Washburn (2008) described the post-mineral deformation of the Silurian cover sequence in the district. Nathan Fox is currently undertaking a PhD study at CODES on the controls on alteration and mineralization of the Cadia East deposit.

Several internal studies and consultant reports have been undertaken at Cadia. These include petrological studies on core samples from the different deposits (Mason 2001; 2002; 2003). An initial investigation of the structural geology of

Ridgeway was conducted by Marjoribanks (2005). Tedder (2001) described the setting and characteristics of the Cadia Au–Cu deposits and presented an exploration model for the district.

Initial investigation of the presence of the Fe-rich magmatic volatiles in the form of magnetite–quartz comb-layered textures at Ridgeway was presented in Harris *et al.* (2006). Recent research results on the volcanic stratigraphy and architecture of rocks at Cadia and the evolution of the porphyry deposits in the Cadia Valley have been discussed in Harris *et al.* (2009a to e). The characteristics of alkalic porphyry Au–Cu deposits of the Macquarie Arc were summarized in Cooke *et al.* (2006, 2007, 2009).

---

# Chapter 2: Regional Geology

---

## 2.1 Introduction

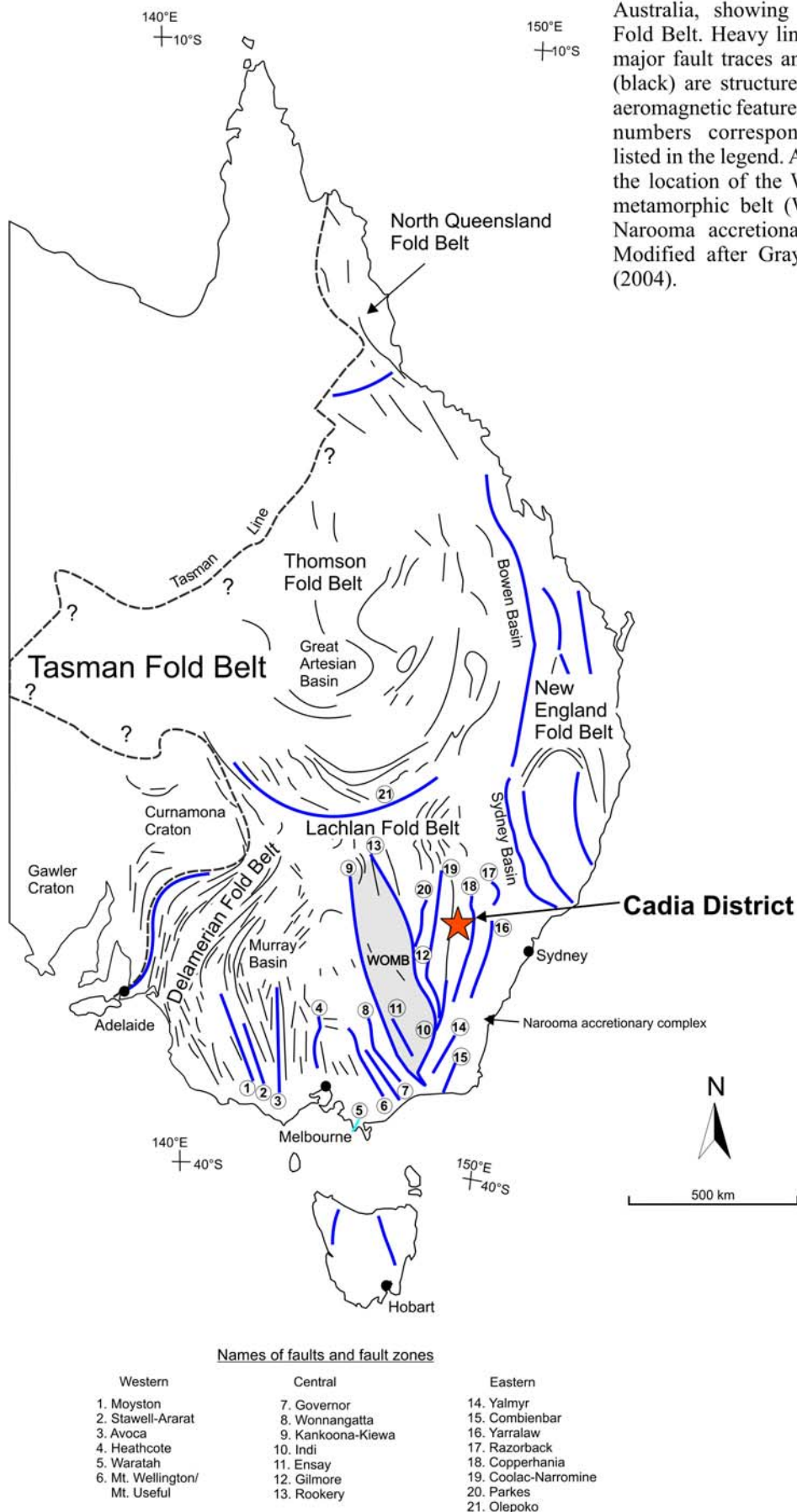
This chapter presents an overview of the regional tectonic setting and geological history of the Cadia district. This includes an overview of the tectonic history of the Lachlan Orogen, specifically of the Macquarie Arc, a major component of the eastern subprovince of the orogen. Reviews of the major structural features and of the different ore deposits in the Macquarie Arc are used to provide a framework for subsequent discussions of the key controls on formation of the Ridgeway deposit.

## 2.2 Tasman Fold Belt

The Cadia district, which hosts porphyry-style Au–Cu deposits and Fe–Cu–Au skarn deposits, is located in the Lachlan Fold Belt of eastern Australia (Fig. 2.1). The Lachlan Fold Belt is one of the major orogenic belts that comprise the Tasman Fold Belt or Tasmanides (Fig. 2.1; Glen, 2005). The Tasmanides resulted from Paleozoic deformational events of accretion and subduction along the eastern margin of Gondwana (Glen, 2005).

The Tasman Fold Belt (Scheibner, 1978), also known as the Tasman Province (Rutland, 1976), is a collection of orogenic belts amalgamated to eastern Australia since the break-up of the Mesoproterozoic supercontinent, Rodinia, and the subsequent establishment of convergent margin orogenic belts along the eastern margin of Gondwana (Glen, 2005). The western edge of the Tasman Fold Belt is bounded by the Tasman Line, a principal suture that crosses the Australian continent from north to south, which separates the Australian craton on the west from younger Paleozoic fold belts on the east (Fig. 2.1).





The Tasman Fold Belt, which makes up one-third of eastern Australia, constitutes five orogenic belts that are progressively younger from west to east: the Delamerian, Thomson, Lachlan, North Queensland, and New England fold belts (Fig. 2.1). The ages of the different rock types and deformation events provided the basis for subdivision of the different orogenic belts (Glen, 2005). The boundaries of these orogens are generally not exposed, mostly being covered by younger rocks, such as the Great Australian Basin in the north and the Murray Basin in the south-west (Fig. 2.1). Other parts of the fold belts are partially covered by thin Tertiary to Holocene sediments and volcanics (Scheibner, 1993).

The fold belts that comprise the Tasman Orogen differ in the timing of their tectonic evolution, from their pre-cratonic stages of turbiditic sedimentation, their orogenic phases characterised by igneous rocks, through a transitional tectonic stage which features molassic sedimentation, bimodal igneous rocks and post-kinematic intrusives, followed by a final cratonic stage and platform sedimentation (Scheibner, 1993).

### **2.3 Lachlan Fold Belt (Lachlan Orogen)**

The Lachlan Fold Belt (also called the Lachlan Orogen and Lachlan terrane) is approximately 700 km wide and 1000 km long (Gray, 1997) and has been a subject of debate for decades. It has the most enigmatic and widely disputed evolutionary history of any component of the eastern margin of Australia (Figs. 2.1 and 2.2). Bounded to the west by the Delamerian Orogen and to the east by the Sydney Basin (Fig. 2.1), the Lachlan Fold Belt (LFB) preserves the most complete, accessible and least reworked rock Palaeozoic rock package of the Tasman Fold Belt.

The LFB is composed of three separate and distinct subduction complexes, each with differences in rock types, metamorphic grades, structural histories and geologic evolution (Glen, 1997). The western and central subprovinces are dominated by metamorphosed quartz and shale turbidite sequences, while the eastern subprovince consists of quartz and shale turbidite sequences as well as mafic volcanic, volcanoclastic and carbonate rocks (Fig. 2.2). Glen (1992) divided the LFB into four subprovinces, structurally separated by major faults. The western

subprovince of Gray (1997) was further segregated into southwestern and western subprovinces by Glen (2005), based on geophysical data showing differences in the geology from north to south.

The western subprovince is dominated by a folded turbidite succession deposited in deep submarine fans composed of quartz-rich sandstone and black shales from Ordovician to Early Carboniferous. The turbidites are underlain by Cambrian volcanic rocks of oceanic affinities (Gray, 1997; Fergusson and Coney 1992; Fig. 2.2). The western subprovince is restricted by the Kiewa Fault to the east and the Mount Wellington Fault to the west (Fig. 2.1). The southwestern subprovince is bounded to the west by the Avoca Fault, to the east by the Mount Wellington Fault, and is closed off to the north by Cambrian greenstones (Glen, 1992). This subprovince is a fold and thrust belt, which comprises the western Bendigo-Ballarat Zone and eastern Melbourne Zone (Fig. 2.2).

The central subprovince is dominated by complexly deformed Ordovician quartz-rich turbidites in the west, and late Silurian turbidites in the east (Fig. 2.2). This region is characterized by the fault-bounded NNW-trending Wagga-Omeo Metamorphic Belt (WOMB; Gray, 1997; Gray *et al.*, 2002; Figs. 2.1 and 2.2). The WOMB has a strike length of almost 500 km, and a width of 150 km (Coney *et al.*, 1990). This metamorphic complex is centered on various deformed N-NW trending elongate syntectonic Silurian granite bodies (Hough *et al.*, 2007).

The eastern subprovince of the LFB includes the Macquarie Arc of Glen *et al.* (2007). It lacks the deep water turbidite quartz-rich and extensive black shale sequences of the western subprovince. Instead, it consists of shallow water feldspathic clastic rocks intercalated with mafic volcanic, volcanoclastic and carbonate rocks (Foster and Gray, 2000; Fig. 2.2). The rocks range from Early Ordovician to Lower Carboniferous, and young towards the east.

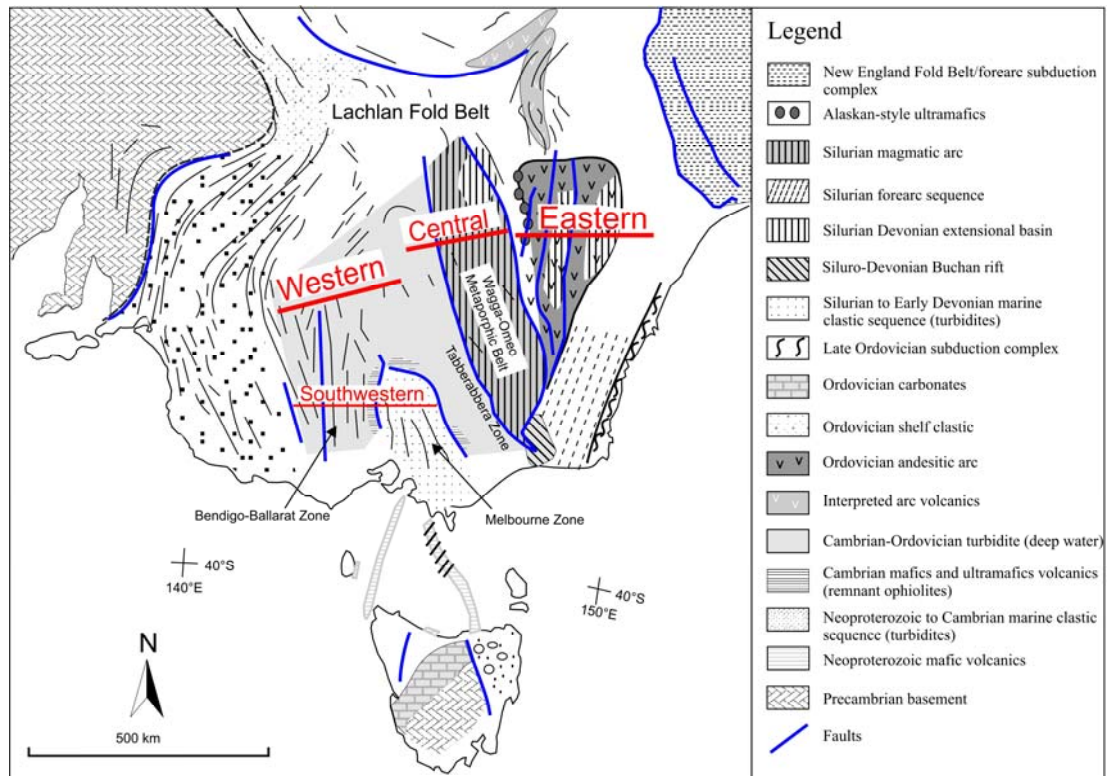


**Figure 2.2** Lachlan Fold Belt subprovinces showing the major tectonic elements. Modified from Glen (2005) and Gray and Foster (2004).

Various models have been put forward to explain the tectonic evolution of the Tasman Fold Belt, particularly the LFB. These theories include strike-slip tectonism as proposed by Vandenberg *et al.* (2000) with eastern and central subprovinces moving dextrally to the south-southeast. In contrast, Glen (2005) proposed a similar theory but employed the opposite sense of terrane movement, where the southwestern subprovince terrane was shunted northwards. The multiple subduction zone model has been proposed by Soesoo *et al.* (1997), Foster and Gray (2000), and Fergusson (2003). Glen (2005) argued against a multiple subduction zone scenario by suggesting that subduction zones require special conditions to form, and are not easily turned on and off. The transpressional strike-slip model of Glen *et al.* (2007) is based primarily on palaeogeographical reconstructions, but there is a lack of kinematic evidence for hundreds of kilometers of strike-slip movement.

## 2.4 Deformation in the Lachlan Fold Belt

The LFB has undergone a long, punctuated history of volcanism, plutonism, metamorphism and deformation. The main orogenic events commenced at 440 Ma and ended by 340 Ma. The recognition of unconformities and major changes in sedimentary facies over time has helped to establish an orogenic framework for the LFB (Andrews, 1938 and Browne, 1957; in Gray *et al.*, 1997). However, Gray *et al.* (1997) argued that unconformities reflect more local tectonic instability and do not define discrete fold belt-wide orogenic pulses across the LFB.

Several orogenies have affected various parts of the LFB. Some events were localized and strongly time-transgressive. Overall, there has been a complex history of deformation during the Ordovician, Silurian, and Devonian (Foster and Gray, 2000). Recent studies suggested that Ar–Ar dating of metamorphic mica in the low-grade meta-sedimentary rocks can give precise estimates on the timing of cleavage formation, and thus record significant deformation events within the LFB (Foster *et al.*, 1999). These workers argued that three major events affected the fold belt – one at ~440 - 430 Ma (Benambran Orogeny), one at ~390 - 380 Ma (Tabberabberan Orogeny), and one at ~360 - 340 Ma (Kanimblan Orogeny).

The Benambran Orogeny caused latest Ordovician to earliest Silurian deformation in the LFB (Glen *et al.*, 2007c). It produced unconformities, diastems and different structural styles and changes in sedimentation patterns (Gray *et al.*, 1997). Important characteristics of the Benambran event are the early E-trending folds and a well-defined N-NW-trending structural grain. Some of the syn-orogenic intrusive rocks are strongly foliated and have high-grade metamorphic aureoles. The series of anticlinorial and synclinorial zones, bounded by E- and W-dipping reverse faults, account for up to 33% tectonic shortening of the eastern subprovince (Gray, 1997).

In the eastern subprovince of the LFB, the Benambran Orogeny deformation records the accretion of the intra-oceanic Macquarie Arc to the Gondawana Plate (Glen *et al.*, 2007c). The Benambran Orogeny caused at least two phases of exhumation-deformations with associated metamorphic and intrusive events,

separated by a basin-forming event. The first phase began at ~443 Ma (Phase I) and the second again at ~ 430 Ma (Phase II; Glen *et al.*, 2007c).

Phase I deformation corresponds to underthrusting and strike-slip faulting, which caused metamorphism and uplift in most parts of the Macquarie Arc (Fig. 2.5F). Oblique compression produced E-W and N-S shortening, with the latter causing the Bega Terrane to be thrust over the Rockley-Gulgong Volcanic Belt (RGVB; Glen *et al.*, 2007c; Fig. 2.5F). Fold and thrust imbrications were more intense in the Girilambone-Wagga Terrane (Fig. 2.5F). Phase I deformation was followed by relaxation and extension, leading to the generation of sedimentary basins such as the Yalmy Basin (Fig. 2.5G). Phase I deformation and subsequent extension were broadly coeval with the emplacement of mineralized monzonitic intrusions at shallow (1 - 3 km) depths in the Cadia and Northparkes districts (Glen *et al.*, 2007c). Phase II deformation affected all parts of the Macquarie Arc and corresponds to underthrusting of the Yalmy Group and emplacement of granitic melts (Glen *et al.*, 2007c; Fig. 2.5H).

. The Tabberabberan Orogeny caused widespread deformation in the LFB from the Early to Middle Devonian (384 - 375 Ma). It resulted in uplift, thrusting and folding of the turbidite successions across the fold belt. The Tabberabberan Orogeny produced the most regionally extensive unconformity separating folded and cleaved Early Devonian rocks and shallow-dipping Late Devonian red beds (Gray *et al.*, 1997). The Tabberabberan event caused a change from marine to terrestrial sedimentation (Rutland, 1976; Cas, 1983; Gray *et al.*, 1997).

The last major Paleozoic deformation event to affect the LFB was the Kanimblan Orogeny in the Early Carboniferous (360 - 340 Ma; VandenBerg, 1999; Gray *et al.*, 1997). It produced an angular unconformity between the flat-lying Permian strata of the Sydney Basin and the underlying folded Late Devonian rocks. The Late Devonian-Early Carboniferous cover sequences in the western and central subprovinces were folded into broad and open folds at this time. The localized development of tight folds was associated with reactivation of older faults (Gray *et al.*, 1997).

Structural studies and Ar–Ar geochronological investigations across the LFB have concluded that the orogen developed by stepwise accretion of deformed oceanic successions (Gray *et al.*, 2002). The ~40 - 45 km-thick crust of the LFB is a result of Late Ordovician-Devonian structural thickening (~300 %) and shortening (~75 %; Gray *et al.*, 2002) and accretionary subduction processes.

## **2.5 Macquarie Arc**

The Macquarie Arc is part of the eastern subprovince of the LFB and hosts porphyry Au–Cu deposits in central western NSW, including the Cadia district (Fig. 2.3). It consists mainly of subduction-related Ordovician intermediate and mafic volcanic, volcanoclastic and associated intrusive rocks (Glen *et al.*, 2003). The Macquarie Arc was accreted to Gondwana in the Early Silurian, and underwent rifting and burial in the Middle to Late Silurian.

The Macquarie Arc crops out in four structural belts, namely, the western (Junee-Narromine), the central (Molong), the eastern (Rockley-Gulgong) Belt, and southern (Kiandra) volcanic belts (Fig. 2.3). The evolution of these belts has been widely debated, but the most generally accepted scenario is that these were formed by rifting and dismemberment of a single arc, the Macquarie Arc, which developed along the boundary between the Australian and proto-Pacific plates during the Ordovician and was subsequently dismembered during the Silurian (Glen *et al.*, 2003; Glen *et al.*, 2007d).

Figure 2.4 summarizes the evolution of the Macquarie Arc showing the major lithostratigraphic units and the different magmatic phases. An entirely intra-oceanic setting is envisaged for the Macquarie Arc (Crawford *et al.*, 2007). It developed through four phases of arc-type magmatism separated by either hiatuses in volcanism that in at least one case coincided with a period of limestone deposition (Table 2.1; Fig. 2.4). Magmatism commenced in the Early Ordovician and culminated in the Late Ordovician to Early Silurian (Crawford *et al.*, 2007). Geochemical and paleontological data indicate that the Macquarie Arc evolved episodically over ~50 million years (Crawford *et al.*, 2007). The relationships between the emplacement



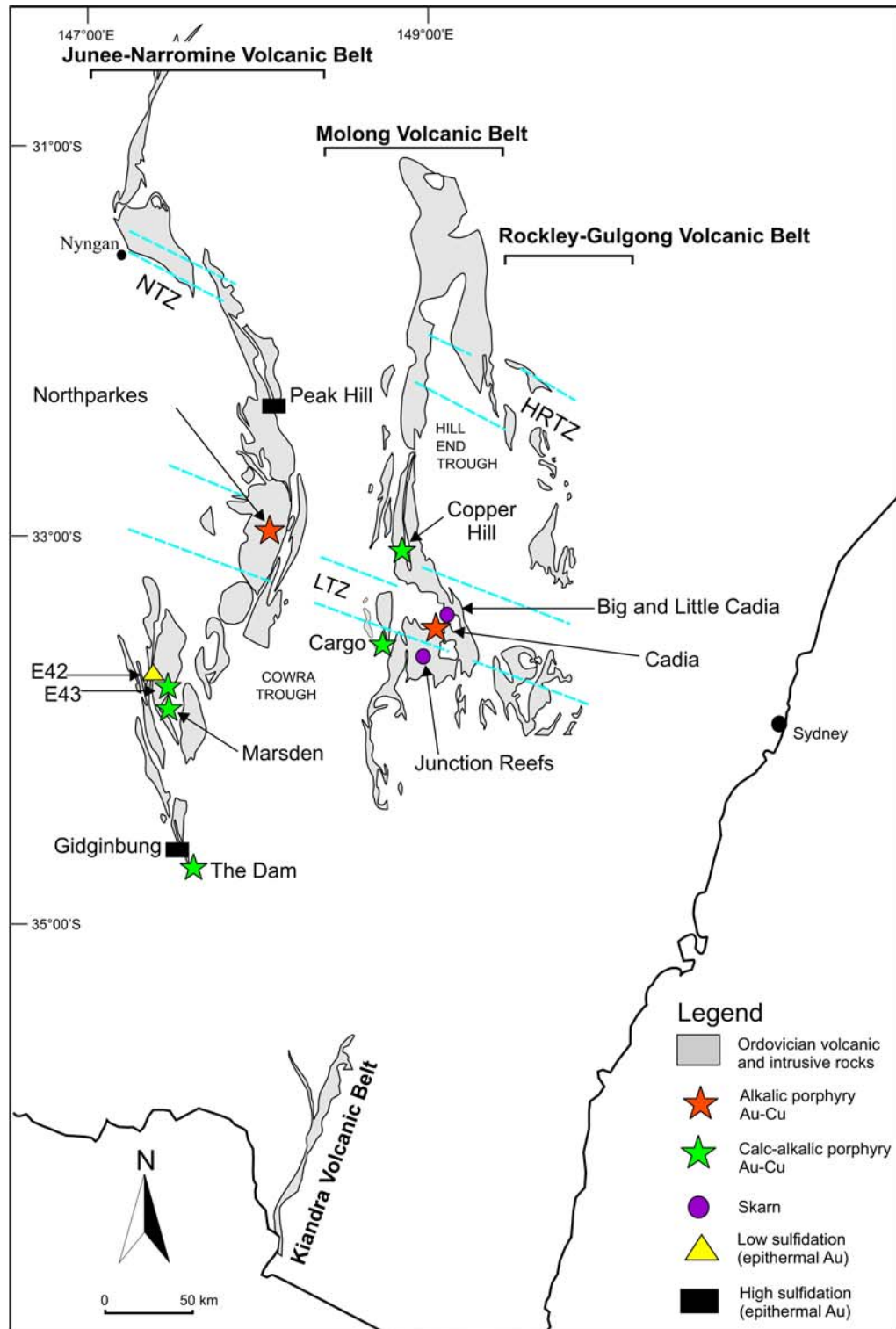


**Figure 2.3** The four main Ordovician volcanic belts comprising the Macquarie Arc showing the location of the different styles of mineralization. Also shown is the Lachlan transverse zone (LTZ) of Glen and Wyborn (1997), Nyngan transverse zone (NTZ) of Hilyard *et al.* (1996) and extension of Hunter River transverse zone (HRTZ). Data for the different deposits are listed in Table 2.2. Modified after Holliday *et al.* (2002) and Glen *et al.* (2007a).



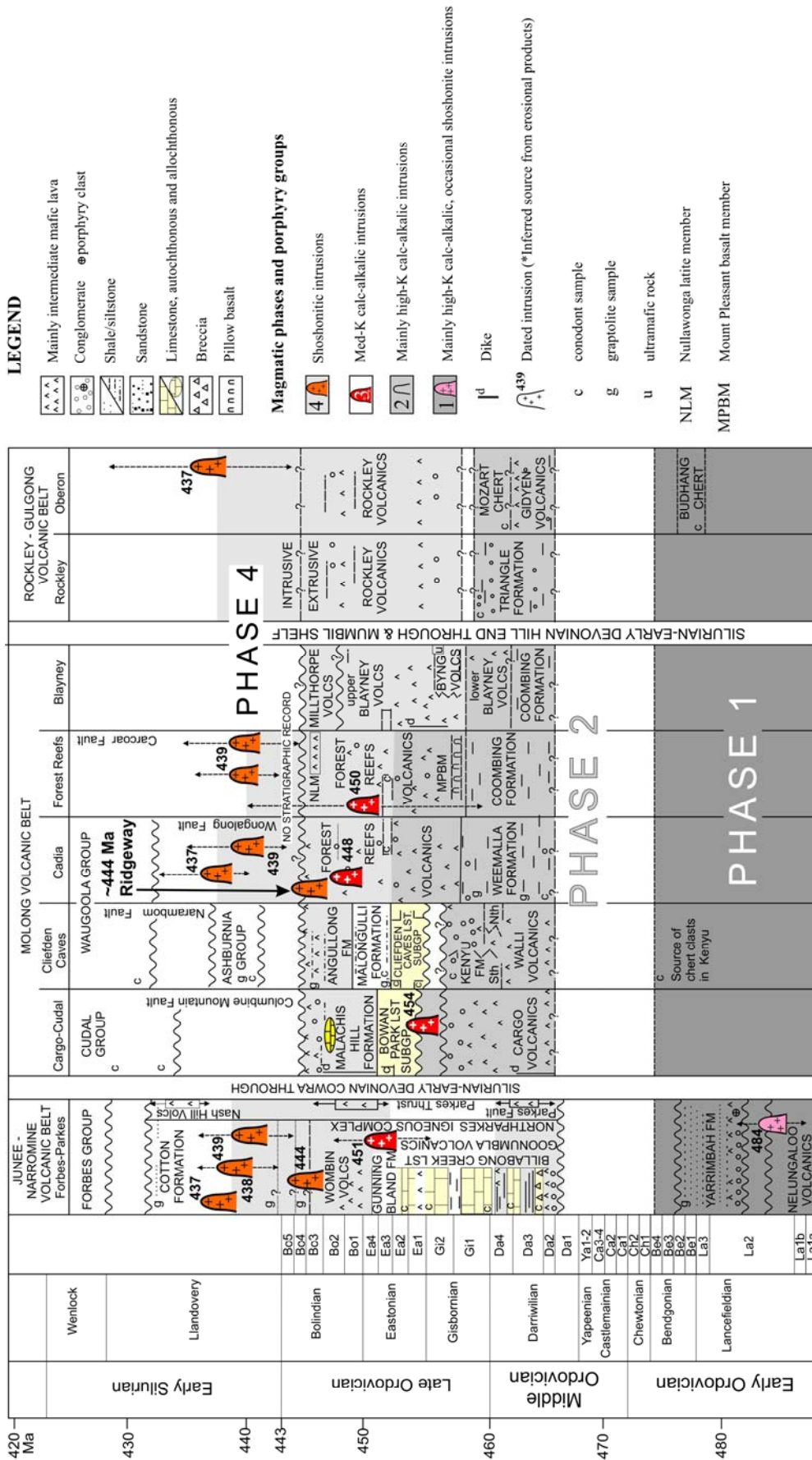


**Figure 2.4** Macquarie Arc showing the magmatic affinities of the major lithostratigraphic units and the different magmatic phases (1 - 4) in the Ordovician to early Silurian history of the arc. Modified from Percival and Glen (2007), Crawford *et al.* (2007) and Glen *et al.* (2007a). Note that Ridgeway has been re-classified to Phase 4 based on new age constraints.

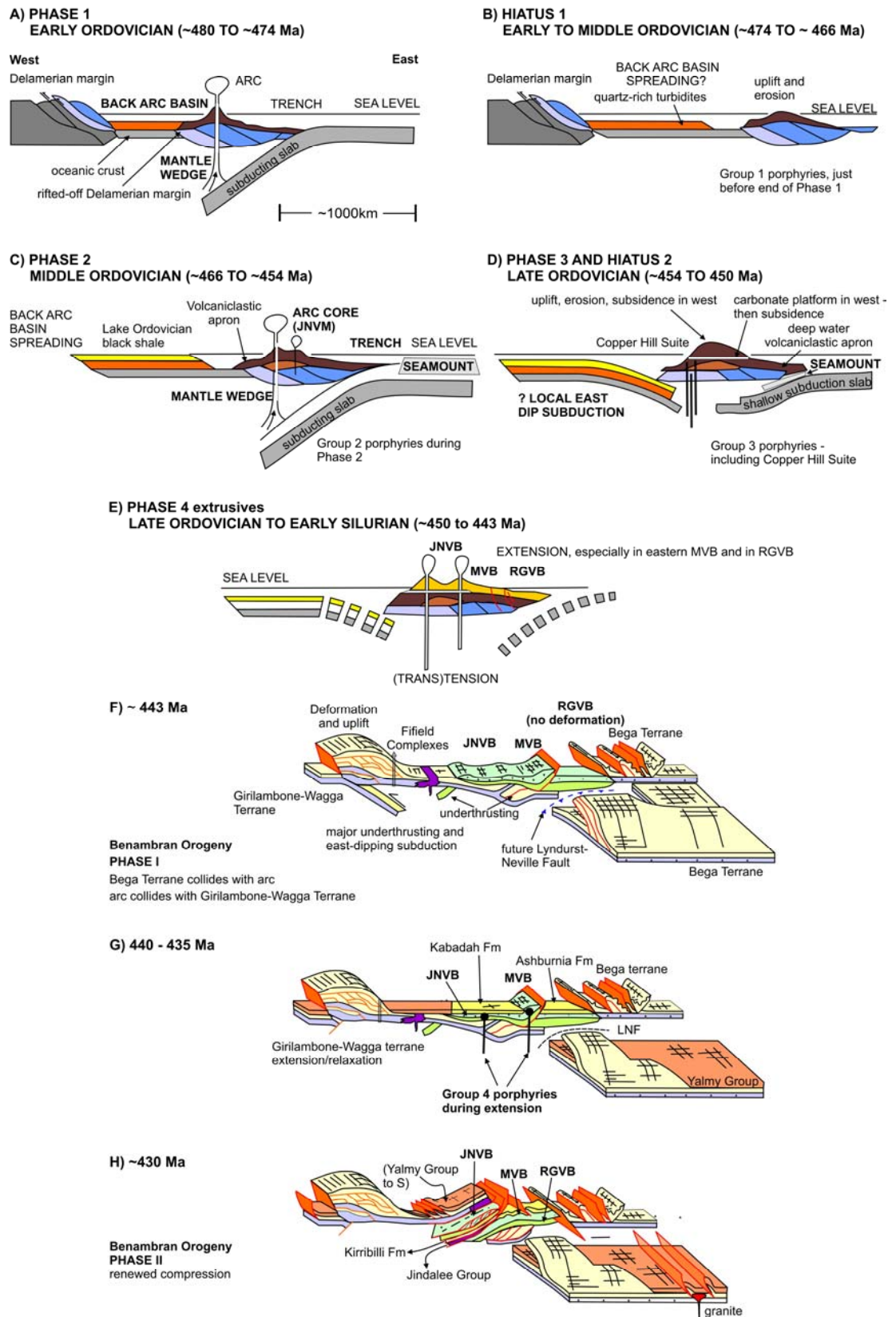


**Figure 2.5** Diagram showing the tectonic evolution of the Macquarie Arc and the different porphyry groups. Modified from Crawford *et al.* (2007) and Glen *et al.* (2007a).

**Table 2.1** Summary of porphyry groups emplaced into the Macquarie Arc. Modified from Glen *et al.* (2007a). Note that Ridgeway has been reclassified as belonging to Group 4 porphyry based on new age constraints.

Porphyry Group	Age (Ma)	Tectonic Event	Host Unit	Chemistry	Examples	Tectonic Setting	Remarks
Group 4	444-435	After end of arc volcanism	Intruded tilted Phase 4 rocks	Shoshonite	Northparkes, Cadia, Ridgeway, Swatchfield	Syn-accretionary	Mineralized
Group 3	454-450 (some extend to 441 Ma)	Coeval with hiatus 2, after the Middle Ordovician cessation of volcanism in the western part of the arc	Phase 2 volcanics and inferred Phase 3 volcanics inferred to have been all eroded	Calc-alkaline (Phase 3) and shoshonite	Copper Hill Complex	Pre-accretionary	Mineralized
Group 2	465-453	Phase 2 magmatism, pre-hiatus 2; and also includes granodiorite at beginning of Phase 2 magmatism	Cowal igneous complex, Narramine igneous complex, Forest Reefs Volcanics	Includes shoshonites and Copper Hill Suites	Copper Hill Complex, granodiorite at E39 (Cowal igneous complex)	Pre-accretionary	Mineralized
Group 1	481	End of Phase 1 magmatism, pre-hiatus 1	Intruded Nellungaloo Volcanics, clasts in overlying unit	High K calc-alkaline to shoshonite	-	Pre-accretionary	-

ages of porphyries and evolution of the Macquarie Arc is shown as schematic diagrams in Figure 2.5.

The four phases of volcanism in the Macquarie Arc are related to distinct groups of porphyritic intrusions that vary from monzodiorite-diorite through monzonite-granodiorite compositions (Glen *et al.*, 2007a; Figs. 2.4 and 2.5, Table 2.1).

The first phase of volcanism (Phase 1) occurred in the Early Ordovician (~490 - 472 Ma; Fig. 2.4). Group 1 porphyries (~484 Ma) were emplaced at the end of the first pulse of volcanic activity in the Junee-Narramine Volcanic Belt (Fig. 2.5A). These intrusive rocks have high-K calc-alkaline composition and have been inferred to be comagmatic with the volcanic rocks (Crawford *et al.*, 2007; Table 2.1; Fig. 2.4). Phase 1 magmatism occurred in an intra-oceanic arc above a W-dipping subduction zone (Glen *et al.*, 2007a; Fig. 2.5A). The emplacement of Group 1 porphyries was followed by a ~9 my hiatus around 470 Ma, between Phase 1 and Phase 2 (Figs. 2.4 and 2.5B). This major hiatus at the end of Phase 1 is interpreted to relate to the cessation of arc magmatism as a consequence of back-arc spreading and/or flat subduction (Glen *et al.*, 2007a) and was characterized by uplift and erosion (Percival and Glen, 2007; Fig. 2.5A).

The second phase of volcanism (Phase 2) occurred during the Middle Ordovician (564 to ~455 Ma), with another ~6.5 my hiatus around 452 Ma (Figs. 2.4 and 2.5C). Magmatic units were emplaced before regional uplift and limestone deposition (Fig. 2.4). Group 2 porphyries were emplaced in the Junee-Narromine Volcanic Belt around ~464 Ma (Group 2A). A second pulse of volcanism was then followed by another episode of intrusive activity around ~455 Ma (Group 2B). Group 2 intrusive rocks range from monzogabbros to monzonites, with high-K magmatic compositions that vary slightly from the Group 1 porphyries (Table 2.1). The major hiatus at the end of Phase 2 is attributed to subduction of a buoyant seamount or inactive ridge and caused a shallowing of subduction which temporarily halted arc volcanism (Glen *et al.*, 1998; Fig. 2.5C).

The third phase of volcanism (Phase 3) occurred during the Late Ordovician (~450 - 455 Ma) and is represented by a widespread but relatively small volume magmatic event, dominated by shallow intrusions found in all three major volcanic belts (Figs. 2.4 and 2.5D; Crawford *et al.*, 2007). Volcanic activity includes the basaltic andesite sequence with subordinate evolved andesites of the Cargo Volcanics (Crawford *et al.*, 2007; Simpson *et al.*, 2007; Fig. 2.4) and the Forest Reefs Volcanics (FRV; ~452 Ma to 455 Ma; Harris *et al.*, 2009c). Phase 3 magmatic activity includes the distinctive medium-K calc-alkaline Copper Hill Suite (Group 3; Crawford *et al.*, 2007) and is best represented by the dominantly dacitic Copper Hill pluton, and diorites to granodiorites in the Cowal and Narromine Igneous Complexes (Glen *et al.*, 2007a; Table 2.1; Fig. 2.4). The main episode of Phase 3 coincided with a ~5 my hiatus in the western part of the arc, associated with regional uplift, erosion and deposition of a widespread carbonate platform (Percival and Glen, 2007; Glen *et al.*, 2007a; Fig. 2.5D).

The most significant phase of magmatic activity (Phase 4) commenced in the Late Ordovician to Early Silurian (~450 - 439 Ma) and is represented only by intrusive activity (Group 4, Table 2.1; Figs. 2.4 and 2.5E). Shoshonitic monzodiorite-monzonite intrusions are inferred to be comagmatic with most of the Late Ordovician volcanics in the Macquarie Arc (Glen *et al.*, 2007). However, geochronological analyses of the Ordovician volcano-sedimentary rocks and igneous intrusions reveals

that there was no volcanism coeval with ore formation in the Cadia district (Wilson *et al.*, 2007; Harris *et al.*, 2009c).

Phase 4 magmatic activity, closely associated with much of the major porphyry Cu–Au mineralization in the Macquarie Arc, is represented by dominantly shoshonitic Group 4 porphyries (Table 2.1; Glen *et al.*, 2007a). Group 4 porphyries are syn-accretionary and were emplaced at shallow depths (2 - 3 km) into tilted and deformed volcanic and volcanoclastic sequences during phase I deformation of the Benambran Orogeny (section 2.4; Fig. 2.5F; Lickfold *et al.*, 2003, 2007; Glen *et al.*, 2007a). Mineralized Group 4 porphyry intrusions are hosts to the Au–Cu porphyry deposits at Ridgeway and Northparkes, and were emplaced between 444 and 437 Ma (Lickfold *et al.*, 2007; Wilson *et al.*, 2007; Harris *et al.*, 2009c; Fig. 2.4; Table 2.1). Glen *et al.* (2007a) suggested that these mineralized porphyries were emplaced after arc volcanism had shut down, and after the initial stages of accretion of the Macquarie Arc and the Wagga Basin to the Gondwana Plate (Figs. 2.5F and G). Arc extension and dismemberment occurred ~438 Ma in the latest Ordovician (Crawford *et al.*, 2007).

## **2.6 Crustal-scale structures and metallogeny of the Macquarie Arc**

The locations of many large ore deposits have been linked to major crustal-scale sutures (Glen and Walshe, 1998; Richards *et al.*, 1994; Kerrich *et al.*, 2000; Glen and Walshe, 2005; Cooke *et al.*, 2005). Complex histories involving episodes of contraction, extension, and strike-slip movement have been documented for the Tasman Fold Belt System. Walshe *et al.* (1995) noted that major N-trending fault systems are the dominant regional-scale features in the Tasman Fold Belt (Fig. 2.6). Most of these N-trending faults are typically from 300 to 500 km in length. They are inferred to be steeply dipping at the surface, but have shallow dips where they merge with mid-crustal detachments. The dominant structure in the North Queensland fold belt is the N-trending Palmerville fault (Fig. 2.6). Other major N-trending structures include the Nebine arch in the Thomson fold belt (Moore, 1986 in Walshe *et al.*, 1995; Fig. 2.6), the Beryl anticline system, and the Canaway fault-ridge, which is marked by a gravity high similar to structures in the LFB (Walshe *et al.*, 1995; Fig. 2.6).

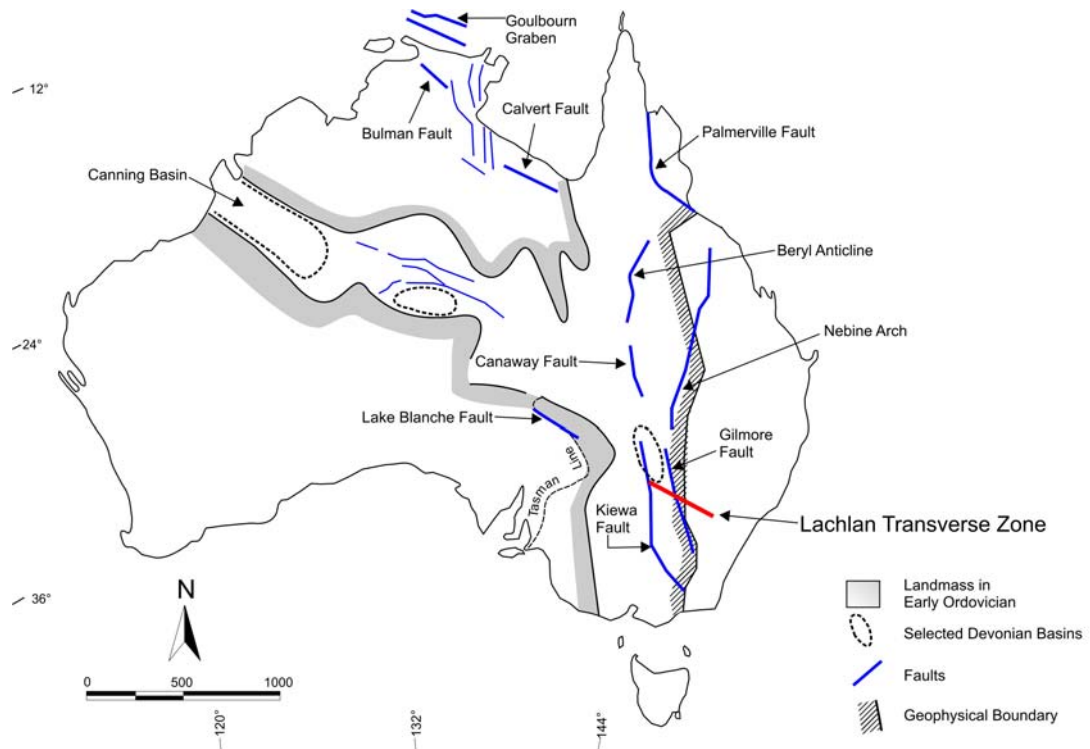


**Figure 2.6** Major crustal-scale north- and west-northwesterly trending structures in the Tasman Fold Belt System. Modified from Walshe *et al.* (1995).

Aside from major N-trending structures, there are other major structural features in the Paleozoic Tasman Fold Belt System that have a WNW trend possibly inherited from the Proterozoic basement (Walshe *et al.*, 1995). These include the Proterozoic Calvert and Bulman Faults, the Palaeozoic Canning Basin, and the Lake Blanche Fault, which defines the northern limit of the Adelaide geosyncline (Plumb *et al.*, 1990; Parkin, 1969 in Walshe *et al.*, 1995; Fig 2.6). At a regional scale, Walshe *et al.* (1995) inferred that the interplay of NW-trending lineaments with the more obvious N-trending faults controlled the location of some major mineral provinces in the Tasman Fold Belt.

### 2.6.1 Lachlan Transverse Zone

The potential importance of W- to NW-trending lineaments and associated structures in NSW was first highlighted by Hill (1956) and Scheibner and Stevens (1974), where they described a 40 x 50 km wide zone of linear features comprising of a series of faults and fractures. Glen and Walshe (1998) named this feature the ‘Lachlan Transverse Zone’ (LTZ). The LTZ (Fig. 2.3; Fig. 2.5) is interpreted to be a



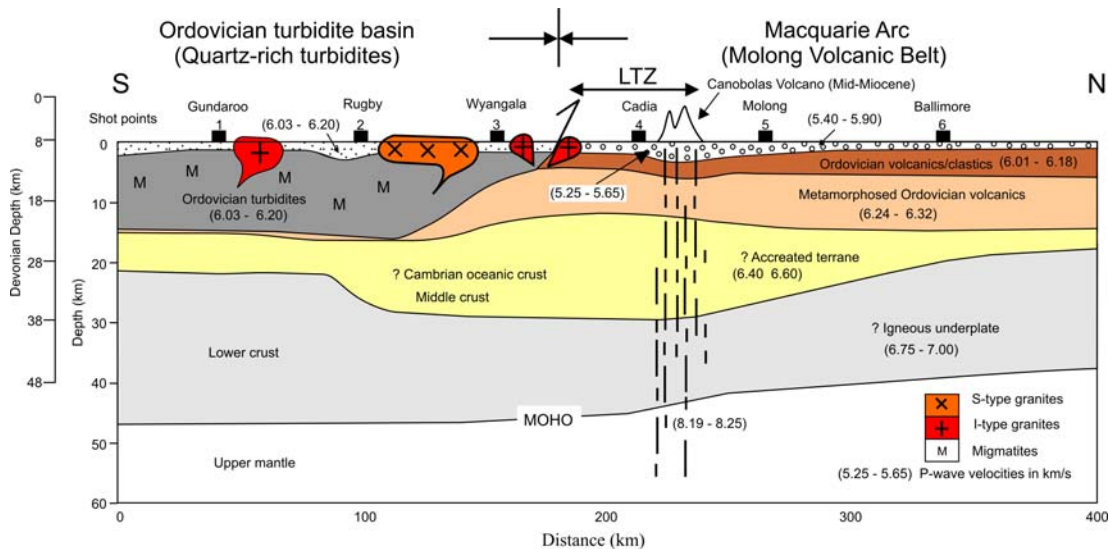


**Figure 2.7** Interpreted crustal architecture and geological features and the seismic crustal-velocity model, showing changes in thickness, spatially, below the surface location of the LTZ. Also shown is the possible depth scale during Devonian times. Modified from Finlayson *et al.* (2002).

deformation zone that contains a variety of rock types and is thought to have been a fundamental crustal-scale structure that localized volcanism in the Macquarie Arc (Glen and Wyborn, 1997; Holliday *et al.*, 2003; Glen *et al.*, 2007a).

Seismic imaging of this zone has shown significant differences in crustal architecture between the upper to middle crustal rock units north and south of the southern margin of the LTZ (Finlayson *et al.*, 2002; Fig. 2.7). Refraction data indicate significant changes in crustal velocities across Molong Volcanic Belt (Finlayson *et al.*, 2002; Fig. 2.7). The near-surface rocks between the Cadia and Molong shot points (between points 4 and 5; Fig. 2.7) produced P-waves velocities significantly lower than the other shot points (i.e., between Molong and Ballimore) that coincide with the Mid-Miocene Canobolas Volcano and the LTZ (Fig. 2.7). Tentative interpretation suggested that there is some indication of lower crustal thinning under the LTZ at greater depths (20 - 30 km; Finlayson *et al.*, 2002). Glen *et al.* (1998) interpreted the LTZ to be the fossilized remnant of seamount subduction, which temporarily interrupted low-angle W-directed subduction during the Mid-Late Ordovician.

Aside from the LTZ, other prominent NW-trending structural corridors that intersect the Macquarie Arc include the Nyngan Transverse Zone (NTZ; Hilyard *et al.*, 1996) and the Hunter River Transverse Zone (HRTZ; Glen and Beckett, 1997;

Fig. 2.3). The localization of the Cadia and Northparkes porphyry Au–Cu districts along the LTZ suggests that the interaction of NNW-trending structures with N-trending structures may have controlled the localization of Ordovician volcanic sequences and their associated Au–Cu deposits (Scheibner and Stevens, 1974; Walshe *et al.*, 1995; Holliday *et al.*, 2002; Glen *et al.*, 2007; Fig. 2.3).

## **2.7 Metallogeny in the Macquarie Arc**

Porphyry Au–Cu deposits worldwide conform to a generalised descriptive model involving their generation at convergent plate boundaries during or immediately following the subduction of oceanic lithosphere (Sillitoe, 2000, 2010). Most deposits are associated with subduction-related magmatic arcs including those in Chile, Peru and the Philippines (Sillitoe, 1998; Camus, 2002). Elsewhere, the back-arc setting above the downdip margins of shallowly dipping lithospheric slabs is responsible for the gold-rich Bingham and Bajo de Alumbrera deposits (Sillitoe, 2000). Across the LFB, however, several distinct metallogenic associations are consistent with an accretion-subduction setting (Cooke *et al.*, 2007; Fig. 2.5), and ore-forming processes are likely to have been similar to those responsible for the formation of other circum-Pacific porphyry Cu–Au systems (Sillitoe, 1998). These commonalities have implications for the assessment of fertility and overall exploration potential of the Macquarie Arc.

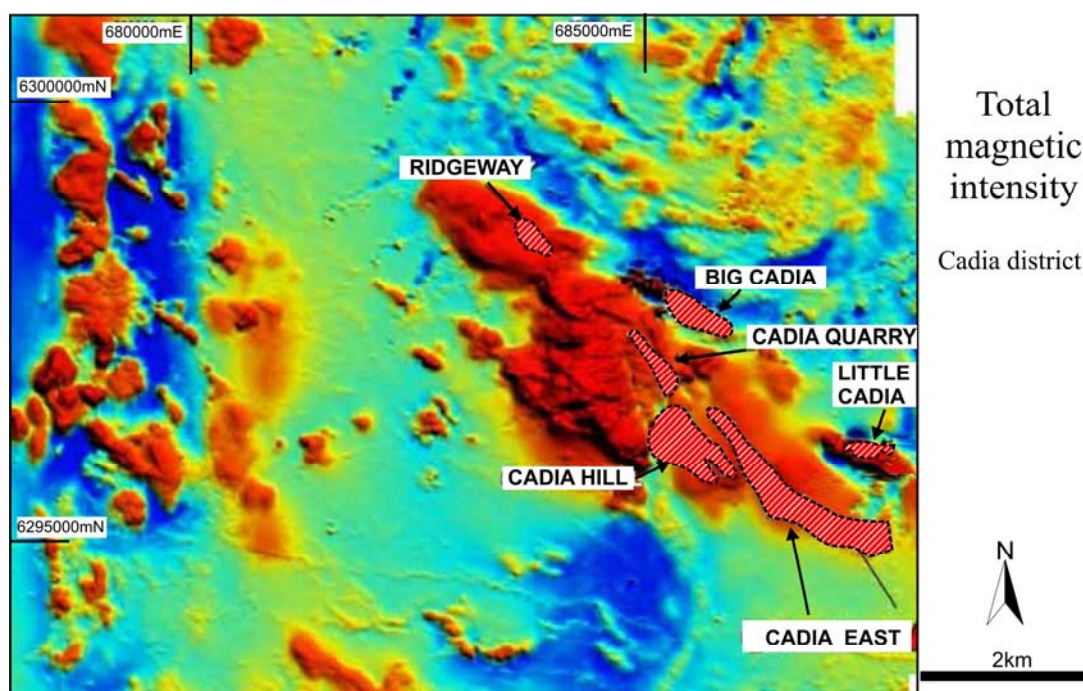
The Late Ordovician to early Silurian Macquarie Arc of the Lachlan Orogen is Australia's only economic porphyry Au–Cu province. The Macquarie Arc is a well-endowed metallogenic province that hosts six active mines with several deposits at the feasibility stage and a number of exploration prospects (Table 2.2). The metallogeny of the Macquarie Arc is characterized by alkalic and calc-alkalic porphyry Au–Cu, skarn, carbonate-base metal epithermal gold, and high sulfidation Au–(Cu) deposits (Cooke *et al.*, 2007; Table 2.2; Fig. 2.3). Significant porphyry Au–Cu mineralization is associated with Ordovician to Early Silurian intrusions in the Cadia district, Northparkes and at Cowal. Other significant mineralized systems include Junction Reefs, Cargo and Copper Hill (Fig. 2.3; Table 2.2).



**Table 2.2** Reserves/resources for the Ordovician gold-copper deposits of the Macquarie Arc.

District / Deposit	Mt	Au (g/t)	Cu (%)	Reference
<b>Alkalic porphyry deposits</b>				
Cadia district	2445.0	0.52	0.28	Table 1.1
Northparkes district	131.7	0.51	1.12	Cooke <i>et al.</i> (2007)
<b>Calc-alkalic porphyry deposits</b>				
Copper Hill <sup>p</sup>	105.0	0.33	0.33	Cooke <i>et al.</i> (2007)
Marsden <sup>p</sup>	76.7	0.30	0.50	Newcrest Mining Limited (2007)
E43 <sup>p</sup>	490m @ 0.19 % Cu			Smith (2004), Cooke <i>et al.</i> (2007)
The Dam <sup>p</sup>	167m @ 1.0 g/t Au, 0.7 % Cu			Smith (2004)
Cargo <sup>p</sup>	108m @ 0.22 g/t Au, 0.52 % Cu			Smith (2004)
<b>Skarn deposits</b>				
<i>Cadia district</i>				
Big Cadia <sup>p</sup>	34.0	0.40	0.50	Newcrest Mining Limited (2008)
Little Cadia <sup>p</sup>	8.0	0.30	0.40	Holliday <i>et al.</i> (2002)
Junction Reefs <sup>m</sup>	1.6	2.80	-	Cooke <i>et al.</i> (2007)
<b>Low sulfidation gold deposits</b>				
E42 (Cowal) <sup>m</sup>	63.5	1.22	-	Cooke <i>et al.</i> (2007)
E41 (Cowal) <sup>p</sup>	No data			
E46 (Cowal) <sup>p</sup>	No data			
<b>High sulfidation gold deposits</b>				
Peak Hill <sup>m</sup>	11.3	1.29	0.11	Cooke <i>et al.</i> (2007)
Gidginbung/Temora <sup>m</sup>	8.7	2.40	-	Cooke <i>et al.</i> (2007)

m - mine; p - prospect

**Figure 2.8** Aeromagnetic image (total magnetic intensity) of the Cadia district showing the distribution and the NW-trending geometry of the different intrusive and intrusive-related mineral deposits. Note the apparent northwest elongation of the high magnetic response (red). The low magnetic responses are represented by blue colours. Data from Newcrest Mining Limited.

The Cadia district, located in the Molong Volcanic Belt, is the largest cluster of known Au–Cu deposits in terms of contained metal (Table 2.2; Holliday *et al.*, 2000). The Cadia district porphyry deposits include the Ridgeway, Cadia East, Cadia Hill and Cadia Quarry, and Fe–Cu–Au skarn deposits at Big and Little Cadia (Fig. 2.8). Au–Cu mineralization is associated with Late Ordovician to Early Silurian intrusions that were emplaced into Ordovician volcanoclastic and metasedimentary rocks of the FRV and Weemalla Formation, respectively.

The Cadia ore deposits are aligned on a NW-trending mineralized corridor that is 6 km long and several hundred meters wide (Holliday *et al.*, 2002). This regional corridor contains a number of geological features and is apparent on the aeromagnetic image (Fig. 2.8). It correlates to the crustal-scale WNW-striking LTZ of Glen and Wyborn (1997).

Current mining operations at Cadia are focused at Cadia Hill and Ridgeway. Cadia Hill comprises sheeted quartz–sulfide veins and disseminated copper sulfides hosted by propylitically altered quartz monzonite porphyry (Holliday *et al.*, 2002; Forster *et al.*, 2004). Located 2 km to the northwest is the Ridgeway deposit, which exploits a stockwork of quartz–sulfide veins hosted in pipe-like intrusions of mafic monzonite, quartz monzonite and adjacent volcanoclastic and sedimentary rocks.

---

# Chapter 3: Geology, Geochronology and Geochemistry

---

## 3.1 Introduction

This chapter describes the geology of Ridgeway, focussing on the intrusive phases and the volcano-sedimentary host rocks. Harper (2000), Wilson (2003), Wilson *et al.* (2003) and Reynolds (2007) previously described the geology of the upper part (~1 km) of Ridgeway. Recent drilling has provided the opportunity to investigate the host rocks of the deeper parts of the Ridgeway orebody, revealing critical new structural, stratigraphic and intrusive relationships that have implications for alteration and mineralization.

## 3.2 District Geology

The Ordovician geology of the Cadia district is characterized by thick successions of arc-derived sedimentary rocks intercalated with trachyandesitic volcanic rocks. The oldest unit in the district is the fine-grained, thinly laminated, siliceous siltstone, massive feldspathic sandstone and calcareous siltstone and sandstone of the Weemalla Formation. This formation is conformably overlain by the FRV, which comprises volcanic and associated volcanogenic sedimentary rocks. Both the Weemalla Formation and FRV sequence have been cut by several phases of Late Ordovician to Early Silurian intrusions that range from mafic to intermediate in composition, including diorite, monzodiorite, monzonite and quartz monzonite stocks, pipes and dikes. The more felsic intrusions are associated with porphyry-style mineralization (Fig. 3.1).

Silurian sedimentary rocks and a thin capping of Tertiary basalts and gravel cover a large section of the late mineralized and altered Ordovician volcano-sedimentary rocks (Holliday *et al.*, 2002; Washburn, 2008; Fig. 3.1). District-wide post-Early Silurian deformation created W-dipping thrust faults throughout the

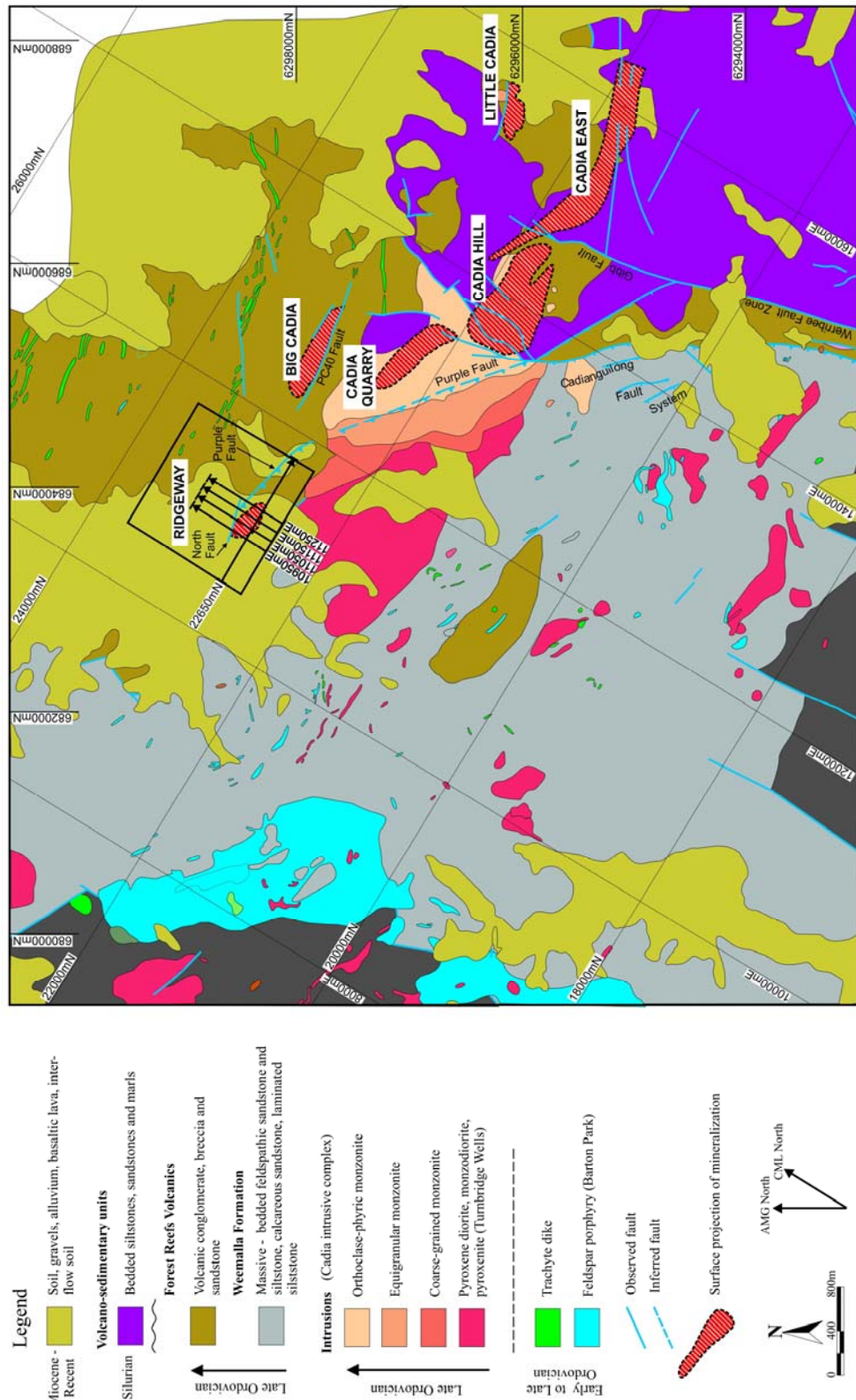


**Figure 3.1** Geology map of the Cadia District showing the major rock units, mineral deposits and major structures. Modified from unpublished mapping Newcrest Mining Ltd. (2006) and Holliday *et al.* (2002). At Ridgeway, the surface projection of the orebody is based on the 0.2 % Cu ore outline at 5400mRL (0.5 km below surface). The Purple Fault and the North Fault are projected from underground mapping. Also plotted are the section lines used in this study (black box). The Purple Fault at Cadia Quarry is inferred to be the contact between the Tumbridge Wells diorite and the coarse grained monzonite (Tedder, 2002).



district, locally mapped as the Cadiangullong Fault System (Fig. 3.1), which juxtaposed Ordovician volcanics to the west in fault contact with the Silurian sedimentary rocks to the east (Glen, 1998; Holliday *et al.*, 2002; Washburn, 2008; Harris *et al.*, 2009a).

### 3.3 Ridgeway Geology

The geology of Ridgeway is based on the results of approximately 14 km of drill core logging by the author. This included numerous underground deep drillholes collared during the development and mining stages of the Ridgeway project and underground mapping. The location of all drillholes logged is projected in 5100mRL (Fig. 3.2).

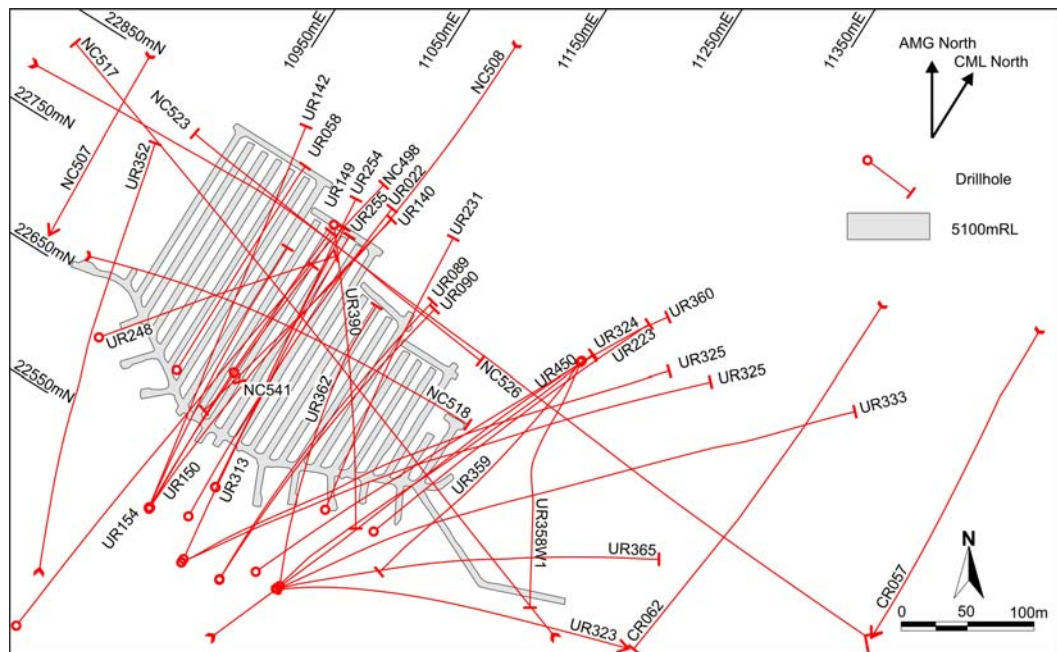


**Figure 3.2** Trace of drillholes logged by the author on Ridgeway deposit (black box in Fig. 3.1), projected on plan at 5100mRL.

Figure 3.4 shows the geology of Ridgeway schematically, based on construction of four parallel cross-sections (Fig. 3.5A to Fig. 3.5D) spaced 100 m apart and a long section (Fig. 3.6). The drillholes have been projected onto these sections by as much as 50 m off section. Spatially, the sections cover 0.8 km x 0.4 km x 2.2 km and incorporate the horizontal and vertical extent of the Ridgeway orebody. The distribution of intrusive rock types is shown in detail on cross-sections and on level plans at different elevations through the ore body (Fig. 3.7). The upper

part (~0.6 km below surface) of Ridgeway, plans at 5255mRL and at 5100mRL (Fig. 3.7A and B, respectively) have been interpreted from underground mine mapping (undertaken by Newcrest) coupled with drillhole observations from the current study. The geological interpretation below the current mine development level plan at 4850mRL (Fig. 3.7C), is based on the results of drillhole logging by the author.

### **3.3.1 Weemalla Formation**

The Weemalla Formation is between 1.3 and 3.5 km thick in the Cadia district. It includes the 50 to 500 m thick Mount Pleasant basalt member (Pogson and Watkins, 1998; Fig. 3.3). The western portion of the Weemalla Formation comprises feldspathic siltstone and fine sandstone in its type locality at Big Box Hill (Fig. 3.3), with some horizons of coarser lithic sandstone, conglomerate, limestone, calcareous mudstone and minor tuffs, lava flow and sills (Taylor, 1988). The siltstone is typically black and has well-defined bedding. The sandstone beds are white to light-grey coloured and are composed predominantly of quartz, feldspar and lithic fragments. The eastern part of the Weemalla Formation, around the Junction Reefs area (Fig. 3.3), is dominated by volcaniclastic sandstone and conglomerate (Taylor, 1988; Squire and McPhie, 2007). Fine-grained cream to dark grey, well-bedded siltstone and mudstone, volcaniclastic siltstone and basaltic lavas are also present.

The Weemalla Formation crops out in the Cadia district to the west of Ridgeway and Cadia Hill (Fig. 3.1). Light and dark grey laminated to thinly bedded fine-grained siltstone, feldspathic sandstone and siltstone, and lesser calcareous siltstone are exposed in this area (Holliday *et al.*, 2002; Harris, *et al.*, 2009a). These rocks contrast with the Weemalla Formation from Big Box Hill and Junction Reefs (cf. Taylor, 1988).

The Weemalla Formation is host to the deeper part of the Ridgeway deposit (Fig. 3.5). This formation has been intersected in underground developments, 0.8 to 1 km below the surface (5100mRL) and has a minimum vertical extent of 1.2 km. At Ridgeway, the Weemalla Formation is characterized by a thick sequence of laminated and siliceous siltstone, feldspathic sandstones and variably calcareous sandstone and siltstone (Table 3.1; Fig. 3.4). Similar rock units were described

briefly by Harper (2000) and Wilson (2003), but due to limited deep drilling at that time, the spatial distribution and detailed discussion of the different rock units in the Weemalla Formation were not constrained. The current study has identified three main lithofacies in the Weemalla Formation (Table 3.1): 1) laminated and siliceous siltstone; 2) massive felspathic sandstone interbedded with siltstone; 3) calcareous sandstone and siltstone.

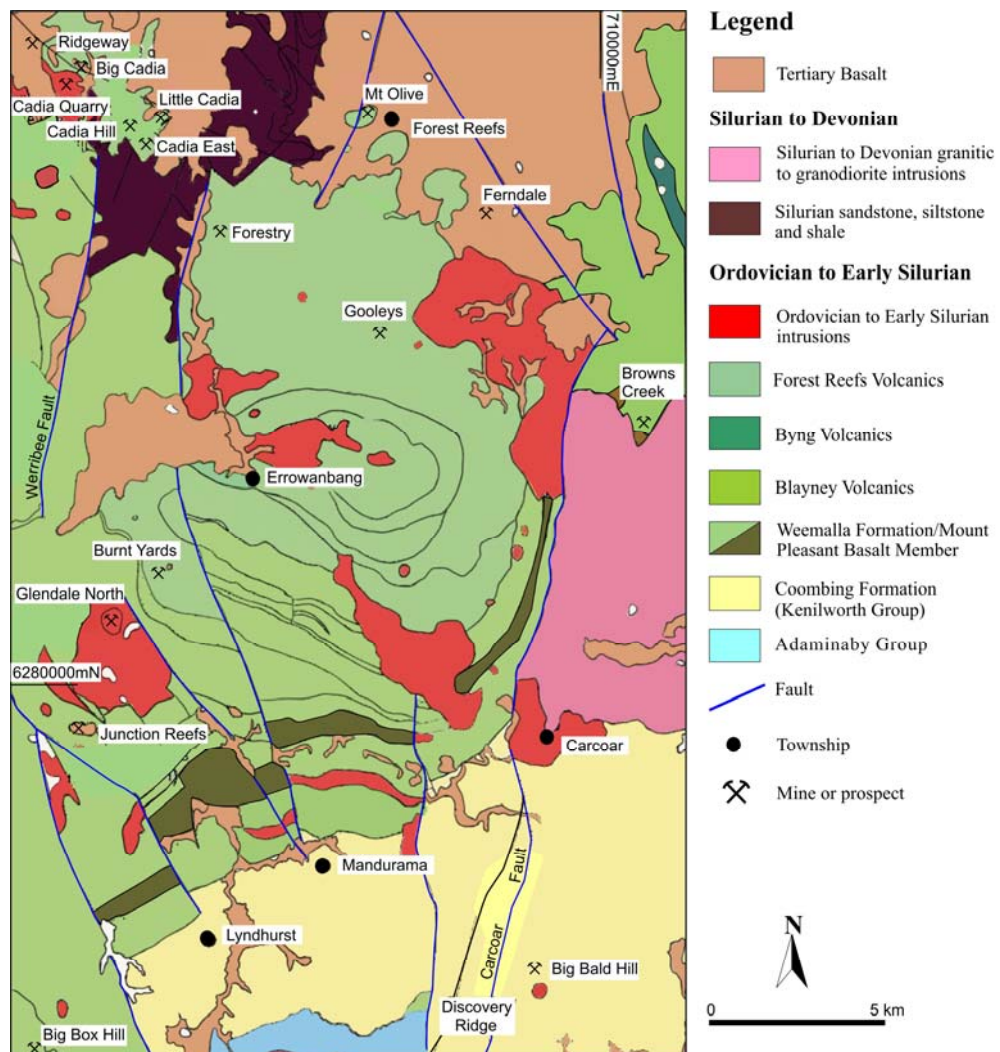


**Figure 3.3** Simplified regional geologic map of the Cadia-Forest Reefs region. Modified from Wyborn and Henderson (1993), Bathurst 1:250,000 map by Pogson and Watkins (1998), Squire (2001), and Squire and McPhie (2007).

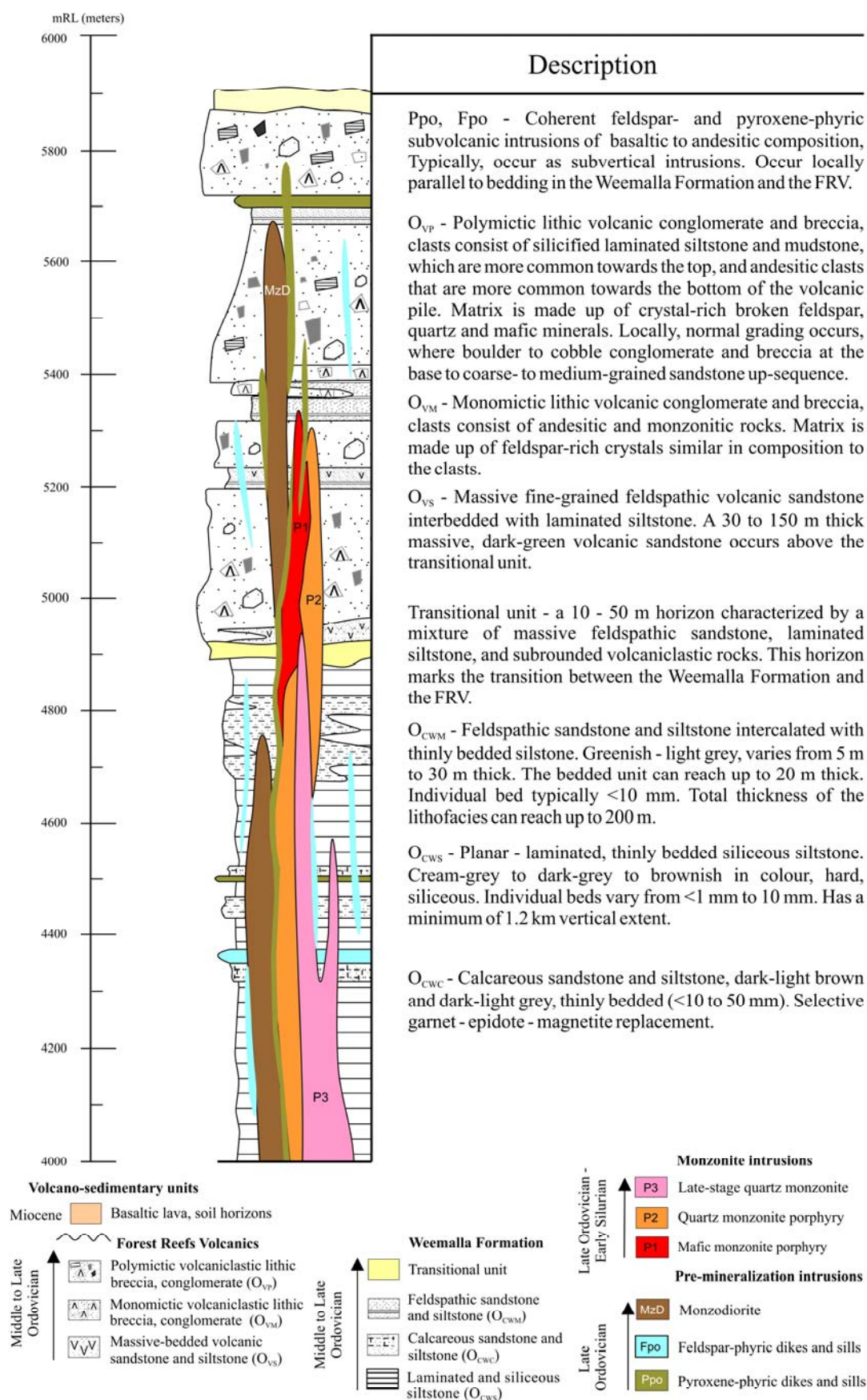


**Figure 3.4** Idealized summary of the Ridgeway lithostratigraphy based on core logging by the author.



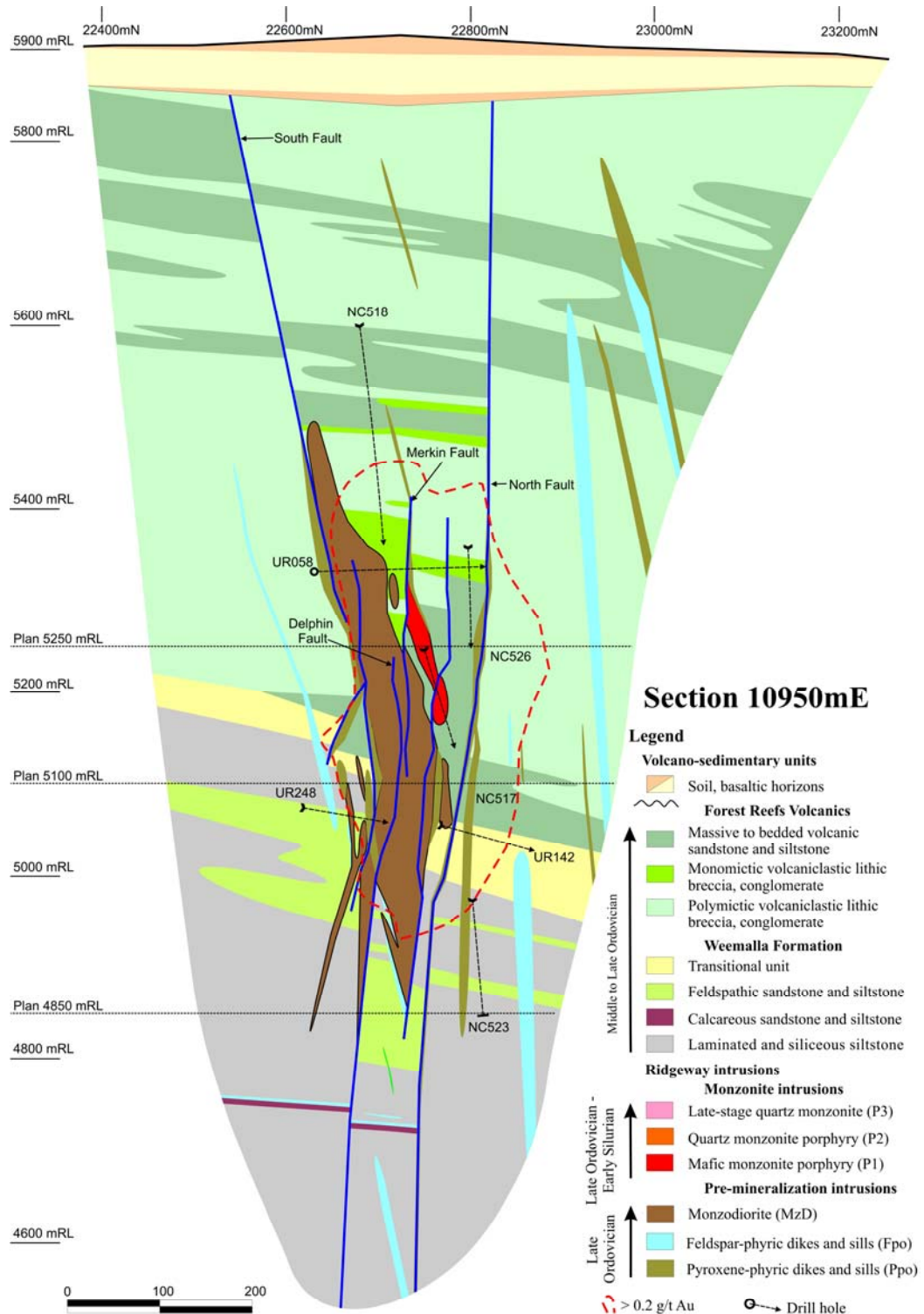
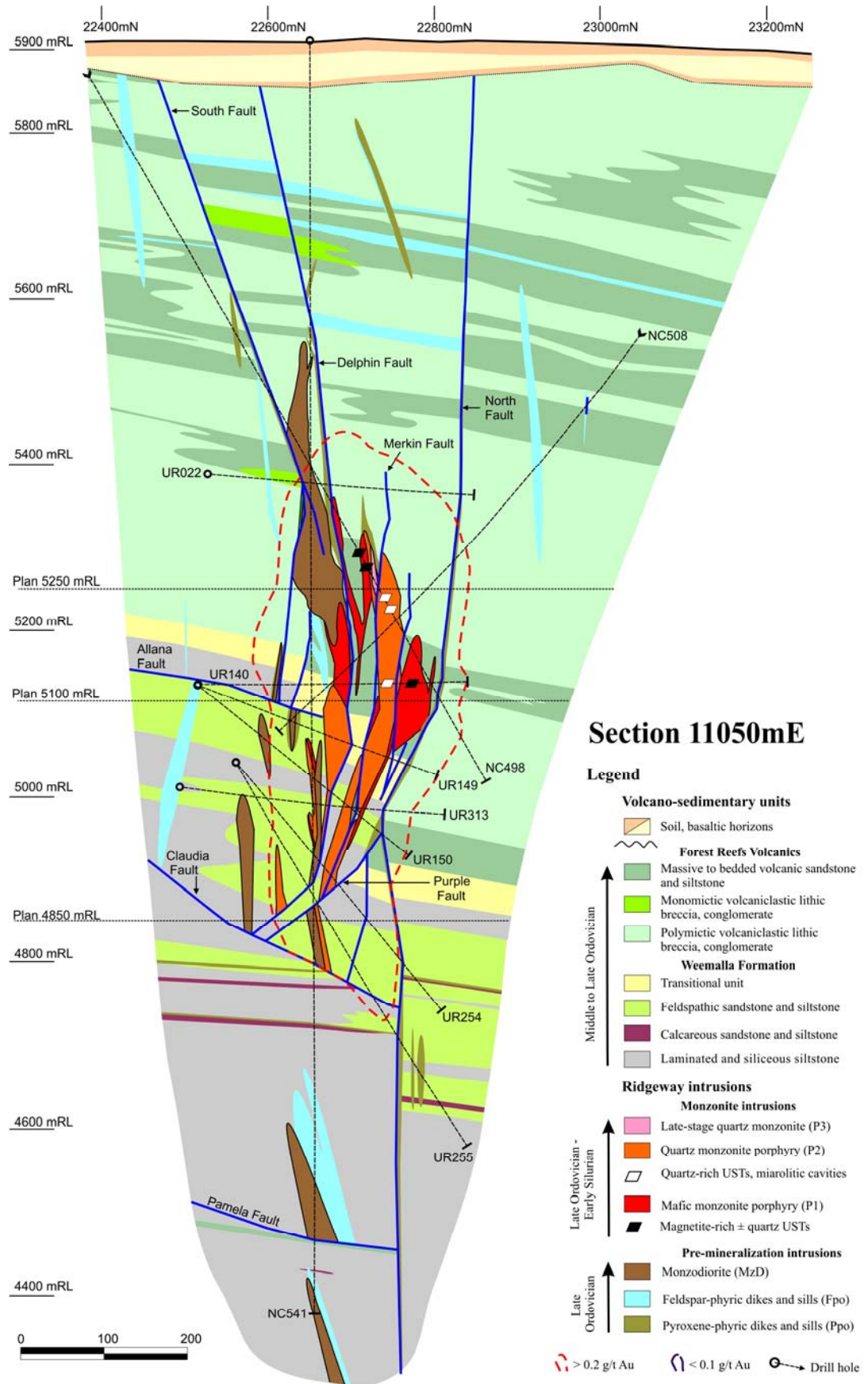


**Figure 3.5A** Interpretive geological cross-section through the western mineralized zone at Ridgeway on section 10950mE. This section is based on underground mapping by Newcrest and detailed core logging by the author from eight diamond drillholes indicated by dashed lines. The earliest intrusions are the pyroxene-phyric (Ppo) dikes emplaced along subvertical NW-striking faults (North and South Faults). The pre-mineralization monzodiorite (MzD) stock dominates in this section, emplaced as tabular, elongate pipe intruding the Weemalla Formation, the Forest Reefs Volcanics (FRV), and along the margins of the Ppo. The massive feldspathic sandstone units of the FRV occurring above the transitional unit appear to thin towards the southwest. The monomictic andesitic volcanic breccia is interbedded with feldspathic sandstone locally. The syn-mineralization mafic monzonite porphyry (P1) is found northeast of the MzD. Orebody is developed in and around P1 and the surrounding wallrocks. The section trace is located in Figure 3.1.

**Figure 3.5B** Interpreted geological cross-section through the center of the mineralized zone at Ridgeway on section 11050mE. This section is based on underground mapping by Newcrest and detailed core logging from 10 diamond drillholes indicated by dashed lines. Pyroxene-phyric (Ppo) dikes are emplaced along subvertical faults (e.g. North Fault, Delphin Fault, South Fault and locally along the Merkin Fault). Thin (<2 m) Ppo and feldspar-phyric (Fpo) sills intrude subparallel to the bedded volcanoclastic sandstone and thinly bedded calcareous sandstone and siltstone units, respectively. The pre-mineralization monzodiorite occur as elongate pipes. The feldspathic sandstone and siltstone units predominate at the upper portion of the Weemalla Formation.

The mafic monzonite porphyry (P1) has an unusual teardrop-shaped intrusion, that appears to pinch-out towards the top and the bottom and swells at its center. The “swelling” of P1 appears to occur just above the transitional unit. The apex and margins of P1 contains a zone of magnetite-rich unidirectional solidification textures (USTs).

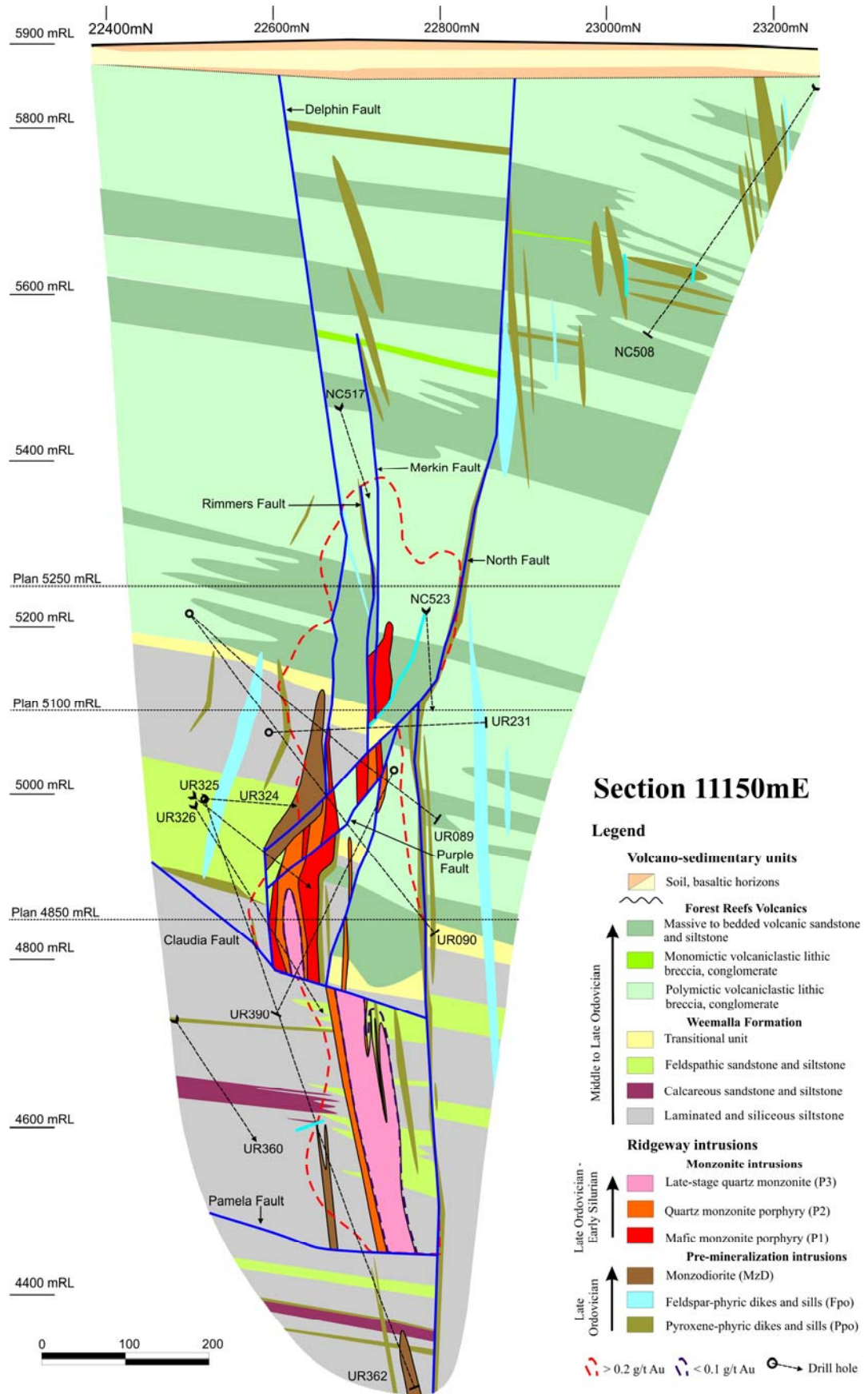
The quartz monzonite porphyry (P2) has an elongate pipe-shaped geometry. Quartz-rich USTs occurs at the apex and margins, miarolitic cavities are found in the intrusion. The section trace is shown in Figure 3.1.



**Figure 3.5C** Interpreted geological cross-section through the center of the mineralized zone on section 11150mE. This section is based on underground mapping by Newcrest and detailed logging from 12 diamond drillholes indicated by dashed lines. A pyroxene-phyric (Ppo) dike is emplaced along the North Fault. Massive feldspathic sandstone and siltstone are the dominant lithofacies of the Weemalla Formation at 5100mRL, southwest of the intrusive complex. The host sequence is cut by a series of subvertical Ppo and feldspar-phyric dikes and sills.

The mafic monzonite porphyry (P1) has a similar geometry to that shown on section 11050mE, where it pinches-out towards the top and swells at the center. The lower extension of P1 at 5100mRL has been cut by post-mineralization faulting. Below 5000mRL, P1 has been intruded by the quartz monzonite porphyry (P2) along its core. Similarly, late-stage quartz monzonite (P3) intruded the core of P2.

The elongate P3 intrusion was the last emplaced monzonite phase at Ridgeway. It produced the low-grade ( $< 0.1$  g/t Au) core of the ore deposit at 4850mRL and below 4800mRL. The intrusions and mineralization are cut by late stage-faults (e.g. Purple, Claudia and Pamela Faults). The section trace is shown in Figure 3.1.





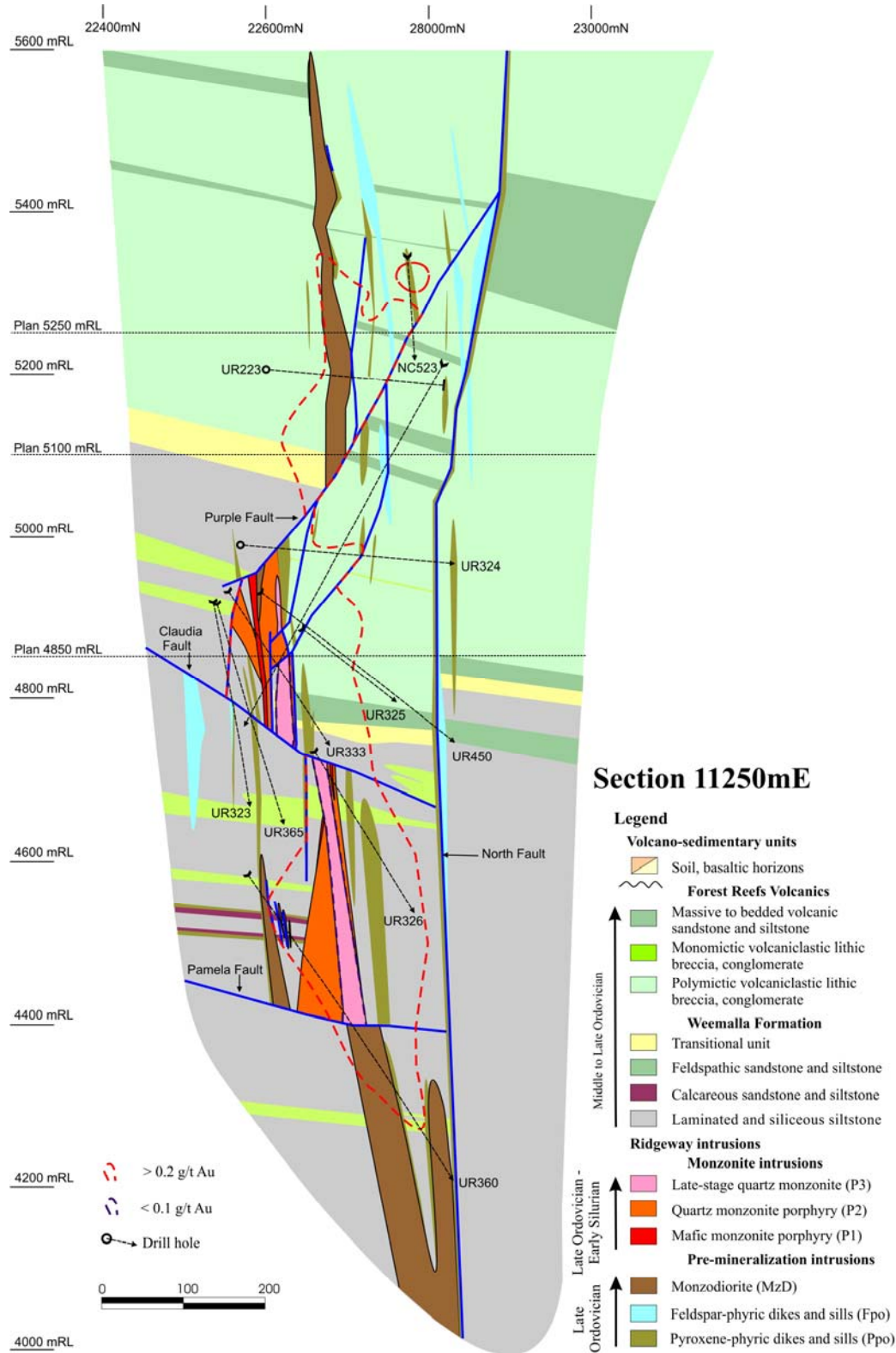


**Figure 3.5D** Interpretive geological cross-section through the eastern mineralized zone on section 11250mE. This section is based on the detailed core logging from 11 diamond drillholes indicated by dashed lines. The pre-mineralization monzodiorite is an elongate plug that intruded the FRV. The FRV is dominated by polymictic volcanic breccia, whereas the Weemalla Formation consists of laminated siliceous siltstone. Mafic monzonite (P1) and quartz monzonite (P2) pipes cut the Weemalla Formation and the FRV. The intrusions and mineralization were cut by moderately dipping reverse faults (e.g. Purple Fault), and low-angle thrust faults (e.g. Claudia and Pamela Faults). The section trace is shown in Figure 3.1.

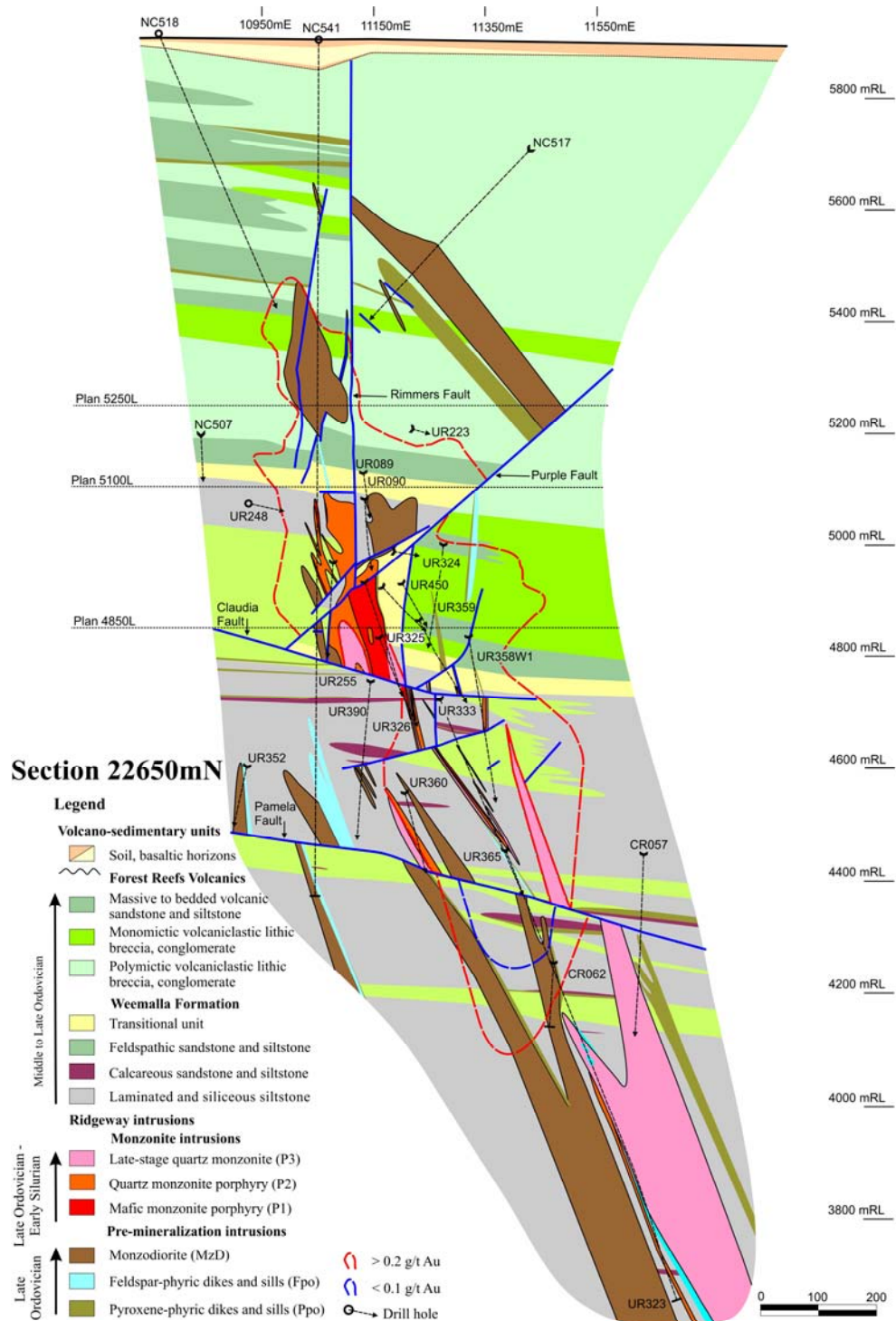


**Figure 3.6** Interpreted geological long-section through the center of the Ridgeway orebody on 22650mN, facing northeast. This section is based on four cross-sections (Figs. 3.5A to D) and detailed core logging of six diamond drillholes on the eastern end of Ridgeway. Drillholes have been projected by as much as 100 m off-section. The section is oriented approximately along the axis of the intrusions, and highlights the plunging of the pre-mineralization monzodiorite (MzD) and the late-stage equigranular quartz monzonite (P3) towards the southeast. The orientation also caused the bedding to appear subhorizontal because the beds are dipping towards the plane of the section. At 4100mRL, P3 truncated the feldspar-phyric (Fpo) dikes. Near the contact, P3 contains abundant fragments of wallrock and quartz veins. P3 is a single intrusion that broadens in diameter and exhibits a gradual change in texture with depth. Gold and copper are associated with mafic monzonite (P1) and quartz monzonite (P2) intrusions. Mineralization is well developed in the feldspathic sandstone unit of the Weemalla Formation, and in the massive volcanic sandstone and monomictic volcanoclastic breccia units of the FRV. The intrusions and mineralization were cut by moderately dipping reverse faults (e.g. Purple Fault), and by the low-angle Claudia and Pamela faults at 4850mRL and at 4400mRL, respectively. The long-section trace is shown in Figure 3.1.



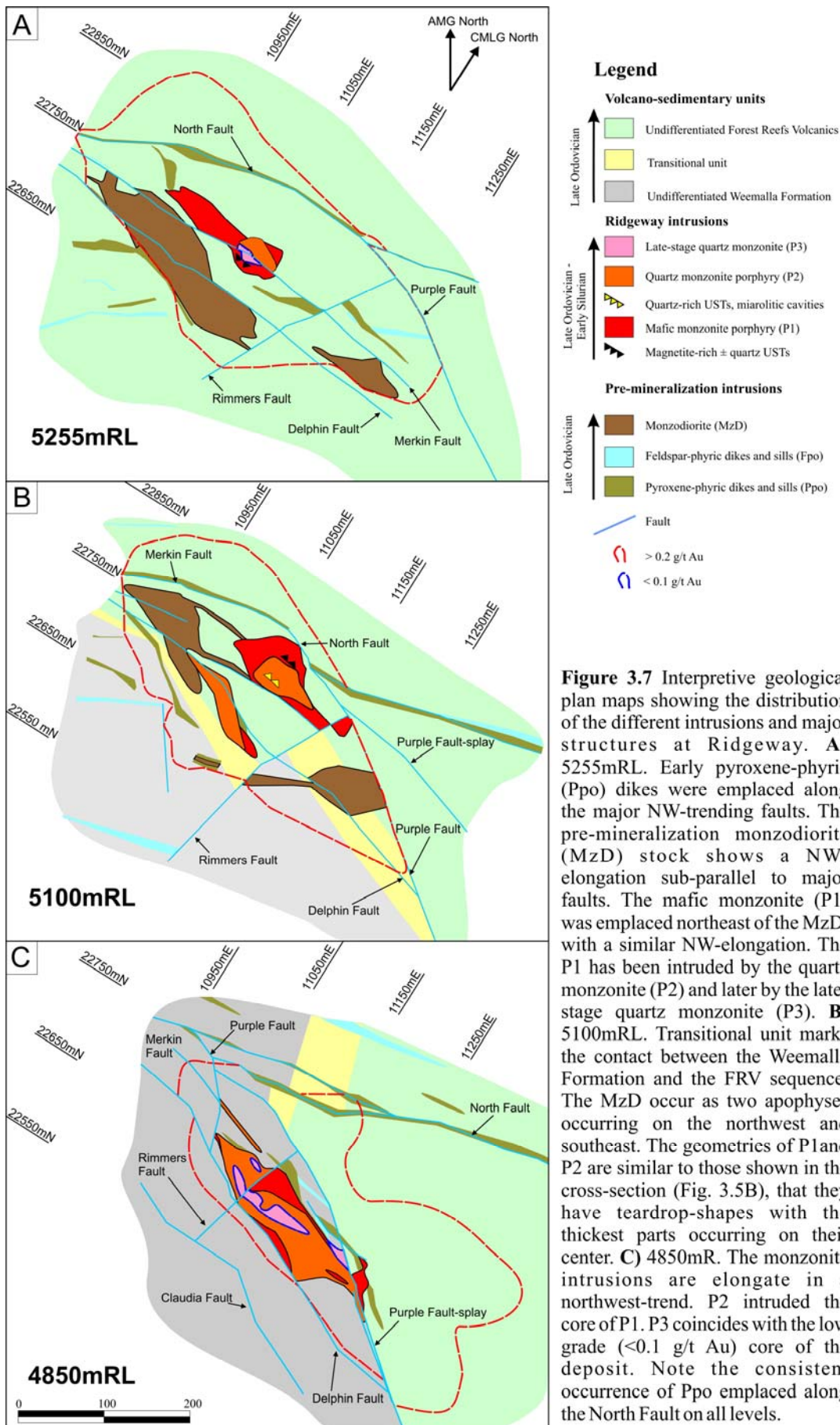




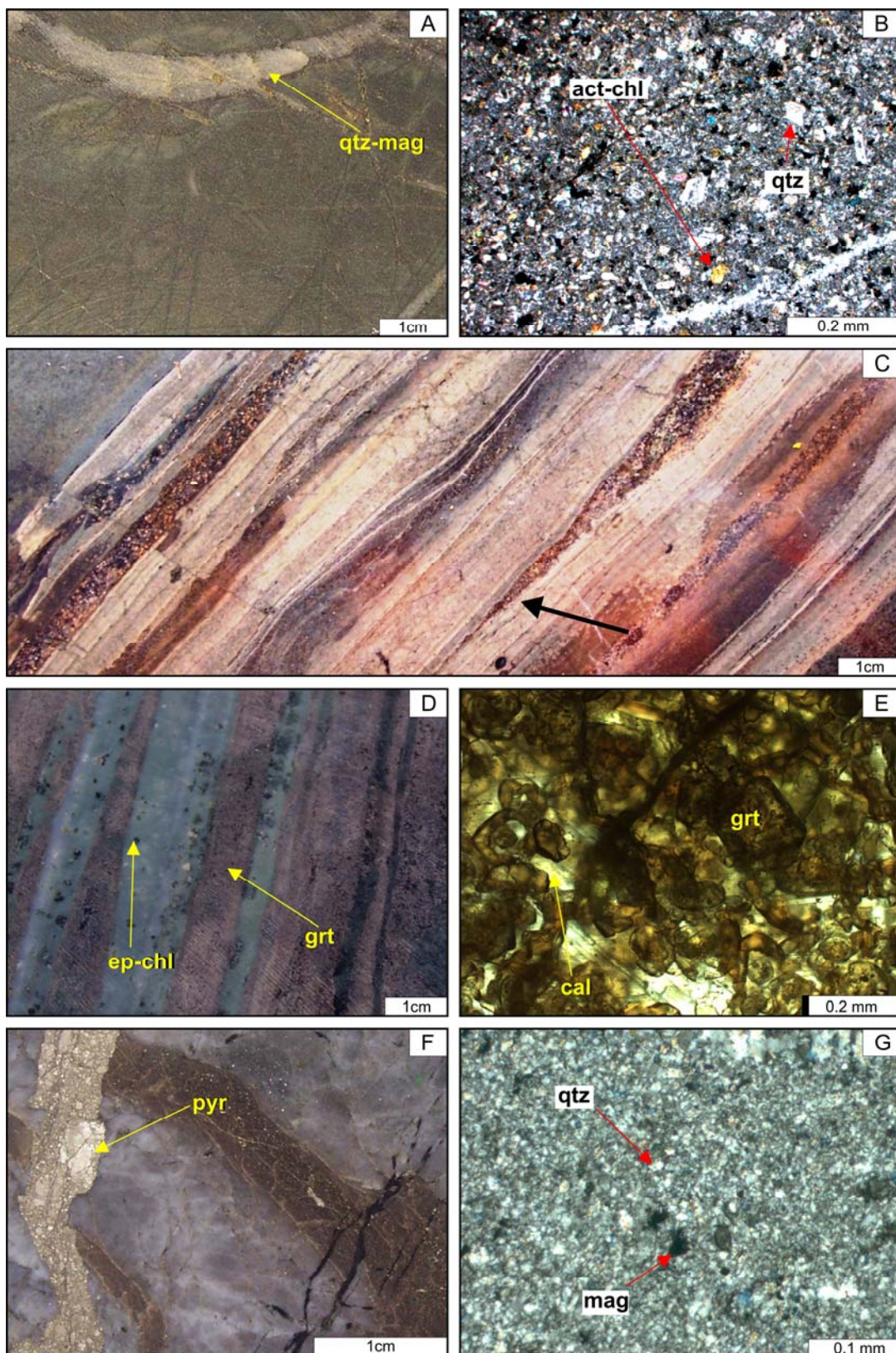
**Table 3.1** Summary of the different rock units of the Weemalla Formation from Ridgeway and their environments of deposition. Terminology is based on the scheme of McPhie *et al.* (1993). \* - abbreviations adopted from Pogson and Watkins (1998); \*\* - this study.

Rock units	Abbreviations	Description/distribution	Environment of formation
Feldspathic sandstone and siltstone	(O <sub>CWM</sub> **)	Dark greenish-grey, massive beds interbedded with thinly bedded siltstone and sandstone. Massive siltstone and fine-grained sandstone can reach up to 30 m thick. The bedded unit locally contains cross bedding and can reach up to 20 cm thick. It is intercalated with the massive feldspathic sandstone. Individual beds are typically 1cm	The thick massive beds suggest rapid deposition from turbidity currents (Squire, 2001). Grading to thinly bedded units indicates a change to low density flows, with lesser tractional and suspension sedimentation (Squire, 2000; Harris <i>et al.</i> , 2009a). The abundant feldspars and mafic minerals indicate a volcanic source
Calcareous sandstone and siltstone	(O <sub>CWC</sub> **)	Interbedded dark-light brown, very thinly bedded to thinly bedded calcareous volcanic sandstone and dark-light grey to greenish coloured, very thinly bedded feldspathic sandstone. Individual beds varies from <1 cm to 5 cm	The laterally extensive and parallel stratified beds suggest low energy conditions. Interbedded feldspathic sandstone suggests a volcanic source wide deposition from direct suspension (Squire, 2001, Wilson <i>et al.</i> , 2003)
Laminated and siliceous siltstone	(O <sub>CWS</sub> *)	Light-dark greyish-brownish, laminated to very thinly bedded siltstone. Individual beds varies from <1 mm up to 10 mm in thickness. Massive siliceous siltstone unit can reach up to 5 m thick. This unit has a vertical extent of more than 1.2 km	The thin, parallel-stratified and planar nature of the bedding, and the lack of ripple-cross laminations suggest low energy conditions (Harris <i>et al.</i> , 2009a). The absence of wave-generated sedimentary structures and the lack of shallow marine facies (e.g. reef limestone) also provide evidence for a below wave-base marine environment (Squire, 2001)

**Figure 3.8** Photographs and photomicrographs of the different lithofacies of the Weemalla Formation from Ridgeway.

- A.** Massive feldspathic siltstone ( $O_{CWM}$ ). The dark green to dark-grey colour is typical, and relates to pervasive chlorite alteration of ferromagnesian minerals (UR149-142m).
- B.** Photomicrograph (xpl) of massive feldspathic siltstone showing broken fragments of quartz and feldspar in a feldspar-rich matrix. The ferromagnesian minerals have been pervasively altered to chlorite  $\pm$  actinolite (UR140-32.4m).
- C.** Bedded to thinly bedded feldspathic sandstone and siltstone ( $O_{CWM}$ ). These beds are typically characterized by massive to normally graded parallel beds and cross-stratification (black arrow) in the feldspathic sandstone. The thin beds have undergone K-feldspar alteration of feldspathic grains, the secondary feldspar have been hematite-dusted (UR360-622.5m).
- D.** Interbedded calcareous feldspathic sandstone and siltstone ( $O_{CWC}$ ). The light-green siltstone has been pervasively silicified and containing disseminated chlorite–epidote. The dark-brown calcareous sandstone beds have undergone intense garnet (andradite) alteration (UR362-666m).
- E.** Photomicrograph (ppl) of garnet (andradite) alteration showing the occurrence of garnet as fine-grained nodules (UR360-603.5m).
- F.** Laminated to thinly bedded siliceous siltstone ( $O_{CWS}$ ). The beds lack internal structure that vary from light-grey to light-brown to buff in colour, and are hard and siliceous (UR362-561.9m).
- G.** Photomicrograph (ppl) of laminated siliceous siltstone ( $O_{CWS}$ ). Abundant (~90 vol %) fine-grained mosaic-textured quartz with accessory disseminated magnetite and chlorite-altered ferromagnesian minerals (UR362-561.9m).

Abbreviations: act = actinolite, cal = calcite, chl = chlorite, ep = epidote, grt = garnet, mag = magnetite, py = pyrite, qtz = quartz, rl = reflected light, xpl = cross polarized light



### 3.3.1.1 Feldspathic sandstone and siltstone ( $O_{CWM}$ )

Dark greenish-grey, massive feldspathic sandstones and siltstones ( $O_{CWM}$ ) interbedded with thinly laminated siltstones are prominent in the upper sequence of the Weemalla Formation (Table 3.1; Figs. 3.4, 3.8A and C). The feldspathic sandstones are composed of broken crystals of quartz, altered plagioclase (10 - 20 %) and pervasively altered ferromagnesian minerals (5 - 10 %) set in a fine-grained microcrystalline matrix of feldspar, quartz and ferromagnesian minerals (Fig. 3.8B). The massive siltstone and sandstone vary from 5 to 30 m thick. Individual bedded units of siltstone and sandstone, locally with cross bedding (Fig. 3.8C), can reach up to 200 cm thick, with individual beds typically <10 mm.

### 3.3.1.2 Calcareous sandstone and siltstone ( $O_{CWC}$ )

The Weemalla Formation includes localized horizons of calcareous sandstone and siltstone below 4800mRL (Fig. 3.4; Fig. 3.5A to D). These beds are characterized by dark to light brown, thinly-bedded calcareous sandstone and light grey to greenish, thinly bedded siltstone (Fig. 3.8D). The calcareous sandstone has typically undergone pervasive garnet (andradite)–epidote–magnetite alteration (Fig. 3.8E). Individual beds vary from <1 to 5 cm thick in a sequence that is up to 20 m thick locally (Table 3.1). This subunit is interbedded with both the siliceous siltstone and the feldspathic sandstone, and has been intruded by pyroxene- and feldspar-phyric sills (Fig. 3.4; Figs. 3.5A to D).

### 3.3.1.3 Laminated and siliceous siltstone ( $O_{CWS}$ )

At Ridgeway, laminated and siliceous siltstones ( $O_{CWS}$ ) form the dominant rock unit of the Weemalla Formation (Fig. 3.4). They have a vertical extent of more than 1.2 km. The sequence is characterized by laminated to thinly bedded, pale-cream to grey (rarely brownish-pinkish) siltstone and siliceous siltstone with rare calcareous feldspathic sandstone interbeds (Table 3.1; Fig. 3.4). The siltstone is fine-grained and indurated (Fig. 3.8F) and composed mainly of fine-grained equigranular mosaic-textured quartz (~80 %) with minor chlorite-altered ferromagnesian minerals and finely disseminated magnetite and pyrite (Fig. 3.8G). Staining of samples with sodium cobaltinitrite showed that K-feldspar is only a minor component (<1 %;

Appendix B). Localized calcareous nodules (<2 mm diameter) in the feldspathic sandstone beds have been selectively replaced by garnet.

Laterally equivalent laminated intervals can be correlated from 50 to 100 m between drillholes in the same area (Fig 3.6). Individual massive siliceous siltstone units can reach up to 5 m thick and single beds vary from <1 mm to up to 10 mm. Faults have offset bedding by a few meters to tens of meters (Fig. 3.5A to Fig. 3.5D).

### **3.3.2 Transitional unit**

The transition between the Weemalla Formation and the FRV is marked by a 10 - 50 m thick unit characterized by sub-angular, massive feldspathic sandstone, laminated and massive siliceous siltstone and sub-angular, polymictic volcanoclastic breccias of andesitic composition (Fig. 3.4; Fig. 3.9A; Harper, 2000; Holliday *et al.*, 2002; Wilson, 2003; Harris *et al.*, 2009a). The breccia clasts comprise <10 vol % of the rock and range from 2 to 5 cm in diameter. They include reworked clasts of sub-angular, massive feldspathic sandstone and siliceous siltstones, and andesite clasts (Fig. 3.9A)." This conformable transition marks the last occurrence of thick successions of laminated siliceous siltstone facies of the Weemalla Formation and the start of the more massive volcanoclastic rocks of the FRV (Fig. 3.4; Harper, 2000; Holliday *et al.*, 2002; Wilson, 2003; Harris *et al.*, 2009a).

### **3.3.3 Forest Reefs Volcanics**

The FRV has an inferred thickness of 2 to 2.5 km and is a gently to moderately NE- to NW-dipping package. In the Cadia-Neville region, Squire and McPhie (2007) subdivided the FRV into lower and upper parts separated by an inferred unconformity and/or fault. The lower part contains the Mount Pleasant basalt member (shoshonitic basaltic lavas), feldspar-rich sandstone, volcanic breccias and mudstone, grading to polymictic volcanic conglomerate with sandstone matrix and calcareous sandstone up-sequence. The upper part is typified by trachyandesite and higher abundances of mafic volcanic fragments and ferromagnesium minerals.

The FRV comprise a large portion of the Cadia district. Here, the FRV has been broadly subdivided into two parts: the basal parts include intermediate



volcanics and volcaniclastic rocks in and around Ridgeway, while the upper parts are composed of more mafic rocks at Cadia East (Holliday *et al.*, 2002; Harris *et al.*, 2009a). Previous studies have identified various lithofacies in the FRV, including intermediate volcanic lithic conglomerates, breccias and sandstones, bedded calcareous sandstones; laminated siliceous volcanic siltstone; massive basaltic to andesitic flows, and hypabyssal dikes and sills (Green, 1999; Harper, 2000; Squire, 2001; Wilson, 2003; Forster, 2005; Kitto, 2005; Harris *et al.*, 2009a).

At Ridgeway, the FRV is the principal host to Cu and Au mineralization and associated hydrothermal alteration (Harper, 2000; Holliday *et al.*, 2002; Wilson, 2003). The FRV package ranges from 650 to 1100 m thick (Fig. 3.4). The variable range in thickness is related to post-mineralization deformation (Fig. 3.5A to D; Fig. 3.6). Harper (2000) and Wilson (2003) have documented in detail the different lithofacies that comprise the FRV from Ridgeway. Similar rock units have been documented during the current study. The rock units in the FRV include (Table 3.2): 1) polymictic lithic conglomerate and breccia; 2) monomictic volcanic breccia; 3) massive to very thinly bedded feldspathic volcanic sandstone; 4) coherent pyroxene- and feldspar-phyrlic basaltic to andesitic subvolcanic intrusions. Units 1, 2 and 3 are equivalent to lithofacies 1, and unit 4 to lithofacies 5 of Wilson *et al.* (2003).

### **3.3.3.1 Polymictic volcaniclastic lithic conglomerate and breccia (O<sub>VP</sub>)**

Polymictic volcaniclastic lithic conglomerate and breccia (O<sub>VP</sub>) are the predominant rock types of the FRV from Ridgeway (Harper, 2000; Wilson, 2003). They occur over a vertical extent of 650 m, extending upwards from the top of the transitional unit to the base of the Tertiary volcanics (Fig. 3.4). The breccias are mostly matrix-supported, with minor clast-supported domains. The clasts, which constitute ~60 vol % of the rock, are massive to poorly sorted (Harper, 2000), angular to subrounded and range from 2 to 64 mm (granule to pebble), mostly ~30 mm in size (Table 3.2). The clast types include basalt, andesite, siliceous siltstone with magnetite interbeds, mudstone, and silicified rock fragments (Fig. 3.9B and C). The matrix constitutes ~30 vol % of the rock and consists of coarse-grained crystal-rich sandstone of broken feldspar and ferromagnesian minerals.

**Table 3.2** Summary of the different rock units of the Forest Reefs Volcanics from Ridgeway and their environment of deposition. Terminology is based on the scheme of McPhie *et al.* (1993). \* - abbreviations adopted from Wilson (2003); \*\* - this study.

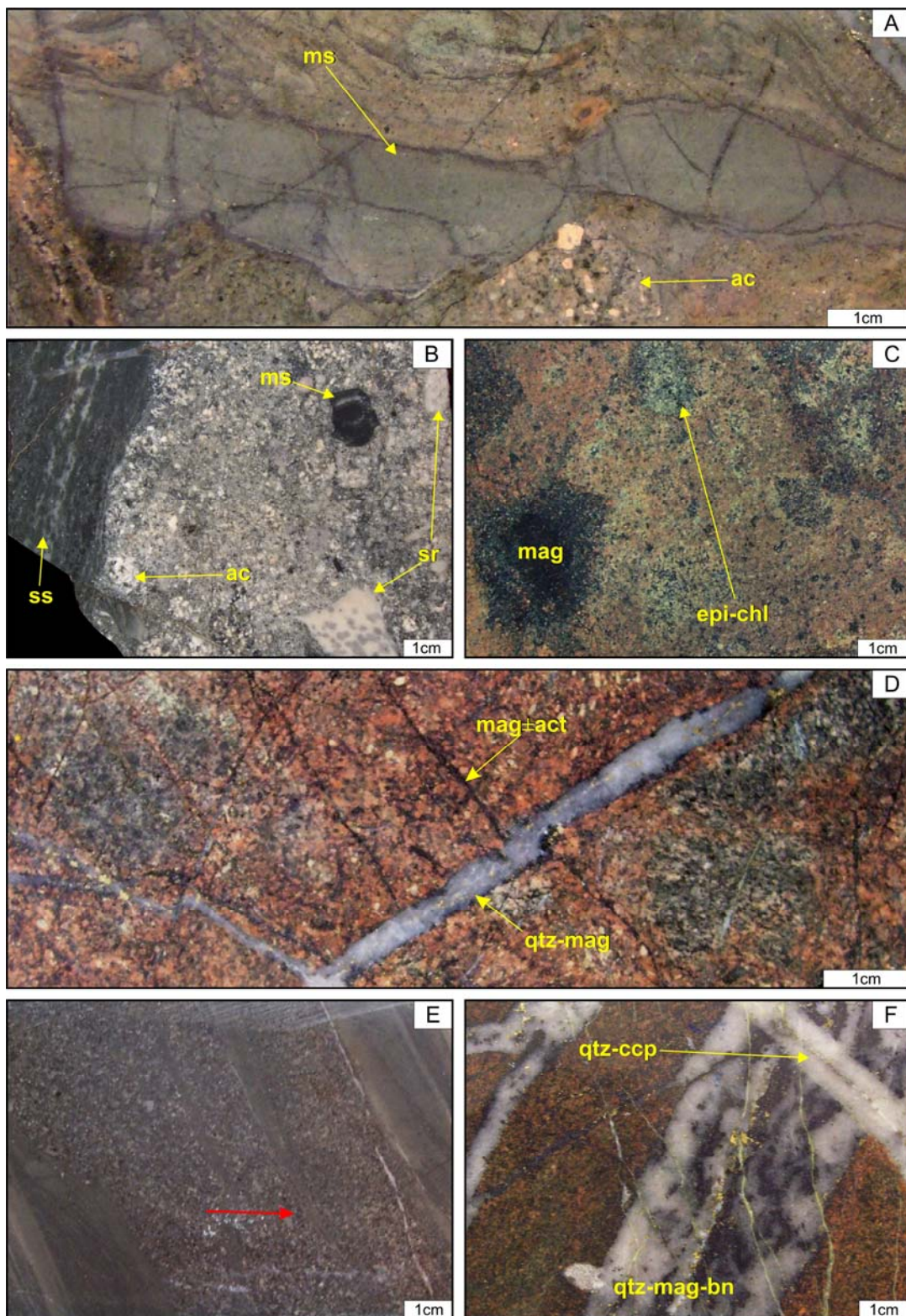
Lithofacies	Rock units	Abbreviations	Description/distribution	Environment of formation
Volcaniclastic lithic breccia, conglomerate, sandstone and siltstone	Polymictic, volcaniclastic lithic breccia, conglomerate	O <sub>VP</sub> **	Massive, poorly sorted, granule to boulder size lithic angular to subrounded clasts of siliceous mudstone, laminated siltstone, feldspar-phyric volcanic rocks. Matrix composed of medium to coarse grained feldspar-rich sandstone	The thick, massive and poorly sorted polymictic nature indicate deposition from concentrated sedimentary flow or direct fall-out from high density turbidity currents (Squire, 2001; Harris <i>et al.</i> , 2009a). This could also be deposited from volcanogenic sedimentary mass flow, or turbulent debris flow (McPhie, <i>et al.</i> , 1993). Diverse clasts compositions reflect variable sources
	Monomictic volcaniclastic breccia	O <sub>VM</sub> **	Massive, poorly sorted, granule to boulder size subrounded clasts of andesitic clasts (~60 %). Matrix composed of medium- to coarse-grained feldspar crystal similar to the clast which gives a "pseudo-breccia" texture	The monomictic andesitic horizons may have been derived from an intermittent influx from erosion of andesitic volcanics, sills or dikes. Alternatively, this could be an in-situ quench fragmentation of coherent lava (Harris <i>et al.</i> , 2009a)
	Massive to bedded crystal-rich volcanic sandstone, thinly bedded siltstone	O <sub>VS</sub> *	Light greenish-grey, massive to bedded coarse grained feldspathic sandstone. Locally with thinly bedded fine-grained siltstone, individual bedding varies from 5 to 30 mm.	The thick massive beds suggest a concentration from high density turbidites, and thin interbeds imply short lived period of below-wave base sedimentation. Intervening cross-stratification record deposition of fluctuating conditions from lower sediment concentration to more turbulent and dilute forms (Squire, 2001)
Coherent feldspar-phyric and pyroxene-phyric intrusions	Pyroxene-phyric dikes and sills	Ppo**	Dark green, with large euhedral to subhedral clinopyroxene phenocrysts (5 - 25 vol %; up to 7 mm diameter). Groundmass is typically greenish to light green-coloured and aphanitic	The porphyritic texture and fine-grained holocrystalline groundmass, and the sharp to irregular contacts (fine-grained, chilled?) with the Forest Reefs Volcanics and Weemalla Formation are interpreted to represent the margins of subvolcanic sills and/or dikes (Kitto, 2005)
	Feldspar-phyric dikes and sills	Fpo**	Greenish, contains abundant evenly distributed subequant plagioclase phenocrysts, (~30 vol %; 2 - 5 mm long) occurring as individual grains	

**Figure 3.9** Photographs of the different rock units of the Forest Reef Volcanics from Ridgeway.

- A.** Transitional unit. Mixture of angular massive feldspathic sandstone (“ms”) and sub-angular andesitic clasts (“ac”). Matrix comprises of volcanic sandstone (UR140-137m).
- B.** Polymictic volcanic lithic breccia ( $O_{VP}$ ). The clasts have been derived from a variety of sources, including bleached, clast-supported, with angular siliceous siltstone clasts (“ss”) that are internally laminated, silicified rock fragments (“sr”), mudstone (“ms”) and andesite clasts (“ac”). Matrix comprises of coarse grained, crystal-rich sand-sized broken fragments of feldspar, quartz and ferromagnesian minerals (NC508-300.1m).
- C.** Polymictic volcanic conglomerate ( $O_{VP}$ ). Matrix-supported, volcanic conglomerate with subrounded to angular clasts of basaltic and andesitic fragments. Matrix comprises volcanic-derived, sand-sized feldspars and mafic minerals. Ferromagnesian minerals both in the clasts and in the matrix have been altered to magnetite, chlorite and epidote (NC508-535.3m).
- D.** Monomictic volcanic breccia ( $O_{VM}$ ). The matrix-supported, subrounded clasts are mostly andesitic in composition. Clasts are typically greenish, composed of hematite-dusted secondary K-feldspar; ferromagnesian minerals are pervasively altered to actinolite–chlorite–magnetite. The matrix comprise of medium- to coarse-grained material that is compositionally similar to clasts. The rock is cut by thin magnetite stringers, which in turn have been cut by a quartz–magnetite vein (UR450-201m).
- E.** Bedded to thinly bedded feldspathic sandstone ( $O_{VS}$ ). Dark-grey, massive, poorly sorted crystal-rich, coarse-grained feldspathic sandstone that grades into diffusely laminated siltstone with localized cross-bedding, as shown by the red arrow (NC508-310.3m).
- F.** Massive feldspathic sandstone ( $O_{VS}$ ). Dark-orange coloured, crystal-rich and coarse-grained. Ferromagnesian minerals have been pervasively altered to actinolite–chlorite–magnetite; primary feldspars have been pervasively altered to hematite-dusted secondary K-feldspar. The rock is cut by a quartz–banded magnetite–bornite vein, which in turn is cut by quartz–chalcopyrite vein (UR450-143.3m).

Abbreviations: act = actinolite, ccp = chalcopyrite, chl = chlorite, ep = epidote, mag = magnetite, qtz = quartz





The clasts become increasingly diverse up-sequence where the abundance of siltstone clasts increases relative to andesitic-basaltic fragments (Harper, 2000). Rare normal grading was observed with cobble to boulder conglomerate at the base grading to coarse- to medium-grained sandstone with thinly bedded siltstone at the top (Fig. 3.4; e.g. NC541-320m; Appendix A; Wilson, 2003).

### **3.3.3.2 Monomictic volcanic breccia ( $O_{VM}$ )**

A minor domain of monomictic, clast- to matrix-supported, sub-rounded to angular volcanic breccia, up to ~30 m thick, has been documented from various drillholes (Figs. 3.5A and 3.6). In these massive and poorly sorted breccias, 60 - 80% of the clasts are andesitic in composition and contain abundant feldspar and lesser mafic phenocrysts (Figs. 3.4 and 3.9D; Table 3.2). The matrix is fine- to medium-grained and is compositionally similar to the clasts. The monomictic breccia is interbedded with the feldspathic sandstone and siltstone locally (Fig. 3.4). This unit is similar to the feldspar-phyric volcanoclastic breccia of Harper (2000) and Wilson (2003).

### **3.3.3.3 Massive feldspathic sandstone and siltstone ( $O_{VS}$ )**

This subfacies consists predominantly of massive sandstone (Fig. 3.4). Fine to coarse-grained feldspar-rich sandstone predominates at the bottom of the sequence, whereas coarser-grained and crystal-rich sandstone are more common up-sequence. Thinly bedded sandstone and siltstone package occurs in the upper portion of the FRV, transected 300 m below surface on section 11050mE (Fig. 3.5B; Wilson, 2003;). The massive sandstone in the upper part of the sequence is characterized by light-cream to light-grey, poorly sorted, crystal-rich coarse-grained feldspathic sandstone. This grades upward to diffusely laminated siltstone with local cross-bedding (Fig. 3.9E). The unit is 5 - 20 m thick, and individual beds vary from 5 - 30 mm thick (Table 3.2).

A significant part of the massive feldspathic volcanic sandstone package occurs at depth, 600 m below surface (below 5300mRL; Fig. 3.5C and D). The sandstone is dark-green to orange, contains moderate amount of secondary magnetite together with fine- to coarse-grained pervasively altered feldspar and pyroxene

crystals (Fig. 3.9F). This volcanic sandstone horizon occurs immediately above the transitional unit, with thicknesses varying from 30 to 150 m (Fig. 3.4). It is strongly mineralized and is cut by vein stockworks immediately around the monzonite intrusions. Pervasive alteration makes identification of the primary lithology difficult in the ore zone. The feldspathic sandstone thins to the southwest of the monzodiorite (Fig. 3.5A and B).

#### **3.3.3.4 Pyroxene-phyric (Ppo) and feldspar-phyric (Fpo) intrusions**

Massive, coherent pyroxene- and feldspar-phyric basalts and andesites have intruded the FRV and Weemalla Formation sedimentary units along fractures, lithologic contacts and bedding planes. These rock types have been classified according to their most abundant phenocryst phase (Table 3.2). Textural, stratigraphic and structural (orientation) evidence has enabled the interpretation that these coherent volcanic rocks occur as sills and dikes (Fig. 3.10A and B, respectively). These dikes and sills commonly exhibit fine-grained (chilled?) margins (Fig. 3.10A). Fluidal peperitic contacts along the upper and lower margins of the massive clinopyroxene-phyric unit, as documented by Squire (2001), were not observed during this study. Cross-cutting relationship shows that Ppo is truncated by Fpo (Fig. 3.16A and B).

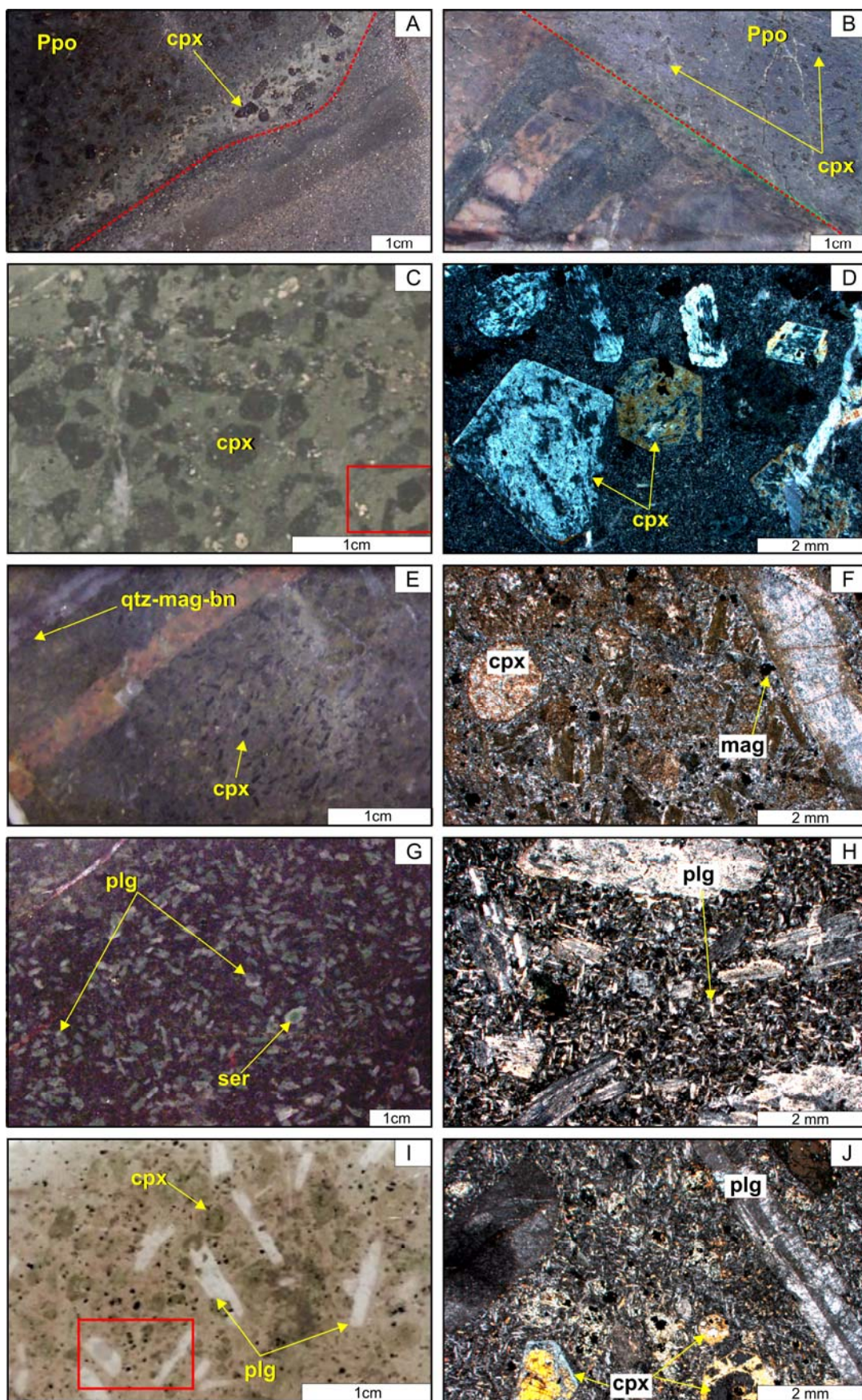
The pyroxene-phyric sills are texturally different from the dikes. The sills are characterized by conspicuously large (>2 to 7 mm) euhedral to subhedral clinopyroxene phenocrysts with light-green aphanitic groundmass (Fig 3.10C). The clinopyroxene phenocrysts have been selectively replaced by chlorite–actinolite (Fig. 3.10D). The groundmass consists of holocrystalline plagioclase, with lesser clinopyroxene. The pyroxene-phyric dikes comprise euhedral clinopyroxene (<2 mm; 5 - 25 vol %), and less euhedral plagioclase phenocrysts. The unit is typically dark-green to dark-brown and moderately to strongly magnetic (Fig. 3.10E). In thin section, small euhedral to subhedral clinopyroxene phenocrysts have been pervasively altered to actinolite–chlorite–magnetite, the plagioclase to secondary hematite-dusted K-feldspar. Minor magnetite phenocrysts are also present (Fig. 3.10F). The clinopyroxene ranges in composition from augite to diopside (Appendix C). The groundmass comprises fine-grained plagioclase, ferromagnesian

**Figure 3.10** Photographs and microphotographs of the coherent lithofacies of the Forest Reefs Volcanics from Ridgeway.

- A.** Pyroxene-phyric (Ppo) basaltic sill unit. Large (up to 7 mm diameter) euhedral to subhedral clinopyroxene phenocrysts have been selectively altered to chlorite. These phenocrysts are set in a dark green to grey coloured aphanitic groundmass. Note the irregular contact (red dashed-line) along bedding of the massive sandstone of the FRV, fine-grained margins (chilled?; NC508-331.4m).
- B.** Pyroxene-phyric basaltic sill unit. Phenocrysts of small (<5 mm) clinopyroxene phenocrysts have been selectively altered to chlorite–actinolite–magnetite. Intrusive contact (red dashed-line) with thinly bedded feldspathic siltstone and sandstone unit of the Weemalla Formation. The contact is discordant to the bedding. The dark grey - green coloured beds contain abundant chlorite–actinolite and magnetite-altered clinopyroxene (?) grains, while the orange-coloured beds are quartz–albite-altered (UR323-583.8m).
- C.** Pyroxene-phyric basaltic sill unit. Conspicuous large (up to 5 mm in diameter), dark-green clinopyroxene crystals (now chlorite–actinolite). Less abundant light-pink feldspar phenocrysts in a light-green aphanitic groundmass (NC508-531.8m).
- D.** Photomicrograph (xpl) part of (C) outlined in red box. Large euhedral phenocrysts of clinopyroxene selectively altered to chlorite–actinolite, set in a fine-grained crystalline groundmass of plagioclase and ferromagnesian minerals.
- E.** Pyroxene-phyric dike. Dark-green, small (<2 mm) subhedral clinopyroxene phenocrysts occur with less abundant fine-grained feldspar set in a fine-grained, dark-brown groundmass. Thin pink aplite vein-dike and quartz–magnetite–bornite veins cut the rock (UR142-181m).
- F.** Photomicrograph (xpl) of Ppo dike. Euhedral phenocrysts of clinopyroxene have been pervasively altered to actinolite–chlorite–magnetite. Orthoclase crystal and lesser euhedral plagioclase phenocrysts have been altered to secondary hematite-dusted K-feldspar. Groundmass is composed of crystalline plagioclase, ferromagnesian minerals and magnetite (UR142-181m).
- G.** Feldspar-phyric (Fpo) andesitic sill unit. Conspicuous euhedral laths of plagioclase phenocrysts (<2 mm long), evenly distributed in a dark greenish-gray aphanitic groundmass. The plagioclase phenocrysts are selectively altered to sericite, preferentially in the cores (UR450-5m).
- H.** Photomicrograph (xpl) of Fpo sill. Phenocrysts of euhedral selectively altered plagioclase set in a fine-grained interlocking skeletal plagioclase crystals and ferromagnesian minerals (UR450-5m).
- I.** Photomicrograph (ppl) of Fpo dike. Conspicuous large (up to 10 mm long) tabular euhedral plagioclase and subhedral pyroxene phenocrysts set in a dark greenish-gray fine-grained groundmass (UR149-3m).
- J.** Photomicrograph (xpl) part of (I) outlined in red box. Phenocrysts of tabular plagioclase selectively altered to albite. Euhedral clinopyroxene phenocrysts selectively altered to actinolite–chlorite–magnetite. The groundmass comprises interlocking network of plagioclase laths, magnetite and actinolite–chlorite-altered ferromagnesian minerals.

Abbreviations: act = actinolite, cpx = clinopyroxene, mag = magnetite, plg = plagioclase, ppl = plane polarized light, xpl = cross polarized light





minerals and magnetite. These pyroxene-phyric dikes are equivalent to the clinopyroxene-phyric dikes of Wilson (2003).

The feldspar-phyric sill contains abundant, evenly distributed euhedral to subhedral subequant plagioclase phenocrysts (2 - 5 mm long) that have been altered to chlorite and sericite (Fig. 3.10G). There are also small euhedral clinopyroxene phenocrysts (~2 mm in diameter) set in a dark-green aphanitic groundmass. The groundmass contains fine-grained interlocking skeletal plagioclase crystals and altered ferromagnesium minerals (replaced by chlorite), together with minor magnetite (Fig. 3.10H). These feldspar-phyric sills are similar to feldspar porphyries from Cadia East (Kitto, 2005)

The feldspar-phyric dikes are texturally distinct from the sills. The dikes are characterized by large (3 - 20 mm diameter), conspicuous subhedral to euhedral plagioclase phenocrysts (Fig. 3.10I). The phenocrysts exhibit faint complex twinning and have undergone moderately to intensely pervasive replacement by alkali-feldspar and sericite (Fig. 3.10J). Relatively fresh euhedral clinopyroxene phenocrysts (<5 mm) have been selectively replaced by chlorite–actinolite. The groundmass is greenish to dark grey and composed of fine-grained interlocking skeletal plagioclase crystals, former ferromagnesium crystals (now replaced by chlorite–actinolite) and magnetite. Plagioclase occurs both as individual crystals and as radial clusters (Fig 3.10J), giving the rock a glomerophyric appearance. The plagioclase crystals have grain size up to 20 mm in diameter. Electron microprobe analyses have identified the feldspar as labradorite (Appendix B). These feldspar-phyric dikes are equivalent to plagioclase-phyric unit of Wilson (2003) and similar to feldspar-pyroxene porphyry from Cadia East (Kitto, 2005).

*Geometry and distribution of the coherent lithofacies:* The continuity across sections shows that many of the coherent units occur as stratiform, sheet-like bodies and as parallel small intrusions (Fig. 3.5A to D). The intersection thickness of the dike units are narrow and vary from 1 to 20 m thick, whereas the thickness of individual sills range from 5 cm to 5 m. Narrow, subvertical Ppo and Fpo dikes are found throughout the deposit. These dikes have intruded W- to NW-striking faults or other zones of structural weakness (Fig. 3.5B). The longest (~ 0.4 km) and most vertically persistent

Ppo dike occurs along the NW-striking North Fault (Figs. 3.5A to D; Fig. 3.7). Dike contacts are sharp, but have been faulted or sheared in places. The Ppo and Fpo dikes are cut by and occur as xenoliths in monzodiorite and monzonite intrusions (Figs. 3.11G and 3.17G). The lower and upper sill contacts are broadly concordant with the bedding of the host FRV and Weemalla Formation.

### **3.4 Ridgeway intrusive complex (RIC)**

The Ridgeway intrusive complex (RIC) is one of several centers that have been emplaced into the FRV and the Weemalla Formation (Fig. 3.1; Wilson *et al.*, 2003). The Cadia intrusive complex (CIC) occupies the center of the Cadia district (Fig. 3.1). It is a 3 x 1.5 kilometers composite, NW-trending stock (Holliday *et al.*, 2002). The CIC comprises diorite to monzodiorite and minor gabbro in the west (Turnbridge Wells diorite), and coarse-grained quartz monzonite porphyry in the east (Fig. 3.1). The Cadia Far East intrusive complex (CFEIC) is located 2.5 km to the southeast of the CIC (Fig. 3.1). It consists of monzodiorite, quartz monzodiorite and quartz monzonite dikes (Wilson *et al.*, 2003).

The RIC is composed of NW-elongated diorite to monzodiorite, monzonite and quartz monzonite intrusions (Wilson *et al.*, 2003). Previous studies at Ridgeway by Wilson (2003) and Wilson *et al.* (2003) used criteria such as intrusive contacts, alteration relationships, abrupt grade changes, and the presence or absence of characteristic veins and mineralization, to discriminate between intrusive phases. This led to the identification of four phases of monzonitic intrusions in the RIC. The earliest phase defined by Wilson *et al.* (2003) is a pre-mineral, equigranular monzodiorite. Three monzonitic intrusions were recognized as being related to mineralization and were subdivided into early-mineral, inter-mineral and late-mineral monzonites (Wilson *et al.*, 2003). The current study has classified individual intrusions using Wilson's (2003) criteria. Additional textural features that have helped to define the intrusive history and intrusion geometries at Ridgeway in the current study include: 1) phenocryst type, size and abundance, 2) distinction of magmatic-hydrothermal textures, and 3) distribution of xenoliths. Although the

**Table 3.3** Textural and mineralogical characteristics of the intrusive rocks from Ridgeway during the current study and by Wilson, 2003 and Wilson *et al.* (2003). The intrusions are listed from oldest (bottom) to youngest (top) based on cross-cutting relationships.

Current study						Wilson (2003); Wilson <i>et al.</i> (2003)				
Relative Age	Rock type	CODE	Texture	Phenocrysts	Distribution/geometry	Rock type	Texture	Quartz vein density (vol %)	Au g/t (average)	Cu (%) (average)
Relative Age	Late-stage quartz monzonite	P3	Equigranular, phaneritic; xenoliths of coherent feldspar-phyric and quartz fragments; has truncated quartz veins	Plagioclase (30 - 60 %; ~3 mm long), interstitial orthoclase (~10 vol %; ~3 mm long; with inclusions of plagioclase, apatite), quartz (<10 vol %), ferromagnesian minerals (<5 m vol %; ~3 mm long)	Northwest-trending; subvertical cylindrical pipe, 5 to 200 m thick; plunges towards the northwest	Late-mineral quartz monzonite	Porphyritic, texturally and compositionally similar to inter-mineral monzonite	1 - 3 locally 8	1.09	0.24
	Quartz monzonite	P2	Porphyritic; crystal-crowded with 50 - 70 vol % phenocrysts in a microcrystalline groundmass; quartz USTs occur near the upper contact; miarolitic cavities and aplite dikes are also present; presence of mafic xenoliths	Plagioclase (15 - 25 vol %; ~2 mm long), orthoclase (~15 vol %; <2 mm long), quartz (2 - 5 vol %), hornblende, pyroxene (<10 vol %); isolated alkali-feldspar and plagioclase megacrysts (up to 20 mm) contain inclusions of apatite and biotite	Elongate along northwest, pinches-out in both ends and swells at its center in plan; subvertical, elongate pipe in section up to 50 m thick	Inter-mineral monzonite	Porphyritic; xenoliths of quartz fragments; truncate quartz veins; comb quartz layers, crenulate bands of euhedral quartz - chalcopyrite - magnetite	2 - 8 locally 20	2.77	0.59
	Mafic monzonite	P1	Porphyritic, with 20 - 50 vol % phenocrysts in a fine-grained anhedral groundmass; magnetite USTs occur at the top of the intrusions; presence of mafic xenoliths common	Orthoclase occurring as isolated tabular crystals (1 to 10 mm long; brick-red to orange); orthoclase and plagioclase (5 - 20 vol %); hornblende, biotite and pyroxene (10 - 25 vol %; <2 mm long)	Elongate along northwest, pinches-out in both ends and swells at its center both in plan and section; subvertical, elongate pipe in section up to 30 m thick	Early-mineral monzonite	Porphyritic, intense alteration has destroyed primary texture	4 - 40 locally 80	5.6	1.24
	Monzodiorite	MzD	Porphyritic to equigranular; holocrystalline, phaneritic; crowded	Plagioclase (30 - 60 vol %; <2 mm long; lath-shaped), interstitial hornblende and pyroxene (5 - 10 vol %; ~2 mm diameter), biotite (<1 vol %), magnetite (<5 vol %)	Elongate along northwest in plan view; subvertical, tabular elongate plug in section up to 100 m thick	Monzodiorite	Equigranular, abundant euhedral plagioclase and euhedral to subhedral mafic phenocrysts in a fine-grained orthoclase- rich groundmass	1 - 4 locally 15	0.92	0.51

Pre-mineralization intrusion

Monzonite intrusions

Relative Age



intrusions have undergone texturally destructive hydrothermal alteration locally, primary features are still recognizable. In this thesis, the intrusions at Ridgeway are subdivided into groups of pre-mineralization, syn-mineralization, and late-stage intrusions. Table 3.3 provides a correlation between the nomenclature for the intrusive phases as documented by Wilson *et al.* (2003) and the current study.

### **3.4.1 Pre-mineralization intrusion**

#### **3.4.1.1 Monzodiorite (MzD)**

The monzodiorite (MzD) at Ridgeway is exposed on the southwest side of the Ridgeway orebody (Fig. 3.7). It is compositionally zoned, with a porphyritic monzodiorite core and an equigranular, more dioritic margin (Table 3.3). There is a gradational contact between the diorite and monzodiorite phases. The monzodiorite is typically greenish-pale cream to orange (Fig. 3.11A). The rock is variably porphyritic, with lath-shaped plagioclase phenocrysts that locally exhibit a preferred alignment (Fig. 3.11B), together with euhedral clinopyroxene (altered to actinolite), and hornblende (altered to biotite–chlorite) set in a fine-grained holocrystalline groundmass of anhedral feldspars with accessory apatite (Fig. 3.11C; Table 3.3).

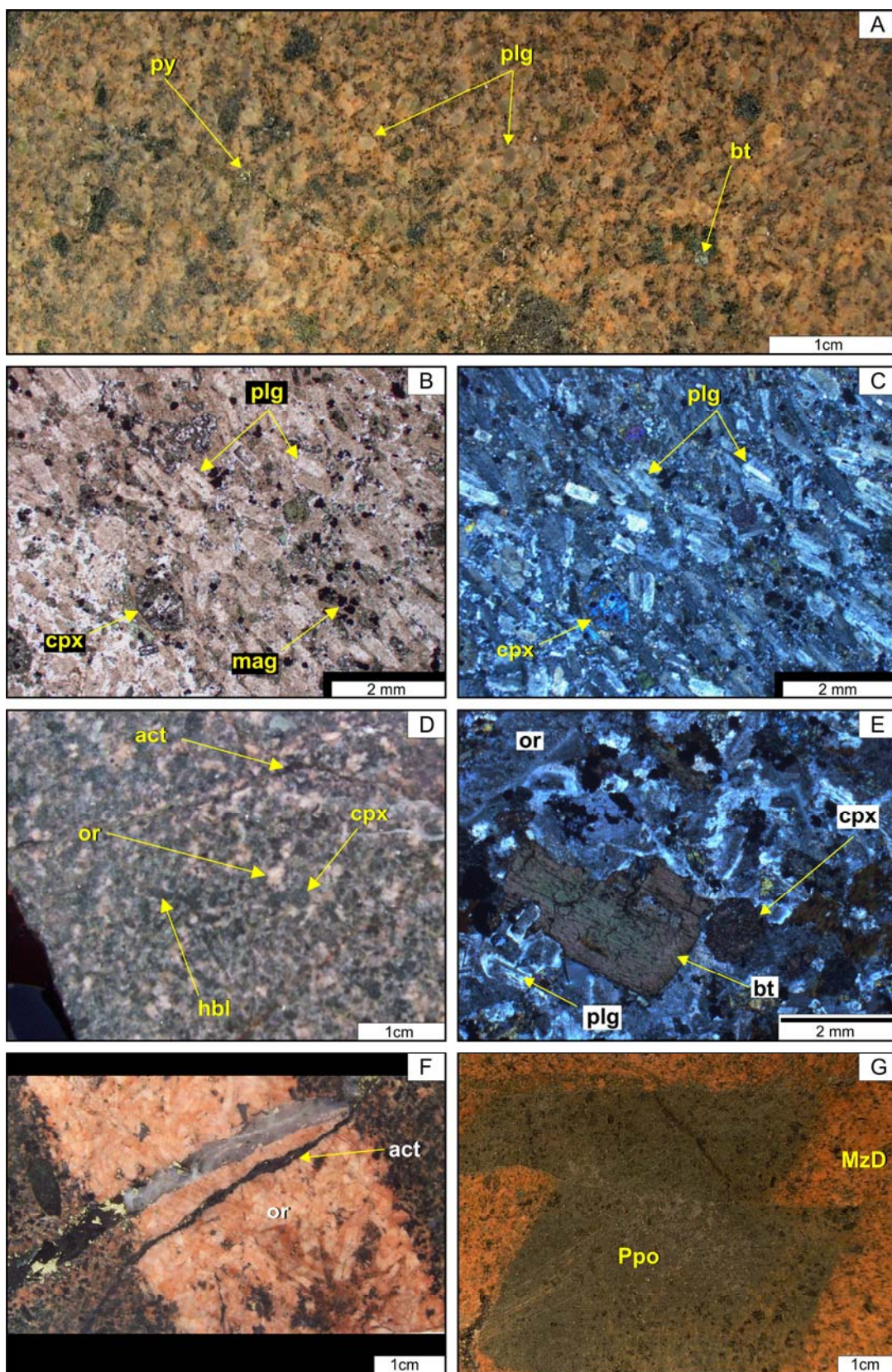
The more dioritic component is typically dark green to grey, equigranular and highly magnetic (Fig. 3.11D). It is composed of interlocking anhedral to subhedral altered plagioclase, orthoclase and dark-green hornblende and clinopyroxene (typically altered to actinolite and chlorite; Wilson, 2003) and relict biotite crystals (Fig. 3.11E). Accessory minerals include apatite and Fe–Ti oxides. The plagioclase and orthoclase are hematite-dusted, giving the rock a pink to red colouration and a ‘wormy’ texture (Fig. 3.11D).

Volumetrically minor salmon-pink to light orange alkali-feldspar syenite has been noted locally in the MzD (Fig. 3.11F). The segregations vary in thickness from 2 to 100 mm and comprise subhedral orthoclase crystals (~80 vol %; typically ~2 mm long, rarely up to 10 mm long), with minor amounts of clinopyroxene, magnetite and apatite.

**Figure 3.11** Textures of the pre-mineralization monzodiorite (MzD) from Ridgeway.

- A.** MzD displaying porphyritic texture. Pale-cream, conspicuous lath-shape turbid plagioclase phenocrysts (< 2mm long) and biotite flakes (after hornblende?) set in K-feldspar altered, hematite-dusted light-orange groundmass (UR150-110.3m).
- B.** Photomicrograph (ppl) of MzD. Abundant euhedral phenocrysts of plagioclase moderately pervasively altered to albite and hematite-dusted secondary K-feldspar. Euhedral clinopyroxene (augite) altered to actinolite–chlorite–magnetite. Small (<2 mm) hornblende phenocrysts totally altered to biotite (now chlorite; UR150-98.7m).
- C.** Photomicrograph (xpl) of (B) showing weakly aligned euhedral plagioclase phenocrysts set in fine-grained crystalline groundmass of orthoclase-rich and altered ferromagnesian minerals (now actinolite–chlorite) and magnetite.
- D.** MzD displaying equigranular texture. This rock is composed of anhedral mass of pale-cream to light orange-coloured feldspar, interstitial with dark-green chlorite–actinolite altered clinopyroxene minerals (UR360-889m).
- E.** Photomicrograph (xpl) of equigranular MzD. Anhedral interstitial selectively albite-altered orthoclase and plagioclase crystals, dark-brown biotite flakes, and altered clinopyroxene minerals (now actinolite–chlorite; UR360; 895m).
- F.** Light orange syenite (~3 cm thick) cutting the MzD. Phenocrysts of orthoclase, with minor few interstitial clinopyroxene (now altered to actinolite–chlorite) and magnetite. Actinolite–magnetite stringer cuts both the MzD and the syenite. Large (~1 cm) subhedral hornblende crystal altered to actinolite–chlorite–magnetite (NC508-955m).
- G.** Dark orange-coloured MzD with dark-green coherent pyroxene-phyric (Ppo) xenolith. The MzD has undergone pervasive K-feldspar alteration of groundmass that has been hematite-dusted. The Ppo has undergone pervasive chlorite–actinolite–magnetite alteration of ferromagnesian phenocrysts and groundmass. Note the distinct colour contrast between the two rocks (UR255-31.6m).

Abbreviations: act = actinolite, bt = biotite, cpx = clinopyroxene, hbl = hornblende, or = orthoclase, plg = plagioclase, ppl = plane polarized light, py = pyrite, qtz = quartz, rl = reflected light, rt = rutile, ttn = titanite, xpl = cross polarized light



*Geometry and distribution:* The MzD occurs on the southern side of the Ridgeway orebody as a subvertical plug with a northwest elongation in plan view (Fig. 3.7A). Underground mapping has helped to define the MzD geometry, and has shown that it is separate from the monzonite intrusions. In plan, the MzD has horizontal dimensions of 200 m by 100 m (Fig. 3.7A), and a vertical extent of at least 2 km (Fig. 3.6A and B). The top of the intrusion is located at 350 m below the present day surface (5500mRL; Fig. 3.5B). Gold grade contours cut through the MzD (Fig. 3.6), and all of the vein stages associated with mineralization at Ridgeway (as described in Chapter 4) have cut the MzD, indicating a pre-mineralization timing for this intrusion (Wilson, 2003).

### **3.4.2 Syn-mineralization intrusions**

At Ridgeway, closely-spaced clusters of monzonite intrusions were emplaced during three phases of magmatism (Fig. 3.4; Fig. 3.5B to D). The oldest of the ore-related intrusions, and the most strongly mineralized, is the mafic monzonite porphyry phase. This was followed by the quartz monzonite, and the equigranular late-stage quartz monzonite. These equates to the three phases of porphyritic intrusion (early-mineral monzonite, and inter- and late-mineral quartz monzonite) recognized by Wilson (2003; Table 3.3).

#### **3.4.2.1 Mafic monzonite porphyry (P1)**

The mafic monzonite porphyry (P1) is characterized by dark-brown to dark orange-red, brick-red to orange, small subhedral to euhedral orthoclase crystals, and smaller, subhedral and pervasively altered ferromagnesian and feldspar phenocrysts (<2 mm long) set in a fine-grained orange-coloured feldspar-rich groundmass (Table 3.3; Fig. 3.12A and B). This rock is notably less crystal crowded than the later monzonite phases. Selectively pervasive to pervasive hydrothermal alteration is ubiquitous throughout the P1. In samples that preserve primary textures, hematite-dusted orthoclase and plagioclase (altered to albite) are the most abundant phenocrysts (5 - 20 vol %), occurring together with subordinate altered subhedral hornblende, biotite and pyroxene phenocrysts that have been altered to chlorite and rutile (Fig. 3.12C). The groundmass is composed of fine-grained, anhedral feldspar



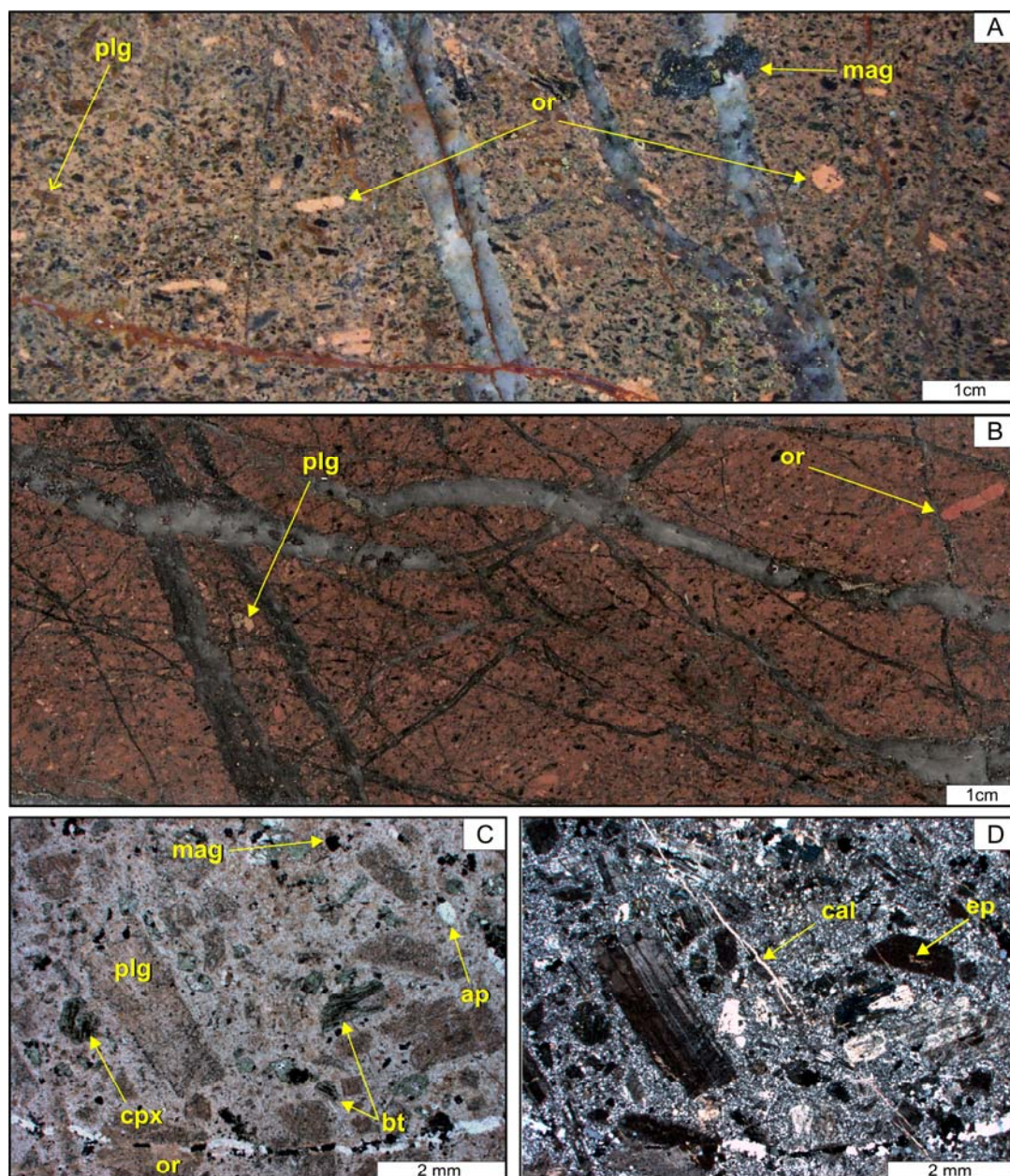


**Figure 3.12** Textures of the mafic monzonite (P1) from Ridgeway. **A)** P1 with conspicuous subhedral orange to reddish orthoclase phenocrysts (<10 mm long), small (<5 mm) subhedral to euhedral hornblende, biotite and pyroxene minerals (altered to chlorite - rutile  $\pm$  actinolite), and dark-brown plagioclase phenocrysts (altered to hematite-dusted albite). The groundmass is composed of light-cream fine-grained alkali-feldspars. Quartz - magnetite veins have cut this rock (NC498-893.5m). **B)** P1 with sparse tabular, dark-orange orthoclase, pale-cream plagioclase and anhedral fine-grained minerals set in a dark-orange groundmass (now pervasively hematite-dusted albite). Abundant quartz - magnetite - bornite veins cut this rock (UR390-47.5m). **C)** Photomicrograph (ppl) of P1 showing euhedral turbid orthoclase and plagioclase (altered to albite), subhedral hornblende, shreddy biotite (after hornblende?), and pyroxene phenocrysts (now chlorite and rutile) surrounded by fine-grained, anhedral alkali-feldspars and accessory apatite, titanite and magnetite. **D)** Photomicrograph (xpl) of **(C)**. Plagioclase phenocrysts (relatively fresh) exhibits twinning, the cores of the other plagioclase crystals have been preferentially altered to epidote. Calcite stringer cuts the rock. Abbreviations: ap = apatite, bt = biotite, cal = calcite, cpx = clinopyroxene, ep = epidote, mag = magnetite, or = orthoclase, plg = plagioclase, ppl = plane polarized light, xpl = cross polarized light



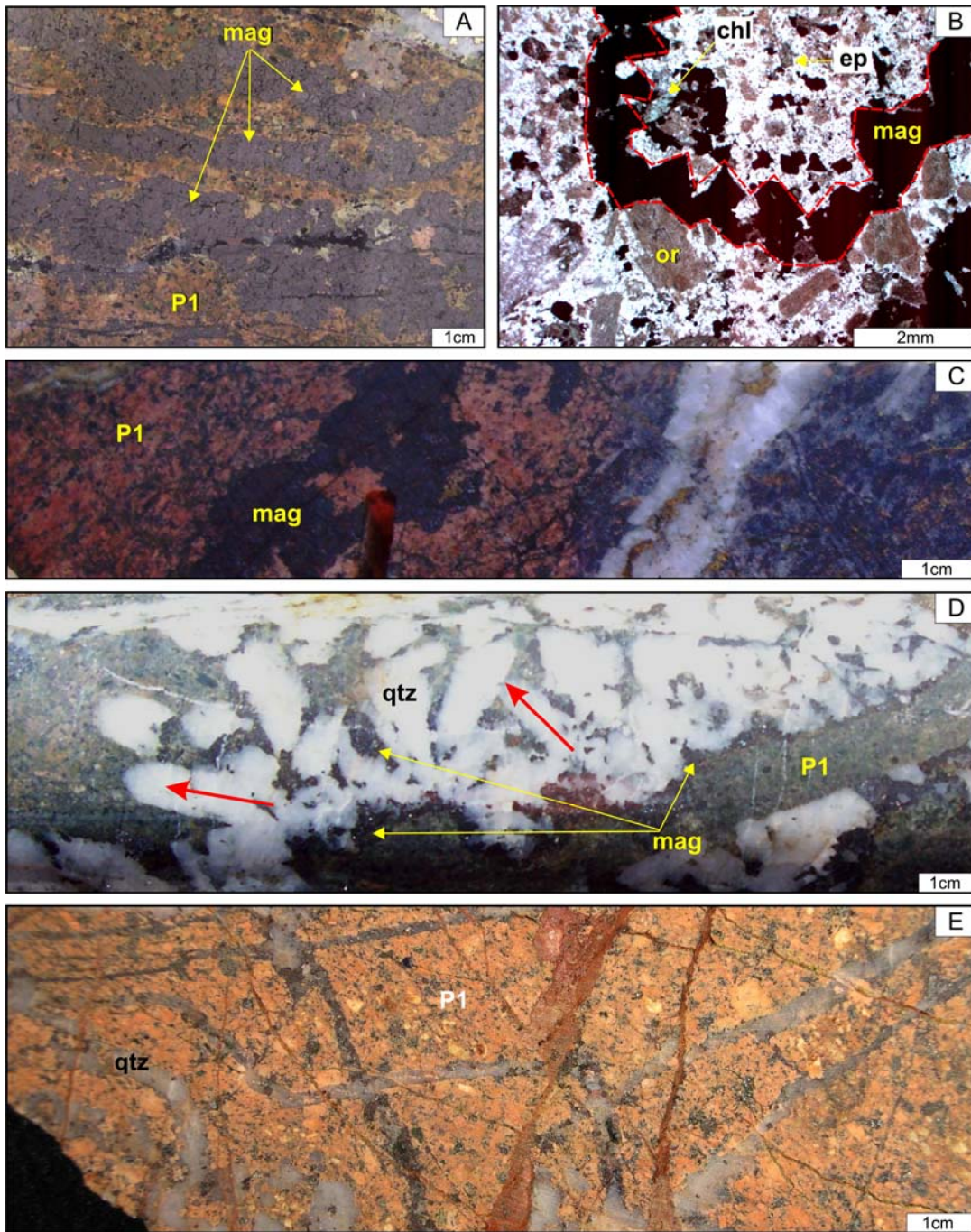


**Figure 3.13** Unidirectional solidification textures (USTs) and “brain-rock” in the mafic monzonite (P1) from Ridgeway. **A)** Crenulate comb layered textures defined by alternating bands of magnetite. The crenulated bands of massive magnetite are interlayered with P1. Grab sample collected near Cadia coreshed (from underground Ridgeway, possibly from 5255mRL-Crosscut 1-chainage 94m, in a similar position to that observed in (D)). **B)** Photomicrograph of magnetite USTs showing the asymmetric crenulate texture (red line) of magnetite. **C)** Crenulate band of massive magnetite in P1. Abundant quartz - magnetite - bornite stockwork veins occur outside the P1 contact, which in turn has been cut by a later quartz - chalcopyrite vein (NC508-883.2m). **D)** Quartz - magnetite comb-texture in P1 intrusion. Euhedral quartz (up to 2 cm) is intergrown with magnetite and chalcopyrite. The quartz crystals points towards the center of the intrusion (NC498-741.4m). **E)** Crenulate bands of discontinuous chains of prismatic quartz (or 'brain-rock'; < 5 mm) in the P1 (NC498-719.3m). Abbreviations: chl = chlorite, ep = epidote, mag = magnetite, or = orthoclase, ppl = plane polarized light, qtz = quartz

intergrowths. Accessory minerals include apatite, titanite and magnetite (Fig. 3.12C). P1 is more strongly mineralized than the later-stage monzonite intrusions (Wilson *et al.*, 2003).

Magnetite  $\pm$  quartz comb-layered textures, interpreted to be unidirectional solidification textures (USTs) occur along the margins and apical portion of P1 (Fig. 3.5B). Magnetite-rich USTs have been observed underground and were logged in some drillholes (Fig. 3.13A and C). The underground location exhibits alternating bands (up to 1 cm) of magnetite and irregular (mm-scale) domains of feldspar-quartz-aplite (Fig. 3.13A and B; Harris *et al.*, 2006). Discontinuous bands of prismatic quartz (up to 5 mm in diameter) are also present Figure 3.13D.

*Geometry and distribution:* P1 occurs as subvertical, steeply-dipping, thin pipes (1 - 30 m thick). The tops of at least three discrete intrusions occur at 550 m below the pre-mining land surface (just above the 5300mRL; 11050mE, Fig. 3.5B). In cross sections, the individual intrusions extend vertically over distances of up to 200 m (Fig. 3.5A to D). Each P1 intrusion is pipe-like and the pipes tend to pinch-out towards their tops and bottoms. P1 is narrow (4 - 10 m wide) in the siliceous siltstone at the bottom, swells to ~20 m inside the massive feldspathic sandstone and the transitional unit, and pinches again in the polymictic volcanoclastic breccia at the top of the deposit (Fig. 3.5B and C).

P1 appears to pinch-out and become rootless along the margins of younger monzonites, possibly due to unrecognized fault offsets (Fig. 3.5B). In plan view, P1 is elongated along a northwest trend, northeast of the MzD (Fig. 3.7A and B). The P1 intrusions typically have sheared and/or brecciated contacts with the pyroxene-phyric dikes, and brecciated contacts with the surrounding host rocks.

#### **3.4.2.2 Quartz monzonite porphyry (P2)**

The quartz monzonite porphyry (P2) has well-preserved primary textures compared to P1. P2 is notably more crystal-crowded (50 - 70 vol % phenocrysts; Fig. 3.14A and B; Table 3.3) and is typically pale-cream to dark orange-red and characterized by a coarse-grained, porphyritic texture. It contains conspicuous (up to 20 mm diameter) light to dark-orange K-feldspar and plagioclase (andesine) crystals



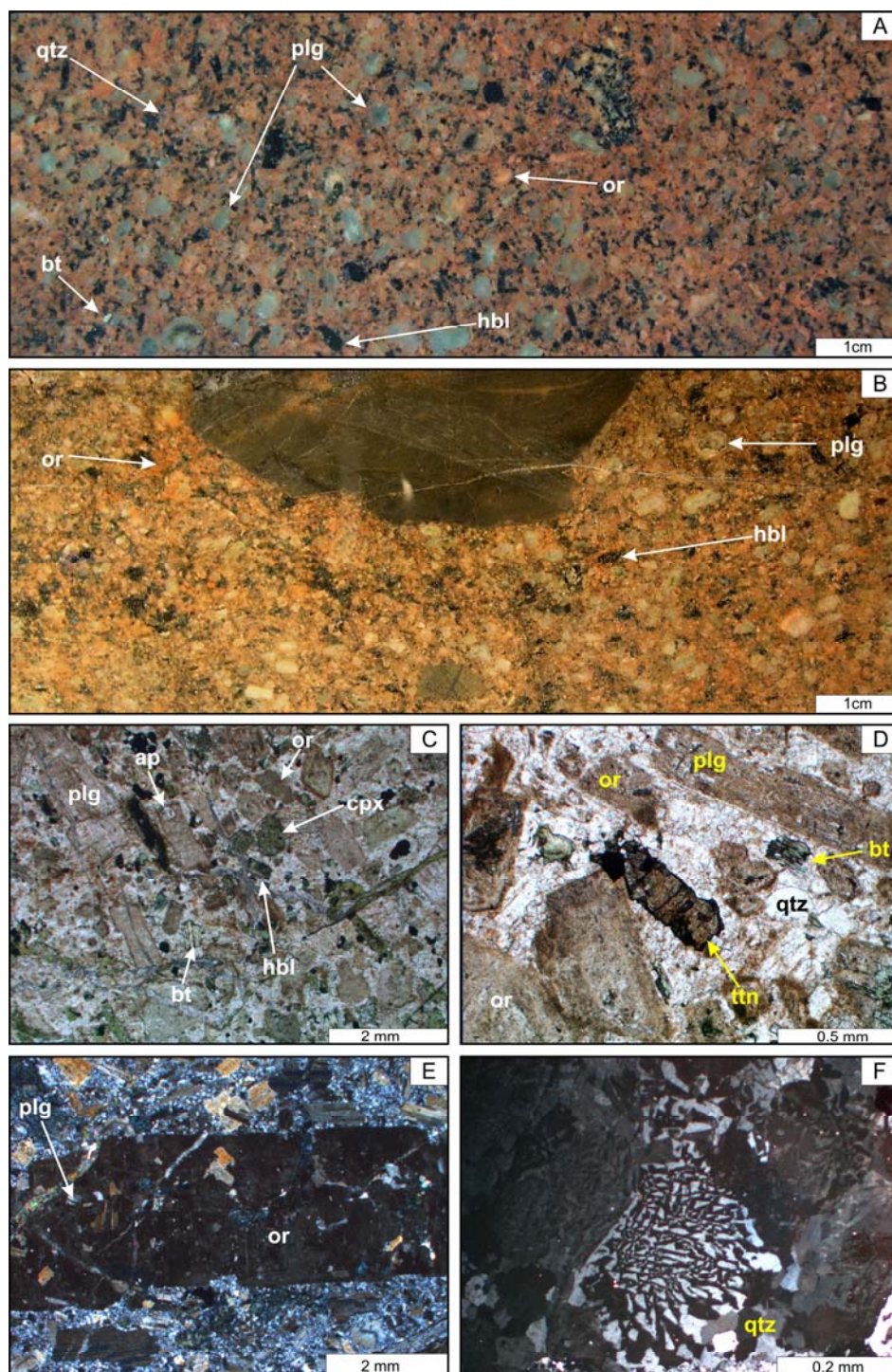


**Figure 3.14** Textures of the quartz monzonite (P2) from Ridgeway. **A)** Crystal-crowded P2 with phenocrysts comprising of abundant subhedral to euhedral, cream plagioclase, subhedral hornblende, biotite, and minor small dark-orange orthoclase and quartz, set in an pale orange groundmass (UR248 - 110.7m). **B)** P2 with abundant phenocrysts of subhedral pale cream plagioclase, subhedral hornblende and orthoclase set in fine-grained K-feldspar altered groundmass (NC541-879m). **C)** Photomicrograph (ppl) of P2. Plagioclase phenocrysts weakly altered to albite, small clinopyroxene and hornblende altered to chlorite, actinolite and rutile. **D)** Photomicrograph (ppl) of P2. The groundmass is composed of anhedral and interstitial quartz and plagioclase crystals, with accessory apatite, titanite and magnetite (UR326-231.6m). **E)** Photomicrograph (xpl) of an orthoclase megacryst (1 cm long) with inclusions of plagioclase, apatite and chlorite-altered biotite (UR 326-267.7m). **F)** Photomicrograph (xpl) of an aplitic vein-dike exhibiting granophyric texture. Intergrowth of quartz and alkali-feldspar radiates out from large plagioclase grains (UR450-122.6m). Abbreviations: ap = apatite, bt = biotite, cpx = clinopyroxene, hornblende = hbl, or = orthoclase, plg = plagioclase, ppl = plane polarized light, qtz = quartz, ttn = titanite, xpl = cross polarized light



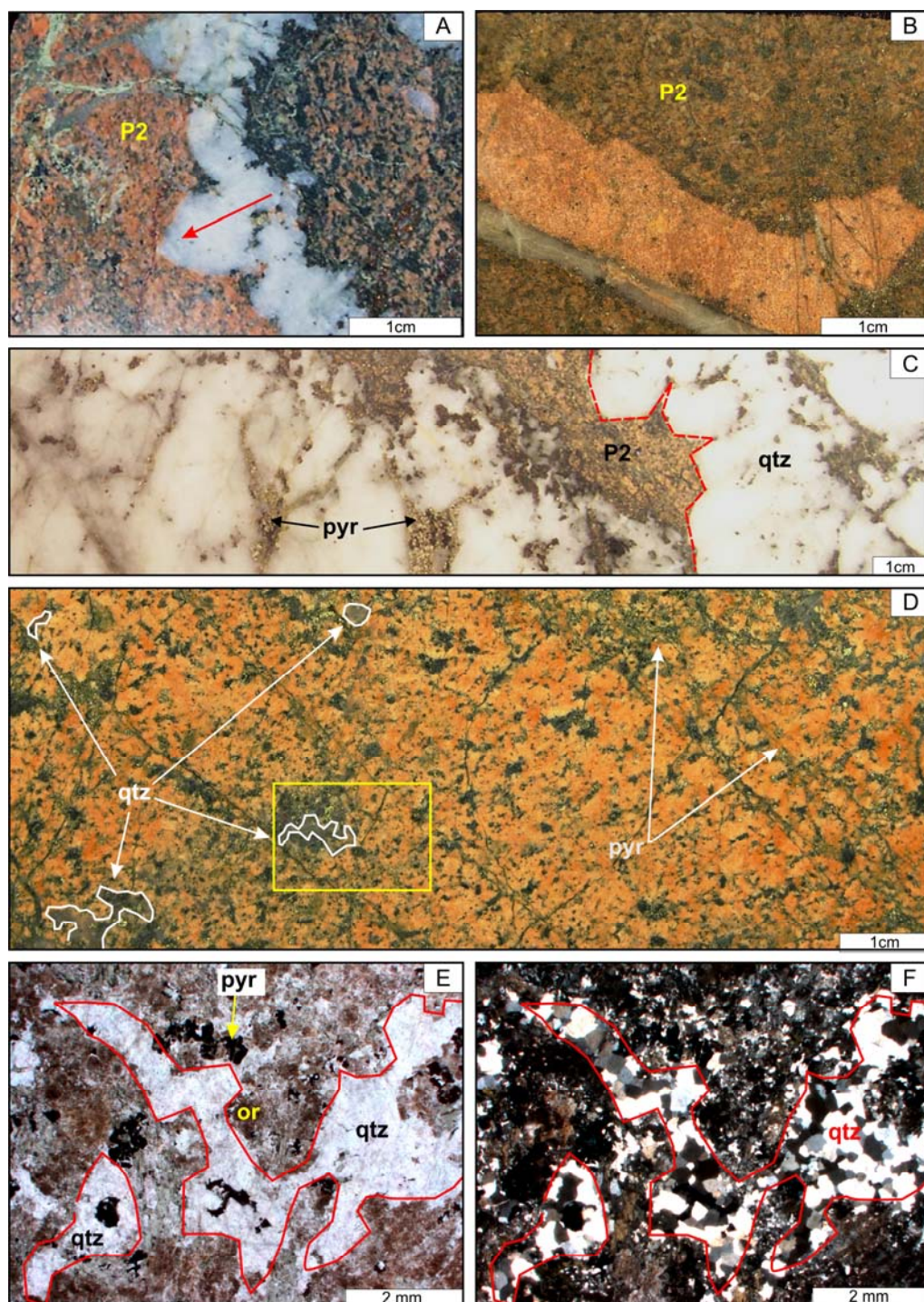


**Figure 3.15** Unidirectional solidification textures (USTs) and miarolitic cavities in the quartz monzonite (P2) from Ridgeway. **A)** Quartz-rich UST occurring near the contact with mafic monzonite (P1). Arrow (red) points downward towards the center of the intrusion (UR140-256m). **B)** Aplite vein-dike with an orange-fined-grained sugary texture defined by alkali-feldspar, quartz, and minor disseminated chalcopyrite (UR149-152.2m). **C)** Quartz-rich UST in P2. Pyrite occurs as coarse-grained crystals intergrown with quartz (UR140-227m). **D)** Pods of sugary quartz crystals (former miarolitic pods; white lines) in P2 (NC498-772.9m). Pyrite occurs as disseminations, chlorite as pervasive replacement of mafic minerals. The dark orange groundmass has been pervasively altered to hematite-dusted alkali feldspar. **E)** Photomicrograph (ppl) part of (D) outlined in white box, showing the pods of quartz crystals (white lines) surrounded by turbid-dark brown orthoclase pervasively altered to albite. **F)** Photomicrograph (xpl) of (E) showing the miarolitic pods (red lines) composed of small aggregates of quartz crystals. Abbreviations: act = actinolite, cpx = clinopyroxene, or = orthoclase, plg = plagioclase, ppl = plane polarized light, pyr = pyrite, qtz = quartz, xpl = cross polarized light



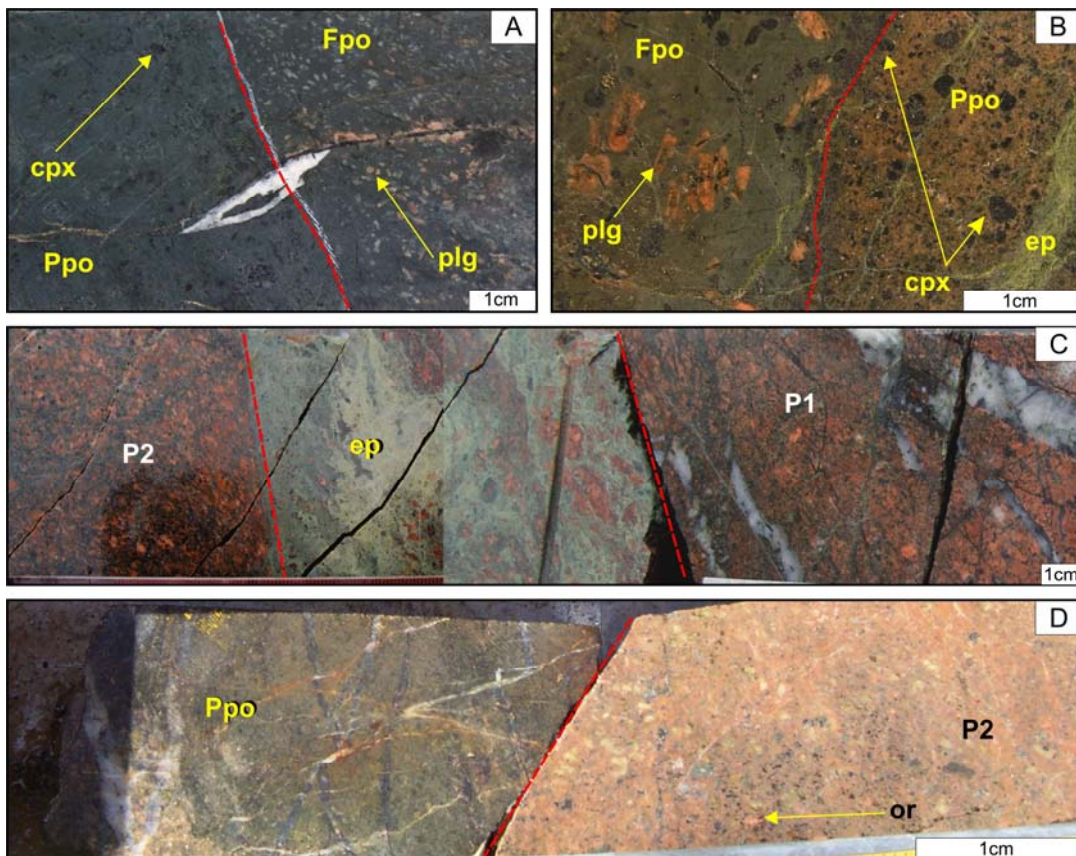


**Figure 3.16** Photographs of intrusive contacts from Ridgeway. **A)** Sharp intrusive contact (red dashed-line) between the pyroxene-phyric (Ppo) dike and feldspar-phyric (Fpo) sill (UR362-103m). **B)** Intrusive contact (red dashed-line) between Fpo sill and Ppo dike. The small (<2 mm) clinopyroxene phenocrysts along the contact probably derived from the Ppo wallrock, implying an early timing for Ppo (UR325-465m). **C)** Healed sheared contact zone (~10 cm, red dashed-lines) with epidote flooding marked the contact between the mafic monzonite porphyry (P1) and the quartz monzonite porphyry (P2). The P1 (right side) has been cut by quartz - magnetite - bornite veins (UR358W1-578m). **D)** Sharp fault (?) contact (red dashed-line) between Ppo and P2. Ppo has undergone pervasive chlorite - actinolite - magnetite alteration of ferromagnesian minerals. P2 has undergone K-feldspar pervasive alteration of the groundmass. The feldspars phenocrysts have been altered to albite and hematite-dusted secondary orthoclase (UR142-181.7m). Abbreviations: cpx = clinopyroxene, ep = epidote, plg = plagioclase, or = orthoclase

and minor phenocrysts of quartz, hornblende, pyroxene and biotite. The groundmass is composed of fine-grained anhedral feldspar, quartz and accessory apatite, titanite, and magnetite (Fig. 3.14C and D). The K-feldspar phenocrysts typically contain inclusions of plagioclase, apatite and biotite (Fig 3.14E).

Abundant quartz USTs between 1 to 30 cm wide occur near the upper contact of P2 (Fig. 3.15A and C; Wilson, 2003; Lickfold *et al.*, 2003). Secondary pyrite occurs as disseminations and clots in the quartz (Fig. 3.15C). The pyrite was not deposited as a primary phase from the hydrothermal fluid-melt mixture – it is a late-stage replacement feature. Inside the P2 intrusions, clusters of spherical anhedral aggregates of quartz occur locally and are interpreted to be miarolitic cavities (Fig.

3.15D). Pale- to dark-orange aplite vein-dikes (1 - 5 cm wide) cross-cut P2 and are locally found along the P2 margins (Fig. 3.15B). The aplite vein-dikes consist of fine-grained intergrowths of K-feldspar and quartz, locally exhibiting granophyric textures (Fig. 3.14F).

*Geometry and distribution:* P2 occurs as a subvertical elongate pipe between 1 to 50 m wide that trends northwest (Fig. 3.7). It has a vertical extent of at least 1.7 km. The top of the intrusion is located 600 m below the pre-mining land surface, below 5300mRL (Fig. 3.5B). P2 intruded along the margins of P1 and along the pyroxene-phyric and feldspar-phyric dikes (Fig. 3.5B). P2 has intruded the core of P1 locally (Fig. 3.5C and Fig. 3.7). Brecciation and pervasive alteration (epidote flooding) characterize the contact between P2 and P1 (Fig. 3.16C). P2 has sharp and discordant contacts with the bedded units of the Weemalla Formation (Fig. 4.12).

### **3.4.3 Late-stage intrusion**

#### **3.4.3.1 Late-stage quartz monzonite (P3)**

The late-stage quartz monzonite (P3) is typically pale-cream to light-pink. The equigranular intrusion is characterized by anhedral to subhedral plagioclase crystals (~3 mm) that account for 30 - 60 % volume of the rock (Table 3.3; Fig. 3.17A to C). Interstitial ferromagnesian minerals are strongly to completely altered to actinolite–chlorite. Plagioclase and orthoclase crystals are anhedral and typically albitized and hematite-dusted. Anhedral quartz crystals occur as interstitial to feldspar and ferromagnesian minerals. Accessory minerals include apatite and titanite ± magnetite.

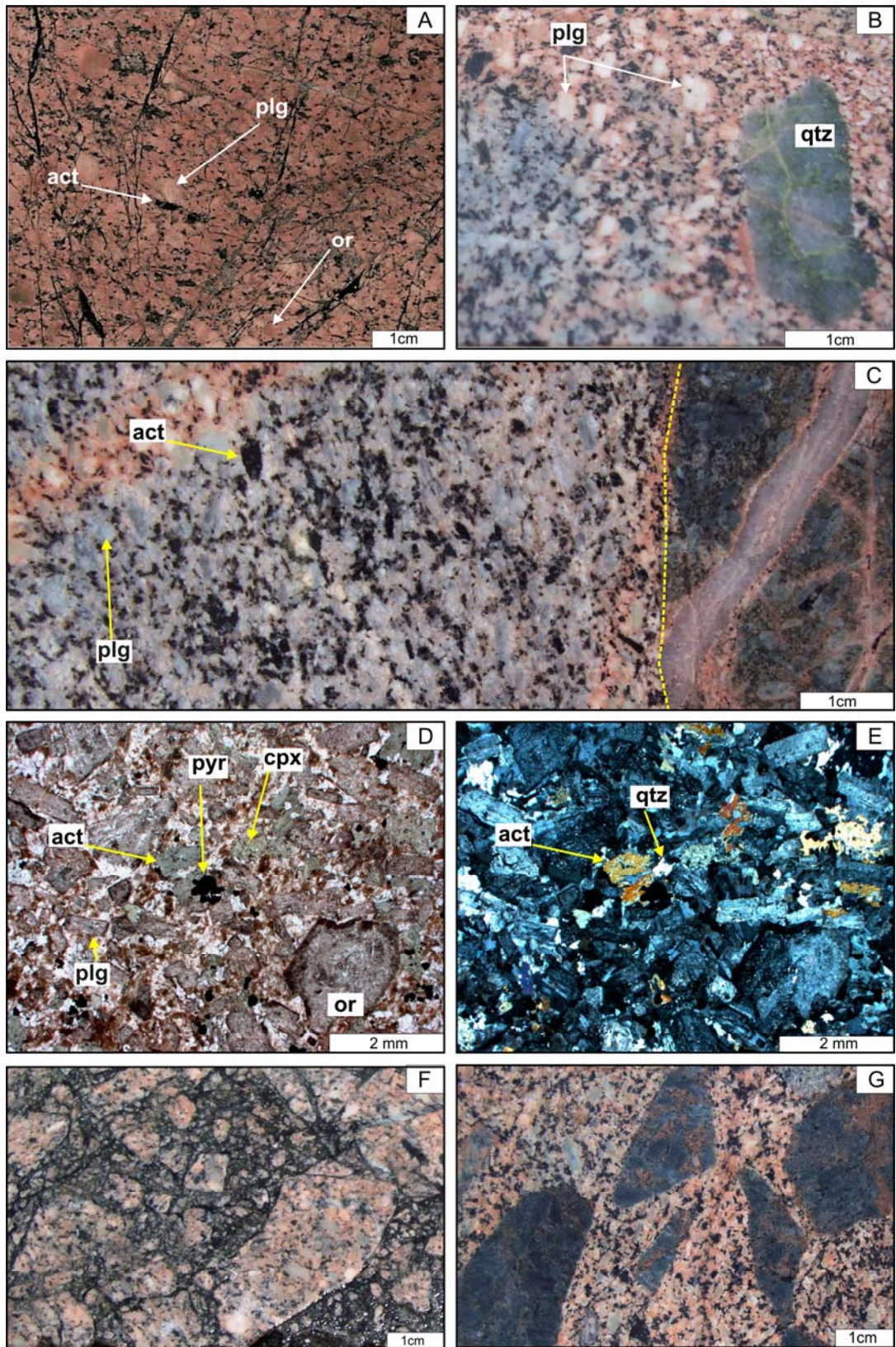
*Geometry and distribution:* P3 occurs as a subvertical pipe, 5 to ~200 m wide, NW-trending, with a vertical extent of at least 1.7 km. Deep in the system, ~1.8 km below the current surface (4100mRL), P3 is the most abundant phase in the intrusive complex occurring as a cylindrical pipe up to 100 m wide and plunging NE (Fig. 3.6). P3 has truncated hydrothermal quartz veins (Fig 3.17C) and is rich in quartz vein fragments (Fig 3.17B) and wallrock xenoliths (Fig 3.17G). Deeper in the system, P3 has been cut locally by a chlorite-altered matrix-rich breccia (Fig. 3.17F). Intrusive contacts with the siliceous siltstone of the Weemalla Formation are sharp and moderately dipping (>70°). P3 is brecciated at its contact with P2.

**Figure 3.17** Textures of the late-stage quartz monzonite (P3) from Ridgeway.

- A.** Equigranular P3 with light-cream subhedral plagioclase crystals with interstitial dark-orange anhedral orthoclase and ferromagnesian minerals. The ferromagnesian minerals have been pervasively altered to chlorite–actinolite  $\pm$  pyrite. This rock is cut by chlorite–epidote veinlets (UR360-835.85m).
- B.** P3 with light-cream subhedral plagioclase crystals, interstitial with anhedral orthoclase and altered ferromagnesian minerals (now chlorite and actinolite). An angular quartz–chlorite vein xenolith is found in P3 (UR323-1303.8m).
- C.** P3 with turbid to pale-cream subhedral plagioclase crystals, interstitial with anhedral orthoclase, and altered anhedral hornblende and clinopyroxene (now chlorite and actinolite). P3 cuts the quartz–orthoclase vein, marked by yellow dashed-line (UR323-1307.5m).
- D.** Photomicrograph (ppl) of P3. Primary feldspars have been altered to hematite-dusted orthoclase, which in turn has been selectively replaced by albite and fine-grained sericite. Primary ferromagnesian minerals have been pervasively altered to chlorite–epidote (UR323-1268m).
- E.** Photomicrograph (xpl) of (D). Subhedral altered plagioclase crystal with interstitial hematite-dusted orthoclase (altered to albite and sericite), quartz and actinolite-altered hornblende and clinopyroxene.
- F.** P3 clasts in a chlorite-altered matrix-rich monomictic breccia. The angular clasts defined a jigsaw-fit to rotated texture (CR057-1932m).
- G.** P3 with xenoliths of coherent feldspar-phyric units of the FRV (UR323-1315.5m).

Abbreviations: act = actinolite, cpx = clinopyroxene, or = orthoclase, plg = plagioclase, ppl = plane polarized light, pyr = pyrite, qtz = quartz, xpl = cross polarized light







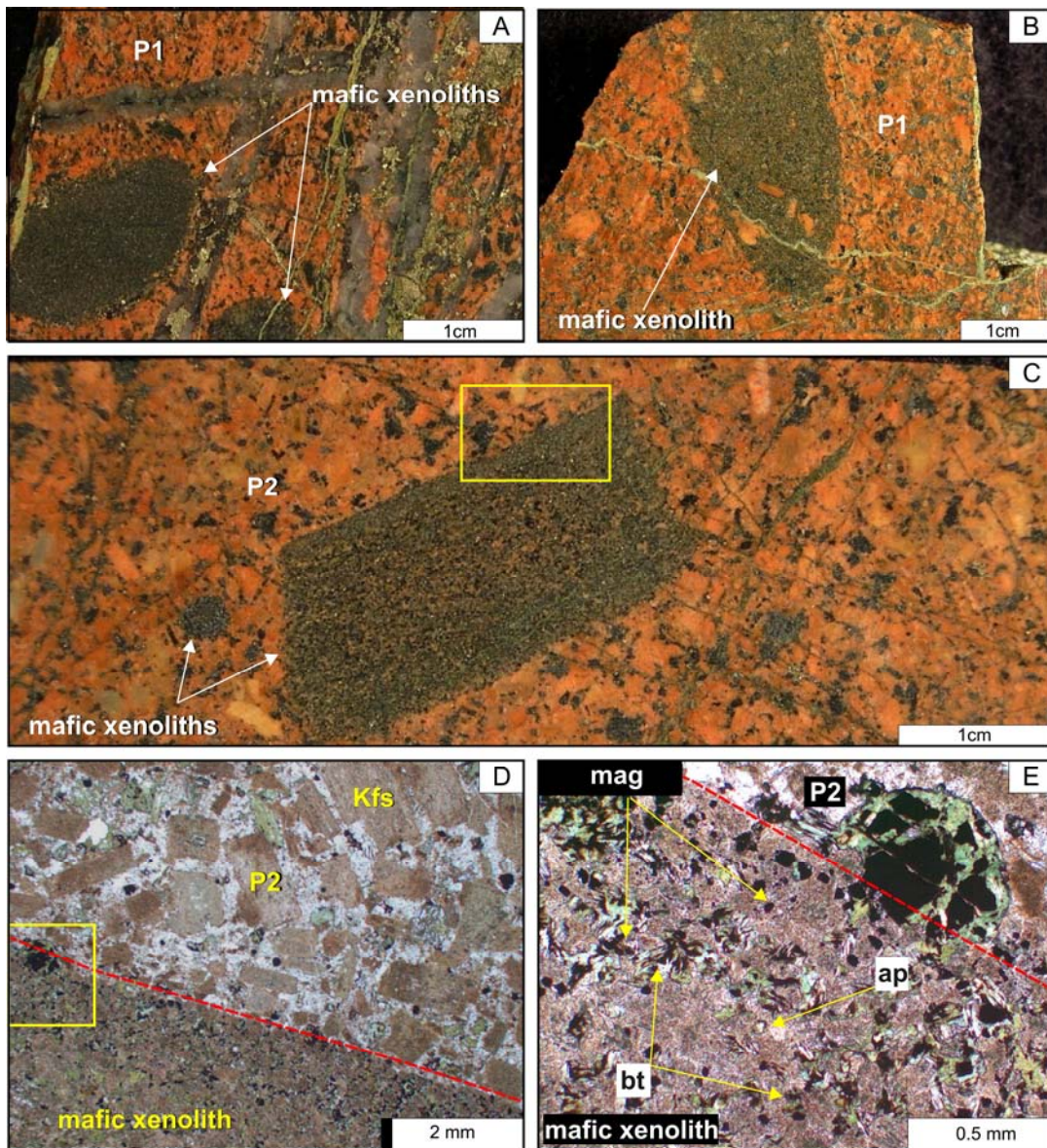


**Figure 3.18** Mafic xenoliths from Ridgeway. **A)** and **B)** Photographs of mafic xenoliths in mafic monzonite (P1; UR140-258-258.3m). **C)** Photograph of mafic xenolith in quartz monzonite porphyry (P2; UR325-178.2m). **D)** Photomicrograph (ppl) showing the sharp contact between the mafic xenolith and P2, outlined in yellow box from (C). The contact is marked by red dashed-line. **E)** Photomicrograph (ppl) of the xenolith, outlined in yellow box from (D). The mafic xenolith comprises of medium-grained, subhedral biotite flakes and interstitial ferromagnesian minerals that have been pervasively replaced by chlorite and magnetite. The groundmass comprises of hematite-dusted K-feldspar alteration; apatite crystals present as accessory minerals. Abbreviations: ap = apatite, bt = biotite, chl = chlorite, Kfs = K-feldspar, mag = magnetite, ppl = plane polarized light

### 3.5 Mafic xenoliths

Mafic xenoliths occur in mineralized monzonites (P1 and P2 porphyries) at Ridgeway (Fig. 3.18). Typically darker in colour than the surrounding rock, these xenoliths vary in shape from spheroidal to ellipsoidal (Fig. 3.18A and B). Some are rectangular (Fig. 3.18C). Their sizes vary from 0.5 to 4 cm in diameter. They are

composed primarily of pervasively chlorite-altered biotite flakes (< 50  $\mu\text{m}$ , 20 - 30 %), interstitial ferromagnesian minerals (pyroxene?) that have been replaced pervasively by chlorite–magnetite; apatite is a common accessory mineral. The groundmass is composed of fine-grained K-feldspar that has been hematite-dusted (Fig. 3.18D and E). The xenoliths are not surrounded by any obvious reaction haloes. These xenoliths are texturally and mineralogically distinct from the more commonly observed xenoliths derived from the Weemalla Formation (Fig. 3.14B) and FRV (Fig. 3.17G).

### 3.6 Tertiary Basalt

The northern and northeastern parts of the Cadia district are covered by Tertiary basalt related to the Canobolas Volcanic Complex (Holliday *et al.*, 2002; Fig. 3.1). At Ridgeway, up to 60 m of Tertiary volcanic rocks conceal the altered FRV (Fig. 3.4). The basal unit is composed mostly of 1 to 3 m of unconsolidated gravel and sands and overlain by coherent basalt lava flows (Harper, 2000).

### 3.7 U–Pb Geochronology

Table 3.4 outlines the previous U–Pb geochronology for the Cadia district (Black, 1994; Squire, 2001; Wilson, 2003; Wilson *et al.*, 2007b; Squire and Crawford, 2007; Harris *et al.*, 2009c). Wilson *et al.* (2007b) concluded that two temporally distinct events of magmatism and related porphyry Au–Cu ore formation occurred in the Cadia district, based on U–Pb and Re–Os geochronology. The first event occurred around 456 - 454 Ma (Late Ordovician) and was related to mineralization at Ridgeway. The second magmatic event occurred at  $437 \pm 4$  Ma (Early Silurian) based on  $^{206}\text{U}/^{238}\text{Pb}$  zircon ages from Cadia Quarry, Cadia Hill and Cadia East. In order to fully evaluate the findings, Harris *et al.* (2009c) analyzed several intrusions from Ridgeway and Cadia Quarry using the  $^{206}\text{Pb}/^{238}\text{U}$  laser ablation-inductively coupled plasma mass spectrometry (LA-ICPMS) technique. These results are outlined below. Specifically, magmatic titanites and zircons from Ridgeway were dated by U/Pb in order to improve the temporal constraints on the age of volcanic and intrusive host rocks. The U–Th–Ph isotopic composition of zircons were analyzed by Dr. Charlotte Allen at the Australian National University

(ANU), Canberra, using Excimer laser ablation inductively coupled plasma mass spectrometry (ELA-ICP-MS).

### 3.7.1 Ridgeway $^{206}\text{Pb}/^{238}\text{U}$ geochronology

No direct age determinations of the mafic volcanic rocks at Ridgeway have been possible due to a lack of zircon, but a U–Pb age for the basal part of the FRV was determined from a quartz-phyric volcanoclastic rock (Harris *et al.*, 2009c). Detrital zircon from this polymictic sedimentary breccia yielded a mean age of  $453.4 \pm 3.6$  Ma. This new U–Pb age overlaps within analytical uncertainty from a detrital  $^{40}\text{Ar}/^{39}\text{Ar}$  hornblende age of  $450 \pm 1.2$  Ma obtained from the intercalated volcanoclastics of the Weemalla Formation by C. Perkins (reported in Pogson and Watkins, 1998). Observed palaeo-fauna in carbonate rocks have a depositional age of  $\sim 452$  Ma (Packham *et al.*, 1999; Harris *et al.*, 2009c). Based on these results, Harris *et al.* (2009c) inferred that the FRV were deposited between 455 and 452 Ma.

**Table 3.4** Summary of SHRIMP  $^{206}\text{Pb}/^{238}\text{U}$  age determinations in the Cadia district.

Deposit	Age (Ma $\pm 2\sigma$ )	Sample description (equivalent intrusive body from the current study at Ridgeway*)	Mineral	Interpreted age	Hole number - depth (m)	Reference
<b>Ridgeway</b>	$456.9 \pm 7.2$	pre-mineralization mafic monzonite (MzD)	titanite	magmatic	NC498-569	Wilson <i>et al.</i> (2007)
	$455.8 \pm 4.4$	inter-mineral quartz monzonite porphyry (P2)	zircon	magmatic	NC498-809	Wilson <i>et al.</i> (2007)
	430 - 440	inter-mineral quartz monzonite porphyry (P2)	zircon	Pb loss	NC498-809	PRISE report; in Harris <i>et al.</i> (2009c)
<b>Cadia Quarry</b>	$456.4 \pm 5.1$	pre-mineralization quartz monzonite porphyry	zircon	magmatic	NC083-35	Wilson <i>et al.</i> (2007)
	$429.7 \pm 4.2$	pre-mineralization quartz monzonite porphyry	zircon	Pb loss or second period of zircon growth	NC083-35	Wilson <i>et al.</i> (2007)
	$453.4 \pm 4.3$	pre-mineralization quartz monzonite porphyry	zircon	magmatic	NC486-467	Wilson <i>et al.</i> (2007)
	$438.7 \pm 5.1$	pre-mineralization quartz monzonite porphyry	zircon	Pb loss or second period of zircon growth	NC486-467	Wilson <i>et al.</i> (2007)
	$436.5 \pm 3.5$	pre-mineralization quartz monzonite porphyry	zircon	magmatic	NC486-608	Wilson <i>et al.</i> (2007)
<b>Cadia Hill</b>	$439 \pm 6.0$	pre-mineralization quartz monzonite porphyry	zircon	magmatic	NC052-116	Black (1994); in Wilson (2003)
	$435.9 \pm 3.7$	pre-mineralization quartz monzonite porphyry	zircon	magmatic	NC384-200	Wilson <i>et al.</i> (2007)
	451.0	pre-mineralization quartz monzonite porphyry	zircon	inherited grains	NC384-200	Wilson (2003)
<b>Cadia East</b>	$451 \pm 1.4$	pre-mineralization quartz monzodiorite porphyry	zircon	magmatic	NC475-1247	Wilson <i>et al.</i> (2007)
	$440.1 \pm 4.2$	pre-mineralization quartz monzodiorite porphyry	zircon	Pb loss or second period of zircon growth	NC475-1247	Wilson <i>et al.</i> (2007)
	$437.1 \pm 3.0$	inter-mineral monzonite porphyry	zircon	magmatic	NC556-1289	Squire (2001)

\*Abbreviations: MzD = monzodiorite, P1 = mafic monzonite porphyry, P2 = quartz monzonite porphyry

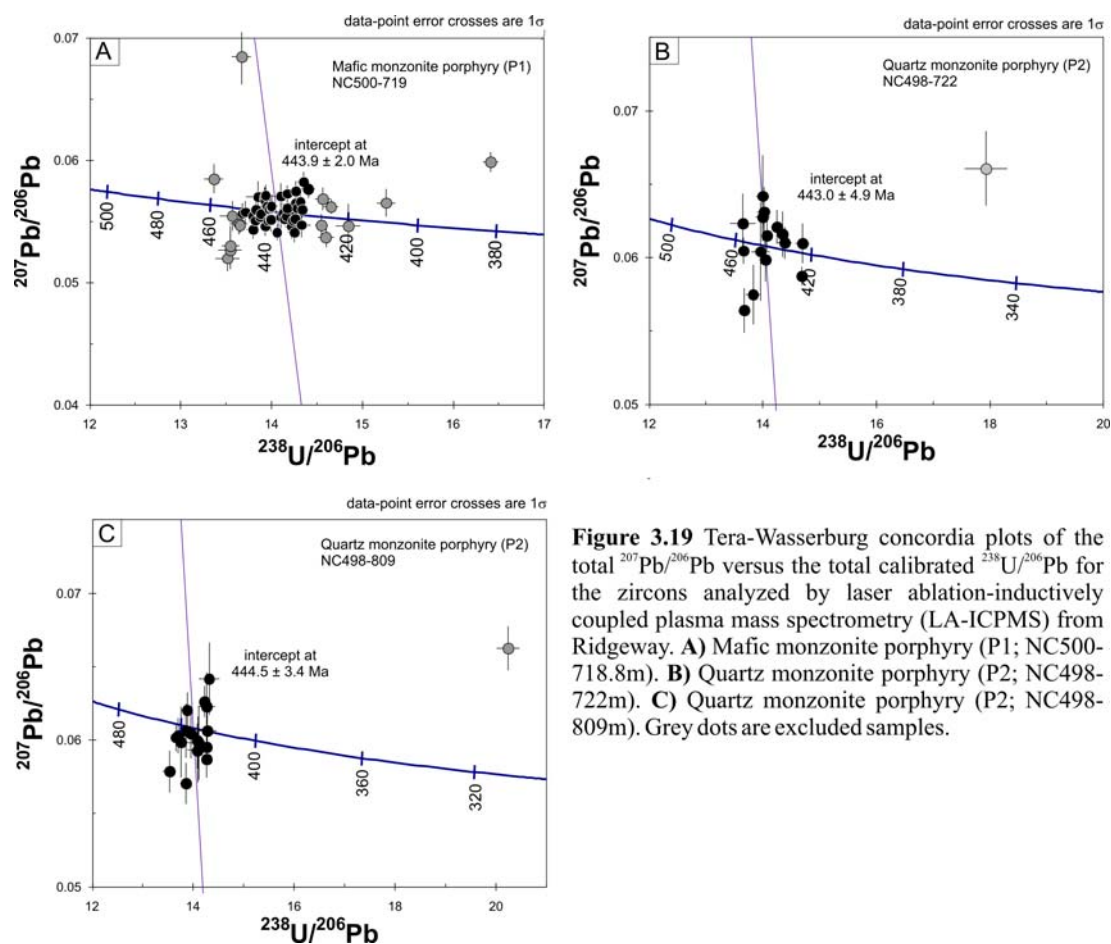


Magmatic titanite from the pre-mineral pyroxene-phyric monzonite at Ridgeway yielded an age of  $456.9 \pm 7.2$  Ma, whereas zircon from the inter-mineral quartz monzonite porphyry yielded  $455.8 \pm 4.4$  Ma (Wilson *et al.*, 2007). Younger ~440 Ma zircons in both samples were reported to be a product of Pb-loss. Similar 455 Ma ages for magmatic zircon were obtained from quartz monzonite porphyry adjacent to the Cadia Quarry deposit ( $456.4 \pm 5.1$  Ma and  $453.4 \pm 4.3$  Ma; Wilson *et al.*, 2007b). By contrast, zircon from quartz monzonite in Cadia Quarry yielded a young age ( $436.5 \pm 3.5$  Ma; Wilson *et al.*, 2007b). From Cadia Hill, zircon yielded a mean age of  $435.9 \pm 3.7$  Ma with two old zircons (~451 Ma) interpreted as inherited crystals, and therefore excluded from the final age determination (Wilson *et al.*, 2007b). Such bimodal distribution of magmatic zircon ages was also recognized in Cadia East quartz monzonite (with populations at  $440.1 \pm 4.2$  Ma and  $451.0 \pm 1.4$  Ma). Despite having near identical U–Pb concentrations and proportions of trace and rare earth elements, the younger 440 Ma zircons have been interpreted as Pb loss and/or unmodified crystallization ages (depending on the sample; Wilson *et al.*, 2007b). Overall, bimodal zircon age distributions were obtained for most samples. Harris *et al.* (2009c) therefore concluded that zircon inheritance is a common feature of monzonitic intrusions in the Cadia district.

Harris *et al.* (2009c) obtained an additional five age determinations from three of the Ridgeway intrusions (Table 3.5). One sample of magmatic titanite from the pre-mineralization MzD yielded an age of  $443.3 \pm 9.7$  Ma (NC500-796m). One sample of magmatic zircon from P1 yielded an age of  $443.9 \pm 2.0$  Ma (NC500-719m; Fig.3.19A). Three different samples of magmatic zircon in P2 were also analyzed and yielded ages that overlap within analytical uncertainty:  $443.0 \pm 4.9$  Ma (NC498-722m; Fig. 3.19B),  $444.5 \pm 3.4$  Ma (NC498-809m; Fig. 3.19C) and  $442.0 \pm 4.9$  Ma (NC519-745m). With these new age determinations, the age of magmatism and associated hydrothermal alteration at Ridgeway is concluded to be  $444.2 \pm 1.3$  Ma (Harris *et al.*, 2009c). Any scatter in concordia is interpreted to be due to zircon inheritance (~455 Ma) from the volcanic basement and/or minor Pb loss (Fig. 3.19).

**Table 3.5** Summary of  $^{206}\text{Pb}/^{238}\text{U}$  LA-ICPMS Age Determinations from Ridgeway. Data from Harris *et al.*, 2009c.

Deposit	Age (Ma $\pm 2\sigma$ )	Sample description	Mineral	Interpreted age	Hole number - depth (m)
Ridgeway	443.3 $\pm$ 9.7	pre-mineralization monzodiorite (MzD)	titanite	magmatic	NC500-796
	442.0 $\pm$ 4.9	mafic monzonite porphyry (P1)	zircon	magmatic	NC519-745
	443.9 $\pm$ 2.0	mafic monzonite porphyry (P1)	zircon	magmatic	NC500-719
	443.0 $\pm$ 4.9	quartz monzonite porphyry (P2)	zircon	magmatic	NC498-722
	444.5 $\pm$ 3.4	quartz monzonite porphyry (P2)	zircon	magmatic	NC498-809

**Figure 3.19** Tera-Wasserburg concordia plots of the total  $^{207}\text{Pb}/^{206}\text{Pb}$  versus the total calibrated  $^{238}\text{U}/^{206}\text{Pb}$  for the zircons analyzed by laser ablation-inductively coupled plasma mass spectrometry (LA-ICPMS) from Ridgeway. **A)** Mafic monzonite porphyry (P1; NC500-718.8m). **B)** Quartz monzonite porphyry (P2; NC498-722m). **C)** Quartz monzonite porphyry (P2; NC498-809m). Grey dots are excluded samples.

### 3.8 Igneous Geochemistry

Selected intrusive rocks have been analyzed geochemically in an attempt to assess geochemical differences between mineralized and pre-mineralization intrusions. This section focuses on both newly discovered and previously documented (Harper, 2000; Holliday *et al.*, 2002; Wilson, 2003) mafic to intermediate alkaline rocks from Ridgeway. The Ridgeway intrusions are discussed in their order of emplacement.

A total of twenty-three intrusive rocks and one mafic xenolith from Ridgeway were analyzed for their major and trace element compositions. Eight samples were analyzed by X-ray fluorescence (XRF) at the University of Tasmania, whereas sixteen samples were analyzed via ICP-MS at the ALS Chemex Laboratory, Brisbane. From this larger suite, two samples from the mafic rocks were analyzed for platinum group of elements (PGE). The results of the twenty-four intrusive samples have been combined with previously generated data from Wilson (2003; 7 samples) and Blevin (2002; 3 samples). In total, thirty-four samples (Appendix D) of intrusive rocks from Ridgeway have been used in the following discussion.

### **3.8.1 Hydrothermal alteration effects and element mobility**

The behaviour of an element during weathering and hydrothermal alteration is commonly related to its ionic potential (Hastie *et al.*, 2007). Thus, elements of low and high ionic potential tend to be preferentially removed in solution as hydrated cations and oxyions, respectively (Hastie *et al.*, 2007). Ions of intermediate ionic potential however, tend to remain in the solid product of alteration and/or weathering and so are relatively immobile elements, e.g. Zr, Hf, Nb, Ta, Y, Ti, Cr and the rare earth elements (REE; Hastie *et al.*, 2007). However, a change in fluid composition and/or increase in temperature and/or extremely high fluid input may mobilize these otherwise immobile elements, and mobility in each case must be tested (Hastie *et al.*, 2007).

At Ridgeway, sampling for igneous geochemistry targeted the least-altered portions of the intrusions. In these samples, primary minerals and igneous textures are still preserved. No hydrothermal veins cut the samples. The effects of hydrothermal alteration on the geochemistry of igneous rocks from Ridgeway have been assessed using a combination of petrography and bivariate plots of mobile versus immobile elements (Fig. 3.20). Bivariate plots of least altered samples from a particular magmatic affinity should show smooth fractionation trends, generally with negative slopes for “immobile” elements (e.g. Zr/TiO<sub>2</sub>; Finlow-Bates and Stumpfl, 1981). Fig. 3.20A shows a theoretical trend for Zr and TiO<sub>2</sub> indicating the stage of differentiation of magma, and the extent of differentiation and alteration (Finlow-Bates and Stumpfl, 1981). The majority of the igneous samples from Ridgeway

define a magmatic fractionation curve (Fig. 3.20B), with one sample of MzD deviated from this trend. There is an apparent “spread” along the X-Y lines in the MzD and Fpo samples, which could suggest that partial mobility of Zr and  $\text{TiO}_2$  occurred in these samples. However, the MzD samples display a coherent pattern in Nb,  $\text{Al}_2\text{O}_3$  and Th bivariate plots (Fig. 3.20C to E), but show some degree of scatter in Y, V and  $\text{P}_2\text{O}_5$  plots (Fig. 3.20F to H) which imply slight modification during alteration. This screening process showed that most samples appear to follow coherent evolutionary trends that are only slightly modified by overprinting alteration.

### 3.8.2 Major element geochemistry

Two petrographically and geochemically distinct intrusive suites are present in the Ridgeway intrusive complex. One suite, dominated by mafic rocks ( $\text{SiO}_2$  from 48 to 54 wt %; Fig. 3.21A) consists of pre-mineralization Ppo and Fpo dikes and sills, and MzD stocks. One MzD sample contains 58 wt %  $\text{SiO}_2$ . The second suite has more intermediate compositions ( $\text{SiO}_2$  from 58 to 62 wt %) and includes the monzonitic rocks (P1, P2 and P3). Mafic xenoliths that are characterized by biotite and pyroxene phenocrysts (typical of lamprophyres) occur only in the monzonites. The one xenolith analyzed has low  $\text{SiO}_2$  (47.8 wt %) and relatively low  $\text{K}_2\text{O}$  (1.7 wt %).

On the  $\text{K}_2\text{O}$  vs  $\text{SiO}_2$  diagram, most of the intrusions, with the exception of one sample of Ppo, lie in the shoshonitic field (Fig. 3.21A). This is consistent with the findings of Wilson (2003) for most of the intrusions in the Cadia district. According to total alkali-silica (TAS) diagram of Le Maitre (1989), the early mafic intrusions (Ppo, Fpo and MzD) at Ridgeway range in composition from trachybasalt to basaltic trachyandesite (Fig. 3.21B), while the intermediate intrusive rocks (P1, P2 and P3) range from trachyandesite to trachyte (Fig. 3.21B). The mafic xenolith is geochemically and mineralogically distinct from the mafic intrusive rocks. Its  $\text{Na}_2\text{O}$  content exceeds its  $\text{K}_2\text{O}$ , unlike all other intrusions analyzed from Ridgeway (Appendix D).

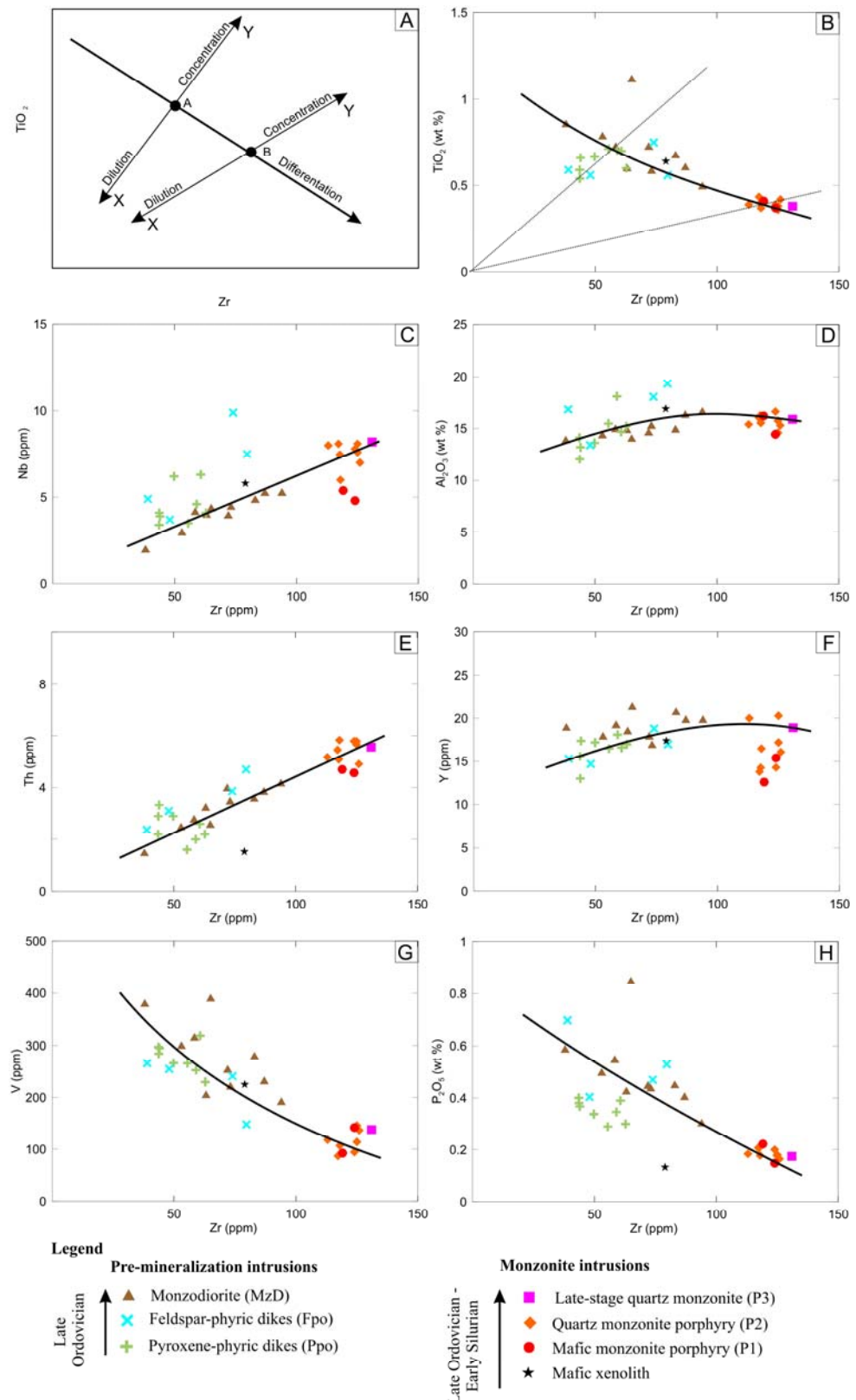


**Figure 3.20** Assessment of the effect of hydrothermal alteration on the whole rock geochemistry for intrusive rocks from Ridgeway. A) Hypothetical diagram showing the effect of differentiation on immobile elements, Zr and  $\text{TiO}_2$ , and the effect of removing or adding other components (modified from Finlow-Bates and Stumpfl, 1981). A magma at point A could differentiate to form other rocks with  $\text{TiO}_2$  and Zr values at point B. The effect of hydrothermal alteration will cause the primary rock composition to “spread” along the lines X-Y. B)  $\text{TiO}_2$  vs Zr. C) Nb vs Zr. D)  $\text{Al}_2\text{O}_3$  vs Zr. E) Y vs Zr. F) V vs Zr. G)  $\text{P}_2\text{O}_5$  vs Zr.

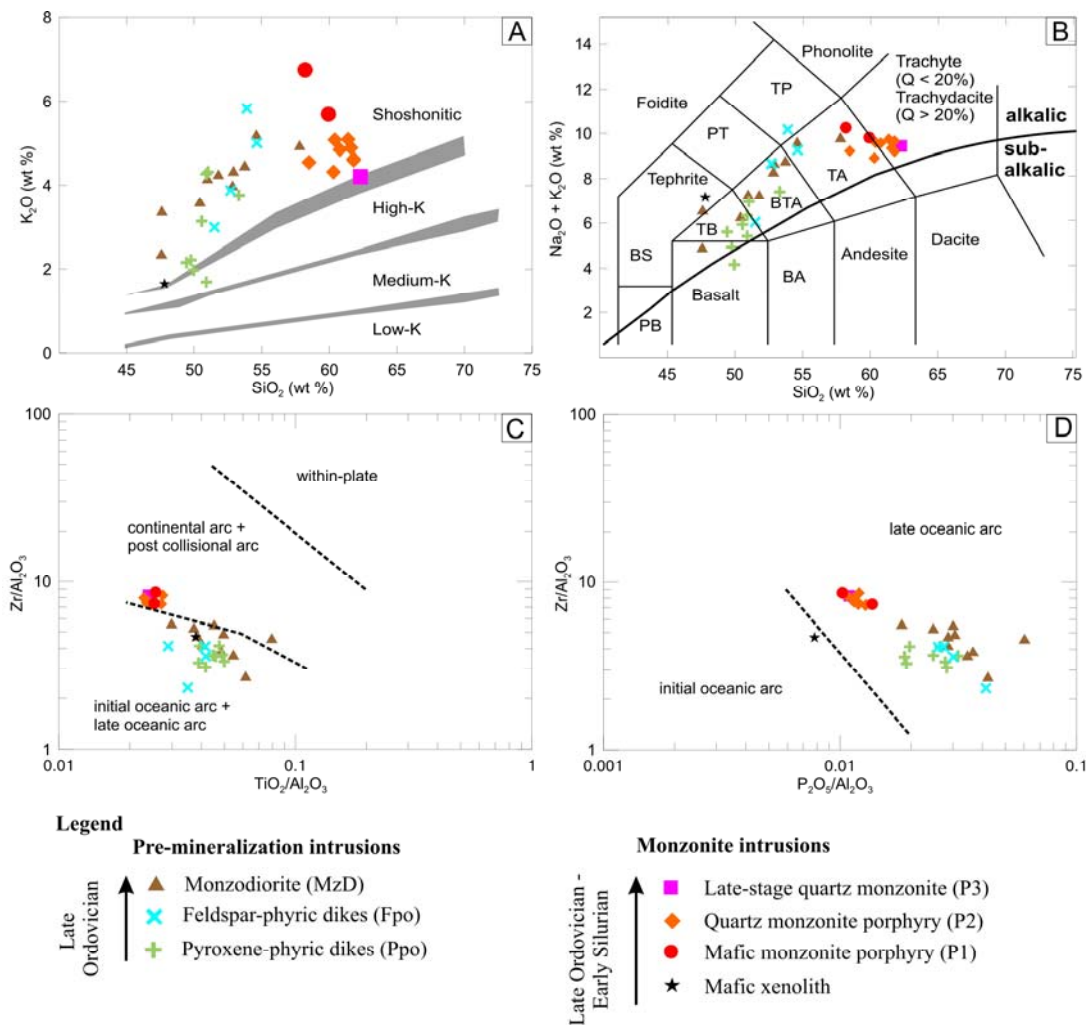


**Figure 3.21** Major- and trace-element discrimination diagrams for intrusive rocks from Ridgeway. **A)**  $K_2O$  vs  $SiO_2$  diagram with magma series boundaries after Peccerillo and Taylor (1976) and Rickwood (1989). **B)** Total alkali - silica (TAS) diagram of Le Maitre *et al.* (1989), showing chemical and rock nomenclature on the basis of  $Na_2O + K_2O$  vs  $SiO_2$ . **C)**  $Zr/Al_2O_3$  vs  $TiO_2/Al_2O_3$  tectonic discrimination diagram (after Muller *et al.*, 1992). **D)**  $Zr/Al_2O_3$  vs  $P_2O_5/Al_2O_3$  oceanic arc discrimination diagram (after Muller *et al.*, 1992). Abbreviations: BA = Basaltic andesite, BS = Basanite, BTA = Basaltic trachyandesite, PB = Picrobasalt, PT = Phonotephrite, TA = Trachyandesite, TB = Trachybasalt, TP = Tephriphonolite

A late intra-oceanic arc tectonic setting has been inferred for the volcanic and intrusive rocks of the Cadia district by previous workers (e.g. Glen *et al.*, 1998; Crawford, 2001; Wilson, 2003). At Ridgeway, immobile element discrimination diagrams (Fig. 3.21C and D) show that the monzonite suite straddles the continental arc and post-collisional arc fields, while most of the mafic rocks, including the mafic xenolith, plot in the initial oceanic arc and late oceanic arc field (Fig. 3.21C). Both the mafic and felsic intrusions from Ridgeway plot in the late oceanic arc on Figure 3.21D, consistent with the interpretation of this setting by Wilson (2003). The Sr and

Nd isotopes analyzed by Wilson (2003) provide evidence for subduction zone geochemical signatures and depleted mantle Nd–Sr–Pb isotopic compositions, precluding the involvement of crustally-derived material.

Figure 3.22 shows bivariate diagrams of major elements versus SiO<sub>2</sub>. The intrusive rocks from Ridgeway exhibit coherent trends with decreasing concentrations of TiO<sub>2</sub>, MnO, MgO, CaO, P<sub>2</sub>O<sub>5</sub> and Fe<sub>2</sub>O<sub>3</sub> and increasing concentrations of K<sub>2</sub>O, and Na<sub>2</sub>O with respect to increasing SiO<sub>2</sub> (Figs. 3.21A and 3.22). Some of the scatter in the K<sub>2</sub>O diagram may be due to feldspar alteration (Fig. 3.21A). The variability in the proportion of the Na<sub>2</sub>O (Fig. 3.22F) may be attributed to contrasting intensities of sodic alterations so common throughout the Cadia district. Al<sub>2</sub>O<sub>3</sub> concentrations increase systematically with increasing SiO<sub>2</sub> up to 55 wt %. A change from positive to negative slope of Al<sub>2</sub>O<sub>3</sub> content with increasing SiO<sub>2</sub> (at 55 wt %) suggests retention of some plagioclase in the magma chamber (Fig. 3.22B). These plots show minor element mobility for Al<sub>2</sub>O<sub>3</sub>, P<sub>2</sub>O<sub>5</sub> and Fe<sub>2</sub>O<sub>3</sub> consistent with mafic rocks overprinted by multiple overprinting alteration events (ref. Fig. 3.20).

Wilson (2003) interpreted that the variation of major and trace element concentrations indicated that pyroxene, Fe–Ti oxides, apatite and plagioclase were fractionating from mafic melts of the Cadia district. The early fractionation and removal of apatite is supported by petrographic observations that this mineral is enriched in the more mafic phases (e.g. the mafic xenoliths found in P2). Although Wilson (2003) concluded that no difference exists between the productive ore-related intrusions and those that lack significant metal accumulation, the monzodiorite (which hosts mineralization) can be discriminated from the monzonite intrusions based on its major elements compositions (Fig. 3.22).



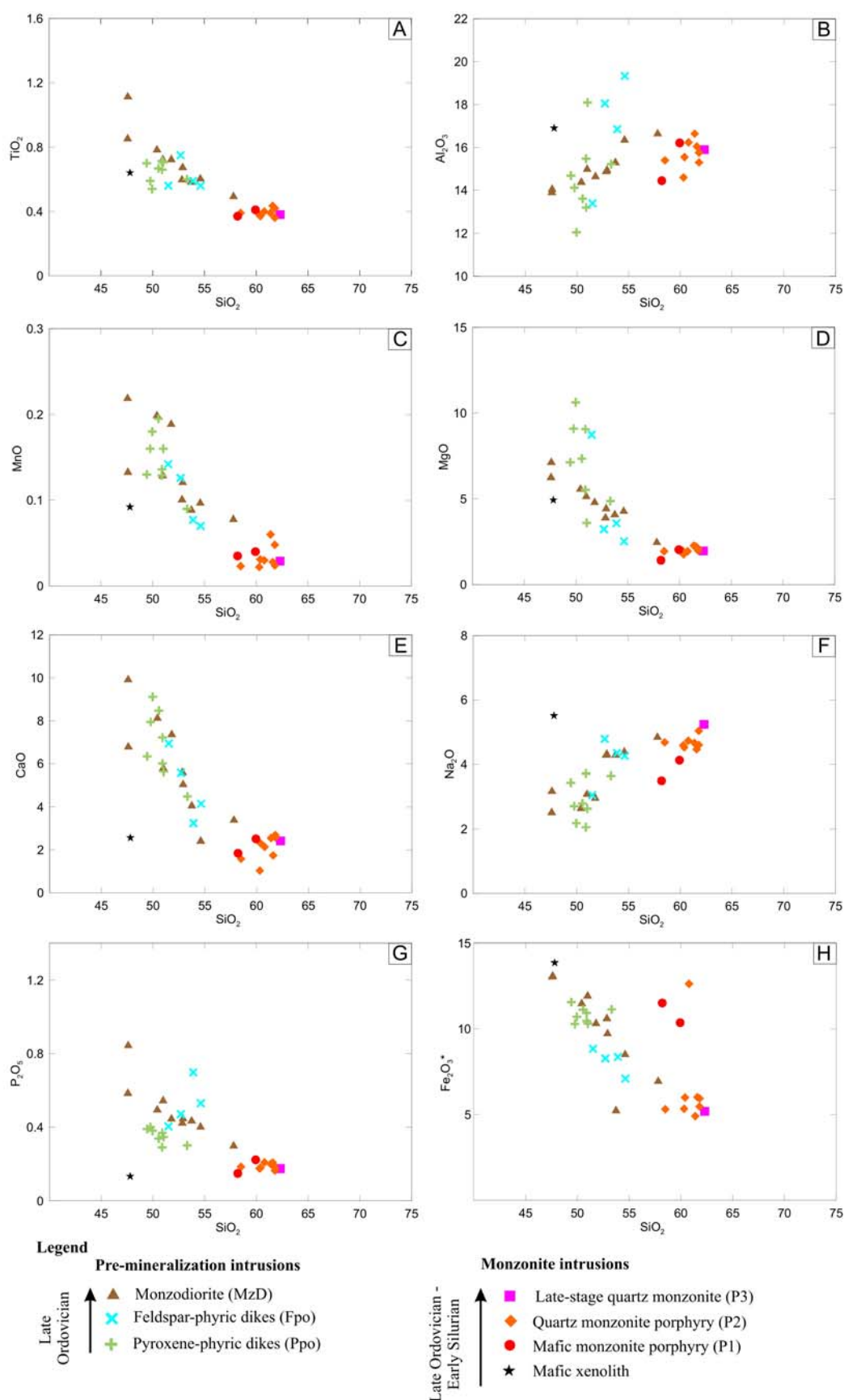


**Figure 3.22** Major element variation diagrams for intrusive rocks from Ridgeway. **A)**  $\text{TiO}_2$  vs  $\text{SiO}_2$ . **B)**  $\text{Al}_2\text{O}_3$  vs  $\text{SiO}_2$ . **C)**  $\text{MnO}$  vs  $\text{SiO}_2$ . **D)**  $\text{MgO}$  vs  $\text{SiO}_2$ . **E)**  $\text{CaO}$  vs  $\text{SiO}_2$ . **F)**  $\text{Na}_2\text{O}$  vs  $\text{SiO}_2$ . **G)**  $\text{P}_2\text{O}_5$  vs  $\text{SiO}_2$ . **H)**  $\text{Fe}_2\text{O}_3^*$  vs  $\text{SiO}_2$ . All values in weight percent.

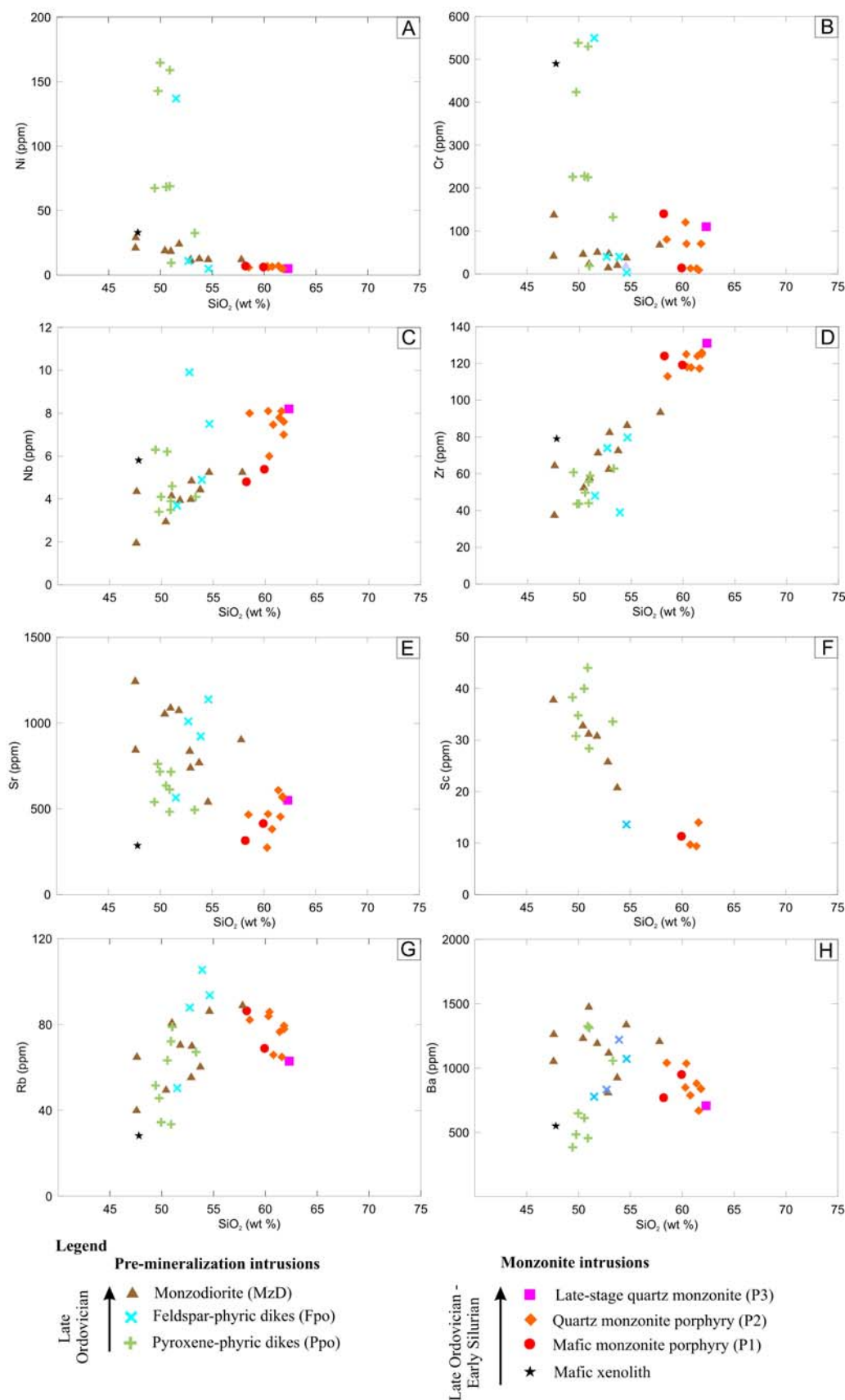
### 3.8.3 Trace and rare earth elements geochemistry

Figure 3.23 shows Harker variation diagrams for trace elements of the intrusive rocks from Ridgeway. These plots show that the mafic suite of rocks ( $\text{SiO}_2 < 55 \text{ wt } \%$ ) are variably enriched in mafic immobile trace elements (Cr, Ni, Sc and V). Compatible elements such as Sc (up to 45 ppm) and V (up to 400 ppm) exhibit clear enrichment compared to the monzonite suite, and show decreasing abundances with increasing  $\text{SiO}_2$  (Fig. 3.23F and I). Pyroxene- and plagioclase-phyric dikes and sills contain up to 165 ppm Ni and as much as 550 ppm Cr (Fig. 3.23A and B). The more mafic intrusions have considerably higher Sc values compared to those of the more evolved monzonites ( $< 12 \text{ ppm}$ ), which have higher concentrations of high field strength (HFS) elements (Nb and Zr) at higher  $\text{SiO}_2$  contents (Fig. 3.23C and D).

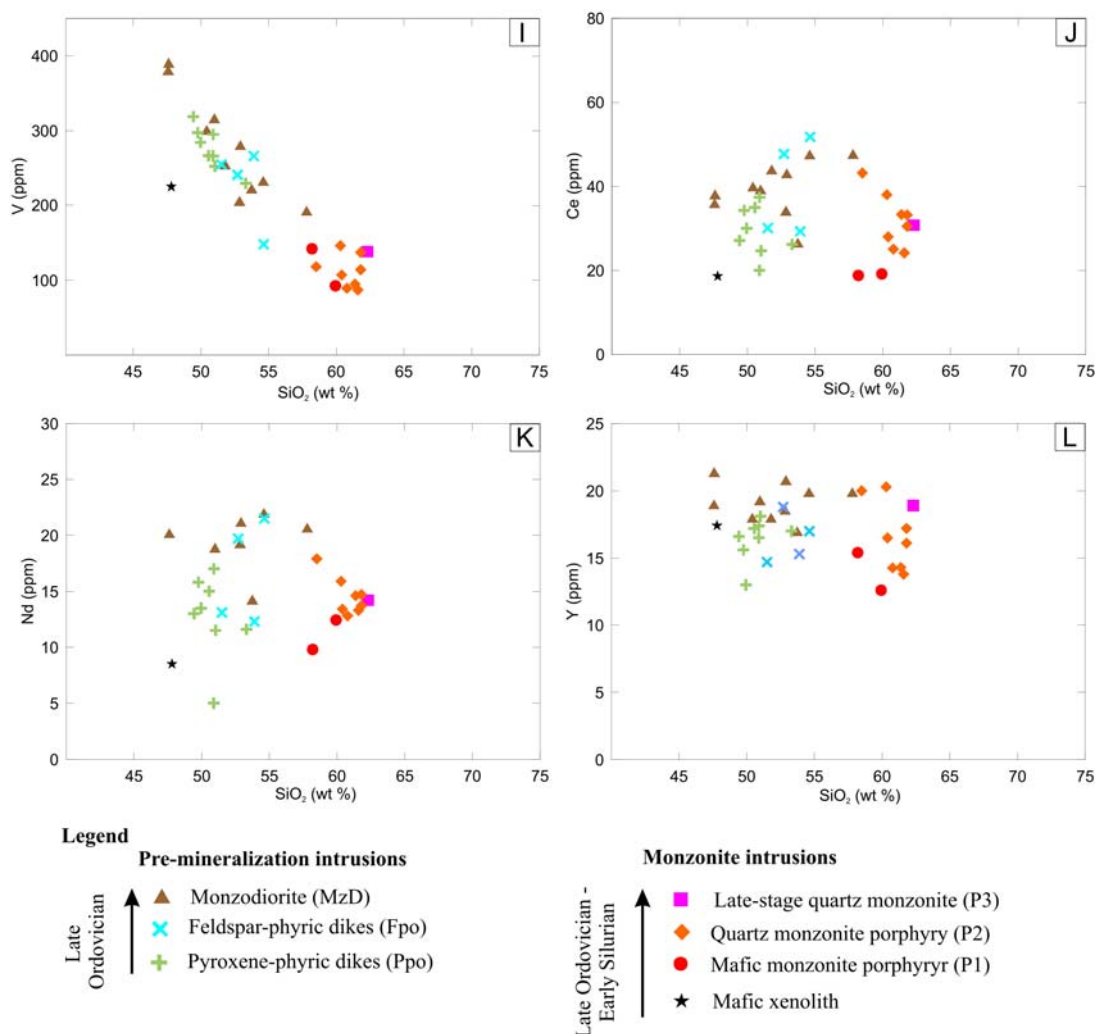
Incompatible elements such as Sr, Rb and Ba have distinctive relationships to  $\text{SiO}_2$  between the two intrusive suites. The mafic intrusions have increasing Rb and Ba up to 54 wt %  $\text{SiO}_2$ , whereas Rb and Ba decreases with increasing  $\text{SiO}_2$  for the monzonite suite (Fig. 3.23G and H). Ba depletion in the monzonite may be due to fractional crystallization of K-feldspar, since Ba substitutes for K in alkali feldspars (Ren, 2004). The mafic intrusions are enriched in Sr relative to the monzonites (Fig. 3.23E), which may reflect a higher proportion of plagioclase to alkali feldspar in the mafic samples (e.g. Blevin, 2002), or feldspar alteration.

Figure 3.24 shows chondrite normalized REE plots for the Ridgeway intrusions. Pre-mineralization intrusions are light rare earth element (LREE)-enriched and do not have prominent Eu anomalies (Fig. 3.24A to C). The MzD has the highest REE concentrations compared to all other intrusions at Ridgeway (Fig. 3.24D to H). The mafic xenolith is depleted in LREE and middle rare earth elements (MREE) relative to P1 and P2, and enriched in heavy rare earth elements (HREE ; Fig. 3.24D and H). P3 has REE profiles similar to P2.

Figure 3.25 plots the REE ratios, as function of  $\text{SiO}_2$ , and age of the intrusions. Ppo and Fpo and MzD have higher total REE abundance and steeper profiles with  $[\text{La/Yb}]_{\text{CN}}$  values from 7.0 to 10.3 (Fig. 3.25A). In contrast, the



**Figure 3.23** Trace elements Harker variation diagrams for intrusive rocks from Ridgeway. **A)** Ni vs SiO<sub>2</sub>. **B)** Cr vs SiO<sub>2</sub>. **C)** Nb vs SiO<sub>2</sub>. **D)** Zr vs SiO<sub>2</sub>. **E)** Sr vs SiO<sub>2</sub>. **F)** Sc vs SiO<sub>2</sub>. **G)** Rb vs SiO<sub>2</sub>. **H)** Ba vs SiO<sub>2</sub>.



**Figure 3.23** (Continued) Trace elements Harker variation diagrams for intrusive rocks from Ridgeway. **I)** V vs SiO<sub>2</sub>. **J)** Ce vs SiO<sub>2</sub>. **K)** Nd vs SiO<sub>2</sub>. **L)** Y vs SiO<sub>2</sub>.

monzonite samples have shallow REE profiles, with  $[La/Yb]_{CN}$  from 3.7 to 7.0 (Fig. 3.25A). The absolute REE abundances decrease systematically with age (Fig. 3.25B). The Ppo and Fpo dikes have the highest degree of LREE enrichment ( $[La/Sm]_{CN} = 3.9 - 4.9$ ; Fig. 3.25C), whereas the monzonites are less enriched in LREE ( $[La/Sm]_{CN} = 1.7 - 4.0$ ). The MzD intrusions have the highest HREE concentrations ( $[Sm/Yb] = 2.2 - 2.8$ ; Fig. 3.25C), whereas the monzonites have  $[Sm/Yb] = 1.4 - 2.2$ . All intrusions exhibit flat HREE patterns (Fig. 3.24). Wilson (2003) noted a broad trend of LREE enrichment with increasing fractionation ( $[La/Sm]_{CN} = 2.0 - 4.4$ ) and a HREE component that systematically decreases with fractionation ( $[Sm/Yb]_{CN}$ ). Change in the MREE has been attributed to apatite fractionation (Squire and Crawford, 2007). Subtle Eu anomalies are present in the REE patterns which maybe

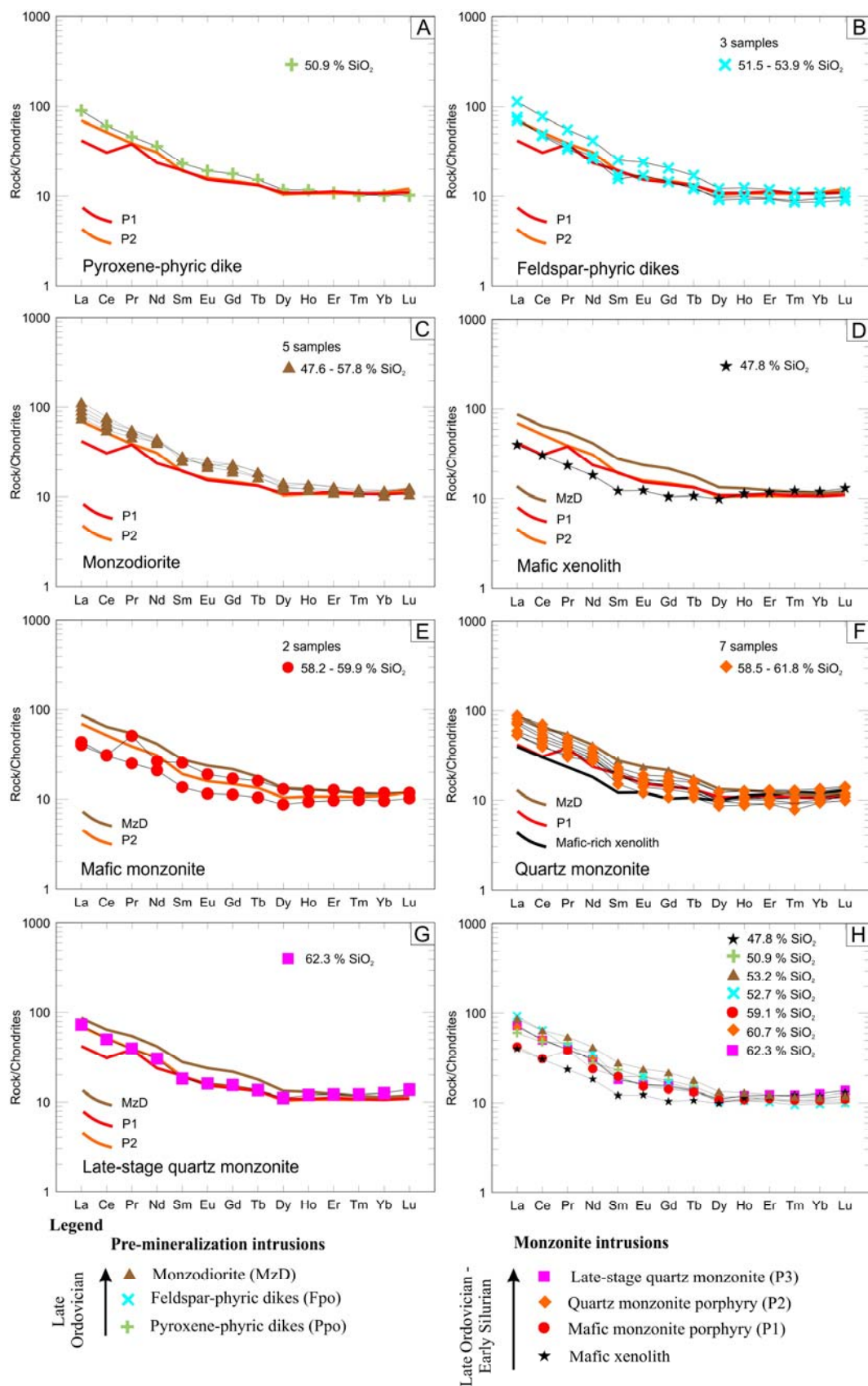
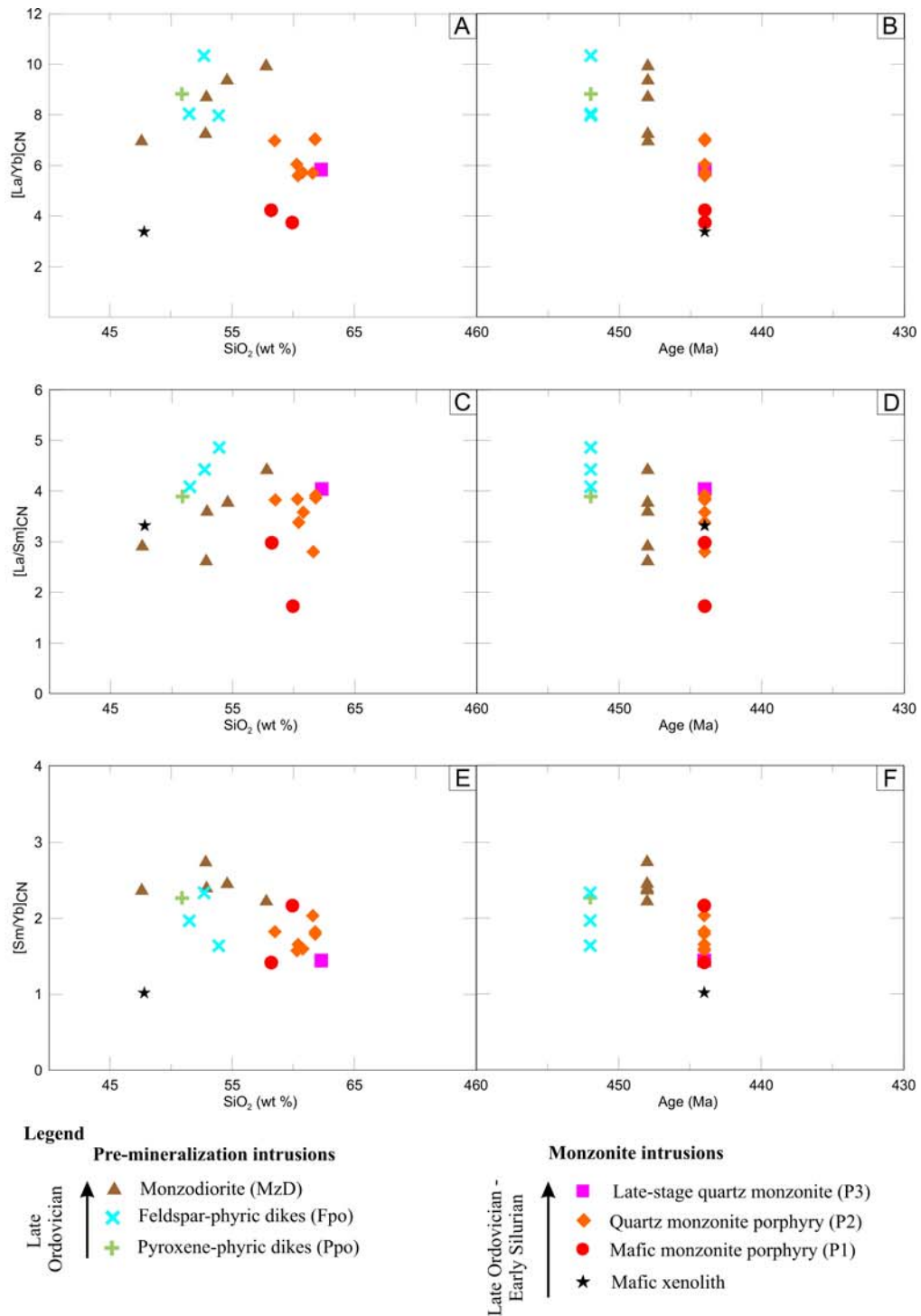


**Figure 3.24** Chondrite-normalized rare earth element (REE) patterns for the intrusive rocks from Ridgeway, normalized to chondrite values of Sun and McDonough (1989). Numbers adjacent to symbol refers to the silica content. The intrusive rocks are plotted against P1, P2, the mafic xenolith and/or MzD for comparison.





consistent with textural and other chemical evidence for local accumulation of plagioclase.

Two samples of mafic rocks were analyzed for their PGE content (Table 3.6). As expected from their mafic character, the mafic xenolith is enriched in Pd (0.083 ppm), Pt (0.033 ppm) and Au (0.1 ppm). The MzD has elevated Au concentration (0.481 ppm) but is lower in Pd (0.028 ppm) and Pt (0.006 ppm). The mafic xenolith and MzD samples from Ridgeway have higher concentrations of Pd, Pt and Au (with the exception of Pt in the MzD) compared to shoshonitic systems similar to those of Bingham Canyon, Fiji, and Lihir, Papua New Guinea (Table 3.6). Given that the mafic xenolith was taken from the mineralized intrusions at the core of the deposit, it may have been that the hydrothermal fluids have modified the PGE. However, this cannot be argued for the MzD, where the sample was taken distal from the mineralizing intrusions (4350mRL; Fig. 3.5D), although overprinted by calc-potassic alteration (Fig. 3.11D). The enrichment of these PGE (i.e. Pd, Pt and Au) may be caused by the relatively high temperature of the alkalic magma, e.g. Bingham Canyon (Maughan *et al.*, 2002). Barnes *et al.* (1985) investigated the extent to which PGE patterns may be modified by alteration in vein ores enriched with Pt and Au and concluded that alteration is not the dominant process in PGE fractionation.

**Table 3.6** PGE and Au abundances of selected samples from Ridgeway compared with abundances of samples from Bingham, Fiji and Lihir. Data from other districts are from Maughan *et al.*, 2003.

Location	Sample	Pd (ppb)	Pt (ppb)	Au (ppb)	Ir (ppb)	Ru (ppb)	Rh (ppb)
<b>Ridgeway</b>	Mafic xenolith (UR323-178.2m)	83.00	33.00	100.0	b.l.d.	b.l.d.	b.l.d.
<b>Ridgeway</b>	Monzodiorite (UR360-895m)	28.00	6.00	478.0	b.l.d.	b.l.d.	b.l.d.
Bingham	Melanephelinite (Tick-38)	8.56	6.27	1.0	0.312	0.280	0.150
Bingham	Melanephelinite (Tick-39)	6.20	6.44	1.5	0.276	0.290	0.200
Bingham	Melanephelinite (Tick-43)	5.52	5.97	0.8	0.289	0.290	0.230
Bingham	Melanephelinite (Tick-44)	9.08	6.59	1.3	0.321	0.360	0.190
Bingham	Melanephelinite (Tick-44)	10.00	9.24	2.3	0.499	0.380	0.180
Bingham	Nb-poor latitic minette (Tick-52A)	2.66	0.93	1.1	0.125	b.l.d.	b.l.d.
Bingham	Trachyte (Tick-59A)	0.55	bld	0.3	0.004	b.l.d.	b.l.d.
Bingham	Nb-rich latitic minette (Tick-66A)	4.73	1.27	0.8	0.212	b.l.d.	b.l.d.
Emperor, Fiji	136136	15.50	6.78	3.0	0.027	0.010	0.090
Emperor, Fiji	136147	11.30	3.42	2.3	0.038	0.000	0.020
Feni, PNG	136166	7.72	2.84	1.4	0.036	0.010	0.070
Lihir, PNG	136167	10.70	9.98	2.4	0.084	0.080	0.150
Lihir, PNG	45DR-1C	1.40	0.87	1.2	0.040	b.l.d.	b.l.d.

\*Abbreviation: bld = below detection

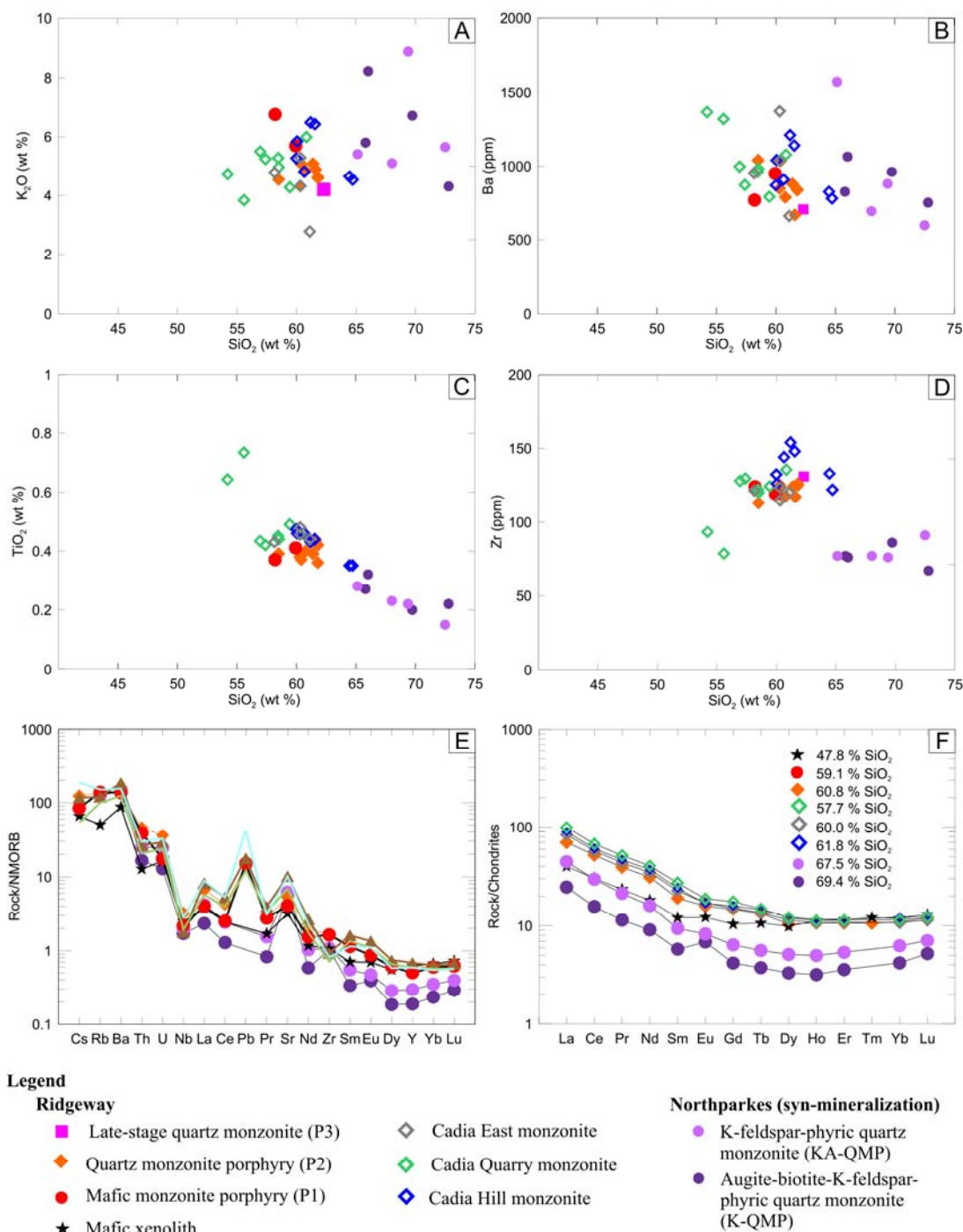


**Figure 3.26** Geochemical comparisons of the different mineralizing intrusions at the Cadia and Northparkes districts. **A)** K<sub>2</sub>O vs SiO<sub>2</sub>. **B)** Ba vs SiO<sub>2</sub>. **C)** TiO<sub>2</sub> vs SiO<sub>2</sub>. **D)** Zr vs SiO<sub>2</sub>. **E)** N-MORB normalized. **F)** Chondrite normalized. All normalization factors from Sun and McDonough (1989). Geochemical data for Cadia Hill, Cadia East and Cadia Quarry from Squire (2001), Blevin (2002) and Wilson (2003). Data for Northparkes taken from Lickfold *et al.* (2007).

### 3.8.4 Comparison to Northparkes district

Figure 3.26 compares the geochemical data of mineralized Ordovician igneous suites from Cadia and Northparkes districts. The Cadia intrusions are similar to the Northparkes intrusions with regards to their K-enrichment and LILE (Fig. 3.26A and B). The Cadia intrusions are enriched in  $\text{TiO}_2$  and Zr relative to the mineralized intrusions from Northparkes (Fig. 3.26C and D). The Ridgeway mineralized intrusions, and other intrusions related to mineralization in the Cadia district, are distinct from the Northparkes mineralizing intrusions in that Northparkes mineralized intrusions are more  $\text{SiO}_2$ -rich and have lower overall REE enrichment (Fig. 3.26E and F).

## 3.9 Discussion

The Ridgeway porphyry Au–Cu deposit is centered on multiple Ordovician dioritic to monzonitic intrusions emplaced into volcanogenic sedimentary rocks of the Weemalla Formation and the FRV. The very thick, diffusely stratified clastic rocks of the FRV display a broad upward-coarsening and thickening trend, from the feldspathic turbidites of the Weemalla Formation (Fig. 3.4). Deposition occurred in an active submarine sedimentary basin (Harris *et al.*, 2009a).

### 3.9.1 Deposition of the Ridgeway host rocks

The predominance of siliceous sandstone and siltstone in the Weemalla Formation suggests the persistence of a marine sedimentary basin throughout its accumulation. The laterally continuous geometries of the laminated siltstone and sandstone package intercalated with the calcareous sandstone unit are consistent with the deposition across a low-relief submarine plain (Harris *et al.*, 2009a). The thick massive, and normally graded beds resulted from turbidity currents with lesser tractional and suspension sedimentation (Squire and McPhie, 2007). The feldspathic nature of this unit indicates a volcanic source. The fine-grained and parallel-stratified bedding grading suggests suspension settling while the thick massive beds towards the top indicate rapid deposition from turbidity currents (Squire and McPhie, 2007).

Overlying the Weemalla Formation is the thick, diffusely stratified polymictic volcanoclastic lithic breccia and conglomerate, massive mafic- and feldspar-rich sandstone rock package of the FRV. The thick massive volcanoclastic sandstones are interpreted to have been deposited from concentrated high-density turbidites. The diverse range in composition, shape and size of the clasts in this rock unit reflects derivation from volcanic sources of contrasting composition (Figs. 3.4 and 3.27A).

The transition from deposition of the Weemalla Formation to the FRV represents the evolution from deeper water sedimentation distal from a volcanic source to a proximal setting to an environment formed on the slopes of a partly emerging volcano (Harris *et al.*, 2009a). Recent research results on the nature, distribution and geometry of the volcanic stratigraphy and architecture of the Cadia district suggested that volcanism and related sedimentation occurred largely in an active sedimentary basin (Harris *et al.*, 2009a). Field observations have shown that the FRV is interfingered and intercalated with the underlying Weemalla Formation, so that they are in part contemporaneous (Wilson, 2003; Harris *et al.*, 2009a). Deposition of the volcanic and associated volcanoclastic detritus is considered to have occurred 455 and 452 Ma, well before the emplacement of the ore-related intrusions (Harris *et al.*, 2009c).

### **3.9.2 Ridgeway intrusive complex**

Figure 3.27 shows a simplified schematic diagram of the volcanic and magmatic evolution of Ridgeway. The structural complexities involved in the emplacement of intrusions are discussed in Chapter 5. The thick volcano-sedimentary sequence at Ridgeway was intruded by a series of mafic dikes and sills (Ppo and Fpo; Fig. 3.27B). These were followed by the equigranular to porphyritic pre-mineralization MzD (Fig. 3.27C), which occur as a plug emplaced along contact with some of the earlier formed dikes. Based on U/Pb geochronology, the MzD is interpreted to have been emplaced at ~448 Ma, several million years after the deposition of the FRV (Harris *et al.*, 2009c). This ~100 m diameter stock intruded prior to the emplacement of the narrower, pencil-like monzonite intrusions that are associated with mineralization. Such relationships are common in many porphyry ore

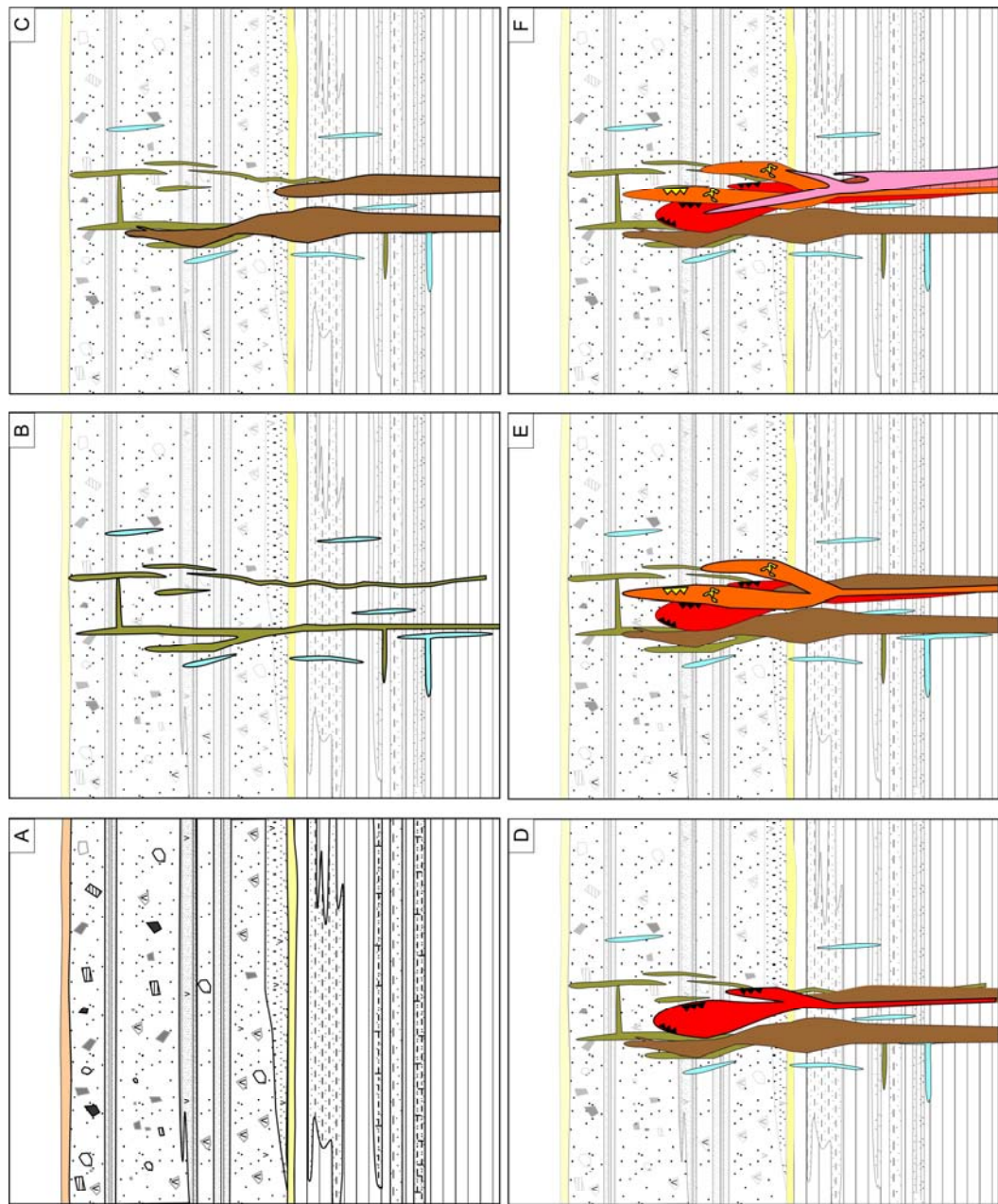


**Figure 3.27** Simplified schematic diagram showing the volcanic and magmatic evolution of Ridgeway (structural complexities are discussed in Chapter 5).

**A)** Accumulation of the Weemalla Formation and Forest Reefs Volcanics (FRV).

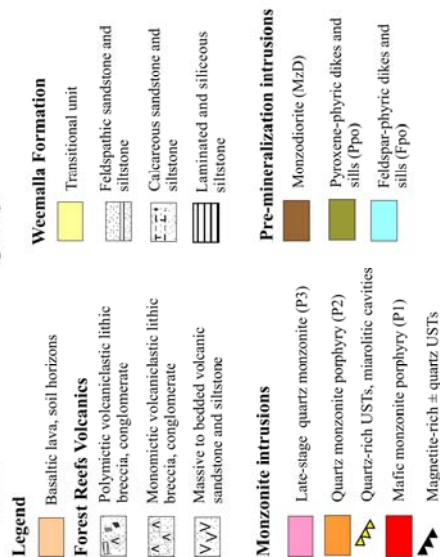
**B)** Intrusion of the coherent pyroxene- and feldspar-phryic dikes and sills.

**C)** Intrusion of the monzodiorite along the margins of some earlier-formed mafic dikes.

**D)** Intrusion of mafic monzonite porphyry northeast of the monzodiorite. Note the swelling of the mafic monzonite at the transitional unit upwards to the FRV. Magnetite-rich unidirectional solidification textures (USTs) occur at the apex and along the margins of the mafic monzonite.

**E)** Intrusion of quartz monzonite porphyry. Quartz-rich USTs occur along the margins, while miarolitic cavities occur within the intrusions.

**F)** Intrusion of the late-stage quartz monzonite along the margins and in the core of the earlier monzonites. This late-stage intrusion truncated mineralization and forms the barren core at Ridgeway.





deposits (e.g. Tanama, Cox, 1985; Santo Tomas II, Sillitoe and Gappe, 1984; Northparkes, Lickfold *et al.*, 2003).

Shoshonitic intrusions associated with mineralization were emplaced at Ridgeway around 444 Ma. The earliest phase was the P1 elongate pipe, northeast of the MzD (Figs. 3.7 and 3.27D). The distribution and geometry of P1 is well understood at higher elevations (Fig. 3.7). At depth, however, this intrusion appears to pinch-out and become rootless along the margins of the younger quartz monzonites (Fig. 3.27E). One possible explanation could be stoping of older intrusion by the more voluminous younger intrusions; evidence that supports stoping-out includes the truncation of mineralized veins by P2. Alternatively, the widely spaced drillholes at depth may have failed to intersect the roots of P1. Either way, this implies that the monzonite porphyries form very narrow pipes at depth as they pass downwards into the siltstones and sandstones of the Weemalla Formation.

P2 is the second phase of the monzonitic suite, occurring as elongate pipes (Fig. 3.27E). The contact between P2 and P1 is obscured by shearing, brecciation or intense hydrothermal alteration (e.g. Fig. 3.16C). P3 is a cylindrical pipe (Fig. 3.27F) that has truncated earlier formed quartz veins and it contains abundant wallrock fragments and quartz vein xenoliths (Fig. 3.17B, C, and G). The contact between P3 and P2 is very subtle texturally, but is obvious from abrupt changes in Cu and Au grades. The contact has been obscured locally by hydrothermal breccias. The absence of xenoliths of P1 or P2, combined with the occurrence of diffuse igneous contacts, implies that P2 and P3 were emplaced in quick succession. P3 has truncated mineralization, and defines the low-grade core of the deposit (Fig. 3.7A and C). As has been observed at many other porphyry deposits, the late-mineral phases commonly intruded into axial portions of stocks, producing low-grade cores, e.g. Panguna, Clark, 1990; Grasberg, Van Nort *et al.*, 1991; Santo Tomas II, Serafica and Baluda, 1977.

An important feature of the Ridgeway intrusive complex is the distinct magmatic hydrothermal transition textures found in P1 and P2. The presence of alternating bands of crenulated magnetite and quartz (including the occurrence of brain-rock textures) implies that Fe-rich magmatic fluids streamed through and

accumulated within the narrow pencil-shaped intrusions at Ridgeway. Preservation of USTs, miarolitic cavities and aplite vein-dikes in mineralized intrusions at Ridgeway provide strong textural evidence that batches of volatile-rich magmas were episodically introduced into the deposit, as reported elsewhere by Carten *et al.* (1988), Lowenstern and Sinclair (1996), Wilson *et al.* (2003), Lickfold *et al.* (2003), and Harris *et al.* (2005). The occurrence and mineralogy of these textures imply that the intrusions were once a dynamic mixture of crystals and magmatic volatiles phases (i.e., an effervescent magma; Burnham, 1979) and that the volatiles were rich in Fe, important ore-forming ligands (including sulfur) and H<sub>2</sub>O. It is likely that these intrusions had considerable permeability (Candela and Blevin, 1995) through which the magmatic volatiles could stream upwards. In essence, the intrusions themselves acted as conduits to supply fluids into the space that was being created at the site of ore deposition.

### 3.9.3 Timing and nature of magmatism

Episodic magmatism in the Cadia district is evident from the new and pre-existing geochronologic data (Harris *et al.*, 2009c). These data reveal that four periods of magmatism occurred in the Cadia district, with the latter two events related to porphyry-style mineralization (Harris *et al.*, 2009c). Submarine volcanism and associated sedimentation occurred prior to 452 Ma. The second period of magmatism occurred during the Late Ordovician ( $448.2 \pm 2.1$  Ma) associated with the emplacement of diorite and monzodiorite intrusions. This was followed by two temporally discrete events during the latest Ordovician (~444 Ma), associated with the emplacement of the Au-rich Ridgeway deposit, and the earliest Silurian (~439 Ma) Cadia East deposit. These two productive ore-forming events are separated only by a few million years (Harris *et al.*, 2009c), rather than 18 million years as previously reported by Wilson *et al.* (2007).

The two productive ore-forming events in Cadia were both part of Phase 4 magmatism in the Macquarie Arc (Glen *et al.*, 2007a) which occurred from the Late Ordovician to Early Silurian (~450 - 439 Ma). Phase 4 magmatism was closely associated with most of the porphyry Cu–Au mineralization in the Macquarie Arc, and is represented predominantly by shoshonitic monzonite intrusions (Glen *et al.*,

2007a). Mineralized intrusions host Au–Cu porphyry mineralization at Ridgeway, Cadia Hill and Cadia East in the Molong Volcanic Belt, and the Northparkes porphyry deposits in the Junee–Narromine Belt. They were emplaced between 446 and 437 Ma (Lickfold *et al.*, 2007; Harris *et al.*, 2009c).

The timing of magmatism at Ridgeway was coeval with ultramafic magmatism in the Macquarie Arc (Harris *et al.*, 2009e). Based on three U–Pb ages (SHRIMP zircon ages of  $445 \pm 6$  Ma and  $448 \pm 8$  Ma; and LA-ICPMS zircon age of  $444 \pm 4$  Ma) from Fifield (Crawford *et al.*, 2007), ultramafic magmatism can be shown to overlap within analytical uncertainty with the Ridgeway and Northparkes porphyry deposits. The PGE-rich ultramafic magmas were sourced from relatively primitive oxidized shoshonitic magmas. Lickfold *et al.* (2003) showed that the causative intrusions in the Northparkes porphyry Au–Cu deposit exhibit distinct geochemistry that has been inherited from the injection of a primitive mafic source. Hattori and Keith (2001) showed that such processes can contribute significant amounts of metals to an evolving magma (e. g. Mount Pinatubo, Philippines; Bingham, Utah). Given the new temporal constraints from U–Pb geochronology, combined with the abundance of mafic (biotite–pyroxene–apatite) xenoliths, anomalous enrichment of PGE and mafic immobile elements, it is plausible that an ultramafic component was introduced into an evolving fractionating melt at Ridgeway. This may help explain the anomalously high concentrations of gold found in the Ridgeway porphyry Au–Cu deposit. Supporting evidence is provided by the mafic xenoliths in P1 and P2, and by the pyroxenite that crops out west of Cadia Hill (Fig. 3.1).

### **3.10 Summary**

The environment of deposition at Ridgeway has evolved from deeper water sedimentation distal from any volcanic source in which well-stratified to massive feldspathic siltstones and sandstones were deposited, to a shallower setting more proximal to volcanism that is dominated by thick, diffusely stratified volcanoclastic units deposited along the slopes of a partly emerging volcano around 455 - 452 Ma. Multiphase mafic to intermediate dikes and sills then intruded the volcano-sedimentary units.

Diorite and monzodiorite intrusions were emplaced around 448 Ma. These were followed by the mineralizing monzonite suite around 444 Ma. Quartz monzonite intrusions associated with the Cadia Hill, Cadia Quarry and Cadia East deposits were emplaced around 439 Ma. The two-ore producing events are separated only by a few million years, rather the 18 million years as reported by Wilson *et al.*, (2007).

The Ridgeway intrusive complex is composed of NW-elongated diorite to monzodiorite, monzonite and quartz monzonite intrusions. The intrusions have pipe-like geometries in cross-sections and swell at their centers. The swelling has tended to occur along the contact of the Weemalla Formation and the FRV. Distinct USTs are developed on the upper margins and apical parts of P1 and P2. Magnetite-rich USTs are developed in P1, whereas quartz-rich USTs and miarolitic cavities are found in P2.

Two petrographically and geochemically distinct intrusive suites are present in the Ridgeway intrusive complex. One suite is dominated by mafic rocks (Ppo and Fpo dikes and sills, and MzD stocks). The second suite (P1, P2 and P3) has more intermediate compositions. Intrusions at Ridgeway had shoshonitic magmatic affinities, which imply that shoshonitic magmatism occurred several times over an 8 m.y. period at Ridgeway, progressing toward more evolved and ultimately mineralized magmatic compositions. P1 and P2 are spatially and temporally associated with mineralization. Mafic xenoliths that comprise phenocrysts of biotite and pyroxene (typical of lamprophyres) occur only in the monzonites, implying mafic magma involvement in mineralization.

---

# Chapter 4: Alteration and Mineralization

---

## 4.1 Introduction

Understanding the distribution of hydrothermal alteration in and around porphyry ore deposits can help to provide important information for exploration targeting. In most cases, the alteration and mineralization features of a prospective target are best understood by comparing features and descriptions of previously discovered deposits developed in similar geologic environments (Sillitoe, 2000; Seedorff *et al.*, 2005). Hydrothermal alteration in porphyry deposits takes place where fluid movement occurs along fractures, veins, intrusion contacts, and in a pervasive fashion within hydrothermal stratigraphic horizons of contrasting permeabilities. The chemical evolution of the hydrothermal fluids and the spatial and temporal distribution of alteration minerals are in part influenced and controlled by the surrounding host rocks.

This chapter describes the temporal and spatial relationships of alteration minerals relative to the intrusive history of Ridgeway. The current study outlines observations of approximately 14 km of drill core (refer to Fig. 3.2 for location of drillholes) which, when combined with petrographic observations and the results of feldspar staining (Appendix B), have provided additional constraints on the distribution of alteration assemblages in and around the deposit. The characteristics of alteration assemblages found in contrasting host rock lithologies, including a variety of volcanic and sedimentary rocks, are discussed to highlight their varying styles of alteration assemblages. Due to compositional difference, the two main categories of host rocks at Ridgeway (siltstone and andesitic volcanics) appear to react differently to hydrothermal fluids, then influencing the distribution of specific alteration and sulfide minerals.



This chapter documents the Ridgeway paragenesis based on observations from different new levels, ranging from above the intrusive center to the deepest accessible portions of the deposit. It builds on previous work by Harper (2000) and Wilson (2003). The integrated deposit-scale vein, alteration and intrusion paragenesis presented in this chapter provides the framework and basis for the vein orientation discussed in Chapter 5.

The spatial distributions of alteration and mineralization assemblages are analyzed using a series of cross-sections. This study extends section 11050mE (originally published by Wilson *et al.*, 2003), by logging numerous underground deep drillholes collared during the development and mining stages of the Ridgeway project and underground mapping that were unavailable in the early parts of the decade. Drillholes logged from representative cross-sections (11050mE) and one long section (22650mN) present the different alteration assemblages and vein stages observed at Ridgeway. Gold and copper grade contours are presented in four different sections (100 m apart) and one long section to show the grade distribution both laterally and vertically. Terminology used to describe the characteristics of the veins and alteration styles is summarized in Table 4.1 (Titley, 1982).

**Table 4.1** Definition of alteration and mineralization terminology, Titley (1982).

<b>Term</b>	<b>Definition</b>
Pervasive alteration	Alteration of the rock that has resulted in the complete change of rock compositions and textures, typically resulting in textural destruction
Selectively pervasive alteration	Alteration in which only specific minerals in the host rock have been altered (e.g. mafic and feldspar phenocrysts), or components of the rock (e.g. groundmass or matrix). This alteration typically preserves or enhances the rock texture
Vein	A fracture >5 mm wide, partially or totally infilled by secondary or hydrothermal minerals
Veinlet	A fracture <5 mm wide, partially or totally infilled by secondary or hydrothermal minerals
Stringer	A fracture <1 mm wide, discontinuous/continuous fracture, filled by secondary or hydrothermal minerals
Vein-dike	A fracture that contains a mix of igneous material and secondary or hydrothermal minerals
Vein selvage	Secondary minerals that occur along edge of veins or veinlets at contact with wallrocks
Alteration halo	Pervasive or selectively pervasive alteration that occurs in the wallrock, surrounding a vein, veinlet or stringer
Weak, moderate, strong	Describes the relative intensity of alteration based on visual estimates in the field

## 4.2 Previous work

Numerous publications and research theses document the mineralization, alteration and vein paragenesis of the major porphyry related gold–copper deposits in the Cadia district (Wood and Holliday, 1995; Holliday *et al.*, 1999; Harper, 2000; Tedder *et al.*, 2001; Holliday *et al.*, 2002; Wilson, 2003; Wilson *et al.*, 2003, Wilson *et al.*, 2004; 2007a and 2007b; Kitto, 2005; Finn, 2006; Reynolds, 2007). At Ridgeway, several detailed studies have characterized the upper parts of the orebody (i.e. Harper, 2000; Wilson, 2003; Reynolds, 2007). Harper (2000) identified six stages of alteration assemblages and twelve vein stages. His pre-mineralization stages included selectively pervasive albite (stage 1) and magnetite–actinolite–biotite (stage 2) alteration assemblages. The main stage K-silicate–sulfide alteration assemblage (stage 3) was found to be associated with the earliest formed sulfides. These alteration stages and associated veins form the inner potassic zone which is restricted to the monzodiorite and monzonite intrusions and immediate adjacent wallrocks. An outer magnetite zone surrounds the inner potassic zone (Harper, 2000). Overprinting and forming a broad shell around the potassic zone is a domain of selectively pervasive propylitic alteration (stage 4), which consists of chlorite, epidote, prehnite and hematite. Late-stage alteration assemblages include structurally controlled and pervasive phyllic alteration (illite–quartz–pyrite; stage 5), and pervasive carbonate alteration (stage 6, Harper, 2000). Cu–Fe sulfides are zoned from a bornite-rich core outwards through chalcopyrite- and pyrite-rich zones (Harper, 2000).

Wilson (2003) recognized fifteen vein types and eight alteration assemblages that are temporally related to the Ridgeway monzonites. Early calc-potassic (actinolite–magnetite–biotite) alteration had four accompanying vein stages and was spatially related to the early-mineral monzonite intrusion and adjacent wallrocks. Transitional stage potassic (orthoclase–biotite  $\pm$  magnetite) alteration is spatially and temporally related to inter-mineral intrusions; this alteration was associated with four vein events characterized by various combinations of quartz–chalcopyrite–pyrite–magnetite–orthoclase. Some late-stage alteration assemblage and associated veins were observed to be associated with the late-mineral monzonite, while other veins are hosted within late stage faults. Peripheral parts of the Ridgeway deposit include four additional vein assemblages that were further segregated into inner propylitic

(characterized by the occurrence of hematite), outer propylitic (lacks hematite), and sodic alteration assemblages. The intensity of alteration and absolute metal concentration decreases from early- to late-mineral intrusions.

Reynolds (2007) characterized the nature of hydrothermal alteration in the upper distal parts of the Ridgeway deposit. Whole-rock geochemical analysis and chemical staining revealed the presence of peripheral magnetite–K-feldspar–biotite (potassic) alteration up to 400 m above from the intrusive centre. This assemblage had been overprinted by chlorite–epidote–hematite–calcite (propylitic) alteration. Three zones of magnetite alteration, defined by different magnetite textures and abundances, were documented. A textural progression occurs from coarse-grained magnetite clots and veins at the mineralized core of the deposit, to fine disseminated magnetite–chlorite intergrowths in the distal parts up to ~500 m outboard from the 0.1 wt % Cu contour.

### **4.3 Ridgeway vein paragenesis**

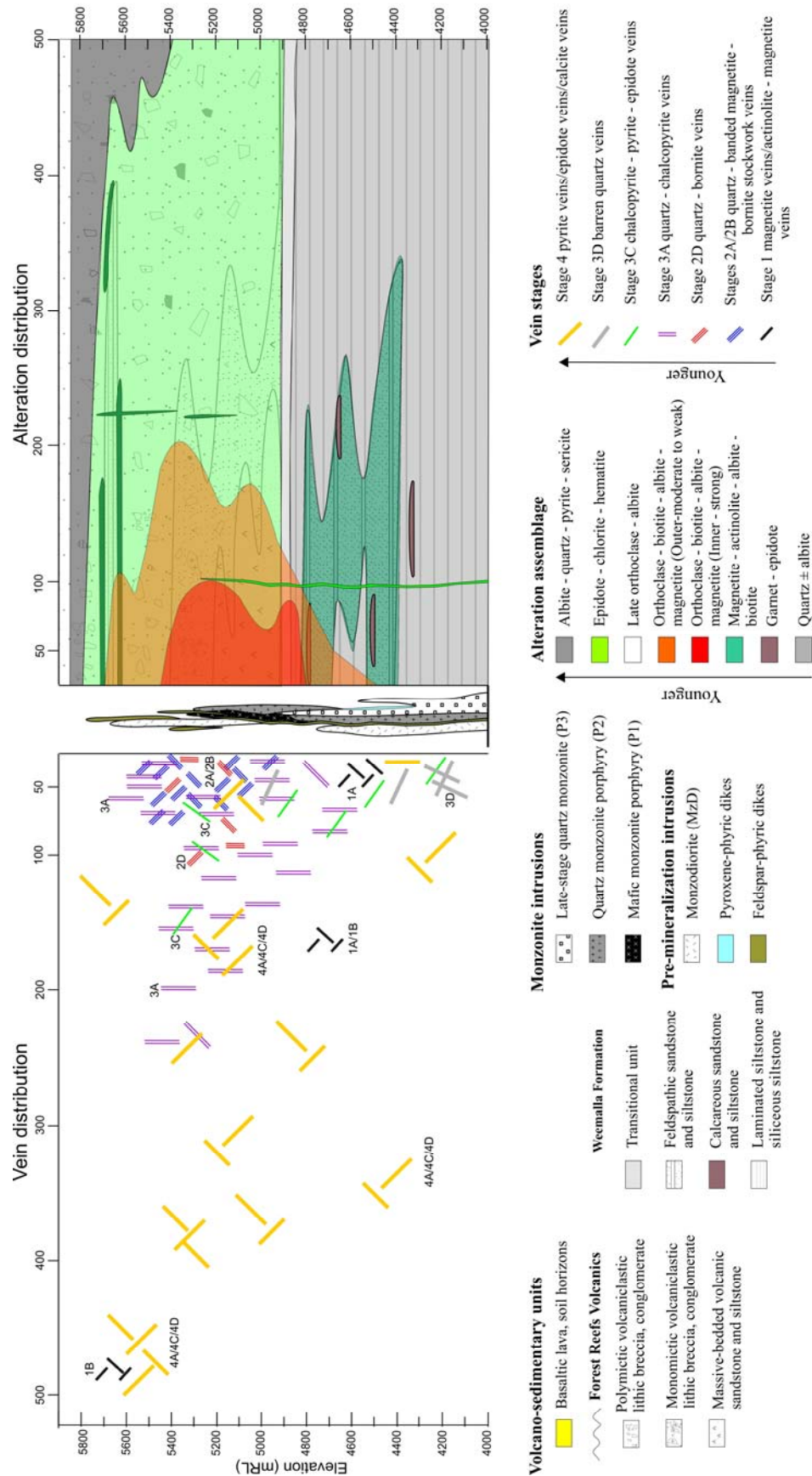
Based on cross-cutting and overprinting relationships, fourteen vein stages and nine alteration assemblages have been identified at Ridgeway in the current study (Table 4.2 and Table 4.3). Figure 4.1 presents a schematic time-space diagram showing the generalized paragenetic sequence and alteration assemblages of the Ridgeway Au–Cu porphyry deposit. Vein assemblages are classified into three main groups (Table 4.2): (A) pre-main mineralization stage; (B) main mineralization stage; and (C) late stage. Significant gold and copper sulfides were deposited during the main mineralization stage. Figure 4.2 and Figure 4.3 illustrate the spatial distribution of the different alteration stages and vein assemblages.

Table 4.4 compares the alteration assemblages and vein paragenesis identified in previous studies (Harper, 2000 and Wilson, 2003) to that of the current study. The current study has provided more detailed description of the deeper parts of the Ridgeway alteration system, and also builds on the previous findings that focussed on the upper parts of the deposit. Specific points of difference between this and earlier studies include: the recognition that peripheral epidote–sulfide veins (Wilson, 2003) formed synchronous with main stage mineralization; the recognition and

**Table 4.2** Summary of vein stages from Ridgeway.

Vein Stage <sup>1</sup>	Veining/Filling		Thickness	Form, mineral associations, internal texture	Distribution and occurrence	Alteration envelope (width)
	Major minerals	Minor minerals				
Pre-main mineralization stage veins						
Stage 1A	Magnetite		1 - 20 mm	Continuous to discontinuous, incipient veinlets; magnetite occurs both as monomineralic stringers and veinlets, chains and/or beads	Abundant in the monzodiorite intrusions and surrounding units	K-feldspar, <3 mm, albite < 3mm
Stage 1B	Magnetite, actinolite	Chlorite, K-feldspar, apatite, chalcopyrite, bornite	1 - 50 mm	Continuous to discontinuous, with diffuse walls and irregular vein shapes, locally wispy with non parallel vein walls; actinolite–chlorite–magnetite occurs as blebby and/or fibrous bands	Abundant in the monzodiorite intrusions, pyroxene-phyric dikes and country rocks	K-feldspar, actinolite <2 mm
Main mineralization stage veins						
Stage 2A	Quartz, magnetite	Actinolite, bornite	3 - 20 mm	Continuous, subparallel, sharp vein walls; magnetite occurs as small (<1 mm) subhedral grains that have overgrown quartz, or as vein selvage	Abundant and well developed in the pyroxene-phyric dikes and the Forest Reefs Volcanics	none
Stage 2B	Quartz, magnetite, bornite	Chalcopyrite, gold, chlorite	5 - 100 mm	Continuous, sharp vein walls; characterized by dark-grey quartz with magnetite laminations (<1 mm) ± bornite ± chalcopyrite ± gold; at depth, sulfides disappear as quartz–laminated chlorite ± magnetite dominate	Well developed on the apical portion and margins of the mafic monzonite intrusions and adjacent Forest Reefs Volcanics wallrocks up to 10 m from the contact	none
Stage 2C	Orthoclase, quartz	Chalcopyrite, bornite, pyrite, magnetite	2 - 10 mm	"Aplite vein-dike"; continuous; aplitic infill with aggregates of chalcopyrite–bornite in the centre of the structure	Occur within the mafic monzonite and adjacent pyroxene-phyric dikes up to 100 m from the contact	none
Stage 2D	Quartz, bornite	Chalcopyrite, magnetite, gold	5 - 20 mm	Continuous, sharp-edged; bornite ± chalcopyrite occupy the central band in the quartz as infill or blebs	Well developed near the contact of the mafic monzonite and the adjacent Forest Reefs Volcanics and pyroxene-phyric dikes	K-feldspar, <2 mm
Stage 3A	Quartz, chalcopyrite	Molybdenite, magnetite, gold	5 - 50 mm	Continuous, subparallel, straight-edged walls; chalcopyrite (1- 10 mm thick) occupies a central band or occurs as discrete aggregates throughout the vein; locally, molybdenite and magnetite have overgrown or are associated with chalcopyrite; flaky molybdenite	Abundant in the quartz monzonite and country rocks.; where found in mafic monzonite, these veins cut the earlier mineralized stage 2 veins	K-feldspar, <2 mm
Stage 3B	Orthoclase, quartz	Chalcopyrite, chlorite	1 - 30 mm	"Aplitic vein-dike"; continuous, straight-sided to wavy, locally with diffuse margins and irregular morphologies; pale to dark-orange; aphanitic, composed primarily of K-feldspar intergrown with quartz ; locally, the dark-orange aplite occupies a central seam with thin hydrothermal selvages of prismatic quartz	Temporally and spatially associated with the quartz monzonite intrusions, typically located near the contact and/or along the contact with the wallrocks	none
Stage 3C	Chalcopyrite, epidote	Pyrite, bornite, apatite, molybdenite	2 – 20 mm	Continuous to discontinuous, wavy-edged to diffuse vein walls; characterized by the presence of epidote selvage up to 2 mm thick, intimately intergrown with sulfides	Occur proximal and distal to the deposit	K-feldspar, <1 mm locally up to 10 mm
Stage 3D	Quartz, chlorite	Pyrite	2 - 20 mm	"Barren quartz "; continuous, straight-sided walls; white quartz with chlorite as central bands or as fine disseminations giving a greenish colouration to the vein; at depth, the vein is sinuous and the quartz has sugary texture; anhedral quartz grains vary from 50 µm to 1 mm	Spatially associated with the quartz monzonite, broadly distributed vertically	K-feldspar, <1 mm
Late stage veins						
Stage 4A	Pyrite, quartz	Quartz, chalcopyrite	1 - 40 mm	Continuous, wavy to straight-sided; typically, pyrite occupies the central band in the quartz veins, locally occurring as monomineralic stringers/veinlets/veins	Present in all intrusions and host rocks, mostly found peripheral to the orebody	K-feldspar (<10 mm); locally with sericite - albite (<5 mm)
Stage 4B	Epidote	Chlorite, quartz, calcite	1 - 10 mm	Continuous to discontinuous; undulating, vary from planar to more irregular diffuse veins	Present in all intrusions and host rocks; typically found peripheral to the orebody, and spatially associated with the intrusion of late-stage quartz monzonite	Occasional K-feldspar, reddening due to hematite dusting (1 - 10 mm)
Stage 4C	Chlorite	Pyrite	centimetre to meters	"Chlorite-rich matrix breccia "; locally exhibiting jig-saw fit, angular to subrounded, clast- to matrix- supported, with matrix composed mostly of chlorite; stage 3A vein fragments observed locally	Present in all intrusions and host rocks	none
Stage 4D	Calcite	Prehnite, quartz	5 – 50 mm	Continuous, straight-sided, sharp contact with wallrocks; locally occurring as late infill to stage 4B veins	Present in all rocks, occurring proximal and peripheral to the core of the deposit	none

<sup>1</sup> Vein stages listed in sequence from oldest to youngest (top to bottom) as observed from cross-cutting relationships in drillcore logging and underground mapping<sup>2</sup> Italized are terms assigned to specific vein stage for clarity



**Figure 4.1** Schematic space-time diagram of alteration assemblages and vein stages for the Ridgeway Au-Cu porphyry deposit. The distance represents how far a feature extends laterally from the center of the monzonite intrusions.

**Figure 4.2** Interpretative cross section along 11050mE showing alteration zonation patterns and distribution of veins stages from Ridgeway.

- A) Interpreted geology along 11050mE. Refer to Fig. 3.1 for section location and Figure 3.5B for detailed geological information.
- B) Distribution of the different alteration assemblages highlighting the strong lithological controls. The pre-mineralization stage formed preferably in the lower part of the orebody, mostly in the Weemalla Formation and early-stage intrusions. Quartz  $\pm$  albite alteration is well developed in the deeper parts of the system. Garnet–epidote alteration is constrained to the reactive calcareous units, whereas magnetite–actinolite–albite alteration is confined to the monzodiorite and pyroxene-phyric dikes, and locally to the more massive feldspathic units of the Weemalla Formation. Remnants of this alteration and associated stage 1B magnetite–actinolite veins occur 600 m from the center of the deposit. Strong orthoclase–biotite–albite–magnetite alteration in the core of the deposit is associated with the mafic monzonite porphyry (P1). This alteration assemblage is surrounded by a domain of moderate to weak orthoclase–biotite–albite  $\pm$  magnetite alteration associated with the quartz monzonite porphyry (P2). Late stage orthoclase–albite alteration is constrained mainly to the late-stage quartz monzonite (P3). Epidote–chlorite–hematite alteration forms a halo around the inner and outer orthoclase–biotite–albite–magnetite alteration zones and has locally overprinted the earlier formed alteration assemblages. The transition between the epidote–chlorite–hematite alteration and the hematite-deficient albite–quartz–pyrite–sericite alteration is marked by the red dashed-line. Albite–quartz–pyrite–sericite alteration has locally encroached and overprinted the epidote–chlorite–hematite alteration assemblage on the northeast side of Ridgeway.
- C) Distribution of the post-mineralization alteration assemblages, which occur presently as selectively pervasive alteration haloes associated with large-scale faults. Note that clay–chlorite alteration is associated with steeply-dipping faults in the centre of the orebody.
- D) Spatial distribution of vein types identified during this study. Stage 1 veins occur peripheral to the orebody and are mostly hosted in the monzodiorite and the pyroxene-phyric dikes at depth. High vein densities associated with main stage mineralization (stages 2 and 3) occur within 400 m of the P1 and P2 intrusive contacts. The vein densities decrease both laterally and vertically. Stage 3C veins occur within 200 m of P2. Stage 4 veins are broadly distributed, occurring in the core of the orebody, but their abundance increases with distance away from the deposit center. Refer to Figure 4.2A for detailed geological information.



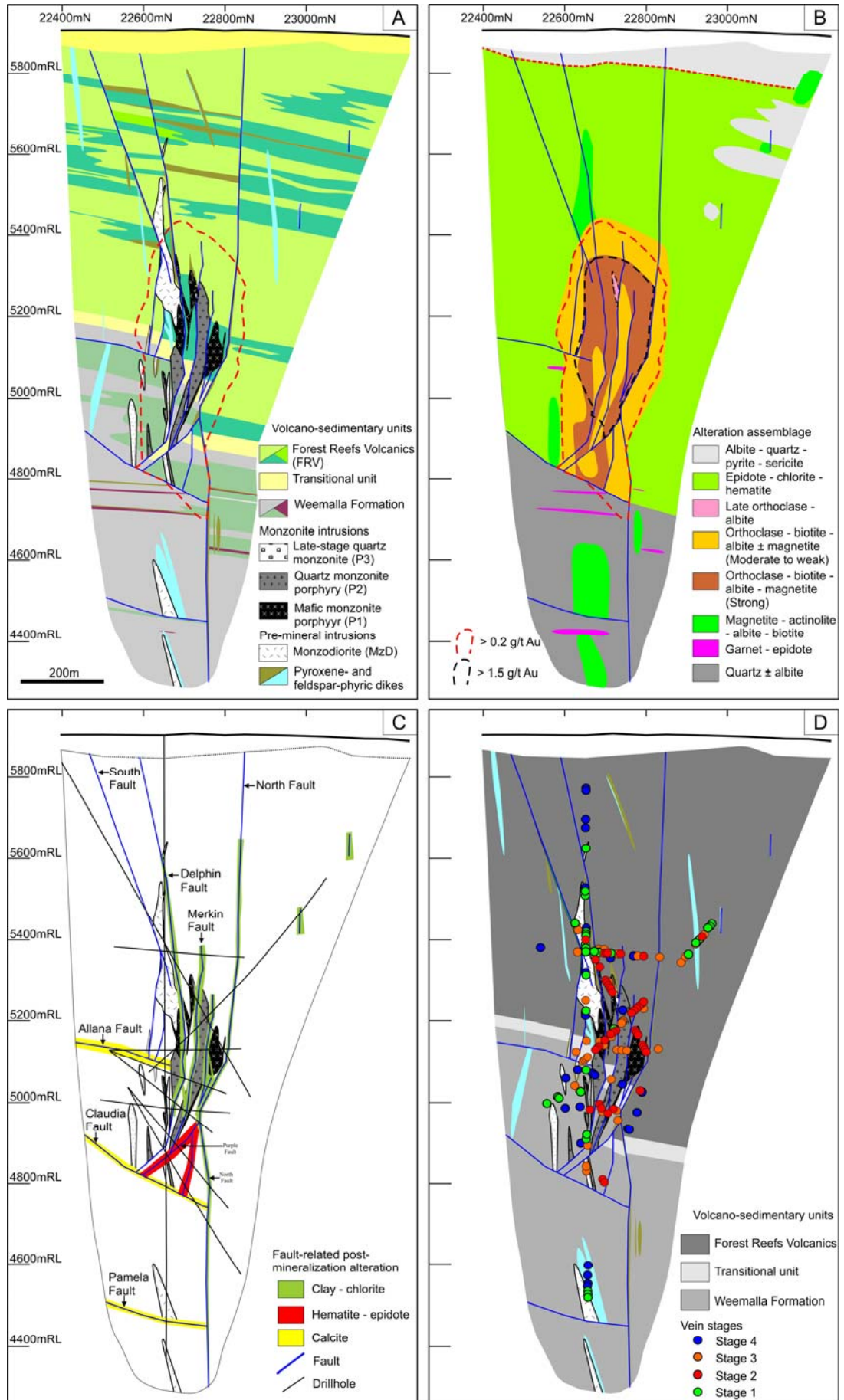
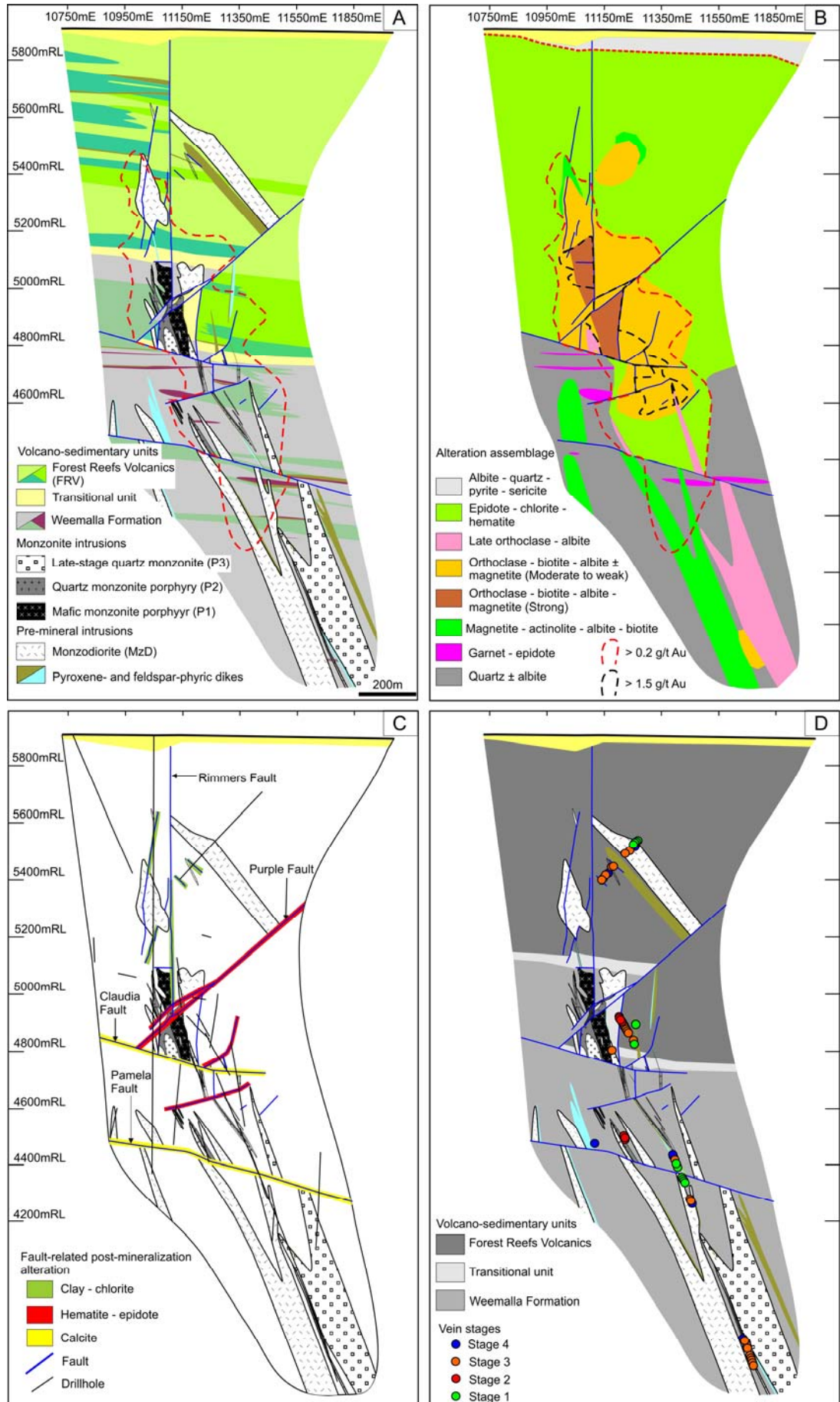


**Figure 4.3** Interpretative long section along 22650mN showing alteration zonation patterns and distribution of veins stages from Ridgeway.

- A) Interpreted geology along 22650mN. Refer to Figure 3.1 for section location and Figure 3.6 for detailed geological information.
- B) Distribution of the different alteration assemblages at Ridgeway. Quartz  $\pm$  albite alteration is constrained to the deeper portion of the deposit, intercalated with actinolite–magnetite–albite alteration in the more calcareous beds of the Weemalla Formation. The actinolite–magnetite–albite alteration assemblage is also well developed in the monzodiorite stocks and pyroxene-phyric dikes. Strong orthoclase–biotite–albite–magnetite alteration is associated with the mafic monzonite (P1) intrusions and extends up to 100 m from the intrusive contact. There is moderate to weakly developed orthoclase–biotite–albite–magnetite alteration domain that surrounds the inner strong orthoclase alteration zone, overprinting the early actinolite–magnetite–albite alteration assemblage in the monzodiorite. Chlorite–epidote–hematite alteration is confined at depth to massive and bedded feldspathic lithofacies of the Weemalla Formation. It is more broadly developed in the FRV, forming a halo around the outer orthoclase–biotite–albite  $\pm$  magnetite alteration. Late-stage orthoclase–albite alteration is centered on late-stage quartz monzonite (P3), and occurs locally in the centre of the orebody.
- C) Distribution of the post-mineralization alteration assemblages, which occur as alteration haloes associated with late-stage faults.
- D) Distribution of the different vein types recognized in this study, based on drill core observations. Stage 1 veins are distributed peripheral to the orebody and mostly hosted in the monzodiorite. Stage 3C chalcopyrite–epidote veins occur about 300 m from the quartz monzonite (P2). Fe–Cu deficient, stage 3D barren quartz veins occur deeper in the system. These veins have been truncated by P3 and, locally occurring as xenoliths in the intrusion. Stage 4 veins are broadly distributed throughout the deposit. Refer to Figure 4.3A for detailed geological information.



documentation of barren quartz (Cu–Fe deficient veins) in the deeper parts of the deposit; confirmation that fault-related peripheral alteration and vein stages are truly post-mineralization, and that the outer propylitic zone is more complicated than previously documented. Details of these findings are provided below. In addition, several pre-mineralization stages have been defined during the current study, based on the recognition of several types of veins that have been truncated by main stage mineralized veins. Particular alteration has been given detailed descriptions of the contrasting alteration assemblages and sulfide distributions found in the contrasting lithologies of the Weemalla Formation and FRV.

### **4.3.1 Pre-main mineralization veins - stage 1**

The pre-existing paragenetic framework for Ridgeway, as outlined in section 4.2, has been modified during the current study. Specifically, a pre-mineralization stage has been added (Table 4.2; Fig. 4.1). Two generations of veining occurred during the pre-mineralization stage. These are best-developed in the pyroxene- and feldspar-phyric dikes, MzD and in the surrounding wallrocks. These veins occur up to 600 m from the intrusive contact. Stage 1 veins are inferred to be associated with the intrusion of the MzD, and have been truncated by mineralized veins (stages 2 and 3).

#### **4.3.1.1 Stage 1A magnetite veinlets**

Stage 1A is characterized by thin, discontinuous magnetite veinlets (Table 4.2; Fig. 4.4A and B). The vein walls are irregular and diffuse, appearing to grade into the adjacent wallrocks locally. Stage 1A veins are abundant in the MzD and surrounding FRV and Weemalla Formation. In the Weemalla Formation, magnetite stringers occur as thin sheeted veinlets (Fig. 4.4B). These veins are cut by later actinolite–magnetite veins (stage 1B; Fig. 4.7E) and by main stage mineralized quartz–magnetite vein (stage 2A; Figs. 4.4 and 4.7F) and quartz–chalcopyrite vein (stage 3A; Fig. 4.7E and F). The fine-grained siltstone and volcanic wallrocks that have been cut by stage 1A magnetite veinlets also occur as xenoliths in the P1 and P2 intrusions (Figs. 4.4C and 4.5H, respectively), suggesting that these veins formed early in the deposit history, i.e. prior to or more likely during the emplacement of the



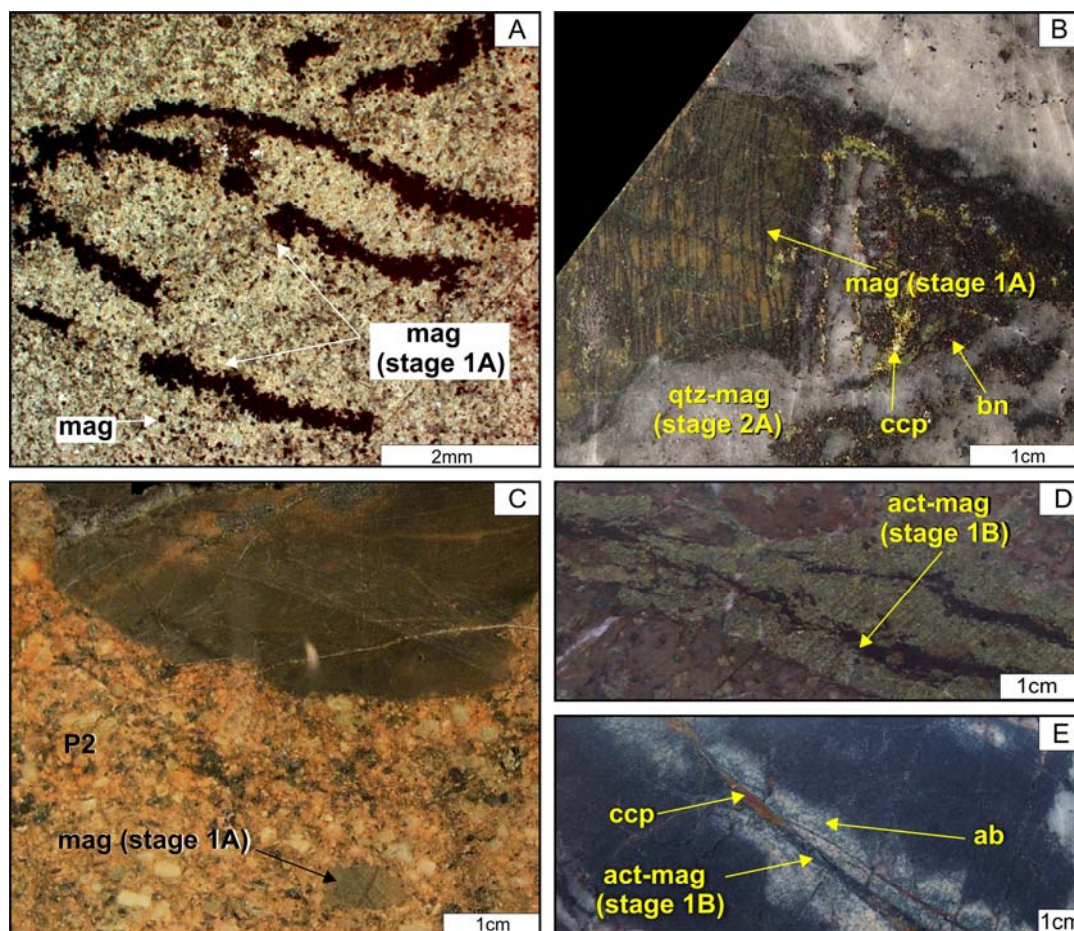


**Figure 4.4** Texture, mineralogy and mineral paragenesis of the pre-mineralization (stage 1) veins from Ridgeway. **A)** Photomicrograph (ppl) of stage 1A magnetite veinlets. The vein walls are irregular to diffuse. These veins have cut the quartz - albite-altered massive siltstone of the Weemalla Formation (UR255-358.8m). **B)** Sheeted stage 1A magnetite veinlets hosted in massive fine-grained siltstone of the Weemalla Formation. The stage 1A veins have been truncated by mineralized quartz - magnetite - bornite veins (stage 2A; UR150-223.3m). **C)** Stage 1A magnetite stringers that have cut the dark-brown quartz  $\pm$  albite-altered fine-grained siltstone occur as xenoliths in orthoclase - biotite - albite altered P2 intrusion (NC541-879m). **D)** Stage 1B magnetite - actinolite veins with irregular walls, hosted in dark-brown quartz  $\pm$  albite altered andesite dike. This vein occurs 600 m away from the center of the orebody. The actinolite has been pervasively replaced by epidote - chlorite (NC507-368.5m). **E)** Stage 1B actinolite - magnetite vein with albite alteration halo, hosted in actinolite - chlorite-altered massive volcanic sandstone of the FRV (UR358W1-611.2m). Abbreviations: ab = albite, act = actinolite, bn = bornite, ccp = chalcopyrite, chl = chlorite, ep = epidote, mag = magnetite, or = orthoclase, ppl = plane polarized light

MzD stocks. Thin K-feldspar and/or albite alteration haloes, up to 3 mm, are developed locally (Figs. 4.4E and 4.11H). Sulfides are absent from these veins.

#### 4.3.1.2 Stage 1B actinolite–magnetite veins

Stage 1B is characterized by actinolite–magnetite ( $\pm$  apatite) veins, generally occurring as irregular and discontinuous fibrous bands (Table 4.2; Fig. 4.4D and E). In other cases, these veins have been reopened by later mineralized quartz–

chalcopyrite veins. In the MzD, stage 1B veins contain traces of chalcopyrite and/or bornite locally. Stage 1B veins range in thickness up to 50 mm. Thin (2 mm) K-feldspar alteration haloes are visible locally when chemical staining is applied. Albite alteration haloes occur as a domain of indurated creamy-white replacement up to 10 mm from the vein (Fig. 4.4E). The massive feldspathic unit of the FRV has been selectively altered to magnetite–actinolite–albite adjacent to stage 1B vein (Fig. 4.7E) whereas in the Weemalla Formation, these veins are typically thinner (up to 5 mm wide) and lack notable alteration haloes. Stage 1B veins have been cut by mineralized quartz–chalcopyrite veins (stage 3A; Fig. 4.7E). Approximately 500 m away from the center of the orebody, northeast of Ridgeway, stage 1B veins are still present and have cut the more coherent (feldspar-phyric lithofacies) parts of the FRV (Figs. 4.1 and 4.2D).

Stage 1 veins are similar to vein stages 2A and 2B described by Harper (2000). These magnetite–actinolite veins were found to be densely concentrated in and around the monzodiorite, implying a genetic link with this intrusion (Harper, 2000).

#### **4.3.2 Main mineralization stage veins - stage 2**

Stage 2 quartz–sulfide veins introduced the bulk of the copper and gold mineralization at Ridgeway, and are associated with the main stage alteration assemblage (orthoclase–biotite–albite–magnetite). The main stage vein stockworks are also associated, both spatially and temporally, with P1 intrusions. Stage 2 veins are abundant in the core of the deposit (Fig. 4.2D). Locally, orthoclase-rich alteration haloes occur around the quartz–bornite veins.

Four substages of veins have been identified as part of stage 2 (Table 4.2). They are best developed in P1 intrusions and in the immediate wallrock contact (up to 100 m away; Fig. 4.1). In the upper part of the deposit, mostly in the FRV, the dominant sulfides in stage 2 veins are bornite and chalcopyrite. In the deeper part of the deposit, bornite is conspicuously absent, and stage 2 quartz–chalcopyrite–magnetite–chlorite veins predominate in the Weemalla Formation.



#### **4.3.2.1 Stage 2A quartz–magnetite veins**

Stage 2A is composed primarily of dark-grey quartz–magnetite  $\pm$  bornite  $\pm$  actinolite veins (Table 4.2). Stage 2A veins are typically sinuous to straight-sided. The proportions of magnetite and quartz are variable, with quartz typically more abundant. Magnetite occurs as small (<1 mm) subhedral crystals that have overgrown quartz, and also occur as vein selvages (Fig. 4.4B). It is possible that the magnetite selvages on stage 2A veins formed early, and that the quartz locally pervaded the center of the structure due to vein reopening (Fig. 4.7F). It is also possible that the magnetite pervaded along the margins of the earlier formed quartz vein. Stage 2A veins are common and well-developed in the pyroxene-phyric dikes and the FRV adjacent to the contact with P1 intrusions. No alteration haloes have been observed around stage 2A veins.

#### **4.3.2.2 Stage 2B quartz–banded magnetite–bornite veins**

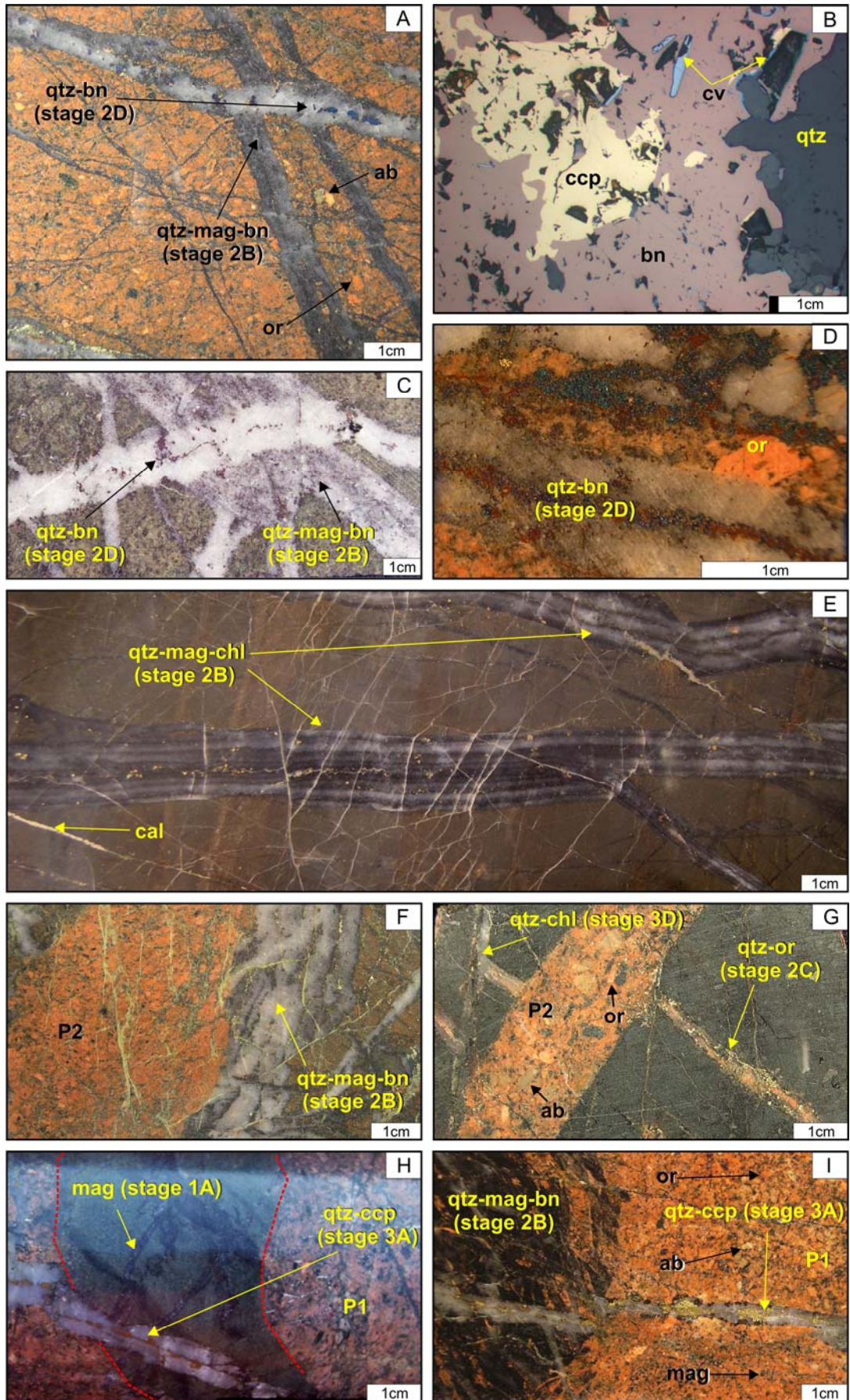
Stage 2B veins are characterized by dark grey quartz intergrown with bands of magnetite  $\pm$  bornite and/or chalcopyrite (Table 4.2). Bornite  $\pm$  chalcopyrite are particularly common in stage 2B veins in the upper part of the deposit, where they are hosted by P1 and andesitic FRV wallrocks (Fig. 4.6A). At depth, bornite is rare to absent, and stage 2B veins consist of quartz intergrown with bands of chlorite  $\pm$  magnetite in quartz  $\pm$  albite altered siltstone of the Weemalla Formation (Fig. 4.5E).

Stage 2B veins have formed dense stockworks in the upper portion of P1 and up to 10 m outboard from contact with the FRV (Figs. 4.1, 4.2D, 4.5I and 4.6). Stage 2B veins are generally formed where magnetite-rich USTs occur along the margins of P1 (section 3.4.2.1). Vein densities locally comprise up to 80% of the rock volume in zones up to 10 m across. Stockwork veins gradually decrease in intensity up to 100 m away from the intrusive contact. Strong, texturally destructive, pervasive orthoclase–biotite–magnetite–actinolite alteration assemblage is associated with the stockwork zones (Fig. 4.6).

**Figure 4.5** Texture, mineralogy and mineral paragenesis of stage 2 veins from Ridgeway.

- A)** Multiple vein stages that have cross-cut a strongly altered mafic monzonite (P1) intrusion. The intrusion exhibiting pervasive orthoclase–biotite–albite–magnetite alteration assemblages has been cut by stage 2A quartz–magnetite veins. The stage 2A veins has been cut by stage 2B quartz–banded magnetite–bornite vein, which in turn has been cut by stage 2D quartz–bornite vein (UR390-47.5m).
- B)** Photomicrograph (rl) of a stage 2D quartz–bornite vein. The bornite is intergrown with chalcopyrite. Parts of the bornite grain have been partially replaced by covellite (dark blue; UR058-95.5m).
- C)** Thick, stage 2B vein with disseminated bornite that has been cut by a stage 2D vein. The veins are hosted in a magnetite–actinolite–albite–altered pyroxene–phyric dike (UR058-95.9m).
- D)** Stage 2D vein hosted in a P1 intrusions with strong orthoclase–biotite–albite–magnetite alteration (NC498-725.3m).
- E)** Stage 2B veins with subparallel laminations of chlorite–magnetite in a quartz  $\pm$  albite-altered siltstone of the Weemalla Formation. This sample comes from deep in the system (4500mRL), approximately 1600 m below the present-day surface. Note the absence of bornite and chalcopyrite, and that late pyrite occurs as disseminations in the veins. The rock and the stage 2D veins have cut been by thin calcite veinlets of indeterminate origin (UR360-719m).
- F)** Stage 2B vein truncated by an orthoclase–biotite–albite–magnetite altered quartz monzonite (P2) intrusion. Late epidote stringers cut the vein and the altered rock (UR254-118.1m).
- G)** Stage 2C quartz–orthoclase vein dike truncated by orthoclase–biotite–albite–magnetite altered P2 intrusion. Quartz–chlorite vein (stage 3D) has cut and offset the stage 2C vein (UR313-173.1m).
- H)** Strong orthoclase–biotite–albite–magnetite altered P1 with xenolith of dark-green actinolite–magnetite–albite altered fine-grained siltstone. Thin, stage 1A magnetite veins occur in the xenolith. The xenolith and the P1 intrusion are cut by quartz–chalcopyrite vein (stage 3A; NC508-930m).
- I)** Stage 2B stockworks developed adjacent to strongly orthoclase–biotite–albite–magnetite-altered P1 intrusion. Both P1 and the stage 2 stockworks have been cut by a quartz–chalcopyrite vein (stage 3A; UR390-247.1m).

Abbreviations: ab = albite, bn = bornite, cal = calcite, ccp = chalcopyrite, cv = covellite, au = gold, mag = magnetite, or = orthoclase, qtz = quartz, rl = reflected light





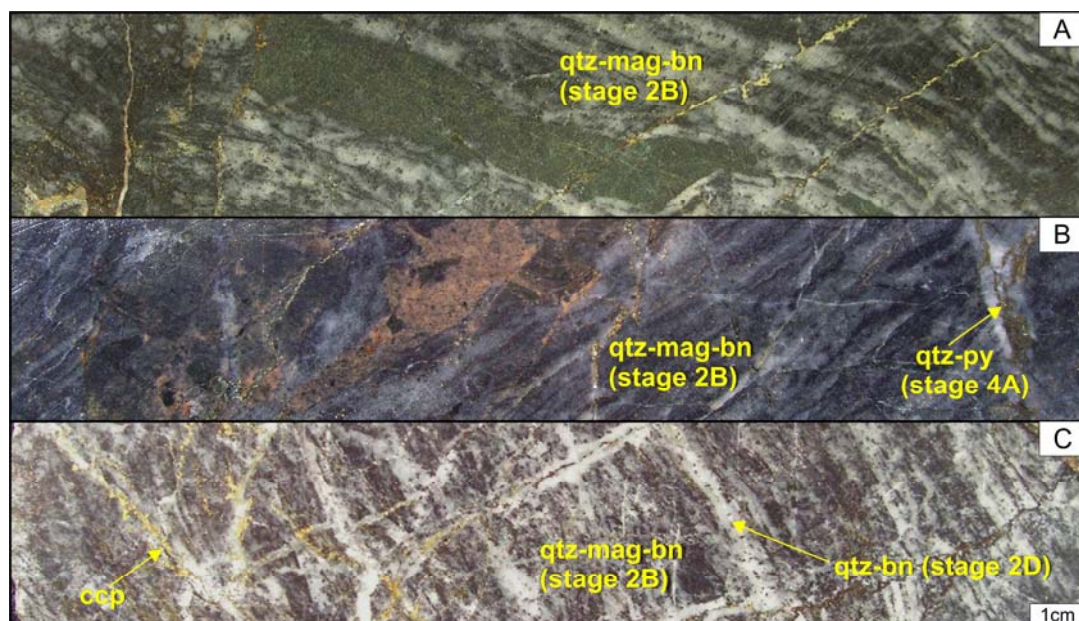


**Figure 4.6** Stage 2B quartz - banded magnetite - bornite stockworks from Ridgeway. These samples are representative of the main stage highly mineralized zones in the core of the orebody. **A)** Massive volcanoclastic sandstone of the FRV, cut by stage 2B veins. This sample is from an interval containing 28.0 g/t Au and 2.63 % Cu (NC498-716.3m). **B)** Massive siltstone of the Weemalla Formation (5.5 g/t Au and 1.48 % Cu). Late stage quartz - pyrite vein (stage 4A) has cut the mineralized vein (UR154-168.3m). **C)** Dense stage 2B veins, grade up to 11.6 g/t Au and 3.59% Cu (UR058-78m). Abbreviations: bn = bornite, ccp = chalcopryite, mag = magnetite, py = pyrite, qtz = quartz

Stage 2B veins have been cut by stage 2D magnetite-poor quartz–bornite veins (Fig. 4.5A and C) and quartz–chalcopryite veins (stage 3A; Fig. 4.5H and I). Stage 2B veins have been truncated by the P2 intrusion (Fig. 4.5F; also see Fig. 4.7A of Wilson, *et al.*, 2003).

Stage 2B veins are similar to E-2 veins of Wilson (2003), who observed gold both within the magnetite–bornite laminations and as disseminations in quartz. Wilson (2003) also noted that the quartz–magnetite–bornite veins lack alteration haloes, suggesting that the causative fluids were in chemical equilibrium with their altered host rocks.

#### 4.3.2.3 Stage 2C vein-dikes

Stage 2C structures comprise fine-grained graphic intergrowths of orthoclase–quartz  $\pm$  chalcopryite (Table 4.2). These magmatic-hydrothermal features are classified as vein-dikes (Lickfold, 2003; Wilson, 2003). They are typically <10 mm wide and contain aggregates of chalcopryite, bornite, and magnetite locally in their centre (Figs. 4.5G and 4.10C). The timing of stage 2C vein-dikes is constrained by

cross cutting relationships. They cut stage 2A and 2B veins, and have been cut by quartz–chlorite veins (stage 3D) and truncated by the P2 intrusion (Fig. 4.5G; Harper, 2000; also see Fig. 4.11C of Wilson *et al.*, 2003).

#### **4.3.2.4 Stage 2D quartz–bornite veins**

Stage 2D veins are characterized by quartz–bornite ( $\pm$  chalcopyrite–magnetite). The Cu–Fe sulfides and magnetite occupy a central band in the quartz vein (Table 4.2; Fig. 4.5A, C and D). Gold occurs locally as disseminations in the quartz veins. Bornite is intergrown with digenite and chalcopyrite. Covellite has partially replaced bornite rims locally (Fig. 4.5B). Previous studies have documented gold inclusions in bornite, and bornite intergrown with hypogene chalcocite (stage E-4 veins of Wilson, 2003).

Stage 2D veins typically have thin K-feldspar alteration haloes in the FRV and pyroxene-phyric dikes. There are also stage 2D veins in the bedded feldspathic sandstone and siltstone units of the upper Weemalla Formation which have undergone strong orthoclase–biotite–albite–magnetite alteration (Fig. 4.1).

### **4.3.3 Main mineralization stage veins - stage 3**

Chalcopyrite is the dominant sulfide mineral in stage 3 veins, typically present as stringers in the quartz veins or as disseminations throughout the vein; locally, as massive chalcopyrite veins together with subordinate pyrite–bornite–epidote. Stage 3 comprises four vein substages that are for the most part localized in and around P2 intrusion, up to 200 m away from the intrusive contacts (Table 4.2; Fig. 4.1). Stage 3 veins are more continuous than stage 2 veins and occur in parallel sets or sheeted veins.

#### **4.3.3.1 Stage 3A quartz–chalcopyrite veins**

Stage 3A is characterized by quartz–chalcopyrite ( $\pm$  molybdenite–magnetite) veins (Table 4.2). Chalcopyrite occupies a central seam (1–10 mm wide), and also occurs as discrete aggregates throughout the quartz veins (Fig. 4.7). Where present, molybdenite occurs as thin center-line seams that in some cases intimately associated

with chalcopyrite (Fig. 4.7A and B). Molybdenite also occurs as acicular clots disseminated throughout the quartz veins (Fig. 4.7C). Gold occurs as inclusions up to 80 microns in diameter in chalcopyrite grains (Fig. 4.7D). Locally, thin, orthoclase-rich alteration haloes occur around FRV-hosted stage 3A veins. No alteration haloes are apparent in P2-hosted stage 3A veins. Stage 3A veins occur throughout the central portion of the deposit and extend up to 200 m laterally from the P2 intrusions (Figs. 4.1 and 4.2D). Stage 3A veins have cut stage 1 and 2B veins (Fig. 4.7B, E and F), and are cut by epidote  $\pm$  chlorite veins (stage 4B, e.g. UR390-389.5m).

Stage 3A veins are similar to stage T-1 veins of Wilson (2003), who also noted the lack of alteration haloes in P2 (inter-mineral monzonite; Wilson *et al.*, 2003). Stage 3A veins are therefore inferred to have been in chemical equilibrium with P2.

#### **4.3.3.2 Stage 3B vein-dikes**

Stage 3B is characterized by pale- to dark-orange aplitic vein-dikes that comprise fine- to medium-grained orthoclase intergrown with quartz (commonly myrmectitic in nature), with minor chalcopyrite, pyrite and chlorite (Table 4.2). Stage 3B veins are compositionally similar to stage 2B, but texturally different. The stage 3B vein-dikes are thicker (up to 20 mm), with narrow bands of hydrothermal quartz (up to 5 mm) locally occurring at the vein-dike margins (Fig. 4.7G and H). Stage 3B vein-dikes are cut by later quartz–chalcopyrite veins (stage 3D; Fig. 4.8G).

Stage 3B veins were emplaced inside and along the margins of the P2 intrusion and rarely in the FRV, suggesting a temporal relationship to P2. Stage 3B aplitic vein-dikes correlate with the T-2 vein-dikes of Wilson (2003), which were observed to be cut by and to have cut quartz–chalcopyrite veins Wilson (2003).

#### **4.3.3.3 Stage 3C chalcopyrite–epidote veins**

Stage 3C veins and veinlets comprise chalcopyrite–epidote ( $\pm$  pyrite–bornite–apatite–molybdenite; Table 4.2); characterized by the presence of aggregates of pale yellow-green epidote as a selvage (up to 2 mm) surrounding a central sulfide seam (Fig. 4.8A and B). Subhedral to euhedral epidote grains occur around the margin of



bornite–chalcopyrite grains (Fig. 4.8C). Apatite is intergrown with the Cu–Fe sulfides. Stage 3C veins have hematite-dusted orthoclase alteration haloes that are typically wider (up to 10 mm) than the related veins. Stage 3C veins are hosted by P2 intrusions in the core of the deposit, and can occur up to 200 m outboard from the intrusive contact (Figs. 4.1 and 4.2D). Stage 3C veins have cut stage 1 and stage 2 veins (e.g. UR058-49.5m), but are cut by epidote and calcite stringers (UR450-216.8m).

Stage 3C veins are equivalent to the peripheral stage epidote–pyrite–chalcopyrite veins (P-1) of Wilson (2003). Wilson (2003) linked these veins to orthoclase–biotite alteration based on limited field observations, and agrees with the occurrence of hematite-dusted K-feldspar alteration haloes documented in the stage 3 veins during the current study.

#### **4.3.3.4 Stage 3D quartz $\pm$ chlorite veins**

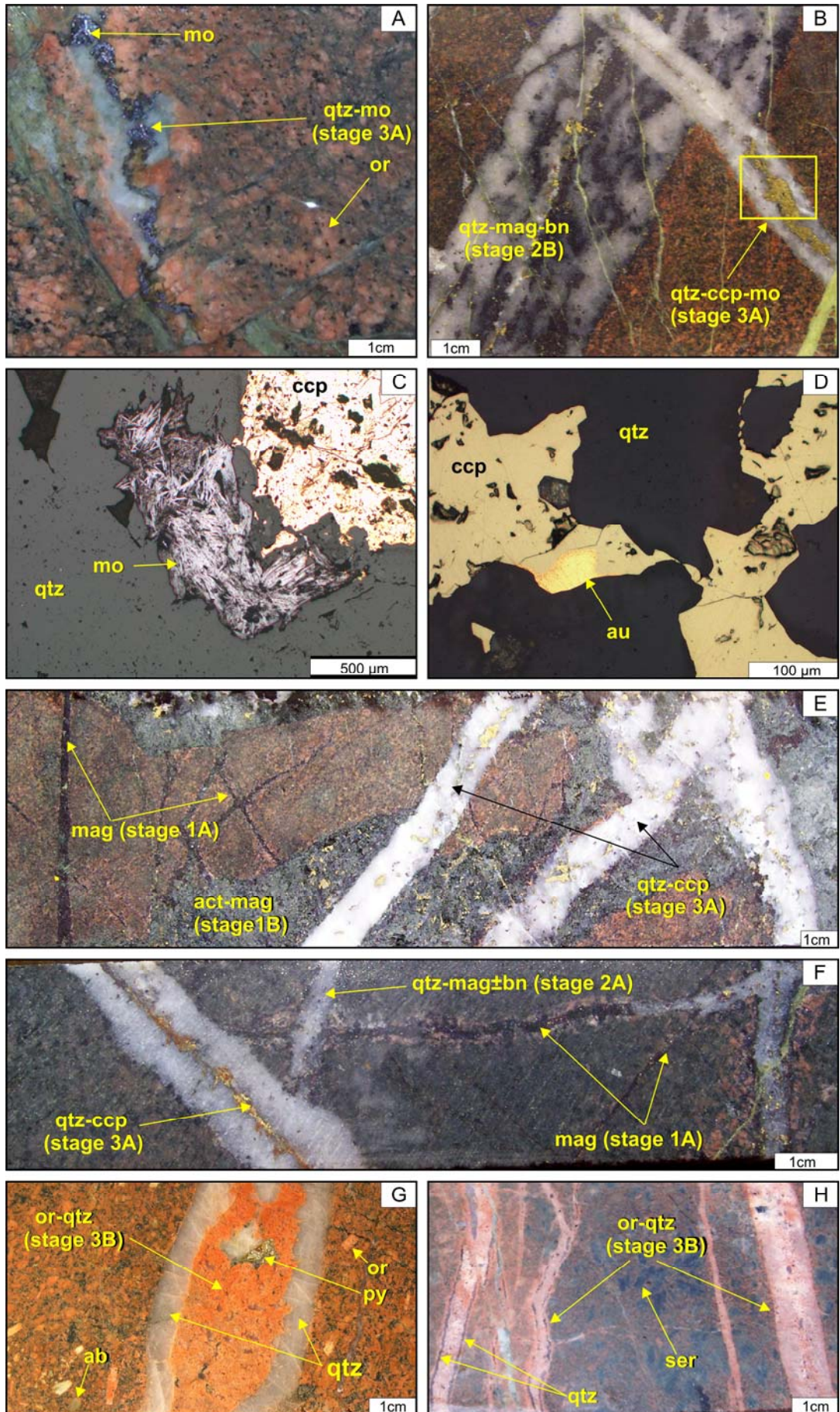
Stage 3D quartz  $\pm$  chlorite veins notably lack Cu–Fe sulfides (Table 4.2). Chlorite occurs as central bands or as crystal clusters that make that quartz veins green (Fig 4.8E and G). Stage 3D quartz veins are typically grey to milky white and exhibit mosaic and interlocked textures and sugary textures (Fig. 4.8F). Thin K-feldspar alteration haloes (<1 mm) surround stage 3D veins that are hosted in the FRV, whereas these K-feldspar alteration haloes are not developed in stage 3D veins hosted in the siltstone units of the Weemalla Formation.

Stage 3D veins were mostly observed in the deeper part of the system (~3750mRL, 2100 m below surface; Fig. 4.1), where a zone of thick (up to 20 mm) barren quartz veins are hosted in the P2 intrusion (Figs 4.8E; e.g. UR323-1376m). Stage 3D veins also occur in the quartz  $\pm$  albite-altered siltstone of the Weemalla Formation, where they are locally developed as sinuous veins (Fig 4.8F). Stage 3D veins have not been previously documented from Ridgeway.

**Figure 4.7** Texture, mineralogy and mineral paragenesis of stage 3 veins from Ridgeway.

- A)** Stage 3A quartz vein with a central molybdenite  $\pm$  chalcopyrite seam, hosted in selectively orthoclase–albite–chlorite-altered quartz monzonite porphyry (P2; CR057-1885.8m).
- B)** A Stage 3A quartz–chalcopyrite–molybdenite vein has cross-cut stage 2B quartz–banded magnetite–bornite vein hosted in massive volcanic sandstone of the FRV that has undergone strongly orthoclase–magnetite alteration. The yellow box shows the approximate location of (C) and (D) (UR450-143.3m).
- C)** Photomicrograph (rl) of stage 3A quartz–chalcopyrite vein. Acicular molybdenite flakes occur interstitial to quartz grains (UR254-376m).
- D)** Photomicrograph (rl) of stage 3A veins in **(B)**. Gold (up to 80  $\mu\text{m}$ ) is intergrown with chalcopyrite.
- E)** Multiple vein stages in actinolite–magnetite–albite-altered massive volcanic sandstone of the FRV. The mineralized stage 3A quartz–chalcopyrite veins have cut stage 1 veins (UR450-158m).
- F)** Multiple vein stages in actinolite–magnetite–albite altered coherent pyroxene-phyric facies of the FRV. Stage 3A quartz–chalcopyrite vein has cut the stage 2A quartz–magnetite vein, which in turn has cut a stage 1A magnetite vein. Note the presence of thin K-feldspar haloes around the earlier veins (NC523-864m).
- G)** Stage 3B aplitic vein-dike with outer bands of anhedral hydrothermal quartz. The aplitic vein-dike contains of equigranular orthoclase intergrown with anhedral quartz. Pyrite occurs as irregular infill at the center of the vein. The P2 host rock has been selectively altered to orthoclase–albite–chlorite (UR140-226m).
- H)** Multi-stage 3B aplitic vein-dikes that comprise myrmecitic intergrowth of orthoclase and quartz with thin marginal bands of hydrothermal quartz, hosted in albite–sericite altered coherent feldspar-phyric coherent facies of the FRV (UR323-1300.3m).

Abbreviations: ab = albite, act = actinolite, bn = bornite, ccp = chalcopyrite, au = gold, mag = magnetite, mo = molybdenite, or = orthoclase, py = pyrite, qtz = quartz, rl = reflected light, ser = sericite





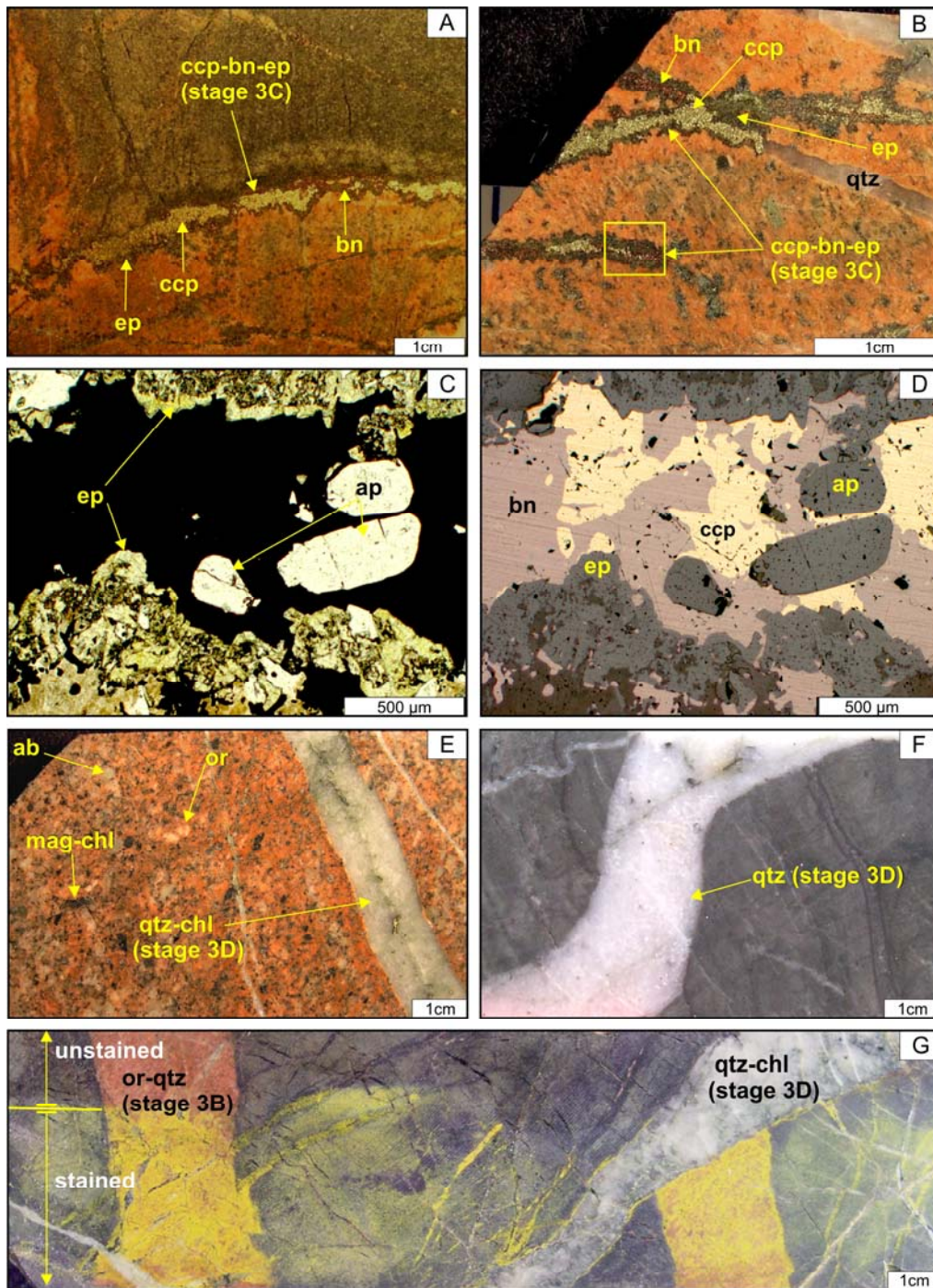


**Figure 4.8** Texture, mineralogy and mineral paragenesis of stage 3 veins from Ridgeway. **A)** Stage 3C chalcopyrite - bornite - epidote vein in orthoclase magnetite - chlorite-altered massive feldspathic sandstone of the Weemalla Formation (NC541-1017.3m). **B)** Stage 3C chalcopyrite - bornite - epidote vein in orthoclase-altered quartz monzonite (P2). The yellow box shows the location of figures C and D (UR149-131.5m). **C)** and **D)** Photomicrograph (ppl) and (rl) of (B), yellow box in (B). Bornite intimately intergrown with chalcopyrite and apatite crystals. Epidote crystals developed along the margins of the Cu-Fe sulfides. **E)** Stage 3D quartz - chlorite vein hosted in altered P2. The intrusion has been moderately altered to orthoclase - albite - magnetite - chlorite (UR325-202m). **F)** Sinuous stage 3D quartz vein hosted in quartz - albite-altered laminated siltstone of the Weemalla Formation (UR323-1348.7m). **G)** Stage 3D quartz - chlorite vein has cut and offset stage 3B aplitic vein-dike. The veins are hosted in pervasive actinolite - chlorite-altered massive siltstone of the Weemalla Formation. The lower half part of the sample has been stained with sodium cobaltinitrite to show the pervasive K-feldspar alteration on the host-rock (UR090-268.3m). Abbreviations: ab = albite, ap = apatite, bn = bornite, ccp = chalcopyrite, chl = chlorite, ep = epidote, mag = magnetite, or = orthoclase, ppl = plane polarized light, qtz = quartz, rl = reflected light.

#### **4.3.4 Late stage veins - stage 4**

Stage 4 veins are associated, both temporally and spatially, with the P3 monzonite. Their occurrence in and around P3, and cross-cutting relationships with earlier mineralized veins resulted in their classification as late-stage veins. Stage 4 comprises four substages of veins (Table 4.2). They are abundant and generally occur throughout the deposit, up to 500 m from the center of the orebody (Fig. 4.1).

##### **4.3.4.1 Stage 4A pyrite $\pm$ quartz veins**

Stage 4A is characterized by pyrite  $\pm$  quartz veins (Table 4.2). Pyrite occupies a central band of some veins and occurs as discrete aggregates in others (Fig. 4.9). The relative proportions of quartz and pyrite are variable. Some veins only contain pyrite (Fig. 4.9). In the core of the deposit, pyrite occurs as irregular veins with diffuse margins that have no alteration haloes, especially where hosted in P3 (Fig. 4.9A). Approximately 300 m outboard from the center, pyrite veins are more abundant, and have cut the orthoclase-altered andesitic FRV (Fig. 4.9B). At a distance of 500 m or greater from the center, pyrite occurs as veinlets, stringers and disseminations, and is associated with the albite–quartz–pyrite–sericite alteration zone (Fig. 4.16J and K). At depth, stage 4A pyrite veins have hematite-dusted K-feldspar alteration haloes (up to 10 mm) and have cut magnetite–actinolite–albite-altered siltstones of the Weemalla Formation (Fig. 4.10A). Numerous examples of stage 4A veins that have cut stage 2 and 3 veins have been observed around the center of the orebody (Fig. 4.6B).

##### **4.3.4.2 Stage 4B epidote $\pm$ chlorite veins**

Stage 4B epidote  $\pm$  chlorite veins and veinlets are abundant throughout the deposit, but are most common in the peripheral zone (Figs. 4.1 and 4.2D; Table 4.2). Where seen in the center of the deposit, stage 4B veins have cut the earlier formed Cu–Fe–sulfide bearing veins (Fig. 4.10C). On the deposit periphery, stage 4B veins have been cut and reopened by calcite–prehnite veins (stage 4D; Fig. 4.10D, E and I). Stage 4B veins have 1 to 10 mm wide alteration haloes of hematite-dusted K-feldspar (Fig. 4.10E). The hematite dusting around epidote-bearing veins implies that these Fe<sup>3+</sup>-bearing minerals formed contemporaneously. Some of stage 4B veins



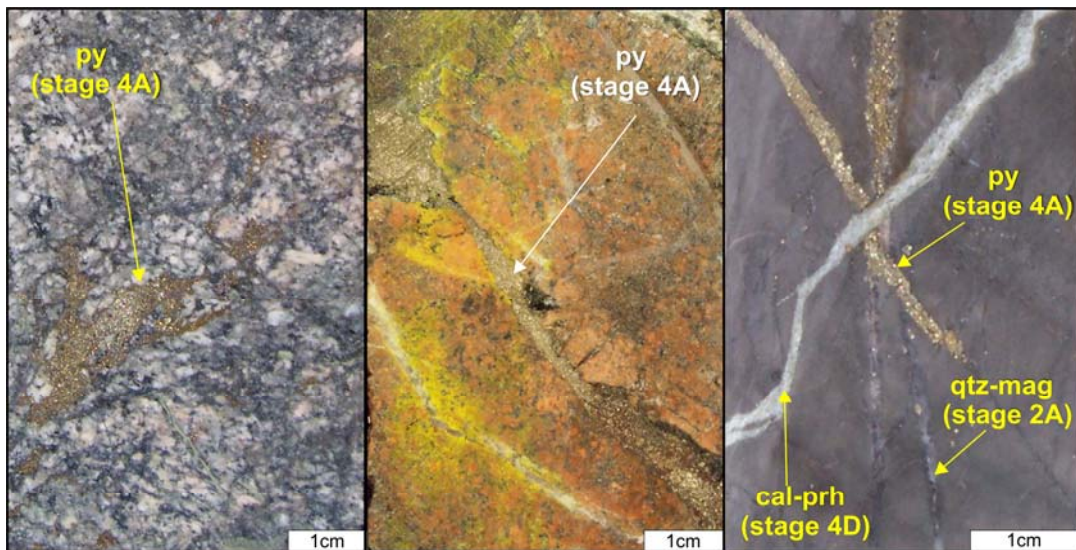


**Figure 4.9** Texture, mineralogy and mineral paragenesis of stage 4 veins from Ridgeway. **A)** Stage 4A pyrite vein with irregular, diffuse margins hosted in weakly altered late-stage quartz monzonite (P3) (CR062-1664.6m). **B)** Stage 4A pyrite vein, with thin K-feldspar haloes, in orthoclase-altered andesitic FRV (UR022-14m). **C)** Thin, stage 4A pyrite vein that has cut stage 2A quartz - magnetite vein, has been cut by a late stage calcite - phrenite vein (stage 4D). These veins are hosted in quartz - albite-altered siltstone of the Weemalla Formation (UR323-611m). Abbreviations: cal = calcite, mag = magnetite, prh = prehnite, py = pyrite, qtz = quartz

could be associated with post-mineralization epidote-hematite alteration (section 4.4.4), which is developed around some fault and fracture zones. Wilson (2003) characterized the epidote-rich zone as associated with brittle fault zones that have locally truncated all of the mineralized intrusions.

#### 4.3.4.3 Stage 4C chlorite-rich matrix breccias

Stage 4C is characterized by irregular centimeter- to meter-wide chlorite-altered matrix-rich breccias (Table 4.2). Fragments in these breccias are composed of subangular to subrounded clasts of monzonite (Fig. 4.10F to H). The fine-grained matrix has been selectively altered to chlorite  $\pm$  pyrite. Most breccias have jigsaw-fit textures, are clast-supported and have angular clasts that are only slightly rotated (Figs. 4.10F to H). At the other extreme, some breccias are matrix-supported, and contain rounded wallrock fragments. Locally, clasts of mineralized stage 3A veins are found in the chlorite-matrix breccia indicating brecciation occurred after the development of stage 3A and the bulk of mineralization at Ridgeway (Fig. 4.10F and G).



The timing of stage 4C breccias is well-constrained by cross-cutting relationships, because the breccias cut P1 monzonite and stage 4B epidote stringers (Fig. 4.10G), and also have cut P3 monzonite (Fig. 4.10H), and in turn have been cut by stage 4D calcite veins (Fig. 4.10H). Stage 4C breccias occur throughout the deposit (Figs. 4.1 and 4.2D) and are correlated with stage T-4 breccias of Wilson (2003; Table 4.4)

#### **4.3.4.4 Stage 4D calcite–prehnite $\pm$ quartz veins**

Stage 4D is the youngest vein stage recognized at Ridgeway. Stage 4D veins comprise intergrowths of calcite, prehnite  $\pm$  quartz (Table 4.2). Stage 4D veins are similar to the L-2 veins of Wilson (2003; Table 4.4), which also contains chlorite, minor pyrite and chalcopyrite interstitial to bladed calcite. Stage 4D veins are broadly distributed throughout the deposit (Figs. 4.1 and 4.2D). They occur as fracture coatings, or as 5 to 50 mm wide veins that are straight walled and planar. In hand specimen, calcite is typically white and slightly translucent, whereas prehnite has a milky white and a massive texture (Fig. 4.10E). In thin section, anhedral aggregates of prehnite are intergrown with calcite (Fig. 4.10K).

Stage 4D veins have cut stage 4B epidote veins (Fig. 4.10D) and stage 4C breccia (Fig. 4.10H). In the core of the deposit, stage 4D calcite–prehnite veins have cut stage 2A quartz–magnetite veins (Fig. 4.10J). No alteration haloes have been observed around stage 4D veins, but they may be associated with the post-mineralization carbonate alteration assemblage (section 4.4.4), which is best developed around low-angle fault zones.

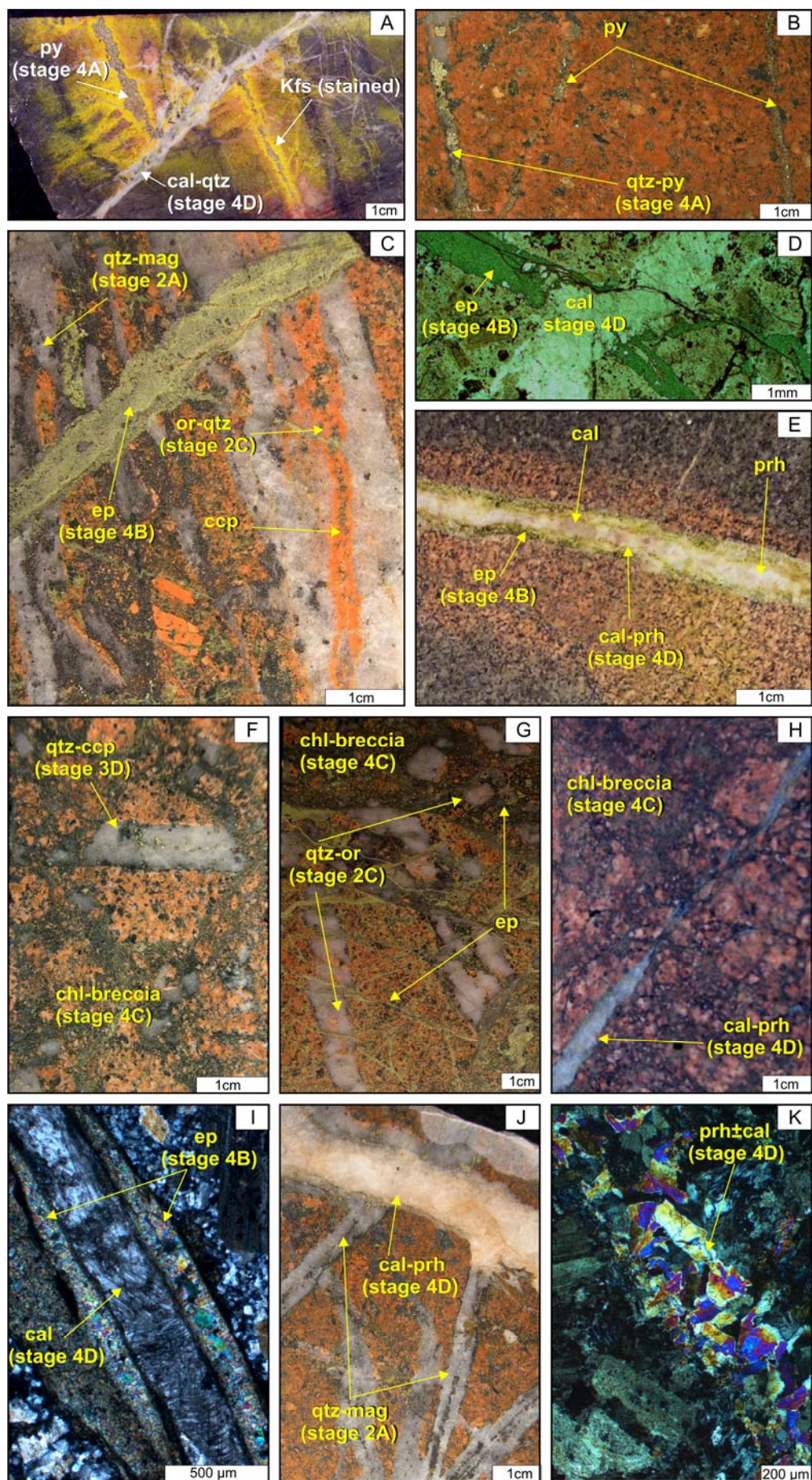
### **4.4 Hydrothermal alteration**

Contrasting compositional differences in host rocks (i.e. siltstone dominant in the Weemalla Formation at depth; permeable andesitic volcanics and volcaniclastics in the FRV) mean that the host rocks reacted differently to infiltrating hydrothermal fluids, and strongly influenced the distribution of alteration mineral assemblages and sulfide minerals.

**Figure 4.10** Texture, mineralogy and mineral paragenesis of stage 4 veins from Ridgeway.

- A)** Stage 4A pyrite vein with hematite-dusted K-feldspar alteration halo hosted by quartz–albite-altered laminated siltstone of the Weemalla Formation. The sample has been stained with sodium cobaltinitrite to highlight the K-feldspar halo around the pyrite vein. A stage 4C calcite–quartz vein has offset the stage 4A vein (UR090-245.3m).
- B)** Stage 4A quartz–pyrite vein in quartz monzonite (P2). The host rock is moderately altered to orthoclase–albite–chlorite (UR149-168.7m).
- C)** A stage 4B epidote vein has cut a stage 2A vein and stage 2C aplitic vein-dike in this sample. The veins are hosted in strong orthoclase–albite–magnetite-altered mafic monzonite (P1; UR140-260m).
- D)** Photomicrograph (ppl) of stage 4B epidote vein cut by late stage 4D calcite vein (UR390-401.5m).
- E)** Composite stage 4B epidote vein with hematite-dusted K-feldspar halo. The center of the vein has been reopened and infilled by stage 4D calcite–prehnite vein (UR089-50.5m).
- F)** Stage 4C chlorite-altered matrix-rich breccia. The clasts consist of P2 monzonite that contain truncated stage 3D quartz–chalcopyrite veins, suggesting that brecciation post-date main stage mineralization (NC541-583.5m).
- G)** Stage 4C chlorite-altered matrix-rich breccia. Clasts of sub-rounded to rounded P1 monzonite contain truncated stage 2C vein and stage 4B epidote stringers (UR390-94m).
- H)** Stage 4C chlorite-altered matrix-rich breccia. Clasts consist of sub-rounded late-stage quartz monzonite (P3). The breccia has been cut by a stage 4D calcite vein (UR362-739.8m).
- I)** Photomicrograph (xpl) of stage 4B epidote vein. The epidote vein has been reopened and infilled by a stage 4D calcite vein (UR326-367.2m).
- J)** Stage 4D calcite–prehnite vein from the center of the high-grade ore zone has cut stage 2A quartz–magnetite veins, and is hosted by strongly orthoclase–albite-altered P1 monzonite (UR390-52.1m).
- K)** Stage 4D prehnite ± calcite vein hosted in orthoclase–biotite-altered P2 monzonite (UR150-96.3m).

Abbreviations: cal = calcite, ccp = chalcopyrite, chl = chlorite, ep = epidote, Kfs = K-feldspar, mag = magnetite, ppl = plane polarised light, prh = prehnite, py = pyrite, qtz = quartz, xpl = cross polarized light



Rather than classifying alteration assemblages (e.g. Lowell and Guilbert, 1970), the Ridgeway alteration types are named here according to their principal alteration minerals, a technique proposed by Rose (1970) and Fountain (1972). At Ridgeway, nine alteration assemblages have been recognized (Table 4.3). They are grouped into four stages including: 1) early alteration stage, 2) main alteration stage, 3) late alteration stage, and 4) post-mineralization fault-related alteration stage. Figures 4.1 to 4.3 illustrate the spatial distribution of the different alteration stages. Table 4.4 shows that the alteration assemblages identified during this study are mostly comparable to those identified by Harper (2000) and Wilson (2003).

#### **4.4.1 Early alteration stage**

##### **4.4.1.1 Quartz $\pm$ albite alteration**

At Ridgeway, a strongly developed, pervasive quartz  $\pm$  albite  $\pm$  pyrite alteration assemblage is the earliest alteration style recognized in the Weemalla Formation (Table 4.3). It is typified by the replacement of primary feldspar by quartz  $\pm$  albite. Several samples from this unit have been stained chemically to test for the presence of K-feldspar and albite (Fig. 4.11B; Appendix B). The pinkish-red stain on the rock suggests the presence of Ca-bearing feldspar, interpreted here to be albite.

Quartz  $\pm$  albite replacement of feldspar has affected the laminated siliceous siltstone of the Weemalla Formation peripheral to the ore zone, and in the deeper parts of Ridgeway (Figs. 4.1, 4.2B and 4.3B). Quartz  $\pm$  albite alteration becomes more widespread with increasing depth, and the alteration assemblage intensifies towards the southeast of the deposit (Fig. 4.3B). Secondary quartz  $\pm$  albite have caused the indurated nature of the laminated siltstone that occur in continuous zones up to 100 m across. In thin section, fine-grained equigranular mosaic-textured quartz  $\pm$  albite comprises ~80 volume % of the rock, occurring with minor chlorite-altered ferromagnesian minerals and disseminated pyrite.

Quartz  $\pm$  albite alteration is inferred to pre-date mineralization at Ridgeway because stage 2A quartz–magnetite vein (Fig. 4.11A) and stage 3C chalcopyrite veins (Fig. 4.11C) have cut quartz  $\pm$  albite-altered rocks. Furthermore, stage 2B veins, which are associated with K-feldspar alteration, have crosscut and overprinted



Table 4.3 Styles and spatial and temporal distribution of alteration facies at Ridgeway.

Alteration stage <sup>1</sup>	Major minerals	Minor minerals	Alteration intensity and styles <sup>2,3</sup>	Spatial and temporal association and distribution	Related Vein Stages
Early alteration stage					
	Quartz, albite	Magnetite, pyrite	Intense, pervasive alteration; fine-grained mosaic quartz–albite has replaced the feldspar components of the rock; pyrite–magnetite–chlorite have altered fine-grained ferromagnesium minerals	Well developed in the deeper parts of the system; typically constrained to the laminated lithofacies of the Weemalla Formation; extends at least 500 m from the intrusions; intensity of alteration increases at depth towards the southeast	No associated veining
	Garnet, epidote	Calcite, quartz, magnetite	Moderate to selectively pervasive alteration of fine- to medium-grained grossularite–andradite (Ad <sub>39-100</sub> to Gr <sub>2-59</sub> ) intergrown with epidote	Restricted; hosted by centimeter- to meter-thick thinly bedded reactive calcareous sandstone and siltstone lithofacies of the Weemalla Formation; proximal to the monzodiorite intrusions and pyroxene-phyric dikes and sills	No associated veining
	Magnetite, actinolite, albite, biotite	Orthoclase	Moderate to strong, pervasive to selectively pervasive actinolite–chlorite–magnetite alteration of clinopyroxene minerals; albite has selectively replaced primary feldspar components; locally, K-feldspar or albite alteration halo occurs around stage 1B and 1C veins	Well developed in the monzodiorite, pyroxene- and feldspar-phyric dikes and sills, and in the surrounding Forest Reefs Volcanics and Weemalla Formation; texturally destructive, especially in the massive lithofacies of the Forest Reefs Volcanics; associated veins occurs at least 600 m from the center of the orebody	Stage 1A, Stage 1B
Main stage alteration					
	Orthoclase, biotite, albite, magnetite,	Actinolite, albite	Moderate to strong, selectively pervasive alteration of plagioclase and alkali feldspar to orthoclase and albite; primary amphibole and pyroxene minerals selectively altered to biotite which in turn has been replaced by chlorite–rutile ± magnetite; orthoclase-rich alteration halo around stage 2 veins	Temporally related to mafic monzonite intrusions with associated veins occurring up to 100 m from the contact	Stage 2A, Stage 2B, Stage 2D
			Weak to moderate, selectively pervasive alteration of primary plagioclase phenocrysts and groundmass to orthoclase; mafic minerals (hornblende) selectively replaced by biotite which is invariably interleaved with chlorite, and clinopyroxene by actinolite–chlorite–rutile ± magnetite; selective pervasive orthoclase-rich alteration envelope mostly occur around stage 3A and 3D veins	Temporally related to quartz monzonite porphyry with associated veins occurring up to 200 m from contact; defines a shell (~100 m thick) around the inner zone of strong orthoclase-biotite alteration	Stage 3A, Stage 3C, Stage 3D
Late stage alteration					
	Orthoclase, albite	Actinolite	Weak to moderate, selectively pervasive alteration of primary plagioclase to albite - orthoclase; orthoclase-rich halo surrounds late stage veins	Restricted to the late-stage quartz monzonite and associated veins	Stage 4A, Stage 4B
	Epidote, chlorite, hematite	Rutile, apatite, calcite	Weak to moderate, selective pervasive alteration of the ferromagnesium minerals to epidote–chlorite ± actinolite; plagioclase phenocrysts selectively altered to epidote and/or sericite preferentially on the core of the crystals; selective pervasive hematite dusting of altered alkali feldspars on all the rock units giving the red colouration and overprinting all earlier alteration assemblages	Defines a 500 m wide shell around orthoclase–biotite alteration domain and monzonite intrusions; has locally overprinted all the earlier alteration zones	Stage 4B
	Albite, quartz, pyrite, sericite	Chlorite	Strong, pervasive alteration of alkali feldspar to albite–quartz, mafic minerals to sericite–chlorite–pyrite; texturally destructive	Defines a cap (50 to 200 m) on the chlorite–epidote alteration at the upper part of the deposit; the contact with the chlorite–epidote alteration is marked by the absence of hematite alteration; patches of this alteration overprints the earlier alteration in the Forest Reefs Volcanics; outer limit is not defined and could extend beyond 600 m from the orthoclase–biotite alteration; this facies thickens both towards the northeast and southwest of the orebody	Stage 4A
Fault related late stage alteration					
	Chlorite, clay	Epidote	Moderate to strong alteration halos associated with the fault zones vary from 0.3 m to 1 m wide; strong, pervasive alteration of feldspar components to clay (kaolinite–sericite–illite), chlorite–epidote pervasively replaced the ferromagnesium minerals	Structurally controlled; associated to steeply dipping faults and shear zones	Epidote flooding up to 1 m from fault zones.
	Epidote, hematite		Strong, pervasive alteration envelope up to 10 m wide around faults; selectively pervasive replacement of altered fine-grained ferromagnesium minerals in the Forest Reefs Volcanics and euhedral clinopyroxene and altered amphibole phenocrysts to chlorite and epidote; strong hematite dusting of primary and secondary feldspars	Associated to post mineralization reverse faults that have cut and offset all of the rock units	Epidote veins up to 1 m around fault zones
	Calcite, quartz	Chlorite	Strong, pervasive bleaching envelope up to 20 m wide around faults; selectively pervasive replacement of altered primary feldspars and ferromagnesium minerals by calcite.	Associated to post-mineralization low-angle thrust faults that generally occur within the Weemalla Formation, sub-parallel to the bedding; these offset the intrusions and mineralization in the deeper part of the system	Calcite stockworks and veinings up to 1 m around fault zones

<sup>1</sup> Alteration stages listed in sequence from oldest to youngest (top to bottom)  
<sup>2</sup> Feldspar, garnet and amphibole compositions confirmed by electron microprobe analysis (Appendix C).  
<sup>3</sup> Definitions of alteration style based on Titley (1982), as defined in Table 4.1.



**Table 4.4** Comparison of alteration assemblages and vein associations observed from Ridgeway during this study with the studies of Harper (2000) and Wilson (2003)

Current study Alteration	Alteration intensity and styles	Vein associations	Wilson, 2003 Alteration	Mineral associations	Alteration intensity and styles	Vein associations	Harper, 2000 Alteration	Characteristics	Vein associations
Early alteration stage							Stage 1 - Sodic alteration	Selective pervasive albitization of plagioclase phenocrysts	Stage 2A; Stage 2B; Stage 2C
Quartz±albite alteration	Intense, pervasive alteration; has fine-grained mosaic quartz–albite replaced the feldspar components of the rock; pyrite–magnetite–chlorite has altered fine-grained ferromagnesium minerals	No associated veining							
Garnet–epidote alteration	Moderate, selectively pervasive alteration of fine- to medium-grained grossularite–andradite (Ad <sub>39-100</sub> to Gr <sub>2-59</sub> ) intergrown with epidote	No associated veining							
Magnetite–actinolite–albite–biotite alteration	Moderate to strong, pervasive to selectively pervasive actinolite–chlorite–magnetite alteration of clinopyroxene minerals; albite has selectively replaced primary feldspar components; locally, K-feldspar or albite alteration halo occurs around stage 1B and 1C veins	Stage 1A, Stage 1B					Stage 2 - Fe-K-Ca alteration	Selective pervasive magnetite, biotite, actinolite alteration.; vein/veinlet controlled, localized orthoclase and apatite alteration; introduction of disseminated chalcopyrite	
Main stage			Early Stage				Stage 3 - K-silicate-sulphide alteration	Vein controlled and localized orthoclase, magnetite, actinolite, biotite, quartz, apatite and sphene alteration; introduction of disseminated chalcopyrite and bornite; irregular orthoclase halos around 3D veins	Stage 3A; Stage 3B; Stage 3C; Stage 3D
Orthoclase–biotite–albite–magnetite alteration	Moderate to strong, selectively pervasive alteration; orthoclase-rich alteration halo occurs around veins stages	Stage 2A, Stage 2B, Stage 2D	Calc-potassic	Actinolite, biotite, orthoclase, albite, quartz, magnetite	Strong, pervasive and locally texturally destructive; locally developed alteration halo occurs around E-1 and E-4 stage veins	Stage E-1A, Stage E-1B, Stage E-2, Stage E-3, Stage E-4			
			Calc-silicate and potassic	Garnet, orthoclase quartz, magnetite, actinolite	Locally strong, selectively pervasive alteration of calcareous beds within the Weemalla Formation	No associated veining			
	Weak to strong, selectively pervasive alteration; orthoclase-rich alteration halo surrounds stage 3A and 3D veins	Stage 3A, Stage 3C, Stage 3D	Transitional Stage Alteration						
			Potassic	Orthoclase, biotite, albite, quartz	Weak to strong, selectively pervasive, typically restricted to vein envelopes; original rock texture preserved; T-1 and L-1 veins with potassic alteration envelopes extend into outer propylitic zone	Stage T-1, Stage T-2, Stage T-3, Stage T-4			
Late Stage			Late Stage and Peripheral Alteration				Stage 4 - Propylitic alteration	Selective pervasive hematite dusting of feldspar; selective replacement of magnetite; selective partial replacement of bornite by covellite, chalcocite and chalcopyrite	Stage 4A
Orthoclase–albite	Weak to moderate, selectively pervasive alteration. Orthoclase-rich alteration halo occurs around late stage veins	Stage 4A, Stage 4B	Potassic	Orthoclase, biotite, albite, quartz		Stage L-1			
Chlorite–epidote–hematite alteration	Weak to moderate, selective pervasive alteration; selective pervasive hematite dusting of altered alkali feldspars in all the rock units gives the red colouration; this assemblages overprinted all earlier alteration assemblages	Stage 4B	Inner Propylitic	Chlorite, albite, hematite, magnetite, epidote	Weak to moderate, pervasive and selectively pervasive alteration of Forest Reefs Volcanics; primary and secondary mafic minerals replaced by chlorite–epidote–calcite–prehnite ± pyrite; plagioclase replaced by albite–chlorite–epidote– white mica	Stage P-1, Stage P-2, Stage P-3			
	Not observed in this study		Outer Propylitic	Epidote, albite, actinolite, calcite	Selectively pervasive district-scale alteration of mafic minerals to chlorite–epidote–calcite and of feldspar to albite	Stage P-3			
Albite–quartz–pyrite–sericite alteration	Strong, pervasive alteration; texturally destructive	Stage 4A	Sodic	Albite, quartz	Strong selectively pervasive alteration of plagioclase to albite–chlorite–quartz and mafic minerals to chlorite–pyrite–calcite	No associated veining			
Fault related late stage alteration							Stage 5 - Phyllic alteration	Structurally controlled pervasive illite, quartz, pyrite ± carbonate ± kaolinite	Stage 6A
Chlorite–clay alteration	Moderate to strong alteration within the fault zones; varies from 0.3 m to 1m wide	Epidote flooding up to 1 m from fault zones	Phyllic	Illite, muscovite, pyrite	Intensely developed alteration halos around late-stage faults; pervasive alteration is absent; local zones of pervasive chlorite alteration; plagioclase altered to calcite–illite–muscovite	Stage P-2			
Epidote–hematite	Strong, pervasive alteration halos up to 10 m around faults; strong hematite dusting of primary and secondary feldspars	Epidote veins up to 1 m around fault zones							
Carbonate alteration	Strong, pervasive bleached halo up to 20 m around faults	Calcite stockworks and veinings up to 1 m around fault zones.					Stage 6 - Carbonate alteration	Selective pervasive carbonate alteration	

quartz  $\pm$  albite-altered rocks (Fig. 4.11B). Albite haloes have been observed around a pre-mineralization stage 1A magnetite vein (Fig. 4.11I). Quartz  $\pm$  albite-altered wallrock fragments occur as xenoliths in some P2 intrusions (Figs. 4.4C and 4.12A). All of these features are consistent with an early timing for the quartz  $\pm$  albite alteration assemblage. This is consistent with the observation of Harper (2000), who stated that selectively pervasive sodic alteration was the oldest alteration style at Ridgeway. Wilson (2003) also noted that intense silicification (quartz  $\pm$  albite–pyrite) occurred in the Weemalla Formation prior to most of the Cu–Au mineralization.

#### **4.4.1.2 Garnet–epidote alteration**

Garnet–epidote ( $\pm$  calcite–quartz–magnetite) alteration was restricted to siltstones and siliceous siltstones of the Weemalla Formation, and extends several hundreds of meters from the monzonite intrusions (Fig. 4.1; Table 4.3). The garnet–epidote assemblage is typically confined to narrow horizons, where replacement of chemically reactive calcareous sandstone and siltstone of the Weemalla Formation occurred (Figs. 4.2B and 4.3B). In hand specimen, pale brown- to dark-brown garnet occurs as thin (<10 mm thick) bands that have replaced sedimentary bedding (Fig. 4.13B). Local selective replacement of relict sandstone occurs as irregular alteration clots up to 10 mm across (Fig. 4.13A). In thin section, granular, subhedral aggregates of dark brown garnet are intergrown with quartz and calcite. Epidote is intergrown with, or more commonly occurs as rims around the garnet (Fig. 4.13C). The garnet–epidote alteration assemblage has been overprinted by chlorite in many samples. Microprobe analysis reveals that most of the garnets have grossularite–andradite compositions (Ad<sub>39-100</sub> to Gr<sub>2-59</sub>; Fig. 4.13D and E; Appendix C).

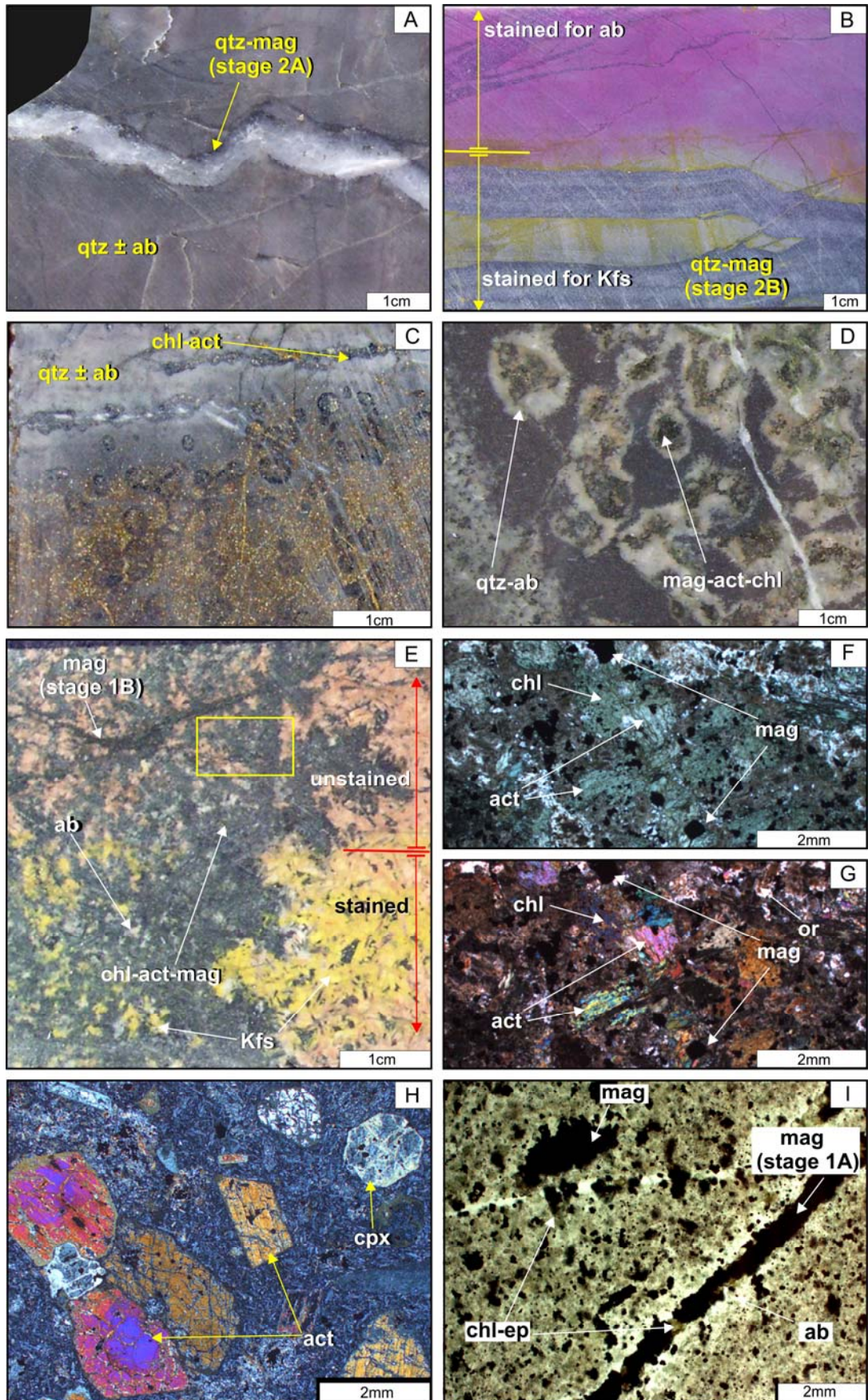
The garnet–epidote alteration assemblage at Ridgeway is interpreted to predate main stage mineralization, because mineralized stage 2A quartz–magnetite and stage 3A quartz–chalcopyrite veins have cut this alteration (e.g. CR062-1630.1m). Previous studies (Harper, 2000; Wilson, 2003) observed similar calc-silicate alteration in the calcareous beds of the Weemalla Formation. Harper (2000) described this alteration as ‘skarn-style’, occurring as horizons of massive fine-grained magnetite–epidote–chlorite–calcite–garnet–pyrite–chalcopyrite and feldspar

**Figure 4.11** Early alteration stage at Ridgeway.

- A)** Strong quartz  $\pm$  albite alteration in massive siltstone unit of the Weemalla Formation, cut by sinuous stage 2A quartz–magnetite vein (CR062-1660m).
- B)** Laminated siltstone unit of the Weemalla formation stained for the presence of albite (upper half-part) and K-feldspar (lower-half). The pink-colouration indicates the presence of Ca-bearing feldspar, interpreted to be weakly calcic albite. The light-yellow stain indicates the presence of K-feldspar, which has overprinted the earlier formed quartz  $\pm$  albite alteration assemblage (UR360-719m).
- C)** Grey fine grain quartz  $\pm$  albite alteration of the Weemalla Formation siltstone, interbedded with selectively pervasive actinolite–chlorite–albite (greenish-coloured) altered sandstone. Actinolite and chlorite have replaced the fine-grained ferromagnesian components. Chalcopyrite occurs as disseminations and stringers associated with main stage mineralization, which has overprinted the earlier formed quartz  $\pm$  albite alteration assemblage (CR062-1644.8m).
- D)** Clots of selectively pervasive actinolite–chlorite–magnetite alteration surrounded by pale white quartz  $\pm$  albite alteration rims in the feldspathic sandstone of the Weemalla Formation (UR352-850.6m).
- E)** Selectively pervasive magnetite–actinolite–albite alteration of the monzodiorite. Note that secondary orthoclase has been hematite dusted. The yellow box shows the approximate location of (F) and (G) (UR022-128.1m).
- F) and G)** Photomicrograph (ppl) and (xpl) of **(D)**, outline in yellow box, showing the selectively pervasive nature of actinolite–magnetite alteration. These minerals have pseudomorphed primary clinopyroxene phenocrysts.
- H)** Photomicrograph (xpl) of feldspar-phyric rock. Euhedral clinopyroxene phenocrysts have been partially altered to actinolite along cleavage planes. The fine-grained feldspathic and mafic components in the groundmass have been selectively replaced by orthoclase–albite which has in turn been overprinted by chlorite. This sample was collected outside the mineralized zone (<0.2 % Au), highlighting the wide spatial extent of the magnetite–actinolite–albite alteration assemblage (UR149-3m).
- I)** Photomicrograph (ppl) of fine-grained feldspathic siltstone of the Weemalla Formation showing selectively pervasive magnetite alteration. The feldspathic component has been selectively altered to epidote–chlorite. The sample is cut by thin discontinuous stage 1A magnetite stringers (NC541-590.8m).

Abbreviations: ab = albite, act = actinolite, ccp = chalcopyrite, chl = chlorite, ep = epidote, mag = magnetite, ppl = plane polarized light, py = pyrite, qtz = quartz, xpl = cross polarized light







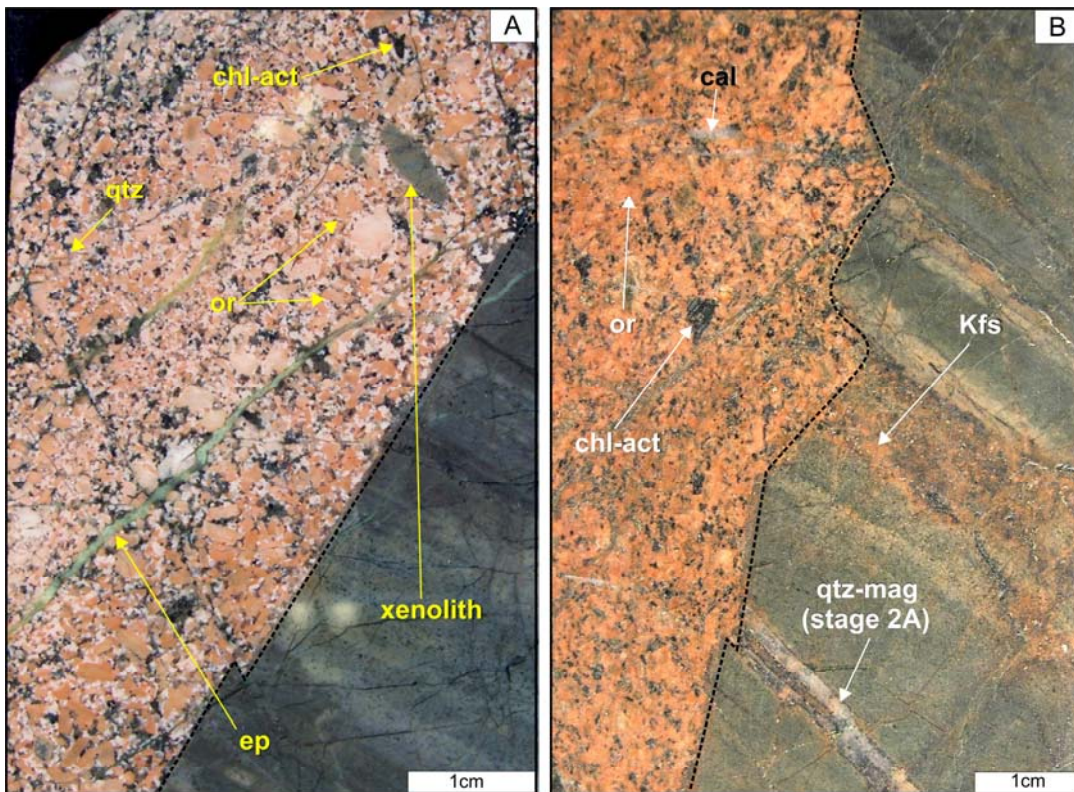


**Figure 4.12** Selectively pervasive to pervasive quartz  $\pm$  albite alteration of laminated siltstone in the Weemalla Formation truncated by quartz monzonite (P2). **A)** Sharp contact of P2 with the laminated silicified siltstone (contact marked by black dashed-line). Note the altered wallrock xenolith in P2 (UR365-720.1m). **B)** Irregular intrusive contact of P2 with altered wallrock. A K-feldspar alteration front has overprinted the feldspathic sandstone horizon of the Weemalla Formation. A stage 2A quartz - magnetite vein has been truncated by P2 (UR254-125m). Black dashed-line marked the contact between the intrusion and the wallrocks. Abbreviations: act = actinolite, chl = chlorite, ep = epidote, Kfs = K-feldspar, mag = magnetite, or = orthoclase, qtz = quartz

that were cut by mineralized quartz–magnetite–chalcopyrite–pyrite veins. Wilson (2003) described selectively pervasive replacement of laminae and beds of the Weemalla Formation by subhedral, granular aggregates garnet–epidote (calc-silicate), with intervening laminae of orthoclase and actinolite alteration (calc-potassic) cut by veinlets of quartz, chalcopyrite and magnetite fractures with orthoclase alteration selvages.

A close spatial association of garnet–epidote alteration with intrusive contacts (i.e. monzodiorite, pyroxene- and feldspar-phyric sills) was observed in several drillholes (e.g. NC541-1181-1191m, UR360-660-672m, UR362-664-681m; rf. section 3.3.1). A genetic relationship is inferred, because Meinert (1997) reported that garnet-rich calc-silicate alteration assemblages in skarn districts typically occur proximal to the causative intrusion.



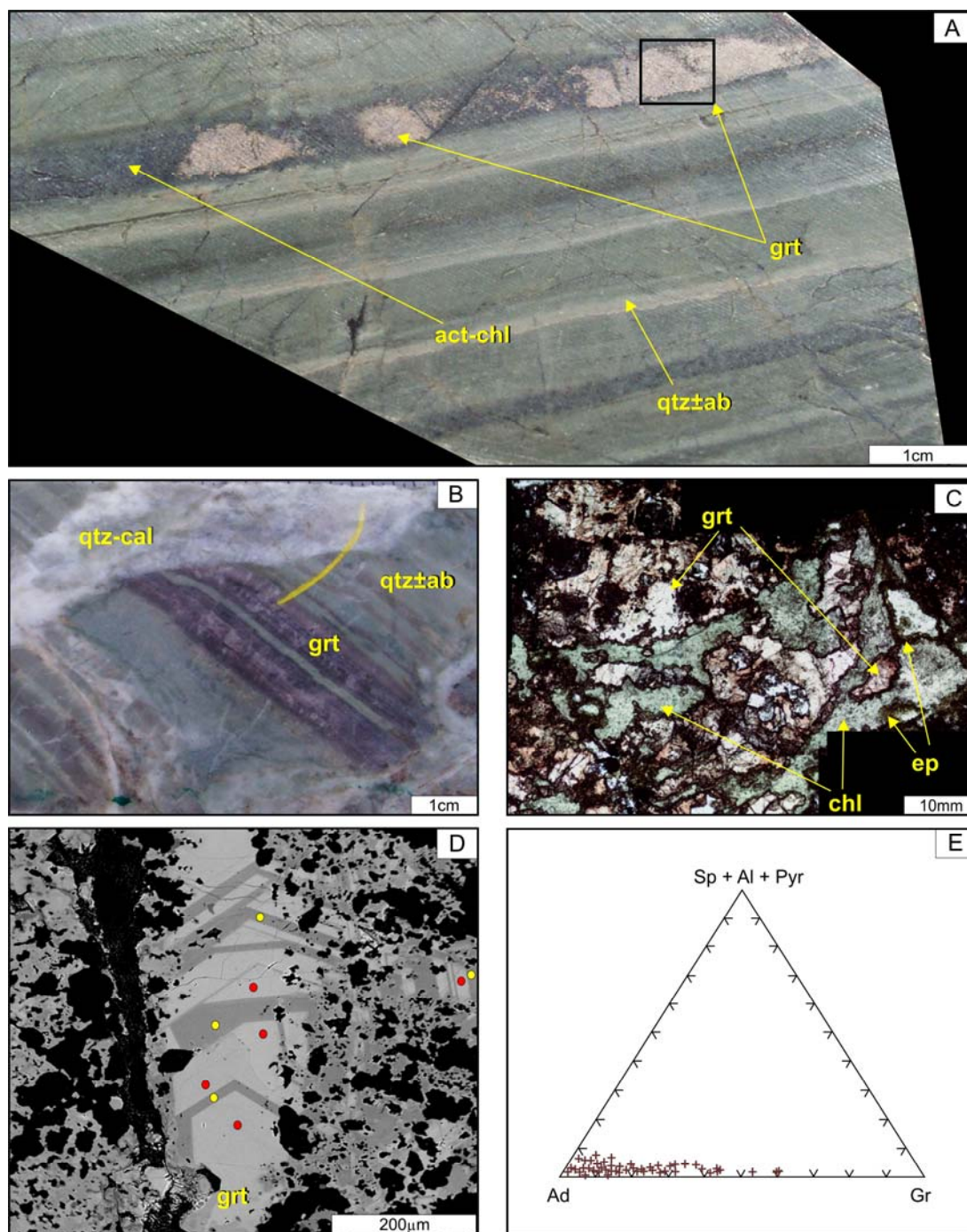


**Figure 4.13** Garnet - epidote alteration in the calcareous units of the Weemalla Formation. **A)** Blebs of garnet - epidote alteration in the actinolite - chlorite altered sandstone units (UR154-110m). **B)** Selectively pervasive garnet (dark-brown) alteration interbedded with quartz - albite altered siltstone (UR323-720.2m). **C)** Photomicrograph (ppl) showing the close association of garnet rimmed by epidote minerals, overprinted by chlorite (light green; UR154 -110m). **D)** Back scattered electron (BSE) microprobe image of andradite crystals from (B), area outlined in black box. The electron microprobe spots showing the compositional variation are marked by red circles (dark-grey bands) composed of  $An_{100}$ , while the yellow circles (light-grey bands) correspond to the more grossularite - andraditic composition,  $An_{67-72}Gr_{25-31}$ . Electron microprobe data are listed in Appendix C. **E)** Composition of garnet. Abbreviations: ab = albite, ad = andradite, al = almandine, cal = calcite, chl = chlorite, ep = epidote, gr = grossularite, grt = garnet (andradite), ppl = plane polarized light, pyr = pyrope, Qtz = quartz, sp = spessartine

#### 4.4.1.3 Magnetite–actinolite–albite–biotite alteration

Selectively pervasive magnetite–actinolite–albite–biotite  $\pm$  orthoclase assemblage is best developed in and adjacent to the MzD, most typically preserved in the felspathic sandstone and siltstone units of Weemalla Formation (Figs. 4.1, 4.2B and 4.3B; Table 4.3). Clots (occurring as pods and lenses) of magnetite–actinolite–chlorite are rimmed by pervasive albite alteration locally (Fig. 4.11D). These clots appear to have nucleated on the margins of fine-grained mafic components.

Where seen in the MzD, magnetite–actinolite alteration has imparted a dark green-grey colour due to the selective replacement of primary hornblende and clinopyroxene by actinolite, biotite, and magnetite (Fig. 4.11E to G). Albite has selectively replaced primary feldspar phenocrysts (Fig. 4.11E). Most of the secondary biotite observed has been pervasively replaced by chlorite; rutile grains are disseminated through the remnant mafic crystals, as documented by Harper (2000). Locally, magnetite occurs as clusters and disseminations, whereas actinolite has partly replaced the primary ferromagnesium minerals (Fig. 4.11F and G). Peripheral to the orebody and outside the 0.2 % Au contour, primary clinopyroxene have been selectively replaced by actinolite (Fig. 4.11H). Apatite and magnetite also occur as fine crystals intergrown with actinolite–chlorite-altered mafic phenocrysts. The intensity of the actinolite–magnetite alteration assemblage is strong in the MzD and pyroxene- and feldspar phyric dikes and sills, and in the immediate host rocks.

The original distribution of magnetite–actinolite alteration assemblage is difficult to determine due to intense texturally destructive overprinting alteration assemblages. Northwest of Ridgeway, remnants of magnetite–actinolite alteration are preserved in andesitic units, where they have been partly overprinted by epidote–chlorite–hematite and late stage albite–quartz–sericite–pyrite alteration (Fig. 4.2B).

Previous studies recognized the occurrence of silicification, calc-silicate and calc-potassic alteration assemblages, locally developed within the Weemalla Formation (Wilson *et al.*, 2003). The distribution and extent of these alteration assemblages and their timing were not fully appreciated due to limited deep drilling at that time. However, these alteration assemblages have been cut by veinlets of

quartz, chalcopyrite and magnetite veins with orthoclase alteration haloes associated with mineralization (Wilson, 2003). Harper (2000) reported that the selectively pervasive biotite–magnetite–actinolite assemblage pre-dated the bulk of Au–Cu mineralization at Ridgeway.

#### **4.4.2 Main stage alteration**

At Ridgeway, most of the Au–Cu mineralization is associated with main stage alteration, which comprises zone of strong (inner) and moderate to weak (outer) orthoclase–biotite–albite–magnetite–actinolite alteration (Fig. 4.1). This alteration assemblage is classified as K-silicate (or potassic) alteration (e.g. Seedorff *et al.*, 2005). At Ridgeway, the transition from inner to outer K-silicate alteration corresponds to the limits of high grade gold mineralization (>1.5 g/t Au). The outer margins of the outer K-silicate alteration zone corresponds approximately to the 0.2 g/t Au contour (Figs. 4.2B and 4.3B).

##### **4.4.2.1 Orthoclase–biotite–albite–magnetite–actinolite alteration**

The earliest K-silicate alteration assemblage in the core of Ridgeway is characterized by a strong, pervasive orthoclase–biotite–magnetite– (albite–actinolite) assemblage (Table 4.3). This alteration is particularly well-developed in P1 intrusion and its adjacent wallrocks. Overall, the strongly developed orthoclase–biotite–magnetite– (albite–actinolite) alteration zone is approximately 200 m wide and up to 800 m in vertical extent (Figs. 4.2B and 4.3B). The alteration assemblage is closely associated spatially with stage 2 stockwork veins that extend up to 100 m from the P1 intrusion (Fig. 4.1), and a genetic link is therefore inferred between the intrusions, veins and alteration assemblage. The K-silicate alteration assemblage has been partially overprinted by epidote and chlorite.

The P1 intrusions are light- to deep-orange due to the selective replacement of primary feldspar phenocrysts and groundmass by hematite-dusted orthoclase and albite (Fig. 4.5A). In thin section, the plagioclase phenocrysts are turbid and pale-brown (Fig. 4.14A). Multiple twins in some of plagioclase crystals are still discernible (Fig. 4.14B). Parts of these phenocrysts have been selectively altered to orthoclase and albite (Ab<sub>92-100</sub>; Appendix C). Shreddy textured hydrothermal biotite

**Figure 4.14** Orthoclase–biotite–albite–magnetite alteration at Ridgeway.

- A) and B)** Photomicrograph (ppl) and (xpl) of a mafic monzonite (P1). The primary amphibole has been selectively altered to biotite, that was in turn retrogressed to chlorite–rutile. The clinopyroxene phenocrysts have been selectively replaced by magnetite and overprinted by chlorite. Turbid, dark-brown feldspar crystals been altered to albite–orthoclase. Submicroscopic hematite dusting has caused a dark-brown colouration of the altered feldspars. The core of the altered plagioclase phenocrysts have been preferentially replaced by epidote–chlorite–apatite. Groundmass is altered to fine-grained albite–orthoclase–quartz with accessory apatite (UR390-47.5m).
- C) and D)** Photomicrograph (ppl) and (xpl) of a pyroxene-phyric dike. The primary ferromagnesian minerals have been replaced by biotite, and partly overprinted by chlorite on the rims. Feldspar phenocrysts and groundmass have been pervasively altered to orthoclase–albite (UR149-123.8m).
- E)** Pyroxene-phyric dike selectively altered to orthoclase–biotite–albite–magnetite. The lower half part of the sample has been stained to show the pervasive K-feldspar alteration on the host-rock (UR022-173.7m).
- F)** Strong orthoclase alteration in laminated siltstone of the Weemalla Formation. Blebs of early actinolite–magnetite alteration have been preserved (UR326-114.5m). The red and yellow boxes show the approximate location of (G) and (H), respectively.
- G)** Photomicrograph (xpl) of (F), outlined in red box. Turbid to dark-brown orthoclase due to hematite dusting. Shreddy actinolite–magnetite alteration still preserved, replacing early biotite.
- H)** Photomicrograph (rl) of (F), outlined in yellow box. Bornite intergrown with gold and magnetite. Covellite and digenite have partly replaced the bornite.

Abbreviations: ab = albite, act = actinolite, ap = apatite, bn = bornite, bt = biotite, chl = chlorite, cv = covellite, dg = digenite, ep = epidote, gold = au, Kfs = K-feldspar, mag = magnetite, or = orthoclase, ppl = plane polarized light, qtz = quartz, rl = reflected light, rt = rutile, xpl = cross polarized light



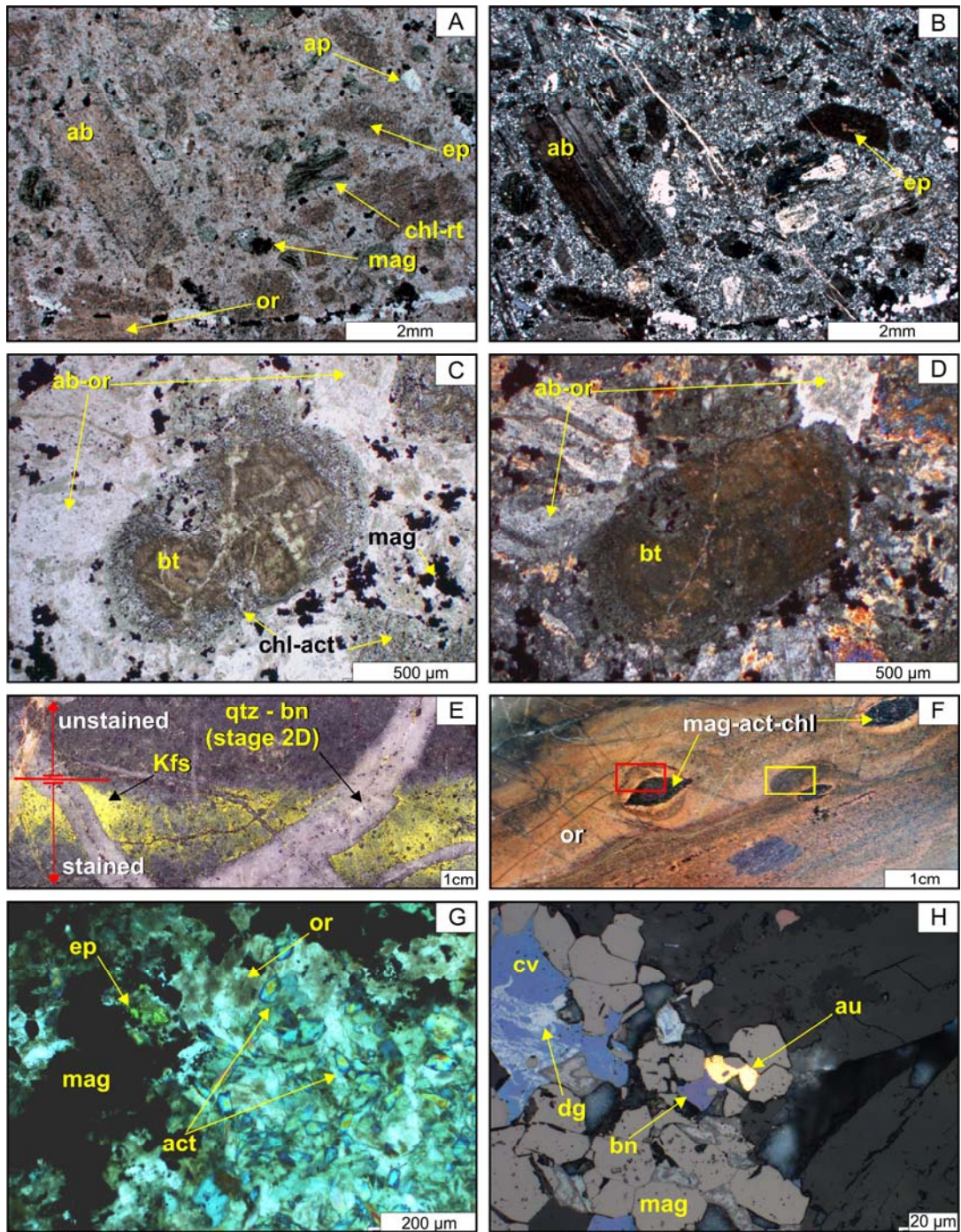
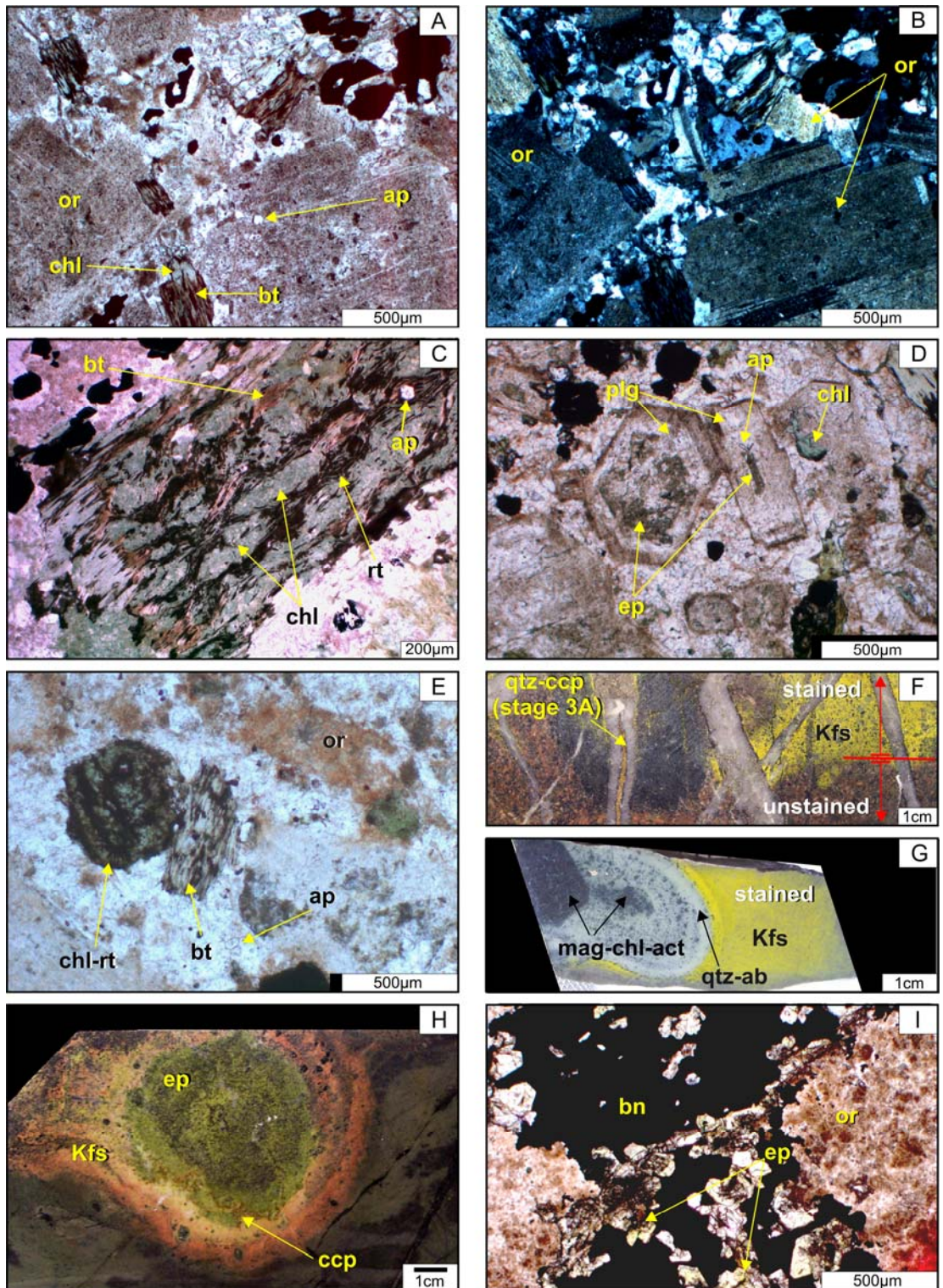




**Fig. 4.15** Orthoclase–biotite–albite alteration and epidote–chlorite–hematite alteration at Ridgeway.

- A) and B)** Photomicrograph (ppl) and (xpl) of quartz monzonite (P2). Turbid, dark brown orthoclase has selectively replaced euhedral plagioclase. The feldspathic groundmass has been altered to orthoclase–albite–quartz. Hornblende phenocrysts have been selectively replaced by biotite interleaved with chlorite–rutile (5130L-XC4-143EW).
- C)** Photomicrograph (ppl) of euhedral primary hornblende selectively replaced by hydrothermal biotite, which has in turn been altered to chlorite–rutile. Relict hydrothermal biotite is still visible along cleavage planes (UR450-106.8m).
- D)** Photomicrograph (ppl) of turbid plagioclase phenocrysts altered to albite–orthoclase. The cores of the altered plagioclase have been preferentially replaced by epidote–chlorite–apatite (UR326-231.6m).
- E)** Photomicrograph (ppl) of selectively pervasive orthoclase–biotite–albite alteration in P2 intrusion. Primary feldspars phenocrysts have been pervasively altered to orthoclase, subhedral hornblende altered to biotite, and euhedral clinopyroxene to chlorite–rutile. The groundmass has been altered to orthoclase–albite–quartz–apatite. Submicroscopic hematite dusting has produced the dark brown colouration of hydrothermal orthoclase (UR360-729m).
- F)** Strong orthoclase alteration in volcanic breccia of the FRV. The top half of the sample has been stained in order to highlight the presence of K-feldspar alteration in the matrix. Stage 3A quartz–chalcopyrite veins that cut the basaltic clast have thin K-feldspar haloes (UR022-164.2m).
- G)** Example of pervasive orthoclase alteration in massive feldspathic siltstone unit of the Weemalla Formation. The sample has been stained in order to highlight the presence of K-feldspar alteration. The sample contains core or pervasive quartz  $\pm$  albite alteration, enveloped by a domain of pervasive K-feldspar flooding (UR248-1.8m).
- H)** Chalcopyrite–epidote dissemination with hematite dusted K-feldspar alteration rind (UR450-9.2m).
- I)** Photomicrograph (ppl) of a stage 3C vein in coherent feldspar-phyric lithofacies of the FRV. The host rock has been pervasively altered to hematite-dusted turbid orthoclase (UR333-535m).

Abbreviations: ab = albite, act = actinolite, ap = apatite, bn = bornite, bt = biotite, ccp = chalcopyrite, chl = chlorite, ep = epidote, Kfs = K-feldspar, mag = magnetite, or = orthoclase, ppl = plane polarized light, qtz = quartz, rt = rutile, xpl = cross polarized light



(now chlorite) occurs together with clusters of needle-like rutile (Fig. 4.14A). Primary mafic minerals (clinopyroxene and hornblende) were altered first to actinolite–magnetite, and then to chlorite  $\pm$  rutile (Fig. 4.14A).

The FRV have undergone textural destruction where stage 2A and 2B veins and stockworks have been intensely developed (Fig. 4.6). In zones of strong stockwork veins, coalesced alteration haloes have created intense K-feldspar flooding (Fig. 4.6). The mafic components have been altered to biotite, which has in turn been selectively replaced by chlorite–actinolite along grain boundaries (Fig. 4.14C and D). The altered FRV are greenish to light-greenish orange, but chemical staining (Appendix B) has shown that these “green” rocks have undergone selectively pervasive K-feldspar alteration of feldspar phenocrysts and groundmass (Fig. 4.14E). Without staining, it is not possible to distinguish the presence of the K-feldspar alteration.

The strong orthoclase–biotite–magnetite– (albite–actinolite) alteration assemblage is similar to the inner potassic alteration assemblage at Endeavour 26, Northparkes (Heithersay and Walshe, 1995) and intense potassic alteration documented for Bingham Canyon, Utah (Redmond and Einaudi, 2010). The inner strong K-silicate alteration assemblage is correlated to calc-potassic assemblage of Wilson (2003).

A zone of moderate to weak orthoclase–biotite–magnetite– (albite–actinolite) alteration occurs as a shell around the inner K-silicate alteration zone (Fig. 4.1; Table 4.3). Magnetite has very restricted occurrences in the outer K-silicate zone, typically occurring as selective replacement of ferromagnesian minerals in P2, in contrast to the inner K-silicate alteration zone. This outer K-silicate alteration forms a shell around the inner zone that is 300 to 400 m wide and has a vertical extent of over 1000 m (Figs. 4.2B and 4.3B). The outer K-silicate alteration assemblage is spatially associated with the P2 intrusion (Fig. 4.2B), and has a spatial and temporal association with stage 3 veins. This is because selectively pervasive orthoclase-rich alteration haloes surround stage 3 veins.

Primary plagioclase and alkali-feldspar phenocrysts in the P2 monzonite have a turbid appearance and dark-brown due to sub-micron hematite dusting (Fig. 4.15A, D and E). Electron microprobe analysis of these phenocrysts has confirmed that they have been altered to orthoclase (Appendix C). Hornblende phenocrysts have been replaced by biotite which is invariably interleaved with chlorite (Fig. 4.15A, C and E). Clinopyroxene has typically been replaced by actinolite–chlorite–rutile (Fig. 4.15E). In parts of the FRV and the Weemalla Formation, ~100 m away from the P2 intrusive contact, chemical staining (Appendix B) has revealed that fine-grained K-feldspar has replaced the matrix (Fig. 4.15F and G).

The outer K-silicate alteration assemblage correlates to the potassic assemblage of Wilson (2003; Table 4.4), which was distinguished from his inner calc-potassic assemblage by the restricted occurrence of actinolite. The current study has found that actinolite has partially replaced primary ferromagnesium minerals in the outer K-silicate alteration zone.

#### **4.4.3 Late stage alteration**

##### **4.4.3.1 Late orthoclase–albite alteration**

Weak, selectively pervasive orthoclase–albite–quartz  $\pm$  actinolite alteration is confined to the P3 monzonite (Table 4.3; Fig. 4.3B). In contrast to the earlier-formed K-silicate alteration assemblages, biotite and magnetite are only sparsely developed. The P3 monzonite has undergone weak orthoclase–albite alteration resulting in partial alteration to complete replacement of primary plagioclase by hydrothermal orthoclase and albite (Fig. 4.16A and B). The ferromagnesian minerals have been partially altered to actinolite–chlorite–epidote (Fig. 4.16A). This alteration assemblage is similar to the late-stage potassic alteration described by Wilson (2003; Table 4.4).

##### **4.4.3.2 Epidote–chlorite–hematite alteration**

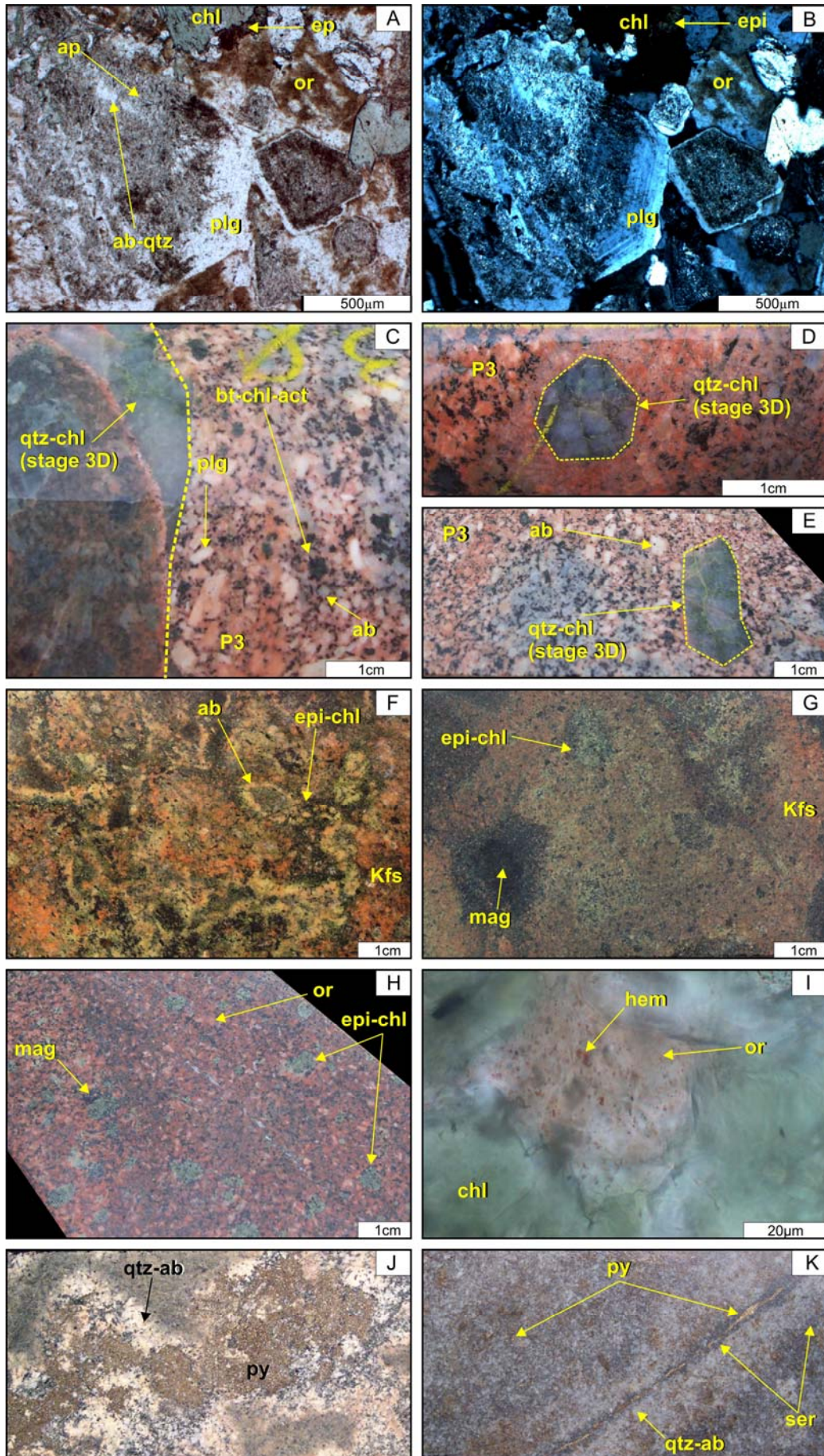
The most widespread alteration assemblage at Ridgeway is a weakly to moderately developed epidote–chlorite–hematite–apatite– (rutile–magnetite). This has caused selectively pervasive alteration of K-feldspar and plagioclase to epidote–chlorite and accessory apatite, and of clinopyroxene and hornblende to chlorite, rutile

**Figure 4.16** Late stage alteration at Ridgeway.

- A)** and **B)** Photomicrograph (ppl) and (xpl) of a late-stage quartz monzonite (P3). Primary feldspars have been altered to hematite-dusted orthoclase, which in turn has been selectively replaced by albite and fine grained sericite. Primary ferromagnesian minerals have been selectively altered to chlorite–epidote (UR323-1268m).
- C)** A late stage orthoclase–albite altered P3 monzonite has truncated a stage 3D barren quartz–chlorite vein hosted by coherent feldspar–phyric lithofacies of the FRV. Subhedral plagioclase crystals in the monzonite have been replaced by albite, and surrounded by orange-coloured orthoclase. Euhedral hornblende crystals have been replaced by biotite–chlorite–actinolite–epidote (UR323-1301.5m).
- D)** and **E)** Xenoliths of stage 3D barren quartz–chlorite veins in P3 monzonite (UR323-1316.5m; UR323-1303.8m).
- F)** Pervasive epidote–chlorite–hematite alteration in andesitic volcanoclastics of the FRV. Epidote and chlorite replaced fine-grained ferromagnesian minerals (UR324-319mm).
- G)** Selectively pervasive epidote–chlorite–hematite alteration in basaltic volcanic breccia of the FRV. Clasts have been altered strongly to epidote, magnetite and chlorite (NC508-535.3m).
- H)** Selectively pervasive epidote–chlorite–hematite alteration of the monzodiorite. Epidote, chlorite and magnetite have totally replaced primary clinopyroxene phenocrysts. Feldspar phenocrysts have been altered to orthoclase–albite–hematite (UR352-768.9m).
- I)** Photomicrograph (ppl) of submicroscopic hematite inclusions in orthoclase-altered feldspar crystals. Mafic minerals have been altered to chlorite (UR149-82.4m).
- J)** Pervasive, texturally destructive albite–quartz–pyrite–sericite alteration of a fine-grained volcanoclastics of the FRV. The rock has been replaced by a fine-grained, granular mass of albite and quartz. Clusters of pyrite have replaced ferromagnesian minerals (UR223-195m).
- K)** Pervasive quartz–pyrite–sericite alteration of a fine-grained volcanic rock (FRV) cut by a stage 4A pyrite veinlet with a thin sericite halo. Fine-grained sericite, chlorite and pyrite have replaced primary mafic minerals, whereas albite and quartz have altered the feldspars (NC508-369.8m).

Abbreviations: ab = albite, act = actinolite, ap = apatite, bt = biotite, chl = chlorite, ep = epidote, hem = hematite, Kfs = K-feldspar, mag = magnetite, or = orthoclase, plg = plagioclase, ppl = plane polarized light, py = pyrite, qtz = quartz, xpl = cross polarized light





and magnetite (Table 4.3; Fig. 4.16F to H). Widespread hematite dusting of primary and secondary feldspars has imparted a dark orange to brown colour to the FRV, and also locally to siltstones and feldspathic sandstones of the Weemalla Formation.

Epidote–chlorite–hematite alteration defines a broad shell around the outer K-silicate alteration that extends up to 500 m (Fig. 4.1). This alteration assemblage has overprinted the early K-silicate alteration in P1 and P2, where the cores of orthoclase-altered plagioclase phenocrysts have been selectively replaced by chlorite–epidote–apatite (Figs. 4.14A and 4.15D). In the volcanic units, ferromagnesian minerals in the andesitic-basaltic clasts have been selectively altered to epidote–chlorite–magnetite, and pervasive hematite dusting of feldspathic components is well-developed in the matrix. The epidote–chlorite–apatite– (rutile–magnetite) mineral assemblage is classified here as propylitic alteration (e.g. Seedorff *et al.*, 2005).

#### **4.4.3.3 Hematite alteration**

The near-ubiquitous hematite dusting of feldspar at Ridgeway makes the timing of hematite alteration difficult to constrain. Hematite dusting results in submicron inclusions in orthoclase-altered crystals (Fig. 4.16I) occurring as haloes around several vein stages, and locally as pervasive replacement. Hematite dusting could therefore have occurred as one alteration event in the evolution of Ridgeway, overprinting early-formed feldspar alteration, or it could have been repeated several times during the evolution of the system. The latter is preferred, as no late-stage hematite alteration front have been observed to overprint earlier-formed alteration haloes.

#### **4.4.3.4 Outer propylitic alteration**

Wilson (2003) defined two subzones of propylitic alteration at Ridgeway based on the presence or absence of finely disseminated red hematite (Wilson, 2003). The hematite-bearing inner propylitic subzone defines a shell asymmetrically distributed between the mineralized potassic alteration and a distal barren hematite-deficient chlorite–albite–actinolite alteration zone (outer propylitic zone; Wilson,

2003; Wilson *et al.*, 2003; Table 4.4). The outer propylitic subzone was not observed during the current study.

#### **4.4.3.5 Albite–quartz–pyrite–sericite alteration**

Pervasive, texturally destructive albite–quartz–pyrite–sericite alteration has affected the upper and distal portions of the FRV (Tables 4.3, 4.4; Figs. 4.1, 4.2B and 4.3B; Wilson, 2003). This alteration assemblage defines a cap above the epidote–chlorite–hematite-altered zone, approximated 600 m above the center of the deposit (Figs. 4.1; 4.2B and 4.3B). The distinct absence of hematite alteration and/or reddening of the rock suggests either that this alteration post dates the hematite dusting that affected all the rock units at Ridgeway, or that this assemblage lies outside the zone of Fe-oxidation at Ridgeway. Albite–quartz–sericite alteration has resulted in the replacement of all ferromagnesian minerals to fine grained sericite, and the feldspathic components of the rocks have been altered to albite–quartz–sericite (Fig. 4.16J). This alteration assemblage is magnetite destructive. In the Weemalla Formation, pervasive alteration of bedded units has resulted in pyrite occurring as clusters or widely distributed as disseminations (Fig. 4.16K). The albite–quartz–pyrite–sericite assemblage is classified here as sodic alteration (c.f. Seedorff *et al.*, 2005) and correlates with the albite–quartz–pyrite (sodic) alteration assemblage of Wilson *et al.* (2003).

#### **4.4.4 Fault-related alteration**

##### **4.4.4.1 Clay–chlorite alteration**

Pervasive clay–chlorite  $\pm$  epidote alteration is associated spatially with steeply-dipping faults (Table 4.3; Figs. 4.2C and 4.3C). This alteration has resulted in the selectively pervasive to pervasive alteration of feldspars to clay within 1 m of the fault planes (Fig. 4.17A). Mafic minerals have been altered to chlorite and epidote. Locally, pervasive epidote flooding occurs within 1 meter of the fault zones. The fault zones vary from 0.3 m up to 1 m thick, and locally contain fragments of quartz–sulfide veins.



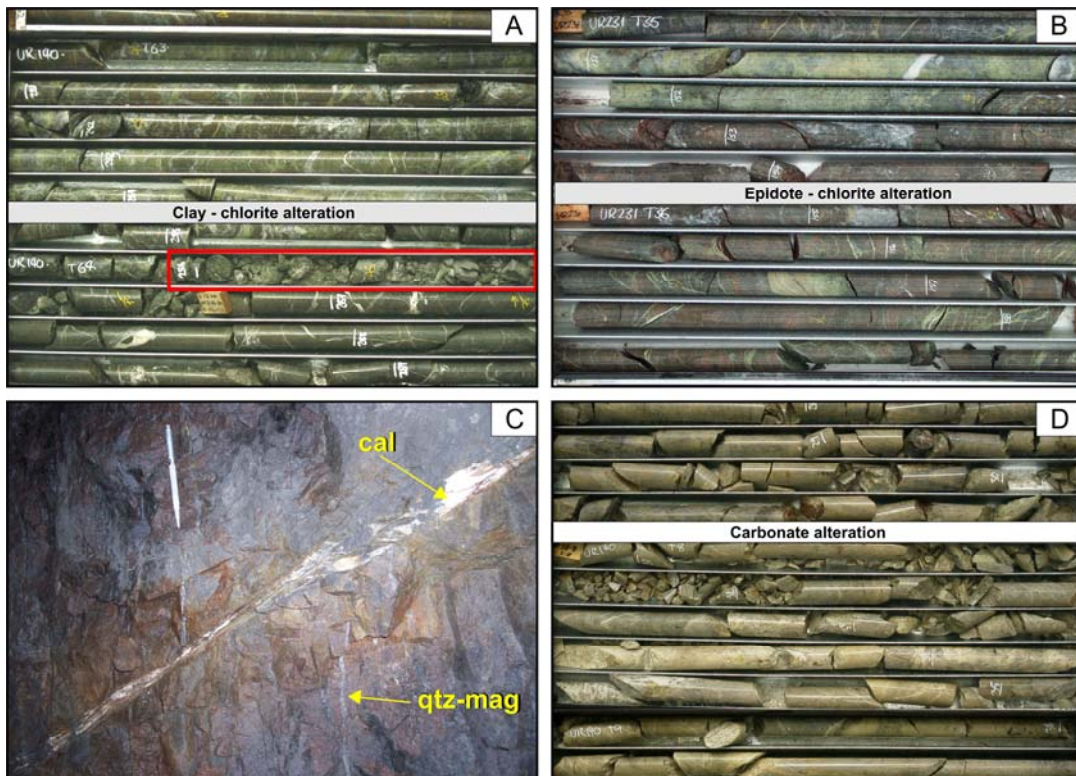


**Figure 4.17** Fault-related late stage alteration assemblage at Ridgeway. **A)** Strong clay - chlorite - epidote alteration associated with 0.5 m fault zone (red box; UR140-286m). **B)** Selectively pervasive epidote - hematite alteration haloes around moderately-dipping reverse fault, epidote flooding has occurred around the fault (UR231-151-153m). **C)** Zone of calcite veins in low-angle thrust fault, dark-brown carbonate alteration haloes occur up to 5 m from the fault (5100L-XC4WW-chainage 68). **D)** Cream to pale white-coloured carbonate alteration haloes around low-angle thrust fault (UR140-22-37m). Abbreviations: cal = calcite, mag = magnetite, qtz = quartz.

Clay–chlorite alteration is correlated to stage 5 phyllic alteration of Harper (2000) and P-2 stage fault zones of Wilson (2003). Clay minerals identified include kaolinite (Harper, 2000) and white mica (Wilson, 2003).

#### 4.4.4.2 Epidote–hematite alteration

Intense epidote–hematite alteration is associated locally with moderately-dipping reverse faults that have truncated the mineralized intrusions and veins at Ridgeway (Table 4.3; Figs. 4.2C and 4.3C). This alteration assemblage has resulted in the selective to pervasive replacement of ferromagnesian minerals to epidote and chlorite, and pervasive hematite alteration of the wallrock up to 10 m from the fault plane (Fig. 4.17B). Locally, epidote stockworks occur around the fault zones. This alteration stage is correlated with the P-4 stage fault zones of Wilson (2003; Table 4.4), Hematite has been recognized as a major component of this alteration

assemblage in the current study, whereas Wilson (2003) did not comment on its presence in stage P-4 fault zones.

#### **4.4.4.3 Carbonate alteration**

Selectively pervasive carbonate–quartz alteration occurs around some low-angle thrust faults and has cut all earlier formed alteration assemblages (Table 4.3; Figs. 4.2C and 4.3C). Carbonate alteration is extensively developed up to 20 m from some faults and has produced characteristic white, buff to brown carbonate-rich alteration haloes (Fig. 4.17C and D). Carbonate alteration is associated with a network of calcite veins and stringers that are concentrated around the fault zones (Fig. 4.17C).

### **4.5 Gold and copper grade distribution**

At Ridgeway, the mineralized ore zone is defined by grades greater than 0.2 g/t Au and 0.2 % Cu. It is approximately 300 m wide, 500 m long and over 1000 m in vertical extent (Figs. 4.18 to 4.22). The ore zone has a pronounced northwest elongation. Deep drilling has established the vertical continuity of mineralization. Ore minerals are zoned laterally and vertically from a bornite-dominant core associated with the quartz–sulfide stockwork, to a domain of bornite > chalcopyrite, to chalcopyrite > bornite ± pyrite (~200 m), and outward to pyrite > chalcopyrite and an outer pyrite-rich fringe >~600 m from the core of the deposit (Harper 2000; Wilson 2003; Wilson *et al.* 2003; Wilson *et al.* 2007a; Reynolds, 2007). Gold occurs as free gold grains and as inclusions in bornite and chalcopyrite. Free gold has been observed as disseminations in stages 2B and 2D veins, and intergrown with chalcopyrite in stage 3A veins (Fig. 4.7D).

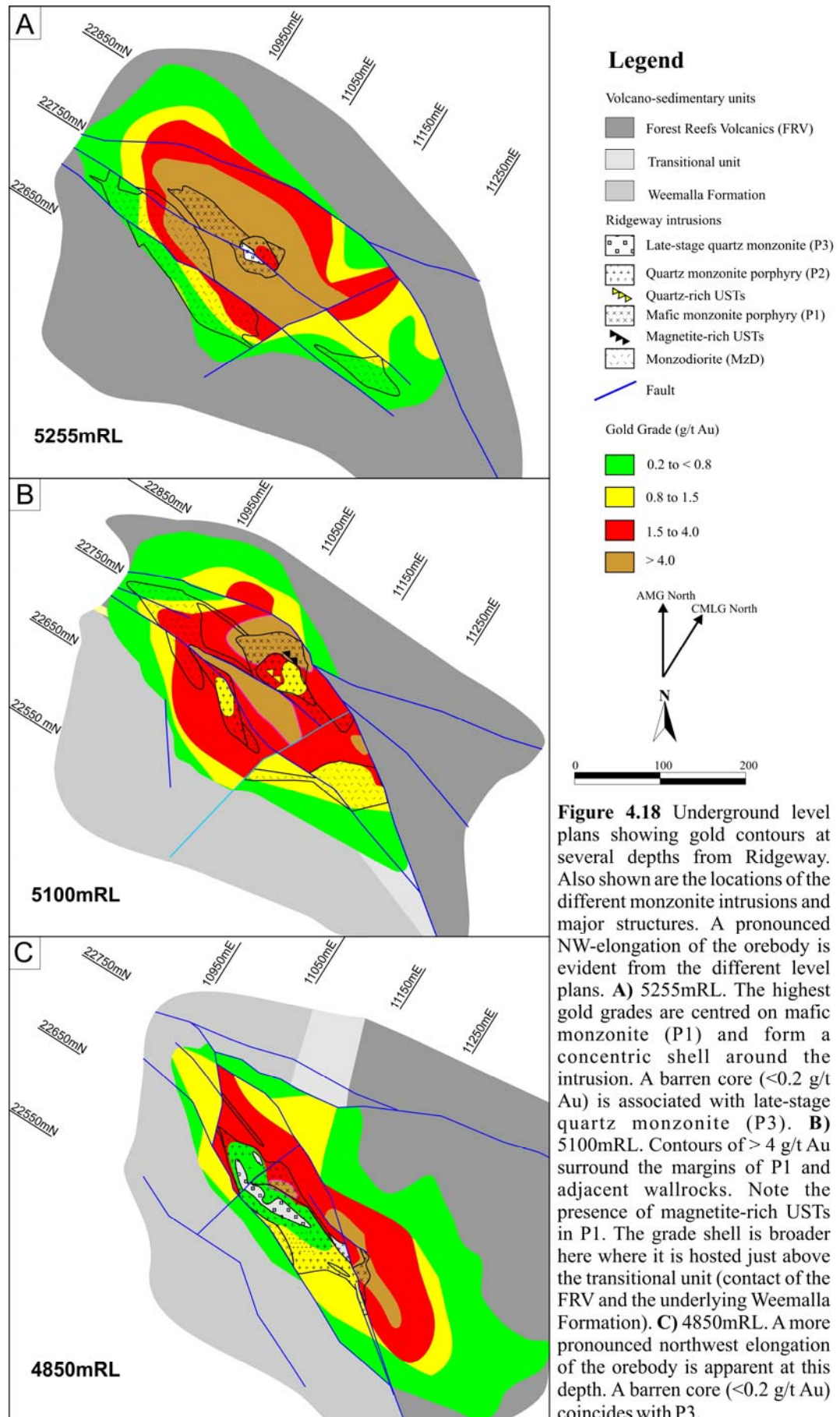
It appears that there were two main stages of copper and gold deposition at Ridgeway. The major stage is due to the formation of bornite-rich stage 2 veins. Stage 2 veins introduced significant gold and copper during emplacement of the P1 monzonite. The formation of stages 2A and 2B stockwork veins adjacent to P1 (with associated magnetite-rich USTs) and the enclosing host rocks resulted in very high gold and copper grades up to 50 m from the contact (Fig. 4.6, Figs. 4.20B and 4.21B; Fig. 4.23). The second major stage of copper-gold endowment was during the

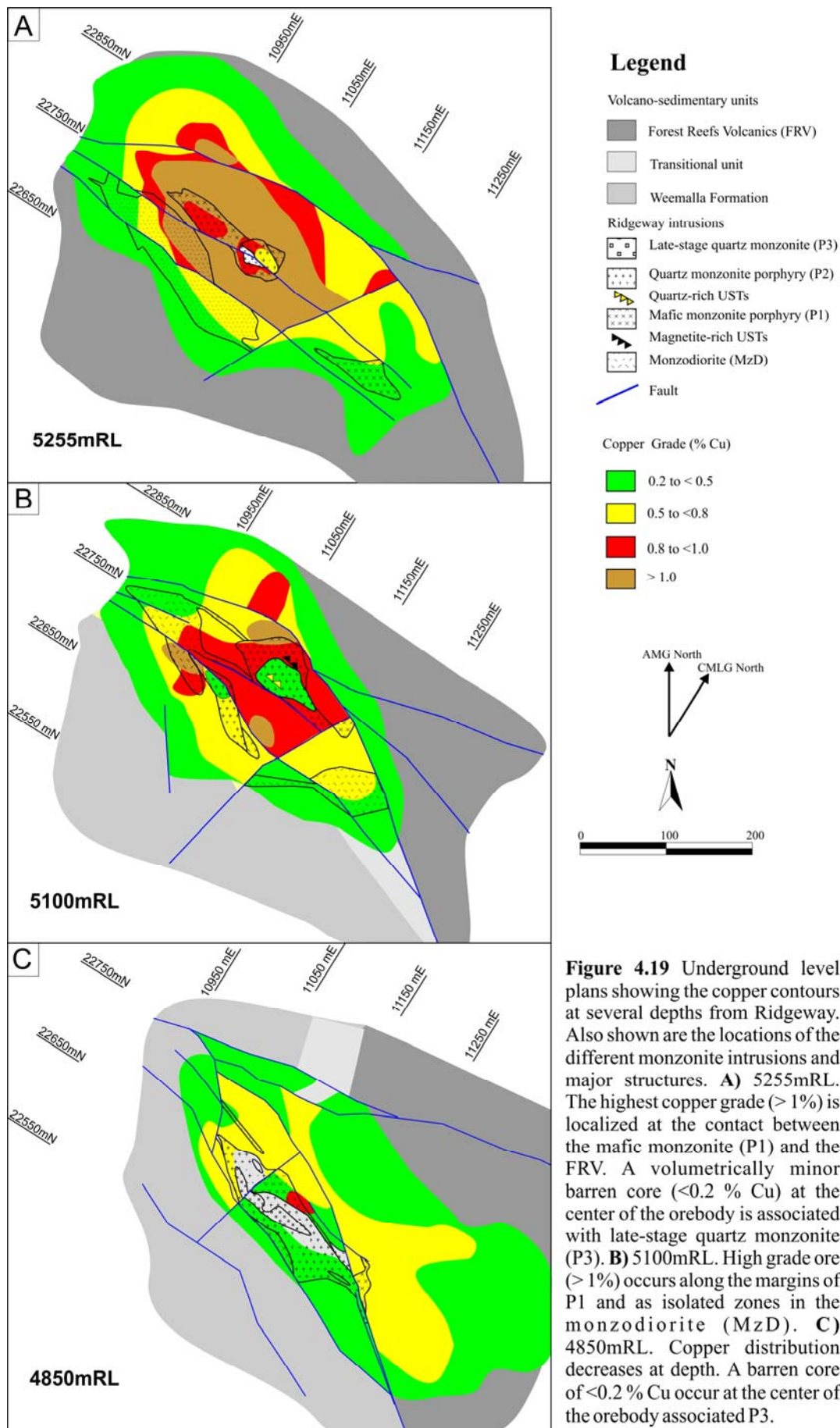


formation of chalcopyrite-rich stage 3, which were spatially and temporally associated with P2 monzonite emplacement (Fig. 4.23). Although these stage 3 veins have lower Cu and Au grade than stages 2A and 2B veins (Fig. 4.23), the wider distribution of the stage 3 veins extended the mineralization to distances of up to 300 m laterally from the center of the orebody (Fig. 4.1; Figs. 4.18 to 4.22 )

Close to P1 and P2 intrusive contact (~50 m), bornite and chalcopyrite occurs in quartz veins as vein fill, as coatings on fractures, and as disseminations through the pervasively altered rocks. Bornite and chalcopyrite are most abundant between elevations 5400mRL and 5000mRL. The abundance of sulfides decreases both downwards and upwards from these elevations, as illustrated in copper grade contour plots (Figs. 4.18 to 4.22).

Well-mineralized stage 2B quartz–banded magnetite–bornite stockwork veins are abundant in the higher parts of the deposit. Below 5000mRL, although stage 2B veins still persist, they are subordinate to stage 3D quartz–chlorite veins that are deficient in Cu–Fe sulfides. The highest Cu and Au grades are therefore located higher in the deposit, where the Au:Cu ratio is nearly 1:1. A decrease in grades from >0.8 % Cu and >1.5 g/t Au in the upper part to < 0.5 % Cu and < 0.8 g/t Au in the lower part is exemplified on several cross-sections (Figs. 4.20 to 4.22). The decrease appears to relate to the following: a) stage 2 veins and stages 3A and 3C were emplaced into reactive, intensely altered volcanoclastic rocks at shallow depth, but alteration of the less reactive quartz  $\pm$  albite altered laminated Weemalla Formation siltstone at depth produced lower Cu and Au grades; b) the P1 and P2 intrusions are wider in the FRV than in the Weemalla Formation, and the local ‘ballooning’ of these mineralizing intrusions above the transitional zones appears to have helped focus fluids and sulfide deposition. It appears that reactive Fe-rich volcanic rocks of the FRV were the favourable site for pervasive mineralization and vein-controlled Cu–Fe sulfides, whereas the Weemalla Formation siltstones and sandstones favoured fracture-controlled mineralization and limited disseminations of sulfides into the finer grained wallrocks.





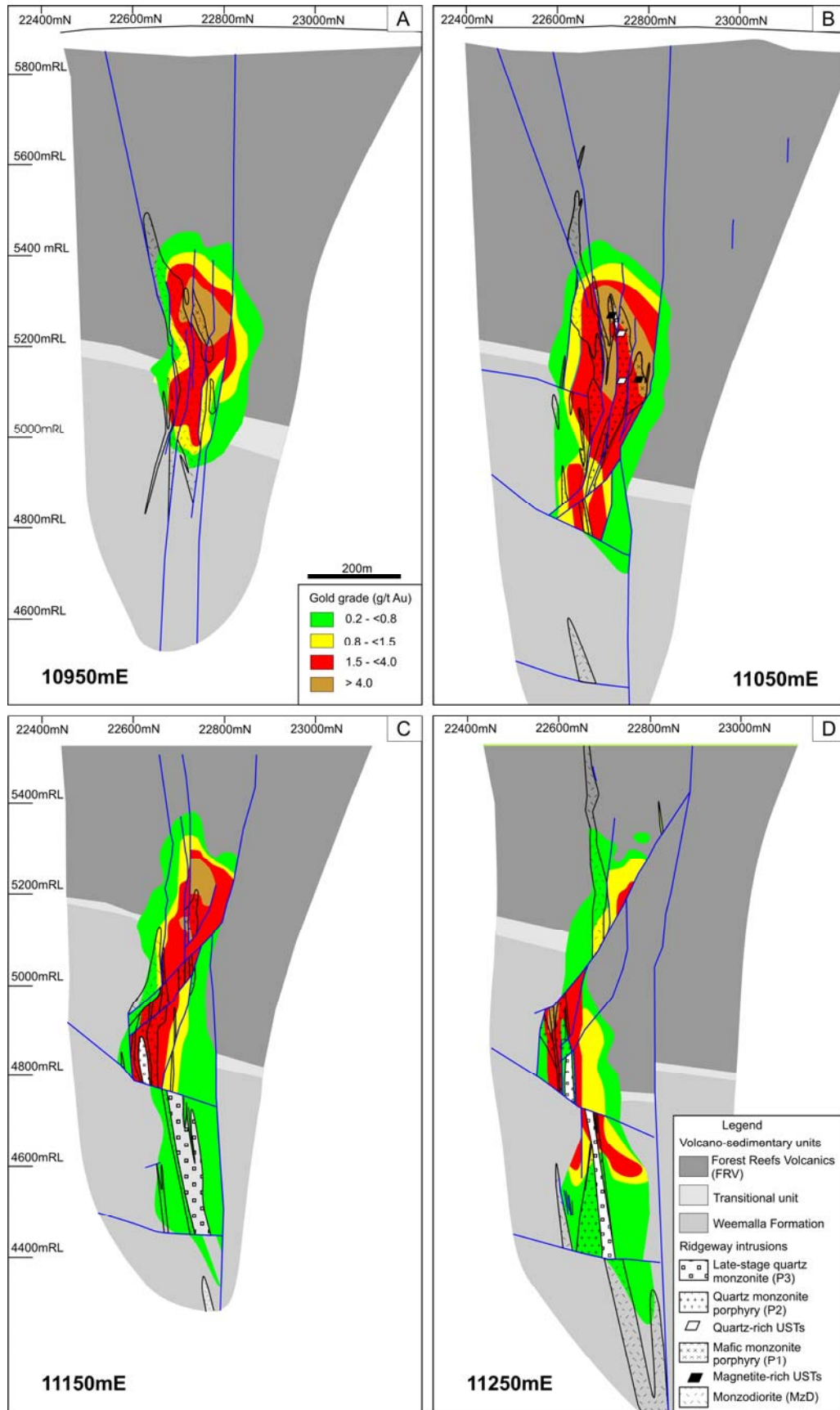


**Figure 4.20** Stacked southwest-northeast cross-sections illustrating gold grade patterns at Ridgeway. Note that the highest gold grade is concentrated at the apical portion of the mafic monzonite (P1) and the quartz monzonite (P2) intrusions. Refer to Figure 3.1 for the location of section lines.



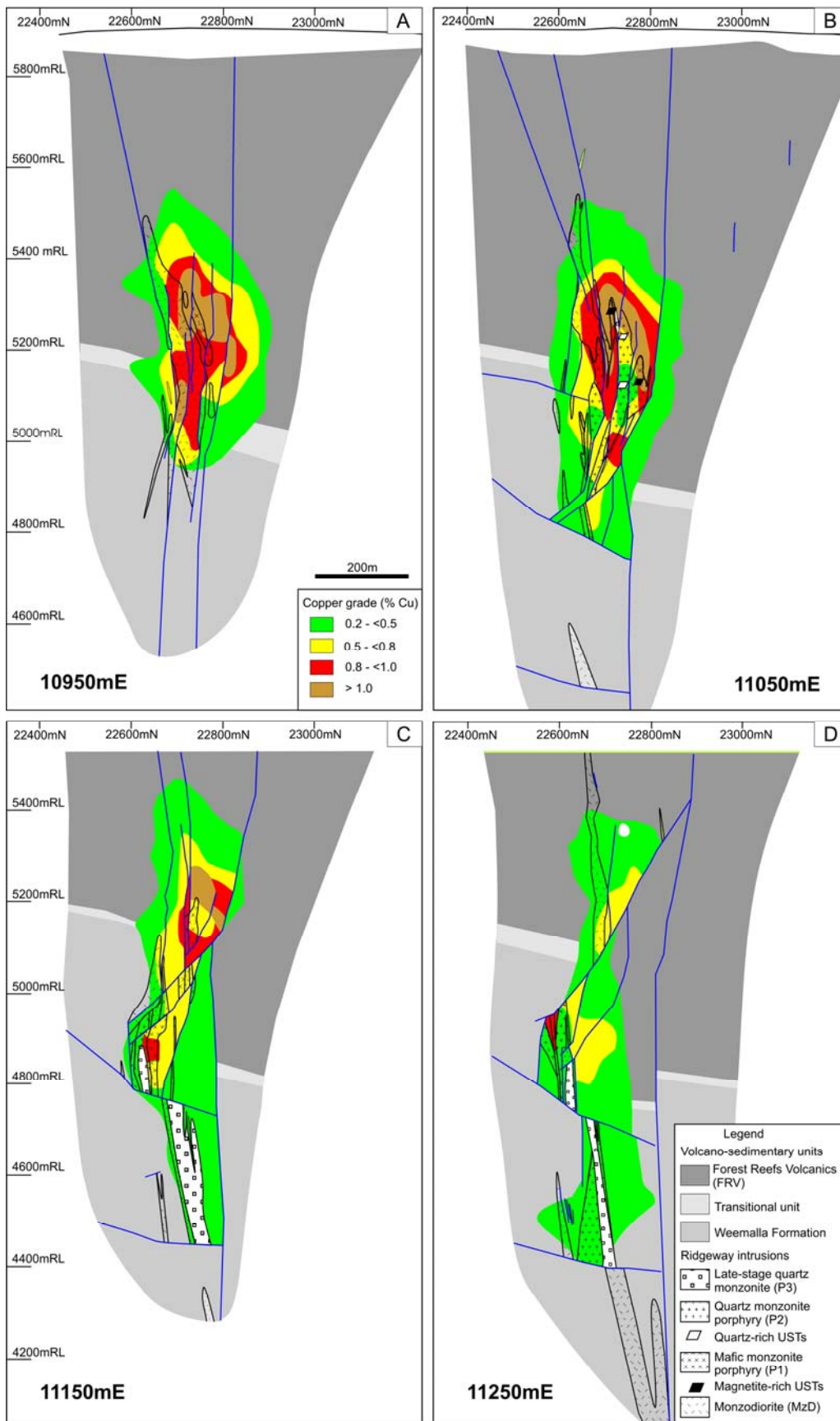


**Figure 4.21** Stacked southwest-northeast cross-sections illustrating copper grade patterns at Ridgeway. Note that the high grade copper is concentrated at the apical portion of the mafic monzonite (P1) and the quartz monzonite (P2) intrusions. Refer to Figure 3.1 for the location of section lines.



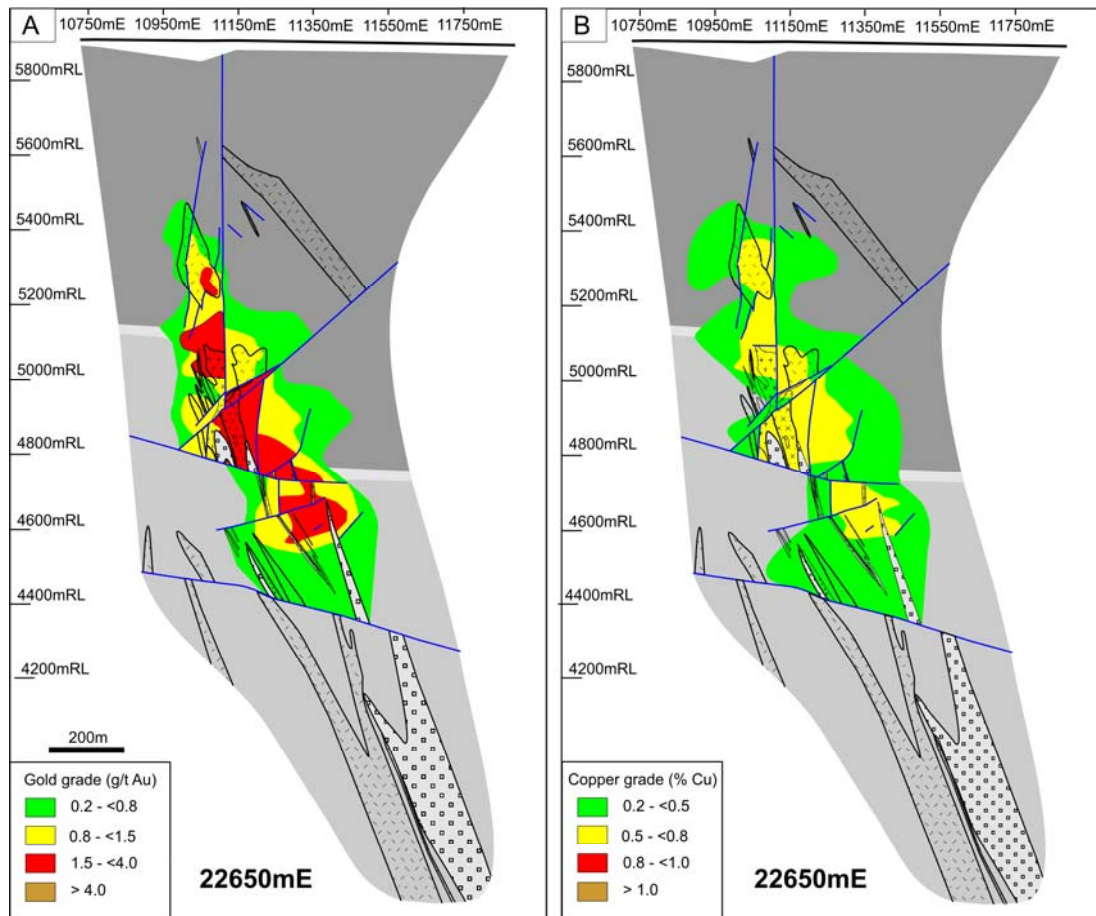


**Figure 4.22** Northwest-southeast interpretative long section along 22650mN through Ridgeway showing gold and copper grade patterns. **A)** Contour of gold assays. Gold grades  $> 1.5$  g/t are highest in and around the apex of mafic monzonite (P1), and occur just above and below the transitional unit. **B)** Contour of copper assays. Copper grades  $> 0.5$  % has the same distribution as the gold ore-grade. Grade distributions have been truncated by major faults. Refer to Figure 4.21 for rock types legend and Figure 3.1 for section line location.

The location of the 0.2 g/t gold contour approximately coincides with the transition inwards from epidote–chlorite–hematite to the outer K-silicate alteration domain (compare Figs. 4.2B and 4.20B). The domain with gold and copper grades exceeding 1.5 g/t Au and  $>0.5$  % Cu is associated spatially with the inner K-silicate alteration assemblage (compare Figs. 4.2B, 4.20B and 4.21B). Grades significantly greater than 4.0 g/t Au and 1.0 % copper grade are associated with abundant stage 2B veins that are localized at the apophysis and margins of P1 (compare Figs. 4.2D and 4.20B). Locally, the 4.0 g/t Au and 1.0 % Cu contours define an inverted-cup shape surrounding the margins of P1 and occurring up to 50 m from the intrusion in the volcanoclastic rocks of the FRV (Figs. 4.20B and 4.21B). Ridgeway has a low-grade core ( $<0.2$  g/t Au;  $<0.2$  % Cu) associated with P3 (Figs. 4.18C and 4.19C).

Copper and gold grade distributions in the Weemalla Formation are strongly controlled by rock type. Elevated grades are confined to the feldspathic-rich and the pyroxene-phyric dikes and sills. Low grades occur in the quartz  $\pm$  albite altered siltstones. Drillhole UR333, (elevation 4600mRL) contains a series of massive stage 3C chalcopyrite–bornite–epidote veins over a 16 m interval with grades of up to 4.5 g/t Au and 3.4 % Cu. This localized high-grade zone is restricted to the massive feldspathic sandstone unit, and the pyroxene- and feldspar-phyric andesitic sill (compare Figs. 4.3A and 4.22).

## **4.6 Re–Os geochronology**

Unlike other porphyry ore deposits of the Cadia district, no direct dating of mineralization at Ridgeway has been previously attempted. In the current study, Re–Os ages were determined for two molybdenite samples for Ridgeway. These results are placed within the context of the revised vein, alteration and intrusion paragenesis outlined above, in order to constrain the absolute timing of hydrothermal events of the Ridgeway deposit.

### **4.6.1 Re–Os analytical methods**

Two molybdenite-bearing drill core samples (UR360-724.5m and UR033; Table 4.6) were sent to Dr. Robert Creaser at the University of Alberta Radiogenic Isotope Facility for mineral separation and dating. Age determinations were based on the Re–Os method outlined by Selby and Creaser (2001). Molybdenite was analyzed with isotope dilution mass spectrometry using Carius-tube, solvent extraction, anion chromatography and negative thermal ionization mass spectrometry techniques. The abundance of  $^{187}\text{Re}$  and  $^{187}\text{Os}$  in these samples were analyzed on a Micromass Sector 54 mass spectrometer and a mixed double spike containing known amounts of isotopically enriched  $^{185}\text{Re}$ ,  $^{190}\text{Os}$  and  $^{188}\text{Os}$  analysis was used (Selby and Creaser, 2004). Blank values used in these analyzes were  $\text{Re} = 5 \pm 2 \text{ pg}$ ,  $\text{Os} = 1.0 \pm 0.2 \text{ pg}$  and  $^{187}\text{Os}/^{188}\text{Os}$  of  $0.30 \pm 0.05$ .

#### 4.6.2 Previous Re–Os geochronological studies

Several studies have sought to constrain the absolute ages of magmatic and hydrothermal activity in the Cadia district (Perkins, 1994; Squire, 2001; Forster and Seccombe (2004); Wilson *et al.*, 2007; Harris *et al.*, 2009c). Previous Re–Os analyses of molybdenite samples from Cadia Quarry, Cadia Hill and Cadia East fall into two ranges, an older age between 460 and 450 Ma and a younger age recorded between 443 and 441 Ma (Table 4.5; Wilson *et al.*, 2007). All molybdenite samples were obtained from transitional stage quartz–sulfide veins. At Cadia Quarry, a single aliquot of molybdenite from texturally and compositionally similar veins returned two age ranges of Re–Os: a younger age of  $443.5 \pm 1.4$  Ma and an older molybdenite age of  $459.7 \pm 1.4$  Ma (Wilson *et al.*, 2007b). A second sample from Cadia Quarry yielded Re–Os ages of  $450.5 \pm 1.7$  Ma,  $466.6 \pm 1.5$  Ma and  $450.8 \pm 1.4$  Ma. A molybdenite sample from Cadia Hill yielded Re–Os ages of  $442.9 \pm 1.4$  Ma and  $443.0 \pm 1.5$  Ma. A similar Re–Os age was determined for molybdenite from Cadia East,  $441.8 \pm 1.4$  Ma.

#### 4.6.3 Results

Re–Os ages determined for two molybdenite samples from Ridgeway are presented in Table 4.6. Sample RWD-moly-01 was taken from a 2 mm wide stage 3C chalcopyrite–pyrite–molybdenite vein that is hosted in quartz  $\pm$  albite altered laminated Weemalla Formation siltstone (UR360-724.5m, 4488mRL). It was collected close to the contact with P2. Analysis of a single aliquot of molybdenite returned a  $^{187}\text{Re}/^{187}\text{Os}$  age of  $442.8 \pm 2.3$  Ma. Sample RWD-moly-02 was taken from UR033-5400mRL, and contains a 20 mm wide stage 3A quartz–chalcopyrite–molybdenite vein hosted in hematite-dusted orthoclase–biotite–magnetite altered volcanoclastic breccia of the FRV. Two separate aliquots of molybdenite from the sample yielded  $^{187}\text{Re}/^{187}\text{Os}$  ages of  $445.7 \pm 2.8$  Ma and  $443.6 \pm 2.1$  Ma (Table 4.6).

**Table 4.5** Analytical results and sample descriptions for Re-Os age determination for molybdenite from Cadia porphyry deposits. Samples are transitional-stage veins from Wilson *et al.* (2007).

Deposit	Drillhole	Depth (m)	Re (ppm)	Os (ppb)	Age (Ma $\pm 2\sigma$ )	Comment	Sample description
Cadia Quarry	NC083	35	25.4	120.4	450.5 $\pm$ 1.7		Quartz–chalcopyrite–orthoclase–
			25.1	123.0	466.6 $\pm$ 1.5	Replicate	molybdenite vein, orthoclase alteration
			12.1	57.4	450.8 $\pm$ 1.4	Replicate	halo
	NC486	431	12.7	61.4	459.7 $\pm$ 1.4		Quartz–chalcopyrite–molybdenite–
	NC486	468	861.0	4013.0	443.5 $\pm$ 1.4		calcite vein, no alteration halo Quartz–molybdenite–chalcopyrite $\pm$ calcite vein, orthoclase alteration halo
Cadia Hill	NC384	200	203.5	947.0	442.9 $\pm$ 1.4		Quartz–chlorite–molybdenite vein,
					443.0 $\pm$ 1.5	Replicate	orthoclase alteration halo
Cadia East	NC335W	959	1057.0	4909.0	441.8 $\pm$ 1.4		Quartz–calcite–molybdenite–bornite vein, orthoclase alteration halo

**Table 4.6** Analytical results for Re–Os geochronology for molybdenite from Ridgeway

Sample No	Drillhole	Depth (m)	Elevation (CML)	Re (ppm)	Os (ppb)	Age (Ma $\pm 2\sigma$ )	Comment	Sample description
RW-moly-01	UR360	724.5	4488	84.61	394	442.8 $\pm$ 2.3		Stage 3D chalcopyrite–pyrite–molybdenite vein, no obvious alteration halo
RW-moly-02	UR033		5400	645.40	3023	445.7 $\pm$ 2.8		Stage 3A quartz–chalcopyrite–molybdenite vein, hematite-dusted orthoclase halo
				651.40	3037	443.6 $\pm$ 2.1	Replicate	

## 4.7 Discussion

The Ridgeway Au–Cu deposit resulted from the superposition of several geologic events over a period of time including multiple phases of intrusive activity, fracturing, alteration and mineralization. Mineralization at Ridgeway was, for the most part, typically vein-controlled and is intimately associated with the emplacement of P1 and to a lesser extent P2. The host rocks strongly controlled the style, distribution and extent of alteration (Figs. 4.1 and Fig. 4.23).

### 4.7.1 Pre-mineralization stage

At Ridgeway, early quartz  $\pm$  albite, calc-silicate and actinolite–magnetite–albite alteration events pre-date mineralization. These alteration zones occur in the different rock units in the Weemalla Formation. Most of these alteration zones are interpreted to be spatially and temporally associated with the monzodiorite. Geochemical data suggest that the monzodiorite shows a different trend to the monzonite suite (section 3.8). The monzodiorite may have formed in association with early-formed calc-silicate and actinolite–magnetite–albite alteration, and acted as passive hosts to mineralizing fluid during the emplacement of P1 and P2 (Fig. 4.23).

#### 4.7.2 Fluid evolution in space and time

Most of the Au–Cu mineralization at Ridgeway was emplaced during the main mineralization stage (stages 2 and 3 veins). Abundant stage 2 veins and strong K-silicate alteration intensity occur in and around the P1. Vein and alteration assemblages are zoned laterally and vertically around the intrusions. In the FRV, Na–K-feldspar-stable vein and alteration assemblages (bornite–chalcopyrite-bearing) occur at the center, passing laterally and vertically outwards to epidote–chlorite–hematite alteration to a more distal quartz–albite–sericite stable alteration assemblage that contains pyrite. The mineralogical zonation is interpreted to reflect thermal and/or chemical gradients in outward migrating fluids, possibly due to cooling, interaction with the wall rocks, and/or by mixing with external fluids. The vertical mineralogical zonation suggests thermal zonation upwards and outwards from the monzonite suite (P1, P2 and P3).

The intensity of K-silicate alteration in the deposit varies with distance from the monzonite suite, rock types and elevation. In the upper levels of the deposit (>5100mRL), large volumes of volcanoclastic rocks of the FRV are pervasively altered to K-silicate assemblage (orthoclase–biotite–magnetite–albite–actinolite). In contrast, below <5100mRL, the K-silicate assemblage only significantly affected the feldspathic horizons of the Weemalla Formation. In the more siliceous rocks, the development of a zone of K-silicate alteration is restricted to thin halo along the margins rather than by laterally varying pressure and temperature-chemical conditions buffered by low permeability of the rock.

Epidote–chlorite–hematite (propylitic) alteration is evident in the FRV and feldspathic sandstone unit of the Weemalla Formation. In the intrusions, this alteration is exemplified as a weak to moderate replacement of feldspars, particularly at the core of plagioclase. Propylitic alteration is interpreted here to reflect the thermal collapse of the hydrothermal system (e.g. Sander and Einaudi, 1990).

Albite–quartz–pyrite–sericite alteration forms a cap and locally extends into the propylitic zone (Fig. 4.2B). This alteration is characterized by intense replacement of the feldspathic components of the FRV by albite, quartz, sericite and



pyrite. Where strongly developed at the top, this later alteration obscures evidence of the earlier propylitic or K-silicate phase.

#### **4.7.3 K-silicate (Potassic) alteration and Au–Cu ore**

At Ridgeway, intense silicate alteration assemblage and highest copper and gold grades occurs in P1 and immediate wallrocks associated with stage 2 veins (Fig. 4.23). The intensely-developed K-feldspar alteration assemblage may be a consequence of the high temperature and high HCl content of hydrothermal fluids (Hithersay and Walshe, 1995). The outer K-silicate alteration forms a shell around the inner K-silicate alteration associated with stage 3 veins. Although lower grade, ore deposition occurred in association with the emplacement of P2. The K-silicate alteration may be due to alkali exchange of K in fluid for Na in wallrock during cooling, and precipitation of Cu–Fe sulfides from H<sub>2</sub>S-bearing fluids by sulfidation of FeO in hornblende and/or magnetite (e.g. Dilles and Einaudi, 1992).

The actual quantity of deposited sulfide is controlled by the host rock chemistry. The basaltic andesite and andesite volcanic rocks contain more sulfide than the siliceous sedimentary rocks. Where seen, the Fe-rich pyroxene-bearing volcanic and sedimentary units of the Weemalla Formation show the same affinity for sulfides as that of the FRV. The Fe-rich rocks in the FRV and the Fe-rich rock units of the Weemalla Formation are chemically more reactive and much better hosts for copper mineralization than the siliceous units of the Weemalla Formation at depth. The occurrence of sulfide mineralization in the mafic reactive units has been documented in other porphyry deposits (e.g. Ray deposit, Phillips *et al.*, 1974).

#### **4.7.4 Relationship of unidirectional solidification textures to Cu–Au mineralization**

Crenulate comb-layered textures (USTs) and miarolitic cavities provide textural evidence for phase separation and metal partitioning from a crystallizing melt (e.g. Kirkham and Sinclair, 1988; Lowenstern and Sinclair, 1996). At Ridgeway, well-developed undulose to crenulate layers dominated by magnetite and

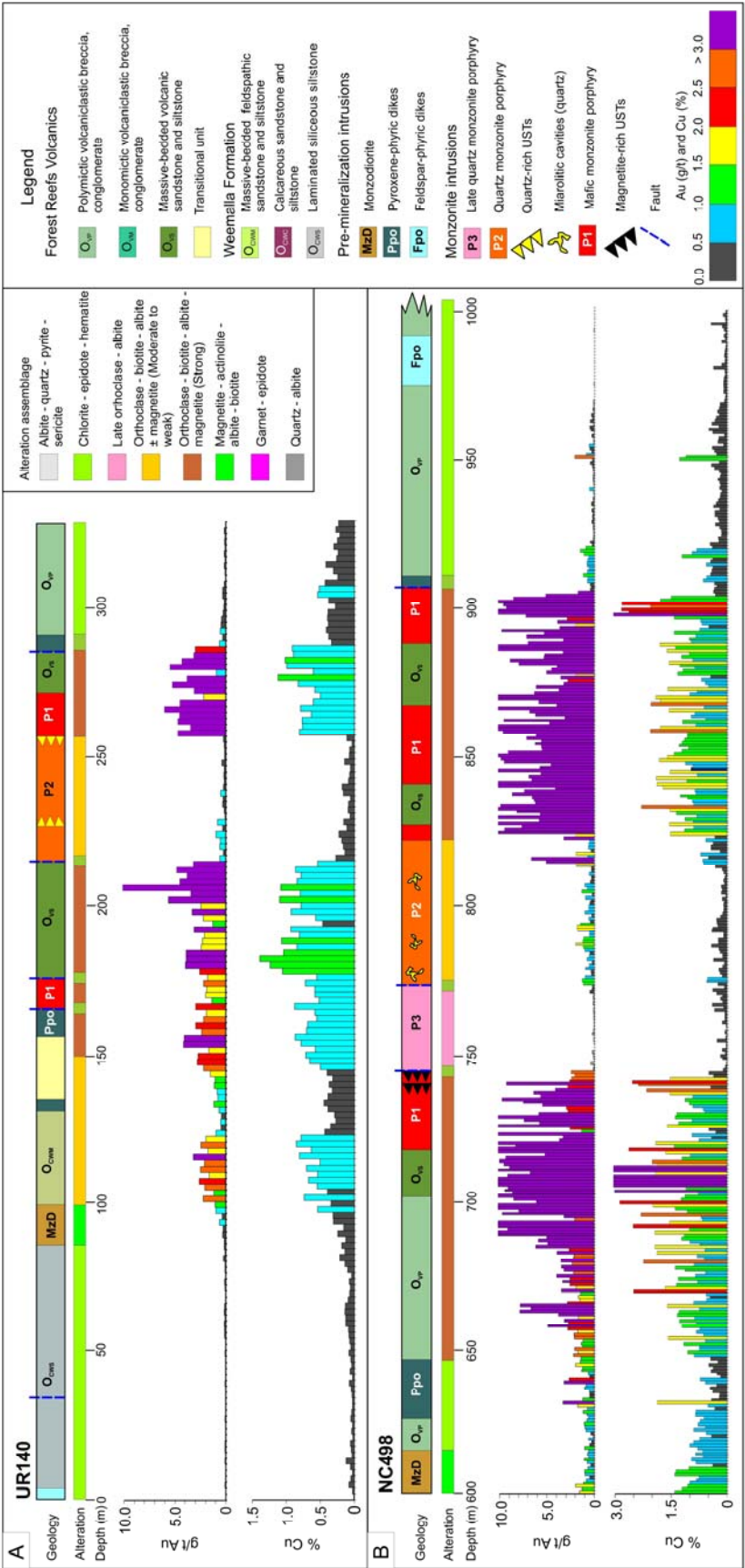


**Figure 4.23** Geology and alteration of selected drillholes through the core of the Ridgeway deposit, showing the rock type, alteration, gold and copper grades (10 g/t Au, 1.5% Cu) coincide with strong K-silicate alteration in the mafic monzonite (P1) and adjacent volcanic sandstone and siltstone units of the FRV. Both gold and copper grades decrease gradually ~ 100 m away from the contact with P1. An abrupt drop in gold and copper grade across the contact with quartz monzonite (P2) from 0.2 to 1 g/t Au and below 0.5 % Cu. A change from strong to moderate K-silicate alteration shows that P2 truncate earlier-formed mineralization. Note the presence of well-developed quartz-rich USTs in P2. The gold and copper grades gradually decrease distal to the center of the intrusions, note also that both grades suddenly drop with the change of rock type to laminated siltstone of the Weemalla Formation. **B)** Elevated gold grade of > 2.5 g/t and copper grade > 0.5 % in P1 and immediate wallrocks, both grades decrease gradually ~100 m away from the contact with P1. Magnetite  $\pm$  quartz-rich USTs occur in the margin of P1. An abrupt drop in gold and copper grade (< 0.2 g/t Au, < 0.2 % Cu) occurs at the fault contact with late-stage quartz monzonite (P3). Quartz miarolitic cavities occur in P2. Note again the discrepancy in grade, P2 is lower (1 g/t Au and <0.24 % Cu) than P1. This diagram provides compelling evidence that P1 added the bulk of the metals, P2 is very weakly mineralized and P3 is barren.

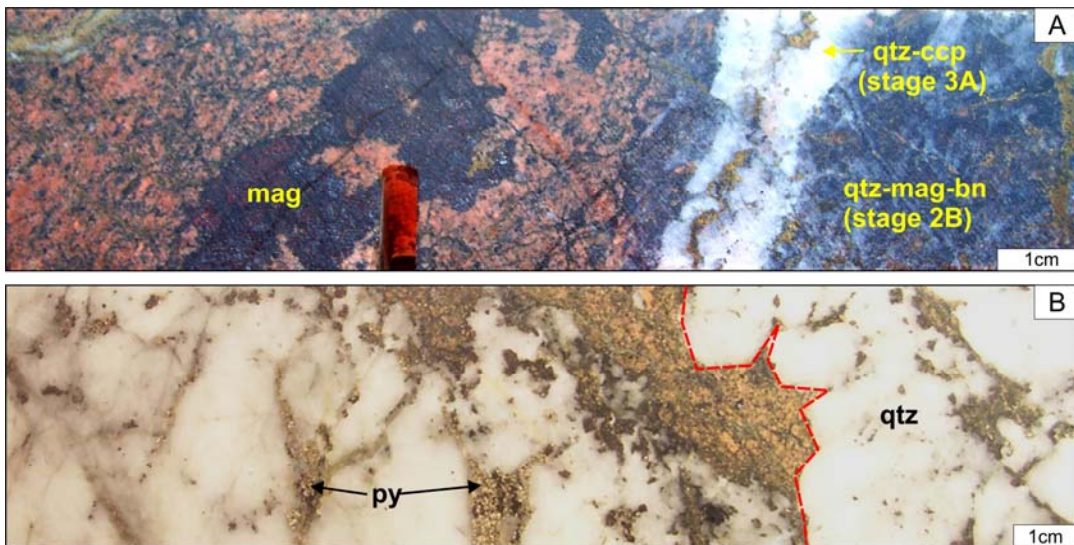


**Figure 4.24** Unidirectional solidification textures (USTs) associated with mafic monzonite (P1) and quartz-monzonite (P2). **A)** Massive magnetite-rich crenulated band in P1. Outboard the contact, a stage 2B quartz - magnetite - bornite stockworks occur, which in turn cut by a stage 3A quartz - chalcopyrite vein. The gold grade for this interval ranges from 4 - 15 g/t and copper grade of up to 1.5 % (NC508-883.2m). **B)** Quartz comb-layered in P2. Pyrite occur as coarse-grained crystals disseminated on the quartz. The gold grades for this interval ranges from 0.2 - 1.0 g/t and copper grade is < 0.5 % (UR140-227m). The red line shows the trace of USTs showing the quartz crystals point downward to the core of the intrusions. Abbreviations: bn = bornite, ccp = chalcopyrite, chl = chlorite, ep = epidote, mag = magnetite, or = orthoclase, py = pyrite, qtz = quartz

quartz were reported by Wilson (2003), Lickfold *et al.* (2003), Wilson *et al.* (2003), and Harris *et al.* (2006). In the current study, USTs have been observed in the apical parts and along the margins of the P1 and P2 monzonite intrusions (section 3.4.1.2; Fig. 4.24).

The crenulated magnetite-rich USTs in P1 have an intimate spatial relationship with the massive stage 2 quartz-magnetite-sulfide stockwork that occurs outboard of the contact with the enclosing FRV volcanoclastic rock units (Fig. 4.24A). The presence of alternating bands of crenulated magnetite implies that Fe-rich magmatic fluids streamed through and accumulated within the narrow pencil-shaped P1 intrusion. When fluid pressure exceeded confining pressure, fracturing occurred and served as a high permeability channel ways for the migration of hydrothermal ore forming fluids, as shown by the elevated gold and copper grade (Fig. 4.23 and 4.24A). As documented, this release of volatiles could have happened repeatedly over a period of time as shown by banded stage 2B veins (section 4.3.2.2).

#### 4.7.5 Ore distribution

At Ridgeway, copper and gold mineralization is interpreted to have occurred during two main mineralizing events. The first event provided high-grade ore in bornite-rich stockwork veins associated with the P1. The second mineralizing event occurred during the intrusion of P2, but the grades were much lower (Fig. 4.23). High-grade ore in P1 and immediate surrounding wall rocks is not a product of multiple episodes of overprinting through a succession of intrusions as has been observed in other porphyry deposits (e.g. Henderson, Colorado, Seedorff and Einaudi, 2004a; Yerington, Nevada, Proffett, 2009). At Ridgeway, it is interpreted that the change of magmatic fluids and the mass of introduced copper and gold decreased markedly through time as each successive intrusions depleted the underlying parent magma chamber of metals and volatiles (from P1 through P3; Fig. 4.23). Similar observations of declining grades associated with successive porphyry intrusions in porphyry deposits have also been observed at El Salvador, Chile (Gustafson and Hunt, 1975), Bajo de Alumbrera, Argentina (Proffett, 2003), Northparkes, Australia (Hiethersay and Walshe, 1995; Lickfold *et al.*, 2003), Boyongan, Philippines (Braxton, 2008) and Bingham, USA (Redmond and Einaudi, 2010).

*Low-grade core:* Low-grade (<0.2 g/t Au, <0.2 % Cu) core, with pyrite veins and disseminations, and weak K-silicate alteration, is developed mostly in P3 (Fig. 4.23). At depth, the large size of P3 compared to P2 (Fig. 4.22) may contribute to slower cooling and higher temperatures. High temperatures may have prevented Cu-sulfide saturation. Alternatively, one factor contributing to the formation of the low-grade core in P3 may have been that the magma was partly depleted of Cu and Au relative to early volatiles by P3 time, compared to P1 and P2 time. This observation was also observed in Bajo de la Alumbrera porphyry Cu–Au, Argentina (Proffett, 2003) and Bingham Canyon porphyry Cu–Mo–Au, Utah (Redmond and Einaudi, 2010).

#### 4.7.6 Timing of the Magmatic - Hydrothermal System

. At Ridgeway, the Re–Os dating of molybdenite from this study and the study of Harris *et al.* (2009c; section 3.7, Table 4.7; Fig. 4.25) on U–Pb age of intrusions supports a broad temporal link between copper–molybdenum mineralization and intrusive activity. This result is broadly concordant with other porphyry deposits in the Cadia district. Wilson *et al.* (2007b) reported the similarity of the estimated ages of intrusions and molybdenite crystallization at Cadia Hill, Cadia East, and the Cadia Quarry which formed between ~443 and 437 Ma (Table 4.7; Figure 4.26). The new Re–Os age determinations of the molybdenite and the U–Pb age determination of the monzonites (ref. section 3.7; Fig. 4.25) constrain the magmatism and mineralization at Ridgeway to  $444.2 \pm 1.3$  Ma, i.e. during the latest Ordovician. This new age implies that the Ridgeway gold–copper deposit is not a separate early Late Ordovician mineralized porphyry as previously reported (Wilson *et al.*, 2007b); instead, Ridgeway is a part of the Au- and Cu-related magmatism associated with the latest Ordovician - earliest Silurian intrusions emplaced between 444 and 437 Ma.

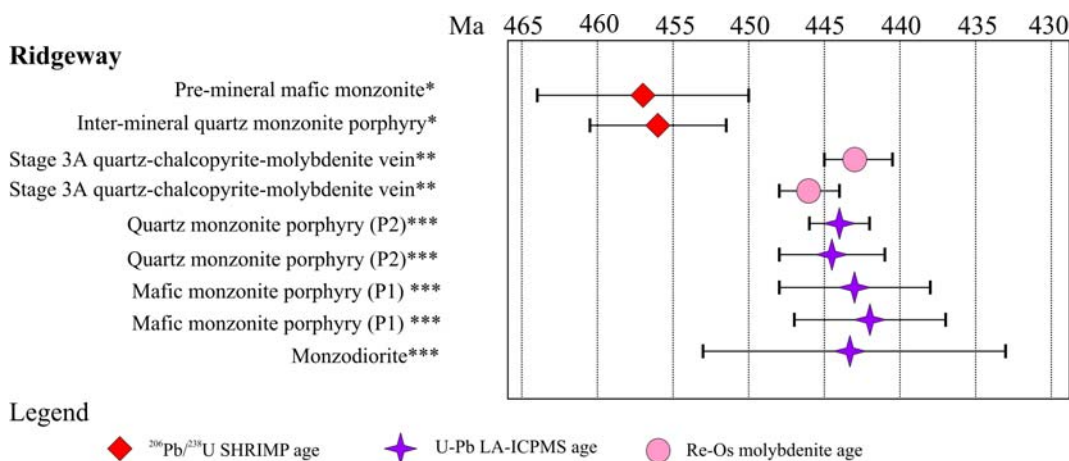


**Figure 4.25** Summary of the geochronology from Ridgeway. Data sources in Table 4.7. \* = Wilson *et al.* (2007), \*\* = this study, \*\*\* = Harris *et al.* (2009c).



Table 4.7 Geochronology data for intrusive units and the associated mineralization at the Cadia district.

Deposit	Age (Ma)	Description	Method	Mineral	Remark	Hole number	Depth	Reference
Ridgeway	456.9 ± 7.2	pre-mineral mafic monzonite	SHRIMP $^{206}\text{Pb}/^{238}\text{U}$	titanite	diorite-monzoniorite	NC498	569	Wilson et al. (2007)
	455.8 ± 4.4	inter-mineral quartz monzonite porphyry	SHRIMP $^{206}\text{Pb}/^{238}\text{U}$	zircon	quartz monzonite porphyry (P2)	NC498	809	Wilson et al. (2007)
	442.8 ± 2.2	stage 3a quartz-chalcopyrite-molybdenite vein	$^{187}\text{Re}/^{187}\text{Os}$	molybdenite	age of Au-Cu mineralization associated with the quartz monzonite porphyry (P2)	UR360	724.5	this study
	445.7 ± 2.8	stage 3a quartz-chalcopyrite-molybdenite vein	$^{187}\text{Re}/^{187}\text{Os}$	molybdenite	age of Au-Cu mineralization associated with the quartz monzonite porphyry (P2)	UR033		this study, Harris et al. (2009c)
	443.9 ± 2.0	early-mineral monzonite***	$^{206}\text{Pb}/^{238}\text{U}$ (LA-ICPMS)	zircon	mafic monzonite porphyry (P1)	NC500	719	Harris et al. (2009c)
Cadia Quarry	443.0 ± 4.9	early-mineral monzonite***	$^{206}\text{Pb}/^{238}\text{U}$ (LA-ICPMS)	zircon	mafic monzonite porphyry (P1)	NC498	722	Harris et al. (2009c)
	444.5 ± 3.4	inter-mineral monzonite**	$^{206}\text{Pb}/^{238}\text{U}$ (LA-ICPMS)	zircon	quartz monzonite porphyry (P2)	NC498	809	Harris et al. (2009c)
	442.0 ± 4.9	Inter-mineral monzonite**	$^{206}\text{Pb}/^{238}\text{U}$ (LA-ICPMS)	titanite	quartz monzonite porphyry (P2)	NC519	745	Harris et al. (2009c)
	443.3 ± 9.7	monzodiorite	$^{206}\text{Pb}/^{238}\text{U}$ (LA-ICPMS)	titanite	diorite-monzoniorite	NC500	796	Harris et al. (2009c)
	456.4 ± 5.1	pre-mineral quartz monzonite porphyry	SHRIMP $^{206}\text{Pb}/^{238}\text{U}$	zircon		NC083	35	Wilson et al. (2007)
	450.7 ± 2.1	transitional stage quartz-chalcopyrite-molybdenite vein	$^{187}\text{Re}/^{187}\text{Os}$	molybdenite		NC083	35	Wilson (2003)
	459.7 ± 1.4	transitional stage quartz-chalcopyrite-molybdenite vein	$^{187}\text{Re}/^{187}\text{Os}$	molybdenite		NC486	431	Wilson et al. (2007)
	453.4 ± 4.3	pre-mineral quartz monzonite porphyry	SHRIMP $^{206}\text{Pb}/^{238}\text{U}$	zircon		NC486	467	Wilson et al. (2007)
	443.5 ± 1.4	transitional stage quartz-molybdenite-chalcopyrite-calcite vein	$^{187}\text{Re}/^{187}\text{Os}$	molybdenite		NC486	468	Wilson et al. (2007)
	436.5 ± 3.5	pre-mineral quartz monzonite porphyry	SHRIMP $^{206}\text{Pb}/^{238}\text{U}$	zircon		NC486	608	Wilson et al. (2007)
Cadia Hill	438.2 ± 4.2	transitional stage muscovite	$^{40}\text{Ar}/^{39}\text{Ar}$	muscovite	Au-Cu mineralization			Foster and Secombe (2004)
	440.0 ± 10	diorite	$^{206}\text{Pb}/^{238}\text{U}$ (LA-ICPMS)	titanite		CH019	74	Harris et al. (2009c)
	447.5 ± 1.5	intermediate monzodiorite	$^{206}\text{Pb}/^{238}\text{U}$ (LA-ICPMS)	zircon		NC489	98	Harris et al. (2009c)
	448.4 ± 2.8	silicic monzonite	$^{206}\text{Pb}/^{238}\text{U}$ (LA-ICPMS)	zircon		CQ089	97	Harris et al. (2009c)
	444.7 ± 2.1	molybdenite vein	$^{187}\text{Re}/^{187}\text{Os}$	molybdenite		CR57/CR70		Harris et al. (2009c)
	439.0 ± 6.0	pre-mineral quartz monzonite porphyry	SHRIMP $^{206}\text{Pb}/^{238}\text{U}$	zircon		NC052	116	Wilson (2003)
	435.9 ± 3.7	pre-mineral quartz monzonite porphyry	SHRIMP $^{206}\text{Pb}/^{238}\text{U}$	zircon		NC384	200	Wilson et al. (2007)
Cadia East	442.9 ± 1.4	transitional stage quartz-chlorite-molybdenite vein	$^{187}\text{Re}/^{187}\text{Os}$	molybdenite		NC384	200	Wilson et al. (2007)
	435.4 ± 0.5	hydrothermal white mica	$^{40}\text{Ar}/^{39}\text{Ar}$	white mica		NC047	251	Wilson (2003)
	451.0 ± 1.4	premineral monzonite porphyry	SHRIMP $^{206}\text{Pb}/^{238}\text{U}$	zircon		NC475	1247	Wilson et al. (2007)
	437.1 ± 3.0	intermineral monzonite porphyry	SHRIMP $^{206}\text{Pb}/^{238}\text{U}$	zircon		NC556	1289	Wilson (2003)
	441.8 ± 1.4	transitional stage quartz-calcite-molybdenite-bornite vein	$^{187}\text{Re}/^{187}\text{Os}$	molybdenite		NC335W	959	Wilson et al. (2007)

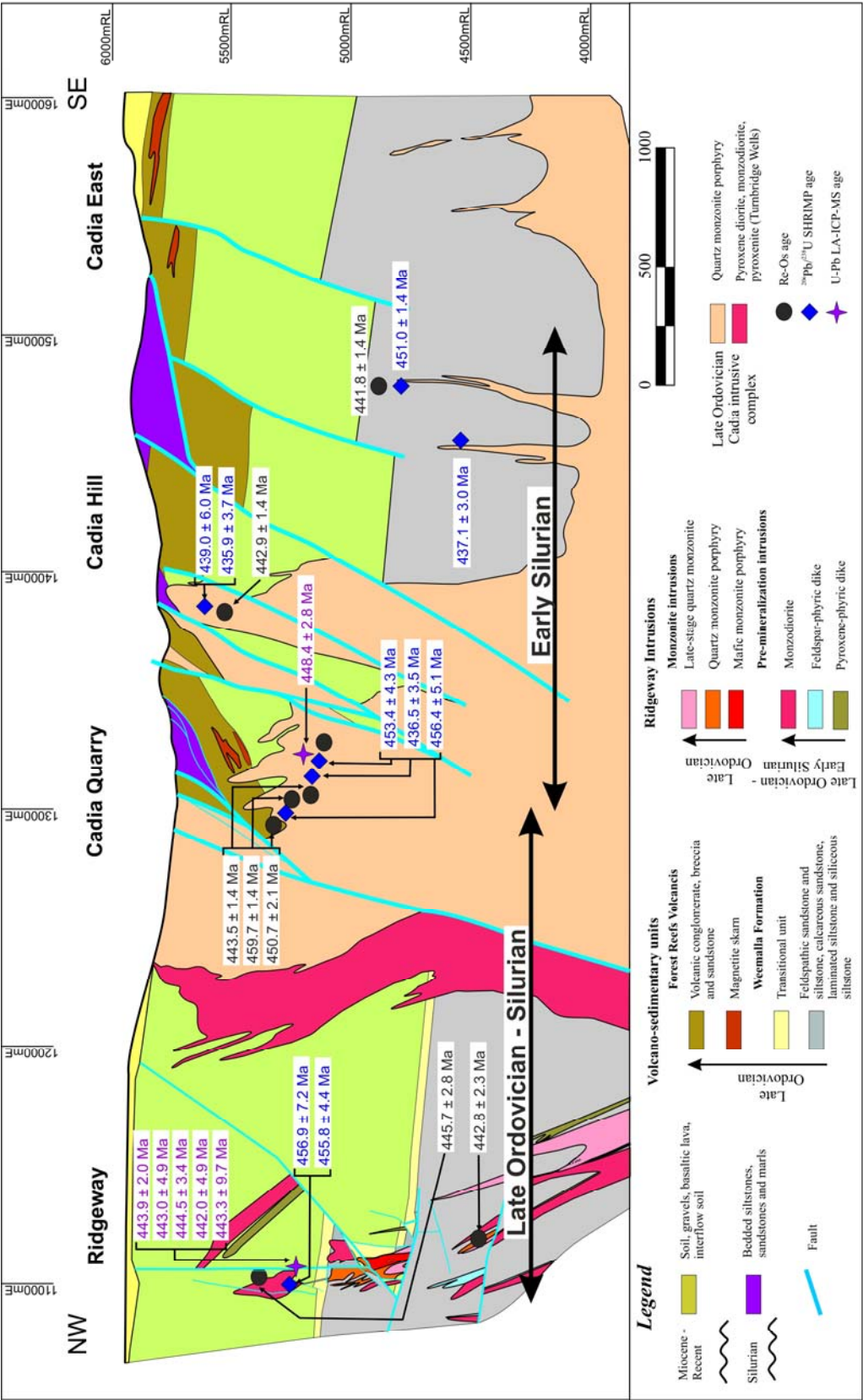


**Figure 4.26** Interpreted NW-SE long section showing the summary of available geochronology for the Cadia district. Modified from Harris *et al.* (2009c). Data summarized in Table 4.7.

## 4.8 Summary

- At Ridgeway, discrete vein stages and associated hydrothermal alteration assemblages were associated with the emplacement of each monzonite intrusion. Contrasting compositional differences in host rocks (i.e. Weemalla Formation, FRV and monzodiorite) causes them to react differently to hydrothermal fluids.
- Quartz  $\pm$  albite, garnet–epidote alteration and actinolite–magnetite–albite alteration assemblages are well-developed in the Weemalla Formation. Pre-mineralization stage 1 veins are associated with the monzodiorite intrusion. Sulfides are absent from these veins.
- Strong K-silicate alteration (inner) characterizes the core of the orebody and the intensity of alteration is a function of stage 2 vein abundance. Stage 2 veins are associated with the emplacement of P1.
- Moderate K-silicate alteration (outer) developed during and/or after the intrusion of P2, and forms a shell around the inner K-silicate alteration zone. Stage 3 veins are associated with the emplacement of P2. The wider distribution of mineralized stage 3 veins extend the zone of Cu-Au mineralization to distances of up to 300 m laterally from the center of the orebody.
- Chlorite–epidote–hematite (propylitic) alteration forms a broad shell around the inner and outer K-silicate alteration zones and has overprinted all earlier-formed alteration assemblages. Stage 4 veins formed mainly in this zone.
- Pervasive albite–quartz–pyrite–sericite alteration occurs in the upper and distal portions of the FRV. This alteration assemblage defines a cap above the epidote–chlorite–hematite-altered zone.
- Au and Cu deposition occurred principally during stage 2 and lesser amounts were added during stage 3. Ore grade decreased markedly through time with each successive porphyry intrusions (from P1 through P3).
- Absolute age constrain (U-Pb zircon and Re-Os molybdenite) indicate that intrusive activity and associated mineralization-hydrothermal alteration at Ridgeway occurred at  $444.2 \pm 1.3$  Ma, a few million years older than the other porphyry-related deposits at the Cadia district.

---

# Chapter 5: Structural Geology

---

## 5.1 Introduction

The link between magmatism and the dynamic structural environment in which porphyry ore deposits form has been a subject of discussion for decades (e.g. Rehrig and Heidrick, 1972, 1976; Gustafson and Hunt, 1975; Heidrick and Titley, 1981; Titley, 1993; Proffett, 2003; Cannell *et al.*, 2005). A complete understanding of the formation of porphyry ore deposits requires a knowledge of both geochemical and structural controls, and the variation in their size and metal concentration may be influenced by either phenomenon. Given the diverse array of geologic environments in which they form, no broad consensus exists on what localizes porphyry ore deposits at the regional scale (e.g. Sillitoe, 1993; Richards, *et al.*, 2001). Most studies have focused on the structural controls on vein and fracture distribution in and around the intrusive centre (e.g. Heidrick and Titley, 1982; Cannell *et al.*, 2005; Gruen *et al.*, 2010).

Stockwork veins, vein arrays and fractures are prominent ore-controlling structures in porphyry-style deposits. Early studies by Rehrig and Heidrick (1972), Titley and Heidrick (1978) and Heidrick and Titley (1982) showed that fractures have systematic, non-random patterns (Tosdal and Richards, 2001). In many porphyry systems, the orientation of the fractures appears to be controlled by brittle failure of the rock column prior to or during magma emplacement into the deposit (Lenzt, 1994).

This chapter documents the geometric and timing relationships between mesoscopic structural elements at Ridgeway (i.e. fractures and veins) with the aim of understanding the emplacement mechanism of the Ridgeway intrusive complex. The structural study attempts to ascertain the dominant structural orientations for each paragenetic stage, so as to determine how emplacement of intrusions and veins related to the far-field crustal stress of the district and the more localized stress and fluid pressure related to episodic magma emplacement. Vein orientations measured

from underground and from drillcore were documented and placed in the previously documented paragenetic framework (outlined in Chapter 4 and summarized in Table 5.1). Additional control on the structural interpretation is provided with use of structural data collected from underground exposures by Newcrest geologists throughout the development of Ridgeway.

## 5.2 Field methods and data presentation

Drillcore structural measurements were collected during this study using “core-orientation equipment” (Fig. 5.1). This equipment is a core cradle that holds the core in its correct plunge and azimuth so that the dip and dip direction of structures can be measured. The data were collected from drillholes that mostly trend NE, with few NW orientations (Fig. 3.2). Limited data were measured from drillholes trending E. Before measuring the orientation of the veins, the equipment was set up on a flat surface with the notched cradle facing the trend of the hole (as determined from downhole surveys). The half-core sample was then placed on the slot, with the orientation lines in place (Fig. 5.1). The dip and dip direction of the veins were then measured using a compass. This equipment was used to take ~640 structural readings from oriented drillholes.

Data collected from drillholes are compared here with measurements made



**Figure 5.1** “Core-orientation cradle” used to measure the dip and dip direction of structures from oriented drillcores at Ridgeway.

during underground mapping. A total of ~160 vein orientation measurements were measured underground from three development drives during this study. All the data collected during the current study are presented as “dip-direction/dip” (e.g. 310/70°NE) for planes. The data are grouped according to the established vein paragenesis. All structural measurements are plotted on the lower hemisphere of an equal area (Schmidt) projection.



Structural data extracted from the Newcrest digital database are also presented in this chapter for comparative purposes. As veins in the Newcrest database are not classified according to vein stages, the structure type and mineral assemblage were used to filter the data and classify them into probable vein stages (Table 5.1). In total, 696 vein measurements were selected from the Newcrest database. Assessment of structural data collected by Newcrest that had been collated on 1:200 scale maps of underground development was also undertaken in order to ascertain the dominant vein strikes at three levels. Vein data were digitized from geology and structural mapping underground from three level plans: 5100mRL, 5255mRL and 5330mRL.

**Table 5.1** Summary of vein stages from Ridgeway.

Vein Stage	Infill		Shape, internal texture, distribution and occurrence
	Major minerals	Thickness	
Pre-main mineralization stage veins			
Stage 1A	Magnetite	1 - 20 mm	Discontinuous, locally as thin sheeted veinlets; abundant in monzodiorite (MzD), Forest Reefs Volcanics (FRV) and Weemalla Formation
Stage 1B	Magnetite, actinolite	1 - 50 mm	Irregular and discontinuous fibrous bands. Abundant in MzD, and FRV, few in Weemalla Formation
Main mineralization stage veins			
Stage 2A	Quartz, magnetite	3 - 20 mm	Continuous, subparallel, sinuous to straight-sided; occur as veins in the upper portion and margins (50 m from the contact) of the mafic monzonite (P1)
Stage 2B	Quartz, magnetite, bornite	5 - 100 mm	Continuous, sharp vein walls; characterized by dark-grey quartz with banded magnetite ± bornite ± chalcopyrite; occur as dense stockwork veins in the upper portion and margins, 10 m from the contact of P1
Stage 2C	Orthoclase, quartz	2 - 10 mm	Continuous, subparallel, sharp vein walls; occur as aplitic dikes
Stage 2D	Quartz, bornite	5 - 20 mm	Continuous, sharp-edged; sulfides occupy the central seam; veins occur in the surrounding wallrocks and within 100 m of the contact of P1
Stage 3A	Quartz, chalcopyrite	5 - 50 mm	Continuous, subparallel, straight-edged walls; chalcopyrite occupies a central band or occurs as discrete aggregates throughout the vein; typically occurring as sheeted veins; occur throughout the central portion of the deposit and extend up to 200 m from the quartz monzonite (P2)
Stage 3B	Orthoclase, quartz	1 - 30 mm	Continuous, straight-sided; occur in parallel sets or sheeted veins
Stage 3C	Chalcopyrite, epidote	2 - 20 mm	Continuous to discontinuous, wavy-edged to diffuse vein walls; characterized by the presence of epidote selvages intimately intergrown with sulfides; occur proximal and distal to the deposit
Stage 3D	Quartz, chlorite	2 - 20 mm	Continuous, well developed in the deeper part of the system hosted in P2 intrusions as sheeted veins; locally, sinuous to wavy veins hosted in Weemalla Formation
Late stage veins			
Stage 4A	Pyrite, quartz	1 - 40 mm	Continuous, wavy to straight-sided; typically, pyrite occupies a central band on the quartz veins, locally pyrite occurs as stringers/veinlets/veins
Stage 4B	Epidote	1 - 10 mm	Continuous to discontinuous, undulating, vary from planar to more irregular diffuse veins
Stage 4C	Chlorite	centimetre to meters	Angular to subrounded, clast- to matrix- supported breccia
Stage 4D	Calcite	5 - 50 mm	Continuous, straight-sided, sharp contact with wallrocks; locally occurring as late infill to stage 4B veins

The local grid at Cadia is called the Cadia Mine Local (CML). It is aligned at 32° east of grid north of the national Australian Map Grid (AMG/GDA94) system. All orientations in this chapter are discussed with reference to the AMG not the local CML. The Relative Level (mRL) used at the mine sets sea level to + 5000 meters.

### 5.3 Previous Work

Several structural models have been proposed to explain the geometry of Ridgeway. Holliday *et al.* (2002) highlighted the occurrence of a pre-existing NW-trending structural corridor that controlled intrusive activity and mineralization. Wilson *et al.* (2003) interpreted the steeply-dipping WNW-striking “normal” fault (North Fault) that bounds the northeastern portion of Ridgeway to have played a role in the emplacement of the Ridgeway intrusive complex.

Marjoribanks (2005) argued that faults at Ridgeway developed during four deformational events. Initial NNE-SSW extension controlled the intrusion of steeply-dipping WNW-striking mafic to intermediate dykes. The second event produced a WNW-ESE oriented right lateral strike-slip fault during NNW-SSE compression. A NNW striking fault bend that developed in the fault system became a zone of extension, marked at Ridgeway by normal faulting, where blocks of the volcanic and sedimentary rocks were downthrown 300 m. The third event occurred after the formation of the orebody and produced steeply-dipping reverse faults as consequence of E-W compression. The North Fault and the Hangingwall Faults were initiated at this stage. Later movement took place along a 50°S-dipping thrust fault (Purple Fault) and displaced the orebody by up to 80 meters to the NNE. The final deformation event produced a series of shallow NNE-dipping thrusts faults that displaced all earlier structures. In summary, Marjoribanks’ (2005) genetic model suggested that Ridgeway formed in a dilational jog. He interpreted the intrusive bodies on level plans to have sigmoidal shapes, and that older intrusions had been rotated clockwise relative to younger intrusions.

Most recently, Harris *et al.* (2009b) conducted a structural analysis and reconstruction of the dismembered porphyry deposits of the Cadia Valley. They suggested the presence of E-W oriented sub-basins that localized fractures and fault-

related features like dikes, stocks and veins. According to Harris *et al.* (2000b), the emplacement of porphyry intrusions occurred during the periods of basin inversion and relaxation phase of the Benambran Orogeny. Washburn (2008) described post-mineralization deformation in the Silurian Waugoola Group sedimentary cover rocks of the Cadia district. She concluded that the faults and folds measured at the surface in the sedimentary cover can be used as a predictive tool to infer basement structures at depth.

## **5.4 Structure of the Cadia district**

The structural evolution of the Macquarie Arc, where the Cadia district is located, is long and complex (Chapter 2), and has influenced the structural architecture. Several deformation phases have been recognised in the Cadia district (Harris *et al.*, 2009b). Most of the shortening has been accommodated by the Early Ordovician rocks which have been deformed locally by reverse faults (Fig. 5.2). Structural dismemberment occurred after the early Silurian, with numerous overprinting brittle deformation events (Washburn, 2008).

### **5.4.1 Regional-scale structures**

Two dominant regional structures are evident in the Cadia district and vicinity. The earliest formed regional structures are the N-striking Wyangalla-Werribee Fault Zone and subsidiary faults (Fig. 5.2). The Werribee Fault has been described by Glen (1998) as a N- to NE-striking, W-dipping thrust (with a strike-slip components) that continues into the Cadia district (mapped and named locally as the Cadiangullong Fault System). The Werribee Fault juxtaposed Ordovician volcanics on western side with Silurian sedimentary rocks on the east (Glen, 1998).

The second generation of regional structures are related to the WNW striking fault zone (Fig. 5.2) that is correlated with the LTZ (Fig. 2.2). The LTZ is a crustal-scale WNW-striking structural zone believed to have played a fundamental role in localizing volcanism and mineralization in the Macquarie Arc (Glen and Wyborn, 1997; Glen *et al.*, 2007a). In the Cadia district, regional magnetic data highlight a strong northwest alignment of faults and intrusions (Fig. 2.8). It appears likely that

the LTZ facilitated and localized the emplacement of the Cadia intrusive complex (Holliday *et al.*, 2002).

#### **5.4.2 District-scale structures**

District-scale faults in Cadia are classified into three major sets based on their association with the major regional structures and their orientation (Washburn, 2008; Harris *et al.*, 2009b). These are: a) N-NE- and NW-striking major thrust faults, exemplified by the Cadiangullong Fault System, b) W-NW oriented faults, and c) E-trending faults.

The Cadiangullong Fault System (Fig. 5.2) is characterized by N-NE- and NW-striking major thrust faults that juxtapose the major lithological units. The NW-striking, SW-dipping Cadiangullong Fault bounds the Cadia Hill deposit on the west and placed the Silurian sedimentary cover in fault contact with the quartz monzonite porphyry (Fig. 5.2; Holliday *et al.*, 2002). The Gibb Fault (Fig. 5.2) is a NE-striking reverse fault, dipping  $\sim 50^\circ$  NW with a minimum displacement of 300 m. It defines the eastern margin of Cadia Hill which is in fault contact with the western end of Cadia East (Holliday *et al.*, 2002; Harris *et al.*, 2009b; Fig 5.2). Parallel to the Gibb Fault is a NE-striking, steeply NW-dipping fault which separates Cadia Quarry from the northern end of Cadia Hill (Holliday *et al.*, 2002). The NW-striking Purple Fault is another major thrust fault. Its dips  $\sim 65^\circ$  SW and is inferred to separate the Turnbridge Wells Diorite from the quartz monzonite porphyry (Fig. 5.2; Tedder, 2002 in Wilson, 2003).

Two major W-NW-oriented faults occur in the Cadia district. The PC40 Fault is a major NW-striking reverse fault. This steeply dipping ( $\sim 80^\circ$  SW) fault splits the Big Cadia skarn deposit on its southern side, south block down (Fig. 5.2; Green, 1999). About 80 - 100 m vertical displacement is inferred for this fault at Big Cadia (Green, 1999). The PC40 fault is interpreted as a strike-slip fault with the south-side down and towards the east, mechanically linked with the strike-slip portion of the Cadiangullong Fault (Groome and Munro, 2009).

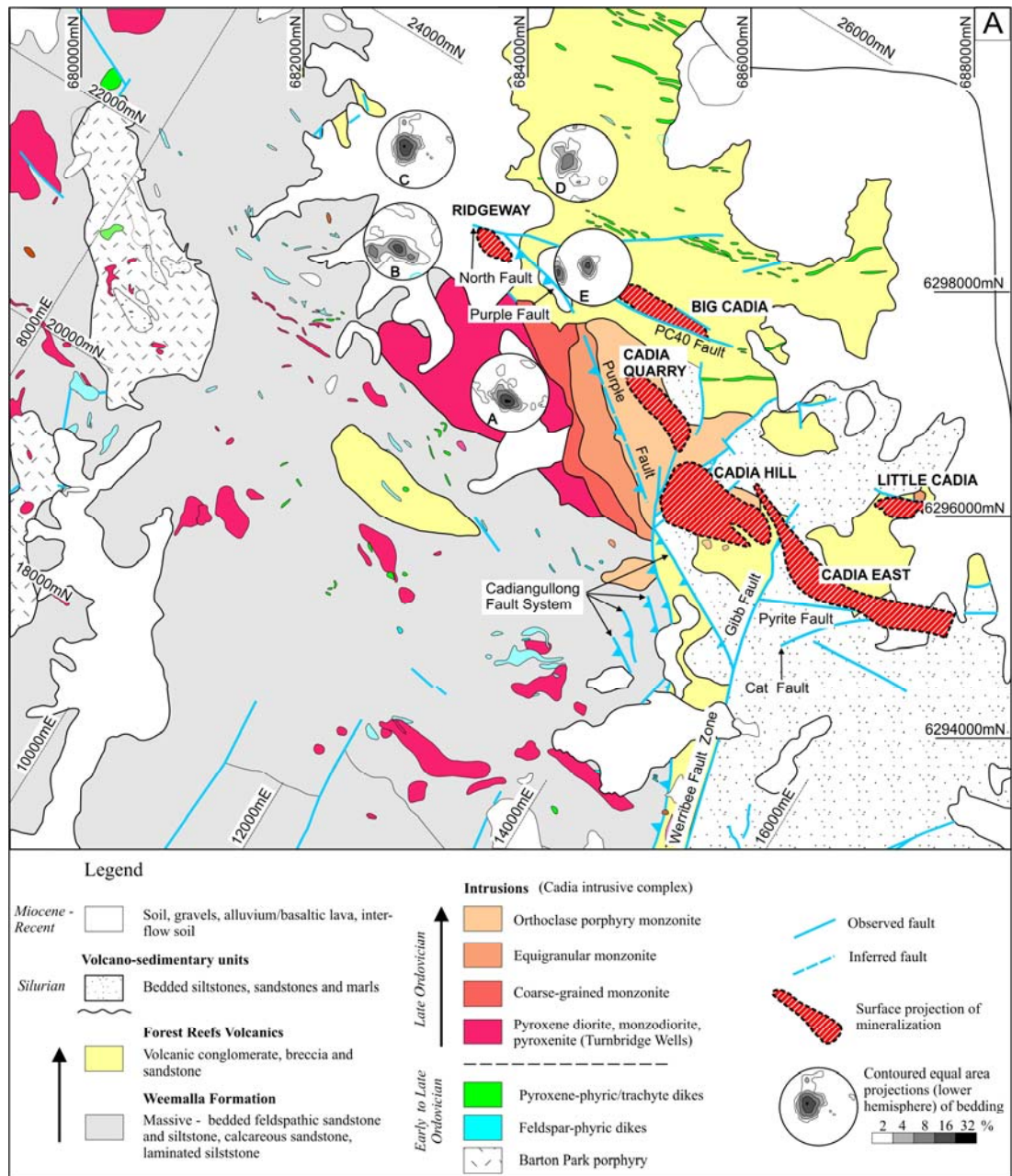


**Figure 5.2** Simplified surface geology map of the Cadia district showing the major rock units, mineral deposits and major structures (modified from Holliday *et al.*, 2003 and Newcrest Mining Limited, 2006). At Ridgeway, the North Fault and the Purple Fault are projected to the surface from underground mapping. Equal area projections (lower hemisphere) of bedding orientations in the Weemalla Formation peripheral to Ridgeway are plotted using data from Newcrest's digital database. Bold letters correspond to domain as summarized in Table 5.2.

The North Fault has been observed in Ridgeway's underground workings. It has a NW-striking near-vertical dip, but has no significant offset of the orebody (Figs. 5.2 and 5.5). Thickness variations of volcanic units across the fault indicate that the North Fault was active during sedimentation (Holliday *et al.*, 2002, Wilson *et al.*, 2003). The North Fault has a similar orientation to the PC40 Fault, which led



Tedder (2002) to suggest that the North Fault at Ridgeway is a northwestern extension of the PC40 Fault. These faults are oriented subparallel to the LTZ.

## **5.5 Structures at Ridgeway**

### **5.5.1 Folds**

Evidence for gentle folds and warps of the laminated siliceous siltstones, of the Weemalla Formation, come from evaluation of the available bedding data (measured from oriented drillcore; Fig. 5.3). Folds in the quartz  $\pm$  albite-altered siltstones are cut by late-stage pyrite veins (stage 4A; Table 5.1; Fig. 5.3B), which suggests that folding occur prior to the development of stage 4 veins. However, the timing of folding relative to pre-mineralization quartz  $\pm$  albite and garnet–epidote alteration assemblages is not certain (Fig. 5.3C). It is possible that folding occurred prior to these alteration events, which would imply ductile deformation occurred prior to the intrusion of the monzonite suite (P1 and P2), but after the emplacement of the MzD.

Bedding measurements from drill core indicate shallow to moderately dipping beds. Figure 5.4 shows poles to bedding separated into domains, mostly measured from oriented drillholes southeast of the deposit. Domain 1 (Fig. 5.4A and Fig. 5.6C), located on the hanging wall of the Claudia Fault and the Purple Fault, has a preferred mean of 35° dipping towards the northeast. Domain 2 (Fig. 5.4B and Fig. 5.6D), located on footwall of the Claudia Fault and hanging wall of the Pamela Fault, has a fold axis plunging 2°SE. This could be interpreted as evidence that Domain 2 has undergone ~13° of block rotation across the Pamela Fault. A fold axis plunging 16°NW was calculated from bedding in the footwall of the Pamela Fault for Domain 3 (not plotted).

Bedding orientations in the Weemalla Formation peripheral to Ridgeway are summarized in Table 5.2. All of the bedding measurements were filtered from Newcrest's digital database. Bedding in Domains A, C and D (Fig. 5.2) generally strikes N-NW and dips 14° to 24°E-NE. On the western and eastern sides of the deposit (Domains B and E, Fig. 5.2), stereonet of poles to bedding show gently and

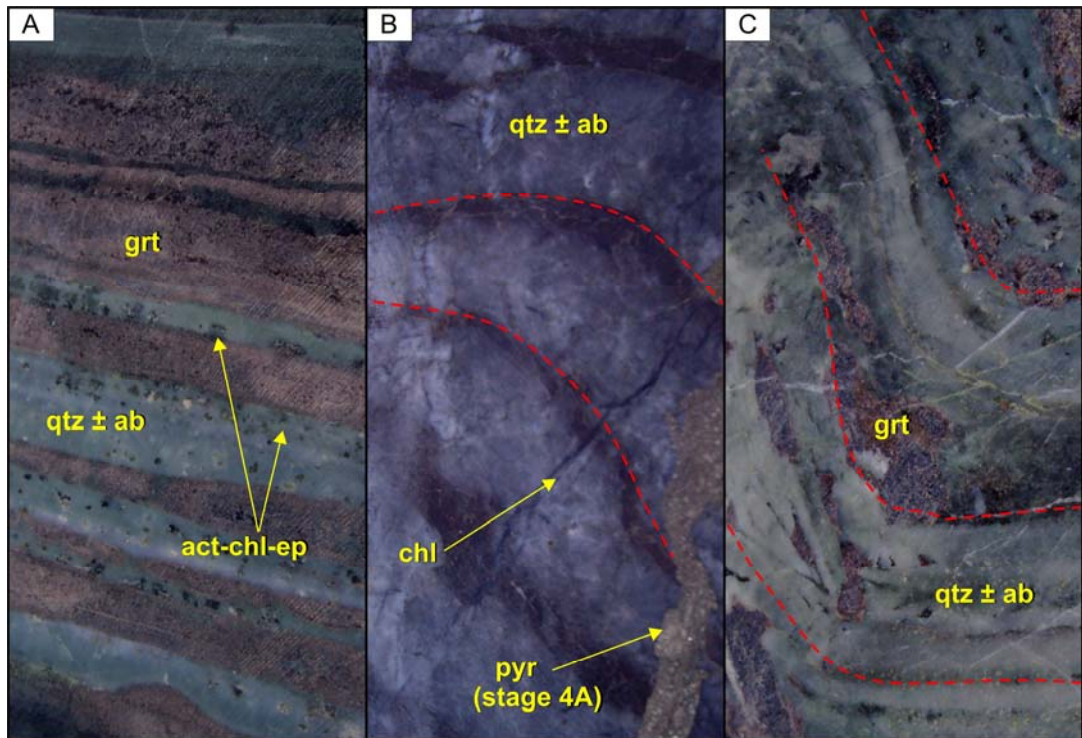


**Figure 5.3** Tilting and folding in the siliceous laminated siltstone and sandstone units of the Weemalla Formation from Ridgeway. **A)** Gently-dipping, NW-striking siltstone interbedded with garnet-altered calcareous sandstone (UR362-666m). **B)** Folded layers (marked by red dashed-line) cut by stage 4A pyrite vein and chlorite stringers (UR362-561.9m). **C)** Folded layers (marked by red dashed-line) in siliceous laminated siltstone and garnet-altered calcareous sandstone (UR362-665m). Abbreviations: ab = albite, act = actinolite, chl = chlorite, ep = epidote, grt = garnet, pyr = pyrite, qtz = quartz

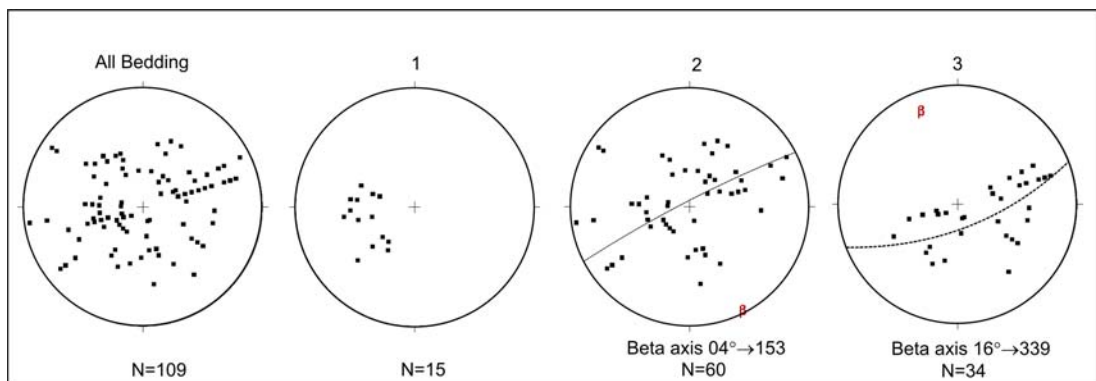


**Figure 5.4** Compilation on equal area projections (lower hemisphere) of bedding orientations in the Weemalla Formation below Ridgeway. The data have been split into domains corresponding to the hanging wall and footwall sides of the Claudia Fault and Pamela Fault. Domain 1 consists of all bedding on the hanging wall of the Claudia Fault and the Purple Fault (Fig. 5.6C). Domain 2 is bounded by Claudia Fault and Pamela Fault (Fig. 5.6D), and Domain 3 consists of all bedding below the Pamela Fault (not plotted).

**Table 5.2** Bedding orientations in the Weemalla Formation from structural domains peripheral to the Ridgeway orebody, plotted in Figure 5.1. Locations are described with respect to the Ridgeway deposit. Data from Newcrest's digital database.

Domain	Number of points	Strike	Dip	Location
Domain A	71	NW	14°NE	South
Domain B	103	NW	14°NE	West
		NW	65°NE	
Domain C	85	NNE	23°E	Northwest
Domain D	43	NNE	25°E	Northeast
Domain E	39	NNW	10°E	Southeast
			80°E	

steeply-dipping bed orientations with fold axis gently plunging to the northwest. These regional bedding orientations correspond with the bedding orientations below the Ridgeway orebody as measured during this study (Domains 1 and 3; Fig. 5.4).

The presence of localized folding peripheral to Ridgeway, gently- and steeply-dipping to the northeast, can be interpreted here for the presence of monocline with fold-axis sub-parallel to the NW-striking structural grain in the district.

### 5.5.2 Faults

At Ridgeway, numerous faults are identifiable underground. Some have offset bedding and veins. Others define zones of intense brittle deformation and fracturing. The faults are classified according to their orientations, which include: NW-striking steeply-dipping faults, NW-striking SW-dipping reverse faults, NE-striking steeply-dipping faults and low-angle thrust faults. Table 5.3 summarizes the orientations and kinematic indicators for these major faults. Their locations are plotted in plan view at 5100mRL (Fig. 5.5A) and along section 11050mE, which highlight the location of the low-angle thrust faults (Fig. 5.5B). The current interpreted offsets are shown on stacked cross-sections (10950mE, 11050mE, 11150mE and 11250mE; Fig. 5.6). These faults were identified by Newcrest geologists based on their underground mapping, and their presence has been confirmed in this study from drillcore logging. The field relationships suggest that NNW-trending low-angle faults postdate the emplacement of the intrusions.

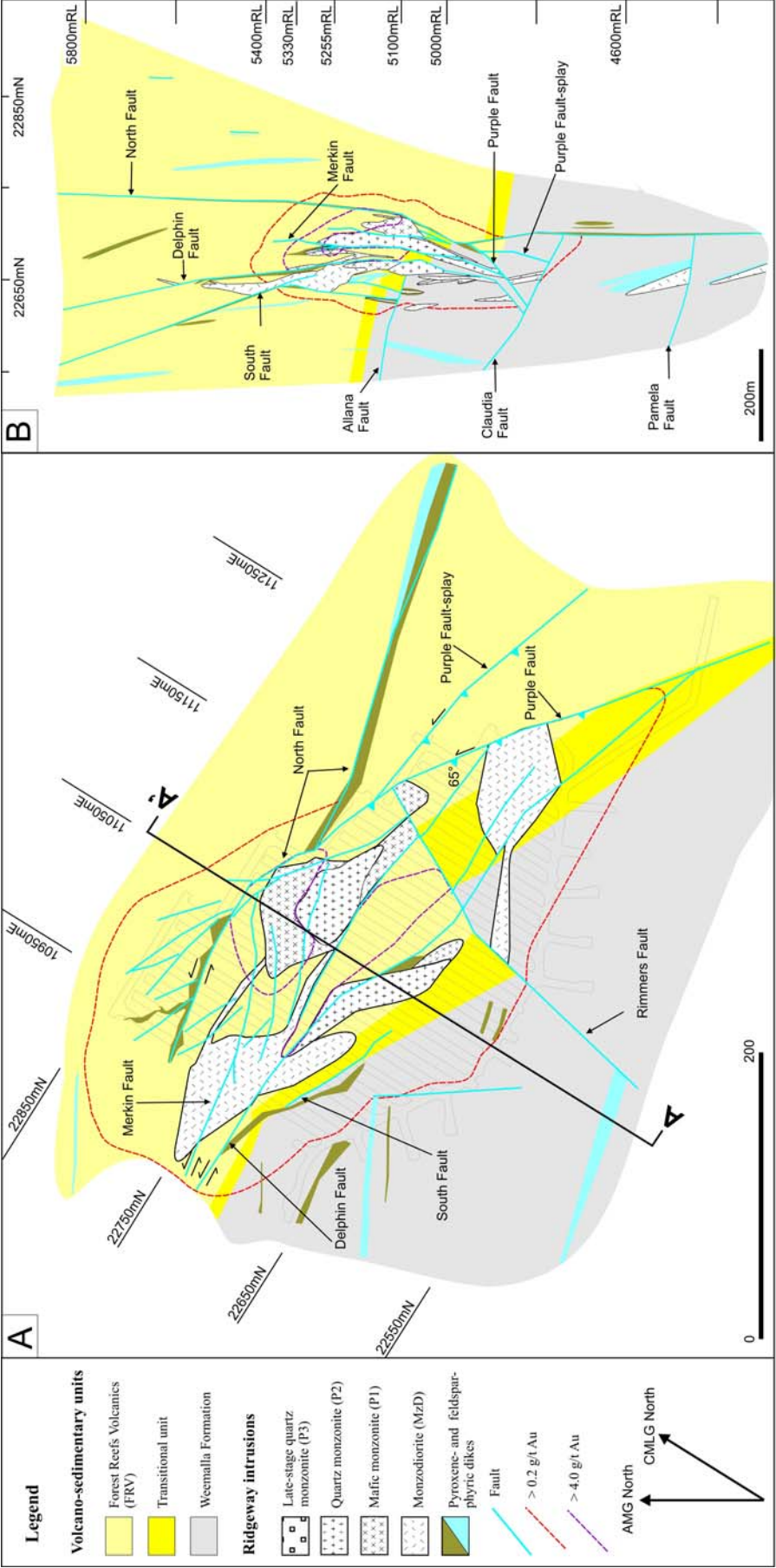
### 5.5.2.1 Northwest-striking, steeply-dipping faults

At Ridgeway the most prominent faults are steeply dipping ( $>80^\circ$ ) NW-striking shear zones and faults that have reverse offsets, as indicated by separations of stratigraphic horizons (Figs. 5.5 and 5.6). Pyroxene-phyric dikes intruded these structures, implying an early timing for fault development.

The North Fault is the largest and the most significant NW-striking fault. This steeply dipping structure bounds the north-northeast sides of the Ridgeway orebody (Table 5.3; Fig. 5.5). Pyroxene-phyric dikes are common in the footwall of the North Fault (Fig. 5.6; Kolkert and Sullivan, 2006). Where exposed underground, the fault is characterized by an intense clay–chlorite–epidote alteration zone that is 0.3 m to 1 m thick (Fig. 5.7A and B). Fragments of brecciated quartz veins occur in the shear zone at 5070mRL-XC13 (Fig. 5.7B and C), which suggests that this fault was reactivated after the development of mineralized veins. Marjoribanks (2005) has identified the presence of a strong SC fabric, and interpreted a south-block-up movement for the North Fault. Although the North Fault has been mapped at many locations underground, the eastern most extension and full depth extent have not yet been established.

**Table 5.3** Major faults at Ridgeway.

Fault	Strike	Dip - dip direction	Latest movement and displacement	Interpretation	Reference
<b>Northwest-striking, steeply-dipping faults</b>					
North Fault	NW	$80^\circ$ SW to vertical	Dip slip movement, south block-up	Pre-existing faults that are active before, during, and after mineralization; pre-mineralization pyroxene-phyric dikes occupy these faults	Holliday <i>et al.</i> (2002); Wilson, <i>et al.</i> (2003); Marjoribanks (2005); this study
Merkin Fault	NW	near-vertical	Parallel to North Fault		Kolkert and O'Sullivan (2006)
Delphin Fault	NW	near-vertical	Parallel to North Fault		Kolkert and O'Sullivan (2006)
South Fault	NW	$\sim 70^\circ$ NE	Parallel to North Fault		this study
<b>North-northwest striking, southwest-dipping reverse faults</b>					
Purple Fault and fault splays	NNW	$\sim 50^\circ - 70^\circ$ SW	Thrust upper block, 50 - 80 m horizontally to the northeast	Post-mineralization structures, displaced the intrusive complex and mineralization	Marjoribanks (2005); Kolkert and O'Sullivan (2006); this study
Rimmers Fault	NE	near-vertical	Oblique-slip movement, 35 m sinistral strike-slip and 12.5 m east-block-up	Accommodation structure or transfer fault zone to Purple Fault	Marjoribanks (2005); this study
			Pure dip-slip, 100 m east-block down		Kolkert and O'Sullivan (2006)
<b>Low-angle thrust faults</b>					
Allana Thrust Fault	NW	$10^\circ - 20^\circ$ NE	limited movement	Latest post-mineralization structures; displaced the intrusive complex at depth	Burgio (2005); Kolkert and O'Sullivan (2006)
Claudia Thrust Fault	NW	$\sim 20^\circ - 30^\circ$ NE	dip-slip, thrust upper block, 30 - 100 m to the SW		Marjoribanks (2005); Kolkert and O'Sullivan (2006)
Pamela Thrust Fault	NW	$10^\circ - 20^\circ$ NE	dip-slip, thrust upper block		Kolkert and O'Sullivan (2006); this study





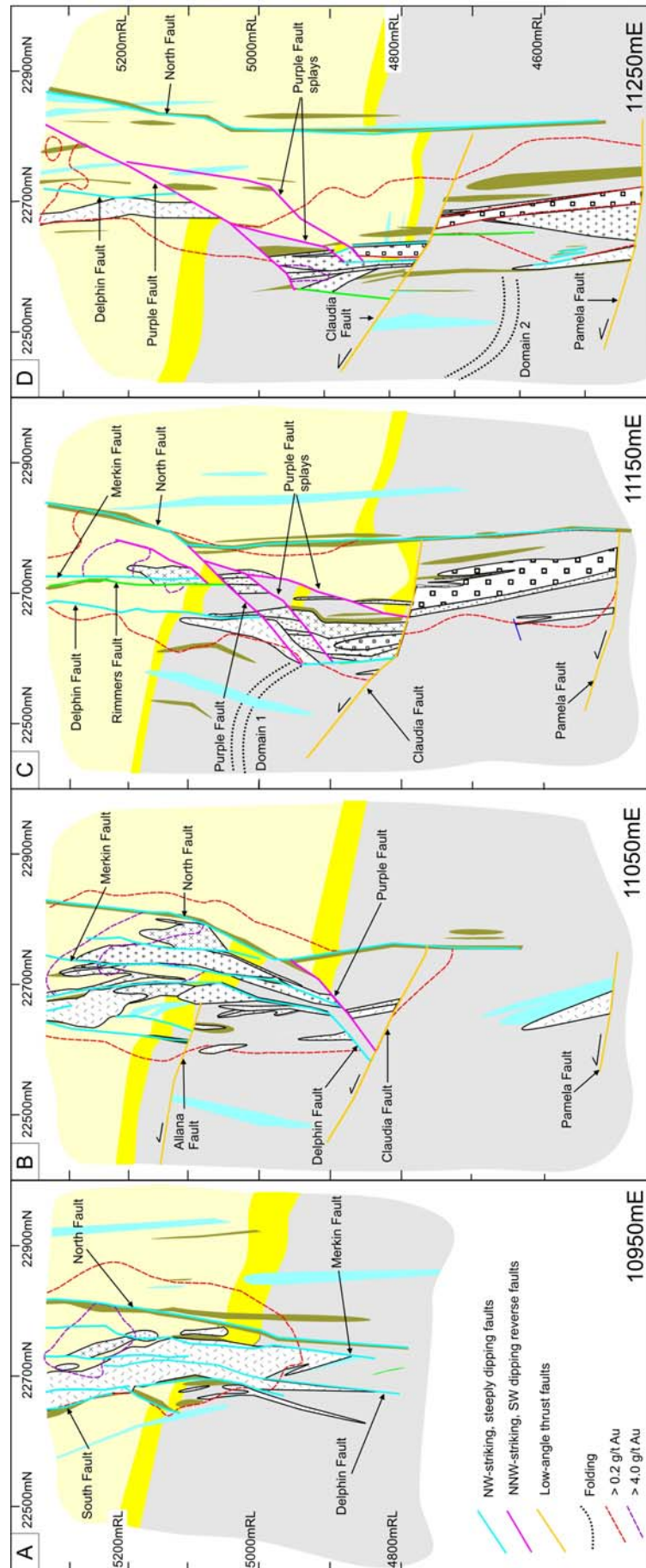


**Figure 5.6** Stacked southwest-northeast (AMG) structural sections through the Ridgeway deposit. Fault interpretations are based on underground mapping of Newcrest and on drillhole logging completed in this study. Sections are going towards the southeast. Refer to Figure 5.5 for details of rock types.

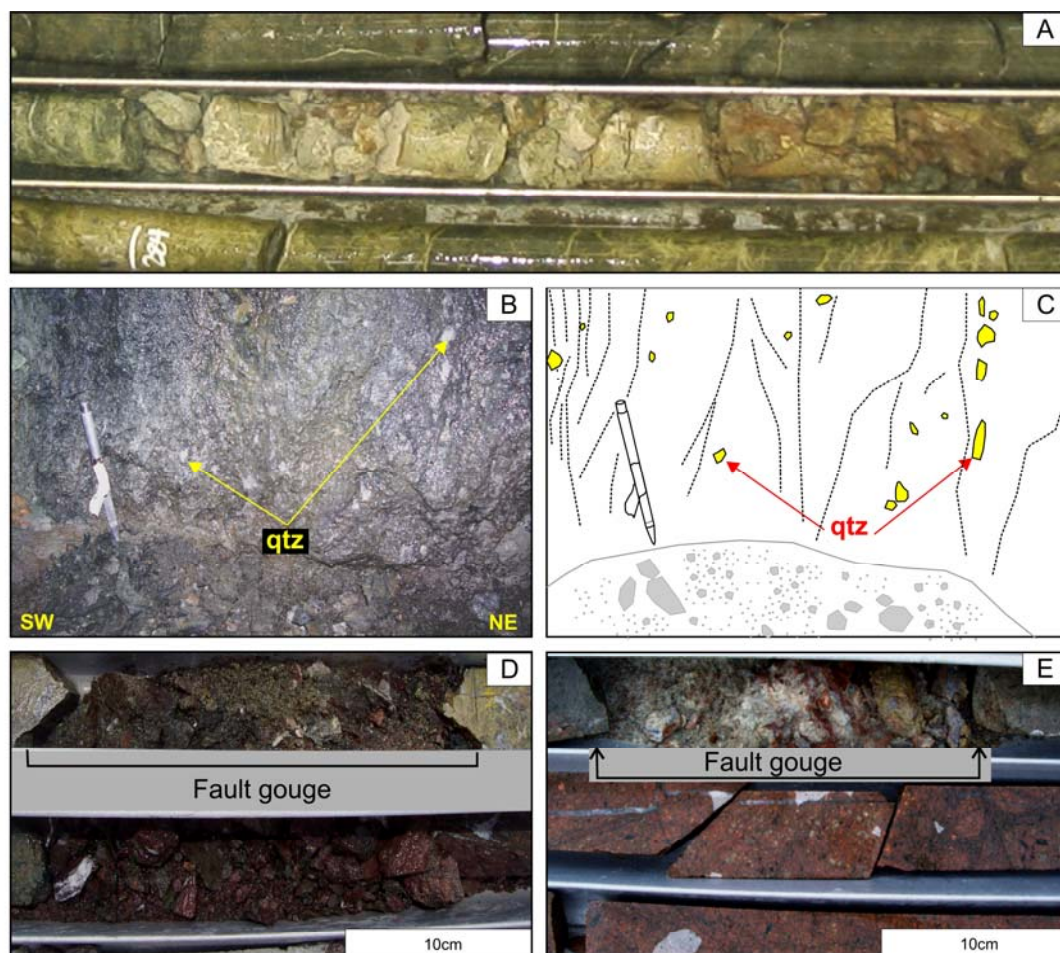


**Figure 5.7** Northwest-striking steeply-dipping faults at Ridgeway. **A)** Core photograph of North Fault (UR142-272m). **B)** North Fault exposed underground (330/85°SW), 1 m gouge zone consists of clay - chlorite - epidote with brecciated quartz fragments (5070mRL-XC13-chainage 137). The length of the scribe is 13.5 cm. **C)** Sketch figure of (B) showing the fragments of brecciated quartz veins. **D)** Core photograph of Merkin Fault, a ~20 cm shear zone comprises of clay - chlorite - epidote (UR248-148m). **E)** Core photograph of Delphin Fault, a ~15 cm shear zone of clay - chlorite with fragments of quartz veins, showing the fault contact between the mafic monzonite and the quartz monzonite (UR248-116.8m). Abbreviation: qtz = quartz

A review of underground mapping by Newcrest geologists, combined with new drill core logging results from the current study has identified several NW-striking structures that are sub-parallel to the North Fault, including the Merkin, Delphin and South Faults (Figs. 5.5 and 5.6). The Merkin Fault is a near-vertical, NW-striking fault characterized by thin ~20 cm shear zone of clay–chlorite–epidote, with fragments of quartz veins (Table 5.3; Fig. 5.7D). Locally, this fault has been cut by calcite stringers. Epidote flooding occurs around the fault zone up to 50 cm from the contact. The Delphin Fault is a steeply-dipping, NW-striking shear zone with clay–chlorite gouge (Table 5.3; Fig. 5.7E). From drillholes logged through the center of the orebody, the contact between P1 and P2 is defined by the Delphin Fault

(Fig. 5.7E). Both the Delphin and Merkin Faults are mostly occupied by altered pyroxene- and feldspar-phyric dikes that host mineralized veins. The Merkin and Delphin Faults do not persist below 4900mRL, and have either merged or have been cut by the Purple Fault (Figs. 5.6B and C; Kolkert and O'Sullivan, 2006).

The southwest side of Ridgeway is bounded by the South Fault (Table 5.3; Fig. 5.6A), a previously unrecognized steeply dipping fault (~70°NE) that has been interpreted during this study from a series of Newcrest level plans. As with the North Fault, the South Fault has been intruded by pyroxene-phyric dikes, predominantly in its footwall (Fig. 5.6A). The South Fault was verified from logged drillhole UR058 (40.6 to 44m; Appendix A), where it is characterized by the presence of a pyroxene-phyric dike, an abrupt change in gold and copper grades, and the appearance of stage 2B veins on the northwest side of the fault.

#### **5.5.2.2 North-northwest striking, southwest-dipping reverse faults**

A series of NNW-striking, SW-dipping faults have been recognized during underground mapping by Newcrest geologists and from drillcore logging below the deposit (Figs. 5.6B to D). This fault set, known locally as the Purple Fault, has truncated the intrusions and associated mineralization. The Purple Fault is a zone of reverse faulting with significant post-mineralization offset (Table 5.3). The faults in this zone have displaced both the intrusions and mineralization by as much as 80 m to the NNE (Marjoribanks, 2005). The main Purple Fault is characterized by a 60 mm domain of fault gouge surrounded by a halo of epidote–hematite alteration up to ~30 mm thick (Figs. 5.8A and B). During the current study, the Purple Fault was observed on 5100L-XC22 (chainage 91-96; Fig. 5.5A), NW-striking and dips ~65° to the SW (Fig. 5.8A). In the footwall, displacements of lithologic units and mineralization have occurred on several minor fault planes (Fig. 5.6B to D). In plan, the Purple Fault curves as it approaches the North Fault towards the northwest (Fig. 5.5A). It may have offset the North Fault and associated dikes (Fig. 5.5A), but this is not clear from the available data.





**Figure 5.8** North-northwest striking low-angle thrust faults at Ridgeway. **A)** Purple Fault exposed underground (340/65°SW), comprise of 6 cm clay - epidote - hematite fault gouge with up to 30 cm epidote - hematite alteration halo from the contact (5100mRL-XC22-chainage 96). **B)** Drillcore intersections of Purple Fault zone (yellow box) characterized by a 3.5 m zone of pervasive epidote - hematite alteration (UR142-152-155.5m). **C)** Photograph of Rimmers Fault (yellow box) characterized by a 1 m pervasive quartz - carbonate alteration halo. The fault contact separates the pyroxene-phyrlic dike and volcanoclastic sandstone (UR231-120-121m). **D)** Drillcore intersection of the Allana Fault with an extensive quartz - carbonate alteration halo transected at 5100mRL (UR140-24-37m). **E)** Photograph of Claudia Fault (yellow box; UR362-178.7m). **F)** Photograph of Pamela Fault (yellow box; 050/10°NW), a 7.5 cm cemented fault breccia with epidote flooding. This fault marked the sharp contact of the late-stage quartz monzonite (hanging wall) and monzodiorite (footwall). Quartz - carbonate alteration haloes are well developed on the monzodiorite (UR360-836m). Abbreviations: ep = epidote, hem = hematite

Rimmers Fault is a NE-striking vertical structure that appears to terminate against the Purple Fault (Table 5.3; Fig. 5.5A). Where exposed, the fault is characterized by a 1-cm wide shear zone filled with clay that has a thin, carbonate-bleached, 1-m wide alteration halo (Fig. 5.8C). The Rimmers Fault was reported to have a 35 m sinistral-offset and 12.5 m east-block-up dip-slip movement on level 5155 (Marjoribanks, 2005). At lower elevations, P1 and the Ordovician volcano-sedimentary units are interpreted here to have similar sinistral offsets (5100mRL; Fig. 5.5A). However, a report by Newcrest geologists interpreted the dip-slip movement to be east-block-down by approximately 100 m based on grade and quartz vein mapping, with no strike-slip offset (Kolkert and O'Sullivan, 2006). A plan view map of grade contours suggests that this fault truncates gold and copper mineralization, indicating that the most recent movements occurred after ore deposition. The Rimmers Fault differs in geometry from one elevation to another and may imply that this fault is a transfer fault zone or an accommodation structure to the Purple Fault (Marjoribanks, 2005; this study). Texturally destructive alteration features obscure the location of the Rimmers Fault below the existing mine development.

### **5.5.2.3 Low-angle thrust faults**

Post-mineralization, low-angle faulting has disrupted the Weemalla Formation below the Ridgeway orebody (Figs. 5.6B to D). These shallowly dipping faults occur subparallel to bedding in laminated siltstone lithofacies of the Weemalla Formation. The thrust faults are characterized by carbonate alteration haloes of varying thickness (section 4.4.4.3). The Allana Fault is located 25 to 50 m below the transitional unit (Fig. 5.5B; Burgio, 2005; Kolkert and O'Sullivan, 2006), and is characterized by a strongly developed creamy-coloured carbonate alteration zone that is up to 2 m wide (Fig. 5.8D; Stoker, 2005). Thin gouge occurs in the fault structure (Stoker, 2005; Burgio, 2005). The Claudia Fault occurs parallel to the Allana Fault and ~300 m below it; it has been intersected in a series of drillholes (and more recently in underground exposures Kolkert, pers. comm. 2010). This fault is characterized by ~ 1 m of sheared rock with abundant carbonate veins (Fig. 5.8E Kolkert and O'Sullivan, 2006). A dip-slip movement up to 30 m was reported



(Stoker, 2005). However, this movement has not affected the Ridgeway deposit, and is interpreted to die out towards the orebody (Kolkert and O’Sullivan, 2006).

The deepest known thrust fault at Ridgeway is the Pamela Fault, which was recognized from four drillholes at 4400mRL during the current study, ~400 m below the Claudia Fault (Fig. 5.5B). The fault strikes NW and dips gently to the NE based on oriented drillcore (Table 5.3). At depth, the contact between P3 and the MzD is marked by the Pamela Fault, and is characterized by a thick cemented fault breccia locally with a quartz–carbonate alteration envelope up to 1 m from the contact (Fig. 5.8F).

## 5.6 Geometry of veins and structures at Ridgeway

There are three general types of fractures that lead to the development of macroscopic fracture networks (Cox, 2005): extension fractures, shear fractures, and hybrid extensional shear fractures (Fig. 5.9). Pure extension fractures form perpendicular to the direction of lowest compressive stress ( $\sigma_3$ ) and open perpendicular to the fracture wall (Fig. 5.9A). Shear fractures, on the other hand, typically form at angles between  $25^\circ$  and  $35^\circ$  to the orientation of the maximum principal stress for intact, isotropic rock (Fig. 5.9B) where the orientation of intermediate stress is contained in the fault plane. No dilation is predicted for these fractures. Hybrid extensional shear fractures have both components of displacement. The hybrid shear fractures form at angles between  $0^\circ$  and  $\sim 25^\circ$  relative to  $\sigma_1$ . The displacement has components that are parallel and perpendicular to the fracture plane (Fig. 5.9C). In porphyry ore systems, vein development occurs in one or more of these fracture types whose dilation is strongly orientation-dependant.

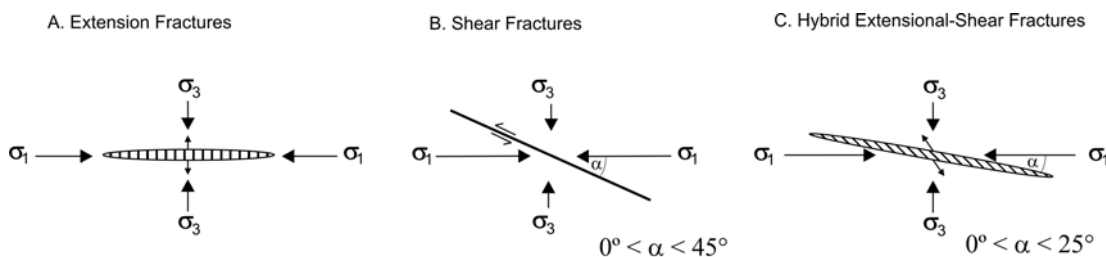


**Figure 5.9** Orientation relationships between stress fields. A) Extension fractures, B) Shear fractures, and C) Hybrid extensional fractures. Modified from Thomson and Sinclair (1990).

At Ridgeway, field observations indicate that the mineralized main stage veins, specifically stages 2A, 2B, 2D, 3A and 3D (Table 5.1), are pure extension fractures which probably formed perpendicular to  $\sigma_3$ . Cathodoluminescence imaging of quartz from stage 2D and 3A (Figs. 5.14A and 5.15A) show that these veins were deposited in open fractures, show no displacement parallel to the vein, and mostly have unstrained quartz crystals perpendicular to vein walls.

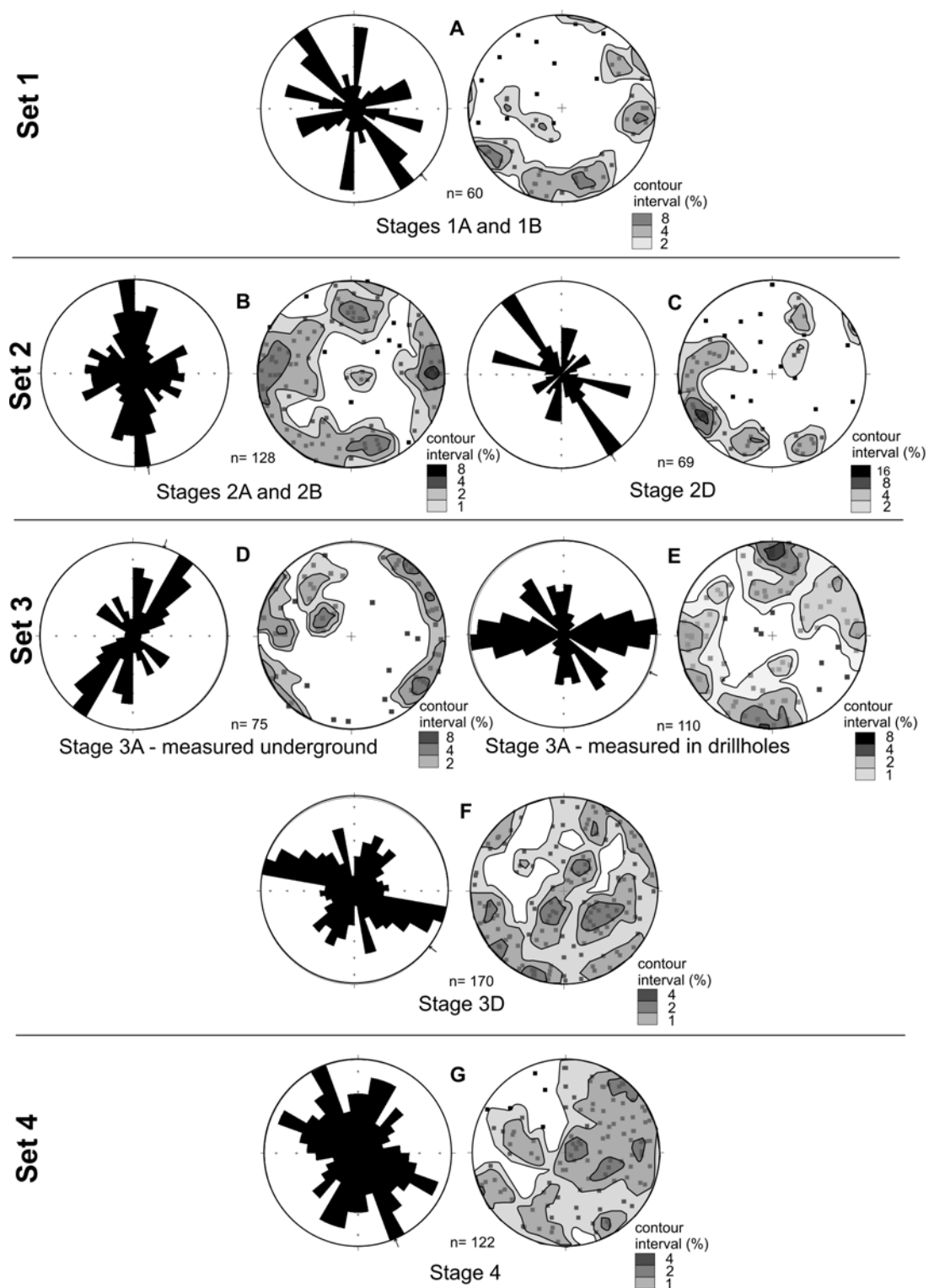
In porphyry-type deposits, fracture orientations are commonly thought to vary through time. They evolved during the hydrothermal process, reflecting the changing stress regimes imposed by the magmatic system and regional tectonic stress (Haynes and Titley, 1980; Tosdal and Richards, 2001). These observations are exemplified at Ridgeway. Based on orientation, mineralogy, and cross-cutting relationships, the vein orientation data can be separated into four temporal sets (Table 5.4; Fig. 5.10), that can be correlated with the well constrained paragenetic vein stages (Table 5.1). The orientations of these four vein sets in the different rock types at Ridgeway are plotted in Figure 5.11. In general, there are no significant differences in vein orientations between rock types.

**Table 5.4** Summary of structural sets at Ridgeway.

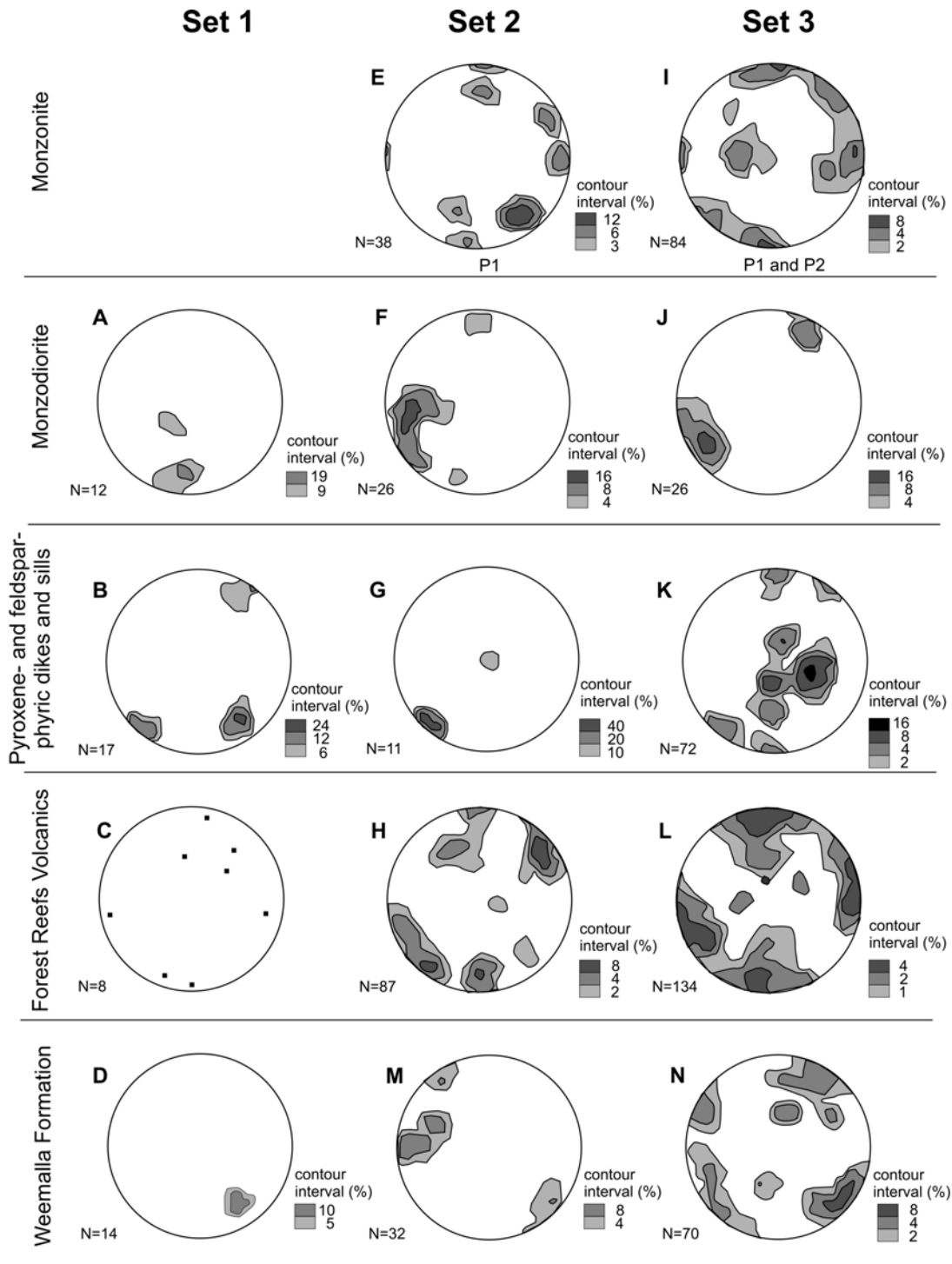
Set	Vein stage	Number of points	Preferred orientation		Secondary orientation	
			Strike	Dip	Strike	Dip dip-direction
Set 1	Stages 1A and 1B (pre-mineralization)	60	variable	moderate to steep		
Set 2	Stages 2A and stage 2B	128	$355 \pm 5^\circ$	moderate to steep - E and W	$060 \pm 10^\circ$	moderate - SE
	Stage 2D	69	$325 \pm 5^\circ$	steep - NE and SW	$285 \pm 5^\circ$	moderate-NE and SW
Set 3	Stage 3A	185	$085 \pm 10^\circ$	steep - N and S	$040 \pm 10^\circ$	moderate to steep - SE and NW
					$320 \pm 10^\circ$	steep - SW and NE
	Stage 3D	170	$290 \pm 10^\circ$	moderate to steep - NE and SW	$N \pm 10^\circ$	steep - E and W
Set 4	Stage 4	122	variable	shallow to moderate	$30 \pm 10^\circ$	shallow to moderate - NW

Figure 5.10 shows the distribution of vein sets and mineralization relative to elevation at Ridgeway. Most of the vein orientations that have been measured from drillcore and underground are mineralized stage 2 and stage 3 veins (Table 5.4). The high-grade ore zone ( $>4.0$  g/t Au) is found above 5100mRL, on the apical part and margins of the P1 intrusion, and comprises mostly well-developed set 2 veins up to 100 m from the contact (section 4.3). Set 3, produced lower grade mineralization and has a wider distribution that extends the mineralized zone to 300 m from the center of the orebody. Below 5100mRL, set 3 veins are hosted in the poorly mineralized Weemalla Formation and P2 intrusions (Figure 5.5B).

Most stages 2A and 2B veins are steep and have a preferred N-strike, with a second population that strike ENE (Table 5.4; Fig. 5.10B). Stage 2D veins are typically steep and NW-striking (Table 5.4; Fig. 5.10C). With regards to Stage 3A veins measured on this study, data collected underground vary from that collected from drillcore (Fig 5.10D and E). Stage 3A veins observed underground are typically steep, and have a dominant NE-strike, with less prominent N- and NW-strikes (Fig. 5.10D). However, there is a bias in the data set towards NE-striking veins, because 50 % of these veins were measured from a single cross-cut on the eastern end of the 5100mRL drive. This domain corresponds to the dominant trend of veins digitized from underground level plans (Domain 8, Fig. 5.19A). Stage 3A veins measured from drillcore samples are moderate-steeply dipping veins with dominant E-strike, and less prominent NW- and N-strikes (Fig. 5.10E). The NE-striking veins are under-represented in the drillcore sample which may be due to a bias in drillhole trends from where the veins were documented (section 5.2). Most of the NE-striking veins are sub-parallel to the core orientations, and hence, were not intersected or measured. Taken together, stage 3A veins measured in this study therefore have a dominant ENE-strike and less dominant NE-, NW-, and N-strikes (Table 5.4). At deeper level, shallow ( $<30^\circ$ ) barren quartz veins (stage 3D) with variable strikes are hosted in P2 and feldspar-phyric sill (Figs. 5.10F and 5.11).



**Figure 5.10** Rose diagram and lower-hemisphere Schmidt equal-area projection of poles for the different vein sets from Ridgeway. **A)** Set 1 pre-mineralization veins (stages 1A and 1B). **B)** Set 2 comprises the bornite-rich stage mineralized stockworks (stages 2A and 2B) and **C)** quartz - bornite veins (stage 2D). **D)** Set 3 comprises sheeted chalcopyrite-rich stage 3A mineralized veins measured from underground development drives (5070mRL and 5100mRL). **E)** Stage 3A veins measured from oriented cores. **F)** Stage 3D veins (barren quartz). **G)** Set 4 comprises late-stage veins, stage 4. Table 5.1 details the vein mineralogy and Table 5.4 summarizes the measured vein orientations.



**Figure 5.11** Lower-hemisphere Schmidt equal-area projection of poles of the different vein sets with respect to the different rock types from Ridgeway.



### 5.6.1 Domain analysis

Figure 5.12 shows the distribution and orientation of set 2 (stages 2A, 2B and 2D), and set 3 (stage 3A) in and around the deposit, projected at 5100mRL. To gain a better understanding of the spatial variability, the vein sets have been grouped into five domains with respect to their locations from the center of the orebody (Fig. 5.12A).

#### 5.6.1.1 Vein set 1

Stage 1 veins developed prior to main mineralization, and are associated with early actinolite–magnetite–albite alteration. Generally, these veins comprise massive magnetite  $\pm$  actinolite, are mostly discontinuous with irregular and diffuse vein walls, and are best developed in the pyroxene- and feldspar-phyric dikes, MzD, and in the surrounding wallrocks (Table 5.1; Figs. 5.11 and 5.13). Because most of the veins are less than 5 mm, these small-scale features were not measured during underground mapping in this study. Limited measurements were taken from veins >5 mm thick when observed in drillcore.

Set 1 structures have variable strikes throughout the deposit. They are generally steep with scattered vein orientations (Table 5.4; Fig. 5.10A), and it is therefore difficult to identify a preferred direction. However, one population is moderately to steeply dipping ( $>60^\circ$ ) towards the NE and SW and has an overall NW-strike (Fig. 5.13A). Other veins have a N-strike (Fig. 5.13B).

The variable orientation of set 1 veins indicates that the fractures were not controlled by a uniform-far-field tectonic stress, but rather by a local stress field (e.g. Engvik *et al.*, 2005). Based on the limited data available, the veins may have developed under conditions where  $\sigma_1$  was oriented sub-vertical, while  $\sigma_2$  and  $\sigma_3$  may have been interchanging in sub-horizontal directions.

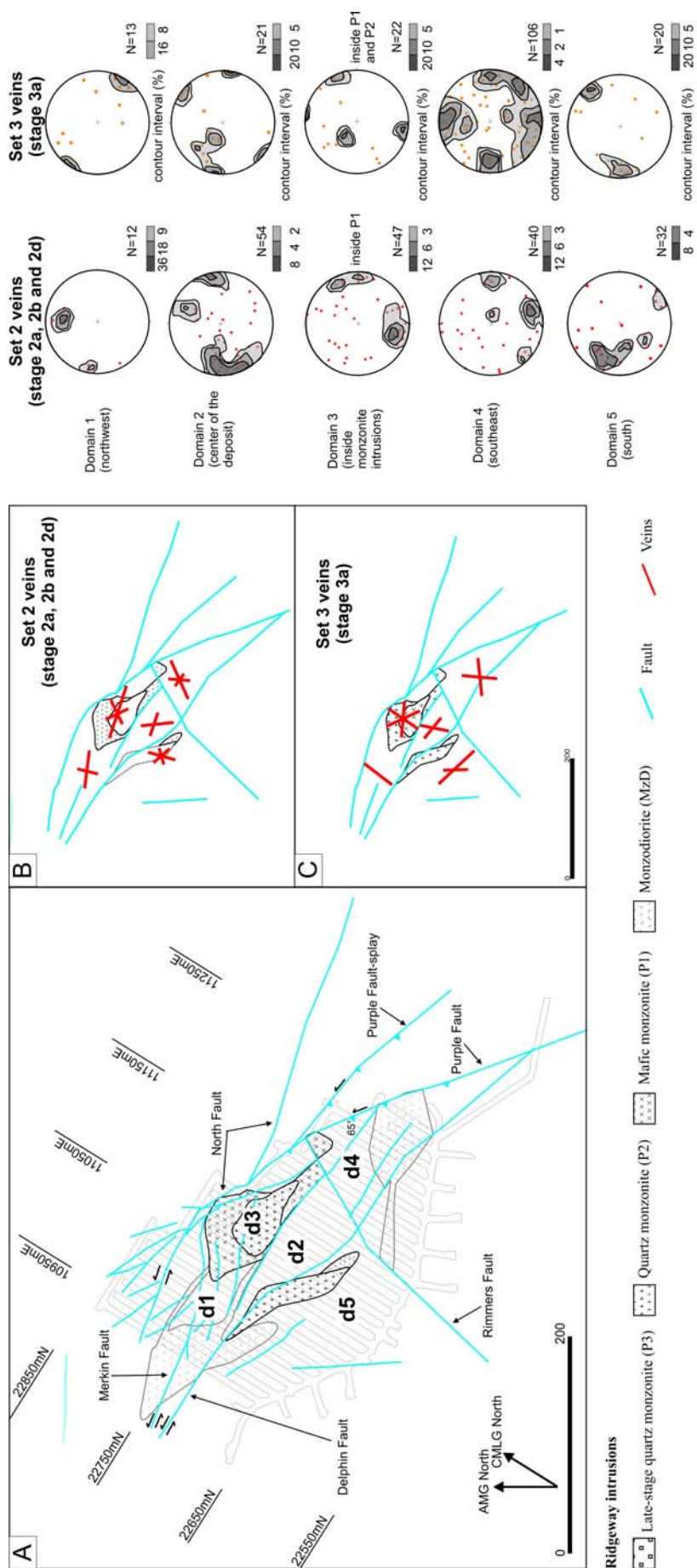


**Figure 5.12** Summary of mineralized veins from Ridgeway set 2 and set 3 measured from drillholes and underground, plotted as lower-hemisphere equal-area (Schmidt net) projection of the poles to veins. The locations are with respect to the center of the Ridgeway orebody projected at 5100mRL. **A)** Simplified geologic map showing the location of measurements by domains. **B)** Summarized orientations of set 2: stages 2A, 2B and 2D veins. **C)** Summarized orientations of stage 3A veins.

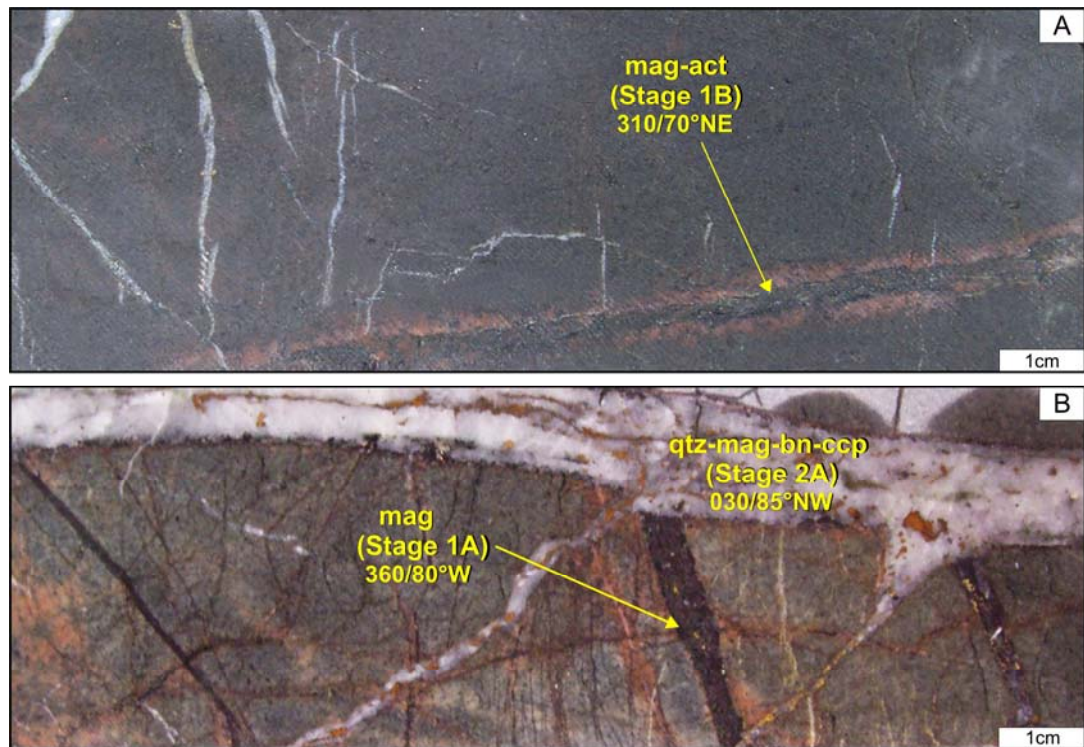


**Figure 5.13** Set 1 veins hosted in massive feldspathic sandstone of the Wemalla Formation. **A)** Moderate to steep, NW-striking magnetite - actinolite vein with hematite-dusted K-feldspar halo (stage 1B; UR323-637.4m). **B)** Steep, NW-striking magnetite vein (stage 1A), showing no offset on vein wall margins. The stage 1A veins is cut by a steeply-dipping, NE-striking quartz - magnetite - chalcopyrite vein (stage 2B; UR326-402m). Abbreviations: act = actinolite, bn = bornite, ccp = chalcopyrite, qtz = quartz, mag = magnetite

### 5.6.1.2 Vein set 2

Set 2 structures include stage 2A, 2B and 2D veins which are all associated with the first phase of mineralization (Table 5.1). These veins occur as stockworks and veins and are most intensely developed in the P1 intrusions and the immediate host rocks, with decreasing intensity away from the contact. Set 2 veins are dominantly steep, and have preferred strike directions: a dominant N-strike and less prominent WNW- and NE-strikes (Table 5.4; Figs. 5.10B and C).

The mineralized set 2 structures have been separated into five domains with respect to their location in and around the orebody, in order to get a better understanding of orientations (Figs. 5.12A and B). Domain 1 (d1) contains moderate to steep, W-striking veins, with less NNE-striking veins. Domain 2 (d2) is the centre of the orebody, and has steep NNW-striking dominant and less WNW-striking veins. Fig. 5.14B shows the high density of steep NNW-striking quartz–magnetite ± bornite



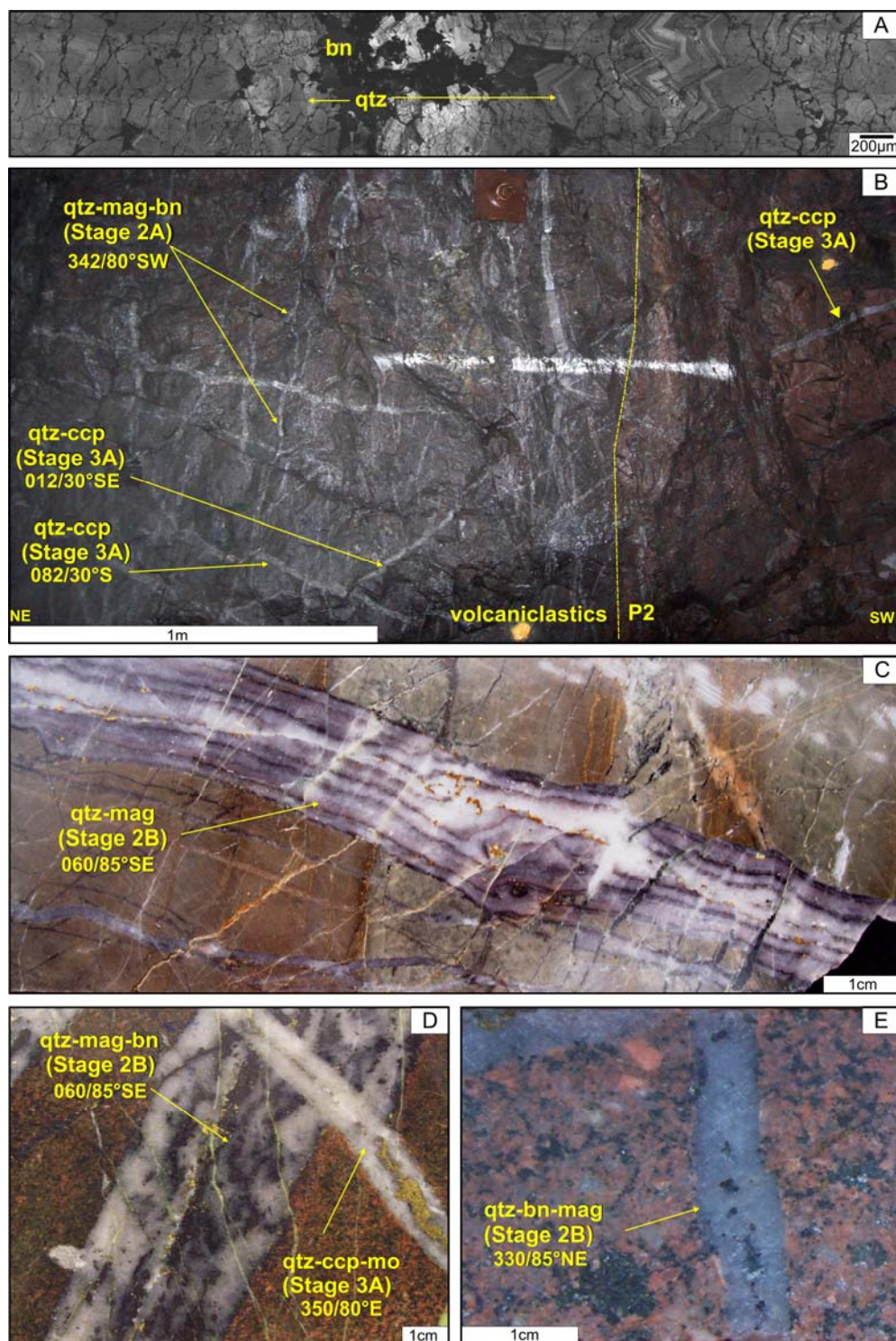


**Figure 5.14** Set 2 veins. **A**) Cathodoluminescence image of a stage 2D vein showing the quartz growth perpendicular to the vein wall (UR022-173.9m). **B**) Steep, NW-striking quartz - magnetite ± bornite veins (stage 2A) cut by thick (10 mm), parallel quartz - chalcopyrite veins (stage 3A) hosted in the massive volcaniclastic units of the FRV. Also shown is the intrusive contact (yellow dashed-line) with the reddish-orange quartz monzonite (P2) with dark-greenish volcaniclastic rocks. Note the intense veining in the volcaniclastic rocks, in contrast to P2 (5100mRL-XC6EW-116-117m, wall facing southeast). **C**) Steep, NE-striking quartz - banded magnetite vein (stage 2B) displaying multiple opening episodes, hosted in laminated siltstone of the Weemalla Formation (UR360-713.8m). **D**) Steep, NE-striking, thick quartz - banded magnetite vein (stage 2B) cut by steep, NW-striking quartz - chalcopyrite vein (stage 3A; UR450-143.3m). **E**) Steep, NW-striking quartz - bornite vein (stage 2D) hosted in mafic monzonite (P1; NC508-928.8m). Abbreviations: bn = bornite, ccp = chalcopyrite, mag = magnetite, mo = molybdenite, qtz = quartz

veins (stages 2A) intensely developed in the massive volcanoclastic lithofacies of the FRV. Domain 3 (d3), has broadly random and diffuse vein orientations centred on P1. Locally, steep mineralized quartz–bornite veins have a preferred NNW-strike (Fig. 5.14E). Domain 4 (d4), southeast of the orebody and east of Rimmers Fault, shows a larger spread of moderate to steep veins with ENE-strike most common. One population of quartz-banded magnetite–bornite veins (stage 2B) has a preferred NE-strike and dips steeply SE (Figs. 5.14C and D). Domain 5 (d5), south of Delphin Fault, has moderate to steep N- to NE-striking veins and less prominent NW-striking veins (Fig. 5.12B).

Stage 2A and 2B stockwork veins in set 2 structures have no uniform cross-cutting relations, suggesting a nearly contemporaneous timing of vein development. The variable orientation of veins inside domains 2 and 3 are interpreted as evidence that the orientation of the fractures was not controlled by a uniform-far-field tectonic stress, but rather by a local stress field. This localized extension regime probably formed with sub-vertical  $\sigma_1$  and significantly smaller but similar  $\sigma_2 \sim \sigma_3$  fluctuating in sub-horizontal directions. Domain 5 could be radial to P1 or just at high angle to the dominant WNW faults.

Set 2 structures are dominated by subvertical stockwork veins (stages 2A and 2B) in the apical portion of P1 and immediately surrounding wallrock, which is interpreted to indicate that fluid pressures were high. Pre-existing fault orientations are widely represented in the vein set. Most domains are dominated by two common orientations that are steep and nearly perpendicular to each other. The most peripheral domains (1, 4 and 5) are dominated by veins that dip towards the deposit center (Fig 5.12B).

### **5.6.1.3 Vein set 3**

Set 3 structures include stage 3A and 3D veins (Tables 5.1), which generally occur as sheeted veins. Set 3 structures are separated into two sub-sets (Table 5.4): chalcopyrite-rich mineralized stage 3A veins, and barren quartz stage 3D veins. Stage 3A veins have moderate to steep dips, and mostly strike E-NE, with lesser NW- and N-striking veins (Table 5.4) In contrast, Cu–Fe deficient stage 3D



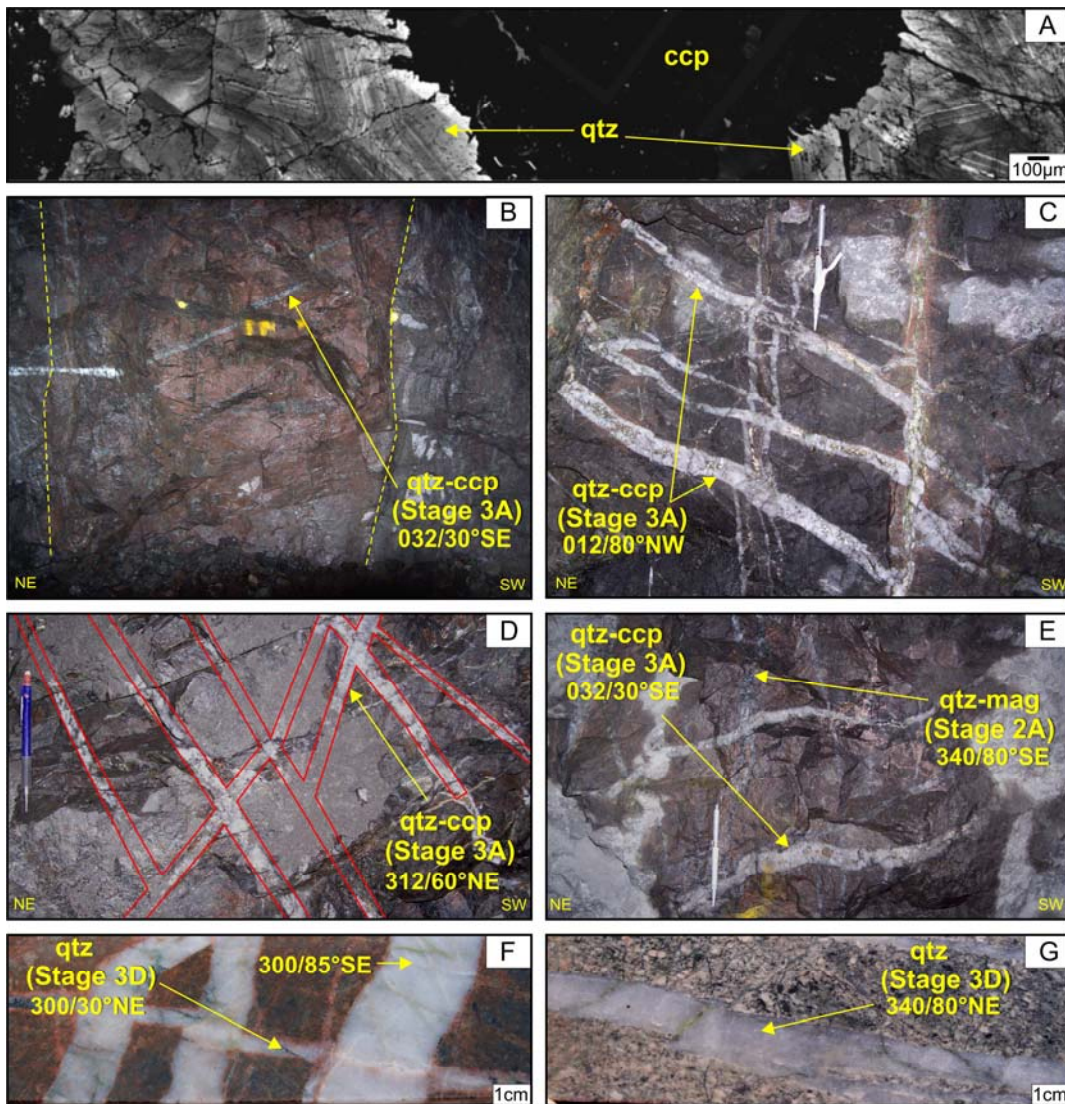


**Figure 5.15** Set 3 veins. **A)** Cathodoluminescence image of a stage 3A vein showing the quartz growth perpendicular to the vein wall (UR450-143.3m). **B)** Shallow, NE-striking, thick (10 mm) parallel quartz - chalcopyrite vein (stage 3A) in quartz monzonite (P2). Also shown is the intrusive contact (yellow dashed-line) of P2 with the massive volcanoclastic unit of the FRV (5100mRL-XC6EW-115.3m, wall facing southeast). **C)** Steep, NNE-striking thick (20 mm) sheeted quartz - chalcopyrite veins (stage 3A; 5100mRL-XC22WW-chainage -56.5m, wall facing northwest). **D)** Moderately-dipping, NW-striking thick (20 mm) parallel quartz - chalcopyrite veins (stage 3A; 5100mRL-XC22WW-chainage-66.5m). **E)** Shallow, NE-striking, thick (25 mm) parallel quartz - chalcopyrite vein (stage 3A). Stage 3A veins cut structural set 2, steep, NW-striking quartz - magnetite veins (stage 2A; 5100mRL-XC6EW-chainage 105m). **F)** Steep, NW-striking thin (3 mm) barren quartz vein (stage 3D) and shallow, NE-striking thick (15 mm) parallel quartz vein (stage 3D) in feldspar-phyric andesitic sill (UR323-1297.8m). **G)** Steep, NW-striking barren quartz vein (stage 3D) inside P2 (UR323-1382.3m). Abbreviations: ccp = chalcopyrite, mag = magnetite, qtz = quartz

quartz veins have extremely variable orientations, and are either steeply dipping or gently dipping (Table 5.4). Figure 5.15F shows the relationship of steep, stage 3D barren quartz veins locally linked with sub-horizontal veins ( $<30^\circ$ ;  $n=39$ ), indicating that veins in both orientations formed synchronously. There is no visible boundary between the quartz infill of intersecting veins.

Set 3 veins have been grouped by domain in Figure 5.12C in a fashion similar to set 2. Only the mineralized stage 3A veins were considered in plotting these domains. Data from stage 3A veins measured underground and in drillholes were combined when compiling the domains (Fig. 5.12C). Domain 1 has steep veins, with dominant NE strike. Domain 2 is dominated by steep NW-striking veins, and fewer steep veins striking NNE. Domain 3 is mostly inside P1 and P2 intrusions, and is dominated by steep, WNW-striking veins, with less common subvertical NW- and shallowly dipping NE-strike. Shallow ( $<30^\circ$ ) quartz–chalcopyrite veins (stage 3A) occur in P2, striking NE and dipping towards the SE (Fig. 5.15B). Domain 4 lies east of Rimmers Fault, and has a larger spread of moderate to steeply dipping veins; one population of veins has an ENE preferred orientation, N- and NW-striking veins are also present. Steeply dipping, NW-striking quartz–chalcopyrite veins (stage 3A) have truncated NE-striking veins in set 2 (e.g. Fig. 5.14D). Thick (~25 mm), steep, NNE-striking (Fig. 5.15C) and moderately-dipping, NE-striking (Fig. 5.15D) parallel sets of quartz–chalcopyrite veins (stage 3A) occur in Domain 4, at the eastern end of 5100mRL (Fig. 5.15C). Domain 5 contains a dominant set of steep NW-striking veins, with less common steep N-striking veins (Fig. 5.12C). The center of the deposit (Domains 2 and 3) contains shallow SE-dipping veins that were not detected to the southeast (Domain 5) or west (Domain 1).

#### **5.6.1.4 Vein set 4**

Set 4 structures include vein stages 4A, 4B and 4D (Table 5.1). These veins are poorly mineralized to unmineralized. Set 4 structures across the entire deposit have scattered orientations (Table 5.4; Fig. 5.10G). Quartz–pyrite veins (stage 4A) are typically steep, with a persistent NW-strike (Fig. 5.16A). One example of a stage 4D calcite–prehnite vein has formed alongside a steep, NE-striking quartz–bornite  $\pm$

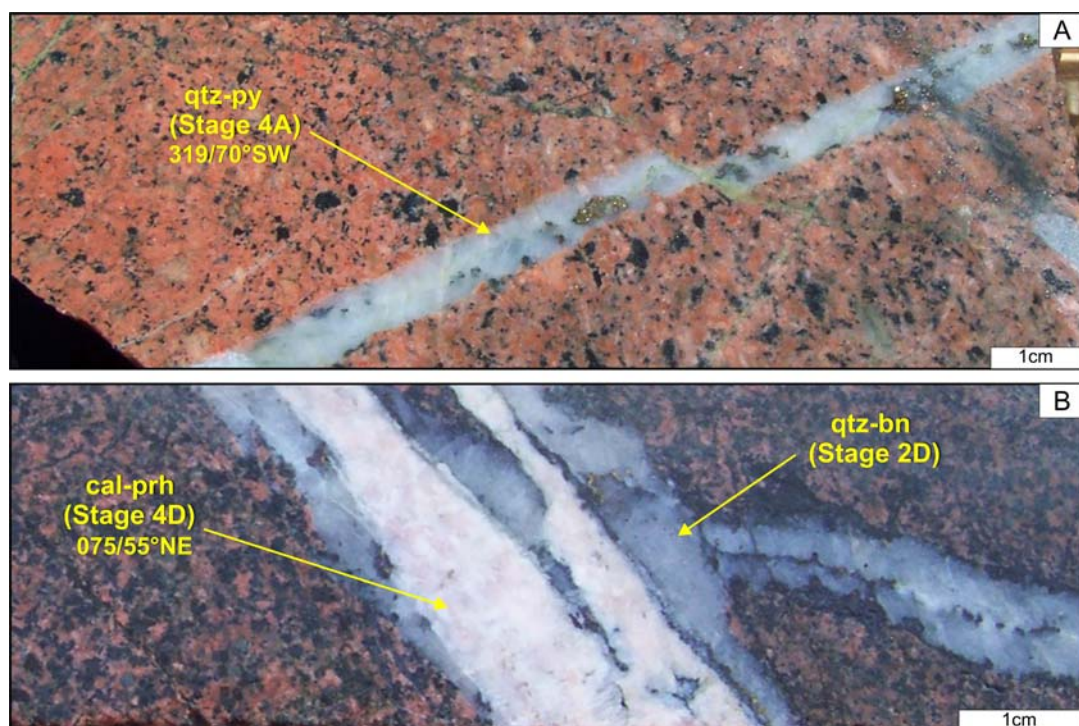


**Figure 5.16** Set 4 veins. **A)** Steep, NW-striking quartz - pyrite vein (stage 4A) hosted in quartz monzonite (P2; CR057-1927m). **B)** Steep, NE-striking calcite - prehnite vein (stage 4D) occupying re-opened quartz - bornite  $\pm$  magnetite vein (stage 2D; NC508-913m). Abbreviations: cal = calcite, prh = prehnite, py = pyrite, qtz = quartz

magnetite vein (stage 2D; Fig. 5.16B), which suggests that the fracturing pattern for set 4 might have been, at least in part, inherited from earlier fractures.

### 5.6.2 Comparison with pre-existing mine data

Structural data recorded by Newcrest geologists for mineralized veins have been filtered using the mineral composition assemblage and structure type from the Newcrest's digital database. Only veins that are easily distinguished mineralogically, specifically bornite- and magnetite-rich veins associated with stages 2A, 2B and 2D, and chalcopyrite-rich stage 3A veins, were reviewed and contoured (Fig. 5.17). In summary, the mine's database shows that stage 2A and stage 2B are dominated by steep NNW-striking ( $340 \pm 20^\circ$ ) and steep E-striking veins with small group of horizontal veins (compare Fig. 5.17A with Fig. 5.10B). Stage 2D consists of steep NW-striking veins ( $\sim 330^\circ$ ), comparable with the data measured in the current study (compare Fig. 5.17B with Fig. 5.10C). Stage 3A veins have moderate to steep dips and are W-striking ( $280 \pm 10^\circ$ ); there are subordinate steep NW- and NE-striking veins. Stage 3A vein orientations are similar to those measured in the current study (compare Fig. 3.17C with Fig. 5.10D and E). Given the reasonable correlation of



results, assumptions used in recovering this data from the Newcrest database appear to be valid.

### 5.6.3 Dikes and sills

Dikes at Ridgeway are broadly NW- to W-trending; a few have northerly strikes (Fig. 5.18A). The dikes are subparallel to the NW-trending structural grain of the Cadia district. Bedding-parallel intrusions (sills) have been documented deep in the system. Such “sills” have variable orientations, generally striking north or northeasterly (Fig. 5.18B). Steep veins hosted in dikes have a similar dominant northwest trend (compare Fig. 5.18A with Fig. 5.11B), while the shallow veins have a similar pattern to the sills (compare Fig. 5.18B with Fig. 5.11K).

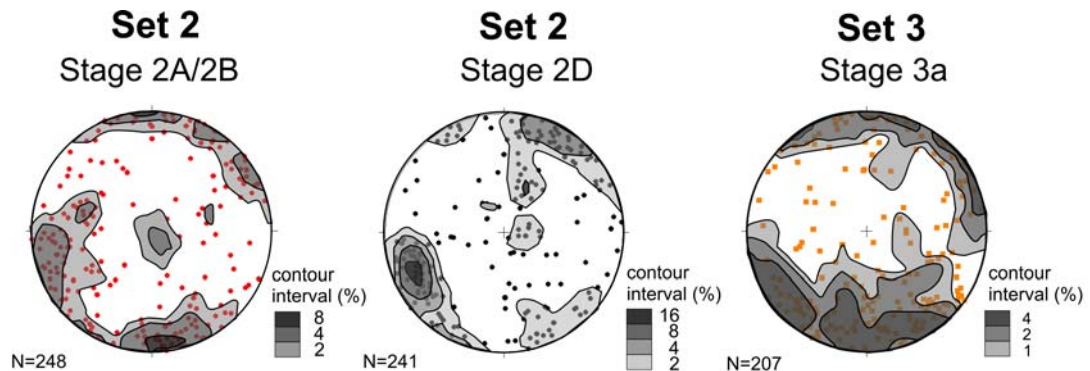


**Figure 5.17** Lower-hemisphere Schmidt equal-area net projection of poles of the vein stages from Ridgeway. The data were extracted from Newcrest’s digital database by assuming all veins with dominant magnetite  $\pm$  bornite are stage 2A/2B veins, bornite-dominant are stage 2D and chalcopyrite-dominant are stage 3A veins.

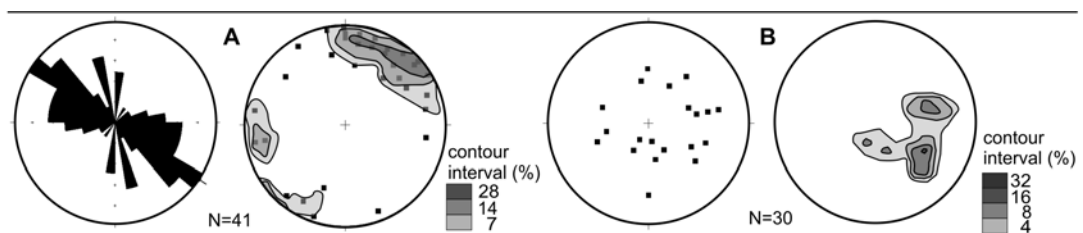


**Figure 5.18** Measured orientations of dikes and sills from Ridgeway. **A)** Dominant, steep NW-trending dikes, and less dominant steep, N-trending dikes. **B)** Bedding parallel pyroxene- and feldspar-phyric sills.

## 5.7 Structural level plans

A review of the available structural data, as compiled on level plans from Ridgeway mine, was undertaken to ascertain the dominant vein orientations, and to compare with the results of the current study. Figure 5.19 shows three representative level plans for Ridgeway. The 5100mRL was the lowest mining level at the time of this study, 5255mRL represents the middle part of the orebody and 5330mRL the highest mining level, 500m below the current surface. Figure 5.5B shows the location of the levels in section. The locations of interpreted faults and intrusion geometries are from Newcrest's interpreted plans, in conjunction with results from this study's drill corelogging (section 3.3). To gain a better understanding of the distribution of veins, structural domains on Figure 5.19 have been defined on the basis of their locations with respect to the center of the orebody. The strike-directions are plotted on a strike-direction histogram (rose diagram) for each domain (Fig. 5.19). For clarity, the dominant and subdominant vein orientations in each domain are simplified, as shown in a small box located on the lower right corner on each figure.

### 5.7.1 5100mRL

The vein array on 5100mRL (Fig. 5.19A) defines a relatively consistent pattern. Veins in domain 1 (d1), north of North Fault, and domains 4 and 5 (d4, d5) on the SW margins of the orebody, are orthogonal to the regional NW structural grain. The veins in domains 3 and 6 (d3, d6) are predominantly NW-trending. In domains 2 and 7 (d2, d7), the veins have variable orientations, however, d7 has two populations (NE- and NW- trending) and the veins are mostly hosted in P1 and P2. East of Rimmers Fault, veins in domain 8 (d8) mostly have NNE- and NW-orientations.

Most of the veins are subparallel to WNW faults in d3, d6, d8 and partly in d2 on level 5100, suggesting strong tectonic control on vein development in these areas. These domains are bounded by the North Fault to the northeast, and by the South Fault and the contact between the FRV and Weemalla Formation to the southwest. Veins in these domains also coincide with the general northwesterly



elongation of P2, and parallel to the regional NW-structural grain. To the NE and SW of this alignment, there is an apparent radial alignment of veins in d1, d4, d5 and partly d7.

Most of the veins on level 5100 strike NW; there is also subordinate NE-trend. Some of the orientations mapped by Newcrest geologists match the data gathered for stage 3A veins in this study, as summarized in Figure 5.12C. For example, the NW orientations in d6 correlate with the subdominant veins in domains 2 and 5 (Fig 5.12C) The two populations of veins with NE and NW orientations in d7 have similar orientation to veins measured inside P1 and P2 in domain 3 (Fig. 5.12C). The predominant NE-striking veins in d8 are similar to stage 3A vein orientations measured underground (Fig. 5.10D). Given the consistent orientation of the veins, and the abundance of set 3 veins based from mapping at 5100mRL by the author, it is inferred here that most of the veins mapped on level 5100 are set 3 veins.

### **5.7.2 5255mRL**

The vein orientations on 5255mRL (Fig. 5.19B) define a very different patterns to those observed on 5100mRL. Specifically, there are abundant veins with orthogonal relationships that are unrelated to the main alignment of the deposit on level 5255. The two perpendicular vein directions most commonly observed are NNW- and ENE-striking veins. These orthogonal relationships are well developed in domains 1, 5 and 8, where they are oriented oblique to the regional northwesterly structural grain and to the elongation of P1 (Fig. 5.19B). In domains 3, 4, 6 and 7, most of the veins trend easterly, with a subordinate NNW-oriented population. Some of the domains mapped on level 5255 by Newcrest geologists can be correlated with the veins measured during the current study from drillcore (Fig. 5.12). For example, the E-trending veins in d3 correlate with set 2 veins (domain1; Fig. 5.12B). The veins observed in d6 and d7 matched the observed dominant strike data for set 2 veins (domain 3; Fig. 5.12B). The predominance of ENE-striking veins in most of the domains on level 5255 are consistent with the measured ENE-striking stage 3A veins measured in drillholes from similar depths (Fig. 5.10E).

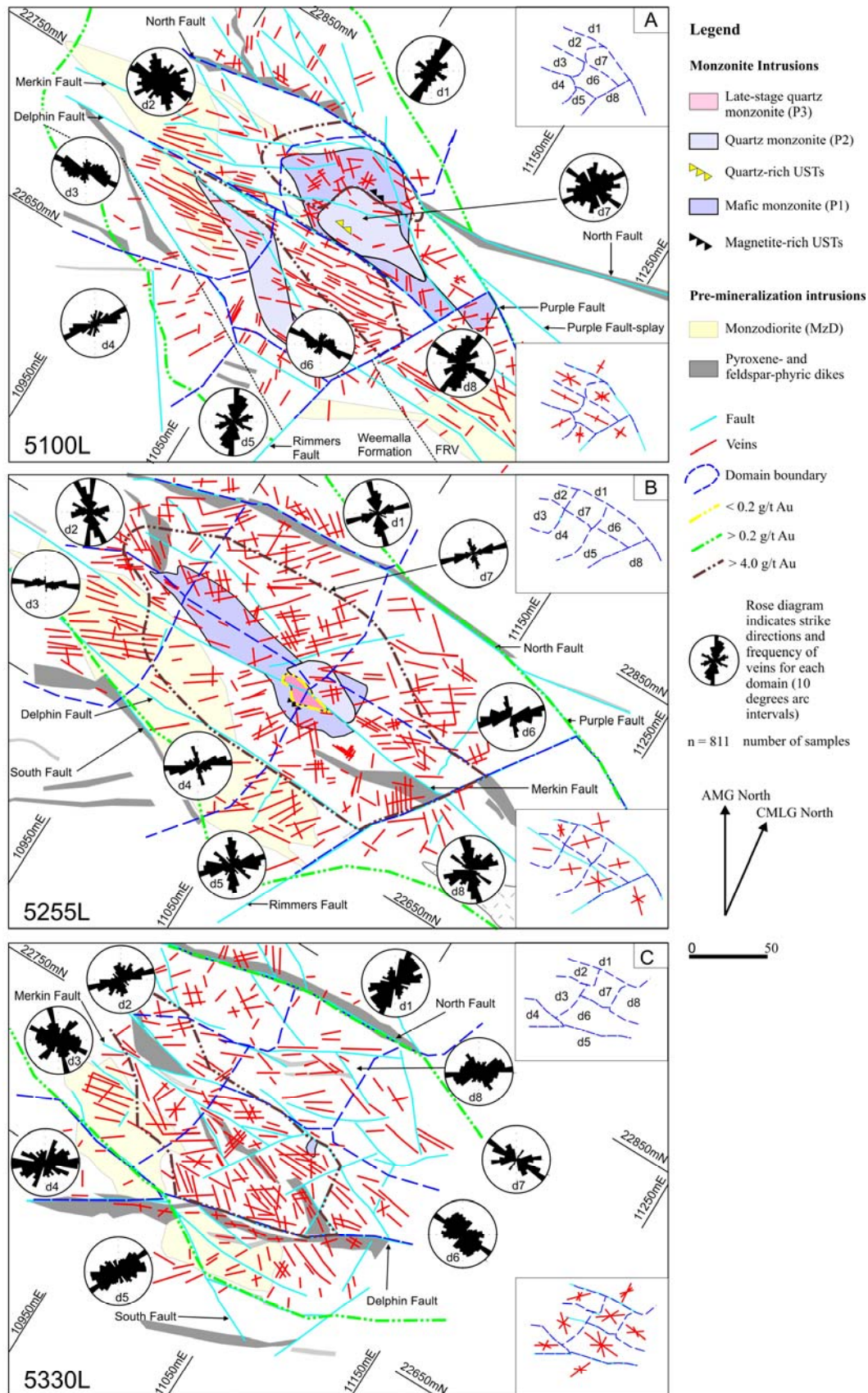


**Figure 5.19** Vein orientations based on underground mapping at Ridgeway by Newcrest geologists. Strike direction histograms (rose diagrams) for veins indicated by domains. Inset box (lower right) shows the summary of vein trends of each domain. Inset box (upper right) shows the domains. Refer to text for detailed explanation.

There is distinct change in vein orientation from generally NW-striking veins at 5100mRL to N- and E-striking orthogonal veins at 5255mRL. A very different pattern of vein orientations occurs at 5255 level which is unrelated to the WNW-striking faults (e.g. North Fault, Delphin Fault, South Fault). These veins appear to record a stress state that reflects regional-scale stresses at a time when local intrusion was taking place, and after both P1 and P2 have solidified, at least on level 5255.

### **5.7.3 5330mRL**

Fault and vein orientations define different patterns on level 5330 to both levels 5100 and 5255 (Fig. 5.19). There are strong WNW-trending components in domains 3 and 7, whereas domain 8 has one W-striking dominant population on level 5330. Veins on the deposit margins (domains 1, 4 and 5) define an apparent radial orientation, similar to that noted for the same domains on 5100mRL. Domain 6, which is bounded by Delphin Fault to the south and the Merkin Fault to the north (Fig 5.19C), has the highest density of veining on level 5330, but the veins have variable orientations. This is a high-grade zone (4.0 g/t Au). The very high vein density in domain 6 suggests a predominance of stockwork veins, which are attributed here to set 2 veins. Based on the locations of the P1 and P2 intrusions on 5255mRL, this domain 6 is interpreted to have been lifted relative to domain 7. Figures 5.5B shows the Merkin Fault dips west and the Delphin Fault dips east at 5255mRL forming a wedge that would allow volume increase as it lifts. The curvature of the Merkin Fault around 5330mRL may reflect this roof lifting within domain 3. In domain 2, the veins are dominantly trending ENE. Domain 2 lies within the 4 g/t Au zone but has a vein pattern similar to domain 8, which has a scattered vein array with one notable population of ENE-striking veins. The random and diffuse trend of veins suggests an overlapping of vein sets at 5330mRL, where dominant trends cannot be recognized easily. This is likely to be due to the presence of vein stockworks, especially above the P1 intrusion.

## 5.8 Discussion and summary

### 5.8.1 Deposit-scale structural interpretations

#### 5.8.1.1 Pre-mineralization deformation

Local bedding orientations at Ridgeway generally strike NW (see Table 5.2) and dip 10° to 35° towards the NE. Localized folding has produced both gently and steeply NE-dipping bed orientations; consistent with monoclinal folding with fold axis gently plunging to the northwest (Fig. 5.2). The similarity of bedding orientations taken proximal and distal from the Ridgeway deposit suggest that folding was district-wide. The strike directions of bedding and the fold-axis are subparallel to the trend of the regional NW-striking faults in the district. The monoclinal folds on the Ridgeway area are of unknown age. The discordant contacts of the subvertical monzodiorite and monzonite intrusions (Fig. 4.12) suggest that folding occurred prior to emplacement of these intrusions. Supporting this, undeformed late stage pyrite veins have been observed which have cut folded layers in the Weemalla Formation (Fig. 5.3). Folding is therefore concluded to have been probably the earliest deformation at Ridgeway. It occurred prior to the emplacement of the Ridgeway intrusive complex (~448 - 444 Ma; section 3.7) during the Late Ordovician.

An alternative hypothesis is that the folds may be in part artefacts that reflect syn-depositional topography and draping over basement fault blocks in the Weemalla basin (e.g., Harris *et al.*, 2009b). Elsewhere in the district, the open to tight folds that have been developed in the FRV and Silurian sedimentary cover sequence are associated with faults formed as a result of E-directed compression during the Devonian-Tabberaberan Orogeny (~380 Ma; Harris *et al.*, 2009b).

#### 5.8.1.2 Mafic dikes as paleostress-direction indicator

Dikes typically intrude normal to the direction of  $\sigma_3$  either with regards to a regional or local stress regime (Valentine and Krogh, 1996). Dikes are believed to propagate by dilation of pre-existing fracture surfaces (Delaney *et al.*, 1986). The geometry of a dike is therefore influenced, at least in part, by the path followed by the tip of the dike as it propagates through its wallrocks (Pollard, 1987). Hence, to

propagate a vertical dike,  $\sigma_3$  must be horizontal and the magma pressure ( $P_m$ ) within a dike must exceed  $\sigma_3$  (Pollard, 1987).

At Ridgeway, pyroxene- and feldspar-phyric dikes have broadly northwesterly strikes and commonly occupy extensional fissures along WNW-striking faults (Fig. 5.19). This implies that the pre-existing faults were a more favorable site for magma emplacement than newly created fractures in intact rock. However, while there was probably a range of pre-existing fault orientations (section 5.5.2), only the WNW-striking faults were intruded by these dikes. The mafic dikes are therefore concluded to have intruded when  $\sigma_3$  was oriented NNE-SSW (Fig. 5.20; Fig. 5.24A).

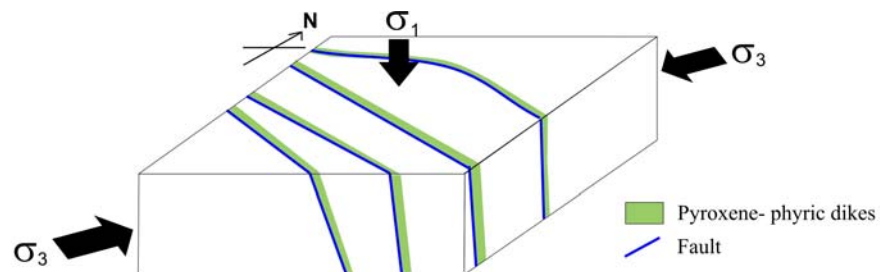


**Figure 5.20** Schematic block diagram showing the emplacement of the pyroxene-phyric dikes at Ridgeway along NW-trending faults.

## 5.8.2 Magma intrusion: a structural model

The ‘space problem’ for pluton emplacement has been a subject of debate for decades. Several classic models have been put forward: cauldron subsidence, stoping, diapiric emplacement and ballooning (in-situ inflation at the emplacement site; Hutton, 1996). In recent years, structural mechanisms for pluton emplacement have received an increased amount of attention (e.g. Petford *et al.*, 2000, Vigneresse and Clemens, 2000). Pluton emplacement models involving dilation along major faults and shear zones are now being applied particularly in transcurrent and extensional settings. These models include space creation in pull-aparts, fault terminations and releasing bends (Hutton, 1996).

At Ridgeway, a model involving a dilation zone on a strike-slip fault and associated dilational jog was proposed for the emplacement of the intrusive complex (Marjoribanks, 2005; Fig. 5.21B). It was suggested that the Ridgeway mine occupies



extensional zone associated with dextral strike-slip fault, with ~100 m of movement along it (Marjoribanks, 2005). This model is similar to the development of a pull-apart basin. Figure 5.21A shows the geometry of the different intrusions at level 5100 to compare the pull-apart basin model with the experimental analogue model (Fig. 5.21B). An experiment by Aydin and Nur (1982), on the evolution of widths and lengths of pull-apart, has shown that the length of the basin is equal to the offset at the bounding strike-slip faults, and the width of the basin is the sum of the widths of the initial pull-apart elements (Fig. 5.21B). To create space for the Ridgeway intrusions, at least 100 m of dextral movement along the NW-striking faults should have occurred. This is unlikely, as significant dextral strike-slip movement has not been documented at Ridgeway. The dilational jog model is therefore discounted.

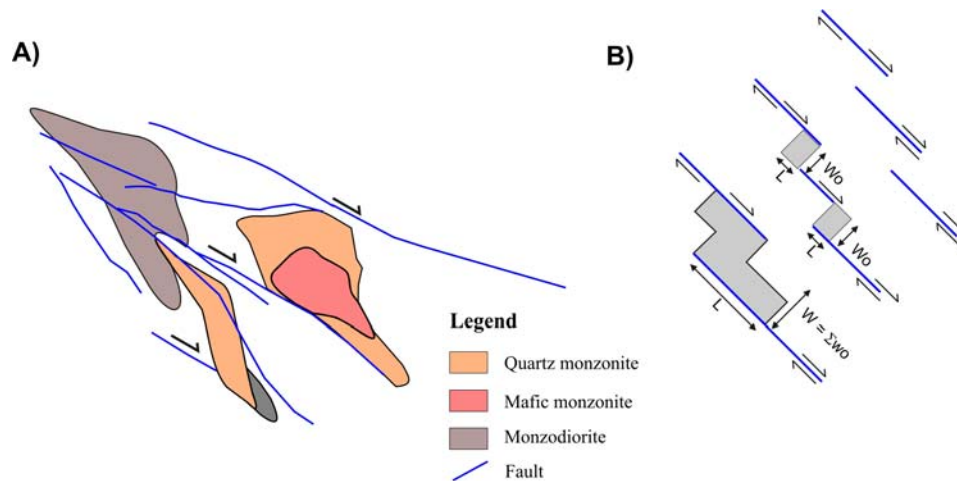


**Figure 5.21** A) Geometry of intrusions at 5100mRL. B) Evolution of widths and lengths of pull-apart basins according to Aydin and Nur (1982).  $W_0$  = initial width of pull-apart basin;  $W$  = width of coalesced pull-apart basin;  $L$  = length of basin equal to fault offset. Modified from Atmaoui, *et al.*, 2006.

Relationships between the geometry of the intrusions and the fault/fracture network at Ridgeway indicate that the faults have been important in the localization of pipe-like intrusions. One potential process for vertical transport of melt in the crust is a model involving the ascent of magmas in narrow conduits along pre-existing faults (Petford *et al.*, 2000). Analogue experiments on magma intrusion into brittle rocks have shown that the analogue liquid exploits existing fractures (Mathieu *et al.*, 2008). Figure 5.22 shows the results of the analogue liquid in the formation of two arms at the dike tip propagating through faults: first, one arm grew faster than the other, soon the liquid abandoned the smallest arm and the largest propagated.

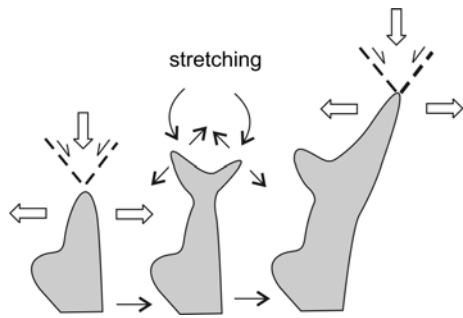


**Figure 5.22** Mechanism for intrusion of dike as it propagates by infiltrating normal faults by repetitive branching (modified from Mathieu *et al.*, 2008).

This type of process may be linked to the formation of a fracture related to tensional stresses created over the dike, between the expanding arms and the formation of hydraulic fracturing.

Ridgeway is located above a NNW-trending monocline (Fig 5.4, domain 1 and Fig 5.6C), specifically where the monocline intersects the WNW- trending North Fault. This geometry strongly suggests that the monocline is draped over a deep-seated fault which provided easy access for the intrusions into the upper crust. At deeper levels, the majority of the intrusions found so far are found in the NNW-striking monocline (sections 11150mE and 11250mE on Fig. 5.6), but at higher levels the intrusions appear to have leaked out along the North Fault (section 10950mE on Fig. 5.6). There are several distinctive features of the final emplacement position of the intrusive bodies above 5000mRL. The sections at 10950mE and 11050mE (Figs. 5.5B and 5.6) show that the porphyry bodies intruded a zone where faults define a wedge-shaped roof. The North Fault dips south and the South Fault and Delphin Fault dip north in this area. Such a wedge shape (assuming it existed at the time of magmatism) would allow easy roof lifting, where even a small roof lift would have provided additional space towards the NE and SW at all levels as the block rose (Fig. 5.23).

Did the wedge shape block exist before the intrusion or was it caused by intrusive activity? The section at 11250mE (Fig. 5.6D) shows a near-vertical North Fault and no significant north dipping-faults. The bend in the North Fault at the intersection with the Purple fault offsets the North Fault by ~50 m. The Purple Fault is generally considered to post-date the intrusion. However on section 11050mE (Figs. 5.5B and 5.6B), the bend in the North Fault is well placed to provide much of the space required to allow the inflation of P2 and P1 porphyry bodies. If this is true, then the later-formed Purple Fault nucleated on this bent segment of the North Fault.

In a wedge model, the stress state in the wedge and outside are very different. The wedge can escape upward and expand as it escapes but the surroundings are under pressure from the inflation of the pluton. The vein pattern at 5100mRL (Fig. 5.19A) is consistent with this model. This level shows a high level of new space created to fit the intrusions. Between the North Fault and the South Fault the veins largely parallel the wedge, suggesting that space is available, while outside this zone veins suggest a radial compression environment indicating forceful inflation. Above the plutons, a zone of roof lifting has been identified on 5330mRL. However the vein structure at 5255mRL shows no evidence that the central block saw a different stress environment to the peripheral zones. Apparently no significant inflation was occurring when these veins were emplaced. The weight of evidence available here supports the conclusion that the inflation was forceful and led to expansion both laterally and vertically (Fig. 5.23). It is not clear if the level of final emplacement was controlled by a pre-existing wedge-shaped roof block. In part, the south dip on the North Fault may have been created by the intrusion. The north-dipping South Fault and perhaps the north-dipping segments of the Delphin Fault define a discrete wedge-shaped roof block that is a significant element in space creation for the intrusions. The dips on these faults may have been inherited, but at least some segments of the Delphin Fault are vertical, so the original dips are uncertain.

The results from the analogue modelling by Aydin and Nur (1982; Fig. 5.22) agree with field observations documented at Ridgeway. Magma has been forced into zones of pre-existing fractures. For Ridgeway, a possible mechanism for magma to reach the upper crust would have been through rapid dike ascent by forceful injection along pre-existing deep-seated structures along a NNW structures. At about 5000mRL, space was created by roof-lifting of a wedge block along the North Fault. Rock material was pushed back around the magma as it swelled when magma reached its neutral buoyancy (Fig. 5.23; Richards, 2003). It should be noted the geometry of the intrusions at Ridgeway is typically subvertical pipes or plugs, with a maximum horizontal dimensions of 200 m by 100 m (section 3.4). This size is relatively small compared to plutons, where roof uplift and displacement can reach up to kilometres (e.g. Amiata, Italy, Acocella, 2000). In the case at Ridgeway, it is

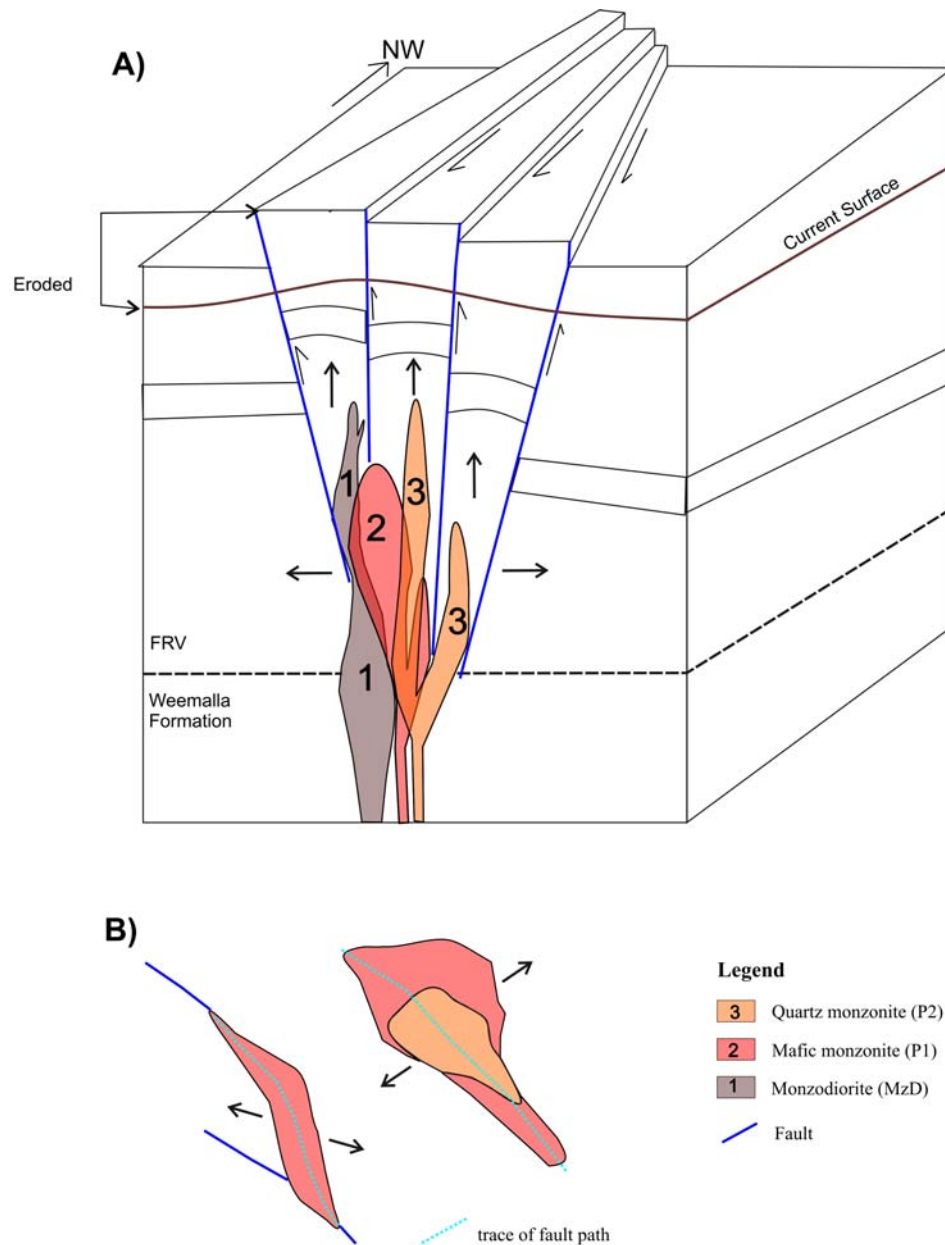


**Figure 5.23 A)** Emplacement model of the Ridgeway intrusive complex to the upper crust by diking and forceful injection along pre-existing crustal faults. The number corresponds to the sequence of intrusions. **B)** Plan showing the geometry of intrusions as it follows the existing fractures and pushes the rock as it swells when they reached neutral buoyancy.

inferred that the uplift would be in the order of tens of meters as evidenced by the change in rock type along faults (section 3.3; Fig. 5.6).

Opinions vary as to the efficacy for felsic magma propagating as dikes, because it has been argued that felsic magma will freeze up close to its source (Rubin, 1995). However, Richards (2003) argued that magma viscosity controls the rate of magma flow, where a faster flowing magma will convect heat rapidly, thus

will tend to stay molten. Moreover, felsic magmas will ascend efficiently through conduits with widths above 3 m (Clemens and Mawer, 1992), up to 10 m (Petford *et al.*, 1994). Any increase in the concentration of volatiles (such as fluorine) will also affect their viscosity (e.g. Mt Pinatubo; Pallister *et al.*, 1996). High volatile proportions have been shown to occur in the alkalic magmatism of central New South Wales. Alkalic magmas are typically enriched in fluorine (Jensen and Barton, 2000).

According to Richards (2003), magma ascent in a dike will continue until the magma freezes or its driving force is exhausted or balanced. At Ridgeway, the magma must have ascended and propagated along faults, cutting through the Weemalla Formation and the overlying volcanoclastic rocks. In this case, the magma started to swell just above the contact between the siltstones of the Weemalla Formation and the volcano-sedimentary succession of the FRV. It is possible that the strong rheological contrast at this contact caused the magma to expand into the more permeable rock package (FRV; Fig. 5.23A). Gow and Walshe (2005) recognized that porphyry-related deposits form at or near the base of competent stratigraphical units. Alternatively, the magma had reached its neutral buoyancy at this level, and the overlying country rocks were lifted along fault blocks, allowing the intrusion to swell, and pushing back the host material around it (Fig. 5.23B). A key feature at Ridgeway is the existence of a roof block along the WNW-striking North Fault which is interpreted to have acted as a relief valve, allowing lateral escape of magma (Fig. 5.6; Fig. 5.23A).

It must be emphasized that the intrusions we now see at Ridgeway were not guided by any fractures now visible. Whatever fracture guided each pipe only remains as the resulting shape of the pipe itself. This is best observed at 5100mRL, where a rhombic-shaped P1 exploited the orthorhombic fault geometry (Fig. 5.23B; e.g. Krantz 1988).

At Ridgeway, the different magma pulses were probably emplaced by the same mechanisms throughout the duration of intrusive activity. The first were the mafic dikes, followed by MzD. The MzD was then followed by P1, which intruded on its northeastern side. Sillitoe (2000) suggested that there is a distinct tendency for



later porphyry stocks to intrude along the shoulders or edges of older plutons, stocks or dikes (e.g., Bajo de la Alumbrera, Proffett, 2003). P1 appears to have been intruded at least in part along the edges of some mafic dikes. This may explain why highly mineralized pyroxene-phyrlic dikes are generally located along the margins and apical portion of P1. The time elapsed between P1 and the intrusion of P2 may have been short. Figure 5.23B shows that P2 intruded along the core of P1, implying that P1 may not have fully crystallized before the injection of P2. A similar scenario could be inferred between P2 and P3.

### **5.8.3 Vein formation, fluid pressure and differential stress**

At Ridgeway, structurally controlled mineralization is dominated by subvertical vein systems: the N-, WNW- and NE-striking mineralized veins in set 2 (stages 2A, 2B and 2D), and the E-, NE- and NW-striking mineralized stage 3A veins (Fig. 5.10). The vein orientations were generally controlled by pre-existing fractures and the prevailing stress state, and in part by the geometry of the intrusions with which the mineralized veins are associated (Fig. 5.19).

In set 2 veins (stages 2A and 2B), the high density of quartz stockworks implies the infiltration of a significant quantity of magmatic fluids derived from a deep level magma body (Lowenstein, 1994). Heidrick and Titley (1982) reported that the stresses in the apical region of a stock are related to the kinetics and thermal history of intrusion in high crustal levels, where  $\sigma_1$  is oriented near-vertical. This near-field stress state is inferred for the development of the P1 intrusion, with  $\sigma_3$  oriented towards the northeast (Fig. 5.24C). The volatile exsolution history of a cooling pluton, as outlined by Burnham (1979), relates the development of fractures to the expansion of fluids from a cooling hydrous magma. Under certain condition, hydrostatic pressure may exceed lithostatic load, causing the rigid tops of intrusions to fail by fracturing of wallrocks adjacent to the pipes (e.g. Burnham, 1979). This event could lead to the development of highly mineralized stockwork veins (stage 2A and 2B) at the roof of the pluton, as seen for P1 (e.g. 5330mRL; Fig. 5.19C). The release of confined stress produced zones of high fracture density, resulting in the development of the high-grade ore shell around P1 (Fig. 5.6). Repeated fracturing and deposition occurred, as demonstrated by multiple lamellae of magnetite in stage

2B veins (Fig. 4.6). Conditions suitable for the formation of vein stockworks, as opposed to a sheeted vein system, exist when the horizontal effective differential stress is near zero (Moore, 1975). However, the dominance of N-striking veins at Ridgeway, at least in stages 2A and 2B (Fig. 5.10B), suggests that  $\sigma_3$  was oriented E. Set 3 structures fit the category of veins controlled by regional structures that may have existed at the time of porphyry emplacement. In this case, set 3 veins exploited dilatant fracture systems in most directions and  $\sigma_2$  was probably similar to  $\sigma_3$ .

At El Teniente and Bingham, Cannell *et al.* (2005) and Gruen *et al.* (2010) who worked on these giant deposits, respectively, have stressed that mineralization is derived from a larger magma sourced at depth. The vein orientations at both deposits have an over-all inward-dipping concentric and radial distribution centered in the middle of the orebody. Non-mineralized veins are common outside the mineralized zone. Cannell *et al.* (2005) and Gruen *et al.* (2010) suggested that these veins formed in response to large pluton at depth and doming of the overlying rocks. Such a scenario cannot be applied to Ridgeway. Concentric veins that dip inwards towards the intrusions may be part of the distal set 2 veins (section 5.6), but this type of vein orientation is very poorly developed. Although apparent radial veins have been observed on some domain at Ridgeway, this is inferred to be in response to the intrusions themselves. Differential block uplift can be related to the high-level intrusions.

At Ridgeway, ore vein formation and mineralization was controlled by local hydraulic fracturing caused by fluid exsolution from the porphyries, rather than from a high fluid pressure from an underlying magma chamber (c.f., El Teniente, Cannell *et al.*, 2003; Bingham, Gruen *et al.*, 2010). The mineralizing fluids at Ridgeway apparently used the porphyry bodies to provide transport to the upper crustal level of ore formation.

#### **5.8.4 Structural History**

The structural history for Ridgeway proposed here is based on the structural orientations, emplacement of intrusions and vein formation and the interplay between far-field crustal stress of the district and the more localized stress and fluid pressure

distribution caused by multiple magmatic intrusions (Fig. 5.24). The following series of events help to explain how the intrusions were localized and how the distinct vein stages were developed on the surrounding rocks which act as hosts for mineralized fluids and the formation of the Ridgeway Au–Cu deposit.

**Event 1:** Emplacement of mafic dikes along WNW-striking faults during relaxation (Fig. 5.24A). An extensional regime resulted in the emplacement of pyroxene- and feldspar-phyric dikes. Magma propagation along these faults required less energy.

**Event 2:** Monzodiorite was emplaced where a NW-striking faults intersected with a NNW-trending monocline. At deeper levels, the plutons lie along the NNW monocline trend but escape into a dilatant zone along the WNW fault at higher levels. Set 1 veins formed during and after the emplacement of the monzodiorite (Fig. 5.24B). The diffuse orientation of veins indicates that the fractures were controlled by a local stress field.

**Event 3:** Emplacement of mafic monzonite, localized on the northeast side of the monzodiorite (Fig. 5.24C). This magma is inferred to have been volatile-rich, and generated significance hydraulic fracturing for the deposition of mineralized veins. Hydraulic pressure exerted from within P1 exceeded the regional confining pressure and the entire periphery of the intrusion was in tension as the pipe expanded. Magnetite-rich USTs developed at the apex of, and along the margins of P1.

**Event 4:** Stage 2 Au–Cu stockwork veins formation (Fig. 5.24D). Mineralized quartz–magnetite–bornite (stage 2A and 2B) stockwork veins immediately followed the emplacement of P1 on its apical portion. Hydraulic fracturing was most intense in the volcanoclastic wallrock, indicating that hydro-magmatic fluid pressures were high. Vein opening occurred in multiple cycles as shown by the banded magnetite textures in stage 2B veins (Fig. 4.6). Quartz–bornite veins (stage 2D) developed later during this event. The dominant veins have N-, WNW- and NE-strikes.

**Event 5:** Emplacement of the quartz monzonite porphyry (Fig. 5.24E), as a second pulse of magma exploited the same plane of weaknesses as P1. P2 intruded along the margins of, and in the core of P1. Quartz-rich USTs and miarolitic cavities developed within P2.

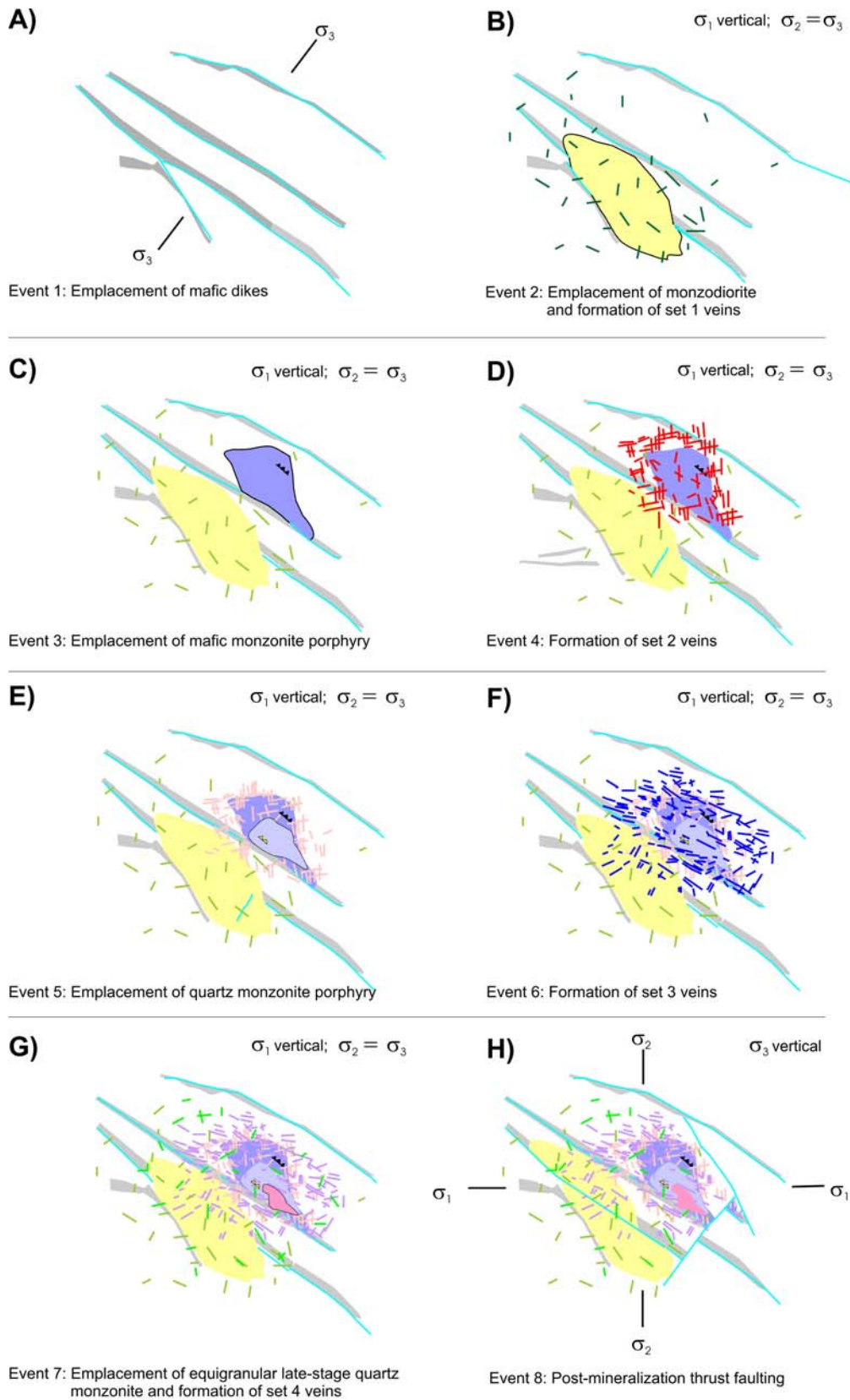


**Figure 5.24** Ridgeway schematic structural history. Plan view sketches illustrating the time sequence of intrusion emplacement and vein formation of the Ridgeway deposit. Shown are geometry of intrusions, distribution and orientation of veins and idealized local stress regime.

**Event 6:** Formation of set 3 veins (Fig. 5.24F). The parallel veins are dominantly steeply-dipping, with preferred E-, NE- and NW-orientations for mineralized stage 3A veins reflecting the prevailing far-field and local stress regimes.

**Event 7** Emplacement of equigranular late-stage quartz monzonite (Fig. 5.24G), followed by emplacement of late stage veins. The veins have a broad range of orientations. Some veins mimic the orientation of earlier-formed veins and have re-opened them. The absence of Cu–Fe sulfides in the late-stage suggests that metals and volatiles had been depleted from the underlying parent magma chamber by this event.

**Event 8:** Late-stage faults have cut and offset the intrusions and mineralization (Fig. 5.24H). A district-scale E-directed compressional event occurred in the early Silurian resulting in the development of NE-directed thrust faults such as the Purple and Claudia Faults.



---

# Chapter 6: Hydrothermal Geochemistry

---

## 6.1 Introduction

Most models of porphyry deposits are highly simplified (e.g. Lowell and Guilbert 1970; Burnham, 1979; Sillitoe 2010). They illustrate shallow intrusions surrounded by a dense fracture network and topped with vein sets and breccia pipes, where hydrothermal fluids deposit their metal loads. To fully understand the detailed mechanics of vein formation and the deposition of ore minerals in a porphyry system, it is essential to examine vein textures and fluid chemistry. The typical vein mineralogy in porphyry copper deposit includes quartz, sulfides and oxides. Paragenetic relationships are easily resolved using optical microscopy, but provide only limited textural information about vein-forming processes.

This chapter presents the results of the cathodoluminescence and trace element studies from hydrothermal quartz on mineralized vein stages from Ridgeway, together with fluid inclusion and stable isotope (sulphur and oxygen) results. These are discussed in the context of constraining the physicochemical environment of ore deposition at Ridgeway and provide the opportunity to investigate the nature of ore deposition in an evolving fracture networks.

## 6.2 Cathodoluminescence

The application of scanning electron microscope-cathodoluminescence (SEM-CL) to the study of hydrothermal quartz from porphyry deposits has only been given attention over the past decade due to recent technological advances (e.g. Penniston-Dorland, 2001; Rusk and Reed, 2002; Landtwing *et al.*, 2005). These workers used CL imaging and laser ablation-inductively coupled plasma mass spectrometry (LA-ICPMS) to reveal complex histories of vein formation with numerous cryptic textural features determined by bright- and dull-luminescing bands in quartz (Penniston-Dorland, 2001; Redmond *et al.*, 2004; Landtwing and Pettke, 2005; Rusk *et al.*, 2006; Mercer and Reed, 2007).

Systematic relationships between the titanium content of quartz and its temperature of equilibration have led to the development of a titanium-in-quartz (TitaniQ) geothermometer, which can serve as an independent geothermometer to constrain the formation temperature of quartz in magmatic systems (Wark and Watson, 2006). At Ridgeway, samples from different stages of quartz veins were investigated by SEM-CL to identify cryptic textures in quartz to establish relationships between quartz and sulfide deposition, and to estimate the temperatures of quartz formation through the application of the TitaniQ geothermometer. Microprobe analyses of  $\text{TiO}_2$  in the quartz USTs were not conducted in this study, and so the Ti in quartz temperature cannot be calculated.

### 6.2.1 Methodology

Veins from well-constrained parts of the Ridgeway paragenesis were selected for this study. A total of ten main-stage quartz–bornite (stage 2B), quartz–chalcopyrite (stage 3A) and quartz veins (stage 3D) were analyzed using SEM-CL, transmitted light, reflected light, and back scatter electron (BSE) imaging. More than 500 SEM-CL images were collected (Appendix F) using FEI Quanta 600 MLA environmental scanning electron microscope using a slow beam scan rate of 30s per image at a resolution of 1024x768 pixels, with an accelerating voltage of 15kV and a magnification of 200X. Trace elements (Ti, Al, Fe and K) were analyzed using the Cameca SX100 electron microprobe at the University of Tasmania with an accelerating voltage of 15kV, a beam current of 200 nA, and a spot size of 5 $\mu\text{m}$ . The limits of detection using these analytical conditions are: Al = 15 ppm, Ti = 22 ppm, Fe = 52 ppm, K = 16 ppm. Chemical mapping using LA-ICPMS has also been undertaken according to the methodology of Large *et al.* (2009) in order to identify the locations of trace metals in the quartz grains, specifically with regards them occurring as discrete inclusions or evenly distributed in the crystal lattice. Table 6.1 summarizes sample locations and characteristics of the veins examined. Detailed microprobe analyses and the estimated temperature of formation for each spot analyzed are provided in Appendix G.

**Table 6.1** Samples analyzed by SEM-CL imaging from Ridgeway.

Vein stage	Hole #	Depth (m)	Elevation (mRL)	Sample description
Stage 2B	UR142	172.5	5081	Quartz-banded magnetite vein; hosted in feldspathic siltstone of the Weemalla Formation; taken from the strong orthoclase–biotite–albite–magnetite alteration zone
	UR450	143.3	4912	Quartz-banded magnetite–bornite vein with thin K-feldspar halo; hosted in volcanoclastic sandstone in the Forest Reefs Volcanics; taken from the strong orthoclase–biotite–albite–magnetite alteration zone
Stage 2D	UR022	173.9	5367	Quartz–bornite vein with thin K-feldspar halo; bornite occurs as disseminations on quartz; hosted in pyroxene-phyric basaltic dike; taken from the magnetite–actinolite–albite–biotite alteration zone
	UR140	205.0	5130	
Stage 3A	UR450	143.3	4912	Quartz - chalcopyrite vein; hosted in pervasive K-feldspar altered volcanoclastic sandstone of the Forest Reefs Volcanics; taken from the strong orthoclase–biotite–albite ± magnetite alteration zone
	CR057	1927.5	4803	Quartz–chalcopyrite–molybdenite vein; hosted in quartz monzonite porphyry; taken from the moderate orthoclase–biotite–albite ± magnetite alteration zone
Stage 3D	UR323	1371.0	3729	Quartz vein, barren, white, sugary vein; hosted in quartz monzonite porphyry; taken from the moderate orthoclase–biotite–albite ± magnetite alteration zone

## 6.2.2 Hydrothermal quartz vein textures

Detailed SEM-CL imaging of the different quartz veins stages from Ridgeway revealed a complex history of mineral deposition and dissolution associated with several hydrothermal events. All quartz veins analyzed show at least three distinct generations of quartz crystallization revealed by contrasting CL light intensity and discrete quartz textures (Table 6.2; Fig. 6.1). The apparent luminescence observed in SEM-CL images depends on numerous operating conditions and absolute CL intensity cannot be easily quantified (Rusk and Reed, 2002). In the following discussion, luminescence intensity is referred to as CL-bright, CL-grey and CL-dark.

The first generation of quartz (Qz-1) is divided into two sub-types: euhedral Qz-1A with well defined growth zones of CL-bright and CL-grey bands, and subhedral Qz-1B with diffuse zoning and CL-grey luminescence (Table 6.2; Fig. 6.1A and B). The second generation of quartz (Qz-2) is generally massive with CL-grey luminescence (Table 6.2; Figs. 6.1A and C). The last generation of quartz (Qz-3) is characterized by CL-dark luminescence, and is closely associated with Cu–Fe sulfide deposition (Table 6.2; Fig. 6.1C).

**Table 6.2** Quartz generations defined by textures using SEM-CL imaging from Ridgeway.

Quartz type	Sub-type	Textures and occurrence	Luminescence	Vein stages
Qz-1	Qz-1A	Euhedral quartz grains with growth zones, characterized by alternating bands and luminescence intensity	CL-bright, CL-grey	Stage 2B, Stage 2D, Stage 3A, Stage 3D
	Qz-1B	Subhedral quartz grains with diffuse and faint oscillatory zoning; equant to rhombohedral shape quartz crystals	CL-grey	Stage 2B, Stage 2D, Stage 3A, Stage 3D
Qz-2		Massive, homogenous luminescence, with no internal texture; truncate early generation Qz-1; locally occurring as indentions or embayments from the edge of quartz crystals	CL-grey	Stage 2B, Stage 2D, Stage 3A, Stage 3D
Qz-3		Occurring near or along the edges of Cu-Fe sulfides; locally occurring along quartz grain boundaries and as microfractures truncating earlier quartz types	CL-dark	Stage 2A, stage 2D, Stage 3A

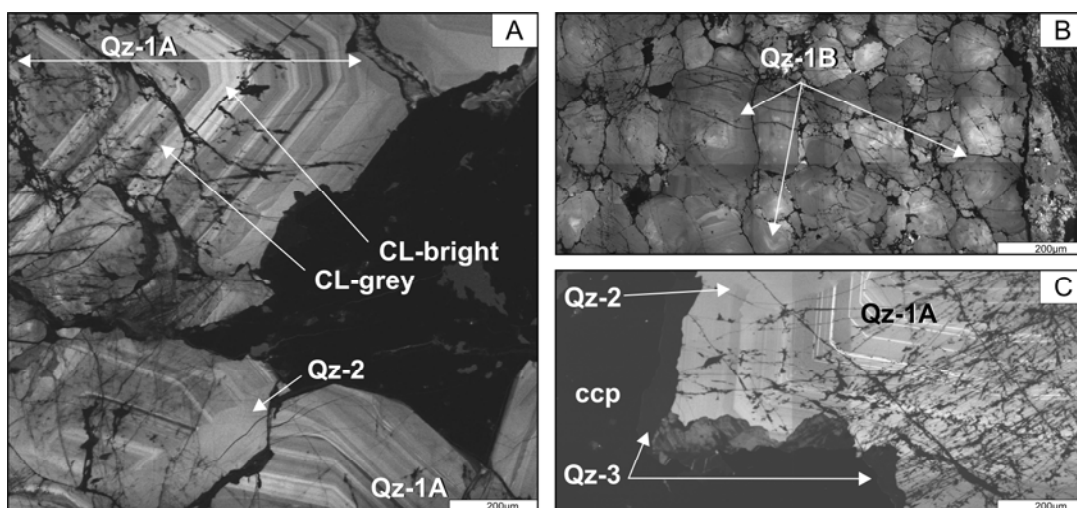


**Figure 6.1** Scanning electron microscope-cathodoluminescence (SEM-CL) images of the different quartz generations showing distinct textures from Ridgeway veins. **A)** Early, Qz-1A quartz, with euhedral growth zoning, exhibiting textures of interlayered CL-bright and CL-grey intensity. Qz-1A growth zones truncated by later quartz generations (UR022-173.9m). **B)** Type Qz-1B quartz, rhombohedral-shaped crystals exhibiting subtle oscillatory zoning (UR323-1371m). **C)** Type Qz-2 has homogeneous CL-grey luminescence, with no evidence of zoning. Qz-2 is a product of dissolution of early quartz. Type Qz-3 has dark grey luminescence, typically occurs near and along the edge of Cu-Fe sulfides. Qz-3 has truncated all of the earlier types of quartz (UR450-143.3m). Abbreviation: ccp = chalcopyrite

### 6.2.2.1 Qz-1A: euhedral growth zones

Type Qz-1A is characterized by euhedral quartz with well-defined alternating bands of CL-bright and CL-grey layers that vary in width from 5 to 50 μm (Fig. 6.1A). Typically, the crystal shapes defined by the concentric growth zones point towards the center of the vein and are oriented parallel to the *c*-axis (Fig. 6.4). Quartz is interpreted to have grown into open extensional fractures (e.g. Penniston-Dorland,

2001). Internal growth zoning has mostly resulted from variations in the physico-chemical conditions during quartz growth, which affected trace element substitutions due to changes in pH or to intrinsic defects caused by the growth conditions (Gotze *et al.*, 2001).

#### **6.2.2.2 Qz-1B: diffuse zones**

Type Qz-1B is characterized by equant, rhombohedral-bipyramidal quartz crystals that display weak CL-grey luminescent regions (Fig. 6.1B). The size of the quartz grain varies from 50 to 500  $\mu\text{m}$  (Fig. 6.2). The cores of individual crystals contain slightly lighter (more luminescent) regions, and subtle oscillatory zoning is visible faintly. Type Qz-1B is most evident in stage 3D barren quartz vein (Fig. 6.8).

#### **6.2.2.3 Qz-2: quartz overgrowths on dissolution surfaces**

The second generation of quartz, Qz-2, is characterized by massive, homogenous CL-grey luminescence with no visible oscillatory zoning (Fig. 6.1A and C). The CL emission of type Qz-2 is uniform with no identifiable internal texture, so only one generation of formation can be identified from CL images. Type Qz-2 has truncated Qz-1 growth zones and occurs as shallow indentions and embayments (Figs. 6.3B and 6.5C). The truncation of growth zones and embayments in quartz grains is interpreted as dissolution or resorption of the earlier-formed quartz generation (Penniston-Dorland, 2001; Harris *et al.*, 2004). Qz-2 occurs in all of the vein stages studied from Ridgeway. It generally occurs near quartz vein margins, or in the centers of veins.

#### **6.2.2.4 Qz-3: CL-dark luminescence**

Type Qz-3 quartz is volumetrically subordinate to Qz-1 and Qz-2, but it is present in all quartz veins analyzed, and associated with Cu–Fe sulfides (Fig. 6.1C). Qz-3 is characterized by CL-dark luminescence and occurs along microfractures, grain boundaries, and edges of sulfide grains. Dark-luminescent regions vary from 10 to 100  $\mu\text{m}$  in width (Fig. 6.5C and G and Fig. 6.7B and C). Typically, Qz-3 has truncated Qz-1 and Qz-2, suggesting that sulfide precipitation post-dates earlier quartz deposition (Fig. 6.5D).



### 6.2.3 Electron microprobe analyses

Variations in trace element concentrations are found to occur in different quartz generations. Chemical mapping of trace elements in type Qz-1A has been conducted to identify the locations of trace metals in the quartz grains. Electron microprobe mapping of quartz from a stage 2B vein (Fig. 6.3) and LA-ICPMS imaging of quartz from a stage 2D vein (Fig. 6.6) were performed to test whether these techniques could map the spatial distributions of the most abundant trace elements (Al, Ti and Fe) in the quartz crystals. The mapping shows a consistency in trace element distributions that suggest Al, Ti and Fe substitute into the quartz crystal lattice. Overall, this technique proved ineffective at mapping element zonation, compared to its effectiveness for mapping trace element distributions in pyrite (e.g. Large *et al.*, 2009).

#### 6.2.3.1 Stage 2B quartz–banded magnetite–bornite veins

SEM-CL imaging of a stage 2B vein revealed three generations of quartz, dominated by irregular Qz-2 that occurs both at the margins and at the center of the vein (Fig. 6.2). Type Qz-1A occurs as euhedral grains up to 30  $\mu\text{m}$  across, while type Qz-1B grains are up to 300  $\mu\text{m}$  in diameter (Figs. 6.2B). Qz-1 occurs as remnants truncated by Qz-2, which suggest that most of the primary quartz crystals have partly dissolved (Fig. 6.3B).

Analyses of trace element concentrations have shown that Al, Ti and K are positively correlated with the bright bands in Qz-1A (Fig. 6.3B to E; Appendix G). For Qz-1A, the CL-bright bands have elevated Al concentrations, from 445 to 1184 ppm, Ti between 132 and 444 ppm and K from 104 and 264 ppm (Fig. 6.3B). These are up to two orders of magnitude higher than the CL-grey bands in Qz-1A, which have Al concentrations between 221 and 412 ppm, Ti from 66 to 114 ppm and K from 24 to 63 ppm (Fig. 6.3B). Type Qz-2 has even lower Ti (68 to 88 ppm), Al (24 to 103 ppm) and K (<16 ppm) concentrations (Fig. 6.3B). Variable concentrations of Fe, between <52 and 341 ppm, were detected for all quartz types in this stage 2B vein.

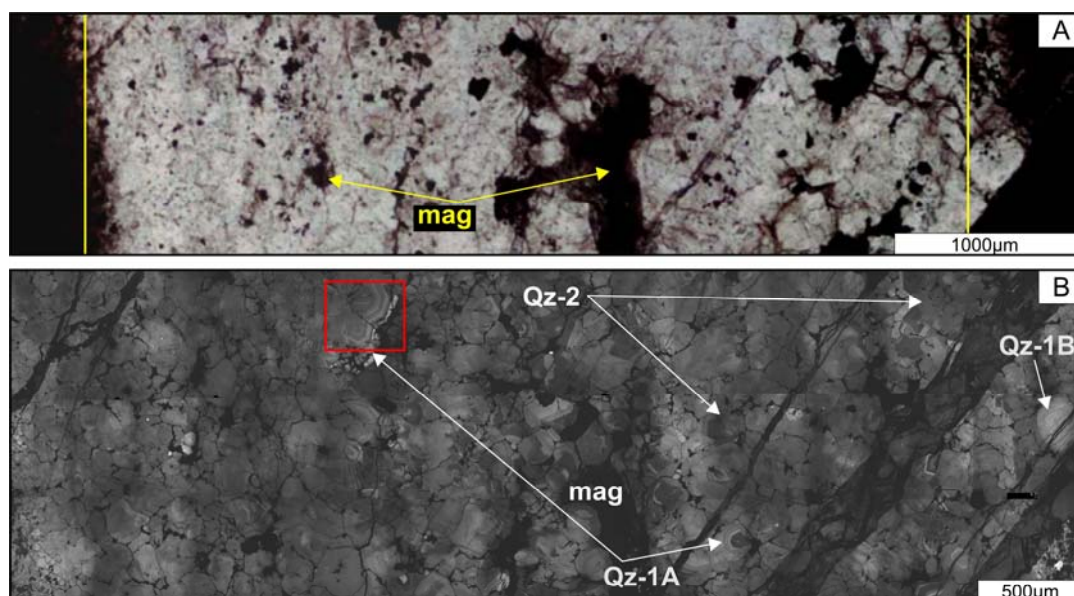
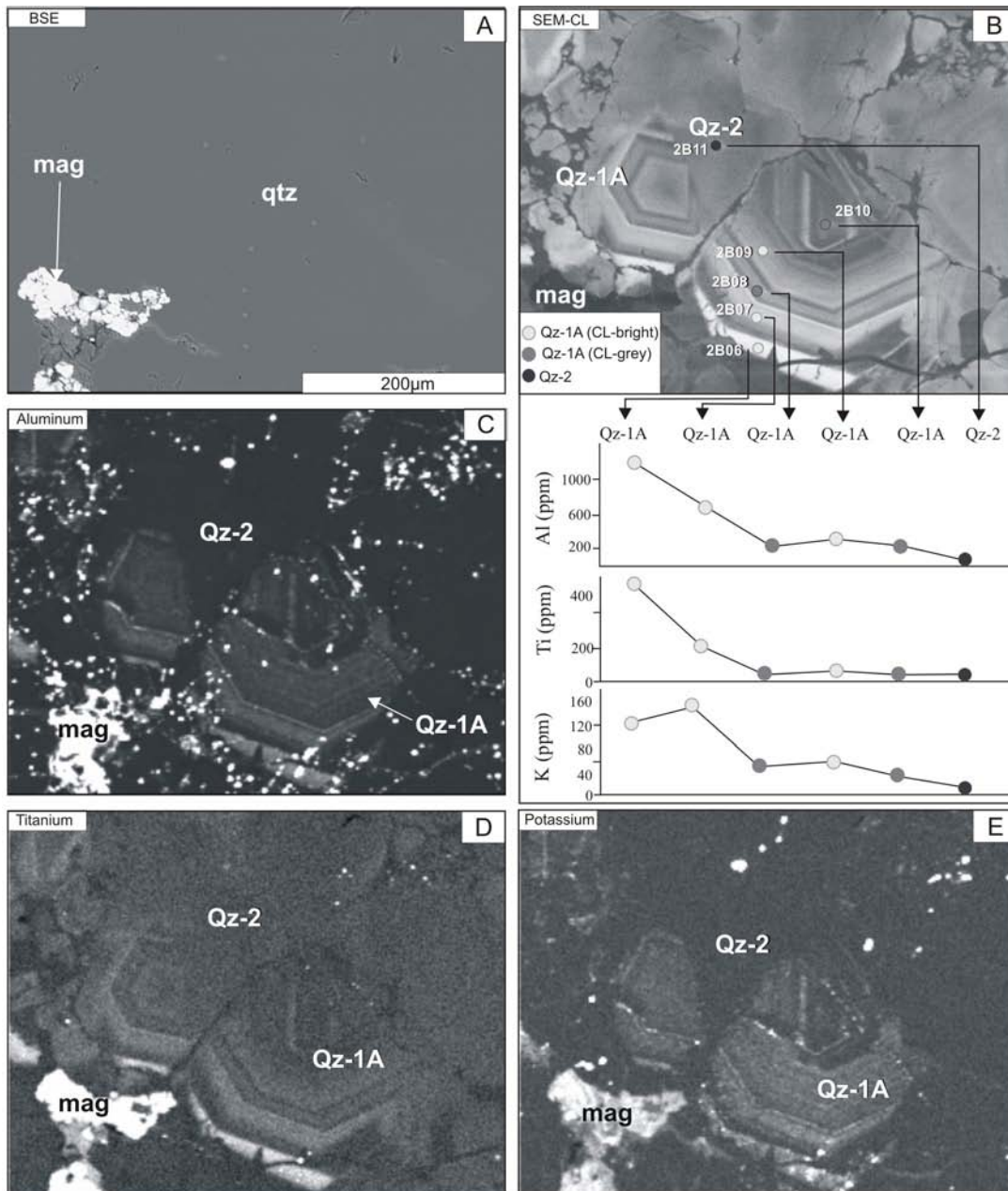


Figure 6.2 Quartz textures observed in a stage 2B quartz - banded magnetite  $\pm$  bornite vein (UR142-172.5m). A) Photomicrograph in plane polarized light. B) SEM-CL imaging of (A) outlined in yellow box. Qz-1A and Qz-1B occur as isolated islands throughout the vein. Qz-2 dominates the vein, truncating earlier quartz generations. Qz-2 occur along the margins and on the center of the vein. A close-up view of the red box in (B) is shown in Figure 6.3. Abbreviation: mag = magnetite

### 6.2.3.2 Stage 2D quartz–bornite vein

The SEM-CL image of a 2D quartz–bornite vein reveals three generations of quartz. Qz-1A comprises >90 vol. % of the vein, and quartz growth zones vary 5 to 30  $\mu\text{m}$  thick (Figs. 6.4 and 6.5C). Qz-2 has cut across Qz-1A growth faces and grain boundaries (Figs. 6.4B and 6.5C). Qz-3 was the last generation of quartz to crystallize, forming fine-grained (<20  $\mu\text{m}$ ) CL-dark luminescent crystals around bornite that have truncated Qz-1A and Qz-2 (Fig 6.5C).

Figures 6.4E and 6.5C show the trace element concentrations in stage 2D veins. All data are listed in Appendix G. CL-bright zones in Qz-1A are positively correlated with elevated Al and Ti concentrations (61 to 2185 ppm Al; 75 to 217 ppm Ti), and K concentrations up to 650 ppm. The darker CL bands in Qz-1A have lower Al (<15 to 1023 ppm), Ti (<21 to 96 ppm), and K (<16 to 307 ppm) concentrations compared to the bright bands. Fe concentrations for Qz-1A vary from <52 to 425 ppm. Qz-2 is characterized by limited variations in trace element concentrations (Al from 147 to 157 ppm; Ti <74 ppm, Fe <161 ppm, and K - below detection limit). Fe contents are highest in Qz-3 between 592 and 1427 ppm. All other trace elements, including Al, Ti and K, are below detection limits in Qz-3.



**Figure 6.3** BSE, CL images, graphs of trace element concentrations, and trace elements mapping of Qz-1A and Qz-2 in stage 2B vein (red box from Figure 6.2B; UR142-172.5m). **A)** BSE and **B)** SEM-CL of Qz-1A and Qz-2. Al, Ti and K are positively correlated with Qz-1A CL-bright bands, but decrease in concentrations for Qz-1A CL-grey bands. Qz-2 have a negative correlation with Al and K concentrations. **C)** to **E)** Trace element maps of Al, Ti, and K of Qz-1A and Qz-2. Note dark to black intensity of Qz-2 in the Al and K trace mapping correspond to very low concentrations of these elements. Details of trace elements concentration listed in Appendix G. Abbreviations: mag = magnetite, qtz = quartz



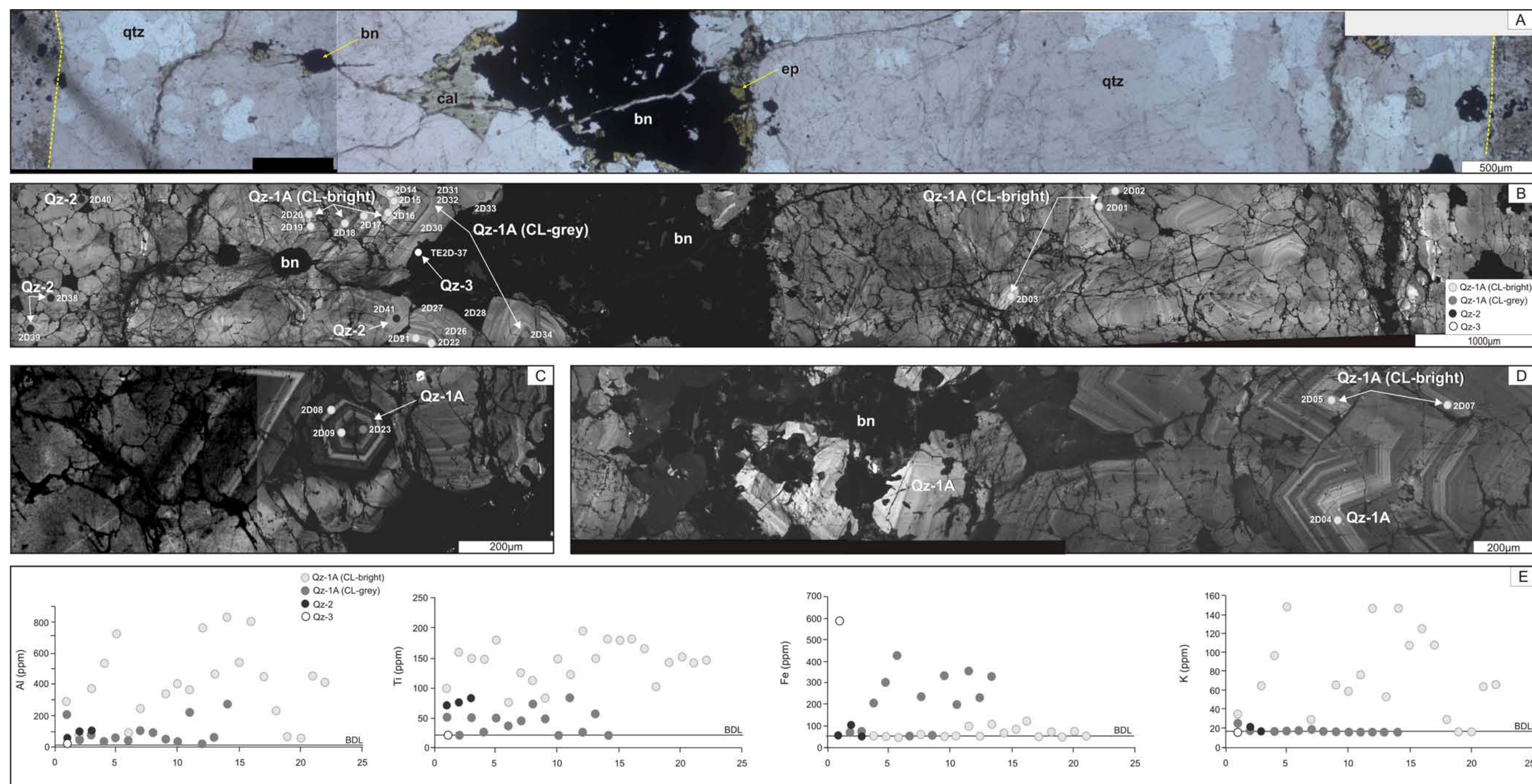


**Figure 6.4** Photomicrograph, CL images and graphs showing the trace element concentrations of Qz-1A, Qz-2 and Qz-3 in stage 2D quartz - bornite vein (UR022-173.9m). **A)** Photomicrograph (ppl). **B)** SEM-CL of (A). Qz-1A prominent pointing towards the center of the vein, Qz-2 is notable along vein margins, close to the wallrock (yellow lines marked the contact). **C)** Qz-1 showing visible growth zones. **D)** Qz-1 facing towards the center of the vein. Note the brecciated Qz-1 crystals on the center of the vein. Bornite filled the open space with Qz-3 precipitated as grain boundaries. **E)** Graphs of trace elements, Al, Ti, Fe and K concentrations from analyzed spots throughout the vein, selected spots shown from (B) to (D). Al, Ti and K elements are positively correlated with Qz-1A, decreasing in concentration to later quartz types. Fe shows a reverse in concentration, where Fe content is highest in Qz-3. Details of trace element concentrations listed in Appendix G. Abbreviations: bn = bornite, BDL= below detection limit, cal= calcite, ep = epidote, ppl = plane polarized light, qtz = quartz



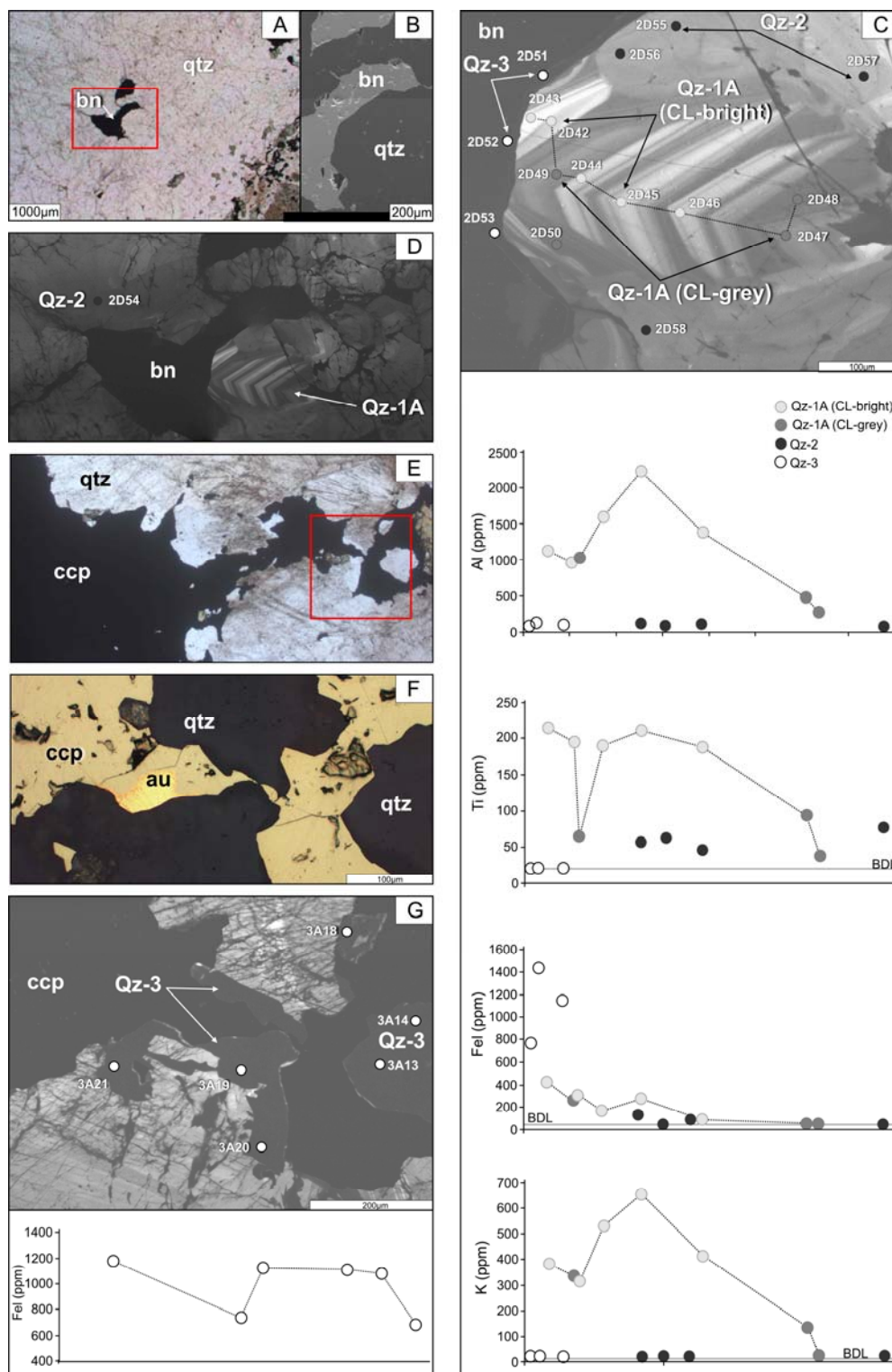


**Figure 6.5** Photomicrographs, CL images and graphs showing trace elements concentrations of Qz-1A, Qz-2 and Qz-3. **A)** Photomicrograph (ppl) of stage 2D quartz - bornite vein (UR140-205m). **B)** BSE of (A). **C)** and **D)** SEM-CL image of (A) outlined in red box and trace element concentrations of the different quartz generations. Qz-1A correlates positively with Al, Ti and K, but negatively with Fe. The concentrations of Al, Ti and K decrease from Qz-1 to Qz-3, but increase in Fe contents (up to 1427 ppm for Qz-3). **E)** Photomicrograph (ppl) of a stage 3A quartz - chalcopyrite vein (UR450-143.3m). **F)** Photomicrograph (rl) of (E), gold intergrown with chalcopyrite. **G)** SEM-CL image of (F), Qz-3 formed along the boundaries of gold and chalcopyrite grain. Qz-3 has elevated Fe concentrations from 744 to 1184 ppm; Al, Ti and K concentrations are all below detection limits. Abbreviations: bn = bornite, BDL = below detection limit, ccp = chalcopyrite, au = gold, ppl = plane polarized light, qtz = quartz, rl = reflected light



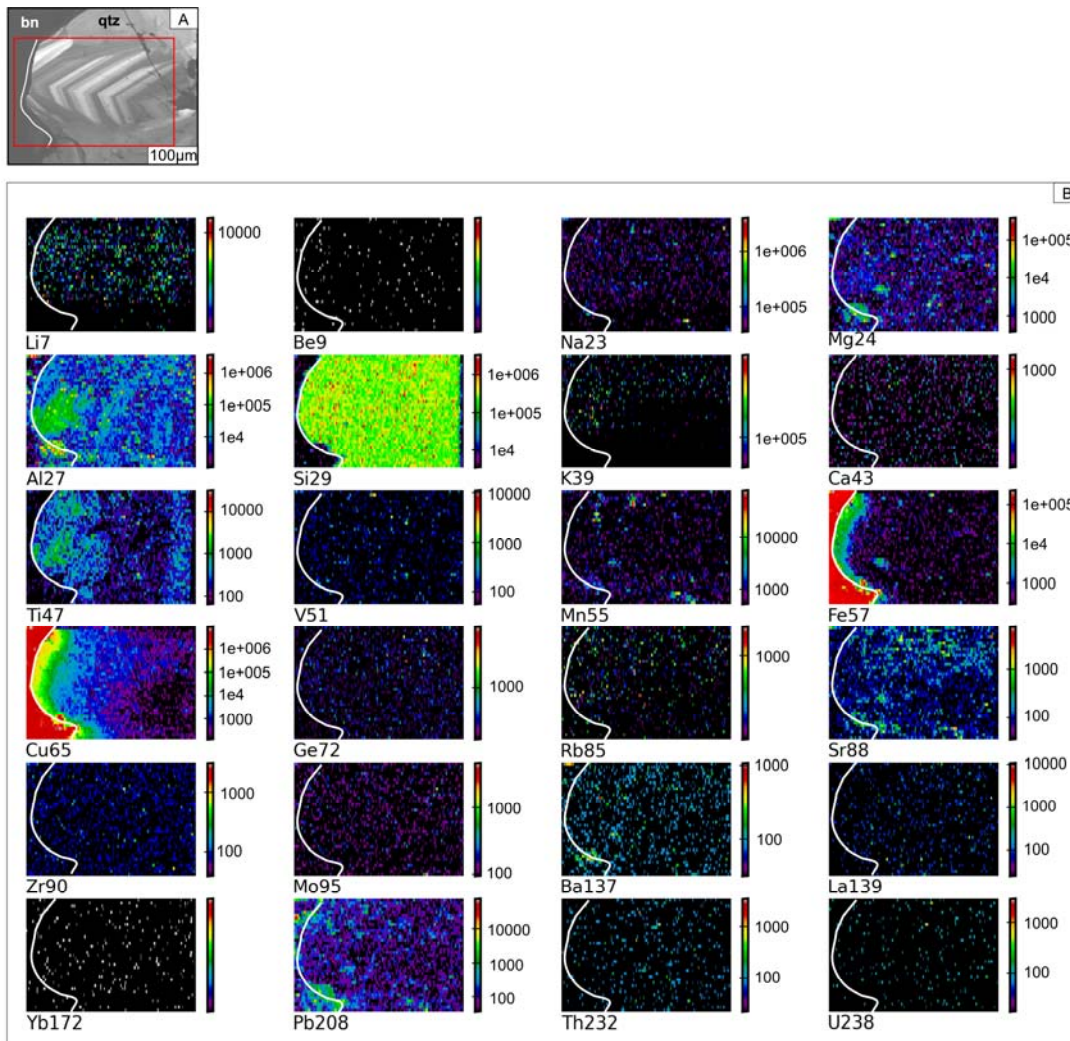


**Figure 6.6** Trace element mapping using LA-ICPMS analysis (methodology of Large *et al.*, 2009). **A)** SEM-CL image of quartz in a stage 2D vein. Quartz types described in Figure 6.5C. **B)** LA-ICPMS trace element maps of (A), enclosed in red box. The element maps show relatively high (hot colours) and low concentrations (cool colours) of various elements in bornite and quartz crystals (white line traces the crystal boundary), based on counts per second detection using the ICPMS. Note the moderately hot colours for Al and Ti that corresponds with type Qz-1. Abbreviations: bn = bornite, qtz = quartz

### 6.2.3.3 Stage 3A quartz–chalcopyrite vein

SEM-CL imaging of stage 3A quartz–chalcopyrite veins defined three types of quartz. The vein is dominated by Qz-1A (> 90 vol. %), which occurs as euhedral quartz crystals up to 1000 µm in diameter (Fig. 6.7). Individual crystals define bright and dark luminescent bands parallel to crystal faces that range between 5 and 30 µm across. Type Qz-2 occur both at the margins and at the centre of the crystals, truncating growth zones of Qz-1A. Qz-3 typically occurs on the edge of chalcopyrite grains in the center of the filled vein (Fig. 6.5G; Figs 6.7B and C).

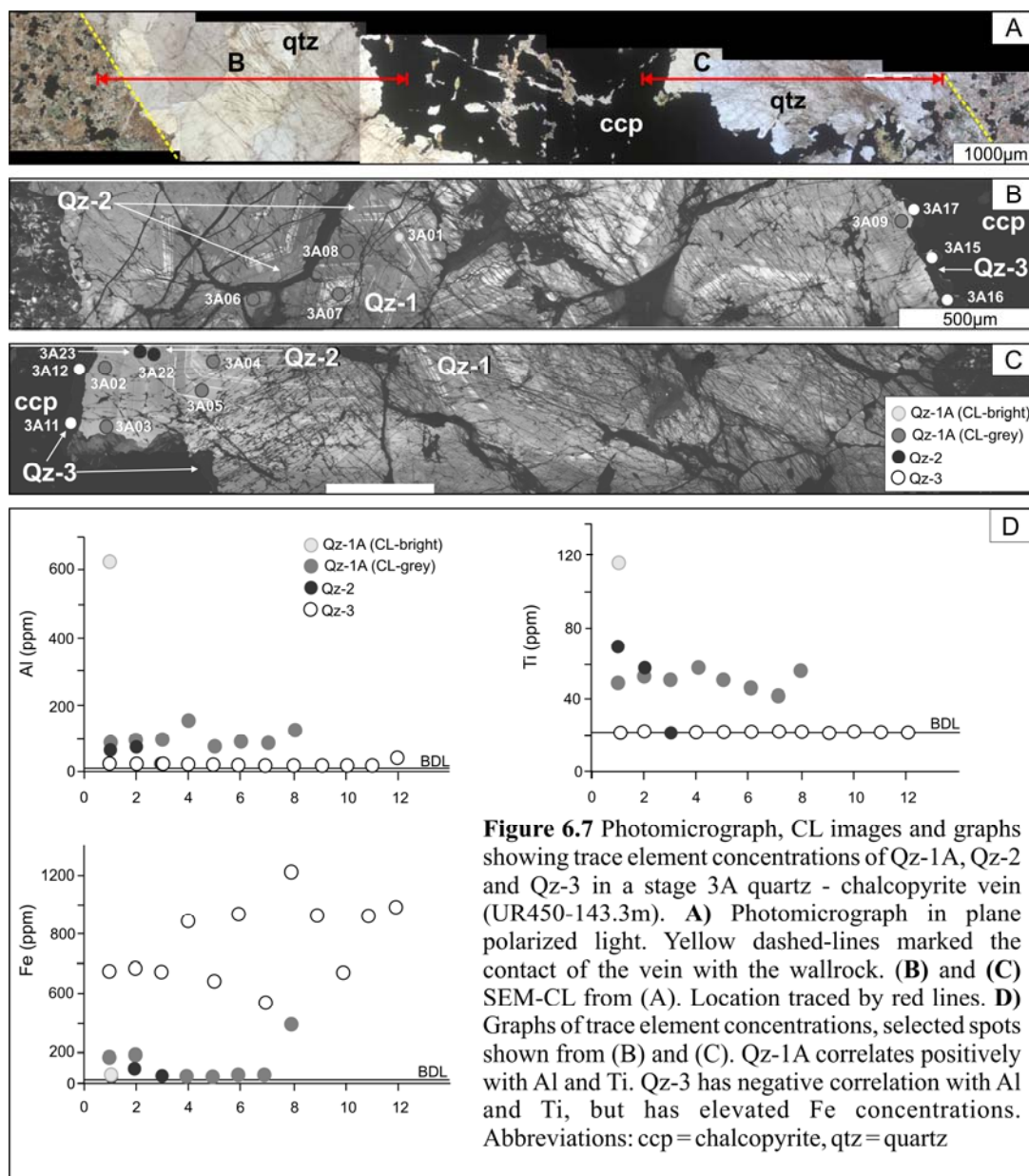
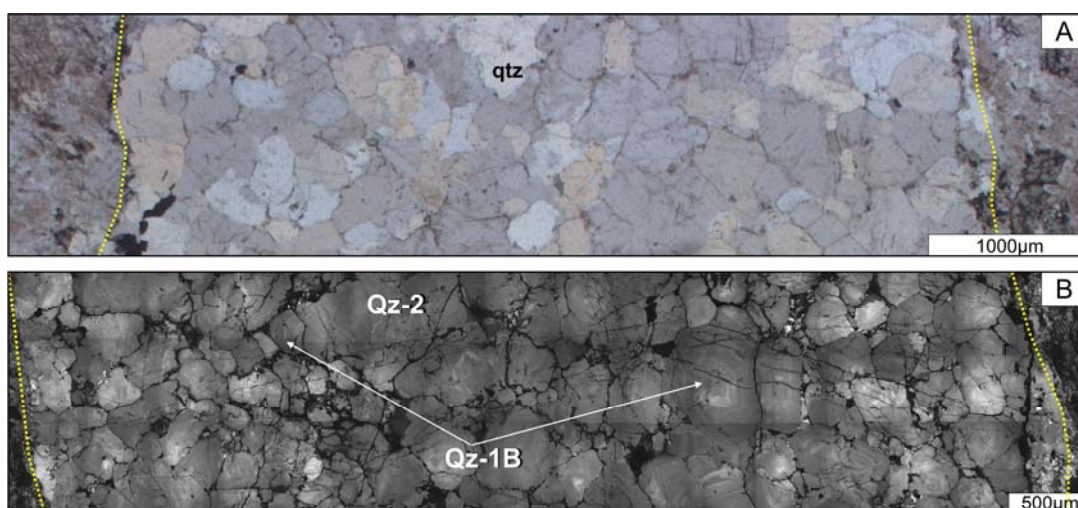


Figure 6.5G and Figure 6.7D show the trace element concentrations in stage 3A veins (details provided in Appendix G). Al and Ti are positively correlated with a single Qz-1A CL-bright spot (Fig. 6.7D). There is a marked decrease in concentrations of these elements in the darker bands of Qz-1A, where Al contents only vary from 76 to 110 ppm, and Ti from 42 to 126 ppm. Qz-2 has Al and Ti below detection limit (<84 ppm and <70 ppm, respectively). Qz-3 has elevated Fe concentrations of 534 to 1417 ppm, while Al, K and Fe are all below detection limits. Qz-3 compositions are consistent with the analysis from other mineralized veins (compare Figs. 6.5G and 6.7D with Figs. 6.4E and 6.5C; Appendix G).

### 6.2.3.4 Stage 3D quartz vein

SEM-CL imaging of a stage 3D barren quartz vein revealed a distinct type of quartz crystals with equant - rhombohedral shapes (Qz-1B) that were up to up to 500  $\mu\text{m}$  in diameter (Fig. 6.8). Qz-1B exhibits diffuse oscillatory zoning with grey to light grey luminescence. Locally, the original grain boundaries have undergone resorption (dissolution), where embayed regions towards the core of the crystal are occupied by Qz-2 (Fig. 6.8B).

Trace element concentrations of five spots (3D01 to 3D05; Appendix G) from Qz-2 shows a limited range of Al (35 to 71 ppm) and Ti (109 to 245 ppm) compared to other quartz types. Only one spot returned Fe concentrations above the detection limit (245 ppm), while K contents are all below detection limit.



**Figure 6.8** Quartz textures in a stage 3D barren quartz vein. **A)** Photomicrograph in plane polarized light. Yellow dashed-lines marked the contact of the vein with the wallrock. **B)** SEM-CL imaging of (A) Type Qz-2 dominates the vein, occurring as embayments on Qz-1B. Few Qz-1B with equant, rhombohedral shape crystal, exhibiting diffuse/faint oscillatory zoning (UR323-1371m). Abbreviation: qtz = quartz

### 6.2.4 Titanium-in-quartz geothermometer

Temperatures of quartz precipitation have been estimated using the TitaniQ geothermometer of Wark and Watson (2006). According to the TitaniQ thermometer, temperatures of quartz equilibration can be determined from the measured Ti contents (in ppm by weight) with the equation:

$$T(^{\circ}\text{C}) = \frac{-3765}{\log\left(X \frac{\text{qtz}}{\text{aTiO}_2}\right)} - 273$$

where  $a\text{TiO}_2$  is the activity of  $\text{TiO}_2$  required for rutile saturation. For Ridgeway, the activity of  $\text{TiO}_2$  is inferred to be equal to one, as hydrothermal rutile has been documented to occur in the deposit (Chapter 4). The minimum temperature that the TitaniQ geothermometer can provide, based on the detection limits for Ti on the electron microprobe (21 ppm), is calculated at 589°C for hydrothermal quartz from Ridgeway (Appendix G). Figure 6.9 shows the concentrations of Al, Ti, Fe and K for the different types of quartz.

Table 6.3 summarizes the range of temperatures estimated for the deposition of the different quartz types and the ranges of trace element concentrations. Calculated temperatures vary from <589 to 974°C (Fig. 6.9E). Overall, temperatures decreased from the earliest-formed quartz (Qz-1 from 601 to 979°C and Qz-2 from 601 to 761°C) to the latest quartz generation (Qz-3 below 589°C). The decrease in temperatures calculated for each quartz type broadly corresponds to the decrease in intensity of quartz luminescence (Table 6.3; Fig. 6.9E). Details for individual spot temperature calculations are listed in Appendix G.

At Ridgeway, it seems that the early quartz (Qz-1 and Qz-2) probably formed at temperatures >600°C. Large fluctuations in calculated temperatures (>100°C) are recorded for Qz-1A (from 610° to 850°C; Fig. 6.9E; Fig. 6.5C; Appendix G). Other samples yielded average temperatures of 761°C (UR142), 735°C (UR022) and 779°C (UR140) for Qz-1A (Appendix G). In these cases, titanium is directly correlated to the intensity of quartz luminescence.

**Table 6.3** Temperature of quartz crystallization calculated using the TitaniQ geothermometer from trace element concentrations for the different quartz types from Ridgeway.

Quartz type	Sub-type	Number of spots <sup>1</sup>	Range °C	Al (ppm) <sup>2</sup>	Ti (ppm) <sup>2</sup>	K (ppm) <sup>2</sup>	Fe (ppm) <sup>2</sup>
Qz-1	Qz-1A CL-bright	34	713 to 979	61 to 2185	75 to 481	<16 to 650	<52 to 415
	Qz-1A-CL-grey	28	601 to 776	<15 to 1023	<21 to 121	<16 to 307	<52 to 425
	Qz-1B	8	717 to 812	35 to 412	77 to 245	<16 to 22	<52 to 341
Qz-2		14	601 to 751	<15 to 157	<21 to 103	<16 to 21	<52 to 161
Qz-3		16	<589	<15 to 44	<21	<16 to 60	534 to 1427

<sup>1</sup> Number of spots used in the calculation of temperature using TitaniQ geothermometer, details listed in Appendix G

<sup>2</sup> Trace element detection limits for Al = 15 ppm, Ti = 21 ppm, K = 16 ppm and Fe = 52 ppm



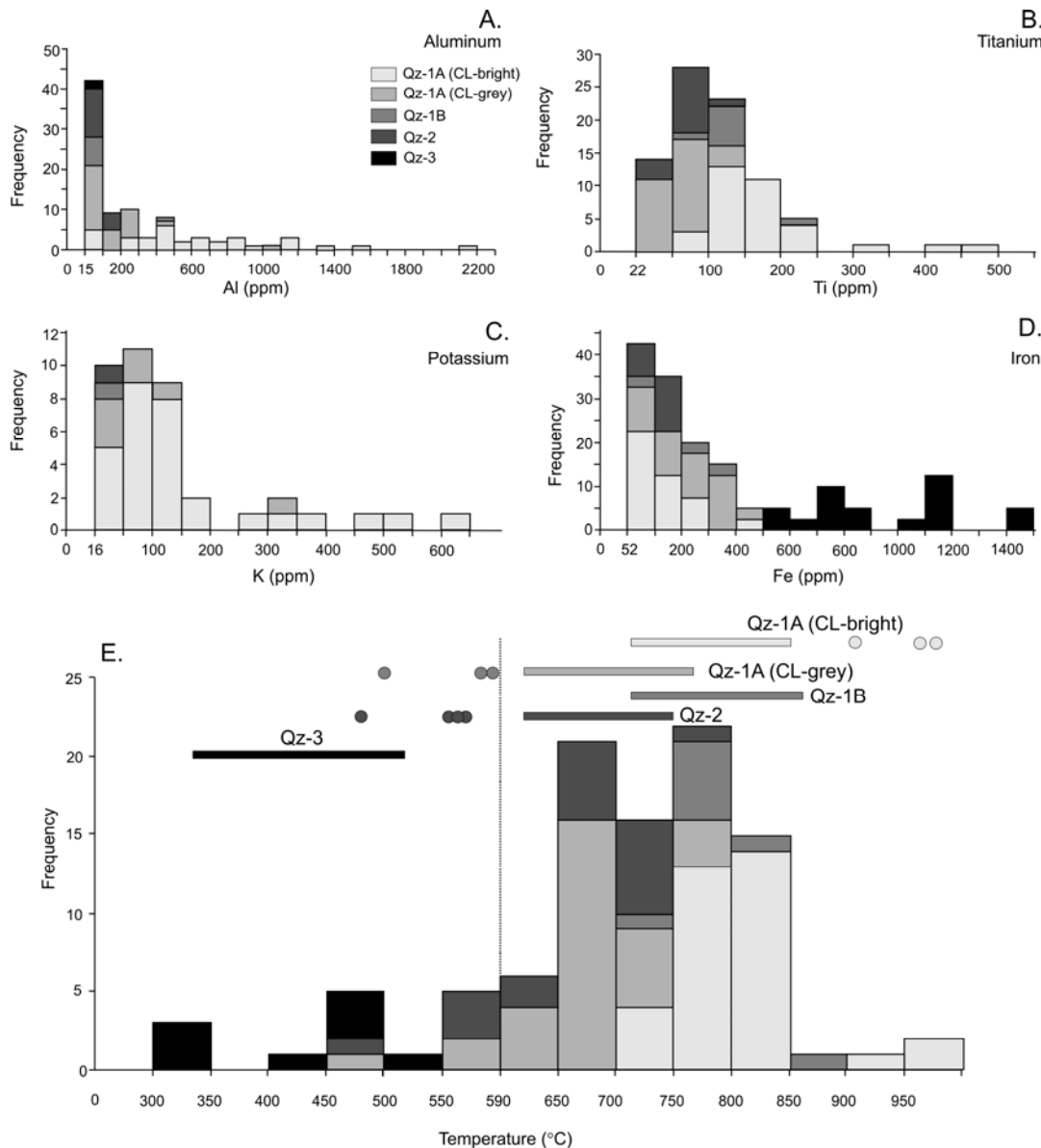


**Figure 6.9** A) to D) Trace element concentrations of Al, Ti, K and Fe for the different types of quartz from Ridgeway. CL-bright bands in Qz-1A have elevated Al and Ti; decreasing concentrations correspond with decreasing luminescence in quartz. K concentrations present in variable amounts in Qz-1A and Qz-2. Fe concentrations in early quartz (Qz-1A and Qz-2) do not exceed 425 ppm. Qz-3 has Fe concentrations from 534 to 1427 ppm. Al, Ti and K concentrations all below detection limits in Qz-3. E) Histogram of temperature of quartz crystallization calculated using the TitaniQ geothermometer (Wark and Watson, 2006). The graph shows a continuous decrease in temperature formation from the earlier quartz types (Qz-1) to the latest type of quartz (Qz-3). The average temperature of Qz-1 is 760°C, Qz-2, is 680°C and below 589°C for Qz-3 where Ti concentrations are below detection limit (21 ppm). The decrease in temperature of quartz crystallization also corresponds to the decrease in intensity of quartz luminescence. Circles represent estimates outside the general temperature population.



### 6.2.5 Discussion

SEM-CL imaging has provided evidence for multiple quartz generations in the Ridgeway quartz veins. The different generations of quartz veins have similar histories of quartz development from early Qz-1 to Qz-2 to Qz-3. This suggests that similar physical and chemical conditions prevailed for quartz deposition during stages 2 and 3. Variations in CL intensity may help to distinguish superimposed mineralization events, if each has its own characteristic trace element concentrations (Redmond *et al.*, 2004; Landtwing and Pettke, 2005; Rusk *et al.*, 2006; Mercer and Reed, 2007). Trace element compositions of quartz may therefore provide insights into geologic processes, and could provide a tool for helping decipher complex paragenetic relationships.

#### 6.2.5.1 Correlation between quartz types, CL intensity and trace elements

At Ridgeway, the earliest generation of quartz initially precipitated into open space as Qz-1, with alternating bands of CL-bright and CL-grey luminescence. Some later time, Qz-1 was fractured, partially dissolved, and then overgrown by Qz-2. Changes in pressure and temperature probably occurred during mechanical fracturing, which created the secondary permeability exploited by Qz-2. Further decrease in pressure and/or temperature may have facilitated the precipitation of Qz-3, prior to or synchronous with Fe–Cu sulfides.

In hydrothermal systems, potential causes for quartz dissolution include pressure fluctuations, pH increase, temperature increase or changes in fluid compositions (Rusk and Reed, 2002). Obvious evidence for quartz dissolution at Ridgeway is provided by truncation of growth zones and the shallow indentions on some Qz-1 crystals filled by Qz-2 (Figs. 6.1, 6.3B and 6.5C). Qz-2 may have formed by local dissolution and reprecipitation of quartz during closure of the fracture or later stresses. Locally, a dissolution front might have moved SiO<sub>2</sub> from the edge of the crystal inward, where it reprecipitated (e.g. Grasberg, Penniston-Dorland, 2001; also Figs. 6.3B and 6.5C).

Rusk *et al.* (2008) used an electron microprobe to map trace element concentration in high temperature quartz samples from quartz-dominated veins with

potassic alteration from porphyry-Cu (Mo-Au) deposits in Butte, Montana; Grasberg, Papua New Guinea Los Pelambres, El Salvador; and El Teniente, Chile. Al and Ti are observed in all samples (Fig. 6.10). The study showed that CL intensity correlates positively with Ti concentrations in quartz veins analyzed from the five porphyry deposits. According to Rusk *et al.* (2008), this relationship suggests that Ti is a CL activator in quartz formed above 400°C and concluded that Ti concentrations broadly reflect temperature of quartz precipitation. The aluminium concentrations, based from the study, are consistently in the range of several hundred ppm (Fig. 6.10; Rusk *et al.*, 2008). Rusk *et al.* (2008) reported that the aluminum concentrations in quartz reflect solubility of Al in hydrothermal fluids, which is strongly controlled by pH. The study concluded that the Al concentrations in quartz reflect fluctuations in pH that may facilitate metal-sulfide precipitation in hydrothermal systems (Rusk *et al.*, 2008). The result of the Ti and Al concentrations in quartz from the different porphyry deposits show that most Ti range from <10 to 200 ppm, and Al between 80 and 400 ppm, with some growth zones in quartz from Grasberg sample have high Ti (476 ppm) and Al (1200 ppm; Fig. 6.10; Rusk *et al.*, 2008). At Ridgeway, the highest Ti and Al concentrations analyzed from the early-formed quartz (Qz-1A) were 481 ppm and 2185 ppm, respectively. Hence, the study of high-temperature quartz in porphyry deposits by Rusk *et al.* (2008) broadly correlates with the results from the early-formed quartz from Ridgeway.

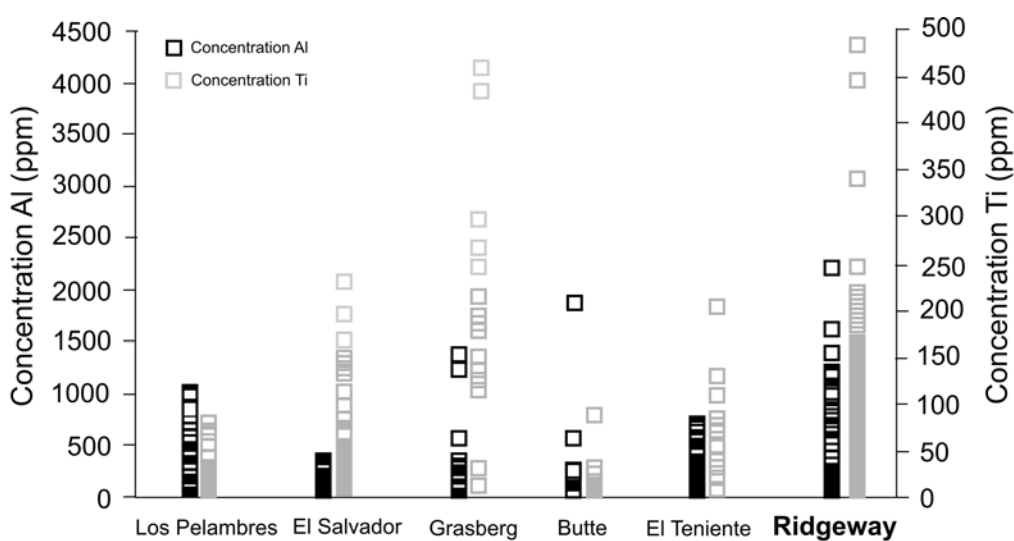


**Figure 6.10** Al and Ti concentration in quartz at Ridgeway compared to six high-temperature hydrothermal ore deposits (data from Rusk *et al.*, 2008). The Ridgeway data is from the current study.

### 6.2.5.2 Temperature of quartz formation and sulfide precipitation

In porphyry deposits, quartz veins associated with potassic alteration usually precipitate from 750° to 500°C, but can be overprinted by cooler fluids (<400°C; Seedorff *et al.*, 2005). A combination of CL petrography with inclusion microthermometry was used to unravel the growth history of individual quartz veins and link this history to copper ore formation at Butte, Montana (Rusk *et al.*, 2006) and Bingham, Utah (Landwing *et al.*, 2005). The early generation CL-bright precipitated at temperature ~550°C (Butte; Rusk *et al.*, 2006) and at ~500°C (Bingham, Landwing *et al.*, 2005). Both studies show that thermal decline to temperatures below 425°C to 350°C was the main driving force for Cu–Fe sulfide deposition together with the later CL-dark luminescing quartz (Rusk and Reed, 2002; Redmond *et al.*, 2004; Landwing *et al.*, 2005). At Ridgeway, high-temperature Qz-1 precipitated during stockwork formation at temperatures between 601 and 850°C, and in equilibrium with hydrothermal K-feldspar. Dissolution of this early-formed quartz was then followed by deposition Qz-2. At temperatures below 589°C, Qz-3 was deposited, together with the Cu–Fe sulfides. By analogy, with the study of Butte and Bingham, Qz-3 may have formed around 425° to 350 °C at Ridgeway.

## 6.3 Fluid Inclusions

Quartz is not a suitable host for fluid inclusions at Ridgeway due to post-mineralization deformation that produced numerous microfractures (e.g. Figs. 6.1, 6.4 and 6.7). This is true both of quartz veins and quartz USTs as revealed from CL. Wilson *et al.* (2003) analyzed quartz-hosted halite-bearing fluid inclusions in pressure shadows around sulfide grains, but concluded that the halite-homogenizing fluid inclusions had re-equilibrated after entrapment.

In the current study, garnet from the garnet–epidote alteration assemblage (Chapter 4) has been investigated as a possible host for workable primary fluid inclusions. The purpose of the current study is to characterize the temperature and pressure of garnet formation in order to help constrain the physiochemical environment of mineralization. Garnet samples were collected from the calcareous

lithofacies of the Weemalla Formation (Chapter 3) at various elevations from ~850 to 1500 m below the current surface (~5070 to ~4360mRL; Table 6.4).

### 6.3.1 Previous work

A systematic fluid inclusion studies of the Cadia porphyry deposits was undertaken as part of the PhD study of Wilson (2003). At Ridgeway, Wilson (2003) analyzed 157 fluid inclusions and reported the presence of aqueous liquid-vapour and hypersaline brine inclusions. Most of these fluid inclusions were concluded to be of secondary origin. The aqueous liquid-vapour inclusions homogenized to liquid at temperature between 53° and 222°C (average 125°C) and had an average salinity of 3.8 wt. % NaCl equiv. One population of hypersaline brine inclusions were reported to occur in the pressure shadows of sulfide minerals in early-, transitional-, and late-stage quartz veins, but were considered secondary in origin because they lie along healed fractures (Wilson *et al.*, 2003). A second population of brine inclusions, interpreted to be of primary origin, homogenized to liquid via halite dissolution, and yielded an average homogenization temperature of 426°C with total average salinity of 50.3 wt % NaCl equivalent. Wilson *et al.* (2003) interpreted that the fluid was a nonboiling, hypersaline brine that exsolved directly from the melt. The inclusions had very low homogenization temperatures (<150°C) suggesting re-equilibration after entrapment.

### 6.3.2 Methodology

Fluid inclusions were analysed from five doubly polished, 150 µm thick garnet-bearing wafers samples collected from the garnet–epidote alteration zone. BSE imaging of selected samples was undertaken in order to ascertain the timing of fluid inclusion entrapment relative to the growth history of the garnet crystals. Primary inclusions were distinguished using the criteria of Roedder (1984), specifically isolated inclusions, random 3-dimensional distributions or fluid inclusions trapped along growth zones.

Microthermometry was carried out on a Linkham MSS600 heating and freezing stage that has an upper temperature of 500°C. All measurements were made using the 100x objective lens. Calibration of the Linkham stage was checked using

synthetic fluid inclusions supplied by Synfl Inc.. The precision of measured temperatures are  $\pm 1.0^{\circ}\text{C}$  for heating experiments and  $\pm 0.3^{\circ}\text{C}$  for freezing. Salinities were determined as NaCl equivalent weight percent (eq. wt. NaCl).

### 6.3.3 Classification

The Ridgeway garnets contain very few fluid inclusions, which range in size from 5 to 20  $\mu\text{m}$ . Inclusion shapes is circular, ellipsoidal, or irregular (Fig. 6.11). The fluid inclusions in garnet have been classified using the scheme of Nash (1976; Table 6.4). Type 1 inclusions are liquid-rich and comprise two sub-groups. Types 1A have a vapour bubble that occupies 10 to 60 vol % of the inclusion, and no daughter crystals (Fig. 6.11A and B). Types 1B have a liquid–vapour ratio similar to type 1A inclusions, but contain a small opaque phase (Fig. 6.11C). Both types 1A and 1B inclusions homogenize to the liquid phase. Type 2 inclusions are vapour-rich. They contain a dark vapour bubble that occupies 60 - 80 vol % of the inclusion, and homogenize to vapour (Fig. 6.11D). These three types of inclusions were found to

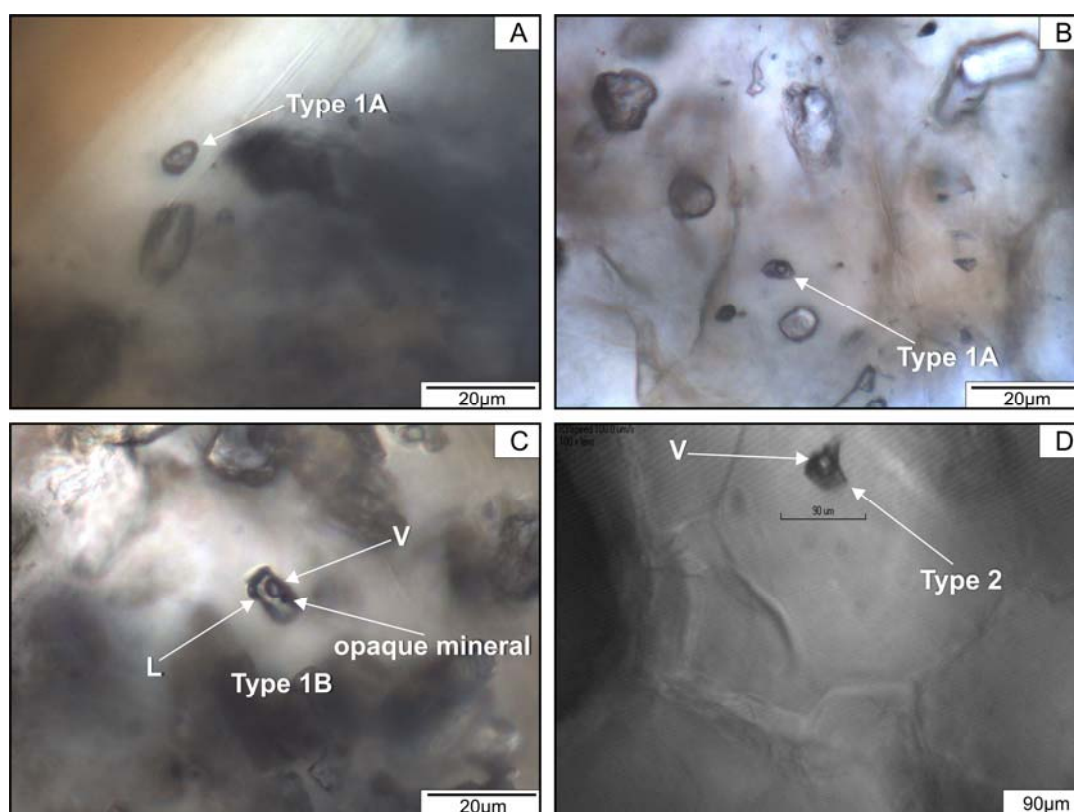


**Figure 6.11** Types and occurrence of fluid inclusions in garnet from Ridgeway. **A)** Primary type 1A liquid-rich isolated inclusion occurring along a growth zone (CR062-1626.3m). **B)** Primary type 1A liquid-rich isolated inclusion (CR062-1626.3m). **C)** Type 1B liquid-rich inclusion containing a small opaque mineral (UR150-90.6m). **D)** Primary type 2 vapour-rich isolated inclusion (CR062-1626.3m). Abbreviations: L = liquid, V = vapour



coexist as a fluid inclusions population only in one sample (i.e. UR323-589m; Table 6.4). The most common fluid inclusion populations consist only of type 1A, or type 1A that coexist with type 1B.

The following abbreviations have been used in the presentation and discussion of microthermometric analyses:  $T_h$  = temperature of homogenization;  $T_e$  = temperature of first melting, i.e. eutectic temperature;  $T_m$  = final or last ice melting temperature. Where possible, homogenization measurements were replicated or triplicated in order to test for reproducibility.

### 6.3.4 Microthermometry results

Microthermometry was carried out on all fluid inclusion types. Most of the analyses were of type 1A, followed by type 1B, and a few type 2 inclusions. Detailed results for the fifty two fluid inclusion analyses are provided in Table 6.4 and histograms are plotted in Figure 6.12. Salinity estimates were calculated from ice-melting temperatures for 19 type 1 inclusions based on the method of Bodnar (1993), assuming a simple NaCl-H<sub>2</sub>O system. Two fluid inclusions from type 1B and one inclusion from type 2 contained a solid phase when frozen that melted at +3.9, +4.5°C, +10 °C, respectively, interpreted to be CO<sub>2</sub> clathrate.

Type 1A fluid inclusions had  $T_h$  ranging from 157° to 321°C (mean = 237°C; Fig. 6.12A). Measured  $T_m$  values ( $n = 11$ ) were between -12° and -2.2°C (mean = -6.3°C; Fig. 6.12B) corresponding to calculated salinities from 3.7 to 11.5 wt. % NaCl equiv (mean = 9.5; Fig. 6.12D). Measured  $T_e$  were all above -20°C except for one inclusion that had  $T_e = -23.2^\circ\text{C}$  (Fig. 6.12C).  $T_e$  values between -21 and -30°C suggest that NaCl and KCl are the predominant salts in solutions (Roedder, 1984; Shepherd *et al.*, 1985).

Type 1B inclusions have  $T_h$  values between 148 and 266°C (mean = 196°C; Fig. 6.12A). The average  $T_h$  for type 1B inclusions is ~40°C lower than that for type 1A inclusions. Measured  $T_m$  values ( $n = 8$ ) range from -10.4° to -3.3°C (mean = -6.0°C; Fig. 6.12B), corresponding to calculated salinities from 5.3 to 13.9 wt. % NaCl equiv (average = 9.0; Fig. 6.12D). On two occasions, frozen inclusions contained a solid phase that dissolved above 0°C, at +3.9°C and +4.5°C. Measured  $T_e$  has a wide range

**Table 6.4** Summary of fluid inclusion microthermometric analyses and location of samples from Ridgeway.

HOLE #	Depth (m)	Elevation (CML) <sup>1</sup>	FI-LABEL	Trials	T <sub>h</sub> (°C)	T <sub>e</sub> (°C)	T <sub>m</sub> (°C)	Salinity (wt. % NaCl equiv)	Type of inclusion	Description
CR062	1626.3	4368	CR062-FI-07		180.8		-2.2	3.7	Type 1A	L-rich
CR062	1626.3	4368	CR062-FI-08		168.5	-10.3	-7.8	11.5	Type 1A	L-rich
CR062	1626.3	4368	CR062-FI-10		177.9				Type 1A	L-rich
CR062	1626.3	4368	CR062-FI-11		173.6				Type 1A	L-rich
CR062	1626.3	4368	CR062-FI-12		156.6				Type 1A	L-rich
CR062	1626.3	4368	CR062-FI-13		263.5				Type 1A	L-rich
CR062	1626.3	4368	CR062-FI-14		211.4				Type 1A	L-rich
CR062	1626.3	4368	CR062-FI-15		260.5				Type 1A	L-rich
CR062	1626.3	4368	CR062-FI-16		307.3				Type 1A	L-rich
CR062	1626.3	4368	CR062-FI-17		296.4				Type 1A	L-rich
CR062	1626.3	4368	CR062-FI-18		218.4				Type 1A	L-rich
CR062	1626.3	4368	CR062-FI-20	1	255.2	-17.6	-5.9	9.1	Type 1A	L-rich
CR062	1626.3	4368	CR062-FI-20	2	256.8		-4.4	7.0	Type 1A	L-rich
UR255	476.8	4629	UR255-FI-01		213.0	-3.0			Type 1A	L-rich
UR323	589.0	4455	UR323-FI-01		217.2	-11.5	-7.8	12.6	Type 1A	L-rich
UR323	589.0	4455	UR323-FI-06		210.8	-9.7	-7.3	10.9	Type 1A	L-rich
UR323	589.0	4455	UR323-FI-08		217.2				Type 1A	L-rich
UR323	589.0	4455	UR323-FI-09		201.8				Type 1A	L-rich
UR323	589.0	4455	UR323-FI-10		215.8				Type 1A	L-rich
UR323	589.0	4455	UR323-FI-11		213.3				Type 1A	L-rich
UR323	589.0	4455	UR323-FI-03		262.1	-23.2	-12.0	16.0	Type 1A	L-rich
UR323	589.0	4455	UR323-FI-07		278.8				Type 1A	L-rich
UR362	665.8	4370	UR362A-FI-01		190.2		-6.2	9.5	Type 1A	L-rich
UR362	665.8	4370	UR362A-FI-02		179.8		-4.5	7.2	Type 1A	L-rich
UR362	666.0	4370	UR362-FI-01		164.7	-11.6			Type 1A	L-rich
UR150	90.6	5073	UR150-FI-01	1	315.8		-5.1	8.0	Type 1A	L-rich
UR150	90.6	5073	UR150-FI-01	2	320.7		-5.9	9.1	Type 1A	L-rich
UR150	90.6	5073	UR150-FI-02		218.8				Type 1A	L-rich
UR150	90.6	5073	UR150-FI-03		299.1				Type 1A	L-rich
UR150	90.6	5073	UR150-FI-04		312.1				Type 1A	L-rich
UR150	90.6	5073	UR150-FI-05	1	306.4				Type 1A	L-rich
UR150	90.6	5073	UR150-FI-05	2	319.0				Type 1A	L-rich
CR062	1626.3	4368	CR062-FI-01		147.8		4.5		Type 1B	L-rich with opaque crystal
CR062	1626.3	4368	CR062-FI-02	1	212.3				Type 1B	L-rich with opaque crystal
CR062	1626.3	4368	CR062-FI-02	2	211.7	-4.3	3.9		Type 1B	L-rich with opaque crystal
CR062	1626.3	4368	CR062-FI-02	3	211.4	-4.5			Type 1B	L-rich with opaque crystal
CR062	1626.3	4368	CR062-FI-03	1	156.2		-6.9	10.2	Type 1B	L-rich with opaque crystal
CR062	1626.3	4368	CR062-FI-03	2	157.2	-7.5	-3.3	5.3	Type 1B	L-rich with opaque crystal
CR062	1626.3	4368	CR062-FI-03	3	155.6				Type 1B	L-rich with opaque crystal
CR062	1626.3	4368	CR062-FI-04		156.3	-7.5	-5.1	8.0	Type 1B	L-rich with opaque crystal
CR062	1626.3	4368	CR062-FI-05		214.7	-22.9	-5.7	8.8	Type 1B	L-rich with opaque crystal
CR062	1626.3	4368	CR062-FI-06		174.3				Type 1B	L-rich with opaque crystal
CR062	1626.3	4368	CR062-FI-09		211.4				Type 1B	L-rich with opaque crystal
CR062	1626.3	4368	CR062-FI-19		221.2				Type 1B	L-rich with opaque crystal
UR323	589.0	4455	UR323-FI-04		265.5	-42.3	-10.4	13.9	Type 1B	L-rich with opaque crystal
UR362	666.0	4370	UR362-FI-02	1	205.0		-5.3	8.3	Type 1B	L-rich with opaque crystal
UR362	666.0	4370	UR362-FI-02	2	205.0		-5.5	8.6	Type 1B	L-rich with opaque crystal
UR362	666.0	4370	UR362-FI-02	3	205.0		-5.5	8.6	Type 1B	L-rich with opaque crystal
UR362	666.0	4370	UR362-FI-03		183.0				Type 1B	L-rich with opaque crystal
UR323	589.0	4455	UR323-FI-02		386.1				Type 2	V-rich
UR323	589.0	4455	UR323-FI-05	1	403.7	-15.3	10.0		Type 2	V-rich
UR323	589.0	4455	UR323-FI-05	2	411.8				Type 2	V-rich

Abbreviations: T<sub>h</sub> = temperature of homogenization, T<sub>e</sub> = temperature of first melting, T<sub>m</sub> = temperature of final ice melting, L = liquid, V = vapour<sup>1</sup> CML = Cadia Mine Lease grid. The mine level (mRL) is 5000+ sea level

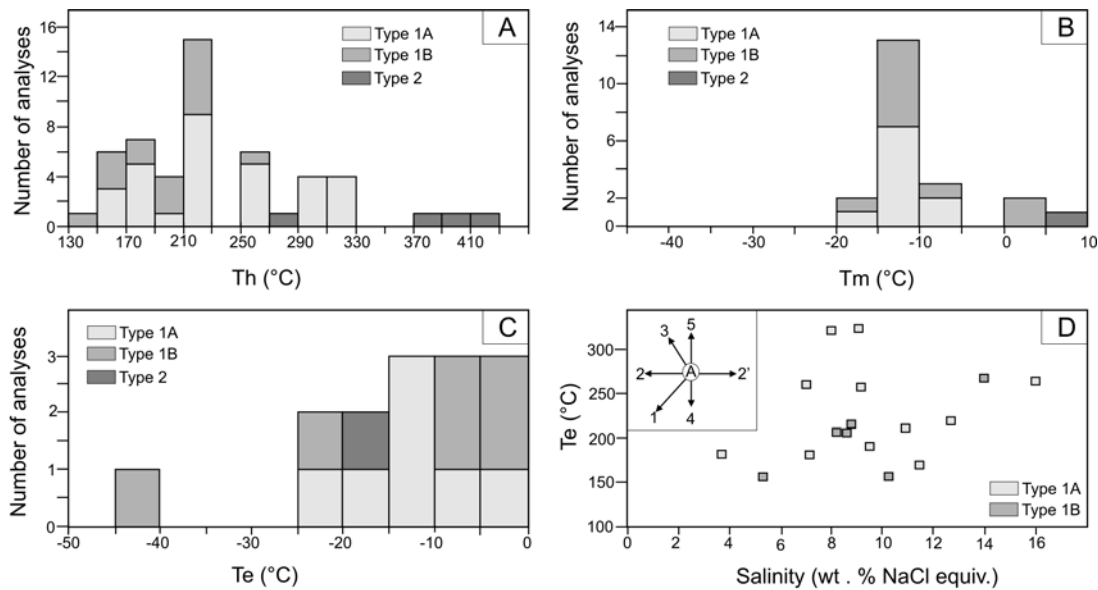


**Figure 6.12** Cumulative frequency plots summarizing the microthermometric measurements of all fluid inclusions in garnet analyzed from Ridgeway. **A)** Homogenization temperatures ( $T_h$ ). **B)** Temperatures of final ice melting ( $T_m$ ). **C)** Temperatures of first ice melting ( $T_e$ ). **D)** Homogenization temperatures ( $T_h$ ) versus salinity. Inset box is the schematic model showing general trends produced as a result of various processes operating on an aqueous fluid or fluid inclusions of composition **A**, modified from Shepherd *et al.*, 1985. 1 - mixing with cooler, less saline fluids; 2/2' - mixing with fluids of contrasting salinity; 3 - boiling with slight cooling; 4 - simple cooling; 5 - leakage of inclusions during heating.

from  $-42.4^\circ$  to  $-4.3^\circ\text{C}$  (Fig. 6.12C), indicating the presence of complex salts (Na, K, Fe and Mg).

The three primary type 2 fluid inclusions analyzed have higher  $T_h$  values ( $386.1^\circ$  -  $411.8^\circ\text{C}$ ) than type 1 inclusions (Fig. 6.12A).  $T_e$  was not measurable for type 2 inclusions, and only one measurement of  $T_m$  was obtained which persisted to  $+10^\circ\text{C}$  (Fig. 6.12B).

### 6.3.5 Discussion

#### 6.3.5.1 Pressure and depth estimates

Two distinct hydrothermal stages characterize most skarn deposits (Meinert *et al.*, 2003); an early prograde stage precipitating anhydrous minerals (e.g. garnet, pyroxene) from relatively high-temperature, hypersaline liquids, and a retrograde stage precipitating hydrous minerals (epidote, amphibole, chlorite) from lower temperature, lower salinity fluids. Experimental results on the temperature of formation of andradite by Taylor and Liou (1978) have reported a maximum at  $650^\circ\text{C}$ , and minimum of  $450^\circ\text{C}$ . Fluid inclusion studies have shown that garnet

formed at temperatures from 425° to 325°C at Santa Rita, New Mexico (Ahmad and Rose, 1980). Johnson and Norton (1985) indicated that garnet is unstable when temperatures are <400°C in the presence of aqueous CO<sub>2</sub> regardless of the garnet composition. Other fluid inclusion studies suggest that early skarn formation in porphyry environments occurs from 500° to 350°C (e.g. Jamtveit and Hervig, 1994).

At Ridgeway, fluid inclusions in andradite homogenize to liquid at 222°C (Type 1). Fluid inclusions that homogenize to vapour (Type 2) have a mean of 401°C. The large difference in homogenization temperatures suggests that these fluid inclusions cannot be representative of garnet formation, based on previous work that shows garnet is stable above 450°C (e.g. Einaudi *et al.*, 1981). It is therefore likely that the Ridgeway fluid inclusions have re-equilibrated after entrapment, or that they were trapped at higher pressures and a pressure correction for the homogenization temperatures is required.

Based from the stratigraphic reconstruction of the middle Ordovician Weemalla Formation and FRV rock sequence at the Cadia district, Harris *et al.* (2009b) estimated that at least 2 km of overburden has been eroded and removed after the Silurian uplift. Garnet–epidote alteration at Ridgeway occurs at depths of 0.9 km to 1.5 km below the current surface. Depth of formation estimated by stratigraphic-structural reconstruction range from 2.9 to 3.5 km for the garnet–epidote alteration zones. These depths are equivalent to lithostatic pressures of 720 to 870 bars and hydrostatic pressures of 290 to 350 bars. This depth of emplacement compares favourably to the depth of formation of porphyry deposits, inferred to be 1 to 6 km (Hedenquist and Richards, 1998; Murakami *et al.*, 2010). In porphyry-related copper skarns, the deepest potassium silicate zones are formed 3 to 5 km depths below the original surface, equivalent to lithostatic pressures of 740 to 1100 bars and hydrostatic pressures of 300 to 500 bars (Einaudi *et al.*, 1981).

For fluid inclusion studies, confining pressures generally need to be estimated from independent evidence of the depth of cover at the time of trapping (Roedder and Bodnar, 1980). In the case of Ridgeway, a pressure correction of 30°C would be required based on geological reconstructions of the thickness of material since removed by erosion (~2000 m). Consequently, trapping temperatures for type 1 fluid

inclusions are calculated to be ~250°C and ~430°C for type 2 inclusions. Even with these pressure corrections, the trapping temperatures estimated for garnet-hosted fluid inclusions are still well below the expected garnet formation temperatures (550° - 450°C, Einaudi *et al.*, 1981). The most likely explanation is that the fluid inclusions have been modified after entrapment, probably during post-mineral deformation. It is therefore concluded that the fluid inclusions of garnet analyzed in the current study were either secondary, and/or were re-equilibrated after entrapment, and cannot constrain formation temperatures.

## 6.4 Sulfur Isotopes

### 6.4.1 Previous Work

Sulfur isotope studies at Cadia porphyry deposits were undertaken by Harper (2000), Wilson (2003), Wilson *et al.* (2007a) and Reynolds (2007). At Ridgeway, a systematic increase in  $\delta^{34}\text{S}_{\text{sulphide}}$  values outward from the core of the deposit was detected (Harper, 2000; Wilson *et al.*, 2007a). The deposit core is characterized by low  $\delta^{34}\text{S}_{\text{sulphide}}$  values ( $\delta^{34}\text{S}_{\text{bornite}} = -4.3\text{‰}$ ;  $\delta^{34}\text{S}_{\text{chalcopyrtie}} = -5.7\text{‰}$ ). These values increase to the propylitically-altered outer and upper margins of the deposit ( $\delta^{34}\text{S}_{\text{pyrite}} = \sim 0\text{‰}$ ). Reynolds (2007) analyzed pyrite grains ( $n = 8$ ) from the distal southern parts of Ridgeway, and reported values of  $\delta^{34}\text{S}_{\text{pyrite}}$  between -3.21 and -1.92‰. Green (1999) reported values of  $\delta^{34}\text{S}_{\text{pyrite}}$  from -5.4 to +5.3‰ and  $\delta^{34}\text{S}_{\text{chalcopyrtie}}$  values from -5.1 to +2.9‰ for the Big Cadia Skarn. Wilson *et al.* (2007a) reported that the Cadia Hill has the largest range of sulfur isotopic composition analyzed, with  $\delta^{34}\text{S}_{\text{sulphide}}$  values from -9.8 to +9.1‰. The results of  $\delta^{34}\text{S}$  from Cadia East have  $\delta^{34}\text{S}_{\text{sulphide}}$  values that range between -5.4 and -1.0‰ (Wilson *et al.* 2007a). Appendix H lists all previous  $\delta^{34}\text{S}$  isotopic results from Ridgeway.

### 6.4.2 Methodology

In the current study, sulfur isotope analyses have been performed on 25 sulfides from several vein stages (Fig. 6.13). Medium- to coarse-grained sulfides were separated manually using a hand-held drill tool. Sulfur isotopic analyses were completed at the Central Science Laboratory (CSL) at the University of Tasmania using the conventional sulfur isotope technique of Robinson and Kusabe (1975). The



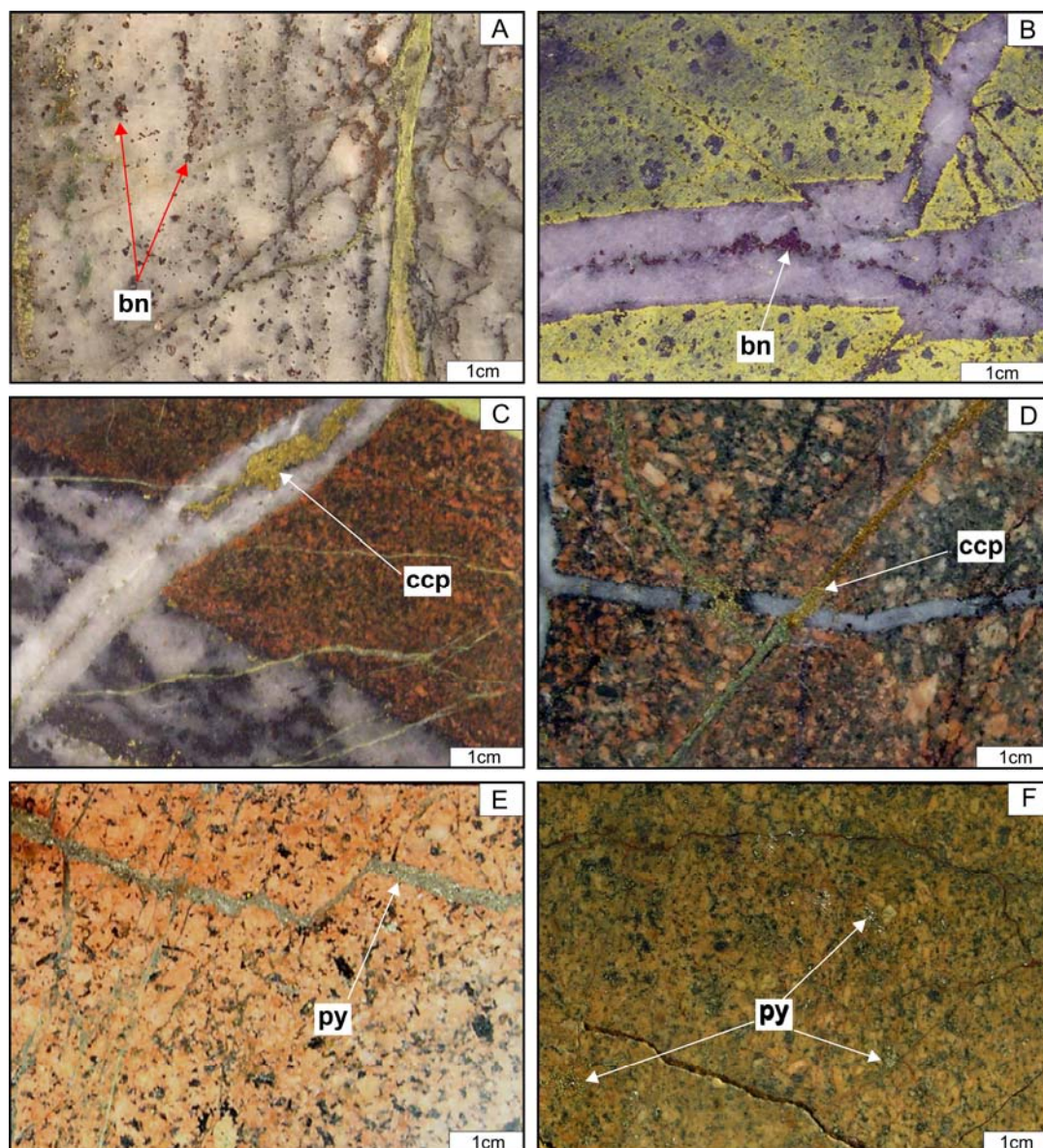


**Figure 6.13** Sulfide samples analyzed for sulfur isotopes from Ridgeway. **A)** Bornite in stage 2B quartz - banded magnetite - bornite vein. **B)** Bornite in stage 2D quartz - bornite vein hosted in K-feldspar-altered pyroxene-phyric dike. **C)** Chalcopyrite in stage 3A quartz - chalcopyrite vein cutting an earlier stage 2B vein. **D)** Chalcopyrite in stage 3C vein cutting stage 2A vein. **E)** Pyrite in stage 4A vein hosted in late-stage quartz monzonite. **F)** Pyrite disseminations in late-stage quartz monzonite. Abbreviations: bn = bornite, ccp = chalcopyrite, py = pyrite

results are expressed in standard  $\delta^{34}\text{S}$  per mil (‰) notation, relative to the Canyon Diablo Troilite (CDT). An analytical uncertainty of  $\pm 0.1\%$  is estimated for this technique. Isotope measurements were performed on a VG Sira Series II mass spectrometer.

Harper (2000) collected and analyzed forty three samples from different vein stages at Ridgeway (Fig. 6.14). Thirty eight of these samples were reviewed as part of the current study. Some of the samples were reclassified based on the updated

paragenesis (Table 4.3). All seventy six sulfide samples, including those from Harper (2000) and Reynolds (2007) were used to contour sulfur isotopic values (per mil) on section 11050mE (Figs. 6.15 and 6.16; Appendix H).

### 6.4.3 Results

Table 6.5 shows the result of twenty-five sulfur isotope analyses, with the associated vein stage, mineralogy, and location of all samples analyzed from the current study. Sulfides analyzed from Ridgeway have  $\delta^{34}\text{S}_{\text{sulfide}}$  values from -6.3 to -0.5‰ (Table 6.5), with sulfur isotopic compositions varying according to their paragenetic stages. Means and ranges of the isotopic data are given in Table 6.6, and plotted on Figure 6.14A. Most of the data are between -5 and -2‰ (Fig. 6.14A). The range of bornite values (stages 2B and 2D) is from -6.3 to -3.0‰. The range for chalcopyrite (stages 3A and 3C) is from -5.7 to -2.3 ‰, and pyrite (stage 4A) has a range from -2.9 to -0.5‰.

The full sulfur isotopic dataset for Ridgeway including the data from Harper (2000) and Reynolds (2007) are plotted on Figure 6.14B (Table 6.7; Appendix H). Figure 6.14C to Figure 6.14H show the data from individual paragenetic stages. The spatial distribution of  $\delta^{34}\text{S}_{\text{sulfide}}$  values is plotted on section 11050mE (Fig. 6.14I). Note that below 4700mRL (i.e. below the Pamela Fault), chalcopyrite and pyrite samples are by necessity projected from 200 - 250 m off-section. Contours of sulfur isotopic values for stages 3A and 3C, and stage 4A are illustrated in Figures 6.15 and 6.16, respectively.

#### 6.4.3.1 Stage 2B and 2D veins

The three  $\delta^{34}\text{S}_{\text{bornite}}$  values obtained from stage 2 veins are between -6.3 and -3.0‰ (Table 6.6; Fig. 6.13A and B). The lowest value (-6.3‰) was obtained from stage 2B bornite, while bornite from stage 2D has a mean value of -3.5‰. These values are consistent with the results from Wilson *et al.* (2007a). The  $\delta^{34}\text{S}_{\text{bornite}}$  values from both studies range between -6.3 and -2.6 ‰ (n = 7; Table 6.7; Fig. 6.14C and D), however, there is insufficient data to comment on the vertical and lateral zonation in  $\delta^{34}\text{S}_{\text{bornite}}$  values for stage 2 veins.

**Table 6.5**  $\delta^{34}\text{S}$  compositions of Ridgeway sulfides from the current study.

Sample ID		Coordinates (CML) <sup>1</sup>			Vein stage - major assemblage/alteration zone	Mineral	$\delta^{34}\text{S}$ (‰)
Hole #	Depth (m)	Northing	Easting	mRL			
UR022	164.2	11073	22691	5368	Stage 3A - quartz–chalcopyrite vein	chalcopyrite	-3.1
UR022	174.1	11074	22701	5367	Stage 2D - quartz–bornite vein	bornite	-4.1
UR022	250.2	11077	22777	5361	Stage 3A - quartz–chalcopyrite vein	chalcopyrite	-2.6
UR140	205.7	11065	22719	5130	Stage 2D - quartz–bornite vein	bornite	-3.0
UR140	227.0	11069	22740	5130	Pyrite dissemination in quartz-rich unidirectional solidification textures	pyrite	-2.9
UR140	257.0	11074	22770	5131	Stage 3C - chalcopyrite–epidote $\pm$ pyrite vein	chalcopyrite	-3.2
UR149	97.0	11041	22605	5094	Stage 3C - chalcopyrite–epidote $\pm$ pyrite vein	chalcopyrite	-5.7
UR149	164.3	11043	22668	5070	Stage 3A - quartz–chalcopyrite vein	chalcopyrite	-3.0
UR149	293.2	11048	22789	5026	Stage 2B quartz–banded magnetite–bornite vein	bornite	-6.3
UR150	185.0	11044	22659	5014	Stage 3A - quartz–chalcopyrite vein	chalcopyrite	-4.1
UR254	376.0	11065	22801	4747	Stage 3A - quartz–chalcopyrite vein	chalcopyrite	-2.5
UR313	56.0	11085	22549	4998	Stage 3C - chalcopyrite–epidote $\pm$ pyrite vein	chalcopyrite	-5.5
UR313	250.5	11064	22741	4978	Stage 3C - chalcopyrite–epidote $\pm$ pyrite vein	chalcopyrite	-4.0
UR326	367.0	11213	22678	4710	Pyrite clots/albite–quartz–pyrite–sericite alteration	pyrite	-1.6
UR326	381.6	11217	22683	4700	Stage 3A - quartz–chalcopyrite vein	chalcopyrite	-2.6
UR326	405.5	11226	22695	4681	Stage 3A - quartz–chalcopyrite vein	chalcopyrite	-3.3
NC541	1094.0	11048	22656	4811	Stage 3C - chalcopyrite–epidote $\pm$ pyrite vein	chalcopyrite	-4.3
NC541	1526.4	11046	22656	4379	Stage 3C - chalcopyrite–epidote $\pm$ pyrite vein	chalcopyrite	-4.8
UR360	765.8	11232	22669	4457	Stage 3C - chalcopyrite–epidote $\pm$ pyrite vein	chalcopyrite	-3.3
UR360	811.6	11242	22695	4420	Stage 4A - Pyrite vein	pyrite	-2.2
UR360	927.2	11266	22757	4327	Stage 3C - chalcopyrite–epidote $\pm$ pyrite vein	chalcopyrite	-3.0
UR450	143.3	11212	22623	4912	Stage 3A - quartz–chalcopyrite vein	chalcopyrite	-2.7
UR450	78.3	11192	22575	4949	Stage 3A - quartz–chalcopyrite vein	chalcopyrite	-4.0
NC498	738.0	11044	22724	5264	Stage 3A - quartz–chalcopyrite vein	chalcopyrite	-2.3
NC498	759.3	11045	22734	5246	Pyrite disseminations/albite–quartz–pyrite–sericite alteration	pyrite	-0.5

<sup>1</sup> CML = Cadia Mine Lease grid. The mine level (mRL) is 5000+ sea level**Table 6.6.** Summary of  $\delta^{34}\text{S}$  compositions for Ridgeway from the current study.

Vein Stage/Alteration	Mineral	Number	Range $\delta^{34}\text{S}$ (‰)	Mean $\delta^{34}\text{S}$ (‰)	Vein assemblage
Stage 2B	bornite	1	-6.3	-6.3	Quartz–banded magnetite–bornite vein
Stage 2D	bornite	2	-4.1 to -3.0	-3.5	Quartz–bornite vein
Stage 3A	chalcopyrite	10	-4.1 to -2.3	-3.0	Quartz–chalcopyrite vein
Stage 3C	chalcopyrite	8	-5.7 to -3.0	-4.2	Chalcopyrite–epidote $\pm$ pyrite vein
Stage 4A	pyrite	2	-2.9 to -2.2	-2.5	Pyrite vein
Albite - quartz - pyrite - sericite alteration	pyrite	2	-1.6 to -0.5	-1.1	Pyrite disseminations/clots

**Table 6.7.** Combined summary of all  $\delta^{34}\text{S}$  compositions for Ridgeway from Harper (2000), Reynolds (2007) and the current study.

Vein Stage/Alteration	Mineral	Number	Range $\delta^{34}\text{S}$ (‰)	Mean $\delta^{34}\text{S}$ (‰)	Vein assemblage
Stage 2B	bornite	1	-6.30	-6.3	Quartz–banded magnetite–bornite vein
Stage 2D	bornite/chalcopyrite	6	-4.3 to -2.6	-3.4	Quartz–bornite vein
Stage 3A	chalcopyrite	20	-5.7 to -0.5	-3.0	Quartz–chalcopyrite vein
Stage 3C	chalcopyrite	11	-5.7 to -2.8	-4.0	Chalcopyrite–epidote $\pm$ pyrite vein
Stage 4A	pyrite	13	-3.4 to +2.4	-1.2	Pyrite vein
Albite - quartz - pyrite - sericite alteration	pyrite	25	-4.0 to +9.2	-1.2	Pyrite disseminations/clots

### 6.4.3.2 Stage 3A and 3C veins

The 18  $\delta^{34}\text{S}_{\text{chalcopyrite}}$  values obtained from stage 3 veins are between -5.7 and -2.3‰ (Table 6.6; Fig. 6.13C and D). The most negative  $\delta^{34}\text{S}_{\text{chalcopyrite}}$  values occur close to P2 (Fig. 6.15), and  $\delta^{34}\text{S}_{\text{chalcopyrite}}$  values increase outward from the intrusion, consistent with the results from Wilson *et al.* (2007a). The  $\delta^{34}\text{S}_{\text{chalcopyrite}}$  values from both studies range between -5.7 and -0.5‰ ( $n = 31$ ; Table 6.7; Fig. 6.14E and F). Vertical and lateral zoning in  $\delta^{34}\text{S}_{\text{chalcopyrite}}$  values is restricted to 100 meters from the center of the deposit (Fig. 6.15), where values become less negative with increasing distance from the core of the deposit.

### 6.4.3.3 Stage 4 pyrite veins and disseminations

The four new  $\delta^{34}\text{S}_{\text{pyrite}}$  values from stage 4 veins and disseminations range from -2.9 to -0.5‰ (Table 6.6; Fig. 6.13E and F). The total dataset of 38  $\delta^{34}\text{S}_{\text{pyrite}}$  values, including the results from previous studies, are mostly between -4 and +2.4‰ (Table 6.7; Fig. 6.14G and H). The  $\delta^{34}\text{S}_{\text{pyrite}}$  values at the center of the deposit range from -2.9 to +0.6‰ ( $n = 4$ ; Fig. 6.16). One anomalously high  $\delta^{34}\text{S}_{\text{pyrite}}$  value (+9.2‰) was obtained from the albite–quartz–pyrite–sericite alteration zone peripheral to the upper northeastern parts of Ridgeway (Harper, 2000; Wilson *et al.*, 2007a; Fig. 6.16; Appendix H). This locally high  $\delta^{34}\text{S}_{\text{pyrite}}$  value has been interpreted to be the product of minor sulfide deposition from trapped connate or convectively circulating seawater (Wilson *et al.*, 2007a). Similar data have been obtained peripheral to Cadia East and Cadia Hill (Wilson *et al.*, 2007a).

A systematic zonation pattern is defined by the  $\delta^{34}\text{S}$  values for stage 4 pyrite. Figure 6.16 illustrates the stage 4 zonation pattern; sulfides have lighter  $\delta^{34}\text{S}_{\text{pyrite}}$  values peripheral to the monzonite intrusions (from +0.6 to -4‰ outwards). In contrast to stage 3  $\delta^{34}\text{S}_{\text{chalcopyrite}}$  values, the  $\delta^{34}\text{S}_{\text{pyrite}}$  values become more negative towards the surface and with increasing distance from the core of the deposit (Fig. 6.16). The consistency of this zonation is evident on the upper western side of the deposit where there is clustering of  $\delta^{34}\text{S}_{\text{pyrite}}$  values of  $\sim -2$ ‰ (Fig 6.16).



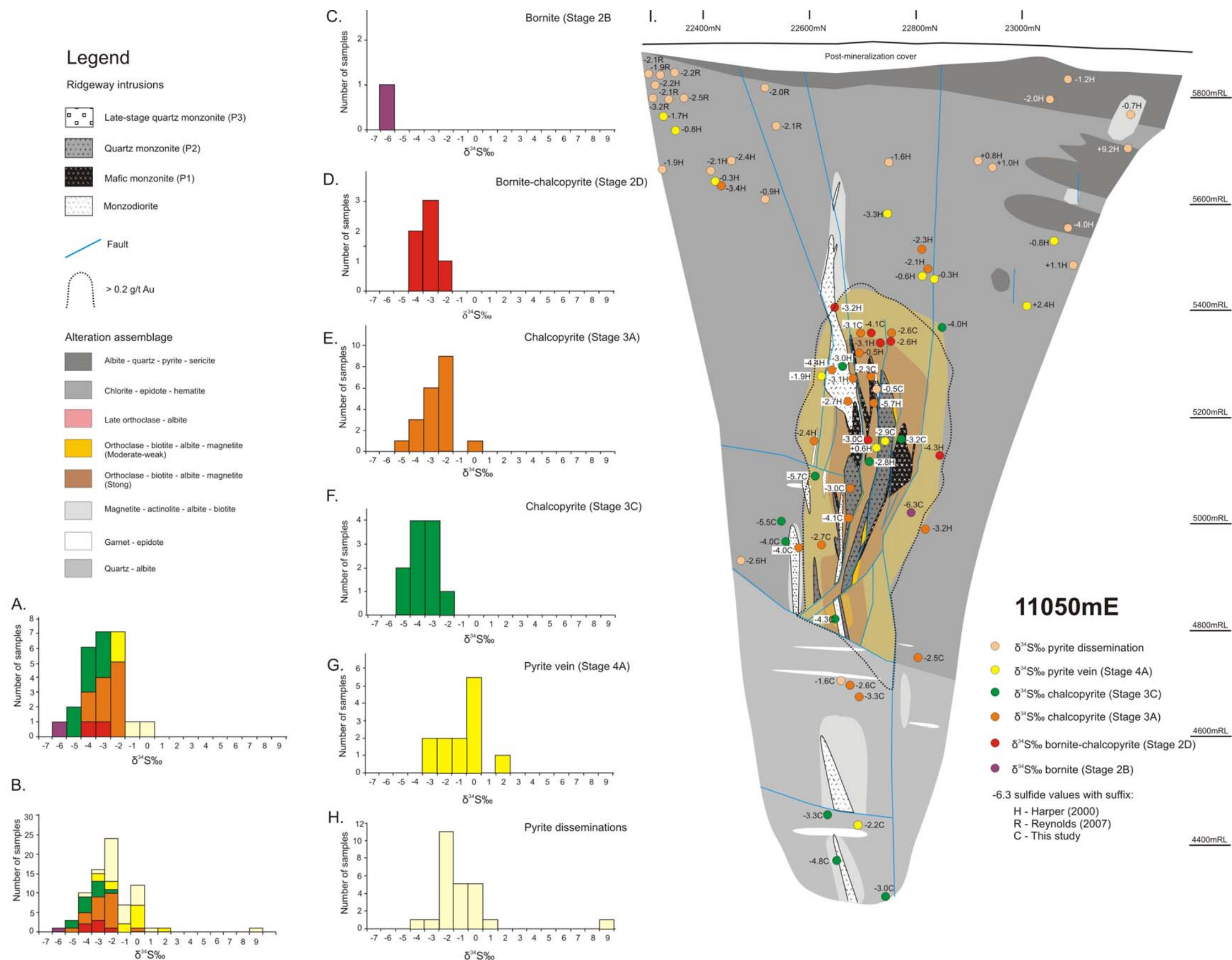


**Figure 6.14** Distribution and location of  $\delta^{34}\text{S}_{\text{sulfide}}$  from section 11050mE at Ridgeway. **A)** Histogram of  $\delta^{34}\text{S}$  (per mil) values for sulfides from selected vein stages in this study (n=25). **B)** Combined histogram of  $\delta^{34}\text{S}$  (per mil) of sulfides (n=76; Harper, 2000; Reynolds, 2007 and this study). **C) to H)** Histograms of  $\delta^{34}\text{S}$  (per mil) values for sulfides from different paragenetic vein stages. **I)** Distribution of combined  $\delta^{34}\text{S}_{\text{sulfide}}$  values at section 11050mE. Also shown are the locations of the Ridgeway monzodiorite and monzonites, hydrothermal alteration zonation and the 0.2 g/t Au grade contour.



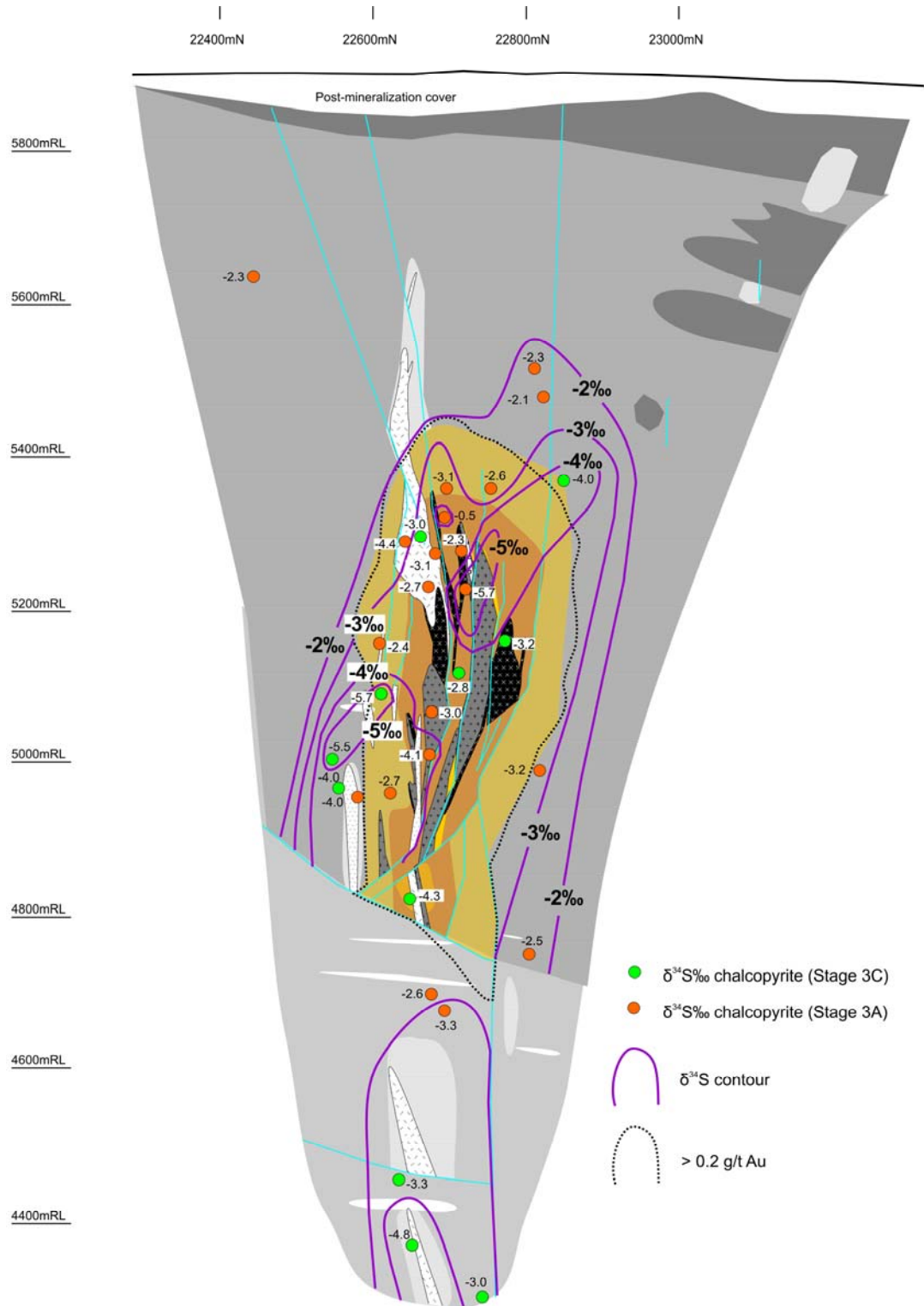


**Figure 6.15** Contoured  $\delta^{34}\text{S}_{\text{chalcopyrite}}$  values for stages 3A and 3C veins. The core is characterized by more negative values. The section also shows the location of the Ridgeway monzodiorite and monzonites, hydrothermal alteration zonation and the 0.2 g/t Au grade contour. Refer to Figure 6.14 for further details.

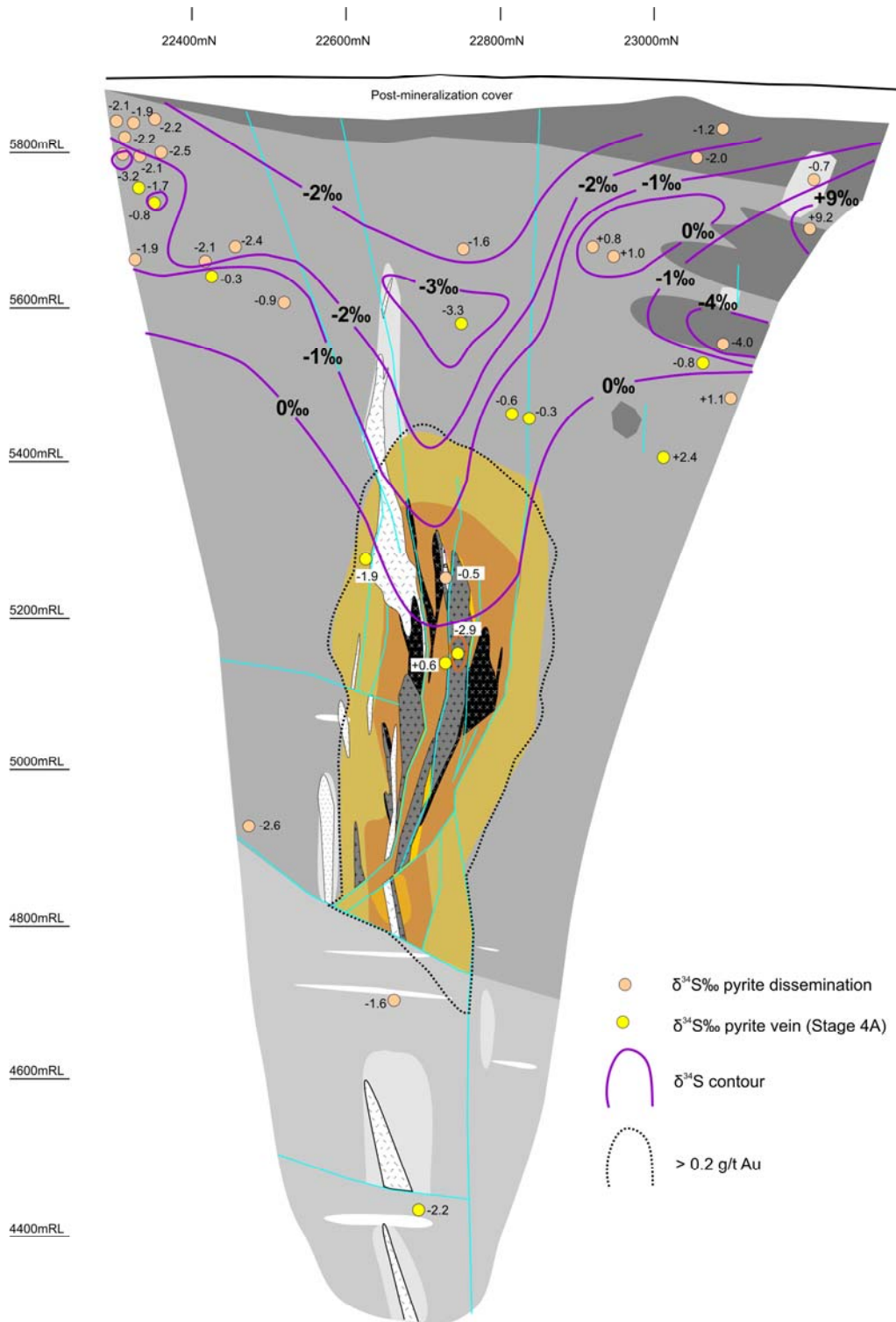


**Figure 6.16** Contoured  $\delta^{34}\text{S}_{\text{pyrite}}$  values from stage 4A pyrite veins and disseminations. There is a systematic decrease in values from the core of the deposit outward to more negative values. The section also shows the location of the Ridgeway monzodiorite and monzonites, hydrothermal alteration zonation and the 0.2 g/t Au grade contour. Refer to Figure 6.14 for further details.

## 6.6.4 Discussion

### 6.6.4.1 Fluid and sulfur sources

In porphyry deposits, most  $\delta^{34}\text{S}_{\text{sulfide}}$  values are between -3 and +1‰, and sulfates have values between +8 and +15‰ (Ohmoto and Rye, 1979). These  $\delta^{34}\text{S}_{\text{sulfide}}$  values imply that the sulfur is derived largely from igneous sources, either directly or by dissolution of igneous sulfides (Ohmoto and Rye, 1979). At Ridgeway, sulfur isotopic compositions of sulfides show increasing  $\delta^{34}\text{S}$  depletion in the sequence of pyrite (ave. -1.8‰), chalcopyrite (ave. -3.6‰) and bornite (ave. -4.9‰; Table 6.7; Fig. 6.14).

Stage 2 and 3 sulfides have isotopically light compositions. The lowest  $\delta^{34}\text{S}$  values analyzed from this study are found at the center with values of  $\delta^{34}\text{S}_{\text{bornite}} = -6.3\text{‰}$  and  $\delta^{34}\text{S}_{\text{chalcopyrite}} = -5.7\text{‰}$  (Table 6.7; Figs. 6.14I and 6.15). The low sulfur isotopic values for sulfides characterize several porphyry copper (-gold) deposits (Fig. 6.17), where the more negative  $\delta^{34}\text{S}$  values found to occur at the center of the orebody, associated with potassic-altered, highly-mineralized ore zones (e.g. Radclyffe, 1995; Lickfold, 2002; Deyell and Tosdal, 2005; Wilson *et al.*, 2007a). The light  $\delta^{34}\text{S}_{\text{bornite}}$  and  $\delta^{34}\text{S}_{\text{chalcopyrite}}$  values in the center of Ridgeway are similar to ranges of  $\delta^{34}\text{S}$  values from other alkalic porphyry deposits (Fig. 6.17). These light  $\delta^{34}\text{S}$  values are interpreted to be a product of sulfide deposition from oxidized, high temperature magmatic-hydrothermal fluids.

According to Ohmoto and Rye (1979), temporal and spatial variations of  $\delta^{34}\text{S}$  minerals can reflect changes in temperature and oxidation state ( $\text{SO}_4\text{:H}_2\text{S}$ ) in magmatic-hydrothermal system. Cooling of a magmatic-hydrothermal fluid will result in progressively decreasing  $\delta^{34}\text{S}_{\text{sulfide}}$  composition (Ohmoto and Rye; Rye, 1993). This study has found that  $\delta^{34}\text{S}_{\text{pyrite}}$  values define a spatial zonation pattern, different from that defined by the Cu-Fe sulfides, where isotopically light  $\delta^{34}\text{S}_{\text{pyrite}}$  (+0.6‰) occur in the core of the deposit, and become more negative (-3.1‰) towards the top creating an open V-shaped pattern (Fig. 6.16). This is consistent with increased isotopic fractionation, which can occur in magmatic systems from cooling or oxidation, in this case of the stage 4 fluid. Lighter distal values has been described

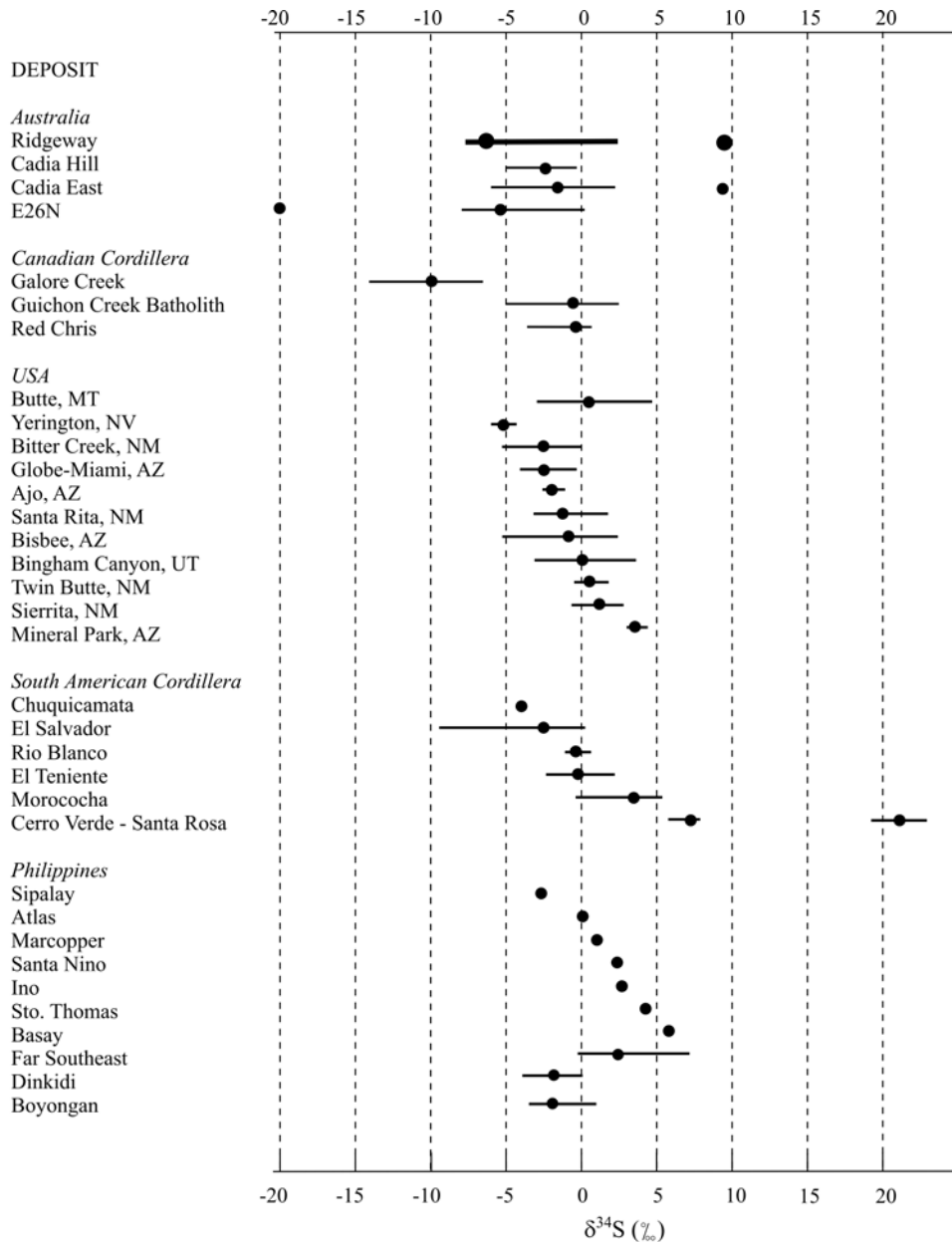


**Figure 6.17** Ranges of  $\delta^{34}\text{S}_{\text{sulfide}}$  values (per mil) determined for sulfides from Ridgeway (Harper, 2000; Reynolds, 2007; this study) compared to other porphyry copper (-gold) deposits. Data sources: Ohmoto and Rye (1979), Heithersay and Walshe (1995), Baker and Thompson (1998), Akira (2000), Wolfe (2001), Lickfold (2002), Wilson, *et al.* (2007a), and Braxton (2007).

in other porphyry deposits, including Butte (Field, 1966), Dinkidi (Wolfe, 2001), and Boyongan (Braxton, 2007). This type of zonation pattern has been attributed to cooling and/or oxidation (e.g. Field, 1966; Wolfe, 2001). These results show that the sulfur isotopic evolution at Ridgeway changed from stage 2 and 3 to stage 4, producing a reversal of sulfur isotopic zonation pattern.

## 6.5 Oxygen Isotopes

Oxygen isotope studies can provide insights into the source(s) of ore-forming fluids. Analyzing quartz–magnetite pairs can help to constrain temperature conditions using oxygen isotope geothermometry. However, CL analysis of quartz–magnetite veins from Ridgeway revealed that these minerals were not precipitated synchronously (Fig. 6.2; Fig 6.18), suggesting that quartz and magnetite are not in isotopic equilibrium. Thus, quartz–magnetite geothermometry has not been used to estimate temperatures of sulfide precipitation at Ridgeway.

Some early isotopic studies of porphyry copper deposits suggested that high-temperature potassic alteration was caused by magmatic-derived fluids whereas late, low-temperature sericitic (phyllic) alteration was caused by meteoric fluids (Sheppard *et al.*, 1969; Sheppard and Taylor, 1974; Sheppard and Gustafson, 1976). More recent works highlighted a magmatic source of fluids for phyllic alteration (e.g. Kusakabe *et al.*, 1984; Wolfe, 1994; Hedenquist *et al.*, 1998; Harris and Golding, 2001; Wilson, 2003). Most skarns have an intimate genetic relationship with intrusions, and their alteration minerals provide a clear record of magmatic-hydrothermal fluid involvement (e.g. Einaudi *et al.*, 1981; Einaudi, 1982; Einaudi and Burt, 1982; Meinert *et al.*, 2003).

Oxygen isotopes have been analyzed from garnet at Ridgeway in order to determine the nature of the sources of hydrothermal fluids responsible for the early stage alteration (garnet) in the calcareous lithofacies of the Weemalla Formation. It was planned to constrain  $\delta^{18}\text{O}$  fluid values using temperature estimates from the fluid inclusion study of garnet. However, all fluid inclusions were found to have unrealistic results, well below the expected garnet formation temperatures (550° to 450°C, Einaudi *et al.*, 1981). Consequently, the  $\delta^{18}\text{O}$  isotopic composition of water in equilibrium with garnet has been calculated at 400°, 450°, 500° and 550°C, representing what is considered here to be the most likely range of garnet forming temperatures.



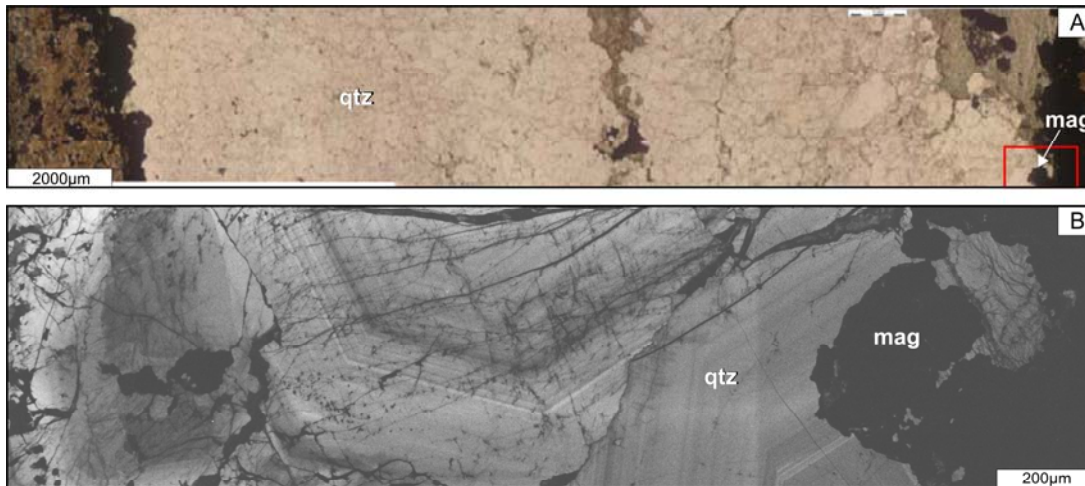


**Figure 6.18** Quartz and magnetite textures observed in a stage 2A quartz - magnetite vein. **A)** Photomicrograph in plane polarized light. **B)** SEM-CL imaging of (A) outlined in red box. The CL image shows that quartz growth zones have been truncated by magnetite, which suggest that magnetite has overgrown quartz (UR140-326m). Abbreviations: mag = magnetite, qtz = quartz

### 6.5.1 Previous work

Harper (2000) conducted oxygen isotope from quartz ( $n = 6$ ) and magnetite ( $n = 4$ ) from Ridgeway. The quartz samples were taken from K-silicate sulfide veins and epidote-quartz-carbonate-chalcopyrite vein, while the magnetite samples were from Fe-K-Ca hydrothermal alteration (Harper, 2000).  $\delta^{18}\text{O}$  values for quartz showed a systematic increase away from the monzonite porphyry, ranging from +7.3‰ in the deposit center to +12.3‰ on the periphery of the 1% Cu contour (Harper, 2000). This systematic increase in  $\delta^{18}\text{O}$  values was interpreted to represent cooling of magmatic-hydrothermal fluids (Harper, 2000). Magnetite  $\delta^{18}\text{O}$  values range from 3.6‰ on the periphery to 2.1‰ in the inner magnetite zone (Harper, 2000).

Wilson (2003) analyzed the  $\delta^{18}\text{O}$  and  $\delta\text{D}$  compositions of illite and muscovite from Cadia Quarry and Cadia East. He reported  $\delta^{18}\text{O}$  values from +9.1 to 12.3‰ and  $\delta\text{D}$  from -41 to -49‰. Based on assumed temperatures at 300°C, 350°C and 400°C for muscovite formation, these data were interpreted to indicate that magmatic-hydrothermal fluids caused phyllic alteration in the Cadia district (Fig. 6.21).

### 6.5.2 Methodology

Twelve samples of garnet were analyzed for their  $^{18}\text{O}$  isotopic composition. Samples were analyzed by Dr. Kevin Faure at GNS Science, Rafter Stable Isotopes Laboratory in New Zealand. Rock samples were crushed, sieved and washed, and garnet crystals were hand-picked manually using a binocular microscope. All results are reported as  $\delta^{18}\text{O}$  relative to Standard Mean Ocean Water (SMOW).

Oxygen was extracted for isotopic analyses from garnet using a  $\text{CO}_2$ -laser and  $\text{BrF}_5$ , using the methodology of Sharp (1990). Samples were normalized to the garnet standard UWG-2 using a value of 5.8 ‰ (Valley *et al.*, 1995). Values for four UWG-2 standards analysed with the samples had values that varied by less than 0.1 ‰. Samples were left overnight in  $\text{BrF}_5$  vapour. Blank  $\text{BrF}_5$  runs were done until yield was less than 0.1 micro moles oxygen. Oxygen was passed through a fluorine-getter (in-line Hg diffusion pump), oxygen converted to  $\text{CO}_2$  by a graphite furnace, yields recorded and the gas analysed on a Geo20-20 mass spectrometer (Sharp, 1990; Valley *et al.*, 1995)

### 6.5.3 Results

The  $\delta^{18}\text{O}_{\text{mineral}}$  values obtained from Ridgeway garnets range between +5.2‰ and +9.9‰ (ave. 7.8‰; Table 6.8). No systematic spatial variation in isotopic compositions was determined for garnet (Fig. 6.19). Waters in isotopic equilibrium with these samples at 400° to 550°C were calculated to have  $\delta^{18}\text{O}$  fluid values of +7.8 to +12.8‰ (Table 6.8; Fig. 6.20), using the fractionation equation of Zheng (1993). Progressive cooling of these waters from 550° to 400°C would drive their isotopic compositions towards lighter  $\delta^{18}\text{O}$  values (+12.8 to +7.8‰; Table 6.8).

### 6.5.4 Discussion

At Ridgeway, temperatures of 550° to 400°C have been assessed to calculate fluid compositions (Table 6.8). These results are interpreted to indicate that the fluids responsible for calc-silicate alteration at Ridgeway were principally of magmatic origin (Fig. 6.20). For these temperature range, compositions of  $\delta^{18}\text{O}$  overlap with

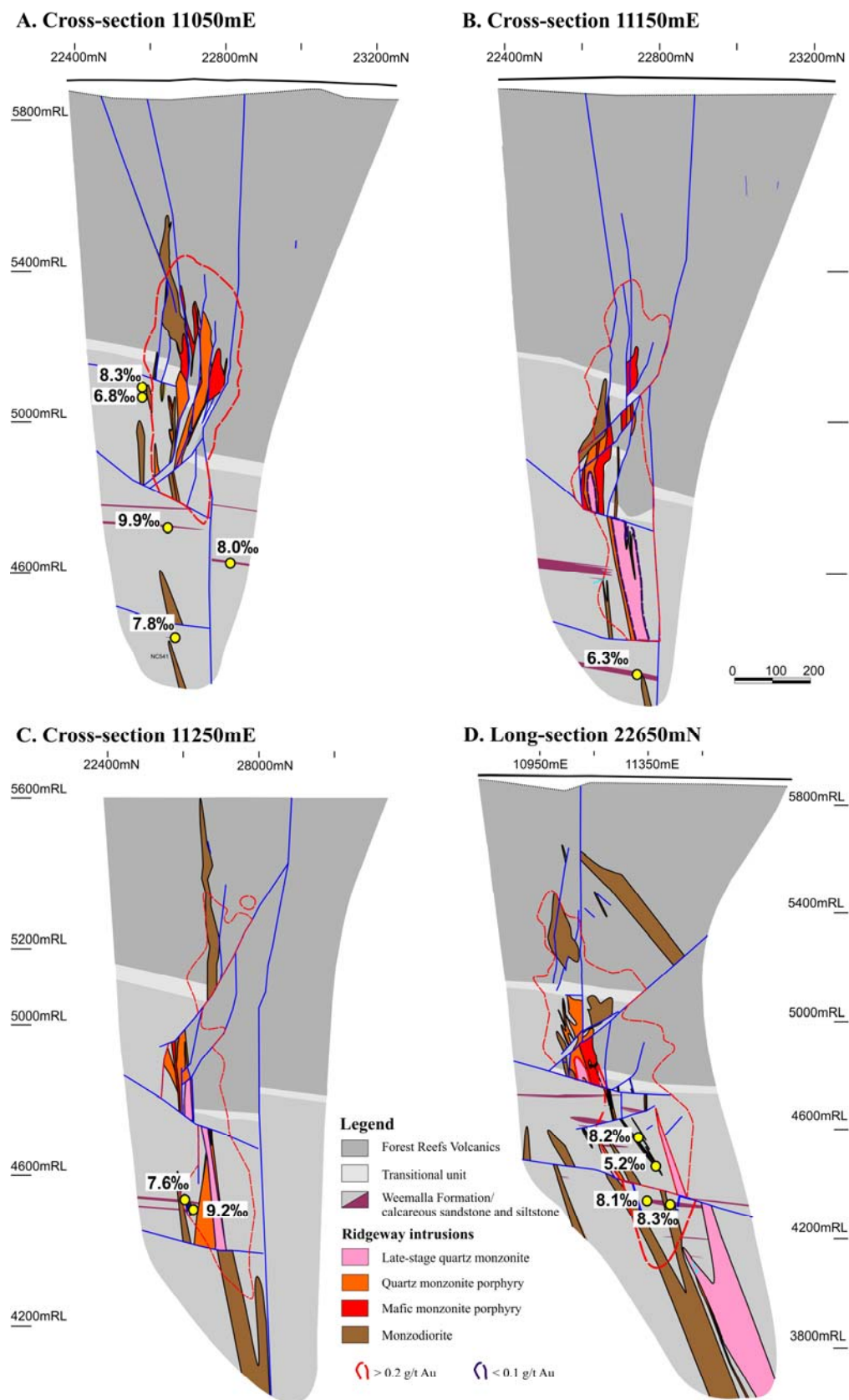


**Figure 6.19** Spatial distribution of  $\delta^{18}\text{O}_{\text{mineral}}$  of garnet from garnet - epidote alteration from different sections at Ridgeway. **A)** Cross-section 11050mE. **B)** Cross-section 11150mE. **C)** Cross-section 11250mE. **D)** Long-section 22650mN. The sections also show the locations of the Ridgeway monzodiorite and monzonites.

**Table 6.8** Measured  $\delta^{18}\text{O}$  compositions of garnet from calc-silicate alteration assemblage from Ridgeway. The  $\delta^{18}\text{O}$  isotopic composition of water in isotopic equilibrium with andradite at 400°C, 450°C, 500°C and 550°C have been calculated using the equations and constants of Zheng (1993).

Sample			Elevation	Measured $\delta^{18}\text{O}\text{‰}$	Calculated $\delta^{18}\text{O}\text{‰}$			
ID	Hole #	Depth (m)	(CML) <sup>1</sup>	(SMOW) <sup>2</sup>	400°C	450°C	500°C	550°C
Grt-01	UR154	110.0	5095	8.3	10.9	11.1	11.2	11.2
Grt-02	UR150	90.6	5073	6.8	9.4	9.6	9.7	9.7
Grt-03	NC541	1189.0	4716	9.9	12.5	12.7	12.8	12.8
Grt-04	UR255	476.8	4629	8.0	10.6	10.8	10.9	10.9
Grt-05	UR360	603.0	4587	7.6	10.3	10.4	10.5	10.6
Grt-06	UR360	664.0	4537	9.2	11.9	12.0	12.1	12.2
Grt-07	UR333	625.8	4523	8.2	10.8	11.0	11.1	11.1
Grt-08	UR323	589.0	4455	5.2	7.8	8.0	8.1	8.1
Grt-09	NC541	1481.6	4424	7.8	10.4	10.6	10.7	10.7
Grt-10	UR362	666.0	4370	6.3	8.9	9.1	9.2	9.2
Grt-11	CR062	1623.0	4368	8.1	10.7	10.9	11.0	11.0
Grt-12	UR365	751.5	4321	8.3	10.9	11.1	11.2	11.2

<sup>1</sup> CML = Cadia Mine Lease grid. The mine level is 5000+ sea level

<sup>2</sup> Results are reported relative to the Standard Mean Ocean Water (SMOW) standard

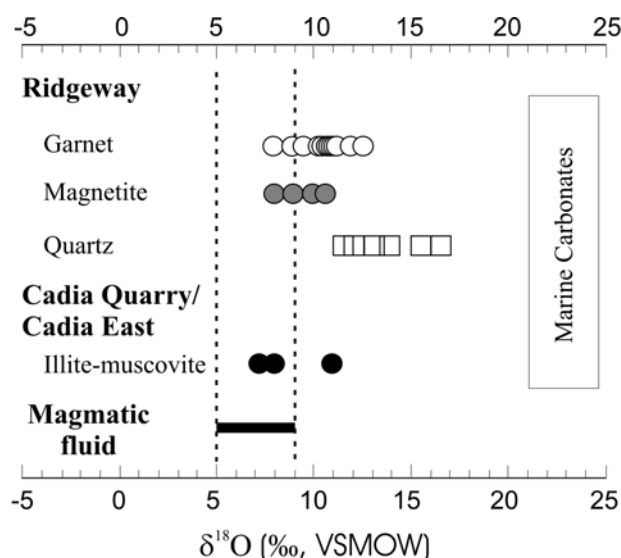


**Figure 6.20** Calculated  $\delta^{18}\text{O}$  (SMOW) composition of fluids in equilibrium with garnet from Ridgeway (open circle). See Table 6.7 for data sources and fractionation factors. Also plotted are calculated  $\delta^{18}\text{O}$  of other minerals from the Cadia district. Data of magnetite and quartz from Harper (2000), and illite-muscovite from Wilson (2003). The average composition of magmatic fluid and the marine carbonate values are from Taylor (1986).

values calculated for magnetite (9.0 - 10.6‰) at 400°C, but slightly lower than the values calculated by Harper (2000) for quartz (11.4 - 16.6‰) at the same temperature (Fig. 6.20). These values are within range for magmatically-derived hydrothermal fluids associated with igneous rocks (Taylor and Sheppard, 1986; Hedenquist and Richards, 1998; Crowe *et al.*, 2001; Fig. 6.20).

## 6.6 Summary

Ridgeway is the product of a complex history of vein formation. SEM-CL imaging reveals multiple generations of quartz in single veins. Cathodoluminescence imaging of quartz show that the bulk of vein quartz (Qz-1) crystallized early in the vein history. Dissolution of Qz-1 followed the deposition of the second generation (Qz-2). Cu-Fe-sulfides were deposited together with a later generation of dark-luminescent quartz (Qz-3). Bright luminescence in quartz correlates with elevated Al, Ti and K concentrations. High-temperature Qz-1 precipitated at temperatures between 601° and 850°C during stockwork formation. Mechanical fracturing occurred when pressure and temperature changes, creating secondary permeability exploited by Qz-2. Further decrease in pressure and/or temperature facilitated the precipitation of Qz-3 at temperatures below 589°C, synchronous with Fe-Cu sulfides.

Fluid inclusions in garnet from calc-silicate alteration assemblage have low homogenization temperatures (average 232°C) that are incompatible with the stability range for garnet, suggesting that these fluid inclusions have re-equilibrated after their formation. A paleodepth of ~2.9 to 3.5 km and lithostatic pressure of 720 to 870 bars is inferred for the depth of garnet–epidote (skarn) alteration formation at Ridgeway based from the stratigraphic reconstruction of the middle Ordovician Weemalla Formation and FRV rock sequence at the Cadia district.

Sulfur isotopic composition of sulfides show low  $\delta^{34}\text{S}_{\text{bornite}}$  and  $\delta^{34}\text{S}_{\text{chalcopyrite}}$  values occur in the core of the deposit. Isotopically light  $\delta^{34}\text{S}_{\text{pyrite}}$  values are also found in the core of the deposit, becoming more negative towards the top, in the epidote–chlorite–hematite alteration zone. This is consistent with increased isotopic fractionation caused by cooling of the magmatic-hydrothermal fluids under oxidizing conditions during late-stage pyrite deposition.

Stable isotopic studies indicate that the fluids responsible for alteration and mineralization at Ridgeway were magmatic-hydrothermal. The calculated  $\delta^{18}\text{O}$  composition of fluids in equilibrium with garnet are within range for magmatically-derived hydrothermal fluids associated with igneous rocks.



---

# Chapter 7: Summary and Genetic Model

---

## 7.1 Introduction

The principal aim of this study has been to investigate the genesis of the Ridgeway alkalic Au–Cu porphyry deposit. Critical to achieving this has been understanding the geometry and distribution of the different intrusions, related magmatic-hydrothermal textures, and vein and fault orientations. Characterization of the discrete veins associated with each intrusion and their associated alteration assemblages have also been fundamental to improving the understanding of this deposit. The results of this study allow constraints to be placed on the absolute ages of intrusion emplacement and sulfide mineralization, and how space was created for the mineralizing intrusions.

This chapter summarizes the findings of the current study. The first section discusses the district-scale features and processes that were important in the genesis of the Ridgeway deposit. The second section integrates all of the preceding chapters into a genetic model for the Ridgeway deposit. The final section comments on exploration implications and recommendations for further research at Ridgeway.

## 7.2 Volcano-sedimentary succession, magmatism and volcanic setting

At Cadia, the porphyry deposits formed during the culmination of a protracted period of magmatic activity that occurred episodically over four cycles. The earliest event deposited the volcano-sedimentary host sequence between 455 and 452 Ma (Fig. 3.27A). The second event is marked by the emplacement of diorite to monzodiorite intrusions around 448 Ma (Fig. 3.27C). The third event was the intrusion of the monzonite suite associated with mineralization at Ridgeway around 444 Ma (Fig. 3.27D and E). Magmatic activity in the district culminated with the emplacement of the quartz monzonite intrusions associated with Cadia Hill, Cadia Quarry and Cadia East around 439 - 436 Ma (Fig. 4.26).

Ridgeway is hosted in a Middle Ordovician sequence of northeast-dipping sedimentary and volcanic rocks (Fig. 3.5). This package is characterized by well-stratified to massive feldspathic siltstones, sandstones and massive mafic- and feldspar-rich sandstones of the Weemalla Formation, grading upwards to thick, diffusely stratified polymictic volcanoclastic lithic breccia and conglomerate of the FRV (Fig. 3.4). This volcano-sedimentary succession is interpreted to have been deposited in an active submarine sedimentary basin (Harris *et al.*, 2009a).

The volcanic sequence was intruded by pyroxene- and feldspar-phyric dikes and sills, diorite to monzodiorite stocks, and pipe-like monzonite and quartz monzonite intrusions. Mafic xenoliths occur only in the monzonites (Fig. 3.18). They are composed primarily of chlorite-altered biotite flakes, interstitial chlorite–magnetite-altered clinopyroxene, and apatite crystals. These xenoliths are texturally and mineralogically distinct from the more commonly observed xenoliths derived from the Weemalla Formation and FRV. Studies of the wholerock geochemistry of the pre-mineralization intrusions and mineralized intrusions have provided the following constraints on their origins and tectonic setting:

- Two petrographically and geochemically distinct intrusive suites are present in the Ridgeway intrusive complex. One suite, dominated by mafic rocks ( $\text{SiO}_2$  from 48 to 54 wt %; Fig. 3.21A) consists of pyroxene- and feldspar-phyric dikes and sills and monzodiorite stocks. The second suite has more intermediate compositions ( $\text{SiO}_2$  from 58 to 62 wt %; Fig. 3.21A) and includes the monzonitic rocks (mafic monzonite and quartz monzonite).
- Discrimination diagram shows that the early mafic intrusions range in composition from trachybasalt to basaltic trachyandesite, while the intermediate intrusive rocks range from trachyandesite to trachyte (Fig. 3.21B).
- All igneous rocks at Ridgeway have compositions consistent with a late oceanic island arc setting based on the  $\text{P}_2\text{O}_5/\text{Al}_2\text{O}_3$  vs  $\text{Zr}/\text{Al}_2\text{O}_3$  tectonic discrimination diagram (Fig. 3.21D).

- The relationships of incompatible elements such as Sr, Rb and Ba to SiO<sub>2</sub> are distinct between the two intrusive suites. The mafic intrusions have increasing Rb and Ba up to 54 wt % SiO<sub>2</sub>, whereas Rb and Ba decreases with increasing SiO<sub>2</sub> for the monzonite suite (Fig. 3.23).
- The mafic monzonite and the quartz monzonite intrusions are spatially and temporally associated with mineralization at Ridgeway.
- The mafic xenoliths are geochemically and mineralogically distinct from the mafic intrusive rocks. These xenoliths are enriched in PGEs (i.e. Pd, Pt and Au; Table 3.6).

Based from the stratigraphic reconstruction of the volcanic architecture at Cadia (Harris *et al.*, 2009b) and the occurrence of distinct garnet–epidote alteration horizon in the sedimentary package provide constraints on the emplacement depths of the intrusions to approximately 2.9 km beneath the paleosurface. This is consistent with the depths of emplacement reported for other porphyry deposits (1 - 6 km, Burnham, 1979; Dilles, 1987; Hedenquist and Richards, 1998, Murakami *et al.*, 2010).

### **7.3 Ridgeway genetic model**

#### **7.3.1 Structural controls and history of emplacement**

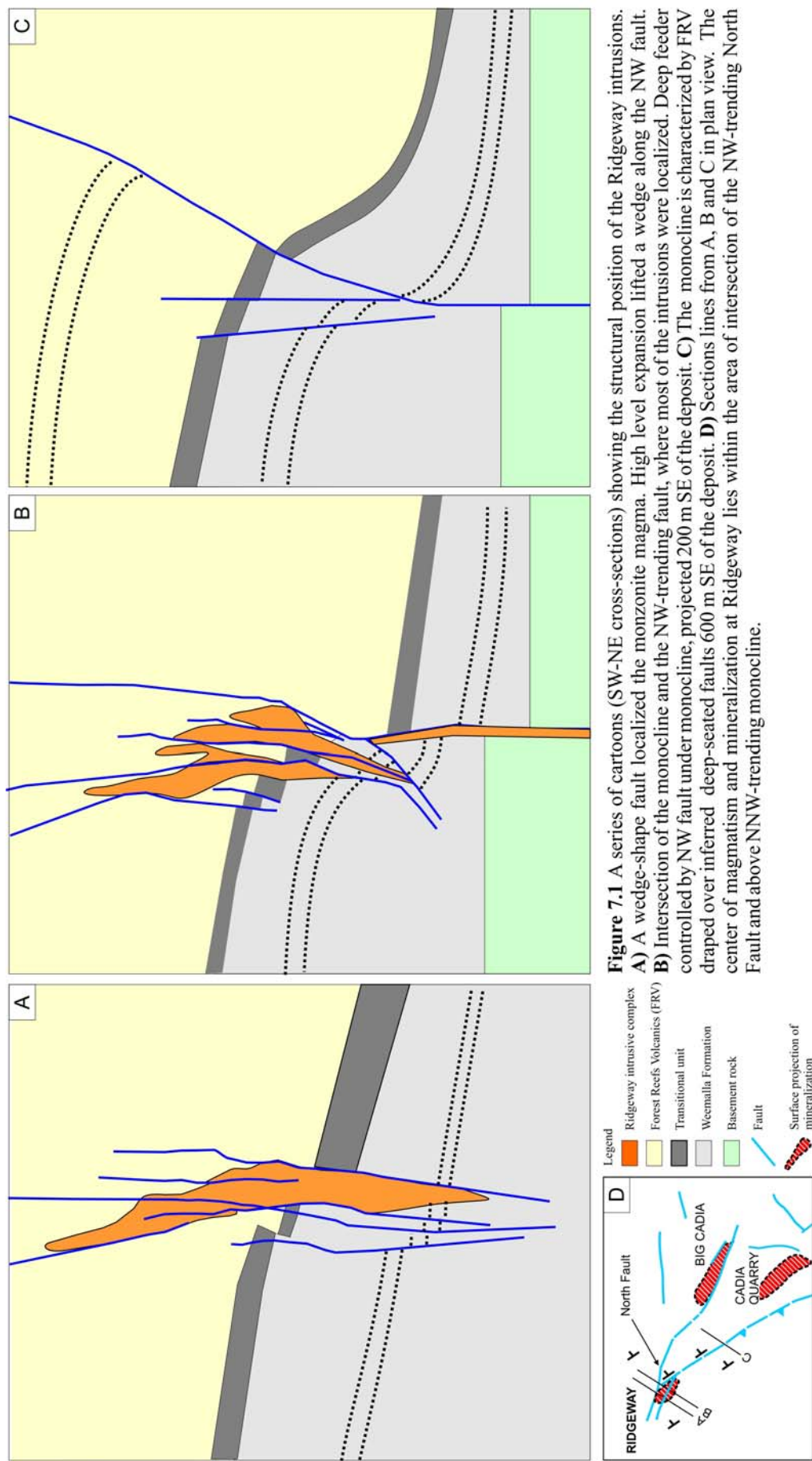
At the district scale, Ridgeway is located in the WNW-trending LTZ (Fig 2.3), and NNW-trending faults appear to have exerted a fundamental control on the localization of volcano-sedimentary facies in the Cadia district (Holliday *et al.*, 2003; Wilson *et al.*, 2003). Similar arc-transverse structures have played important roles in localizing mineralization in other porphyry copper belts around the world, such as the Teniente Fault Zone in Chile (Cannell *et al.*, 2005), the Archibarca lineaments in northern Chile (Richards *et al.*, 2001) and transfer structures in the Papua New Guinea-Irian Jaya region (Gow and Walshe, 2005).

The structural analysis of Ridgeway has shown that the main center of magmatism and mineralization lies within the area of intersection of the NW-trending North Fault and above the NNW-trending monocline. Figure 7.1 provides a

series of cartoons that highlight the features that influenced the emplacement of the porphyry bodies. Figure 7.1A shows a wedge-shape fault array that provided the pathways for the deep-seated magma to rise to shallow crust by forceful injection. Subsequent enlargement of the intrusion occurred by lateral spreading of wall rocks (Fig. 7.1B). Figure 7.1C shows that the monocline was draped over an inferred deep-seated fault, which most likely provided the conduit for the monzonite to ascend to the upper crust. In summary, space was created for the emplacement of the mineralizing intrusions at Ridgeway by host-rock rigid displacements via lateral flexure of wall rocks to the sides of intrusions, and via faulting and uplift of roof rocks (Fig. 5.23 and Fig. 7.1).

The rheological contrast between the sedimentary rocks and the overlying volcaniclastic rocks, in part, appeared to have exerted an important control over the localization and geometry of the Ridgeway deposit. The intrusions and mineralization are aligned along a northwest trend which is parallel to the strike of the district's structural grain (Fig. 5.2). Typically, the pipe-like intrusions tend to “swell” as they reached the contact of the sedimentary rocks and the more permeable volcaniclastic rock package (Fig. 3.5). These relationships suggest that the emplacement of Ridgeway intrusions was guided by the faults, localized at the intersection of the monocline with the NW-trending faults (Fig. 7.1D), and maximum dilation was achieved immediately above the contact between the two Ordovician volcano-sedimentary packages.

Quartz vein orientations show that mineralizing fluids were preferentially emplaced into two subvertical vein systems. The older veins (set 2) strike N, WNW and NE, whereas the younger mineralized structures (set 3) strike E, NE and NW (Fig. 5.12 and Fig. 5.24). Vein formation and mineralization is interpreted to have been controlled by local hydraulic fracturing caused by fluid exsolution from the monzonite porphyries (i.e. mafic monzonite and quartz monzonite). The mineralizing fluids at Ridgeway apparently used the porphyry bodies to provide transport up to the level of ore formation.





### 7.3.2 Intrusions, alteration and mineralization

The Ridgeway intrusive complex includes monzodiorite, monzonite and quartz monzonite. It is elongated to the NW, and has dimensions of at least 400 x 100 x 2000 m. Emplacement of the Ridgeway intrusive complex began with an early monzodiorite stock, followed by the mafic monzonite and quartz monzonite pipes. Discrete vein stages and associated hydrothermal alteration assemblages followed the emplacement of each intrusion at Ridgeway (Tables 4.2 and 4.3). The spatial configuration of the reconstructed Ridgeway intrusive complex, viewed along 11050mE, is shown schematically from Figure 7.2 to Figure 7.4. The sequence shown in Figure 7.2A begins with the deposition of the volcano-sedimentary successions and intrusion of the pyroxene- and feldspar-phyric dikes and sills. The following subsections describe the key events that are inferred to have led to ore formation at Ridgeway.

#### 7.3.2.1 Pre-mineralization: monzodiorite, stage 1 veins and related hydrothermal alteration events

The early stage alteration is characterized by widely developed quartz  $\pm$  albite and locally developed garnet–epidote alteration and actinolite–magnetite–albite alteration assemblages. These alteration assemblages are well-developed in the Weemalla Formation (e.g. Figs. 3.8, 4.11 and 4.13).

. Significant events include:

- Emplacement of the pre-mineralization monzodiorite stocks as a subvertical plug (200 x 100 x 2000 m), with the top located 350 m below the current surface (Fig. 7.2B).
- Widespread quartz  $\pm$  albite alteration, which extended at least 500 m from the center of what would become the orebody. Local replacement of calcareous unit throughout the Weemalla Formation by garnet–epidote, whereas actinolite–magnetite–albite have replaced the feldspathic siltstone and sandstone horizons locally. Actinolite–magnetite–albite alteration also affected the monzodiorite, pyroxene- and feldspar-phyric dikes and sills and the FRV (Fig. 7.2B).

- Formation of stage 1 veins up to 600 m from the monzodiorite contact. Sulfides are absent from these veins (Fig. 7.2B). Stage 1A magnetite veins at Ridgeway are similar to ‘M’ veins from Island Copper porphyry, British Columbia (Arancibia and Clark, 1996), stage 1A veins from Boyongan, Philippines (Braxton and Cooke, 2005), and the earliest vein type seen in the Rosario porphyry Cu–Mo deposit, Chile (Masterman *et al.*, 2005).

#### **7.3.2.2 Main-stage mineralization: mafic monzonite porphyry, stage 2 veins and related hydrothermal alteration events**

Main stage magmatic-hydrothermal events produced the earliest-formed orthoclase–biotite–magnetite–(albite–actinolite) alteration assemblage. This alteration defines the inner K-silicate alteration zone at Ridgeway. The bulk of the copper and gold mineralization at Ridgeway is associated with the main stage event.

Significant events during this stage include:

- Emplacement of the mafic monzonite porphyry (P1). These intrusions occur as thin subvertical pipes (1 - 30 m thick), with the top generally located 550 m below the current surface (Fig. 7.3A).
- Development of magnetite-rich USTs at the apex of the mafic monzonite (Fig. 7.3A).
- Formation of bornite-rich stage 2 veins associated, both spatially and temporally, with the mafic monzonite. These veins are best developed within the intrusions and in the immediate wallrock up to 100 m from the contact (Fig. 7.3A).
- The stage 2B quartz–banded magnetite–bornite stockwork produced high-grade ore (>4 g/t Au) and is centred on, and most intensely developed along the margins of P1 and the adjacent volcanic rocks to distances of up to 10 m from the intrusive contact. The high-grade contours define an inverted-cup shape surrounding the margins of the mafic monzonite (Figs. 4.20B and 4.21B). Mineralized quartz–bornite veins (stage 2D) formed late during this event.

- Development of intense orthoclase–biotite–magnetite–(albite–actinolite) alteration formed during and/or after the intrusion of P1 (Fig. 7.3A). This alteration assemblage associated with stage 2 stockworks and veins that locally exhibit K-silicate alteration haloes.

P1 appears to have been particularly productive, exsolving and focussing large volumes of high temperature magmatic-hydrothermal fluids, as exemplified by the magnetite-rich USTs at its apex and the intense quartz vein stockwork developed within and around it (Fig 7.3A). Hydrostatic pressure in the crystallizing intrusion must have exceeded the combined effects of lithostatic load and tensile strength of the FRV in order to cause extensive fracturing of surrounding rocks during a major decompression event, creating a dilatant fracture network where hydrothermal fluids precipitated the quartz–sulfide veins stockwork and generated strong orthoclase–biotite–magnetite–(albite–actinolite) alteration of the P1 intrusion and the FRV wallrocks.

Hydraulic fracturing was most intense in the volcanoclastic wallrocks. Vein opening occurred in multiple cycles, as shown by the banded magnetite textures in stage 2B veins (e.g. Fig. 4.5E, Fig. 4.6), and the complex history of quartz growth and dissolution apparent in the CL images (Figs. 6.1, 6.3 and 6.5).

### **7.3.2.3 Main-stage mineralization: quartz monzonite porphyry, stage 3 veins and related hydrothermal alteration events**

A second stage of gold and copper deposition occurred during the emplacement of the quartz monzonite porphyry (P2). Although this stage has lower Cu and Au grades than stage 2, the wider distribution of mineralized veins extend the zone of Cu–Au mineralization to distances of up to 300 m laterally from the center of the orebody.

Significant events during this stage include:

- Intrusions of P2 as thin, subvertical pipe (1 - 50 m thick), with tops generally located 600 m below the present-day surface (Fig. 7.3B).

- Development of quartz-rich USTs at the apical portion and along the margins of P2, while miarolitic cavities occur within the intrusions (Fig. 7.3B).
- Formation of chalcopyrite-rich stage 3 veins associated, both spatially and temporally, with P2. These veins are best developed within the intrusions and in the immediate wallrock up to 200 m from the intrusive contact (Fig. 7.3B). Barren quartz veins (stage 3D) were formed during the later stage of this event. Stage 3 veins occur in parallel sets or sheeted veins.
- Development of moderate orthoclase–biotite alteration during and/or after the intrusion of P2. This outer K-silicate alteration forms a shell around the inner K-silicate alteration zone (Fig. 7.3B). The location of the 1.5 g/t gold contour approximately coincides with the transition from the inner K-silicate domain to the outer K-silicate alteration assemblage.
- Chlorite–epidote–hematite (propylitic) alteration of the wallrocks adjacent to the K-silicate alteration zones may have formed at this time, although the timing is difficult to constrain precisely due to a lack of cross-cutting relationships (Fig. 7.3B).

#### **7.3.2.4 Late-stage: equigranular quartz monzonite, stage 4 veins and related hydrothermal events**

The final stage of magmatic activity at Ridgeway resulted in the emplacement of the equigranular quartz monzonite (P3) that was followed by the development of unmineralized stage 4 veins that contain milky quartz, pyrite, chlorite, epidote, prehnite and calcite. This intrusion has truncated hydrothermal quartz veins and is rich in quartz vein fragments and wallrock xenoliths. P3 occurs as a subvertical pipe, 5 to ~200 m wide, with a vertical extent of at least 1.7 km.

Other significant events during this stage include:

- Weak, selectively pervasive orthoclase–albite–quartz  $\pm$  actinolite alteration is confined in P3 (Fig. 7.3C). In contrast to the earlier-formed K-silicate alteration assemblages, biotite and magnetite are only sparsely developed.
- Continued development distal chlorite–epidote–hematite (propylitic) alteration, resulting in a broad shell around the inner and outer K-silicate

alteration domain (Fig. 7.3C). The propylitic alteration assemblage has overprinted all earlier-formed alteration assemblages locally. The abundant sub-micron size hematite grains that have selectively altered hydrothermal feldspars throughout the deposit are inferred to be part of the propylitic assemblage, and are responsible for the characteristic orange-pink colouration of the altered rocks. The location of the 0.2 g/t gold contour approximately coincides with the transition from the outer K-silicate alteration domain from the epidote–chlorite–hematite zone.

- Development of pervasive, texturally destructive albite–quartz–pyrite–sericite alteration in the upper and distal portions of the FRV (Fig. 7.3C). This alteration assemblage defines a cap above the epidote–chlorite–hematite-altered zone and is magnetite-destructive.
- Stage 4 veins formed mainly in the epidote–chlorite–hematite alteration zone but also occur locally in the K-silicate alteration zones, and in P3 (Fig. 7.3C). The absence of Cu–Fe sulfides in stage 4 veins suggests that metals had been depleted from the underlying parent magma chamber by this time.
- The  $\delta^{34}\text{S}$  compositions of pyrite from stage 4 veins and disseminations (–4 to +2.4‰) are consistent with a magmatic origin for sulfur. There is a systematic spatial zonation of  $\delta^{34}\text{S}_{\text{pyrite}}$  values, where isotopically light  $\delta^{34}\text{S}_{\text{pyrite}}$  values occur in the core of the deposit. These values become more negative towards the top, consistent with increased isotopic fractionation, which can occur in magmatic systems from cooling or oxidation (Ohmoto and Rye, 1979).

The peripheral setting of the epidote–chlorite–hematite alteration assemblage, and observed cross-cutting and overprinting relationships suggest that the propylitic assemblage formed both synchronous with and after K-silicate alteration. This is consistent with interpretations of a protracted history of propylitic alteration from other alkalic porphyry systems; (e.g. Mount Polley, Copper Mountain, Cu–Au deposits of the Iron Mask batholith; Lang and Stanley, 1995).



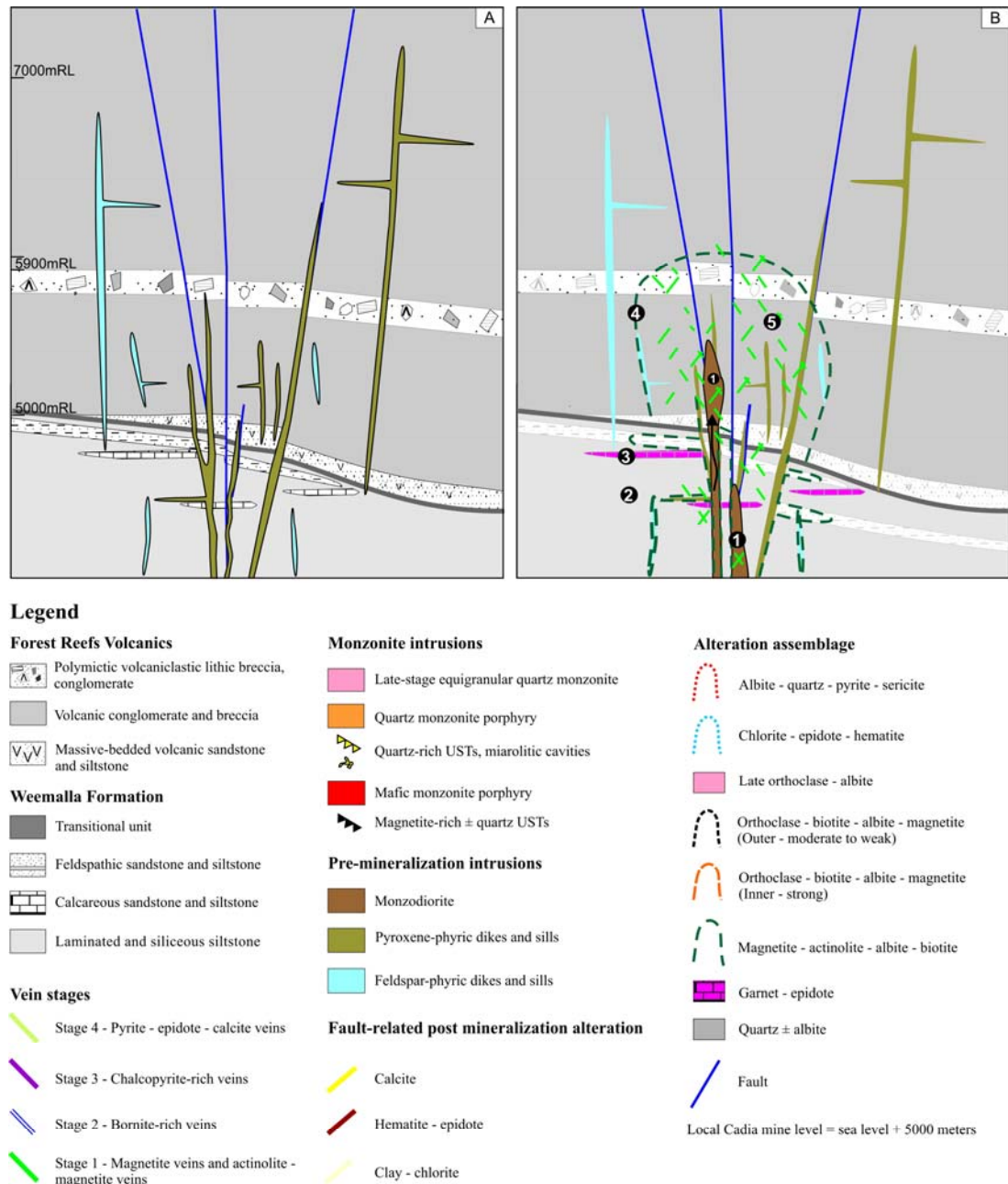


**Figure 7.2** Conceptual genetic model for Ridgeway. Pre-mineralization magmatic and hydrothermal events. The vertical axis plots the elevation from stratigraphic reconstruction of the volcano-sedimentary succession with respect to current surface level at 5900mRL (Cadia mine elevation). Horizontal axis not to scale. **A)** Deposition of siltstones, sandstones and volcaniclastic sandstones, conglomerates and breccias between 455 Ma and 452 Ma. After consolidation, the volcano-sedimentary package was intruded by pyroxene- and feldspar phyric dikes and sills exploiting pre-existing faults. **B)** Intrusion of the monzodiorite (1) around 448 Ma and formation of pervasive quartz ± albite alteration (2) in the siltstone units, pervasive garnet - epidote alteration (3) in the calcareous units, and selectively pervasive magnetite - actinolite - albite alteration (4; green line) in the feldspathic sandstone and siltstone units at depth, and the massive volcaniclastics and basaltic to andesitic breccia in the upper sequence that may extend for several hundreds of meters away from the temporally-related monzodiorite stock. Stage 1 veins (5) may have developed at this event, and extended up to 600 m or more from the intrusion. Stage 1 veins are deficient with Cu-Fe sulfides.

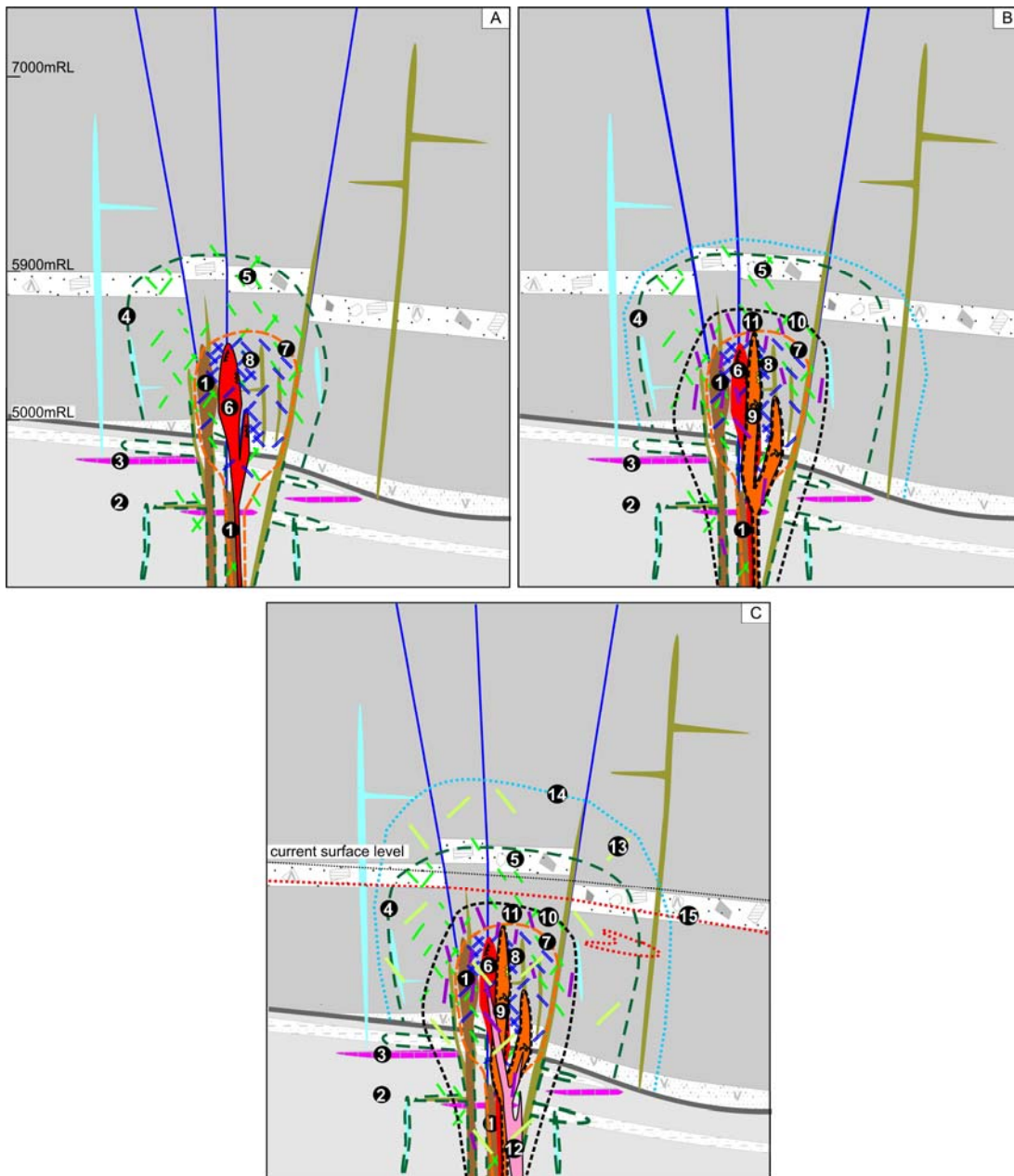


**Figure 7.3** Conceptual genetic model for Ridgeway. Main mineralization and late-stage magmatic and hydrothermal alteration events. **A)** Intrusion of mafic monzonite porphyry (6) around 444 Ma, and development of magnetite-rich unidirectional solidification textures (USTs) along the apex. Development of intense pervasive orthoclase - biotite - magnetite - albite (inner K-silicate) alteration assemblage (7; orange line). The mafic monzonite may be associated with bornite-rich stage 2 veins (3) occurring as stockworks and veins concentrated within and along the margins of the intrusion. Later stage 2 veins may be developed up to 100 m away from the intrusive contact. **B)** Intrusion of quartz monzonite porphyry (9), and development of USTs along the margins and miarotitic cavities within the intrusion. Development of moderate selectively pervasive orthoclase - biotite (outer K-silicate) alteration assemblage (10; black line). The quartz monzonite porphyry may be associated with the chalcopyrite-rich stage 3 veins (11) occurring as sheeted veins, up to 200 m from the contact. Chlorite - epidote - hematite alteration may be developed at this stage. **C)** Intrusion of late-stage equigranular quartz monzonite. Weak orthoclase - albite alteration is developed inside this intrusion (12). Stage 4 veins (15) may be associated with this intrusion. Continued development of chlorite - epidote - hematite alteration around the outer K-silicate alteration (11; light blue line), and may have overprinted the earlier K-silicate alteration zone. Development of texturally destructive albite - quartz - pyrite - sericite alteration (16; red line) and may have overprinted all the earlier alteration assemblage. Refer to Figure 7.2 for legend.

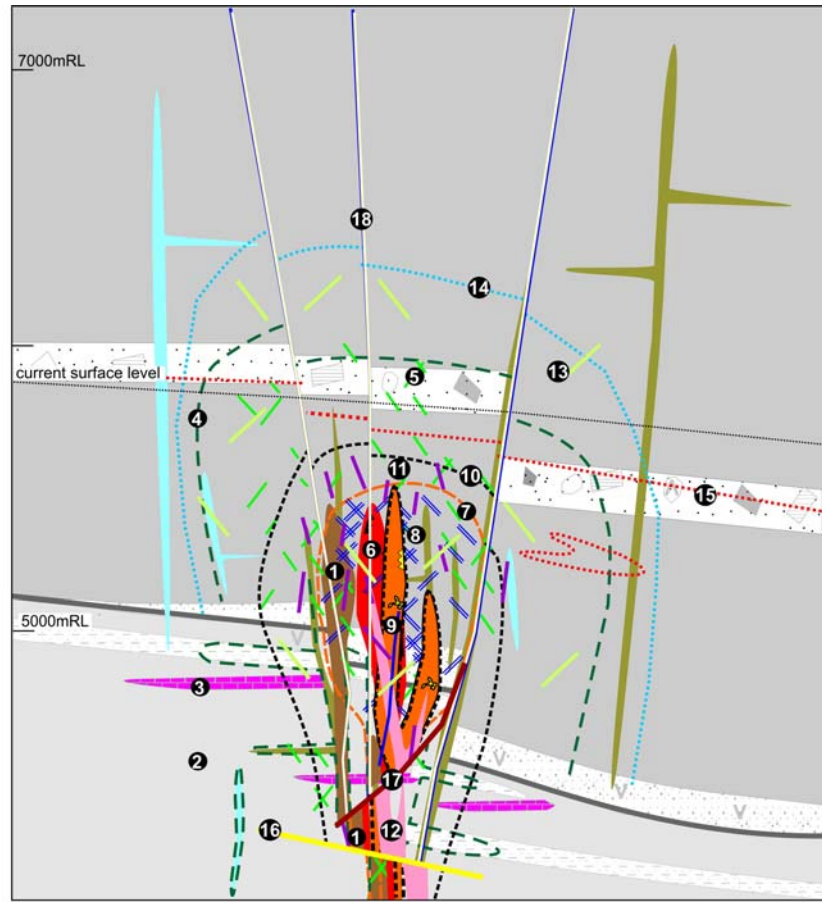


**Figure 7.4** Conceptual genetic model for Ridgeway. Post-mineralization fault-related events. Deformation in the early Silurian generated low-angle reverse and thrust faults, with intense alteration haloes developed for a few meters from the fault plane. Pervasive carbonate - quartz  $\pm$  chlorite halo (16; yellow thick line) occur in low-angle reverse fault, with associated calcite veins and stringers. Intense epidote - hematite alteration of the wall rock occur in moderately dipping thrust fault (17; maroon line), locally with associated epidote stockworks. Pervasive clay (sericite) - chlorite  $\pm$  epidote alteration halo developed in steeply dipping faults (18; light yellow line). Refer to Figure 7.2 for legend.

### 7.3.2.5 Post-mineralization: fault-related hydrothermal events

The last hydrothermal activity events at Ridgeway were structurally controlled and produced post-mineralization alteration assemblages around the faults that dismembered the orebody (Fig. 7.4). A district-scale E-directed compressional event during the Benambran Orogeny (~435 Ma) probably caused at least some of the post-mineralization faulting that has cut and offset the intrusions and mineralization at Ridgeway (Harris *et al.*, 2009b).

Significant events include:

- NW-striking, steeply-dipping shear zones and faults that have offset stratigraphic horizons (Fig. 7.4). Pervasive clay–chlorite  $\pm$  epidote alteration haloes up to 0.3 - 1 m wide are associated with these faults. The fault zones locally contain fragments of quartz–sulfide veins suggesting that these faults were reactivated after the development of mineralized veins.
- N-NW striking, southwest-dipping reverse faults truncated the intrusions and associated mineralization. Intense epidote–hematite alteration haloes of up to ~30 mm thick occur around the fault zones (Fig. 7.4).
- Low-angle faults disrupted the Weemalla Formation below the Ridgeway orebody (Fig. 7.4). Pervasive carbonate– quartz  $\pm$  chlorite alteration haloes up to 2 m wide characterize these faults (Fig. 7.4). Locally, carbonate alteration was associated with a network of calcite veins and stringers that formed around the fault zones.

### **7.3.3 Timing of igneous activity and sulfide mineralization**

The absolute timing of mineralization at Ridgeway has been constrained by Re–Os dating of molybdenite and U–Pb dating of the monzonites. Intrusive activity and associated sulfide mineralization occurred at  $444.2 \pm 1.3$  Ma, a few million years older than the other porphyry-related deposits at the Cadia district (c.f. Wilson *et al.*, 2007b). The new geochronologic results imply that the Ridgeway Au–Cu deposit is not early Late Ordovician in age as previously reported (Wilson *et al.*, 2007b) but is part of the Au- and Cu-related magmatism associated with the latest Ordovician - earliest Silurian intrusions of the Cadia district that were emplaced between 444 and 437 Ma.

Overall, the magmatic evolution of the Ridgeway deposit occurred over approximately 8 m.y., with hydrothermal activity occurring as discrete events towards the end of the system. Intrusions at Ridgeway had shoshonitic magmatic affinities, which imply that shoshonitic magmatism occurs several times in the district, progressing toward more evolved and ultimately mineralized magmatic compositions. The abundant mafic xenoliths observed in the intrusions associated

with mineralization (i.e. P1 and P2 porphyries) could imply mafic magma involvement during mineralization at Ridgeway, although more work is required to test this hypothesis.

### **7.3.4 Sulfide precipitation**

Hydrothermal quartz veins from Ridgeway comprise multiple generations of quartz with cryptic textural features (e.g. Figs. 6.1 to 6.8). Cathodoluminescence imaging of these veins has revealed a consistent evolution of early euhedral quartz with well defined growth zones (Qz-1) and massive, homogenous quartz with no visible zoning (Qz-2) that predate the deposition of bornite, chalcopyrite ( $\pm$  gold), from a later generation of dull-luminescing quartz (Qz-3) consistently associated with Cu–Fe sulfides. Similar relationships have been reported from other porphyry deposits, such as in quartz–sulfide veins at Grasberg, Irian Jaya, Indonesia (Penniston-Dorland, 2001); in stockwork veins at Bingham (Redmond *et al.*, 2004), and in quartz–molybdenite veins at Butte (Rusk and Reed, 2006). Titanium-in-quartz geothermometry for quartz veins from Ridgeway has showed that the early generation quartz precipitated at high-temperatures ( $>600^{\circ}\text{C}$ ). In contrast, the late Qz-3 dark-luminescing quartz is inferred to have formed below  $589^{\circ}\text{C}$ , the lower limit of applicability of the geothermometer. Cooling combined with sulfate reduction and neutralization of the fluid by wall rock interaction are considered to be the processes most likely to have lead to sulfide precipitation at Ridgeway.

### **7.3.5 Gold enrichment in the alkaline melts at Ridgeway**

The gold-rich nature of the Ridgeway deposit may be attributed to a range of factors: enrichment of the melt at its source (e.g. Keith *et al.*, 1995, Clark and Arancibia, 1995), favourable conditions within the magma chamber that allowed transportation of the gold into volatile phase during fractionation (e.g. Candela, 1989), and/or favourable physicochemical conditions at the site of deposition (e.g. Burnham, 1979; Cline and Bodnar, 1991, 1994). No single factor is likely to have been responsible for the gold-rich nature of the deposit.

The highest gold-grades at Ridgeway are associated with the hydrothermal quartz–magnetite–bornite stockwork and veins. This probably relates to the ability of



bornite to contain one order of magnitude more gold than co-existing chalcopyrite (Simon *et al.*, 2000). This association is well-documented from other gold-rich porphyry deposits (e.g. Grasberg, MacDonald and Arnold, 1994; Panguna, Clark, 1990; Batu Hijau, Garwin, 2000; Northparkes, Lickfold *et al.*, 2003; Santo Tomas, Serafica and Baluda, 1977; Far Southeast, Garcia 1991).

At Ridgeway, mafic xenoliths occur in the mineralized monzonite intrusions (P1 and P2 porphyries), and are enriched in PGEs (i.e. Pd, Pt and Au). Bingham, Utah, Emperor, Fiji, and Lihir, Papua New Guinea are reported to have high contents of Au, Pt, and Pd (Hattori and Kieth, 2001; Maughan *et al.*, 2002). Hattori and Keith (2001) concluded that elevated concentrations of these elements in many deposits suggest a contribution from primitive mafic melt derived from the mantle. Mafic alkaline magmas are also considered to have been critical in the generation of the gold-rich Bingham deposit (Sillitoe 2000; Maughan *et al.* 2002) and Northparkes (Lickfold *et al.*, 2007). This could also be the case for the anomalously high concentrations of Au found in Ridgeway.

## **7.4 Exploration Implications**

Understanding how Ridgeway formed will hopefully aid exploration for other porphyry Au–Cu deposits (both alkalic and calc-alkalic) at both the district and regional scale. Given that many porphyry Au–Cu districts lack marked lithological contacts such as the Weemalla Formation-FRV transition, those that do should be given particular emphasis during exploration, as the rheological and chemical changes at such contact may be important for high grade ore formation. The types and compositions of the wallrocks were important influences on the distribution and extent of alteration and mineralization assemblages at Ridgeway, and were markedly different in the feldspathic, mafic and siliceous protoliths. Exploration models therefore need to allow for alteration assemblages forming in different protoliths, particularly in distal locations.

Ridgeway was localized at the intersection of the NNW-trending monocline and NW-trending faults. Similar structural intersections may have been focal points for magmatic emplacement and are therefore prospective for exploration. The

structures related to both regional and local stress regimes at Ridgeway were important pathways that facilitated fluid flow and ore localization at different times during the evolution of the system. Early NW-trending major faults pre-dated intrusions and were most likely reactivated during and after magmatism (Fig. 7.2). Recognition of these early deformation features helped to improve the structural understanding of Ridgeway. Similar work could enhance exploration opportunities for deposits concealed beneath the Ordovician sequence elsewhere in the Cadia district and the broader Macquarie Arc.

#### **7.4 Further Work**

Recommendations for future research on Ridgeway include:

- Detailed geochemical and petrographic study of the mafic xenoliths in P1 and P2 to investigate whether interaction between mafic and felsic magmas played a role in the generation of this gold-rich porphyry deposit.
- Detailed investigation of the peripheral chlorite–epidote–hematite alteration assemblage may broaden our understanding of the temporal evolution and distal footprint of Ridgeway.
- Detailed investigation of the geochemistry of secondary apatite and rutile may help to define distal alteration signatures of Ridgeway that could help to provide a vector towards similar concealed porphyry deposits.
- Detailed age dating of fault-related sericite could constrain the timing of post mineralization deformation at Ridgeway.
- Detailed LA-ICPMS analyses of epidote, chlorite and pyrite could help to determine the distal trace elements signal of alteration mineral at Ridgeway.
- Further investigation and study of favourably oriented structures and facies analysis and provenance of the volcano-sedimentary sequence at the Cadia district and surrounds could help to evaluate where structural intersections similar to the monocline-fault intersection at Ridgeway exist, and provided a locus for mineralization.
- Further studies of quartz-rich USTs, including analyses of fluid inclusions (if possible),  $\text{TiO}_2$  contents and TitaniQ calculations, could help to constrain temperature and provide additional insights into magmatic-hydrothermal transitional processes that led to the formation of Ridgeway.

---

# References

---

- Acocella, V., 2000**, Space accommodation by roof lifting during pluton emplacement at Amiata (Italy): *Terra Nova*, v. 12 (4), p. 149-155.
- Ahmad, S. N., and Rose, A. W., 1980**, Fluid inclusions in porphyry and skarn ore at Santa Rita, New Mexico: *Economic Geology*, v. 75, p. 229-250.
- Aydin, A. and Nur, A., 1982**, Evolution of pull-apart basins and their scale independence: *Tectonics*, v. 1, p. 91-105.
- Atmaoui, N., Kukowski, N., Stockhert, B. and Konig, D., 2006**, Initiation and developement of pull-apart basins with Riedel shear mechanism: insights from scaled clay experiments: *International Journal of Earth Sciences*, v. 95, p. 225-238.
- Arancibia, O. N., and Clark, A. H., 1996**, Early magnetite-amphibole-plagioclase alteration mineralization in the Island Copper porphyry copper-gold-molybdenum deposit, British Columbia: *Economic Geology*, v. 91, p. 402-438.
- Bajwah, Z. U., 1985**, Geology, geochemistry and genesis of the Big Cadia iron-copper-gold deposit, NSW.: Unpublished PhD thesis, University of Newcastle, Australia, 412 p.
- Baker, T., Ash, C. H., and Thompson, J. F. H., 1997**, Geologic setting and characteristics of the Red Chris porphyry copper-gold deposit, northwestern British Columbia: *Exploration and Mining Geology*, v. 6, p. 297-316.
- Barnes, S., Naldrett A. J., and Gorton, M. P., 1985**, The origin of the fractionation of platinum-group elements in terrestrial magma: *Chemical Geology*, v. 53, p. 303- 323.
- Beane, R. E., 1982**, Hydrothermal alteration in silicate rocks, *in* Titley, S. R., ed., *Advances in Geology of the Porphyry Copper Deposits, Southwestern North America*, Tucson, The University of Arizona Press, p. 117-138.
- Bierlein F.P., Gray D.R., Foster D.A., 2002**. Metallogenic relationships to tectonic evolution - the Lachlan Orogen, Australia: *Earth and Planetary Science Letters* 202, p. 1-13.
- Black, L., 1994**, SHRIMP dating of Cadia and Copper Hill samples, Newcrest Mining Limited.
- Blenkinsop, T. G., 2008**, Relationships between faults, extension fractures and veins, and stress: *Journal of Structural Geology*, v. 30, p. 622-632.
- Blevin, P. L., 2002**, The petrographic and compositional character of variably K-enriched magmatic suites associated with Ordovician porphyry Cu-Au mineralisation in the Lachlan Fold Belt, Australia: *Mineralium Deposita*, v. 37, p. 87-99.

- Blevin, P. L., and Chappell, B. W., 1995**, Chemistry, origin, and evolution of mineralized granites in the Lachlan fold belt, Australia; the metallogeny of I- and S-type granites: *Economic Geology*, v. 90, p. 1604-1619.
- Bodnar, R. J., 1993**, Revised equation and table for determining the freezing point depression of H<sub>2</sub>O-NaCl solutions: *Geochimica et Cosmochimica Acta*, v. 57, p. 683-684.
- Bodnar, R. J. and Vytik, M. O., 1994**, Interpretation of microthermometric data for H<sub>2</sub>O-NaCl fluid inclusions: *in* Fluid Inclusions in Minerals, Methods and Applications, De Vivo, B. and Frezzotti, M. L., eds, published by Virginia Tech, Blacksburg, V. A. p. 117-130.
- Bonn, P.D., 2000**. The formation of veins in their microstructures. In: Stress , Strain and Structures: A volume in honour of W. D. Means, M.W. Jessell and J.L. Urai, eds., v. 2, Journal of the Virtual Explorer.
- Braxton, D. P., 2007**, Boyongan and Bayugo Porphyry Copper-Gold Deposits, NE Mindanao, Philippines: Unpublished PhD thesis, University of Tasmania, Australia, 277 p.
- Braxton, D. P. and Cooke, D. R., 2005**, The Boyongan porphyry Cu-Au deposit: Repeated hydrothermal cycles tied to discrete intrusive events: *Mineral Deposit Research: Meeting the Global Challenge*, p. 257-360.
- Burnham, C. W., 1979**, Magmas and hydrothermal fluids, *in* Barnes, H. L., ed., *Geochemistry of Hydrothermal Ore Deposits*, New York, Wiley, p. 71-136.
- Burnham, C. W., 1997**, Magmas and hydrothermal fluids: *in* Barnes, H. L., ed., *Geochemistry of ydrothermal ore deposits*, Pennsylvania, John Wiley and Sons Inc., p. 63-123.
- Burgio, N., 2005**, Ridgeway Deeps Geotechnical Information Base Report, Newcrest Mining Limited, 57 p.
- Candela, P. A., 1989**, Felsic magmas, volatiles, and metallogenesis: *in* Whitney J. A. and Naldrett, A. J., eds., *Ore deposition associated with magma*, volume 4, *Reviews in Economic Geology*, p. 223-233.
- Candela, P. A., 1997**, A Review of Shallow, Ore-related Granites: Textures, Volatiles, and Ore Metals: *Journal of Petrology*, v. 38 (12), p 1619-1633.
- Candela, P. A., and Blevin, P. L., 1995**, Do some miarolitic granites preserve evidence of magmatic volatile phase permeability?: *Economic Geolgy*, v. 90, p. 2310-2316.
- Cannell, J. C., 2004**, El Teniente porphyry copper-molybdenum deposit, central Chile: Unpublished PhD thesis, University of Tasmania, Australia, 317 p.
- Cannell, J. C., Cooke, D. R., Walshe, J. L., and Stein, H., 2005**, Geology, mineralization, alteration, and structural evolution of the El Teniente porphyry Cu-Mo deposit: *Economic Geology*, 100, p 979-1003.
- Carten, R. B., 1986**, Sodium - calcium metasomatism: Chemical, temporal and spatial relationships at the Yerington, Nevada, porphyry copper deposit: *Economic Geology*, v. 81, p. 1495-1519.

- Carten, R. B., Walker, B. M. and Geraghty, E. P., 1988**, Comparison of field-based studies of the Henderson porphyry molybdenum deposit, Colorado, with experimental and theoretical models of porphyry systems: *in* Taylor, R. P. and Strong, D. F., eds., Recent advances in the geology of granite-related mineral deposits, Special volume 39: Ottawa, Canadian Institute of Mining and Metallurgy, p. 351-366.
- Cas, R., 1983**, Palaeogeographic and tectonic development of the Lachlan fold belt, southeastern Australia, Sydney, N.S.W., Australia, Geological Society of Australia, 104 p.
- Chang, Z. and Meinert, L. D., 2008**, The magmatic–hydrothermal transition-evidence from quartz phenocryst textures and endoskarn abundance in Cu–Zn skarns at the Empire Mine, Idaho, USA: *Chemical Geology*, v. 210, p. 149-171.
- Chappell, B. W., White, A. J. R., and Hine, R., 1988**, Granite provinces and basement terranes in the Lachlan fold belt, southeastern Australia: *Australian Journal of Earth Sciences*, v. 35, p. 505-521.
- Chernicoff, C.J., Richards, J.P., and Zappettini, E.O., 2002**, Crustal lineament control on magmatism and mineralization in northwestern Argentina: Geological, geophysical, and remote sensing evidence: *Ore Geology Reviews*, v. 21, p. 127-155.
- Ciavarella, V. and Wyld, S. J., 2008**, Wall rocks as recorders of multiple pluton emplacement mechanisms - Examples from Cretaceous intrusions of northwest Nevada: *The Geological Society of America Special Paper* 438, 34p.
- Clark, G. H., 1990**, Panguna copper-gold deposit: *in* Hughes F. E., ed.: *Geology of the Mineral Deposits of Australia and Papua New Guinea*, v. 2, p. 1807-1816.
- Clemens, J. D. and Mawer, C. K., 1992**, Granitic magma transport by fracture propagation: *Tectonophysics*, v. 204, p. 339-360.
- Cline, J. S., and Bodnar, R. J., 1991**, Can economic porphyry copper mineralization be generated by a “typical” calc-alkaline melt?: *Journal of Geophysical Research*, v. 96, p. 8113-8126.
- Cline, J. S., and Bodnar, R. J., 1994**, Direct evolution of brine from a crystallizing silicic melt at the Questa, New Mexico, molybdenum deposit: *Economic Geology*, v. 89, p. 1780-1802.
- Collins, W. J., and Vernon, R. H., 1992**, Palaeozoic arc growth, deformation and migration across the Lachlan fold belt, southeastern Australia, *Tectonophysics*, *Tectonophysics* 214, Amsterdam, Netherlands, Elsevier, p. 381-400.
- Coney P.J., 1992**, The Lachlan belt of eastern Australia and Circum-Pacific tectonic Evolution - the Palaeozoic eastern margin of Gondwanaland, tectonics of the Lachlan fold belt, southeastern Australia and related orogens: *Tectonophysics*, v. 214, p.1-25.
- Coney, P. J., Edwards, A., Hine, R., Morrison, F., and Windrim, D., 1990**, The regional tectonics of the Tasman orogenic system, eastern Australia: *Journal of Structural Geology*, v. 12, p. 519- 543.



- Cooke D.R., Hollings P., Walshe J.L., 2005**, Giant Porphyry Deposits: Characteristics, Distribution, and Tectonic Controls: *Economic Geology*, v. 100 (5), p. 801-818.
- Cooke, D. R. and Holliday, J. R., 2007**, Advances in Geological Models and Exploration Methods for Copper  $\pm$  Gold Porphyry Deposits: *in* "Proceedings of Exploration 07: Fifth Decennial International Conference on Mineral Exploration" edited by B. Milkereit, 2007, p. 791-809.
- Cooke, D.R., Wilson, A.J., House, M.J., Wolfe, R. C., Walshe, J. L., Lickfold, V., and Crawford, A. J., 2007**, Alkalic porphyry Au-Cu and associated mineral deposits of the Ordovician to Early Silurian Macquarie Arc, New South Wales: *Australian Journal of Earth Sciences*, v. 54, p. 445-463.
- Cooke, D. R., Wilson, A. J., Lickfold, V. and Crawford, A. J., 2002**, The alkalic Au-Cu porphyry province of NSW: AusIMM 2002 - 150 Years of Mining, Auckland, The Australasian Institute of Mining and Metallurgy, p. 197-202.
- Corbett, G. J., and Leach, T. M., 1998**, Southwest Pacific Rim gold-copper systems; structure, alteration, and mineralization: *Economic Geology Special Publication 6*, 237 p.
- Cox, D. P., 1985**, Geology of the Tanama and Helecho porphyry copper deposits and their vicinity: professional paper no. 1327, US Geological Survey, Government Printing Office, Washington, 59 p.
- Cox, S. F., 2005**, Coupling between Deformation, Fluid Pressures, and Fluid Flow in Ore-Producing Hydrothermal Systems at Depth in the Crust: *Society of Economic Geologists, 100th Anniversary Volume*, p. 39-75.
- Crawford, A. J., 2001**, Tectono-magmatic development of the Ordovician volcanic belts in central western NSW, and the timing and location of porphyry-style mineralisation within the Macquarie Arc: *in* Crawford, A. J., Cooke, D. R., and Glen, R. A., eds., *Final Report: CODES-DMR-SPIRT Ordovician Project*, Hobart, Centre for Ore Deposit Research, p. 7.41-7.52.
- Crawford, A. J. and Berry, R. F., 1991**, Early tectonic evolution of the Lachlan Foldbelt: a Tasmanian perspective: *Tectonics and Metallogenesis of the Lachlan Fold Belt*, Canberra, Geological Society of Australia, p. 11.
- Crawford, A. J., Cooke, D. R. and Fanning, C. M., 2007**, Geochemistry and age of magmatic rocks in the unexposed Narromine, Cowal and Fairholme Igneous Complexes in the Ordovician Macquarie Arc, New South Wales: *Australian Journal of Earth Sciences*, v. 54, p. 243-271.
- Crowe, D.E., Riciputi, L.R., Bezenek, S. and Ignatiev, A., 2001**, Oxygen isotope and trace element zoning in hydrothermal garnets: windows into large-scale fluid flow behavior. *Geology* 29, p. 479-482.
- Delaney, P. T., Pollard, D. D., Ziony, J. I. and McKee, E. H., 1986**, Field relations between dikes and joints: Emplacement processes and paleostress analysis: *Journal of Geophysical Research*, v. 91, p. 4920-4938.
- Deyell, C. L. and Tosdal, R., 2005**, Sulfur Isotopic Zonation in Alkalic Porphyry Cu-Au Systems: Application to Mineral Exploration in British Columbia, B. C.: Ministry of Energy of Mines, Geological Field Work Vol 2004, p. 191-208.

- Dilles, J. H., 1987**, Petrology of the Yerington Batholith, Nevada: Evidence for Evolution of Porphyry Copper Ore Fluids: *Economic Geology*, v. 82, p. 1750-1789.
- Dilles, J. H. and Einaudi, M. T., 1992**, Wall-rock alteration and hydrothermal flow paths about the Ann-Mason porphyry copper deposit, Nevada - A 6 km vertical reconstruction.: *Economic Geology*, v. 87, p. 1963-2001.
- Dilles, J. H., Solomon, G. C., Taylor, H. P. J. and Einaudi, M. T., 1992**, Oxygen and hydrogen isotope characteristics of hydrothermal alteration at the Ann-Mason porphyry copper deposit, Yerington, Nevada.: *Economic Geology*, v. 87, p. 44-63.
- Eastoe, C. J., 1982**, Physics and chemistry of the hydrothermal system at the Panguna porphyry copper deposit, Bougainville, Papua New Guinea: *Economic Geology*, v. 77, p. 127-153.
- Engvik, A. K., Bertram, A., Kalthoff, J. F., Stockhert, B., Austrheim, H. and Elvevold, S., 2005**, Magma-driven hydraulic fracturing and infiltration of fluids into the damaged host rock, an example from Dronning Maud Land, Antarctica: *Journal of Structural Geology*, v. 27, p. 839-854.
- Einaudi, M.T., 1982**, Description of skarns associated with porphyry copper plutons, southwestern North America: *in* Titley, S.R., ed., *Advances in the geology of porphyry copper deposits, southwestern North America*: Tucson, University of Arizona Press, p. 139-184.
- Einaudi, M.T. and Burt, D.M., 1982**, Introduction: Terminology, classification, and composition of skarn deposits: *Economic Geology*, v. 77, p. 745-754.
- Einaudi, M. T., Meinert, L. D. and Newberry, R. J., 1981**, Skarn Deposits: *Economic Geology*, 75th Anniversary Volume, p. 317-391.
- Fergusson, C. L., and Coney, P. J., 1992**, Convergence and intraplate deformation in the Lachlan fold belt of southeastern Australia: *Tectonophysics*, v. 214, p. 417-439.
- Field, C. W., 1966**, Sulfur isotope abundance data, Bingham District, Utah: *Economic Geology*, v. 61, p. 850-871.
- Finn, D., 2006**, Late-stage phyllic alteration in the Cadia East copper-gold porphyry deposit, NSW: implication to mineralization: Unpublished Honours thesis, University of Tasmania, 108 p.
- Finlayson, D. M., Korsch, R. J., Glen, R. A., Leven, J. H. and Johnstone, D. W., 2002**, Seismic imaging and crustal architecture across the Lachlan Transverse Zone, a possible early cross-cutting feature of eastern Australia: *Australian Journal of Earth Sciences*, v. 49 (2), p. 311-321.
- Finlow-Bates, T. and Stumpfl E. F., 1981**, The Behaviour of So-Called Immobile Elements in Hydrothermally Altered Rocks Associated with Volcanogenic Submarine-Exhalative Ore Deposits: *Mineral Deposita*, v. 16, p. 319-328.
- Forster., D. B., 2005**, The Geology, Genesis and Significance of Skarn Mineralisation and Alteration in the Cadia Gold-Copper District, New South Wales, Australia: Unpublished PhD thesis, University of Newcastle, 222 p.

- 
- Forster D. B., Seccombe P.K. and Phillips D., 2004**, Controls on skarn mineralization and alteration at the Cadia deposits, New South Wales, Australia: *Economic Geology*, v. 99, p. 761-788.
- Foster, D. A. and Gray, D. R., 2000**, Evolution and structure of the Lachlan fold belt (orogen) of eastern Australia: *Annual Review of Earth and Planetary Sciences*, v. 28, p. 47-80.
- Fountain, R. J., 1972**, Geological Relationships in the Panguna Porphyry Copper Deposit, Bougainville Island, New Guinea: *Economic Geology*, v. 67, p. 1049-1064.
- Fournier, R. O., 1999**, Hydrothermal processes related to movement of fluid from plastic into brittle rock in the magmatic-epithermal environment: *Economic Geology*, v. 94 (8), p. 1193-1212.
- Garcia, 1981**, Geology and Mineralization Characteristics of the Mankayan Mineral District, Benguet, Philippines: *Geological Survey of Japan Report*, No. 277, p. 21-30.
- Garwin, S. L., 2000**, The setting, geometry and timing of intrusion-related hydrothermal systems in the vicinity of the Batu Hijau porphyry copper-gold deposit, Sumbawa, Indonesia: Unpublished PhD thesis, University of Western Australia, 452 p.
- Gerbi, C., Johnson, S. E. and Paterson, S. R., 2004**, Implications of rapid, dike-fed pluton growth for host-rocks strain rates and emplacement mechanisms: *Journal of Structural Geology*, v. 26, p. 583-594.
- Glen, R. A., 1992**, Thrust, extensional and strike-slip tectonics in an evolving Palaeozoic orogen; a structural synthesis of the Lachlan Orogen of southeastern Australia: *Tectonophysics*, v. 214, p. 341-380.
- Glen, R. A., 1998**, Structural Geology: *in* Stewart, J. R., ed., Bathurst 1:250 000 geological sheet SI/55-8 Explanatory Notes, Sydney, Geological Survey of New South Wales, p. 287-310.
- Glen, R. A., 2005**, The Tasmanides of eastern Australia: *in* Vaughan, A.P.M., Leat, P. T. and Pankhurst, R. J., eds., *Terrane Processes at the Margins of Gondwana*, Geological Society of London, Special Publications, v. 246, p. 23-96.
- Glen, R. A., Crawford, A. J., and Cooke, D. R., 2007a**, Tectonic setting of porphyry Cu–Au mineralisation in the Ordovician - Early Silurian Macquarie Arc, Eastern Lachlan Orogen, New South Wales: *Australian Journal of Earth Sciences*, v. 54, p. 465-479.
- Glen, R. A., Korsch, R. J., Direen, N. G., Jones, L. E. A., Johnstone, D. W., Lawrie, C., Finlayson, D. M. and Shaw, R. D., 2002**, Crustal structure of the Ordovician Macquarie Arc, Eastern Lachlan Orogen, based on seismic-reflection profiling: *Australian Journal of Earth Sciences*, v. 49 (2), p. 323-348.
- Glen R.A., Meffre S. and Scott R.J., 2007c**, Benambran Orogeny in the eastern Lachlan Orogen, Australia; Geological evolution and metallogenesis of the Ordovician Macquarie Arc, Lachlan Orogen, New South Wales: *Australian Journal of Earth Sciences* 54, p. 385-415.

- Glen, R. A. and Walshe, J. L., 1999**, Cross-structures in the Lachlan Orogen: the Lachlan Transverse Zone example: *Australian Journal of Earth Sciences*, v. 46, p. 641-658.
- Glen, R. A., Walshe, J. L., Barron, L. M. and Watkins, J. J., 1998**, Ordovician convergent-margin volcanism and tectonism in the Lachlan sector of east Gondwana: *Geology*, v. 26 (8), p. 751-754.
- Glen, R. A. and Wyborn, D., 1997**, Inferred thrust imbrication, deformation gradients and the Lachlan Transverse Zone in the Eastern Belt of the Lachlan Orogen, New South Wales: *Australian Journal of Earth Sciences*, v. 44 (1), p. 49-68.
- Götze, J., Plötze, M., and Habermann, D., 2001**, Origin, spectral characteristics and practical applications of the cathodoluminescence of quartz-a review: *Mineralogy and Petrology*, v. 71, p. 225-250.
- Gow, P. A. and Walshe, J. L., 2005**, The Role of Pre-existing Geologic Architecture in the Formation of Giant Porphyry-Related Cu  $\pm$  Au Deposits: Examples from New Guinea and Chile: *Economic Geology*, v. 100, p. 819-833.
- Gray D.R., and Foster D.A., 2004**. Tectonic evolution of the Lachlan Orogen, southeast Australia: historical review, data synthesis and modern perspectives: *Australian Journal of Earth Sciences* v. 51 (6), p. 773-817.
- Gray, D. R., Foster, D. A. and Bierlein, F. P., 2002**, Geodynamics and metallogeny of the Lachlan Orogen: *Australian Journal of Earth Sciences*, v. 49, p. 1041-1056.
- Gray, D. R., Foster, D. A. and Bucher, M., 1997**, Recognition and definition of Orogenic events in the Lachlan Fold Belt: *Australian Journal of Earth Sciences*, v. 44 (4), p. 489-501.
- Gray D.R., Foster D.A., Korsch R.J., Spaggiari C.V., 2006**. Structural style and crustal architecture of the Tasmanides of eastern Australia; example of a composite accretionary orogen; Styles of continental contraction: *Special Paper - Geological Society of America* 414, 119-132.
- Green, D., 1999**, Geology, geochemistry and genesis of the Big Cadia deposit, N.S.W.: Unpublished BSc (Honours) thesis, University of Tasmania, 187 p.
- Grocott, J., Arevalo, C., Wekner, D. and Cruden, A., 2009**, Fault-assisted vertical pluton growth: Coastal Cordillera, north Chilean Andes: *Journal of the Geological Society, London*, v. 166, p. 295-301.
- Groome, W. and Munro, D., 2009**, Preliminary Report on the Holman Lode Occurrence, Cadia Extended (Quarry) Deposit, Cadia Valley Operations, Orange NSW: Newcrest Mining Limited, 60 p.
- Gruen, G., Heinrich, C. A. and Schroeder, K., 2010**, The Bingham Canyon Porphyry Cu-Mo-Au Deposit. II. Vein Geometry and Ore Shell Formation by Pressure-Driven Rock Extension: *Economic Geology*, v. 105, p.69-90.
- Guillou-Frottier, L. and Burov, E., 2003**, The development and fracturing of plutoic apexes: implications for porphyry ore deposits: *Earth and Planetary Science Letters* 214, p. 341-356.

- Gustafson, L. B. and Hunt, J. P., 1975**, The porphyry copper deposit at El Salvador, Chile: *Economic Geology*, v. 70, p. 857-912.
- Gustafson, L. B. and Quiroga, J., 1995**, Patterns of mineralization and alteration below the porphyry copper orebody at El Salvador, Chile: *Economic Geology*, v. 90, p. 2-16.
- Gustafson, L. B., and Titley, S. R., 1978**, Porphyry Copper Deposits of the Southwestern pacific islands and Australia: *Economic Geology*, v. 73, 597–599.
- Harper, B. L., 2000**, Hydrothermal alteration at the Ridgeway porphyry gold-copper deposit, NSW: Unpublished Honours thesis, University of Tasmania, 130 p.
- Hastie, A. R., Kerr, A. C., Pearce, J. A. and Mitchell, S. F., 2007**, Classification of Altered Volcanic Island Arc Rocks using Immobile Trace Elements: Development of the Th-Co Discrimination Diagram: *Journal of Petrology*, v. 48, p. 2341-2357.
- Harris, A. C., and Golding, S. D., 2002**, New evidence of magmatic-fluid-related phyllic alteration: implications for the genesis of porphyry Cu deposits: *Geology*, v. 30, p. 335-338.
- Harris, A. C., Golding, S. D., and White, N. C., 2005**, Bajo de la Alumbrera Cu-Au: Stable isotope evidence for a porphyry-related hydrothermal system dominated by magmatic aqueous fluids: *Economic Geology*, v. 100, p. 863-886.
- Harris, A., Cuison, A. G., Chang, Z., Cooke, D. R., Bonnici, N., Faure, K. and Cross, C., 2006**, Fe-rich magmatic volatiles in the Ridgeway Au-Cu porphyries: evidence from magnetite-quartz comb-layered textures.
- Harris, A. C., Kamenetsky, V. S., White, N. C. and Steele, D. A., 2004**, Volatile phase separation in silicic magmas at Bajo de la Alumbrera porphyry Cu-Au deposit, NW Argentina: *Resource Geology*, v. 54 (3), p. 341-356.
- Harris A., Percival, I., Allen, C., Tedder, I., McMillan, C., Cooke, D. R., McPhie, J., Dunham, P. and Collett, D., 2009a**, Volcanic Stratigraphy and Architecture of the Cadia Valley, New South Wales: *in* Cadia Valley Alkalic Porphyry Ore Deposits: Deconstructing the System Architecture, Final Project Report, 18 p.
- Harris A., Washburn, M., Tosdal, R., Cooke, D. R., Fox, N., Cuison A. G., Berry, R., McMillan, C., Holliday, J., Dunham, P. and Collett, D., 2009b**, Reconstruction of the dismembered Cadia Valley porphyry ore deposits, New South Wales: *in* Cadia Valley Alkalic Porphyry Ore Deposits: Deconstructing the System Architecture, Final Project Report, 22 p.
- Harris A., Allen, C., Creaser, R., Cooke, D. R., Cuison A. G., Washburn, M. and Tosdal, R., 2009c**, Evolution of the Cadia Valley porphyry ore deposits, New South Wales: an integrated model based on U-Pb and Ar isotope data: *in* Cadia Valley Alkalic Porphyry Ore Deposits: Deconstructing the System Architecture, Final Project Report, 11 p.
- Harris A., Cooke, D. R., Cuison A. G. and Fox, N., 2009d**, New insights into the geochemistry of the Forest Reefs Volcanics: implication for the evolution of



the Macquarie Arc: *in* Cadia Valley Alkaline Porphyry Ore Deposits: Deconstructing the System Architecture, Final Project Report, 10 p.

- Harris A., Cooke, D. R., Washburn, M., Tosdal, R. and Fox, N., 2009e**, Evolution of the Cadia Valley porphyry ore deposits, New South Wales: an integrated model based on U-Pb and Ar isotope data: *in* Cadia Valley Alkaline Porphyry Ore Deposits: Deconstructing the System Architecture, Final Project Report, 15 p.
- Hastie, A. R., Kerri, A. C., Pearce, J. A. and Mitchell, S. F., 2007**, Classification of Altered Volcanic Island Arc Rocks using Immobile Trace Elements: Development of the Th-Co Discrimination Diagram: *Journal of Petrology*, v. 48 (12), p. 2341-2357.
- Hattori, K. H., and Keith, J. D., 2001**, Contribution of mafic melt to porphyry copper mineralization: evidence from Mount Pinatubo, Philippines, and Bingham Canyon, Utah, USA: *Mineralium Deposita*, v. 36, p. 799-806.
- Haynes, F. M. and Titley, S. T., 1980**, The Evolution of Fracture-Related Permeability within the Ruby Star Granodiorite, Sierrita Porphyry Copper Deposit, Pima County, Arizona: *Economic Geology*, v. 75, p. 673-683.
- Hedenquist, J. W., Arribas, A. and Reynolds, T. J., 1998**, Evolution of an intrusion-centered hydrothermal system: Far Southeast Lepanto porphyry and epithermal Cu-Au deposits, Philippines: *Economic Geology*, v. 93, p. 374-404.
- Hedenquist, J. W., and Richards, J. P., 1998**, The influence of geochemical techniques on the development of genetic models for porphyry copper deposits: *in* Richards, J. P., and Larson, P. B., eds., *Reviews in Economic Geology Volume 10. Techniques in Hydrothermal Ore Deposits Geology*, Littleton, Society of Economic Geologists, p. 235-256.
- Heidrick, T. L., and Titley, S. R., 1982**, Fracture and dike patterns in Laramide plutons and their structural and tectonic implications, *in* Titley, S. R., ed., *Advances in Geology of the Porphyry Copper Deposits, Southwestern North America*, Tucson, The University of Arizona Press, p. 73-91.
- Heithersay, P. S., and Walshe, J. L., 1995**, Endeavour 26 North: A Porphyry Copper-Gold Deposit in the Late Ordovician, Shoshonitic Goonumbla Volcanic Complex, New South Wales, Australia: *Economic Geology*, v. 90, p. 1506-1532.
- Hilyard, D., Drummond, M., Clare, A., Sanders, Y., Aung, Z., Glen, R., Ruszkowski, P., Fleming, G., Lewis, P. and Robson, D., 1996**, Preliminary Palaeozoic bedrock interpretation of the Narromine & Nyngan 1:250000 sheet areas: *Geological Survey of New South Wales Quarterly Notes*, v. 101, p. 1-16.
- Hill, D., 1951**, *Geology, Handbook of Queensland*, Brisbane, Australasian Association for the Advancement of Science, p. 13-24.
- Hill, E. S., 1956**, A contribution to the morphotectonics of Australia: *J. geol. Soc. Aust.*, 3. p. 1-15.
- Holliday, J., McMillan, C., and Tedder, I., 1999**, Discovery of the Cadia Ridgeway Gold-Copper Porphyry Deposit – discovery case history: *Data Metallogenica*, 5 p.

- Holliday, J., and Wood, D., 1993**, Discovery and exploration of porphyry-associated gold/copper mineralisation at Cadia: New South Wales - The State of Exploration, Sydney, NSW Department of Mineral Resources, p. 19-22.
- Holliday, J. R., Wilson, A. J., Blevin, P. L., Tedder, I. J., Dunham, P. D., and Pfitzner, M., 2002**, Porphyry gold-copper mineralisation in the Cadia district, eastern Lachlan Fold Belt, New South Wales, and its relationship to shoshonitic magmatism: *Mineralium Deposita*, v. 37, p. 100-116.
- Hough, M.A. Bierlein, F.P., Wilde, A.R., 2007**. A review of the metallogeny and tectonics of the Lachlan Orogen: *Mineralium Deposita*, v. 42, p. 435-448.
- Hutton, D. H. W., 1996**, The 'space problem' in the emplacement of granite: *Episodes*, v. 19 (4), p. 114-119.
- Jamveit, B. and Hervig, R. L., 1994**, Constraints on Transport and Kinetics in Hydrothermal Systems from Zoned Garnet Crystals: *Science*, v. 263, p. 505-508.
- Jensen, P. J., and Barton, M. D., 2000**, Gold deposits related to alkaline magmatism: *in* Hagemann, S. G., and Brown, P. E., eds., *Gold in 2000, Reviews in Economic Geology* v. 13, Society of Economic Geologists, p. 279-314.
- Johnson, J. W. and Norton, D., 1985**, Theoretical Prediction of Hydrothermal Conditions and Chemical Equilibria during Skarn Formation in Porphyry Copper Systems: *Economic Geology*, v. 80, p. 1797-1823.
- Keith, J. D., Christiansen, E. H., Maughan, D. T., and Waite, K. A., 1998**, The role of mafic alkaline magmas in felsic porphyry-Cu and Mo systems: *in* Lentz, D. R., ed., *Mineralized intrusion related skarn systems. Short Course Handbook*, v. 26, Ottawa, Mineralogical Association of Canada, p. 211-243.
- Keith, J. D., Whitney, J. A., Canna, T. M., Hook, C. and Hattori, K., 1995**. The role of magmatic sulphides and mafic alkaline magmatism in the formation of giant porphyry and vein systems: examples from the Bingham and Tintic mining districts, Utah: *in* Clark A. H. ed., *Giant Ore Deposits—II*, QMinEx, Department of Geological Sciences, Queen's University, Kingston, Ontario, p. 316-339.
- Kerrich, R., Goldfarb, R., Groves, D. I. and Garwin, S., 2000**, Geodynamics of world-class gold deposits: Characteristics, space-time distribution and origins: *Reviews in Economic Geology*, v. 13, p. 501-551.
- Kirkham, R. V., 1971**, Intermineral intrusions and their bearing on the origin of porphyry copper and molybdenum deposits: *Economic Geology*, v. 66, p. 1244-1249.
- Kirkham, R. V., and Dunne, K. P. E., 1999**, World distribution of porphyry, porphyry-associated skarn and bulk-tonnage epithermal deposits and occurrences - Open File Report 3792a: Vancouver, Geological Survey of Canada, p. 87.
- Kirkham, R. V., and Sinclair, W. D., 1988**, Comb layer quartz in felsic intrusions and their relationship to porphyry deposits: *in* Taylor, R. P., and Strong, D. F., eds., *Recent Advances in the Geology of Granite-Related Mineral Deposits*,

- Canadian Institute of Mining and Metallurgy Special Volume 31, Montreal, Canadian Institute of Mining and Metallurgy, p. 50-71.
- Kirkham, R.V., and Sinclair, W.D., 1996**, Porphyry copper, gold, molybdenum, tungsten, tin, silver: *in* Eckstrand, O.R., Sinclair, W.D., and Thorpe, R.I., eds., *Geology of Canadian mineral deposit types: Geological Survey of Canada, Geology of Canada no. 8*, p. 421-446
- Kitto, J. C., 2005**, Lithostratigraphy, alteration and geochemistry of the Cadia East Gold-Copper porphyry deposit, NSW: Unpublished Honours thesis, University of Tasmania, 136 p.
- Koide, H. and Bhattacharji, S., 1975**, Formation of Fractures Around Magmatic Intrusions and Their Role in Ore Localization: *Economic Geology*, v. 70, p. 781-799.
- Kolkert, R. and O'Sullivan, T., 2006**, Resource Model July 2006 Report, Ridgeway Gold Mine: Newcrest Mining Limited, 80 p.
- Krantz, R. W., 1988**, Multiple fault sets and three-dimensional strain: theory and applications: *Journal of Structural Geology*, v. 10 (3), p. 225-237.
- Kroll, T., Muller, D., Seifert, T., Herzig, P. M. and Schneider, A., 2002**, Petrology and geochemistry of the shoshonite-hosted Skouries porphyry Cu-Au deposit, Chalkidiki, Greece: *Mineralium Deposita*, v. 37, pp. 137-144.
- Kusakabe M, Nakagawa S, Hori M, Matsuhisa Y, Ojeda JM, Serrano L, 1984** Oxygen and sulfur isotopic compositions of quartz, anhydrite and sulfide minerals from the El Teniente and Río Blanco porphyry copper deposits, Chile: *Bulletin Geological Survey Japan* 35: p. 583-614.
- Landtwing, M. R., Furrer, C., Redmond, P. B., Pettke, T., Guillong, M. and Heinrich, C. A., 2010**, The Bingham Canyon Porphyry Cu-Mo-Au Deposit. III. Zoned Copper-Gold Ore Deposition by Magmatic Vapor Expansion: *Economic Geology*, v. 105, p. 91-118.
- Landtwing, M. R. and Pettke, T., 2005**, Relationships between SEM-cathodoluminescence response and trace-element composition of hydrothermal vein quartz: *American Mineralogist*, v. 90, pp. 122-131.
- Landtwing, M, R., Pettke, T., Halter, W. E., Heinrich, C. A., Redmond, P. B., Einaudi, M. T. and Kunze, K., 2005**, Copper deposition during quartz dissolution by cooling magmatic-hydrothermal fluids: The Bingham porphyry: *Earth and Planetary Science Letters* 07544, 15 p.
- Lang, J. R. and Stanley, C. R., 1995**, Contrasting styles of alkalic porphyry copper-gold deposits in the northern part of the Iron Mask batholith, Kamloops, British Columbia.: *in* Schroeter, T. G., ed., *Porphyry Deposits of the Northwestern Cordillera of North America* 46, Vancouver, Canadian Institute of Mining, Metallurgy and Petroleum, p. 581-592.
- Lang, J. R. and Titley, S. R., 1998**, Isotopic and geochemical characteristics of Laramide magmatic systems in Arizona and implications for the genesis of porphyry copper deposits: *Economic Geology*, v. 93, pp. 138-170.
- Large, R. R., Danyushevsky, L. V., Hollit, C., Maslennikov, V., Meffre, S., Gilbert, S. E., Bull, S., Scott, R. J., Emsbo, P., Thomas, H., Singh, B. and**

- Foster, J., 2009**, Gold and trace element zonation in pyrite using a laser imaging technique: implications for the timing of gold in orogenic and carlin-style sediment-hosted deposits: *Economic Geology*, v. 104 (5), pp. 635-668.
- Le Maitre, R. W., 1989**, A classification of igneous rocks and glossary of terms: recommendations of the International Union of Geological Sciences Subcommission on the Systematics of Igneous Rocks, Oxford, Blackwell Scientific Publications, 193 p.
- Lentz, D. R., 1994**, Alteration and alteration processes associated with ore-forming systems: *in* Lentz, ed.: Geological Association of Canada, Short Course Notes v. 11, pp. 69-99.
- Lickfold, V., 2002**, The Endeavour Porphyry Cu-Au Deposits, Australia: Unpublished PhD thesis, University of Tasmania, Australia, 245 p.
- Lickfold, V., Cooke, D. R., Smith, S. G. and Ullrich, T. D., 2003**, Endeavour Copper-Gold Porphyry Deposits, Northparkes, New South Wales: Intrusive History and Fluid Evolution: *Economic Geology*, v. 98, p. 1607-1636.
- Lickfold, V., Cooke, D. R., Crawford, A. J. and Fanning, C. M., 2007**, Shoshonitic magmatism and formation of the Northparkes porphyry Cu-Au deposits, New South Wales: *Australian Journal of Earth Sciences*, v. 54, p. 417-444.
- Linnen, R. L. and Williams-Jones, A. E., 1987**, Tectonic Control of Quartz Vein Orientation at the Trout Lake Stockwork Molybdenum Deposit, Southeastern British Columbia: Implications for Metallogeny in the Kootenay Arc: *Economic Geology*, v. 82, p. 1283-1293.
- Lowell, J. D., and Guilbert, J. M., 1970**, Lateral and vertical alteration-mineralization zoning in porphyry ore deposits: *Economic Geology*, v. 65, p. 373-408.
- Lowenstern, J. B., and Sinclair, W. D., 1996**, Exsolved magmatic fluid and its role in the formation of comb-layered quartz at the Cretaceous Logtung W-Mo deposit, Yukon Territory, Canada: *Transactions of the Royal Society of Edinburgh, Earth Sciences*, v. 87, p. 291-303.
- MacDonald, G. D., and Arnold, L. C., 1994**, Geological and geochemical zoning of the Grasberg igneous complex, Irian Jaya, Indonesia: *in* van, L. T. M., Hedenquist, J. W., James, L. P., and Dow, J. A. S., eds., *Mineral deposits of Indonesia; discoveries of the past 25 years.*, *Journal of Geochemical Exploration* 50, Amsterdam-New York, International, Elsevier, p. 143-178.
- Marjoribanks, M., 2005**, Structural observations on the Ridgeway gold-copper deposit, Cadia Camp, New South Wales: Newcrest Mining Limited, 20 p.
- Masterman, G.J., 2003**, Structural and geochemical evolution of the Rosario Cu-Mo porphyry deposit and related Cu-Ag veins, Collahuasi district, northern Chile: Unpublished PhD thesis, University of Tasmania, Australia, 253 p.
- Masterman, G. J., Cooke, D. R., Berry, R. F., Walshe, J. L., Lee, A. W., and Clark, A. H., 2005**, Fluid Chemistry, Structural Setting, and Emplacement History of the Rosario Cu-Mo Porphyry and Cu-Ag-Au Epithermal Veins,

- Collahuasi District, Northern Chile: *Economic Geology*, v. 100 (5), pp. 835-862.
- Mathieu, L., van Wyk de Vries, B., Holohan, E. P. and Troll, V. R., 2008**, Dykes, cups, saucers and sills : Analogue experiments of magma intrusion into brittle rocks : *Earth and Planetary Science Letters*, v. 271, pp. 1-13.
- Maughan, D. T., Keith, J. D., Christiansen, E. H., Pulsipher, T., Hattori, K. and Evans, N. J., 2002**, Contributions from mafic alkaline magmas to the Bingham porphyry Cu-Au-Mo deposit, Utah, USA: *Mineralium Deposita*, v. 37, p. 14-37.
- McPhie, J., Doyle, M. and Allen, R., 1993**, Volcanic textures: a guide to the interpretation of textures in volcanic rocks, University of Tasmania, Centre for Ore Deposit and Exploration Studies (publisher), Australia, 196 p.
- Meinert, L. D., 1997**, Application of skarn deposit zonation models to mineral exploration: *Exploration and Mining Geology*, v. 6, p. 185-208.
- Meinert, L. D., Hedenquist, J. W., Satoh, H. and Matsuhisa, Y., 2003**, Formation of Anhydrous and Hydrous Skarn in Cu-Au Ore Deposits by Magmatic Fluids: *Economic Geology*, v. 98, p. 147-156.
- Mercer, C.N. and Reed, M. H., 2007**, Insights into the formation of deep hydrothermal quartz from the porphyry copper-molybdenum deposit at Butte, Montana: American Geophysical Union, abstract # V41D-0816.
- Moore, J. M., 1975**, A Mechanical Interpretation of the Vein and Dyke System of the S. W. England Orefield: *Mineral Deposita*, v. 10, p. 374-388.
- Müller, D., and Forrestal, P., 1998**, The shoshonite porphyry Cu-Au association at Bajo de la Alumbrera, Catamarca Province, Argentina: *Mineralogy and Petrology*, v. 64, p. 47-64.
- Murakamin, H., Seo, J. H. and Heinrich, C., 2010**, The relation between Cu/Au ratio and fromtion depth of porphyry-style Cu-Au  $\pm$  Mo deposits: *Mineralium Deposita*, v. 45, p. 11-21.
- Nash, J. T., 1976**, Fluid-inclusion petrology - data from porphyry copper deposits and applications to exploration: U.S. Geological Survey Professional Paper, v. 907-D, p. D-1 - D-15.
- Newcrest Mining Staff, 1996**, The Cadia "wallrock-porphyry"-style gold-copper deposit, N.S.W.: Porphyry-related copper and gold deposits of the Asia-Pacific region., Cairns, Australian Mineral Foundation, p. 16.1-16.10.
- Newcrest Mining Staff, 1997**, The Cadia gold-copper deposit, NSW, New developments in research for ore deposit exploration, Third national conference of the Specialist Group in Economic Geology, Geological Society of Australia v. 44, Sydney, Geological Society of Australia, p. 54.
- Newcrest Mining Staff, 1998**, Cadia gold-copper deposit: *in* Berkman, D. A., and Mackenzie, D. H., eds., *Geology of Australian and Papua New Guinean mineral deposits.*, Australasian Institute of Mining and Metallurgy, Monograph Series v. 22, Melbourne, Australasian Institute of Mining and Metallurgy, p. 641-646.



- Newcrest Mining Limited, 2006**, Concise Annual Report to shareholders, 92 p.
- Newcrest Mining Limited, 2008**, Concise Annual Report to shareholders, 68 p.
- Norman, D. K., Parry, W. T., and Bowman, J. R., 1991**, Petrology and geochemistry of propylitic alteration at Southwest Tintic, Utah: *Economic Geology*, v. 86, p. 13-28.
- Ohmoto, H., and Lasaga, A. C., 1982**, Kinetics of reactions between aqueous sulfates and sulfides in hydrothermal systems: *Geochimica et Cosmochimica Acta*, v. 46, p. 1727-1745.
- Ohmoto, H. and Rye, R. O., 1979**, Isotopes of sulfur and carbon: *in* Barnes, H. L., ed., *Geochemistry of Hydrothermal Ore Deposits*, New York, John Wiley and Sons, p. 509-567.
- Packham, G., Percival, I. and Bischoff, G., 1999**, Age constraints on strata enclosing the Cadia and Junction Reefs ore deposits of central New South Wales, and tectonic implications: *Geological Survey of New South Wales, Quarterly Notes*, v. 110, p. 1-12.
- Packham, G. H., 1987**, The eastern Lachlan fold belt of Southeast Australia; a possible Late Ordovician to Early Devonian sinistral strike slip regime: *in* Leitch, E. C., and Scheibner, E., eds., *Terrane accretion and orogenic belts.*, *Geodynamics Series 19*, Washington, DC, United States, American Geophysical Union, p. 67-82.
- Pallister, J. S., Hoblitt, R. P., Meeker, G. P. Knight, R. J. And Siems, D. F., 1995**, Magma mixing of Mount Pinatubo: petrographic and chemical evidence from the 1991 deposits: *in* Newhall, C. G. and Punongbayan, R. S., eds., *Fire and Mud: Eruptions and Lahars of Mount Pinatubo*, Philippines, Seattle, W.A.: University of Washington Press, p. 687-731.
- Penniston-Dorland, S. C., 2001**, Illumination of vein quartz textures in a porphyry copper ore deposit using scanned cathodoluminescence: *Grasberg Igneous Complex, Irian Jaya, Indonesia: American Mineralogist*, v. 86, p. 652-666.
- Percival, I. G., Morgan, E. J. and Scott, M. M., 1999**, Ordovician stratigraphy of the northern Molong volcanic belt; new facts and figures: *Quarterly Notes - Geological Survey of New South Wales*, v. 108, p. 8-27.
- Percival I.G. and Glen R.A., 2007**, Ordovician to earliest Silurian history of the Macquarie Arc, Lachlan Orogen, New South Wales; Geological evolution and metallogenesis of the Ordovician Macquarie Arc, Lachlan Orogen, New South Wales: *Australian Journal of Earth Sciences* v. 54, p. 143-165.
- Perkins, C., 1994**, Report on  $^{40}\text{Ar}/^{39}\text{Ar}$  and K-Ar dating, Cadia, NSW: Newcrest Mining Limited, 4 p.
- Perkins, C., Walshe, J. L. and Morrison, G., 1995**, Metallogenic episodes of the Tasman Fold Belt system, Eastern Australia: *Economic Geology*, v. 90, p. 1443-1466.
- Petford, N., 2003**, Rheology of granitic magmas during ascent and emplacement: *Annual Reviews Earth Planetary Science*, v. 31, p. 399-427.

- Petford, N., Cruden, A. R., McCaffrey, K. J. W. and Vigneresse, J. L., 2000**, Granite magma formation, transport and emplacement in the Earth's crust: *Nature*, v. 408, p. 669-673.
- Petford N, Lister, J. R. and Kerr R. C., 1994**, The ascent of felsic magmas in dykes: *Lithos*, v. 32, p. 161-68.
- Phillips, C. H., Gambell, N. A. and Fountain D. S., 1974**, Hydrothermal Alteration, Mineralization, and Zoning in the Ray Deposit: *Economic Geology*, v. 69 (8), p. 1237-1250.
- Pollard, D.D., 1987**, Elementary fracture mechanics applied to the structural interpretation of dykes: *in* Halls, H.C., Fahrig, W.F., eds., *Mafic Dyke Swarms*, Geological Association of Canada Special Paper 34, p. 5-24.
- Pollard, P.J., Taylor, R.G. and Peters, L., 2005**, Ages of intrusion, alteration and mineralization at the Grasberg Cu-Au deposit, Papua, Indonesia: *Economic Geology*, v. 100, p. 1005-1020.
- Pogson, D. J. and Watkins, J. J., 1998**, Bathurst geological sheet 1:250 000, Sydney, Australia: Geological Survey of New South Wales, Department of Mineral Resources, 430 p.
- Raymond, O. L., Pogson, D. J., Wyborn, D., Henderson, G. M. A., Krynen, J., Meakin, S., Morgan, E. J., Scott, M. M., Stuart-Smith, P., Wallace, D., Warren, A. Y. E., Watkins, J. J. and Glen, R. A., 1998**, Bathurst Geology Second Edition, 1:250 000 Geological Sheet SI 55-8: Geological Survey of New South Wales. Sydney, Australian Geological Survey Organization, Caberra.
- Potter, R. W., Clynne, M. A. and Brown, D. L., 1978**, Freezing point depression of aqueous sodium chloride solutions: *Economic Geology*, v. 73, p. 284-285.
- Proffett, J. M., 2003**, Geology of the Bajo de la Alumbrera Porphyry Copper-Gold Deposit, Argentina: *Economic Geology*, v. 98, p. 1535-1574.
- Proffett, J. M., 2009**, High Cu grades in porphyry Cu deposits and their relationship to emplacement depth of magmatic sources: *Geology*, v. 37 (8), p. 675-678.
- Radclyffe D., 1995**, Regional scale propylitic alteration in the Northparkes mineral field, Parkes New South Wales: Unpublished BSc Hons thesis, University of Tasmania, 118 p.
- Redmond, P. B. and Einaudi, M. T., 2010**, The Bingham Canyon Porphyry Cu-Mo-Au Deposit. I. Sequence of Intrusions, Vein Formation, and Sulfide Deposition: *Economic Geology*, v. 105, p. 43-68.
- Redmond, P. B., Einaudi, M. T., Inan, E. E., Landtwing, M. R. and Heinrich, C. A., 2004**, Copper deposition by fluid cooling in intrusion-centered systems: New insights from the Bingham porphyry ore deposit, Utah: *Geology*, v. 32, p. 217-220.
- Reed, M. H., 1997**, Hydrothermal alteration and its relationship to ore fluid composition: *in* Barnes, H. L., ed., *Geochemistry of Hydrothermal Ore Deposits*, New York, John Wiley and Sons, p. 303-365.

- Rehrig, W. A. and Heidrick, T. L., 1972**, Regional fracturing in Laramide stocks of Arizona and its relationship to porphyry copper mineralization: *Economic Geology*, v. 67, p 198-213.
- Rehrig, W. A. and Heidrick, T. L., 1976**, Regional tectonic stress during the Laramide and Late Tertiary intrusive periods, Basin and Range Province, Arizona: *Arizona Geological Society Digest X*, p. 205-228.
- Ren, M., 2004**, Partitioning of Sr, Ba, Rb, Y, and LREE between alkali feldspar and peraluminous silicic magma: *American Mineralogist*, v. 89, p 1290-303.
- Reynolds, T. J. and Beane, R. E., 1985**, Evolution of hydrothermal fluid characteristics at the Santa Rita, New Mexico, porphyry copper deposit: *Economic Geology*, v. 80, p. 1328-1347.
- Reynolds, W. J., 2007**, Characterisation of Distal Alteration Assemblages at the Ridgeway Gold-Copper Deposit, New South Wales: Unpublished Honours thesis, University of Tasmania, 86 p.
- Reynolds, W., Harris A., Cooke, D. R., Chang, Z. and Cuison, A. G., 2009**, Peripheral alteration assemblages to the Ridgeway porphyry Au-Cu deposit, Cadia, central New South Wales: *in* Cadia Valley Alkalic Porphyry Ore Deposits: Deconstructing the System Architecture, Final Project Report, 11 p.
- Richards, J. P., 2000**, Lineaments revisited: *Society of Economic Geologists Newsletter*, 42, p. 14-20.
- Richards, J. P., 2003**, Tectono-Magmatic Precursors for Porphyry Cu-(Mo-Au) Deposit Formation: *Economic Geology*, v. 98, p. 1515–1533.
- Richards, J. P., 2005**, Alkalic-type epithermal gold deposits-a review: *Mineralogical Association of Canada Short Course Volume 23*, p. 267-400.
- Richards, J.P., Boyce, A.J. and Pringle, M.S., 2001**, Geologic Evolution of the Escondida Area, Northern Chile: A Model for Spatial and Temporal Localization of Porphyry Cu Mineralization: *Economic Geology*, v. 96, p. 271-305.
- Richards, J. P. and Kerrich, R., 1993**, The Porgera gold mine, Papua New Guinea: magmatic hydrothermal to epithermal evolution of an alkalic precious metal deposit: *Economic Geology*, v. 88, p. 1017-1052.
- Robinson, B. W. and Kusakabe, 1975**, Quatitative preparation of sulphur dioxide for 34S/32S analyses, from sulphides by combustion with cuprous oxide: *Analytical Chemistry*, v. 47, p. 1179-1181.
- Roedder, E., 1984**, Fluid Inclusions: *Mineralogical Society of America, Reviews in Mineralogy*, v. 12, 646 p.
- Roedder, E. and Bodnar, R. J., 1980**, Geologic pressure determinations from fluid inclusion studies: *Annual Review of Earth and Planetary Sciences*, v. 8, p. 263-301.
- Rollinson, H., 1993**, Using geochemical data: evaluation, presentation, interpretation, Harlow, Longman, 352 p.
- Roman, D. C. and Cashman, K. V., 2006**, The origin of volcano-tectonic earthquake swarms: *Geological Society of America*, v. 34 (6), p. 457-460.

- Rose, A. W., 1970**, Zonal Relations of Wallrock Alteration and Sulfide Distribution at Porphyry Copper Deposits: *Economic Geology*, v. 65, p 920-936.
- Ross, K. V., Godwin, C. I., Bond, L., and Dawson, K. M., 1995**, Geology, alteration and mineralization of the Ajax East and Ajax West copper-gold alkalic porphyry deposits, southern Iron Mask batholith, Kamloops, British Columbia: *in* Schroeter, T. G., ed., *Porphyry Deposits of the Northwestern Cordillera of North America*. Canadian Institute of Mining, Metallurgy and Petroleum Special Volume 46, Quebec, Canadian Institute of Mining, Metallurgy and Petroleum, p. 565-580.
- Rubin., A. M., 1995**, Propagation of magma-filled cracks: *Annual Reviews Earth Planet. Science*, v. 23, p 287-336.
- Rusk, B. G. and Reed, M. H., 2002**, Scanning electron microscope-cathodoluminescence analysis of quartz reveals complex growth histories in veins from the Butte porphyry copper deposit, Montana: *Geology*, v. 30, p. 727-730.
- Rusk, B. G., Reed, M. H., Dilles, J. H., and Kent, A. J. R., 2006**, Intensity of quartz cathodoluminescence and trace-element content in quartz from the porphyry copper deposit at Butte, Montana: *American Mineralogist*, v. 91, p. 1300-1312.
- Rusk, B.G., Reed, M.H., Krinsley, D., Bignall, G. and Tsuchiya, N., 2005**, Natural and synthetic quartz growth and dissolution revealed by scanning electron microscope cathodoluminescence: *in* M. Nakahara, N. Matubayasi, M. Ueno, K. Yasuoka, and K. Watanabe, eds., *Proceedings of 14th international conference on the properties of water and steam*, p. 296.302.
- Rusk, B.G., Lowers, H. A. and Reed, M.H., 2008**, Trace elements in hydrothermal quartz: Relationships to cathodoluminescent textures and insights into vein formation: *Geology*, v. 36 (7), p. 547-550.
- Rutland, R. W. R., 1976**, Orogenic evolution of Australia: *Earth Science Reviews*, v. 12, p. 161-196.
- Rye, R. O., 1993**, The evolution of magmatic fluids in the epithermal environment: The stable isotope perspective: *Economic Geology*, v. 88, p. 733-753.
- Sander, M. V. and Einaudi, M. T., 1990**, Epithermal deposition of Gold during transition from propylitic to potassic alteration at Round Mountain, Nevada: *Economic Geology*, v. 85, p. 285-311.
- Scheibner, E., 1978**, Tasman fold belt system or orogenic system; introduction: *Tectonophysics*, v. 48, p. 153-157.
- Scheibner, E., 1987**, Paleozoic tectonic development of eastern Australia in relation to the Pacific region: *in* Monger, J. W. H., and Francheteau, J., eds., *Circum-Pacific orogenic belts and evolution of the Pacific Ocean basin.*, *Geodynamics Series 18*, Washington, DC, United States, American Geophysical Union, p. 133-165.
- Scheibner, E., 1993**, Strucutral Framework of New South Wales: *Geological Survey of New Southwales, Quarterly Notes*, v. 93, p. 1-36.

- Scheibner, E., and Basden, H., 1996**, Geology of New South Wales - Synthesis Volume 1: Structural Framework, NSW Geological Survey, 295 p.
- Scheibner, E., and Basden, H., 1998**, Geology of New South Wales - Synthesis Volume 2: Geological Evolution, Sydney, NSW Geological Survey, 666 p.
- Scheibner, E., and Stevens, B. P. J., 1974**, The Lachlan River lineament and its relationship to metallic deposits: Journal and Proceedings of the Royal Society of New South Wales, v. 122, p. 35-74.
- Seedorf, E., 1988**, Cyclic development of hydrothermal mineral assemblages related to multiple intrusions at the Henderson porphyry molybdenum deposit, Colorado: *in* Taylor, R. P., and Strong, D. F., eds., Recent advances in the geology of granite-related mineral deposits, CIM Special Volume 31, p. 367-393.
- Seedorff, E., Dilles, J. H., Proffett, J. M., Einaudi, M. T., Zurcher, L., Stavast, W. J. A., Johnson, D. A. and Barton, M. D., 2005**, Porphyry deposits: Characteristics and origin of hypogene features: Economic Geology 100th Anniversary Volume, p. 251-298.
- Seedorff, E. and Einaudi, M.T., 2004a**, Henderson porphyry molybdenum system, Colorado: I. Sequence and abundance of hydrothermal mineral assemblages, flow paths of evolving fluids, and evolutionary style: Economic Geology and the Bulletin of the Society of Economic Geologists, v. 99, p. 3-37.
- Seedorff, E. and Einaudi, M.T., 2004b**, Henderson porphyry molybdenum system, Colorado, II, Decoupling of introduction and deposition of metals during geochemical evolution of hydrothermal fluids: Economic Geology and the Bulletin of the Society of Economic Geologists, v. 99, p. 39-72.
- Selby, D., and Creaser, R. A., 2001**, Re-Os geochronology and systematics in molybdenite from the Endako porphyry molybdenum deposit, British Columbia, Canada: Economic Geology, v. 96, p. 197-204.
- Selby, D and Creaser, R. A., 2004**, Macroscale NTIMS and microscale LA-MC-ICP-MS Re-Os isotopic analysis of molybdenite: Testing spatial restrictions for reliable Re-Os age determinations, and implications for the decoupling of Re and Os within molybdenite: Geochimica et Cosmochimica Acta, v. 68, p. 3897-3908.
- Serafica, V. S. and Baluda R. P., 1977**, Geology of the Philex Santo Tomas II ore body: *in* Proceedings 5th Symposium on Mineral Resources Development, Baguio City, 1977, Section 1, Paper 3.
- Shannon, J. R., Walker, B. M., Carten, R. B. and Geraghty, E. P., 1982**, Unidirectional solidification textures and their significance in determining relative ages of intrusions at the Henderson Mine, Colorado: Geology, v. 10, p. 293-297.
- Sharp, Z. D., 1990**, Laser-based microanalytical method for the in situ determination of oxygen isotope ratios of silicates and oxides: Geochimica et Cosmochimica Acta, v. 54, p. 1353-1357.
- Shepherd, T. J., Rankin, A. H. Alderton, D. H. M. 1985**. A Practical Guide to Fluid Inclusion Studies: Blackie and Son, London , 240 p.



- Sheppard, M. F. and Gustafson, L. B., 1976**, Oxygen and hydrogen isotopes in the porphyry copper deposit at El Salvador, Chile: *Economic Geology*, v. 71, p. 1549-1559.
- Sheppard, M. F., Nielsen, R. L. and Taylor, H. P., Jr., 1969**, Oxygen and hydrogen isotope ratios of clay minerals from porphyry copper deposits: *Economic Geology*, v. 64, p. 755-777.
- Sheppard, M. F. and Taylor, H. P. Jr., 1974**, Hydrogen and oxygen isotope evidence for the origins of water in the Boulder batholith and Butte ore deposits, Montana: *Economic Geology*, v. 69, p. 926-946.
- Sibson, R.H., 2000**, A brittle failure mode plot defining conditions for high-flux flow: *Economic Geology*, v. 95, p. 41-48.
- Sillitoe, R. H., 1973**, The tops and bottoms of porphyry copper deposits: *Economic Geology*, v. 68, p. 799-815.
- Sillitoe, R. H., 1979**, Some thoughts on gold-rich porphyry copper deposits: *Mineralium Deposita*, v. 14, p. 161-174.
- Sillitoe, R. H., 1993**, Epithermal models: Genetic types, geometrical controls and shallow features: *Geological Association of Canada Special Paper 40*, p 403-417.
- Sillitoe, R. H., 1997**, Characteristics and controls of the largest porphyry copper-gold and epithermal gold deposits in the circum-Pacific region: *Australian Journal of Earth Sciences*, v. 44 (3), p. 373-388.
- Sillitoe, R. H., 2000**, Gold-rich porphyry deposits: descriptive and genetic models and their role in exploration and discovery: *in* Hagemann, S. E., and Brown, P. E., eds., *Gold in 2000, Reviews in Economic Geology* v. 13, Boulder, Society of Economic Geologists, p. 315-345.
- Sillitoe, R. H., 2010**, Porphyry Copper Systems: *Economic Geology*, v. 105, p. 3-41.
- Sillitoe, R.H. and Gappe, I.M., 1984**, Philippine porphyry copper deposits: Geologic setting and characteristics: United Nations Development Program, Coordinating Committee for Geosciences Programmes in East and Southeast Asia, Technical Publication 14, 89 p.
- Simon, G., Kesler, S. E., Essene, E. J. and Chryssoulis, S. L., 2000**, Gold in porphyry copper deposits: experimental determination of gold in the Cu-Fe-S system at 400 to 700 C: *Economic Geology*, v. 95, p. 259-270.
- Stephens, J. R., Mair, J. L., Oliver, N. H. S., Hart, C. J. R. and Baker, T., 2004**, Structural and mechanical controls on intrusion-related deposits of the Tombstone Gold Belt, Yukon, Canada, with comparisons to other vein-hosted ore-deposit types: *Journal of Structural Geology*, v. 26, p. 1025-1041.
- Soesoo, A., Bons, P. D., Gray, D. R. and Foster, D. A., 1997**, Divergent double subduction; tectonic and petrologic consequences: *Geology (Boulder)*, v. 25, p. 755-758.
- Solomon, M., and Groves, D. I., 2000**, The geology and origin of Australia's mineral deposits, Oxford University Press, 1002 p.

- Squire, R. J., 2001**, Volcanological and tectono-magmatic evolution of the Cadia - Neville region, NSW: Unpublished PhD thesis, University of Tasmania, 221 p.
- Squire R. J. and Crawford A. J., 2007**. Magmatic characteristics and geochronology of Ordovician igneous rocks from the Cadia-Neville region, New South Wales: implications for tectonic evolution; Geological evolution and metallogenesis of the Ordovician Macquarie Arc, Lachlan Orogen, New South Wales: *Australian Journal of Earth Sciences*, v. 54, p. 293-314.
- Squire, R. J. and McPhie, J., 2007**, Complex volcanic facies architecture of the Forest Reefs Volcanics near Cadia, New South Wales, associated with prolonged arc-related volcanism: *Australian Journal of Earth Sciences*, v. 54, p. 273-292.
- Squire, R. J., and Miller, J. Mc. L., 2003**, Synchronous compression and extension in East Gondwana: tectonic controls on world-class gold deposits at 440Ma: *Geology*, v. 31, p1073-1076.
- Stanley, C. R., Holbek, P. M., Huyck, H. L. O., Lang, J. R., Preto, V. A. G., Blower, S. J., and Bottaro, J. C., 1995**, Geology of the Copper Mountain alkalic copper-gold porphyry deposits, Princeton, British Columbia: *in* Schroeter, T. G., ed., *Porphyry Deposits of the Northwestern Cordillera of North America*. Canadian Institute of Mining, Metallurgy and Petroleum Special Volume 46, Quebec, Canadian Institute of Mining, Metallurgy and Petroleum, p. 537-564.
- Stein, H. J., Markey, R. J., Morgan, J. W., Delby, D., Creaser, R. A., McCuaig, T. C. and Behn, M., 2001a**, Re-Os Dating of Boddington molybdenite, SW Yilgarn: two Au mineralization events: *AGSO - Geoscience Australia Record*, v. 37, p. 469-471.
- Stein, H. J., Markey, R. J., Morgan, J. W., Hannah, J. L., and Scherstén, A., 2001b**, The remarkable Re-Os chronometer in molybdenite: how and why it works: *Terra Nova*, v. 13, p. 479-486.
- Stein, H. J., Morgan, J. W., Markey, R. J. and Hannah, J. L., 1998**, An introduction to Re-Os: what's in it for the mineral industry: *SEG Newsletter*, 32, p. 18-15.
- Stoker, P., 2005**, Cadia Valley Operations Site Visit Report: Newcrest Mining Limited, 15 p.
- Sun, S. S. and McDonough, W. F., 1989**, Chemical and isotopic systematics of oceanic basalts: implications for mantle composition and processes, *in* Saunders, A. D., and Norry, M. J., eds., *Magmatism in Ocean Basins*, London, Geological Society of London, Special Publication 42, p. 313-345.
- Taylor, H. P., 1997**, Oxygen and hydrogen isotope relationships in hydrothermal mineral deposits: *in* Barnes, H. L., ed., *Geochemistry of Hydrothermal Ore Deposits*, New York, John Wiley and Sons, p. 229-302.
- Taylor, J. M., 1988**, The geology of 'Weemalla' and 'Narambon' near Panuara, central western New South Wales: Unpublished Honours thesis, University of Sydney.

- Taylor, B. E. and Liou, J. G., 1978**, The low-temperature stability of andradite in C-O-H fluids: *American Mineralogist*, v. 63, p. 378-393.
- Tedder, I. J., Holliday, J. and Hayward, S., 2001**, Discovery and evaluation drilling of the Cadia Far East gold-copper deposit: NewGen Gold 2001 - Case Histories of Discovery, Perth, Australian Mineral Foundation, p. 171-184.
- Tedder, I. J., 2002**, Summary and Conclusions of Preliminary Structural Report: Tunbridge Wells, Orange: Newcrest Mining Limited, p. 19.
- Tikoff, B. B. and Teyssier, C., 1994**, Strain modeling of displacement-field partitioning in transpression orogens: *Journal of Structural Geology*, v. 16, p. 1575-1588.
- Thomson, M. L. and Sinclair, A. J., 1990**, Syn-hydrothermal development of fractures in the Silver Queen Mine Area, Owen Lake, Central British Columbia, *Geological Fieldwork*, p. 191-197.
- Titley, S. R., 1981**, Geologic and geotectonic setting of porphyry copper deposits in the southern cordillera: in Dickinson, W. R. and Payne, W. P., eds., *Relations of Tectonics to Ore Deposit in the Southern Cordillera*, Tucson, Arizona Geological Society Digest, v. 14, p. 79-97.
- Titley, S. R., 1982**, The style and progress of mineralization and alteration in porphyry copper systems: in Titley, S. R., ed., *Advances in geology of the porphyry copper deposits, southwestern North America*, Tucson, The University of Arizona Press, p. 93-116.
- Titley, S. R., 1993**, Characteristics of porphyry copper occurrence in the American Southwest: *Geological Association of Canada Special Paper 40*, p. 433-464.
- Titley, S. R. and Heidrick, T. L., 1978**, Intrusion and Fracture Styles of Some Mineralized Porphyry Systems of the Southern Pacific and Their Relationships to Plate Interactions: *Economic Geology*, v. 73, p. 891-903.
- Tobey, E., Schneider, A., Aleria, A., Olcay, L., Perantonis, G., and Quiroga, J., 1998**, Skouries porphyry gold-copper deposit, Chalkidiki, Greece: setting, mineralization and resources: in Porter, T. M., ed., *Porphyry and hydrothermal copper and gold deposits: A global perspective*, Glenside, Australian Mineral Foundation, p. 159-168.
- Tosdal, R. M. and Richards, J. P., 2001**, Magmatic and structural controls on the development of porphyry Cu  $\pm$  Mo  $\pm$  Au deposits: in Tosdal, R. M., and Richards, J. P., eds., *Structural Controls on Ore Genesis: Reviews in Economic Geology 14*, Society of Economic Geologists, p. 157- 181.
- Ulrich, T., Gunther, D. and Heinrich, C. A., 2002**, The evolution of a porphyry Cu-Au deposit, based on LA-ICP-MS analysis of fluid inclusions: Bajo de la Alumbrera, Argentina: *Economic Geology*, v. 97, p. 1889-1920.
- Ulrich, T. and Heinrich, C. A., 2002**, Geology and alteration geochemistry of the porphyry Cu-Au deposit at Bajo de la Alumbrera, Argentina: *Economic Geology*, v. 97, p. 1865-1888.
- Valentine, G. A. and Krogh, K. E.C., 1996**, Structural Control on Basaltic Dike and Sill Emplacement, Paiute Ridge Mafic Intrusion Complex, Southern Nevada: Los Alamos National Laboratory Report, v. LA-13157-MS, 22 p.

- Valentine, G. A. and Krogh, K. E.C., 2006**, Emplacement of shallow dikes and sills beneath a small basaltic volcanic center – The role of pre-existing structure (Paiute Ridge, southern Nevada, USA): *Earth and Planetary Science Letters*, v. 246, p. 217-230.
- Valley J. W., Kitchen, N., Kohn, M. J., Niendorf, C. R. and Spicuzza, M. J., 1995**, UWG-2, a garnet standard for oxygen isotope ratios: Strategies for high precision and accuracy with laser heating: *Geochimica et Cosmochimica Acta* 59: p.5223-5231.
- VandenBerg A. H. M., 1999**. Timing of orogenic events in the Lachlan Orogen: *Australian Journal of Earth Sciences* 46, p. 691-701.
- VandenBerg A. H. M., Willman, C. E., Maher, S., Simons, B. A., Cayley, R. A., Taylor, D. H. Morand, V. J., Moore, D. H. and Rajojvic, A., 2000**, The Tasman Fold Belt System in Victoria: Geological Survey of Victoria Special Publication.
- Van Nort, S. D., Atwood, G. W., Collinson, T. B., Flint, D.C. and Potter, D. R., 1991**, Geology and mineralization of the Grasberg porphyry Cu–Au deposit, Irian Jaya, Indonesia: *Min Eng*, p. 300-303.
- Vigneresse, J. L., 2007**, The role of discontinuous magma inputs in felsic magma and ore generation: *Ore Geology Reviews*, v. 30, p. 181-216.
- Vigneresse, J. L. and Clemens, J. D., 2000**, Granitic magma ascent and emplacement: neither diapirism nor neutral buoyancy: *in* Vendeville B., Mart, Y. and Vigneresse, J. L., eds., *Salt, Shale and Igneous Diapirs in and around Europe*, Geological Society, London, Special Publications 174, p. 1-19.
- Vityk, M. O. and Bodnar, R. J., 1995**, Textural evolution of synthetic fluid inclusions in quartz during reequilibration, with applications to tectonic reconstruction: *Contributions to Mineralogy and Petrology*, v. 121, p. 309-323.
- Walshe, J. L., Heithersay, P. S. and Morrison, G. W., 1995**, Toward an understanding of the metallogeny of the Tasman fold belt system: *Economic Geology*, v. 90, p. 1382-1401.
- Wark, D. A. and Watson, B. E., 2006**, TitaniQ: A titanium in quartz geothermometer: *Contributions to Mineralogy and Petrology*, v. 152, p. 743-754.
- Washburn, M., 2008**, Architecture of the Silurian sedimentary cover sequence in the Cadia porphyry Au-Cu district, NSW, Australia: Implications for post-mineral deformation, MSc thesis, University of British Columbia, 165p.
- Weinberg, R., 2004**, Granite Transport and Emplacement: a Review: *in* The Ishihara Symposium: Granites and Associated Metallogenesis, p. 125-127.
- Wilson, A., Cooke, D., and Thompson, J., 2002**, Alkaline and high-K calc-alkaline porphyry Au- deposits: a summary: *in* Cooke, D. R., and Pongratz, J., eds., *Giant Ore Deposits: Characteristics, Genesis and Exploration*, Hobart, Centre for Ore Deposit Research, University of Tasmania, p. 51-55.
- Wilson, A. J., 2003**, The geology, genesis and exploration context of the Cadia gold–copper porphyry deposits, New South Wales, Australia: Unpublished PhD thesis, University of Tasmania, Hobart, 335 p.

- 
- Wilson, A. J., Cooke, D. R. and Harper, B. L., 2003**, The Ridgeway Gold-Copper Deposit: A High-Grade Alkalic Porphyry Deposit in the Lachlan Fold Belt, New South Wales, Australia. *Economic Geology*, v. 98 (8), p. 1637-1666.
- Wilson, A.J., Cooke D.R., and Richards, T., 2004**, Veins, pegmatites and breccias: Examples from the alkalic Cadia Quarry Au-Cu porphyry deposit, NSW, Australia: University of Tasmania, Centre for Ore Deposit Research Special Publication 5, p. 45-56.
- Wilson, A. J., Cooke, D. R., Harper, B. J. and Deyell, C. L., 2007a**, Sulfur isotopic zonation in the Cadia district, southeastern Australia: exploration significance and implications for the genesis of alkalic porphyry gold-copper deposits: *Mineralium Deposita*, v. 42, p. 465-487.
- Wilson, A. J., Cooke, D. R., Stein, H. J., Fanning, C. M., Holliday, J.R. and Tedder, I. J., 2007b**, U-Pb and Re-Os Geochronologic Evidence for Two Alkalic Porphyry Ore-Forming Events in the Cadia District, New South Wales, Australia: *Economic Geology*, v. 102, p. 3-26.
- Wolfe, R. C., 1994**, The geology, paragenesis and alteration geochemistry of the Endeavour 48 Cu-Au porphyry, Goonumbla, New South Wales: Unpublished Honours thesis, University of Tasmania, 102 p.
- Wolfe, R. C., 2001**, Geology of the Didipio region and paragenesis of the Dinkidi Cu-Au porphyry deposit: Unpublished PhD thesis, University of Tasmania, Hobart, 200 p.
- Wood, D. and Holliday, J., 1995**, Discovery of the Cadia gold-copper deposit in New South Wales - by refocussing the results of previous work: *New Generation Gold Mines - case histories of discovery*, Perth, Australian Mineral Foundation, p. 11.1-11.10.
- Wyborn, D., 1992**, The tectonic significance of Ordovician magmatism in the eastern Lachlan fold belt: *Tectonophysics*, v. 214, p. 177-192.
- Zheng, Y. F., 1993**, Calculation of oxygen isotope fractionation in hydroxyl-bearing silicates: *Earth and Planetary Science Letters*, v. 120, p. 246-263.
- Zheng, Y. F., 1990**, Oxygen isotope fractionation in carbonate and sulfate minerals: *Geochemical Journal*, v. 33, p. 109-126.